

NO-A179 563

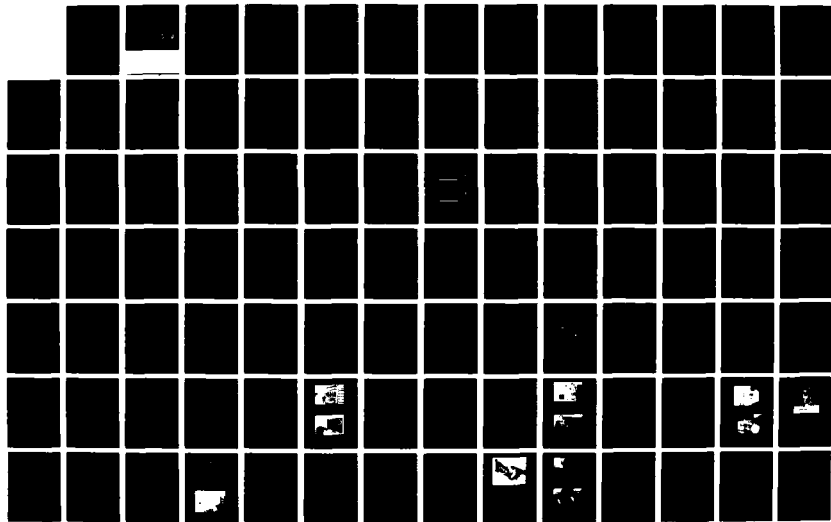
INVESTIGATION OF LOW-AMPLITUDE SHEAR WAVE VELOCITY IN
ANISOTROPIC MATERIAL (U) TEXAS UNIV AT AUSTIN
GEOTECHNICAL ENGINEERING CENTER S H LEE ET AL. AUG 86
AFOSR-TR-87-0483 AFOSR-83-0062

1/4

UNCLASSIFIED

F/G 8/13

NL





PHOTOCOPY RESOLUTION TEST CHART

AD-A179 563

INVESTIGATION OF LOW-AMPLITUDE SHEAR WAVE
VELOCITY IN ANISOTROPIC MATERIAL

DTIC FILE COPY

by

Shannon H.H. Lee and Kenneth H. Stokoe, II

a report on research
sponsored by
United States Air Force
Office of Scientific Research
Bolling Air Force Base

DTIC
S APR 23 1987 D

DISTRIBUTION STATEMENT A
Approved for public release
Distribution Unlimited

UNCLASSIFIED

SECURITY CLASSIFICATION OF THIS PAGE

ADA179563

REPORT DOCUMENTATION PAGE

1a. REPORT SECURITY CLASSIFICATION UNCLASSIFIED			1b. RESTRICTIVE MARKINGS		
2a. SECURITY CLASSIFICATION AUTHORITY			3. DISTRIBUTION/AVAILABILITY OF REPORT Approved for Public Release; Distribution Unlimited.		
2b. DECLASSIFICATION/DOWNGRADING SCHEDULE					
4. PERFORMING ORGANIZATION REPORT NUMBER			5. MONITORING ORGANIZATION REPORT NUMBER(S) AFOSR-TR- 87-0483		
6a. NAME OF PERFORMING ORGANIZATION UNIVERSITY OF TEXAS AT AUSTIN		6b. OFFICE SYMBOL (If applicable)	7a. NAME OF MONITORING ORGANIZATION AFOSR/NA		
6c. ADDRESS (City, State and ZIP Code) DEPARTMENT OF CIVIL ENGINEERING AUSTIN, TX 78712			7b. ADDRESS (City, State and ZIP Code) AFOSR/NA BLDG. 410 Bolling AFB, DC 20332		
8a. NAME OF FUNDING/SPONSORING ORGANIZATION AIR FORCE OFFICE OF SCIENTIFIC RESEARCH		8b. OFFICE SYMBOL (If applicable) AFOSR/NA	9. PROCUREMENT INSTRUMENT IDENTIFICATION NUMBER AFOSR-83-0062		
8c. ADDRESS (City, State and ZIP Code) Bldg 410 BOLLING AFB, DC 20332			10. SOURCE OF FUNDING NOS.		
			PROGRAM ELEMENT NO. 61102F	PROJECT NO. 2307	TASK NO. C1
11. TITLE (Include Security Classification) INVESTIGATION OF LOW-AMPLITUDE SHEAR WAVE VELOCITY IN ANISOTROPIC			WORK UNIT NO.		
12. PERSONAL AUTHOR(S) SHANNON H.H. LEE AND KENNETH H. STOKOE, II					
13a. TYPE OF REPORT FINAL TECHNICAL		13b. TIME COVERED FROM 2/1/83 TO 6/15/86	14. DATE OF REPORT (Yr., Mo., Day) AUGUST, 1986		15. PAGE COUNT 370
16. SUPPLEMENTARY NOTATION					
17. COSATI CODES			18. SUBJECT TERMS (Continue on reverse if necessary and identify by block number)		
FIELD	GROUP	SUB. GR.	BIAXIAL STRESS STATE, BODY WAVES, CONSTRAINED MODULUS, CROSS-ANISOTROPIC MODEL, EXPERIMENTAL TESTING, LINEAR BEHAVIOR, POLARIZED SEISMIC WAVES, PRINCIPAL STRESSES, SAND, (cont.)		
19. ABSTRACT (Continue on reverse if necessary and identify by block number) An understanding of the relationship between low-amplitude shear wave velocity and state of stress is necessary for correctly measuring and properly utilizing seismic shear waves in geotechnical engineering. Theoretically, the mean effective stress has been shown to be the stress state controlling shear wave velocity in an isotropic, homogeneous, elastic medium. Mean effective stress has been assumed to be the stress state controlling anisotropically loaded soil even though several researchers have shown discrepancies with this assumption. Therefore, a 7-ft cubical sample of dry sand was constructed in a large-scale triaxial device. Instrumentation was embedded in the sample during construction so that shear waves could be excited and monitored within the sand while loaded under true triaxial conditions. Extensive seismic tests were conducted under isotropic, biaxial and triaxial confinements in order to compare measured shear wave velocities with previous research and to investigate the influence of anisotropic velocity. (continued on reverse)					
20. DISTRIBUTION/AVAILABILITY OF ABSTRACT UNCLASSIFIED/UNLIMITED <input checked="" type="checkbox"/> SAME AS RPT. <input type="checkbox"/> DTIC USERS <input type="checkbox"/>			21. ABSTRACT SECURITY CLASSIFICATION UNCLASSIFIED		
22a. NAME OF RESPONSIBLE INDIVIDUAL DR. SPENCER T. WU			22b. TELEPHONE NUMBER (Include Area Code) (202) 767-4935	22c. OFFICE SYMBOL AFOSR/NA	

18. (cont.) SEISMIC WAVES, SHEAR MODULUS, SHEAR WAVES, SMALL STRAINS, STRESS HISTORY, STRUCTURAL ANISOTROPY, VELOCITY SURFACE, WAVE SURFACE, WAVE VELOCITY

19. (cont.)

The behavior of shear waves under isotropic loading agrees with the results of previous investigations and indicates the importance of mean effective stress in estimating shear wave velocity. Nonetheless, the shortcomings of the "mean-effective-stress" method are clearly demonstrated in the biaxial and triaxial test series. A "three-individual-stresses" method is shown to be a more correct model for predicting the variation of shear wave velocity under anisotropic stress conditions, as well as being a more sound approach based on stress-strain laws. The "three-individual-stresses" method is based on shear waves which have the directions of particle motion and wave propagation polarized along principal stress directions. Under these conditions, shear wave velocity is controlled about equally by the principal stresses in the directions of particle motion and wave propagation, with the (third) principal stress in the out-of-plane direction having only a minor influence.

Due to structural anisotropy, the sand sample behaves as a cross-anisotropic material under isotropic confinement. When the axis of symmetry of applied stresses coincides with the axes of symmetry for structural anisotropy, the cross-anisotropic model can still be used to represent the sand sample. This model requires five elastic constants which can be measured using compression and shear waves propagating along principal stress and inclined directions. Determination of the five elastic constants is presented, along with the results of measurements of oblique compression wave velocities from a companion study (Lee and Stokoe, 1986). Finally, applications are presented which illustrate use of the results of this study for: in situ measurement of the coefficient of earth pressure at rest, understanding the distinction between measured wave velocities in crosshole and downhole seismic tests, and evaluation of dynamic shear moduli from laboratory tests.

AFOSR-TR- 87-0483

**INVESTIGATION OF LOW-AMPLITUDE SHEAR WAVE VELOCITY
IN ANISOTROPIC MATERIAL**

Approved for public release;
distribution unlimited.

by

Shannon H.H. Lee and Kenneth H. Stokoe, II

a report on research
sponsored by
United States Air Force
Office of Scientific Research
Bolling Air Force Base

AIR FORCE OFFICE OF SCIENTIFIC RESEARCH (AFSC)
NOTICE OF TRANSMITTAL TO DTIC
This technical report has been reviewed and is
approved for public release IAW AFR 190-12.
Distribution unlimited.
MATTHEW J. ROSE
Chief, Technical Information Division



August, 1986

Geotechnical Engineering Report GR86-6
Geotechnical Engineering Center
Civil Engineering Department
The University of Texas at Austin

Accession For	
NTIS	CRARI
DTIC	TAB
Unannounced	<input type="checkbox"/>
Justification	<input type="checkbox"/>
By	
Distribution	
Availability Codes	
Dist	Availability for Special
A-1	

ACKNOWLEDGEMENTS

The authors wish to express their gratitude to the following people for their valuable assistance in this project:

- Drs. Jose M. Roesset, Augusto L. Podio and Ching-Hsie Yew for their advice during this project,
- Mr. Herbert Y.H. Chu, for help in completing some of the tests,
- fellow graduate students in geotechnical engineering for their assistance in the sample construction,
- Mr. Glenn J. Rix, for allowing us to use relevant data obtained during his M.S. research,
- Meei-Ling Lin, Chang-Hu Lin, Jung-Hua Chang, and Ignacio Sanchez-Salinero for their valuable discussions,
- Linda M. Iverson for her assistance in the typing of this report,
- Regina Lin-Ling Chi (wife of the first author) for her encouragement, understanding and typing,
- the staff of the Phil Ferguson Laboratory, Balcones Research Center, especially Mrs. Laurie Goldin,
- the technical staff of the Department of Civil Engineering, especially James Stewart, Marvin Howse and Tom Phillips, and
- The United States Air Force Office of Scientific Research (AFOSR), Bolling Air Force Base, Washington, D.C., for supporting this research under grant AFOSR 83-0062, Major John J. Allen was the initial project manager, after which Lt. Col. Dale Hokanson became the project manager.

ABSTRACT

An understanding of the relationship between low-amplitude shear wave velocity and state of stress is necessary for correctly measuring and properly utilizing seismic shear waves in geotechnical engineering. Theoretically, the mean effective stress has been shown to be the stress state controlling shear wave velocity in an isotropic, homogeneous, particulate medium. Mean effective stress has been assumed to be the stress state controlling anisotropic, particulate material even though several researchers have shown discrepancies with this assumption. Therefore, a 7-ft cubical sample of dry sand was constructed in a large-scale triaxial device. Instrumentation was embedded in the sample during construction so that shear waves could be excited and monitored within the sand while loaded under true triaxial conditions. Extensive seismic tests were conducted under isotropic, biaxial and triaxial confinements in order to compare measured shear wave velocities with previous research and to investigate the influence of anisotropic stress state on velocity.

The behavior of shear waves under isotropic loading agrees with the results of previous investigations and indicates the importance of mean effective stress in estimating shear wave velocity. Nonetheless, the shortcomings of the "mean-effective-stress" method are clearly demonstrated in the biaxial and triaxial test series. A "three-individual-stresses" method is shown to be a more correct model for predicting the variation of shear wave velocity under anisotropic stress conditions, as well as being a more sound approach based on stress-strain laws.

Due to structural anisotropy, the sand sample behaves as a cross-anisotropic material under isotropic confinement. When the axis of symmetry of applied stresses coincides with the axes of symmetry for structural anisotropy, the cross-anisotropic model can still be used to represent the sand sample. This model requires five elastic constants which can be measured using compression and shear waves propagating along principal stress and inclined directions. Determination of the five elastic constants is presented, along with the results of measurements of oblique compression wave velocities from a companion study (Lee and Stokoe, 1986). Finally, applications of this study to: in situ measurement of the coefficient of earth pressure at rest, understanding the distinction between measured wave velocities in crosshole and downhole seismic tests, and evaluation of dynamic shear moduli from laboratory tests are presented.

TABLE OF CONTENTS

	<u>Page</u>
ACKNOWLEDGMENTS.....	iii
ABSTRACT.....	iv
LIST OF FIGURES.....	ix
LIST OF TABLES.....	xix
LIST OF SYMBOLS.....	xxiii
 CHAPTER ONE	
INTRODUCTION.....	1
1.1 Background.....	1
1.2 Organization.....	2
1.3 Objectives.....	3
 CHAPTER TWO	
REVIEW OF LITERATURE.....	5
2.1 Introduction.....	5
2.2 Wave Motion in an Isotropic Full Space.....	5
2.2.1 Shear and Constrained Moduli.....	7
2.2.2 Young's Modulus and Poisson's Ratio.....	8
2.2.3 Previous Theoretical Studies.....	8
2.2.4 Previous Experimental Studies of P-Wave Velocity.....	10
2.2.5 Previous Experimental Studies of S-Wave Velocity.....	14
2.3 Wave Motion in An Anisotropic Full Space.....	16
2.3.1 Theory for Cross-Anisotropic Medium.....	17
2.3.2 Young's Modulus and Poisson's Ratio.....	21
2.3.3 C_{13} and Its Limitation.....	23
2.3.4 Velocity Surface and Wave Surface.....	24
2.3.5 Previous Experimental Studies of P-Wave Velocity.....	26
2.3.6 Previous Studies of S-Wave Velocity.....	28
2.4 Summary.....	38
 CHAPTER THREE	
EXPERIMENTAL EQUIPMENT.....	43
3.1 Experimental Technique Considerations.....	43
3.2 Large-Scale Triaxial Device.....	45
3.2.1 Structure of the Device.....	45
3.2.2 Rainer Used to Place Sand.....	48
3.2.3 Excitation Ports.....	52
3.3 Monitoring and Recording Systems.....	57
3.3.1 Accelerometers.....	57
3.3.2 Charge Amplifiers.....	62
3.3.3 Digital Oscilloscopes.....	62
3.3.4 Stress Cells.....	62
3.3.5 Strain Sensors.....	66
3.4 Sample Construction and Dynamic Testing.....	66
3.5 Determination of Wave Velocity.....	75

	<u>Page</u>
CHAPTER FOUR	
MATERIAL AND TESTING PROCEDURES.....	77
4.1 Introduction.....	77
4.2 Sand Classification.....	77
4.3 Static Shear Strength and Stress-Strain Behavior.....	82
4.4 Dynamic Parameters.....	86
4.5 Predominant Frequency, Strain Amplitude and Wavelength.....	86
CHAPTER FIVE	
ISOTROPIC CONFINEMENT.....	107
5.1 Introduction.....	107
5.2 Effects of Stress State and Stress History.....	108
5.2.1 Continuous Sequence of Loading and Unloading.....	108
5.2.2 Repeated Tests at Similar Pressures.....	113
5.2.3 Effect of Confinement Period at One Pressure.....	113
5.3 Effect of Structural Anisotropy.....	121
5.4 Effect of Isotropic Confinement.....	127
5.5 Summary.....	130
CHAPTER SIX	
BIAXIAL CONFINEMENT.....	131
6.1 Introduction.....	131
6.2 Effect of Stress History.....	131
6.2.1 Continuous Sequence of Loading and Unloading.....	134
6.2.2 Repeated Tests at Similar Pressures.....	137
6.2.3 Confining Period at One Pressure.....	137
6.3 Tests with Direction of Major Principal Stress Remaining Constant....	139
6.3.1 Effect of Principal Stress in Direction of Wave Propagation...	139
6.3.2 Effect of Principal Stress in Direction of Particle Motion...	150
6.3.3 Effect of Principal Stress in Out-of-Plane Direction.....	159
6.4 Tests with Direction of Major Principal Stress Reorienting.....	166
6.4.1 Effect of Principal Stress in Direction of Wave Propagation...	166
6.4.2 Effect of Principal Stress in Direction of Particle Motion...	166
6.4.3 Effect of Principal Stress in Out-of-Plane Direction.....	173
6.4.4 Comparison of Effects of Constant and Reoriented Major Principal Stress Directions.....	173
6.5 Comparison of Shear Wave Velocity Under Isotropic Confinement and Biaxial Confinement.....	178
6.6 Effect of Structural Anisotropy.....	188
6.7 Summary.....	194
CHAPTER SEVEN	
TRIAXIAL CONFINEMENT.....	197
7.1 Introduction.....	197
7.2 Effect of Confining Period at One Pressure.....	197
7.3 Effect of Triaxial Confinement.....	201
7.4 Comparison with Previous Empirical Equations.....	205
7.5 Summary.....	220
CHAPTER EIGHT	
OBLIQUE SHEAR WAVES.....	223
8.1 Introduction.....	223
8.2 Cross-Anisotropic Condition.....	223
8.3 Orthotropic Condition.....	230

	<u>Page</u>
CHAPTER NINE	
CROSS-ANISOTROPIC MODEL AND BODY WAVE PROPAGATION.....	233
9.1 Introduction.....	233
9.2 Constrained Modulus.....	234
9.3 Shear Modulus.....	235
9.4 C_{13} in a Cross-Anisotropic Model.....	238
9.5 Young's Modulus.....	241
9.6 Poisson's Ratio.....	241
9.7 Wave Surfaces in a Cross-Anisotropic Medium.....	241
9.8 Comparison with Isotropic Model for Natural Soil.....	254
9.9 Summary.....	265
CHAPTER TEN	
APPLICATIONS.....	269
10.1 Introduction.....	269
10.2 Estimation of Coefficient of Earth Pressure at Rest.....	269
10.2.1 P-Wave Method.....	269
10.2.2 Shear Wave Method.....	270
10.2.3 K_0 from a Combination of Body Wave Velocities.....	278
10.3 In-Situ Seismic Surveys.....	278
10.4 Resonant Column Tests.....	279
10.4.1 Structural Anisotropy.....	279
10.4.2 Void Ratio.....	282
10.4.3 Variation of Shear Modulus Due to Initial Stress.....	282
10.5 Earthquake Engineering Analysis.....	283
10.6 Summary.....	285
CHAPTER ELEVEN	
SUMMARY, CONCLUSIONS AND RECOMMENDATIONS.....	287
11.1 Summary.....	287
11.2 Conclusions.....	288
11.3 Recommendations.....	291
APPENDIX A	
CALIBRATION CURVES AND READINGS FOR STRESS CELLS.....	293
APPENDIX B	
CALIBRATION CURVES FOR STRAIN SENSORS.....	301
APPENDIX C	
TYPICAL SHEAR WAVEFORMS.....	309
APPENDIX D	
MAGNITUDE OF LINEAR SPECTRUM OF SHEAR WAVEFORMS IN APPENDIX C.....	319
REFERENCES.....	329

LIST OF FIGURES

<u>Figure</u>	<u>Page</u>
2.1	Characteristic Motions of Body Waves.....6
2.2	Variation of P-Wave Velocity with Confining Pressure in a Rod of Dry Granular Particles.....11
2.3	Effect of Confining Pressure on the Compression Wave Velocity in Granular Materials Elastic Half-Space.....12
2.4	Different Sets of Symbols Used in Cartesian Coordinates in this Study.....18
2.5	Elastic Wave Velocities in a Cross-Anisotropic Medium.....19
2.6	Directions of Ray and Wave Normal on the Wave Surface from a Point Source at the Origin in Isotropic and Anisotropic Full Spaces.....25
2.7	Time-Distance Curves of SH, SV, and P Direct Waves Observed at Depth.....27
2.8	Variation in Shear Modulus with Increasing Stress Difference.....31
2.9	Results of Shear Wave Velocity Tests Under Biaxial Confinement...32
2.10	Variation of Shear Wave Velocity with Directions of Wave Propagation and Particle Motion for TB-NS Plane of Motion for Triaxial Confinement with a Constant $\bar{\sigma}_0$34
2.11	Variation of Normalized Small-Amplitude Shear Modulus with Nor- malized Stress Ratio K_{13} Using the "Average-Stress" Method.....36
3.1	Cut-Away, Isometric View of Large-Scale Triaxial Device.....46
3.2	Schematic Diagram of Large-Scale Triaxial Device and Associated Systems.....46
3.3	Side View of Large-Scale Triaxial Device.....47
3.4	Panel Board Used to Pressurize Membranes in Large-Scale Triaxial Device.....47
3.5	Schematic Diagram of Air/Water System Used to Pressurize Membranes.....49
3.6	Top View of New Rainer.....50
3.7	View of New Rainer Loaded with Sand and Ready for Raining Process.....51
3.8	Raining Sand into the LSTD Using New Rainer.....51
3.9	Excitation Port with Clamping Tool.....53
3.10	Completed Excitation Port in Place.....54
3.11	Generation of SV-Wave at North Excitation Port.....54

<u>Figure</u>	<u>Page</u>
3.12	Set-Up for Calibrating Strain Gages on Each Excitation Port.....55
3.13	Calibration Curve for Strain Gages on the Excitation Port along the Z-Direction.....56
3.14	Calibration Curve for Strain Gages on the Excitation Port along the X-Direction.....56
3.15	Schematic View of Instrumentation Locations.....58
3.16	Isometric View of 3-D Accelerometer Package.....59
3.17	Two-Dimensional and Three-Dimensional Accelerometer Blocks.....59
3.18	Accelerometer Block Used to Monitor Oblique Shear Waves.....61
3.19	Accelerometer Being Assembled in Aluminum Accelerometer Block which is Part of NS Excitation Port.....64
3.20	Electric Set-Up Used in Calibrating Endevco Model 2735 Charge Amplifiers.....64
3.21	Stress Cell and Strain Sensors.....65
3.22	Strain Calibration Curve for Strain Sensor SN-1.....67
3.23	Instrumentation at Mid-Depth Plane in the LSTD.....68
3.24	Membranes Hung on Adjacent Vertical Sides of LSTD and Covered with Greased Plastic Sheets.....70
3.25	Raining Device on Top of Elevation Collar that is Bolted to LSTD.....71
3.26	Overhead Crane Used to Fill Rainer with Sand.....71
3.27	Working Platform Hanging from Rainer.....72
3.28	Placement of Accelerometers at Desired Locations and Elevations.....72
3.29	Instruments Being Placed at the Mid-Depth Plane.....73
3.30	Placement of Density Sampler at Designated Elevation and Location.....74
3.31	Data Acquisition System.....74
3.32	Determination of Shear Wave Velocity from a Linear Source-Receivers System.....76
4.1	Grain Size Analysis of Washed Mortar Sand.....78
4.2	Photomicrograph of Washed Mortar Sand.....79
4.3	Stress-Strain Relationship from Consolidated-Drained Triaxial Tests on Washed Mortar Sand.....83

<u>Figure</u>		<u>Page</u>
4.4	Stress-Strain Behavior Along Each Principal Direction Under Isotropic Confinement.....	84
4.5	Variation in Low-Amplitude Shear Modulus with Effective Confining Pressure.....	87
4.6	Variation in Low-Amplitude Material Damping Ratio with Effective Confining Pressure.....	88
4.7	Variation in Shear Modulus with Shearing Strain.....	89
4.8	Variation in Material Damping Ratio with Shearing Strain.....	90
4.9	Variation in Normalized Shear Modulus with Isotropic Confining Pressure.....	91
4.10	Variation in Shear Modulus with Shearing Strain Under Anisotropic Confinement.....	91
4.11	Relationship between Shear Modulus and Isotropic Stress State....	92
4.12	Relationship between Shear Modulus and Anisotropic Stress State..	92
4.13	Relationship between q_c and V_s for Washed Mortar Sand Confined Under Normally Consolidated Conditions.....	93
4.14	Determination of Particle Amplitudes and Predominant Periods from a Typical S-Wave Accelerometer Record.....	94
4.15	Initial Subset of First Series of Biaxial Confinement Tests with Variation of Stress in One Principal Direction (BIA1).....	101
4.16	Second Series of Biaxial Confinement Tests with Variations of Stresses in Two Principal Directions (BIA2).....	102
4.17	Second Subset of First Series of Biaxial Confinement Tests with Variation of Stress in One Principal Direction (BIAR).....	104
4.18	Loading Conditions for Triaxial Confinement Tests.....	105
5.1	Effect of Stress History on Variation of S-Wave Velocities, V_{xy} and V_{yx} , with Isotropic Confining Pressure.....	110
5.2	Effect of Stress History on Variation of S-Wave Velocities, V_{xz} and V_{yz} , with Isotropic Confining Pressure.....	111
5.3	Effect of Stress History on Variation of S-Wave Velocities, V_{zx} and V_{zy} , with Isotropic Confining Pressure.....	112
5.4	Effect of Repeated Loading on Variation of S-Wave Velocities, V_{xy} and V_{yx} , with Isotropic Confinement.....	116
5.5	Effect of Repeated Loading on Variation of S-Wave Velocities, V_{xz} and V_{yz} , with Isotropic Confinement.....	117

<u>Figure</u>	<u>Page</u>
5.6	Effect of Repeated Loading on Variation of S-Wave Velocities, V_{zx} and V_{zy} , with Isotropic Confinement.....118
5.7	Effect of V_s of Confining Period at an Isotropic Pressure of 40 psi.....120
5.8	Effect of Structural Anisotropy on S-Wave Velocities under Isotropic Confinement.....128
6.1	Biaxial Confinement Tests with Direction of Major Principal Stress Remaining Constant.....132
6.2	Biaxial Confinement Tests with Direction of Major Principal Stress Reorienting.....133
6.3	Shear Wave Velocities, V_{xy} , V_{yx} , and V_{zx} Under BIA1Z Loading....135
6.4	Shear Wave Velocities, V_{xy} , V_{yx} , and V_{zx} Under BIA2Z Loading....136
6.5	Effect of Confining Period on S-Wave Velocity Under Biaxial Confinement BIA1.....141
6.6	Effect on V_{xy} and V_{yx} of Varying Only Principal Stress in Direction of Wave Propagation Under Biaxial Loading.....142
6.7	Effect on V_{xz} and V_{yz} of Varying Only Principal Stress in Direction of Wave Propagation Under Biaxial Loading.....143
6.8	Effect on V_{zx} and V_{zy} of Varying Only Principal Stress in Direction of Wave Propagation Under Biaxial Loading.....144
6.9	Effect on V_{xy} and V_{yx} of Principal Stress in Direction of Wave Propagation Under Biaxial Loading When $\bar{\sigma}_a$ and $\bar{\sigma}_c$ are Varied.....146
6.10	Effect on V_{xz} and V_{yz} of Principal Stress in Direction of Wave Propagation Under Biaxial Loading When $\bar{\sigma}_a$ and $\bar{\sigma}_c$ are Varied.....147
6.11	Effect on V_{zx} and V_{zy} of Principal Stress in Direction of Wave Propagation Under Biaxial Loading When $\bar{\sigma}_a$ and $\bar{\sigma}_c$ are Varied.....148
6.12	Effect on V_{xy} and V_{yx} of Varying Only Principal Stress in Direction of Particle Motion Under Biaxial Loading.....151
6.13	Effect on V_{xz} and V_{yz} of Varying Only Principal Stress in Direction of Particle Motion Under Biaxial Loading.....152
6.14	Effect on V_{zx} and V_{zy} of Varying Only Principal Stress in Direction of Particle Motion Under Biaxial Loading.....153
6.15	Effect on V_{xy} and V_{yx} of Principal Stress in Direction of Particle Motion Under Biaxial Loading When $\bar{\sigma}_b$ and $\bar{\sigma}_c$ are Varied....155

<u>Figure</u>		<u>Page</u>
6.16	Effect on V_{xz} and V_{yz} of Principal Stress in Direction of Particle Motion Under Biaxial Loading When $\bar{\sigma}_b$ and $\bar{\sigma}_c$ are Varied....	156
6.17	Effect on V_{zx} and V_{zy} of Principal Stress in Direction of Particle Motion Under Biaxial Loading When $\bar{\sigma}_b$ and $\bar{\sigma}_c$ are Varied....	157
6.18	Effect on V_{xy} and V_{yx} of Principal Stress in Out-of-Plane Direction Under Biaxial Loading.....	160
6.19	Effect on V_{xz} and V_{yz} of Principal Stress in Out-of-Plane Direction Under Biaxial Loading.....	161
6.20	Effect on V_{zx} and V_{zy} of Principal Stress in Out-of-Plane Direction Under Biaxial Loading.....	162
6.21	Effect on V_{xy} and V_{xz} of Varying Only Principal Stress in Direction of Wave Propagation Under Biaxial Loading for BIAR Series.....	167
6.22	Effect on V_{zx} and V_{zy} of Varying Only Principal Stress in Direction of Wave Propagation Under Biaxial Loading for BIAR Series.....	168
6.23	Effect on V_{yx} and V_{xz} of Varying Only Principal Stress in Direction of Particle Motion Under Biaxial Loading for BIAR Series.....	170
6.24	Effect on V_{yz} and V_{zx} of Varying Only Principal Stress in Direction of Particle Motion Under Biaxial Loading for BIAR Series.....	171
6.25	Effect on V_{xy} and V_{yx} of Varying Only Principal Stress in Out-of-Plane Direction Under Biaxial Loading for BIAR Series....	174
6.26	Effect on V_{yz} and V_{zy} of Varying Only Principal Stress in Out-of-Plane Direction Under Biaxial Loading for BIAR Series....	175
6.27	Effect on V_{xy} and V_{yx} of Varying Principal Stress in Both Directions of Wave Propagation and Particle Motion Under Biaxial Loading for BIA2 Series.....	180
6.28	Effect on V_{xz} and V_{yz} of Varying Principal Stress in Both Directions of Wave Propagation and Particle Motion Under Biaxial Loading for BIA2 Series.....	181
6.29	Effect on V_{zx} and V_{zy} of Varying Principal Stress in Both Directions of Wave Propagation and Particle Motion Under Biaxial Loading for BIA2 Series.....	182

<u>Figure</u>		<u>Page</u>
6.30	Regression Analysis of Slopes of Shear Wave Velocity (V_{SI}) for Idealized Cross-Anisotropic Model.....	191
6.31	Regression Analysis of Slopes of Shear Wave Velocity (V_{SA}) for Idealized Cross-Anisotropic Model.....	192
7.1	Mohr-Coulomb and Stress-Space Diagrams for Triaxial Confining Pressure Tests.....	198
7.2	Effect of Confining Period on S-Wave Velocity Under Triaxial Confinement TRI3.....	200
7.3	Variation of S-Wave Velocities Under Triaxial Confinement, TRI1, Based on Eq. 7.1.....	206
7.4	Variation of S-Wave Velocities Under Triaxial Confinement, TRI2, Based on Eq. 7.1.....	207
7.5	Variation of S-Wave Velocities Under Triaxial Confinement, TRI3, Based on Eq. 7.1.....	208
7.6	Shear Wave Velocities Measured During Loading Sequence of ISO, BIA1, BIA2 and TRI2.....	218
7.7	Trend in Shear Wave Velocities Predicted by Different Methods: (a) Three-Individual-Stresses Method, (b) Average-Stress Method, and (c) Mean-Effective-Stress Method.....	219
8.1	Waveforms of Shear Wave V_{zx} , and Oblique Shear Wave V_{SH45} Under Isotropic Confinement with $\bar{\sigma}_0 = 40$ psi.....	224
8.2	Waveforms of Shear Wave V_{zx} and Oblique Shear Wave $V_{SH22.5}$ Under Isotropic Confinement with $\bar{\sigma}_0 = 40$ psi.....	225
8.3	Waveforms of Shear Wave V_{zx} and Oblique Shear Wave V_{SH45} Under Biaxial Confinement BIA1Z with $\bar{\sigma}_x = \bar{\sigma}_y = 15$ psi, and $\bar{\sigma}_z = 40$ psi.....	226
8.4	Waveforms of Shear Wave V_{zx} and Oblique Shear Wave $V_{SH22.5}$ Under Biaxial Confinement BIA1Z with $\bar{\sigma}_x = \bar{\sigma}_y = 15$ psi, and $\bar{\sigma}_z = 40$ psi.....	227
8.5	Velocities of Oblique Shear Waves, V_{SH45} , and $V_{SH22.5}$, Under Isotropic Confining Pressures.....	228
8.6	Velocities of Oblique Shear Waves, V_{SH45} , and $V_{SH22.5}$, Under Biaxial Confinement with Only One Stress in the Z-Direction Varying, BIA1Z.....	229

<u>Figure</u>		<u>Page</u>
8.7	Waveforms of Oblique Shear Waves, V_{SH45} , in the Orthotropic Condition BIA1X with $\bar{\sigma}_x = 40$ psi and $\bar{\sigma}_y = \bar{\sigma}_z = 15$ psi.....	231
8.8	Waveforms of Oblique Shear Waves, $V_{SH22.5}$, in the Orthotropic Condition BIA1X with $\bar{\sigma}_x = 40$ psi and $\bar{\sigma}_y = \bar{\sigma}_z = 15$ psi.....	232
9.1	Distribution of Particle Displacements Associated with Seismic Waves from a Circular Footing on a Homogeneous, Isotropic, Elastic Half-Space.....	245
9.2	Comparison of Velocity Surfaces with Measured S-Wave, P-Wave and Oblique P-Wave Velocities Under Isotropic Confinement with $\bar{\sigma}_0 = 15$ psi.....	246
9.3	Comparison of Wave Surface with Measured S-Wave, P-Wave and Oblique P-Wave Velocities Under Isotropic Confinement with $\bar{\sigma}_0 = 15$ psi.....	247
9.4	Comparison of Velocity Surfaces with Measured S-Wave, P-Wave and Upper Limit of C_{13} Under Isotropic Confinement with $\bar{\sigma}_0 = 15$ psi.....	248
9.5	Comparison of Velocity Surfaces with Measured S-Wave, P-Wave and 1/7 of Upper Limit of C_{13} Under Isotropic Confinement with $\bar{\sigma}_0 = 15$ psi.....	249
9.6	Comparison of Velocity Surfaces with Measured S-Wave, P-Wave and 1/16 of Upper Limit of C_{13} Under Isotropic Confinement with $\bar{\sigma}_0 = 15$ psi.....	250
9.7	Comparison of Wave Surfaces with Measured S-Wave, P-Wave and Upper Limit of C_{13} Under Isotropic Confinement with $\bar{\sigma}_0 = 15$ psi.....	251
9.8	Comparison of Wave Surfaces with Measured S-Wave, P-Wave and 1/7 of Upper Limit of C_{13} Under Isotropic Confinement with $\bar{\sigma}_0 = 15$ psi.....	252
9.9	Comparison of Wave Surfaces with Measured S-Wave, P-Wave and 1/16 of Upper Limit of C_{13} Under Isotropic Confinement with $\bar{\sigma}_0 = 15$ psi.....	253
9.10	Comparison of Velocity Surfaces with Measured S-Wave, P-Wave, and Oblique P-Wave Velocities Under Isotropic Confinement with $\bar{\sigma}_0 = 30$ psi.....	255

<u>Figure</u>		<u>Page</u>
9.11	Comparison of Wave Surfaces with Measured S-Wave, P-Wave, and Oblique P-Wave Velocities Under Isotropic Confinement with $\bar{\sigma}_0 = 30$ psi.....	256
9.12	Comparison of Velocity Surfaces with Measured S-Wave, P-Wave, and Oblique P-Wave Velocities Under Biaxial Confinement BIA1Z with $\bar{\sigma}_z = 20$ psi.....	257
9.13	Comparison of Velocity Surfaces with Measured S-Wave, P-Wave, and Oblique P-Wave Velocities Under Biaxial Confinement BIA1Z with $\bar{\sigma}_z = 30$ psi.....	258
9.14	Comparison of Wave Surfaces with Measured S-Wave, P-Wave, and Oblique P-Wave Velocities Under Biaxial Confinement BIA1Z with $\bar{\sigma}_z = 20$ psi.....	259
9.15	Comparison of Wave Surfaces with Measured S-Wave, P-Wave, and Oblique P-Wave Velocities Under Biaxial Confinement BIA1Z with $\bar{\sigma}_z = 30$ psi.....	260
9.16	Comparison of Velocity Surfaces with Measured S-Wave, P-Wave, and Oblique P-Wave Velocities Under Biaxial Confinement BIA2Z with $\bar{\sigma}_x = \bar{\sigma}_y = 20$ psi.....	261
9.17	Comparison of Velocity Surfaces with Measured S-Wave, P-Wave, and Oblique P-Wave Velocities Under Biaxial Confinement BIA2Z with $\bar{\sigma}_x = \bar{\sigma}_y$	262
9.18	Comparison of Wave Surfaces with Measured S-Wave, P-Wave, and Oblique P-Wave Velocities Under Biaxial Confinement BIA2Z with $\bar{\sigma}_x = \bar{\sigma}_y = 20$ psi.....	263
9.19	Comparison of Wave Surfaces with Measured S-Wave, P-Wave, and Oblique P-Wave Velocities Under Biaxial Confinement BIA2Z with $\bar{\sigma}_x = \bar{\sigma}_y = 25$ psi.....	264
10.1	Ratio of SH- to SV-Wave Velocities at a Soft Clay Site.....	276
10.2	Comparison of Low-Amplitude Shear Moduli of Dry Sand Determined from Relationships Developed with Different Testing Devices.....	277
10.3	Variations of Maximum Shear Modulus Under Constant Mean Effective Stress with Initial Stress.....	284

FigurePage

A.1	Calibration Curve for Stress Cell SS-1.....	294
A.2	Calibration Curve for Stress Cell SS-2.....	295
A.3	Calibration Curve for Stress Cell SS-3.....	296
A.4	Comparison of Principal Stress Measured by Stress Cell SS-1 with Applied Stress in the Triaxial Device.....	297
A.5	Comparison of Principal Stress Measured by Stress Cell SS-2 with Applied Stress in the Triaxial Device.....	298
A.6	Comparison of Principal Stress Measured by Stress Cell SS-3 with Applied Stress in the Triaxial Device.....	299
B.1	Strain Calibration for Strain Sensor SN-2.....	302
B.2	Strain Calibration for Strain Sensor SN-3.....	303
B.3	Strain Calibration for Strain Sensor SN-4.....	304
B.4	Strain Calibration for Strain Sensor SN-5.....	305
B.5	Strain Calibration for Strain Sensor SN-6.....	306
B.6	Strain Calibration for Strain Sensor SN-7.....	307
B.7	Strain Calibration for Strain Sensor SN-8.....	308
C.1	Typical Shear Waveforms from which V_{xy} was Determined at $\bar{\sigma}_0 = 40$ psi under Isotropic Confinement.....	310
C.2	Typical Shear Waveforms from which V_{yx} was Determined at $\bar{\sigma}_0 = 40$ psi under Isotropic Confinement.....	311
C.3	Typical Shear Waveforms from which V_{xz} was Determined at $\bar{\sigma}_0 = 40$ psi under Isotropic Confinement.....	312
C.4	Typical Shear Waveforms from which V_{yz} was Determined at $\bar{\sigma}_0 = 40$ psi under Isotropic Confinement.....	313
C.5	Typical Shear Waveforms from which V_{zx} was Determined at $\bar{\sigma}_0 = 40$ psi under Isotropic Confinement.....	314
C.6	Typical Shear Waveforms from which V_{zy} was Determined at $\bar{\sigma}_0 = 40$ psi under Isotropic Confinement.....	315
C.7	Typical Shear Waveforms from which V_{45} was Determined at $\bar{\sigma}_0 = 40$ psi under Isotropic Confinement.....	316
C.8	Typical Shear Waveforms from which $V_{22.5}$ was Determined at $\bar{\sigma}_0 = 40$ psi under Isotropic Confinement.....	317
D.1	Magnitude of Linear Spectrum of Waveform of V_{xy} in Fig. C.1.....	320
D.2	Magnitude of Linear Spectrum of Waveform of V_{yx} in Fig. C.2.....	321
D.3	Magnitude of Linear Spectrum of Waveform of V_{xz} in Fig. C.3.....	322
D.4	Magnitude of Linear Spectrum of Waveform of V_{yz} in Fig. C.4.....	323

FigurePage

D.5	Magnitude of Linear Spectrum of Waveform of V_{zx} in Fig. C.5.....	324
D.6	Magnitude of Linear Spectrum of Waveform of V_{zy} in Fig. C.6.....	325
D.7	Magnitude of Linear Spectrum of Waveform of V_{45} in Fig. C.7.....	326
D.8	Magnitude of Linear Spectrum of Waveform of $V_{22.5}$ in Fig. C.8...	327

LIST OF TABLES

<u>Table</u>	<u>Page</u>
2.1 Summary of Values of the Slope of the $\log V_p - \log \bar{\sigma}_0$ Relationship in Dry Sand Under Isotropic Confinement.....	13
2.2 Summary of Values of the Slope of the $\log V_s - \log \bar{\sigma}_0$ Relationship in Dry Sand Under Isotropic Confinement.....	15
2.3 Summary of Values of the Slope of the P-Wave Velocity-Confining Pressure Relationships for Dry Sand Under Anisotropic Confinement.....	29
2.4 Summary of Values of the Slope of the S-Wave Velocity-Confining Pressure Relationships for Dry Sand Under Anisotropic Confinement.....	39
3.1 Distances Between Accelerometers Inside the Triaxial Device.....	63
4.1 Summary of Soil Characteristics and Properties of Washed Mortar Sand.....	80
4.2 Densities and Void Ratios of Sand at Various Elevations in the Large-Scale Triaxial Device.....	81
4.3 Ratios of Calibrated Readings of Stress Cells to Applied Confining Pressures.....	85
4.4 Loading Pressure Sequences.....	98
5.1 Shear Wave Velocities Measured During First Continuous Loading Sequence Under Isotropic Confinement.....	109
5.2 Shear Wave Velocities Measured During First Continuous Unloading Sequence Under Isotropic Confinement.....	109
5.3 Shear Wave Velocities Measured from Repeated Tests under Isotropic Confinement.....	114
5.4 Average Value of Shear Wave Velocities from All Tests under Isotropic Confining Pressures.....	115
5.5 Shear Wave Velocities at Different Times under an Isotropic Pressure of 40 psi.....	119
5.6 Comparison of Shear Wave Velocities on First Loading, First Unloading and Complete Set of Tests under Isotropic on Confinement.....	122

<u>Table</u>	<u>Page</u>
5.7 Comparison of Shear Wave Velocities, V_{xy} and V_{yx} , in the Isotropic Plane Measured under Isotropic Confinement.....	124
5.8 Comparison of Shear Wave Velocities, V_{xz} , V_{yz} , V_{zx} and V_{zy} , in Anisotropic Planes Measured under Isotropic Confinement.....	125
5.9 Results of Linear Regression Analysis of V_s Values Used in Representing Cubical Sample as a Cross-Anisotropic Model.....	126
5.10 Regression Analysis of Shear Wave Velocities from Complete Set of Tests Under Isotropic Confinement.....	129
6.1 Effect of Repeated Tests on Shear Wave Velocity Under Biaxial Confinement.....	138
6.2 Effect of Confining Period at One Biaxial Stress State.....	140
6.3 Effect on V_s of Varying Only Principal Stress in Direction of Wave Propagation Under Biaxial Confinement.....	145
6.4 Effect on V_s of Principal Stress in Direction of Wave Propagation Under Biaxial Confinement When $\bar{\sigma}_a$ and $\bar{\sigma}_c$ Varied.....	149
6.5 Effect on V_s of Varying Only Principal Stress in Direction of Particle Motion Under Biaxial Loading.....	154
6.6 Effect on V_s of Principal Stress in Direction of Particle Motion Under Biaxial Loading When $\bar{\sigma}_b$ and $\bar{\sigma}_c$ Varied.....	158
6.7 Effect on V_s of Varying Principal Stress in Out-of-Plane Direction Under Biaxial Loading.....	163
6.8 Effect on V_s of Principal Stress in Out-of-Plane Direction Under Biaxial Confinement Calculated from Eqs. 6.4 and 6.5.....	165
6.9 Effect on V_s of Varying Only Principal Stress in Direction of Wave Propagation Under Biaxial Loading for BIAR Series.....	169
6.10 Effect on V_s of Varying Only Principal Stress in Direction of Particle Motion Under Biaxial Loading for BIAR Series.....	172
6.11 Effect on V_s of Varying Only Principal Stress in Out-of-Plane Direction Under Biaxial Loading for BIAR Series.....	176
6.12 Comparison of Slopes, Constants and S-Wave Velocities Between the State of Constant Principal Stress Directions and the State of Reorientation of Principal Stress Directions Under Biaxial Confinement.....	177

<u>Table</u>	<u>Page</u>
6.13 Effect of Variation of Principal Stresses in Both Directions of Wave Propagation and Particle Motion on S-Wave Velocity Under Biaxial Confinement.....	183
6.14 Values of Constants and Slopes of Eq. 2.52 for Each Type of Shear Wave Velocity Under Biaxial Confinement.....	185
6.15 Ratio of Shear Wave Velocity Predicted by Eq. 2.52 with Constants and Slopes Listed in Table 6.14 to the Test Results of BIA1 and BIA2.....	186
6.16 Ratio of Shear Wave Velocities Measured in BIA1 to BIA2.....	187
6.17 Ratio of Shear Wave Velocity Predicted by Eq. 2.52 with Constant and Slopes of BIA1 to BIA2 Under Same Biaxial Confining Pressures.....	189
6.18 Results of Regression Analysis of the Sand Sample Based on an Idealized Cross-Anisotropic Model and BIA1 Test Series.....	190
6.19 Ratio of Shear Wave Velocity Predicted by Idealized Cross-Anisotropic Model to the Best-Fit Value Predicted by Table 6.14.....	195
7.1 Effect of Confining Period on S-Wave Velocities Under Triaxial Confinement, TRI3.....	199
7.2 Comparison of Measured Shear Wave Velocities to Values Predicted by "Three-Individual-Stresses" Method in Test Series TRI1.....	202
7.3 Comparison of Measured Shear Wave Velocities to Values Predicted by "Three-Individual-Stresses" Method in the Test Series of TRI2.....	203
7.4 Comparison of Measured Shear Wave Velocities to Values Predicted by "Three-Individual-Stresses" Method in the Test Series of TRI3.....	204
7.5 Loading Sequence and Shear Wave Velocities Measured Under TRI2.....	210
7.6 Loading Sequence and Shear Wave Velocities Measured Under TRI3.....	210
7.7 Test Results of Shear Wave Velocities Measured Under Triaxial Confinement, TRI2.....	211

<u>Table</u>	<u>Page</u>
7.8 Comparison of Shear Wave Velocities Predicted by Eqs. 7.3, 7.4 and 7.5 Under Isotropic Confinement.....	213
7.9 Shear Wave Velocities Predicted by Eqs. 7.3, 7.4, and 7.5 Under Biaxial Confining Pressure Conditions of BIA1.....	214
7.10 Shear Wave Velocities Predicted by Eqs. 7.3, 7.4, and 7.5 Under Biaxial Confining Pressure Conditions of BIA2.....	215
7.11 Shear Wave Velocities Predicted by Eqs. 7.3, 7.4, and 7.5 Under Triaxial Confining Pressure Conditions (TRI1).....	216
7.12 Comparison of Constants and Slopes for Eq. 2.52 Relating V_s to $\bar{\sigma}_a$, $\bar{\sigma}_b$, and $\bar{\sigma}_c$ with Those Reported by Knox et al (1982).....	221
9.1 Constants and Slopes of the $\log M - \log \bar{\sigma}_a$ Relationship for This Sand Sample.....	236
9.2 Constants and Slopes of the $\log G - \log \bar{\sigma}$ Relationship for This Sand Sample.....	239
9.3 Comparison of Values of C_{13} for the Sand Sample from Theoretical Limits, Measured Results, and Values Suggested by Drnevich (1974).....	240
9.4 Limits and Measured Values of Young's Moduli for a Cross-Anisotropic Material.....	242
9.5 Limits and Measured Values of Poisson's Ratio for a Cross-Anisotropic Material.....	243
9.6 Comparison of Young's Modulus Estimated by Cross-Anisotropic and Isotropic Models.....	266
9.7 Comparison of Poisson's Ratio Estimated by Cross-Anisotropic and Isotropic Models.....	267
10.1 Comparison Between Applied and Calculated Coefficient of Earth Pressure at Rest, K_0 , from Compression Wave Velocity, V_{xx}	271
10.2 Comparison Between Applied and Calculated Coefficient of Earth Pressure at Rest, K_0 , from Shear Wave Velocity, V_{xz} and V_{yz}	273
10.3 Comparison Between Applied and Calculated Coefficient of Earth Pressure at Rest, K_0 , from Shear Wave Velocity, V_{zx} and V_{zy}	277

LIST OF SYMBOLS

A_1	= amplitude of accelerometer record
A_2	= double amplitude of accelerometer record
b	= stress level, defined as $(\bar{\sigma}_1 - \bar{\sigma}_3)/(\bar{\sigma}_1 - \bar{\sigma}_3)_f$
C	= constant
c	= dimensionless constant for G_{\max}
C_1	= constant for V_p
C_2	= constant for V_s
C_4	= constant of C_{44} , defined as $\rho(C_{xz})^2$
C_6	= constant of C_{66} , defined as $\rho(C_{xy})^2$
C_{11}	= one of five independent constants for cross-anisotropic model
C_{12}	= additional constant for cross-anisotropic model
C_{13}	= one of five independent constants for cross-anisotropic model
C_{33}	= one of five independent constants for cross-anisotropic model
C_{44}	= one of five independent constants for cross-anisotropic model
C_{66}	= one of five independent constants for cross-anisotropic model
C_G	= constant of the $\log G - \log \bar{\sigma}$ relationship, which equals $\rho \cdot (C_S)^2$
C_M	= constant, which equals $\rho \cdot (C_p)^2$, for $\log M - \log \bar{\sigma}_a$
C_{xz}	= constant of V_{xz}
C_{xy}	= constant of V_{xy}
d	= distance
dia	= diameter
D	= depth
e	= void ratio
E	= Young's modulus
E_{11}	= Young's modulus along the 1- or X-axis
E_{33}	= Young's modulus along the 3- or Z-axis
E_A	= Young's modulus for anisotropic plane
E_a'	= pseudo-Young's modulus, defined as $2G(1+\nu_A')$
E_I	= Young's modulus for isotropic plane
E_I'	= pseudo-Young's modulus, defined as $2G(1+\nu_I')$
E_{Sp}	= Young's Modulus of spherical particles
EW	= east-west direction in large-scale triaxial device
F	= gage factor
f	= wave frequency
g	= acceleration of gravity
G	= shear modulus

G_{\max}	= low-amplitude shear modulus
G_{OH}	= maximum shear modulus determined from resonant column tests with hollow samples
G_{OS}	= maximum shear modulus determined from resonant column tests with solid samples
G_s	= specific gravity of solid particles
G_{Sp}	= shear modulus of spherical particles
k	= factor based on plasticity index
K_o	= coefficient of earth pressure at rest
K_{13}	= principal stress ratio, defined as $\bar{\sigma}_1/\bar{\sigma}_3$
K_{23}	= principal stress ratio, defined as $\bar{\sigma}_2/\bar{\sigma}_3$
mm	= slope of $\log V_p - \log \bar{\sigma}_o$ relationship
ma	= slope of $\log V_p - \log \bar{\sigma}_a$ relationship
max	= maximum value
M	= constrained modulus
Mm	= slope of the $\log M - \log \bar{\sigma}_o$ relationship and equals $2mm$
n	= porosity
ne	= slope of $\log V_s - \log (\bar{\sigma}_a \cdot \bar{\sigma}_b)$, defined as $ne = na = nb$ with $nc = 0$
na	= slope of $\log V_s - \log \bar{\sigma}_a$ relationship
nb	= slope of $\log V_s - \log \bar{\sigma}_b$ relationship
nc	= slope of $\log V_s - \log \bar{\sigma}_c$ relationship
nt	= slope of $\log V_s - \log [(\bar{\sigma}_a + \bar{\sigma}_b)/2]$ relationship
nl	= slope of $\log V_s - \log t$ relationship
Na	= slope of $\log G - \log \bar{\sigma}_a$ relationship and equals $2na$
Nb	= slope of $\log G - \log \bar{\sigma}_b$ relationship and equals $2nb$
Nc	= slope of $\log G - \log \bar{\sigma}_c$ relationship and equals $2nc$
Nm	= slope of $\log G - \log \bar{\sigma}_o$ relationship and equals $2nm$
Ne	= slope of $\log G - \log (\bar{\sigma}_a \cdot \bar{\sigma}_b)$ relationship and equals $2ne$
NS	= north-south direction in large-scale triaxial device
OCR	= overconsolidation ratio
P	= compression wave (P-wave)
Pa	= atmospheric pressure
ΔR	= change in resistance in ohms
R	= gage resistance in ohms
S	= shear wave (S-wave)
t	= confinement time at one pressure
t	= wave travel time

T	= wave period
TB	= top-bottom direction in large-scale triaxial device
V	= wave velocity
V_C	= compression wave velocity in a bar
V_P	= compression wave velocity of a low-amplitude wave
V_{PA}	= velocity of P-wave in the anisotropic plane
V_{PI}	= velocity of P-wave in the isotropic plane
$V_{P,\theta}$	= oblique P-wave velocity
V_S	= shear wave velocity of a low-amplitude wave
V_{S1}	= V_S in BIA1 series
V_{S2}	= V_S in BIA2 series
V_{SA}	= velocity of S-wave in the anisotropic plane
V_{SI}	= velocity of S-wave in the isotropic plane
V_{SH}	= SH-wave velocity
$V_{SH,\theta}$	= oblique SH-wave velocity
$V_{SH\bar{\theta}}$	= oblique SH-wave velocity with particle motion at an angle $\bar{\theta}$ to the principal stress direction
$V_{SV,\theta}$	= oblique SV-wave velocity
V_{xx}	= velocity of P-wave along x-axis
V_{yy}	= velocity of P-wave along y-axis
V_{zz}	= velocity of P-wave along z-axis
V_{xy}	= velocity of S-wave in xy-plane
V_{xz}	= velocity of S-wave in xz-plane
V_{yx}	= velocity of S-wave in yx-plane
V_{yz}	= velocity of S-wave in yz-plane
V_{zx}	= velocity of S-wave in zx-plane
V_{zy}	= velocity of S-wave in zy-plane
\bar{z}	= peak particle amplitude
$\dot{\bar{z}}$	= peak particle velocity
$\ddot{\bar{z}}$	= peak particle acceleration
γ	= shearing strain
γ_d	= dry unit weight of sand
γ_{xy}	= shearing strain in xy-plane
γ_{yz}	= shearing strain in yz-plane
γ_{zx}	= shearing strain in zx-plane
γ_w	= unit weight of water
ϵ	= strain in microstrains (10^{-6} cm/cm)

- ϵ = axial strain
- ϵ_x = axial strain in x-axis
- ϵ_y = axial strain in y-axis
- ϵ_z = axial strain in z-axis
- θ = angle between the direction of wave propagation and the axis of symmetry
- Λ = Lamé's constant
- λ = wavelength
- ν = Poisson's ratio
- ν_{12} = Poisson's ratio for 1- and 2-axes when normal stress is applied in 2-axis
- ν_{13} = Poisson's ratio for 1- and 3-axes when normal stress is applied in 3-axis
- ν_{31} = Poisson's ratio for 3- and 1-axes when normal stress is applied in 1-axis.
- ν_A' = pseudo-Poisson's ratio for anisotropic plane
- ν_I' = pseudo-Poisson's ratio for isotropic plane
- ν_{sp} = Poisson's ratio of spherical particles
- ρ = mass density = γ/g
- ρ_{sp} = mass density of spherical particles
- $\bar{\sigma}_a$ = axial stress in a resonant column sample
- $\bar{\sigma}_a$ = effective principal stress in direction of wave propagation
- $\bar{\sigma}_b$ = effective principal stress in direction of particle motion
- $\bar{\sigma}_c$ = effective principal stress in out-of-plane direction (direction perpendicular to $\bar{\sigma}_a$ and $\bar{\sigma}_b$ directions)
- $\bar{\sigma}_N$ = effective stress in the plane perpendicular to the direction of P-wave propagation
- $\bar{\sigma}_r$ = radial stress in a resonant column sample
- $\bar{\sigma}_x$ = effective principal stress along the x-axis or north-south direction
- $\bar{\sigma}_y$ = effective principal stress along the y-axis or east-west direction
- $\bar{\sigma}_z$ = effective principal stress along the z-axis or vertical (top-bottom) direction
- $\bar{\sigma}_0$ = mean effective principal stress
- $\bar{\sigma}_1$ = major principal effective stress
- $\bar{\sigma}_2$ = intermediate principal effective stress
- $\bar{\sigma}_3$ = minor principal effective stress
- τ_0 = initial shearing stress

- τ_{xy} = shearing stress in xy-plane
- τ_{yz} = shearing stress in yz-plane
- τ_{zx} = shearing stress in zx-plane
- $\bar{\phi}$ = effective angle of internal friction
- $\bar{\theta}$ = angle between the direction of particle motion and the principal stress direction

CHAPTER ONE

INTRODUCTION

1.1 BACKGROUND

Seismic shear wave velocities are often used to estimate small-strain shear moduli in the laboratory and in the field. These shear moduli can then be used to evaluate directly soil-structure interaction problems such as machine foundations or they can be used as reference levels for large-strain problems such as earthquake shaking and blast loading. An understanding of the relationship between shear wave velocity and state of stress is necessary for correctly measuring and properly utilizing shear moduli in such problems. Knowledge of the effects of stress level, overconsolidation ratio, period of confinement and ratio of major-to-minor principal stresses on shear wave velocity is important.

In most geotechnical engineering studies involving measurement of dynamic soil properties, the soil is assumed to be isotropic and the isotropic (or equivalent isotropic) state of stress is assumed to control. Therefore, measurement of one shear wave velocity and one compression wave velocity is assumed sufficient to characterize the material. Poisson's ratio is estimated once these wave velocities are measured. Laboratory tests such as the traditional resonant column, cyclic triaxial and cyclic simple shear tests are conducted under this supposition. Data reduction in geophysical surveys such as from reflection, refraction, crosshole, and downhole surveys are almost always treated with the same hypothesis.

However, natural soils exhibit more complicated characteristics than that assumed for an isotropic material because of structural and/or stress-induced anisotropy. The behavior of compression and shear waves in an anisotropic material can be quite different from that in an isotropic material. Additionally, more sophisticated constitutive models have to be employed to fit measured behavior. Fortunately, many natural soils seem to be reasonably well approximated by a cross-anisotropic model which can be handled quite economically in both analytical and experimental work.

To study the effects of state of stress and anisotropy on seismic measurements, crosshole and downhole tests were emulated in a large-scale triaxial device in the laboratory. Compression (P) and shear (S) wave velocities of a sand specimen were measured along principal stress directions

under isotropic and anisotropic conditions. These measurements permit calculation of four of the five elastic constants needed in a cross-anisotropic model. The fifth elastic constant necessary in this model was also measured with inclined P-waves. The measurements of P-wave velocities are presented by Chu et al (1984) and Lee and Stokoe (1986). This study concentrates on investigating the behavior of the S-waves.

One important characteristic of seismic waves when employed for in situ testing is that the waves sample a large zone of undisturbed soil as compared to other field measurements and almost all laboratory measurements. Therefore, the results of wave velocities measured in situ reflect the gross properties of the zone through which they propagate. However, the understanding presented herein is necessary if these seismic waves are to be used and analyzed properly.

1.2 ORGANIZATION

This study attempts to form a bridge between measurements of low-amplitude body wave velocities in engineering practice and velocities predicted from analytical studies. Basic principles of seismic waves in elastic media are presented in Chapter Two. The propagation of elastic body waves in anisotropic material are emphasized. The design of the true triaxial device and the construction of the sand sample in the device are detailed in Chapter Three. The testing program of the states of stress at which wave propagation tests were conducted are presented in Chapter Four along with a discussion of the engineering properties of the sand.

The effect of isotropic confinement on shear wave velocity for shear waves propagated along principal stress directions is presented in Chapter Five. Propagation velocities of shear waves along principal directions under biaxial confinement are presented in Chapter Six. The effects of triaxial confining pressures on shear wave velocity is discussed in Chapter Seven. Finally, shear waves propagated along the top-bottom principal axis in the triaxial device, which is in the direction of the force of gravity, with particle motions not in another principal direction were treated as oblique shear waves in this study. The behavior of oblique shear waves is briefly presented in Chapter Eight.

A cross-anisotropic model is examined in Chapter Nine and is shown to be the best model for the sand tested. Determination of the five elastic

constants necessary in this model as well as Young's moduli and Poisson's ratios are discussed. Chapter Nine also includes a discussion of the three wave fronts of body wave surfaces that exist in a cross-anisotropic material; two shear wave surfaces and one compression wave surface, as compared with only two wave fronts in an isotropic medium.

Applications of this study are presented in Chapter Ten to illustrate the use of seismic waves for measurement of the coefficient of earth pressure at rest (K_0) in situ, understanding the distinction between measured velocities in the crosshole and downhole seismic tests, and estimation of elastic stiffnesses for use in earthquake engineering analyses. An improved understanding of the elastic shear modulus measured with resonant column tests on natural soil is also discussed.

Finally, a brief summary and conclusions along with recommendations for future work are presented in Chapter Eleven.

1.3 OBJECTIVES

One objective of this study is to define the relationship between low-amplitude shear wave velocities and effective principal stresses. In the last two decades, mean effective confining stress has been used as the key stress component influencing shear wave velocity over a wide variation in strains ranging from very small strains (less than 0.001%) to quite large strains (more than 10%). This stress component may be adequate at large strains, but it is still questionable at small strains. One reason for questioning its use is that only a few tests of S-wave velocity under biaxial and triaxial confinements have been performed. A large number of shear wave velocity measurements under biaxial and triaxial states of stress were successfully performed as discussed in Chapters Six and Seven.

Another objective is to evaluate material models used to characterize natural soil deposits. According to structural and stress-induced anisotropy uncovered in this research, a cross-anisotropic model as well as measurement of the five associated constants are recommended in Chapter Nine. Moreover, the spread-out wave fronts of body waves in natural deposits of soil, which are more correctly modeled as cross-anisotropic materials rather than isotropic materials, were detected and presented herein.

Finally, the third objective of this study is to illustrate some areas where this research can be applied. When properly applied and interpreted,

seismic wave velocities can be used to estimate in situ anisotropy and state of stress. In addition, these field measurements can form a critical link in translating laboratory measurements to field behavior. Several of these points are discussed in Chapter Ten.

CHAPTER TWO

REVIEW OF LITERATURE

2.1 INTRODUCTION

For the past two decades, mean effective confining pressure, $\bar{\sigma}_0$, has been considered to be the major factor affecting the low-amplitude shear wave velocity of sand. (For the purposes of this research, low-amplitude strains are considered to be shearing strains which do not exceed about 0.001 percent.) The effects of structural anisotropy and stress-induced anisotropy were generally ignored. The aim of this research is to study shear wave velocities in the soil skeleton under anisotropic loadings. With the companion research on compression wave velocities (Lee and Stokoe, 1986), a cross-anisotropic model for level soil deposits is investigated as well. Theoretical models and past research related to the scope of this study for both compression and shear waves are presented in the following sections.

2.2 WAVE MOTION IN AN ISOTROPIC FULL SPACE

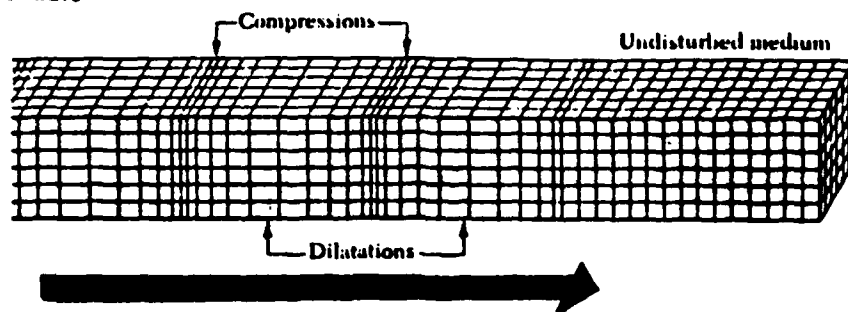
The equations of motion for stress waves in an isotropic full space have been treated in detail by many authors (Timoshenko and Goodier, 1951; Ewing, Jardetzky, and Press, 1957; Kolsky, 1963; and others), and therefore only essential results are presented. The solution of the equations of motion yield two types of waves, compression and shear waves. These waves are called body waves because they travel throughout the body of the full space. Compression waves are also referred to as P-waves, primary waves, irrotational waves or dilatational waves while shear waves are also referred to as S-waves, distortional waves, equivoluminal waves or secondary waves.

Compression waves are those body waves which exhibit pure volume change. As such, compression waves exhibit a pushpull motion in which particle motions are excited parallel to the direction of wave propagation as shown in Fig. 2.1a. Compression waves propagate with a velocity which can be expressed as:

$$V_p = [(\lambda + 2G)/\rho]^{1/2} \quad (2.1)$$

where V_p is the compression wave velocity, λ and G are Lamé's constants (G is also called the shear modulus or modulus of rigidity), and ρ is the mass

a. P-wave



b. S-wave

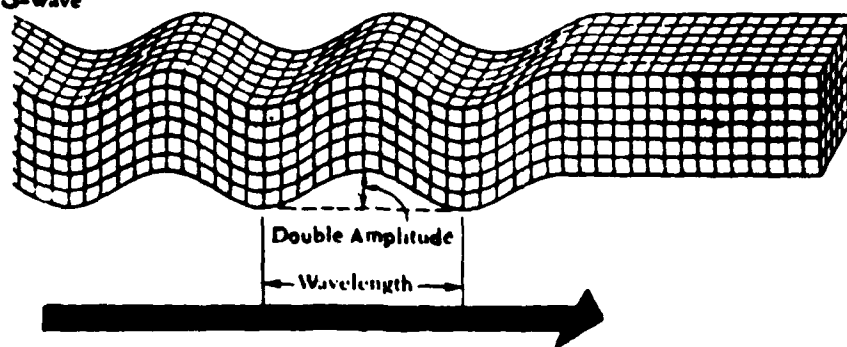


Fig. 2.1 - Characteristic Motions of Body Waves (from Bolt, 1976)

density of the soil. The unit weight of soil divided by the acceleration of gravity is defined as the mass density of the soil.

Shear waves are those body waves which exhibit pure rotational motion. Therefore, shear waves excite particle motion perpendicular to the direction of wave propagation. There are two special cases of shear waves: (1) a shear wave so polarized that particle motion is contained in a vertical plane is designated as an SV-wave as shown in Fig. 2.1b, and (2) a shear wave so polarized that particle motion is solely in the horizontal plane which is called an SH-wave (Dobrin, 1976). Shear waves propagate with a velocity, V_s , which can be expressed as:

$$V_s = [G/\rho]^{1/2} \quad (2.2)$$

The feature of directionality of particle motion of shear waves has been used by many researchers to study shear waves. For instance, Jolly (1956) used polarized sources to control the direction of particle motion and to identify SH- and SV-waves through reversible wave signals in geophysical surveys. Schwarz and Musser (1972), Tanimoto and Kurzeme (1973), Mooney (1974), Ballard (1976), Stokoe and Hoar (1977), and Auld (1977) employed this characteristic to identify S-waves in geotechnical engineering studies. Ballard, Stokoe, and McLemore (1983) recommend a source with controlled directionality for identifying the S-wave in their proposed ASTM (American Society for Testing and Materials) standard test method for crosshole seismic testing.

2.2.1 SHEAR AND CONSTRAINED MODULI

By measuring shear and compression wave velocities in an isotropic full space, seismic tests provide a direct means of evaluating shear and constrained moduli, G and M , respectively, from:

$$G = \rho V_s^2 \quad (2.3)$$

$$M = \rho V_p^2 \quad (2.4)$$

2.2.2 YOUNG'S MODULUS AND POISSON'S RATIO

For an isotropic full space, Poisson's ratio can be calculated once V_p and V_s have been measured as follows:

$$\nu = [1 - (V_p/V_s)^2/2] / [1 - (V_p/V_s)^2] \quad (2.5)$$

where ν is Poisson's ratio. Young's modulus, E , can then be calculated from:

$$E = 2G (1 + \nu) \quad (2.6)$$

Equations 2.5 and 2.6 have been used to estimate Young's modulus and Poisson's ratio of media in geotechnical engineering (Mooney, 1974; Hardin, 1978, Abbiss, 1981; and Nazarian and Stokoe, 1983), rock engineering (Podio, Gregory and Gray, 1968; and Hamilton, 1979), and geophysical prospecting (Davis, 1980; and Hamilton, 1979). Results of such calculations for soils tested in this study are presented and discussed in Chapters Nine and Ten.

2.2.3 PREVIOUS THEORETICAL STUDIES

Evaluation of the behavior of body waves propagating in porous material comprised of equal-sized spheres loaded with normal forces is customarily based on Hertz theory (Hertz, 1881; see also Timoshenko and Goodier, 1951). The material of the spheres is assumed to be homogeneous and isotropic with known values for the elastic constants. The contact deformation can, then, be estimated in terms of elastic constants and contact pressures. Consequently, the elastic constants of the whole porous material are related to the fundamental constants of the spheres. Gassmann (1951) derived the formula for compression wave velocity through a hexagonal packing of spheres as:

$$V_p = 800 \{ [2\pi E_{sp} g^2] / [(1 - \nu_{sp}^2)^2 n^2 \rho_{sp}] \}^{1/6} \cdot D^{1/6} \quad (2.7)$$

where E_{sp} , ν_{sp} , and ρ_{sp} are Young's modulus, Poisson's ratio, and mass density of the individual spheres, respectively, n is the porosity of the packed medium, g is the acceleration of gravity and D is the depth of burial.

By adopting the theories from Cattaneo (1938), Mindlin (1949), Mindlin and Deresiewicz (1953) along with Hertz theory, Duffy and Mindlin (1957)

derived the differential stress-strain relations for a face-centered cubic array with both normal and tangential forces in the contact area. In the principal stress direction, x or (1,0,0) direction, they derived the equation for Young's modulus of the medium as:

$$E_{(1,0,0)} = \frac{2(8-7\nu_{sp})}{8-5\nu_{sp}} \left[\frac{3G_{sp}^2 \bar{\sigma}_0}{2(1-\nu_{sp})^2} \right]^{1/3} \quad (2.8)$$

where G_{sp} is the shear modulus of the spheres and $\bar{\sigma}_0$ is the gross hydrostatic confining pressure (typically called the mean effective confining pressure in geotechnical engineering).

If the linear dimensions of the cross section of a bar are sufficiently small in comparison with the wavelength, the compression wave velocity in a slender bar can be written as:

$$V_c = [E/\rho]^{1/2} \quad (2.9)$$

From Eqs. 2.8 and 2.9, it can be seen that the variation of compression wave velocity in a bar composed of spheres is proportional to the one sixth power of pressure, i.e.,

$$V_c = C \bar{\sigma}_0^{1/6} \quad (2.10)$$

where C is the constant of the equation in functions of ρ , ν_{sp} , and G_{sp} . By comparing Eqs. 2.7 through 2.10, one can see that the mean effective confining pressure has been shown theoretically to be one of the main factors affecting compression wave velocity. It is interesting to note that Eq. 2.8 is based on the static stress-strain relationship.

Another approach is to treat the porous material macroscopically as having a homogeneous, isotropic, and elastic frame. For such material which is saturated, stress-strain relations can be derived for the medium in terms of elastic constants of the frame and fluid. Three solutions for wave velocities are obtained; two for P-wave velocities and one for S-wave velocities. The higher value of P-wave velocity is referred to as the velocity of the fluid, or wave of the first kind, while the lower value is called the velocity of the frame or wave of the second kind (Kosten and Zwikken, 1949; Morse, 1952; Brandt, 1955; and Biot, 1956). The relationship

between P-wave velocity and mean effective confining pressure has also been found to vary with a power of $1/6$ for the wave of the second kind, while the velocity of the wave of the first kind is rather independent of the applied confining pressure.

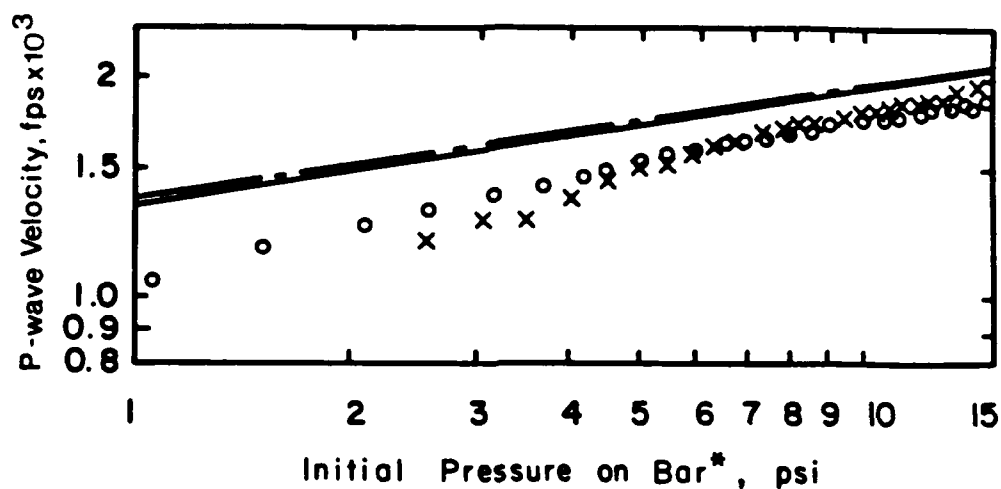
Biot (1956) also derived the relationship between shear wave velocity and confining pressure. He found the slope of the relationship to be the same as that of the compression wave velocity relationship, i.e., shear wave velocity varies with about the $1/6$ power of the hydrostatic confining pressure.

2.2.4 PREVIOUS EXPERIMENTAL STUDIES OF P-WAVE VELOCITY

Wave propagation tests with a rod composed of dry granular particles were conducted by Duffy and Mindlin (1957), as shown by Fig. 2.2. Compression wave velocity was found to vary with the $1/6$ power of pressure down to about 10 psi (68.9 kPa), and about the $1/4$ power of pressure below 10 psi (68.9 kPa). Duffy and Mindlin attributed the change of slope to the poor initial contact between particles at low confining pressures.

Richart (1962) pointed out that, based on experimental results presented by many researchers, the slopes of the compression wave velocity to confining pressure relationship on a log-log scale range between $1/6$ and $1/2$. Data from in situ up-hole tests (Smoots and Stickel, 1962), and resonant column tests (Hardin, 1961; and Wilson and Miller, 1962) have also shown that the exponent of the power of confining pressure may vary over a range from 0.16 to 0.40, as shown in Fig. 2.3. The results of pulse tests with large specimens (Schmertmann, 1978; Kopperman, et al, 1982; and Chu, et al, 1984) have also shown a range in the value of the slope from 0.14 to 0.24. All of these results are summarized in Table 2.1.

One additional point of note is that specimens used in these experimental tests may not be an isotropic medium, especially in large samples, even under isotropic confinement. Accordingly, some of the researchers concluded that structural anisotropy existed in the samples. However, the theory for an isotropic full space presented in the earlier equations does not take into account this anisotropy, and one must exercise care in using the equations as noted in Section 2.2.3.



Orientation	$\langle 1, 0, 0 \rangle$	$\langle 1, 1, 0 \rangle$
Theory	—	—
data	o	x

* Composed of stainless steel spheres with $\frac{1}{8} \pm 10 \times 10^{-6}$ in. in diameter

Fig. 2.2 - Variation of P-Wave Velocity with Confining Pressure in a Rod of Dry Granular Particles (from Duffy and Mindlin, 1957)

From Duffy and Mindlin (12) - tests on steel balls $1/8 \pm 0.00010$ " dia.
 From Gassmann (13) - theoretical - assuming dry spheres of granite, $e = 0.36$.
 From MIT (14) - range of test data for Ottawa Standard Sand, $e = 0.53$.
 From Matsubara and Hunter (15) - test data for dry sand, $e = 0.64$.
 From Shannon, Yamane, and Dietrich (16) - computed from test data for
 Ottawa Standard Sand, $e = 0.61$.

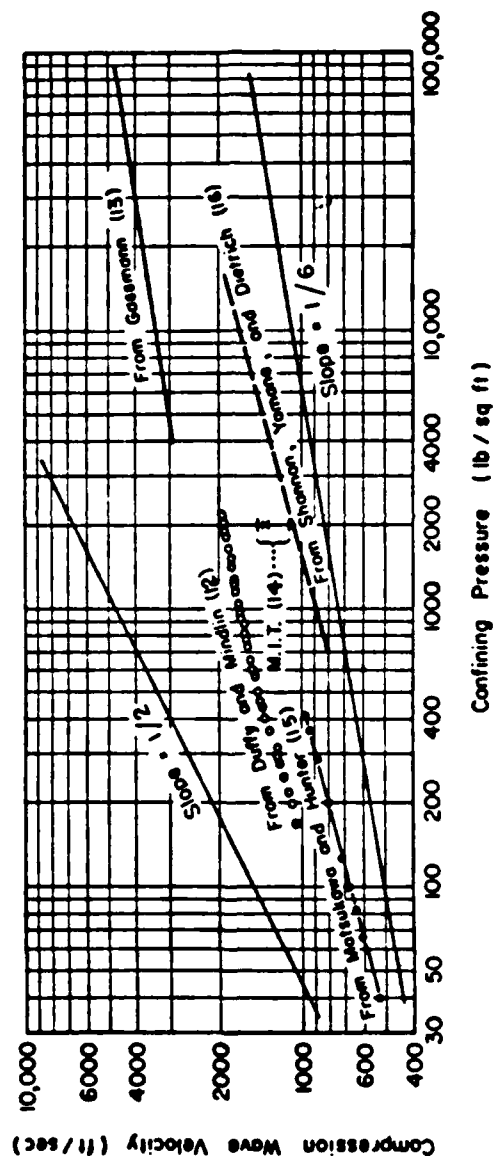


Fig. 2.3 - Effect of Confining Pressure on the Compression Wave Velocity in Granular Materials (from Richart, 1962)

Table 2.1 - Summary of Values of the Slope of the $\log V_p - \log \bar{\sigma}_0$ Relationship+ in Dry Sand Under Isotropic Confinement

Reference	Slope	Confining Pressure	Remark++
Matsukawa and Hunter (1956)	0.20	40-400 psf	1
Duffy and Mindlin (1957)	0.17 0.25	>700 psf <700 psf	1
Shannon, et al (1959)	0.25	>600 psf	1
Hardin (1961)	0.23-0.31▽ 0.23-0.40▽▽	400-8000 psf 400-8000 psf	1
Smoots and Stickel (1962)	0.16-0.28	>600 psf	1
Wilson and Miller (1962)	0.20-0.25	>600 psf	1
Hardin and Richart (1963)	0.27-0.35 0.23-0.25	<2000 psf >2000 psf	1
Schmertmann (1978)	0.20-0.23* 0.14-0.18**	720-2880 psf	2
Kopperman, et al (1983)	0.20* 0.23-0.24**	1440-5760 psf 1440-5760 psf	3
Chu, et al (1984)	0.17* 0.22-0.23**	1440-5760 psf	3
Lee and Stokoe (1986)	0.21* 0.22**	2160-4320 psf 2160-4320 psf	3

+ Relationship is: $V_p = C_1 \bar{\sigma}_0^{mm}$

* V_p in vertical plane of sand sample, i.e., V_{pA}

** V_p in horizontal plane of sand sample, i.e., V_{pI}

++1 Resonant Column Test

++2 Pulse Test (Cylindrical Chamber)

++3 Pulse Test (Large-Scale Triaxial Device)

▽ Dry Sand

▽▽ Saturated Sand

2.2.5 PREVIOUS EXPERIMENTAL STUDIES OF S-WAVE VELOCITY

By substituting Eqs. 2.10 and 2.6 into Eq. 2.2, the relationship between shear wave velocity and confining pressure also exhibits a 1/6 power as:

$$V_s = C_2 \bar{\sigma}_0^{1/6} \quad (2.11)$$

where C_2 is the constant in a function of v_{sp} , G_{sp} , and ρ . Hardin (1961) investigated Eq. 2.11 by performing a comprehensive study of shear wave velocity of dry and saturated Ottawa sand specimens with the resonant column method. Hardin found that, to fit Eq. 2.11, the values of the power of confining pressure for dry sand ranged from 0.23 to 0.32. Furthermore, a curved line instead of a straight one more correctly fit the $\log V_s - \log \bar{\sigma}_0$ relationship. A value of confining pressure of 2000 psf was adopted as the break point in the relationship (Hardin and Richart, 1963), and two straight lines were then used to fit the data. For dry sand, the curve above 2000 psf had 0.238 for the average slope compared with 0.293 for the average slope below 2000 psf.

Based on much work with resonant column tests (Hardin, 1962; Gardner, 1964; and Drnevich, Hall, and Richart, 1967), Hardin and Black (1966 and 1968) concluded that the small-strain shear modulus of soil is independent of the deviatoric component of the initial static state of stress and depends only on the mean effective confining pressure for both clay and sand. The slope value, 1/2, was adopted for either angular grains or rounded grains for $\bar{\sigma}_0$ above or equal to 2000 psf, while 3/5 was used for rounded grains with $\bar{\sigma}_0$ below 2000 psf.

A summary of test results for shear wave velocities determined under isotropic confining pressures is given in Table 2.2. Additional recent work, which has focused on the effect of isotropic confining pressure on V_s and G in resonant column tests, agrees with Hardin and Black in that shear wave velocity and shear modulus estimated with powers of 0.25 and 0.50, respectively, of the mean effective confining pressure are sufficiently accurate for practical purposes (Hardin and Drnevich, 1972; Hardin, 1978; Iwasaki, Tatsuoka, and Takagi, 1978 and 1979; Tatsuoka, Iwasaki, Yoshida, Fukushima, and Sudo, 1979; Tatsuoka, Iwasaki, Fukushima, and Sudo, 1979; and Uchida, Sawada, and Hasegawa, 1980). However, slightly lower values for the power of $\bar{\sigma}_0$ have come from most large-scale specimens tested with the pulse

Table 2.2 - Summary of Values of the Slope of the $\log V_s - \log \bar{\sigma}_0$
Relationship+ in Dry Sand Under Isotropic Confinement

Reference	Slope	Confining Pressure	Remark++
Hardin (1961)	0.23-0.32	300-10,000 psf	1
Hardin (1962)	0.25 ≥0.25	2000-9800 psf 15-2000 psf	1
Wilson and Miller (1962)	0.15-0.20	700-12,000 psf	1
Hardin and Richart (1963)	0.23-0.25 0.27-0.31	>2000 psf <2000 psf	1
Gardner (1964)	0.25 0.17	<1000 psi 1000-5000 psi	1
Lawrence (1965)	0.25-0.33	2880-14,400 psf	2
Hardin and Drnevich (1972)	0.25		1
Schmertmann (1978)	0.20-0.29* 0.16-0.20**	720-2880 psf	3
Iwasaki, et al (1978)	0.25	511-4088 psf	1
Tatsuoka, et al (1979)	0.25	511-4088 psf	1
Roesler (1979)	0.25-0.26	1044-3600 psf	4
Knox, et al (1982)	0.18* 0.19-0.22**	1440-5760 psf	5
This Report	0.18* 0.20**	1440-5760 psf	5

+ Relationship is: $V_s = C_2 \bar{\sigma}_0^{nm}$

* propagation in vertical plane, i.e., V_{SA}

** propagation in horizontal plane, i.e., V_{SI}

++1 Resonant Column Test

++2 Pulse Test (Small Cylindrical Sample)

++3 Pulse Test (Cylindrical Chamber)

++4 Pulse Test (Medium Cubical Sample)

++5 Pulse Test (Large-Scale Triaxial Device)

method (Schmertmann, 1978; Roesler, 1929; Knox, et al, 1982; and Lee and Stokoe, 1985). These lower values (about 1/6 to 1/5) are closer to the theoretical value and are discussed in detail in Chapter Nine.

2.3 WAVE MOTION IN AN ANISOTROPIC FULL SPACE

An anisotropic full space is considered herein to be a linear elastic full space which may be either a homogeneous material under anisotropic loading or an anisotropic medium under isotropic loading. As such, the elastic properties of the material vary with direction. Therefore the anisotropy of the material must be considered. The number of static constants needed to describe the material can be as many as 36 for a completely anisotropic system. Due to energy considerations, the stress-strain relationship is symmetrical, and the 36 constants reduce to 21 independent coefficients. For elastic symmetry in three planes, (i.e., an orthotropic medium), there are only nine independent constants (Desai and Christian, 1977). In geotechnical engineering, the most common model for level soil conditions is a cross-anisotropic (or transversely isotropic) model which has one axis of symmetry and requires five independent constants (Love, 1927). The relationship for a material having the z-axis (vertical axis) as the axis of symmetry can be expressed in matrix form as:

$$\begin{bmatrix} \sigma_x \\ \sigma_y \\ \sigma_z \\ \tau_{yz} \\ \tau_{zx} \\ \tau_{xy} \end{bmatrix} = \begin{bmatrix} C_{11} & C_{12} & C_{13} & 0 & 0 & 0 \\ C_{12} & C_{11} & C_{13} & 0 & 0 & 0 \\ C_{13} & C_{13} & C_{33} & 0 & 0 & 0 \\ 0 & 0 & 0 & C_{44} & 0 & 0 \\ 0 & 0 & 0 & 0 & C_{44} & 0 \\ 0 & 0 & 0 & 0 & 0 & C_{66} \end{bmatrix} \begin{bmatrix} \epsilon_x \\ \epsilon_y \\ \epsilon_z \\ \gamma_{yz} \\ \gamma_{zx} \\ \gamma_{xy} \end{bmatrix} \quad (2.12)$$

where C_{11} is the constrained modulus in the x- and y-directions, C_{33} is the constrained modulus in the z-direction, C_{44} is the shear modulus for yz- and xz-planes, C_{66} is the shear modulus for the xy-plane, and $C_{66} = (C_{11} - C_{12})/2$. The normal stresses are σ_x , σ_y , and σ_z ; the shear stresses are τ_{yz} , τ_{zx} , τ_{xy} ; the normal strains are ϵ_x , ϵ_y , ϵ_z ; the shear strains are γ_{yz} , γ_{zx} , and γ_{xy} . The five independent constants are C_{11} , C_{33} , C_{44} , C_{66} , and C_{13} . Therefore, the constrained modulus and shear modulus, which had only one value each in

the case of isotropic material, now each have two values for a cross-anisotropic medium. The equivalent symbols used in Cartesian coordinates for this study are shown in Fig. 2.4.

2.3.1 THEORY FOR CROSS-ANISOTROPIC MEDIUM

The simplest anisotropic material exhibits, at a minimum, cross-anisotropic (transversely isotropic) behavior. This behavior may be caused by several reasons such as stress-induced anisotropy or structural anisotropy. Dahlen (1972a and 1972b) extended the work of Biot (1940 and 1965) to take into account the effect of anisotropic stress state on the velocity of body waves in an otherwise isotropic material. This type of anisotropy is referred to as stress-induced anisotropy. Backus (1965) investigated the opposite situation; that is, where the anisotropic behavior is due to structural anisotropy under an isotropic initial stress condition. Structural anisotropy is also called inherent anisotropy, which may be caused by inclusions (Melia and Carlson, 1984), microcracks inside materials (Eshelby, 1957; Tocher, 1957; Birch, 1960; Matsushima, 1960; and Nur, 1971), interparticle contact orientation (Parkin et al, 1968; and Oda, 1972), or the stress history of the medium (Saada, Bianchini and Shook, 1978; and Hardin, 1983). Additionally, laminated media have been shown to be cross-anisotropic (transversely isotropic) materials by many investigators when the thicknesses of the layers are smaller than a wavelength (Postma, 1955; White and Angona, 1955; Helbig, 1958; Backus, 1962; Berryman, 1979; and Ross, Sierakowski and Sun, 1980).

By applying a plane wave in the xz-plane, White (1965) derived three equations for body wave velocities in terms of the five constants of a transversely isotropic medium as:

$$V_{sh,\theta} = \{(C_{66}\sin^2\theta + C_{44}\cos^2\theta)/\rho\}^{1/2} \quad (2.13)$$

$$V_{sv,\theta} = \{(C_{11}\sin^2\theta + C_{33}\cos^2\theta + C_{44} - \Delta)/(2\rho)\}^{1/2} \quad (2.14)$$

$$V_{p,\theta} = \{(C_{11}\sin^2\theta + C_{33}\cos^2\theta + C_{44} + \Delta)/(2\rho)\}^{1/2} \quad (2.15)$$

where $\Delta = \{[(C_{11} - C_{44})\sin^2\theta - (C_{33} - C_{44})\cos^2\theta]^2 + 4(C_{13} + C_{44})^2\sin^2\theta\cos^2\theta\}^{1/2}$,
and

θ = the angle between the direction of propagation of the plane wave and the axis of symmetry (z-axis) as shown in Fig. 2.5.

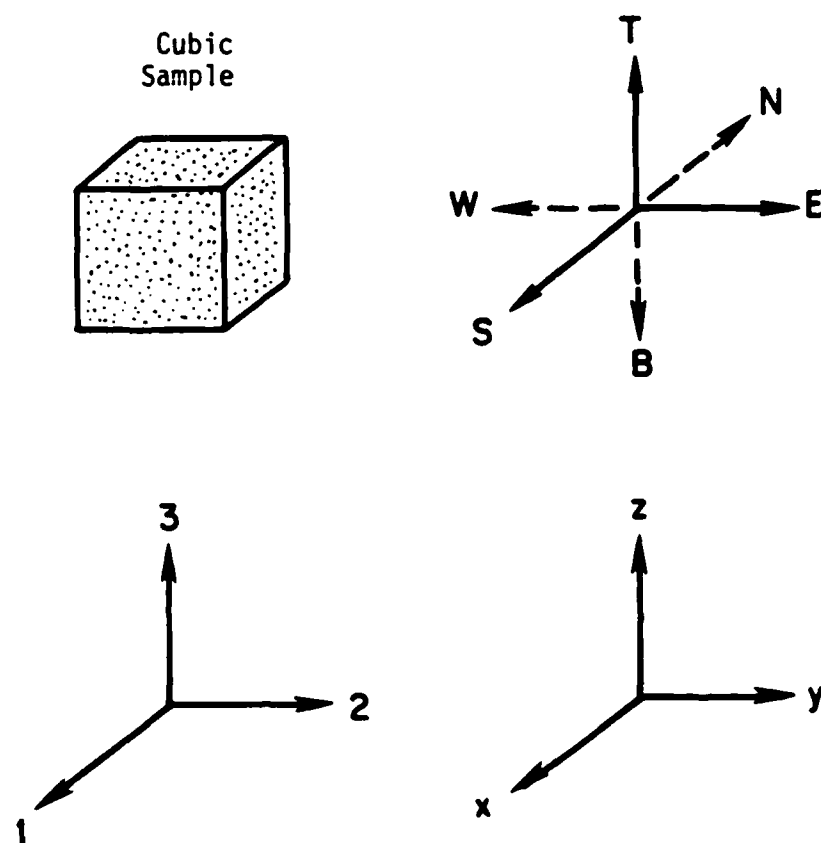


Fig. 2.4 - Different Sets of Symbols Used in Cartesian Coordinates in this Study

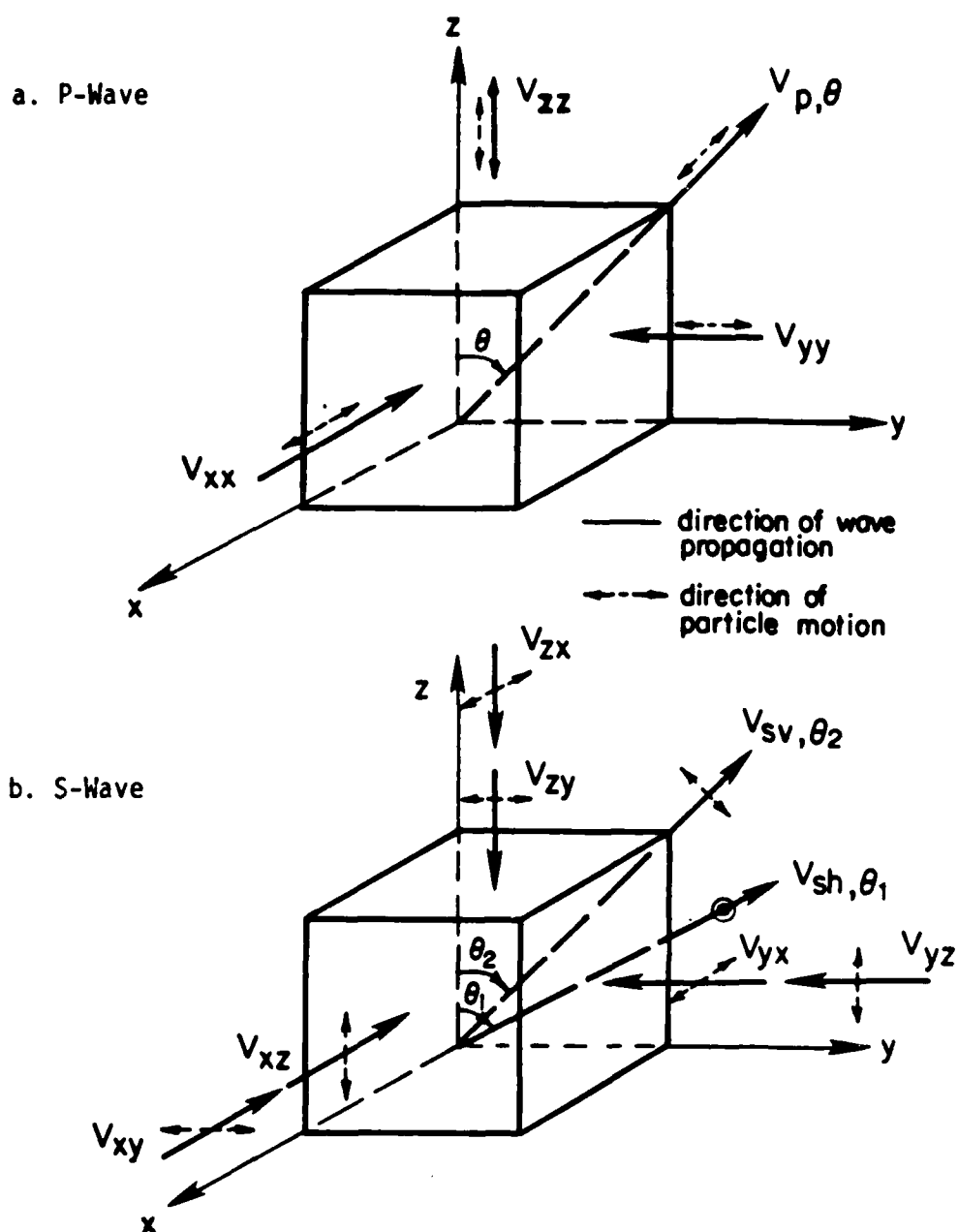


Fig. 2.5 - Elastic Wave Velocities in a Cross-Anisotropic Medium

SH-waves propagate as plane shear waves at any angle (θ) with the z-axis with a velocity $V_{sh,\theta}$. Particle motions associated with SH-waves are always purely horizontal, hence, perpendicular to the xz-plane for plane waves in the xz-plane. Particle motions of SV-waves are perpendicular to the direction of wave propagation and, for plane waves in the xz-plane, are contained in the xz-plane. SV-waves propagate with a velocity $V_{sv,\theta}$ in this case. For compression waves, the directions of wave propagation and particle motion coincide, and these waves propagate with velocity $V_{p,\theta}$.

The magnitudes of the three wave velocities (P, SV and SH) depend on the angle θ as follows: When $\theta = 0$ degrees, plane waves propagate in the z-direction with velocities:

$$V_{p,0} = [C_{33}/\rho]^{1/2} \quad (2.16)$$

$$V_{sh,0} = [C_{44}/\rho]^{1/2} \quad (2.17)$$

$$V_{sv,0} = [C_{44}/\rho]^{1/2} \quad (2.18)$$

When wave propagation is in the x-direction, i.e. $\theta = 90$ degrees, the values of velocity are:

$$V_{p,90} = [C_{11}/\rho]^{1/2} \quad (2.19)$$

$$V_{sh,90} = [C_{66}/\rho]^{1/2} \quad (2.20)$$

$$V_{sv,90} = [C_{44}/\rho]^{1/2} \quad (2.21)$$

The velocities of body waves propagating along principal directions (Eqs. 2.16 through 2.21) can then be expressed as V_{xx} , V_{yy} , and V_{zz} for P-waves, and V_{xy} , V_{yx} , V_{xz} , V_{yz} , V_{zx} , and V_{zy} for S-waves. The first subscript of the velocity term denotes the direction of wave propagation while the second subscript denotes the direction of particle motion. For a material with the z-axis as the axis of symmetry (as is the sample tested in this study), the relationship between wave velocities is as follows:

$$V_{p,90} = V_{xx} = V_{yy} \quad (2.22)$$

$$V_{p,0} = V_{zz} \quad (2.23)$$

$$V_{sh,90} = V_{xy} = V_{yx} \quad (2.24)$$

$$V_{sh,0} = V_{zx} = V_{zy} \quad (2.25)$$

$$V_{sv,90} = V_{xz} = V_{yz} \quad (2.26)$$

$$V_{sv,0} = V_{zx} = V_{zy} \quad (2.27)$$

where $V_{xz}=V_{yz}=V_{zx}=V_{zy}$. Hence, the nine possible waves (three P-waves and six S-waves) result in four different wave velocities. For convenience in this study, the following four symbols will sometimes be used to denote the wave velocities along the principal directions (for the sample which would be idealized as having the z-axis as the axis of symmetry):

$$V_{PI} = V_{xx} = V_{yy} \quad (2.28)$$

$$V_{PA} = V_{zz} \quad (2.29)$$

$$V_{SI} = V_{xy} = V_{yx} \quad (2.30)$$

$$V_{SA} = V_{xz} = V_{yz} = V_{zx} = V_{zy} \quad (2.31)$$

where the first subscript is used to denote the type of wave, and the second subscript "I" is used to denote the isotropic plane and "A" is used to denote the anisotropic plane in which wave propagation and particle motion are contained. For body waves not propagating along principal directions, wave velocities will still be denoted as $V_{sh,\theta}$, $V_{sv,\theta}$, and $V_{p,\theta}$.

Figure 2.5 illustrates these waves for a cross-anisotropic material having the z-axis as the axis of symmetry.

2.3.2 YOUNG'S MODULUS AND POISSON'S RATIO

For a cross-anisotropic medium, the stress-strain relation can be written following Hook's formulation as:

$$\begin{bmatrix} \epsilon_x \\ \epsilon_y \\ \epsilon_z \end{bmatrix} = \begin{bmatrix} 1/E_{11} & -\nu_{12}/E_{11} & -\nu_{13}/E_{33} \\ -\nu_{12}/E_{11} & 1/E_{11} & -\nu_{13}/E_{33} \\ -\nu_{31}/E_{11} & -\nu_{31}/E_{11} & 1/E_{33} \end{bmatrix} \begin{bmatrix} \sigma_x \\ \sigma_y \\ \sigma_z \end{bmatrix} \quad (2.32)$$

in which

$$\nu_{31}/E_{11} = \nu_{13}/E_{33} \quad (2.33)$$

In the above equations, E_{11} is Young's modulus in the x- (or 1-) direction and is the same as E_{22} . E_{33} is Young's modulus in the z- (or 3-) direction. Poisson's ratio in the plane of isotropy, ν_{12} , is simply the ratio of the negative strain in the x- (or 1-) direction to the positive strain in y- (or 2-) direction when normal stress is applied along the y-direction. Similar definitions are also used for Poisson's ratios ν_{13} and ν_{31} . For convenience in this report, the following notations are used:

$$\nu_I/E_I = \nu_{12}/E_{11} \quad (2.34)$$

$$\nu_A/E_A = \nu_{13}/E_{33} \quad (2.35)$$

Therefore, ν_{31} can be calculated from Eqs. 2.33 and 2.35, and Eq. 2.32 can be simplified as following:

$$\begin{bmatrix} \epsilon_x \\ \epsilon_y \\ \epsilon_z \end{bmatrix} = \begin{bmatrix} 1/E_I & -\nu_I/E_I & -\nu_A/E_A \\ -\nu_I/E_I & 1/E_I & -\nu_A/E_A \\ -\nu_A/E_A & -\nu_A/E_A & 1/E_A \end{bmatrix} \begin{bmatrix} \sigma_x \\ \sigma_y \\ \sigma_z \end{bmatrix}$$

where $E_I (= E_{11})$ is Young's modulus in the isotropic plane (horizontal plane or xy-plane in this study), $E_A (= E_{33})$ is Young's modulus in the anisotropic plane (any vertical plane in this study), $\nu_I (= \nu_{11})$ is Poisson's ratio in the isotropic plane, and $\nu_A (= \nu_{13})$ is Poisson's ratio in the anisotropic plane.

From the generalized stress-strain law (Eq. 2.12), $\epsilon_x (= \epsilon_y)$ and ϵ_z are:

$$\epsilon_x = [\sigma_x(C_{11}C_{33} - C_{13}^2) - \sigma_y(C_{12}C_{33} - C_{13}^2) + \sigma_z(C_{12}C_{13} - C_{11}C_{13})]/|C| \quad (2.37)$$

$$\epsilon_z = [\sigma_x(C_{12}C_{13} - C_{13}C_{11}) - \sigma_y(C_{11}C_{13} - C_{13}C_{12}) + \sigma_z(C_{11}^2 - C_{12}^2)]/|C| \quad (2.38)$$

where

$$|C| = \begin{vmatrix} C_{11} & C_{12} & C_{13} \\ C_{12} & C_{11} & C_{13} \\ C_{13} & C_{13} & C_{33} \end{vmatrix}$$

By comparing Eq. 2.36 and 2.37, it follows that:

$$E_I = |C|/(C_{11}C_{33} - C_{13}^2) \quad (2.39)$$

and

$$\nu_I = (C_{12}C_{33} - C_{13}^2)/(C_{11}C_{33} - C_{13}^2) \quad (2.40)$$

From Eqs. 2.36 and 2.38, it follows that

$$E_A = |C|/(C_{11}^2 - C_{12}^2) \quad (2.41)$$

and

$$\nu_A = (C_{11}C_{13} - C_{12}C_{13})/(C_{11}^2 - C_{12}^2) \quad (2.42)$$

Obviously, two values of Young's moduli and three values of Poisson's ratios (Eqs. 2.33-2.35) exist in a cross-anisotropic medium rather than only one of each for an isotropic material. Values of Young's modulus and Poisson's ratio are discussed in Chapter Nine.

2.3.3 C_{13} AND ITS LIMITATION

Since there are five independent constants in a transversely isotropic material, there are at least five measurements necessary for evaluation of these constants. Wave velocities along principal axes give four constants, C_{11} , C_{33} , C_{44} , and C_{66} (See Eqs. 2.16 through 2.21). Either a compression or

shear wave inclined to the axis of symmetry can be used to calculate C_{13} (Eqs. 2.14 and 2.15). A value of C_{13} calculated by either Eq. 2.14 or 2.15 will be sound in theory as opposed to one determined by an empirical equation such as the one suggested by Drnevich (1974) ($C_{13} \approx (C_{11} + C_{33})/2 - 2 \cdot C_{66}$). Nye (1957) pointed out that a relation of C_{13} with the other constants has been derived by Ferrar (1941) as:

$$C_{13} < [(C_{11} + C_{12})C_{33}/2]^{1/2} \quad (2.43)$$

The value calculated by the right side of Eq. 2.43 can be used as an upper limit for C_{13} , which is done throughout this report.

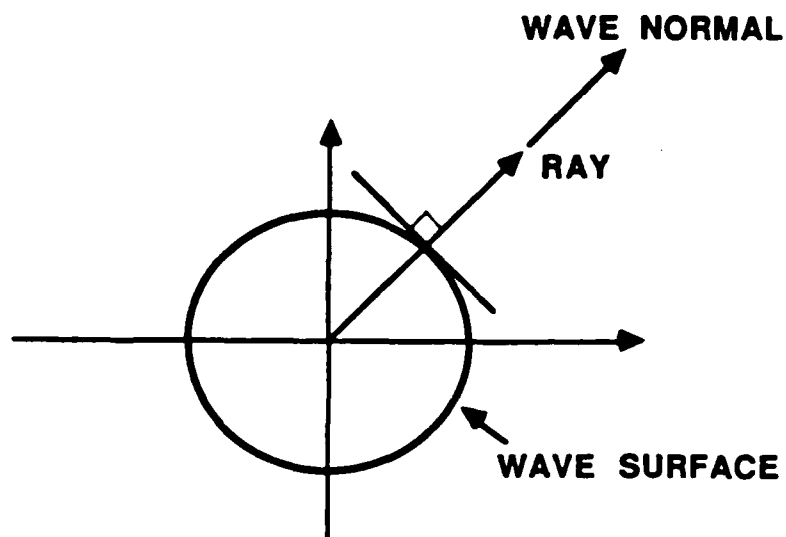
2.3.4 VELOCITY SURFACE AND WAVE SURFACE

In discussions of body waves, the terms velocity surface and wave surface often arise. The velocity surface is defined as the wave front resulting from the wave normal. The wave surface is defined as the wave front constructed from energy flow.

When a plane wave moves through an isotropic medium, the wave normal always coincides with the direction of energy flow (also called ray path) as shown in Fig. 2.6a. So, the velocity surface is also the wave surface. However, for a plane wave propagating through an anisotropic medium, the wave normal is in the direction along which the plane wave propagates whereas the energy flow moves along a different direction if the wave normal is not in any one of the principal directions. Therefore, the wave surface may be different from the velocity surface (Wooster, 1938; and Joos, 1958).

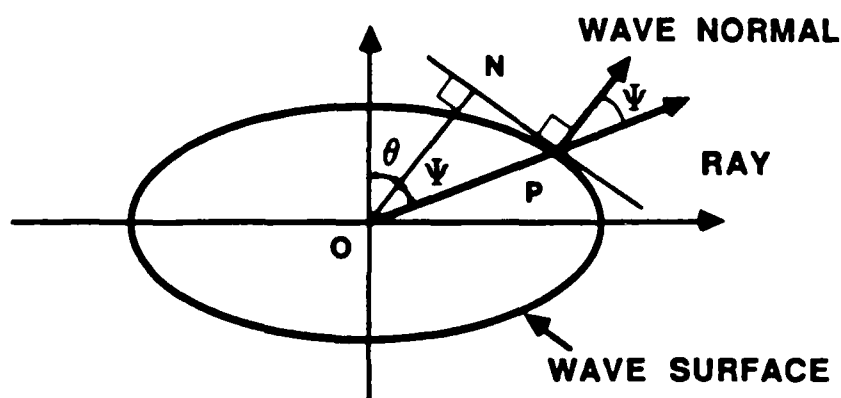
A difference between the directions of ray and wave normals has been found through research on crystals (Love, 1927 and Nye, 1957). All statements for-wave velocities mentioned in discussing Eqs. 2.16 through 2.31 have referred to the wave normal. The wave velocity (i.e. the velocity of the wave normal) is proportional to the magnitude of \overline{ON} in Fig. 2.6, while the ray velocity (i.e. the velocity of the energy flow) is proportional to the magnitude of \overline{OP} . An analytical treatment of wave velocity to ray velocity by Joos (1934) and Postma (1955) has shown:

$$\text{Ray Velocity} = \text{Wave Velocity}/\cos\psi \quad (2.44)$$



RAY VELOCITY =
WAVE VELOCITY

(a) ISOTROPIC FULL SPACE



RAY VELOCITY =
 $\frac{\text{WAVE VELOCITY}}{\cos \Psi}$

(b) ANISOTROPIC FULL SPACE

Fig. 2.6 - Directions of Ray and Wave Normal on the Wave Surface from a Point Source at the Origin in Isotropic and Anisotropic Full Spaces

where ψ is the angle between the directions of the ray and wave normals. Through the measured ray velocities, the velocity surface and the wave surface can, therefore, be constructed with Eq. 2.44. In some conditions, the combination of the five constants for a cross-anisotropic medium may cause a cusp in the wave surface for the SV-wave. Figure 2.7 is the first observation which resulted in a cusp in shale reported by Jolly (1956). The velocities of SV-waves in the vertical direction is about the same as that for P-waves. Such behavior results in a near-vertical cusp of the SV-wave. Levin (1978), Helbig (1979 and 1983), and Byon (1984) extended this concept to more complex geophysical prospecting work, such as cross-anisotropic media with inclined layers.

2.3.5 PREVIOUS EXPERIMENTAL STUDIES OF P-WAVE VELOCITY

From the results of extensive studies on in situ velocities of seismic waves in sedimentary formations, Faust (1953) suggested an equation for rock as:

$$V_p = C L^{1/6} D^{1/6} \quad (2.45)$$

where V_p is in fps, L is a parameter of "lithology" in ohm-ft, D is depth in ft, and C is a constant with an average value of about 2000. From observations in western Canada, Acheson (1963) formulated an equation similar to Eq. 2.45 as:

$$V_p = C D^{1/n} ; 8 < n < 20 \quad (2.46)$$

in which V_p is in fps, and D is depth in feet. Many other researchers have also noticed the importance of depth on V_p (Hamilton, 1970; Hamilton, 1971a and 1971b; Hamilton, Bachman, Curray and Moore, 1977; Hamilton, 1976 and 1979; and Bachman, 1983). Nevertheless, detailed studies of compression wave velocity under biaxial confining pressures were not reported until 1982 by Kopperman, et al.

Kopperman et al (1982) and Chu, et al (1984) conducted a complete series of tests on the effect of both biaxial and triaxial states of stress on compression wave velocity for waves propagating along principal stress directions. Sand samples were used which were tested in a large-scale

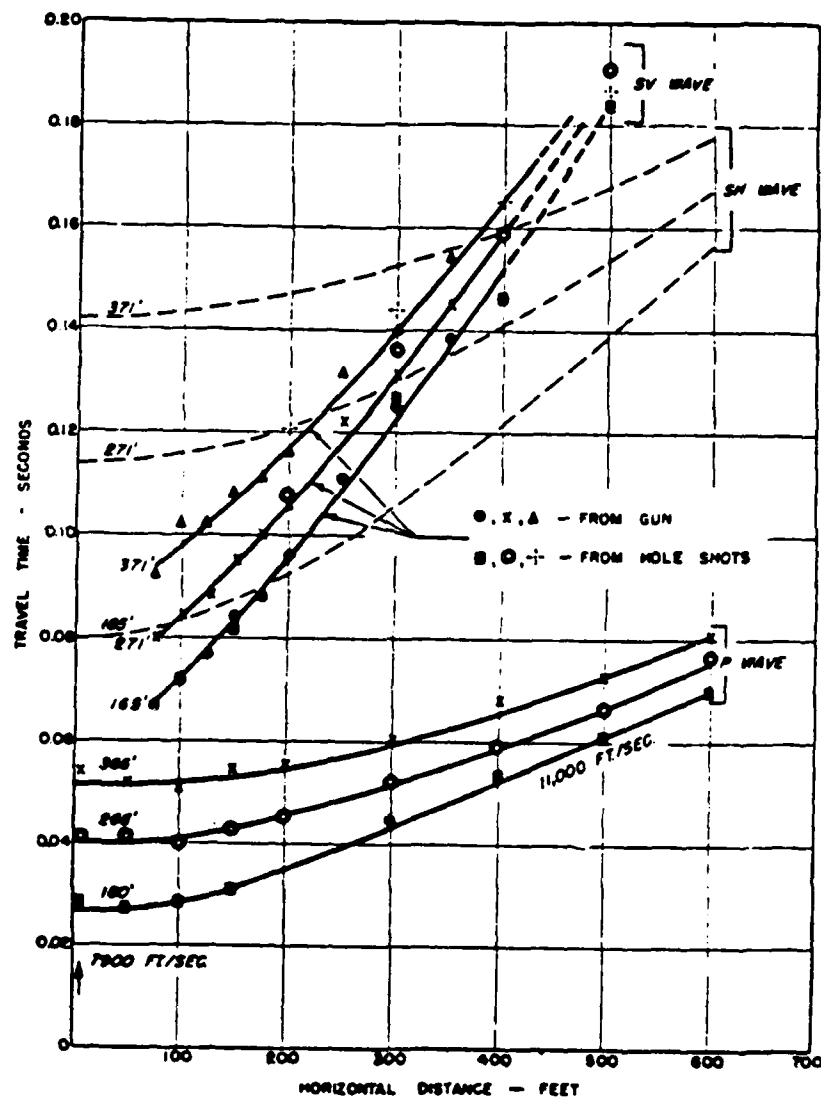


Fig. 2.7 - Time-Distance Curves of SH, SV, and P Direct Waves Observed at Depth (from Jolly, 1956)

cubical device measuring 7 ft (2.1 m) on each side. An equation for compression wave velocity along principal axes for all states of stress, (i.e., isotropic, biaxial, or triaxial conditions), was suggested as:

$$V_p = C_1 \bar{\sigma}_a^{ma} \quad (2.47)$$

where V_p is the P-wave velocity in principal directions in fps, C_1 is a constant with values of 327, 292, and 317 for the x-, y-, and z-directions, respectively, $\bar{\sigma}_a$ is the effective stress in the direction of wave propagation in psf, and ma is the dimensionless exponent. The values of the exponent for the $\log V_p$ - $\log \bar{\sigma}_a$, $\log V_p$ - $\log \bar{\sigma}_0$, and $\log V_p$ - $\log D$ relationships from the above research are summarized in Table 2.3. Results from Lawrence (1963) with uniaxial pressure in a confined sample and from Schmertmann (1978) with biaxial confinement in a chamber specimen have been re-analyzed in this study, and the results are also listed in Table 2.3. Compression wave velocity is a function of effective stress in the direction of wave propagation as shown in the table. A discussion of these results is presented by Lee and Stokoe (1986).

2.3.6 PREVIOUS STUDIES OF S-WAVE VELOCITY

Before one can discuss the effect of stress state on shear wave velocity, a notation set must be developed so that the stress components in the directions of shear wave motions can be described. Following standard mechanics nomenclature, $\bar{\sigma}_1$ is the major effective principal stress, $\bar{\sigma}_2$ is the intermediate effective principal stress, and $\bar{\sigma}_3$ is the minor effective principal stress for an anisotropically confined system. The principal stress ratios, K_{13} and K_{23} , can then be defined as:

$$K_{13} = \bar{\sigma}_1 / \bar{\sigma}_3 \quad (2.48)$$

and

$$K_{23} = \bar{\sigma}_2 / \bar{\sigma}_3 \quad (2.49)$$

The values of K_{13} and K_{23} range from 1 to 2.67 in this study. Also, a stress level, b , is defined as:

$$b = (\sigma_1 - \sigma_3) / (\sigma_1 - \sigma_3)_f \quad (2.50)$$

Table 2.3 - Summary of Values of the Slope of the P-Wave Velocity-Confining Pressure Relationship for Dry Sand Under Anisotropic Confinement

Reference	ma*	mm**	Remark†
Faust (1953)	1/6	---***	1
Acheson (1963)	1/20 - 1/8	---	1
Lawrence (1963)	0.20-0.25	---	2
Schmertmann (1978)	0.19 0.19	0.23 0.22	3□ 3□□
Kopperman, et al (1982)	0.20-0.24 0.20	0.23-0.24 0.20	4□ 4□□
Chu, et al (1984)	0.21-0.22 0.19	0.22-0.23 0.20	4□ 4□□
Lew and Campbell (1985)++	0.288-0.305	---	1

* $V_p = c_1 \bar{\sigma}_a^{ma}$; with V_p in fps and $\bar{\sigma}_a$ in psf

** $V_p = c_1 \bar{\sigma}_o^{mm}$; with V_p in fps and $\bar{\sigma}_o$ in pfs

*** not applicable

□ parameter for V_{pI}

□□ parameter for V_{pA}

++ Depth (D) < 110 ft

+ 1. in situ measurement

+ 2. Pulse Test (one-dimensional compression wave test in laterally constrained specimen)

+ 3. Pulse Test (Cylindrical Chamber)

+ 4. Pulse Test (Large-Scale Triaxial Device)

where $(\sigma_1 - \sigma_3)_f$ is the stress difference of major and minor principal stresses at failure. Other symbols used to relate the stress components to wave behavior are (from Knox, et al, 1982):

$\bar{\sigma}_a$ = effective principal stress in the direction of wave propagation,
 $\bar{\sigma}_b$ = effective principal stress in the direction of particle motion, and
 $\bar{\sigma}_c$ = effective principal stress in the out-of-plane direction which is perpendicular to the plane that includes σ_a and σ_b .

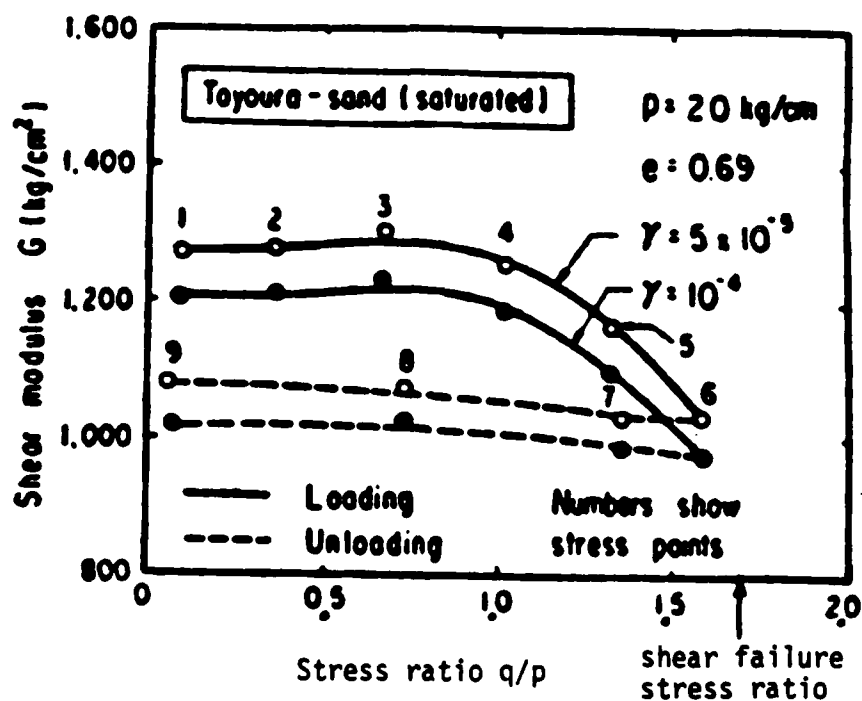
As discussed in Section 2.2 and Fig.2.1, the directions of $\bar{\sigma}_a$ and $\bar{\sigma}_b$ are perpendicular for S-waves. For P-waves, $\bar{\sigma}_a$ and $\bar{\sigma}_b$ are in the same direction.

The resonant column method has been employed in the laboratory to study whether or not the mean effective confining pressure ($\bar{\sigma}_o$) is the best parameter to estimate shear wave velocities and shear moduli. Although some scattering of data has been noticed, most researchers accept $\bar{\sigma}_o$ as an appropriate parameter (Hardin, 1961; Hardin and Richart, 1963; Hardin and Black, 1966 and 1968; Iwasaki, et al 1978; Kuribayashi, et al 1974; Tatsuoka, et al 1979; Uchida, et al 1980; and Bianchini and Saada, 1981). The maximum shear modulus for sand under triaxial confinement suggested by Hardin (1978) is:

$$G_{\max} = [(C \cdot OCR^k)/(0.3 + 0.7 e^2)] P_a^{1-N_m} \bar{\sigma}_o^{N_m} \quad (2.51)$$

where: G_{\max} = shear modulus in desired units,
 C = dimensionless constant,
 OCR = overconsolidation ratio,
 K = factor related to soil plasticity,
 P_a = atmospheric pressure in same units as G_{\max} ,
 e = void ratio,
 $\bar{\sigma}_o$ = mean effective principal stress in same units as G_{\max} , and
 N_m = slope of $\log G - \log \bar{\sigma}_o$ relationship.

Figure 2.8, from Kuribayashi, et al (1975) in which resonant column tests were used, shows that the variation of maximum shear modulus with increasing stress level (they used the term stress ratio) under constant mean effective stress. A permanent change in deformation exists once the stress ratio exceeds some value like 1.2 in their sample. Lawrence (1965) also concluded that $\bar{\sigma}_o$ is one of the major parameters for estimating shear wave velocity from his results in pulse tests with a rod specimen (see Fig. 2.9).



Notes: 1. $\frac{q}{p} = \frac{\bar{\sigma}_a - \bar{\sigma}_r}{(\bar{\sigma}_a + 2\bar{\sigma}_r)/3}$

2. tests conducted at $\bar{\sigma}_0 = p = \text{constant}$
 3. torsional resonant column with anisotropic loading

Fig. 2.8 - Variation in Shear Modulus with Increasing Stress Difference (from Kuribayashi et al, 1975)

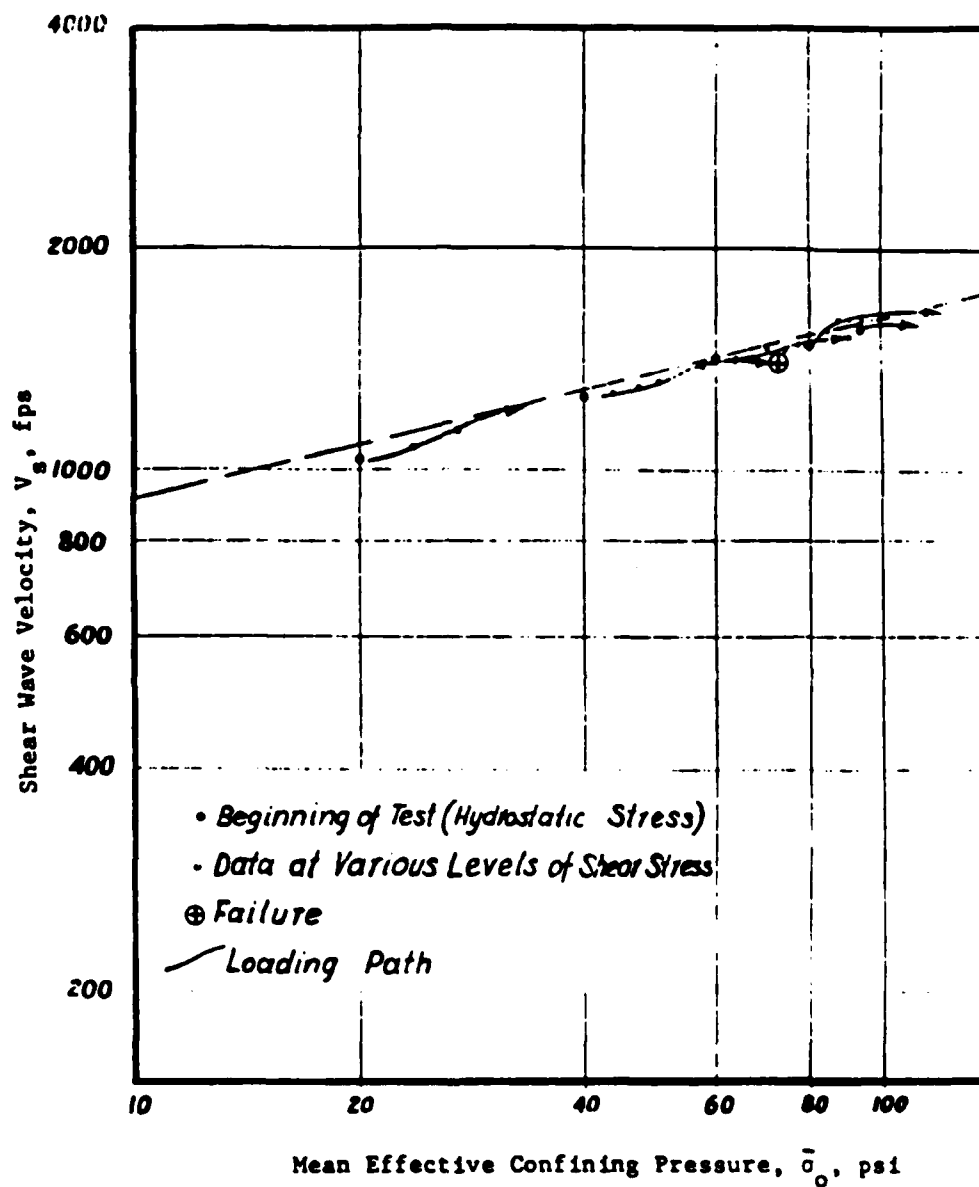


Fig. 2.9 - Results of Shear Wave Velocity Tests under Biaxial Confinement (from Lawrence, 1956)

Schmertmann (1978) used the effective octahedral stress, $\bar{\sigma}_o$, to evaluate shear wave velocities, as well.

The above conclusion implies that the mean effective confining pressure is also applicable to a stress-induced anisotropic medium and that body wave velocities will be the same in all directions in this material. However, just the opposite characteristic for wave velocities has been shown for anisotropic media in Sections 2.3.1 and 2.3.4.

In 1979, Roesler used stationary stochastic signals to measure shear wave velocities in a triaxial cube which measured 30 cm on a side. He concluded that only stress components in the directions of wave propagation and particle motion affect shear wave velocity along principal stress directions. Equation 2.52 was, consequently, suggested by Roesler (with the notation used in this report) as:

$$V_s = C \bar{\sigma}_a^{na} \bar{\sigma}_b^{nb} \bar{\sigma}_c^{nc} \quad (2.52)$$

where $na=0.149$, $nb=0.107$, $nc=0$. This equation is referred to as the "two-individual-stresses" method hereafter (because $nc = 0$).

Pulse tests conducted in a large-scale triaxial device measuring 7 ft (2.1 m) on a side under biaxial and triaxial confinements were presented by Knox et al (1982). Their data were re-analyzed in this study with the following results:

$$V_{SI} = 201 \bar{\sigma}_a^{0.09} \bar{\sigma}_b^{0.09} \bar{\sigma}_c^{0.01} \quad (2.53)$$

$$V_{SA} = 156 \bar{\sigma}_a^{0.11} \bar{\sigma}_b^{0.11} \bar{\sigma}_c^{-0.00} \quad (2.54)$$

in which V_{SI} and V_{SA} are the S-wave velocities for isotropic and anisotropic plane in fps, respectively, and $\bar{\sigma}_a$, $\bar{\sigma}_b$, and $\bar{\sigma}_c$ are the effective stresses in fps. Values in Eq. 2.53 are the values for the best-fit curves for the two shear waves in the isotropic plane (V_{xy} and V_{yx}), and values in Eq. 2.54 are the best-fit curves for the four shear wave velocities in the anisotropic planes (V_{xz} , V_{yz} , V_{zx} , and V_{zy}). The equations demonstrate the structural anisotropy in the sand sample used.

An "average-stress" method has been proposed by Knox, et al (1982) and discussed by Allen and Stokoe (1982) (see Fig. 2.10) in which:

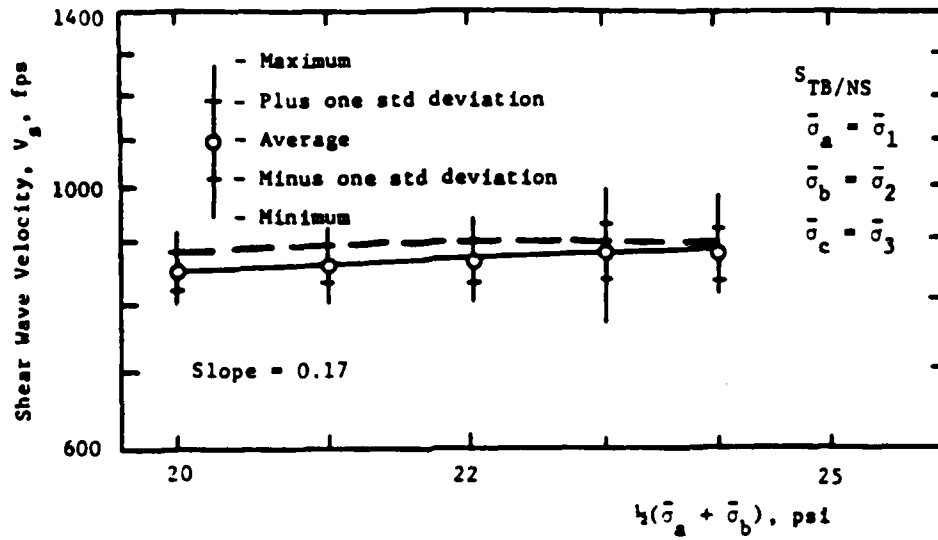
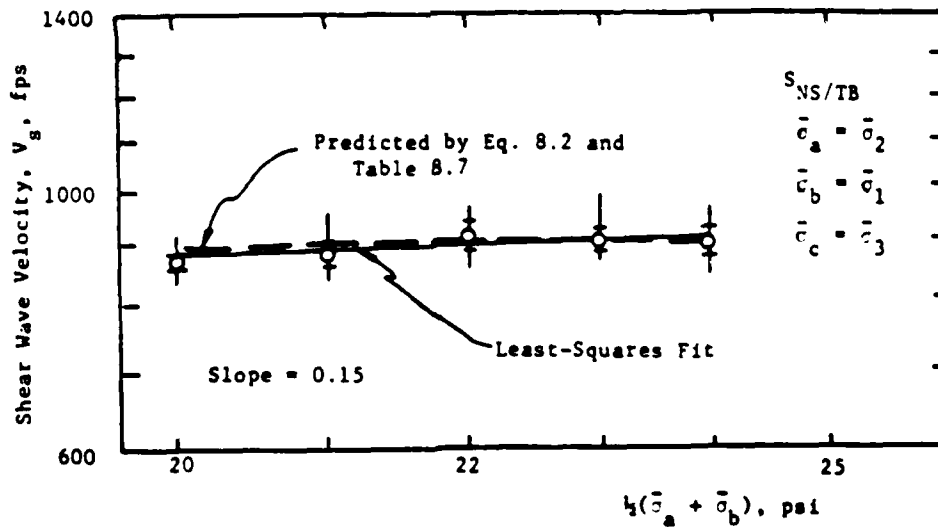
a) For the $S_{TB/NS}$ -Waveb) For the $S_{NS/TB}$ -Wave

Fig. 2.10 - Variation of Shear Wave Velocity with Directions of Wave Propagation and Particle Motion for TB-NS Plane of Motion for Triaxial Confinement with a Constant $\bar{\sigma}_0$ (from Knox, et al, 1982)

$$V_s = C [(\bar{\sigma}_a + \bar{\sigma}_b)/2]^{nt} \quad (2.55)$$

where nt is the slope for the $\log V_s \log [(\bar{\sigma}_a + \bar{\sigma}_b)/2]$ relationship. Yu and Richart (1984) employed the resonant column method to test the dry sand under biaxial loading and extended their data to the range of large shearing strains. The "average-stress" method was preferred in their report as shown in Fig. 2.11. For convenience in comparisons, the equation for shear modulus in their report was transformed to one for shear wave velocity as:

$$V_s = C p_a^{0.25} [(\bar{\sigma}_a + \bar{\sigma}_b)/2]^{0.25} (1 - 0.32K_{13}^{1.7})^{0.5} \quad (2.56)$$

According to Hook's law, however, the stress component in the out-of-plane direction ($\bar{\sigma}_c$) should be considered for a more precise value of shear wave velocity. The shortcomings of the "mean-effective-stress" method and the "average-stress" method is discussed in Chapter Seven along with the "three-individual-stresses" method. For a practical standpoint, Stokoe et al (1985b) agreed with the "two-individual-stresses" method as a result of tests in the large-scale triaxial device.

The anisotropy of rock has long been recognized by researchers (Adams and Williamson, 1923; Tocher, 1957; Brace, 1960; and Podio, 1968). Because confining pressures used in rock testing typically exceed those used in soil testing by orders of magnitude, most stress-induced anisotropy has been attributed to the closure of microcracks (Nur, 1971; Nur and Simmon, 1969). Therefore, test results on rock are not be compared herein with results from soil tests.

Shear wave velocity has also been related to depth (D) or effective overburden pressure ($\bar{\sigma}_v$) in geophysics. Toki (1969) developed the following theoretical relation between shear wave velocity V_s , porosity n , and effective overburden pressure $\bar{\sigma}_v$ as:

$$V_s^2 = A(n_{\max} - n)\bar{\sigma}_v^{0.5} \quad (2.57)$$

where V_s is in fps, and $\bar{\sigma}_v$ is in psi. The constant, A , is equal to 5.7×10^5 as determined by ultrasonic pulse tests performed in a triaxial compression device. Hamilton (1971) collected in situ information from on-land and offshore S-wave velocity studies. With twenty-nine selected in situ

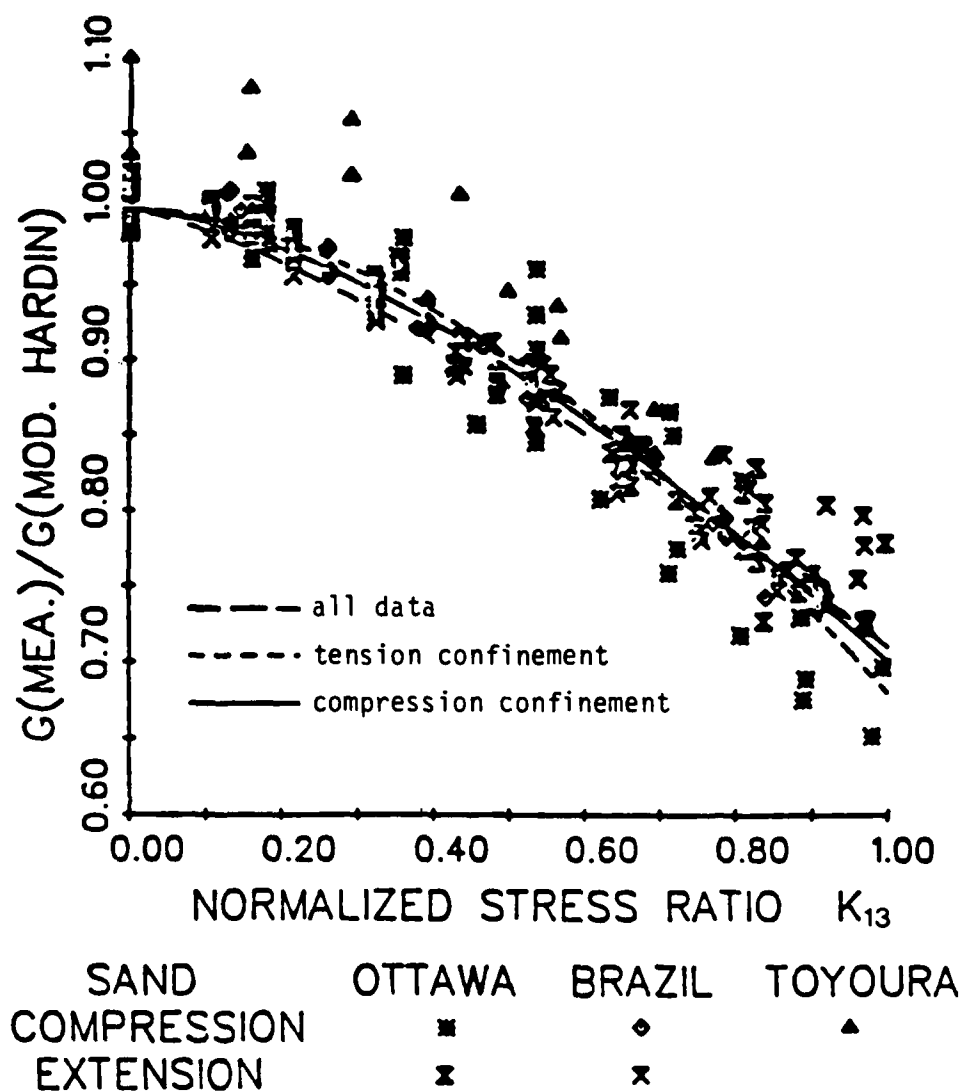


Fig. 2.11 - Variation of Normalized Small-Amplitude Shear Modulus with Normalized Stress Ratio K_{13} Using the "Average-Stress" Method (from Yu and Richart, 1984)

measurements of shear wave velocity, Hamilton (1971 and 1979) suggested an equation for V_s from a regression analysis as:

$$V_s = 128 D^{0.28} \quad (2.58)$$

where D is depth in ft, and V_s is in fps. Ohta and Goto (1978) considered geologic age, depth, soil type, and standard penetration resistance as factors for developing an equation for shear wave velocity. For sand, assuming V_s only a function of depth, they suggested:

$$V_s = 232.5 D^{0.308} \quad (2.59)$$

where V_s is in fps, and D is in ft. Equation 2.60 was suggested by Fumal (1978) for sand with the same units as in Eq. 2.59:

$$V_s = 471 D^{0.20} \quad (2.60)$$

Sykora and Stokoe (1983) presented two equations relating in situ shear wave velocity to both total and effective overburden pressure (σ_v and $\bar{\sigma}_v$, respectively) for sands as:

$$V_s = 790 \sigma_v^{0.30} \quad (2.60)$$

$$V_s = 720 \bar{\sigma}_v^{0.36} \quad (2.61)$$

where V_s is in fps, and σ_v and $\bar{\sigma}_v$ are in tsf and less than or equal to 10.0 tsf (10.0 Kg/cm²).

It should be noted that the overburden pressure is usually the major principal stress in normally consolidated soils and the state of stress is not isotropic. In addition, the density of soil is usually increasing with depth, i.e., the void ratio decreases as depth increases. Consequently, the exponent in the $V_s - D$ relationship from in situ measurement may be larger than that predicted from laboratory measurements. This point is demonstrated by noting that values of the exponent of the effective overburden pressure (0.25 to 0.36) determined from in situ seismic surveys are slightly higher

than those values determined from the summation of n_a , n_b , and n_c (0.17 to 0.25) from most laboratory tests.

A summary of previous work on sand under anisotropic stress conditions is listed in Table 2.4. Test results in this study are presented and discussed in Chapters Six and Seven.

2.4 SUMMARY

The theory of wave motion in an isotropic space yields one compression wave velocity and one shear wave velocity. Once these wave velocities are measured, values of dynamic constrained modulus (M), shear modulus (G), Young's modulus (E), and Poisson's ratio (ν) can then be determined. However, for nearly all level soil deposits, either inherent or stress-induced anisotropy exists. This anisotropy results in (at least) two compression wave velocities and two shear wave velocities present for wave measurements along principal stress directions. The material model which best describes this condition is known as a cross-anisotropic model. The four wave velocities are related to four of the five independent constants required to describe a crossanisotropic model, i.e., C_{11} , C_{33} , C_{44} , and C_{66} . Therefore, any simple equation relating shear modulus or shear wave velocity to the mean effective stress, like Eq. 2.51, cannot reflect the anisotropy of the material. The intent of this study is to develop a rational equation relating anisotropic stress state and shear wave velocity.

Stress-induced anisotropy may cause an isotropic medium to behave as a cross-anisotropic material. This is one of the main reasons for the discrepancy between measured values of V_s and values predicted by the "mean-effective-stress" method as shown in Sections 2.3.5 and 2.3.6. As such, a "three-individual-stresses" method is employed in this study as compared to the "mean-effective-stress" method or the "average-stress" method as discussed in Chapter Seven.

The fifth constant, C_{13} , of the cross-anisotropic medium theoretically can be estimated from velocities of either oblique P-waves or oblique S-waves. Oblique P- and S-wave velocities are a function of the angle θ between the axis of symmetry and the direction of the wave normal as discussed in Section 2.3.1. (A mathematical limitation for C_{13} may be used for checking the measured value of C_{13} .) Three wave fronts, one for the P-wave and two for S-waves, exist in a cross-anisotropic material. The

Table 2.4 - Summary of Values of the Slope of the S-Wave Velocity-Confining Pressure Relationships for Dry Sand Under Anisotropic Confinement.

Reference	na*	nb*	nc*	nm**	nt***	nd	Remark [∇]
Lawrence (1965)+	0.06- 0.16	0.08- 0.17	----	0.25	----	----	2
Hardin and Black (1966)+	0.11- 0.13	0.13- 0.14	----	0.25	----	----	1
Toki (1969)	----	----	----	----	----	0.25	3a
Hamilton (1971)	----	----	----	----	----	0.28	1
Kuribayashi, et al (1975)	----	----	----	0.25	----	----	1
Ohta and Goto (1978)	----	----	----	----	----	0.308	3b
Campbell and Duke (1976)	----	----	----	----	----	0.386 0.358	3d 3e
Fumal (1978)	----	----	----	----	----	0.20	3c
Iwasaki, et al (1978)	----	----	----	0.25	----	----	1
Schmertmann (1978)	0.09- 0.12	----	----	0.47- 0.19	----	----	4
Tatsuoka, et al (1979)	----	----	----	0.25	----	----	1
Roesler (1979)	0.149	0.107	0	----	----	----	5
Uchida, et al (1980)	----	----	----	0.25	----	----	1
Knox, et al (1982)	0.10 0.12	0.09 0.11	0.01 ----	0.20- 0.24	0.18- 0.24	----	6□ 6□□

(see notes on next page)

Table 2.4 (cont.) - Summary of Values of the Slope of the S-Wave Confining-Pressure Relationships for Dry Sand Under Anisotropic Confinement.

Reference	na*	nb*	nc*	nm**	nt***	nd	Remark [∇]
Allen and Stokoe (1982)	0.12	0.11	----	0.24	0.24	----	1
Sykora and Stokoe (1983)	----	----	----	----	----	0.30 0.36	3a 3b
Yu and Richart (1984)	0.12- 0.14	0.11- 0.14	----	----	0.25	----	1
Stokoe, et al (1985)	0.10 0.09	0.10 0.09	0 0	----	0.20 0.18	----	6□ 6□□
Stokoe and Ni (1985)	0.11	0.11	----	0.22	----	----	1
Lew and Campbell (1985)	0.28- 0.40	----	----	----	----	0.30	3b

∇ 1: Resonant Column Test

∇ 2: Pulse Test (Small Cylindrical Sample)

∇ 3: In-Situ Test

∇ 4: Pulse Test (Cylindrical Chamber)

∇ 5: Pulse Test (Medium Cubical Sample)

∇ 6: Pulse Test (Large-Scale Triaxial Device)

□ parameter for V_{SI}

□□ parameter for V_{SA}

+ data or slopes, na and nb,
reduced in this study

---- not applicable

$$*V_s = C_2 \bar{\sigma}_a^{na} \bar{\sigma}_b^{nb} \bar{\sigma}_c^{nc}$$

$$**V_s = C_2 \bar{\sigma}_o^{nm}$$

$$***V_s = C_2 [(\bar{\sigma}_a + \bar{\sigma}_b)/2]^{nt}$$

a..... $V_s = C_2 \sigma_V^{nd}$

b..... $V_s = C_2 \bar{\sigma}_V^{nd}$

c..... $V_s = C_2 D^{nd}$

d..... Equation c for
recent alluvium

e..... Equation c for
older alluvium

shapes of the wave fronts are based on the combination of the five elastic constants. Anisotropy also causes the wave surface to differ from the velocity surface, and a cusp may appear in the wave surface of SV-wave in some conditions. A schematic representation of the variation of wave fronts and the cusp in the SV-wave front are shown in Chapter Nine.

CHAPTER THREE

EXPERIMENTAL EQUIPMENT

3.1 EXPERIMENTAL TECHNIQUE CONSIDERATIONS

Extensive work has been done in the field of dynamic testing of materials. McSkimin (1961), Richart (1975), and Woods (1978) have reviewed the methods developed for the laboratory and field testing. Basically, two types of methods, pulsed and steady-state-vibrations, can be used to determine propagation velocities of body waves or Rayleigh waves.

A steady-state-vibration test can be either a slow cyclic test or one at a resonant frequency. The stiffness of the specimen in the cyclic test is calculated from the relationship between applied stress and measured strain; while the stiffness in the resonant test is usually obtained from a wave equation with the appropriate boundary conditions. The most common types of steady-state-vibration tests used in the laboratory to measure the dynamic behavior of soils are: (1) cyclic triaxial tests with stress control (Murahama and Shibata, 1960; and Seed and Lee, 1966), or with strain control (Taylor and Hughes, 1965; and Thiers and Seed, 1969), (2) cyclic simple shear tests with the Norwegian Geotechnical Institute's (NGI) device (Kjellman, 1951) or the Cambridge University apparatus (Roscoe, 1953), (3) cyclic torsional shear tests (Hardin and Drnevich, 1972; and Yoshimi and Oh-Oka, 1973), and (4) resonant column tests with isotropic confinement (Ishimoto and Iida, 1936; Hardin, 1961; and Drnevich, 1972), or with anisotropic confinement (Hardin and Music, 1965; and Allen and Stokoe, 1982).

In laboratory pulse tests, the time (or time delay) for a disturbance at one point within a sample to travel to a detecting sensor at a second point is used to estimate wave velocity. Specimen stiffness is then calculated from the velocity (Hughes and Cross, 1951; and Wyllie, Gregory, and Gardner, 1956). Paterson (1956) and Lawrence (1963) used piezoelectric crystals or ceramics to generate and detect disturbances in a traditional triaxial cell. Schmertmann (1978) generated pulsed P- and S-waves by striking a rod with a ball and with a scissor-type wave generator in a test chamber. A DC motor exciter buried in a 30 cm x 30 cm x 30 cm cubical sample was used to generate S-waves by Roesler (1979). Knox, et al (1982) constructed a large-scale triaxial device in which cubical samples measuring 7 ft (2.1 m) on a side were loaded in true triaxial states of stress. Pulsed P- and S-waves were successfully measured by the accelerometers buried inside the cubical sample.

A critical-angle method was employed by Jeffreys (1926), Aremberg (1948), and Gregory (1967) for generating pure shear waves, and by Van Stevenink (1967), and Gregory and Podio (1970) for exciting either compression or shear waves in rock tests.

For in situ tests, the steady-state-vibration technique has been used to measure the transmission of Rayleigh waves at soil sites (Fry, 1963 and 1965). The phase difference between two peaks of wave motion are used to calculate the surface wave velocity. However, this technique has seen limited use because of the expense and size of the source needed to sample depths greater than about 50 ft (5 m).

Numerous pulsed testing techniques are utilized in field testing. One or more boreholes are necessary depending on the methods such as (1) refraction prospecting (Gardner, 1939; and Richart, et al 1970), (2) reflection surveying (Dix, 1955), (3) crosshole tests (Stokoe and Woods, 1972; Stokoe and Hoar, 1978a; and Ballard, et al 1983), (4) downhole tests (Jolly, 1956; and Hoar and Stokoe, 1978), (5) uphole tests (Meissner, 1961; and Kovalex and Molotova, 1960), (6) in-hole tests or sonic logging (Carroll, 1966; and Ogura, 1979), (7) bottom-hole tests (Stokoe, et al 1978; Arnold, 1981; and Olson and Stokoe, 1983), and (8) the "Spectral-Analysis-of-Surface-Waves" (or SASW) method (Heisey, 1982; and Stokoe and Nazarian, 1983).

Steady-state-vibration methods are used to generate small-strain waves in field testing and either small- or large-strain vibrations in laboratory testing. The pulsed methods are usually used to excite small-strain vibrations in both laboratory and field testing. Recently, two methods, called the in situ impulse test and the cylindrical in situ test (CIST), were employed to conduct large-strain in situ pulsed testing (Troncoso, 1975; Wilson, et al 1978; Air Force Weapons Laboratory, 1977; and Bratton and Higgins, 1978).

The threefold purpose of this study is to examine: (1) the effect of stress state on shear wave velocities, (2) the influence of structural anisotropy on shear wave velocities, and (3) the importance of items (1) and (2) in in situ testing. To perform such research, it is necessary to have a true triaxial device with which polarized seismic waves can be generated. The device should accommodate a large specimen so that the structural composition of deposited soil can be reflected and so that seismic tests can be conducted in a manner similar to field seismic testing. Some true

triaxial devices have been used to investigate the constitutive laws of soil (Kjellman, 1936; Ko and Scott, 1967; and Lade and Duncan, 1973). Nonetheless, all of these devices use small samples (less than 4 in. (10 cm) on a side), and the tests are conducted only statically or very slowly cyclically (30 seconds in a period). Both isotropic and biaxial resonant column apparatus measure only the secant shear modulus rather than tangent shear modulus. The large-scale triaxial testing devices developed by Stokoe, et al (1980) is the best apparatus for this research. The principal stresses can be controlled individually to obtain isotropic, biaxial, or triaxial confinement conditions. A careful arrangement of sensors (see Section 3.3.1) allows crosshole tests to be simulated in this device. The excitation ports can be used to generate polarized waves which is very important in identifying the initial arrival of the shear wave (Jolly, 1956; Ballard and Leach, 1969; and Stokoe and Hoar, 1978b).

3.2 LARGE-SCALE TRIAXIAL DEVICE

3.2.1 STRUCTURE OF THE DEVICE

A large-scale triaxial device (LSTD) was designed and constructed during 1980 and 1981 under the sponsorship of a grant from the United States Air Force Office of Scientific Research (AFOSR) (Kopperman et al, 1982). The triaxial testing device is a reinforced steel box with interior dimensions of 7 ft (2.1 m) on a side. A sketch of the device is shown in Fig. 3.1, and a picture of the device is shown in Fig. 3.3. Figure 3.2 shows the equipment associated with the device for: (1) placing sand into the device, (2) pressurizing the sand mass to the desired stress state, (3) generating compression or shear waves in the sand mass, (4) monitoring and digitally recording these waveforms, and (5) monitoring stress and strain throughout the sand sample during testing.

Axes perpendicular to the walls of the device represent principal stress directions. Membranes (water pressure bags) were used to apply independent pressures in each of the three principal directions. Each membrane has two ports to fill up or drain the water. The membranes were placed on top and on two adjacent sides (north and west sides) of the device. (The other three walls of the device had no membranes because excitation ports existed in these walls.)

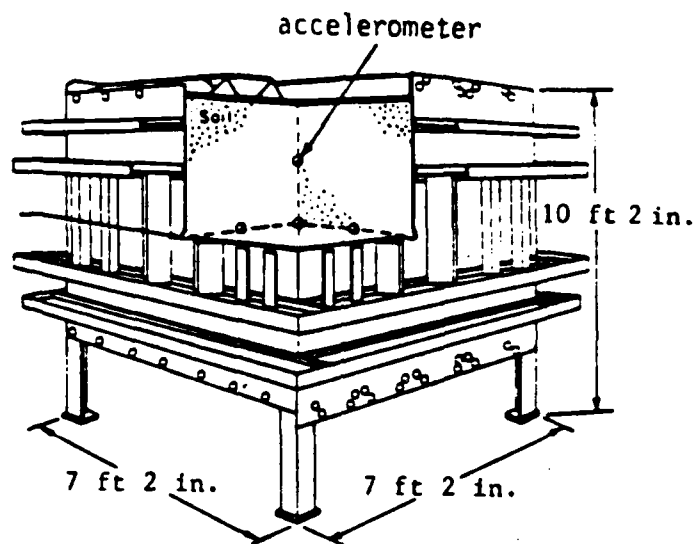


Fig. 3.1 - Cut-Away, Isometric View of Large-Scale Triaxial Device

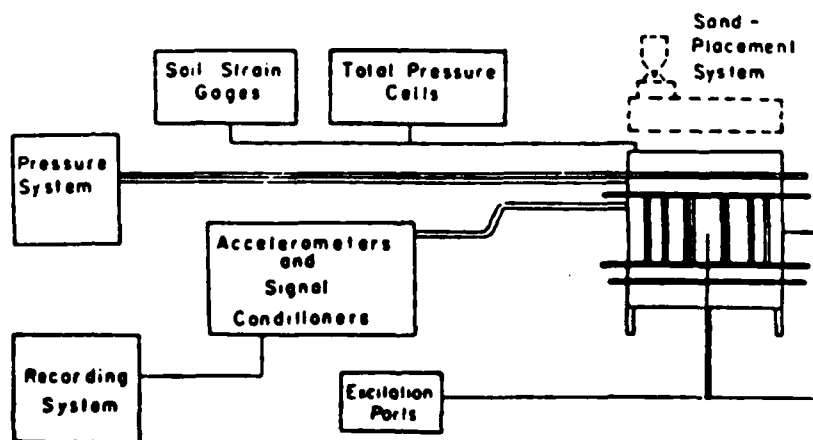


Fig. 3.2 - Schematic Diagram of Large-Scale Triaxial Device and Associated Systems



Fig. 3.3 - Side View of Large-Scale Triaxial Device
(with Shannon H.H. Lee standing beside it)

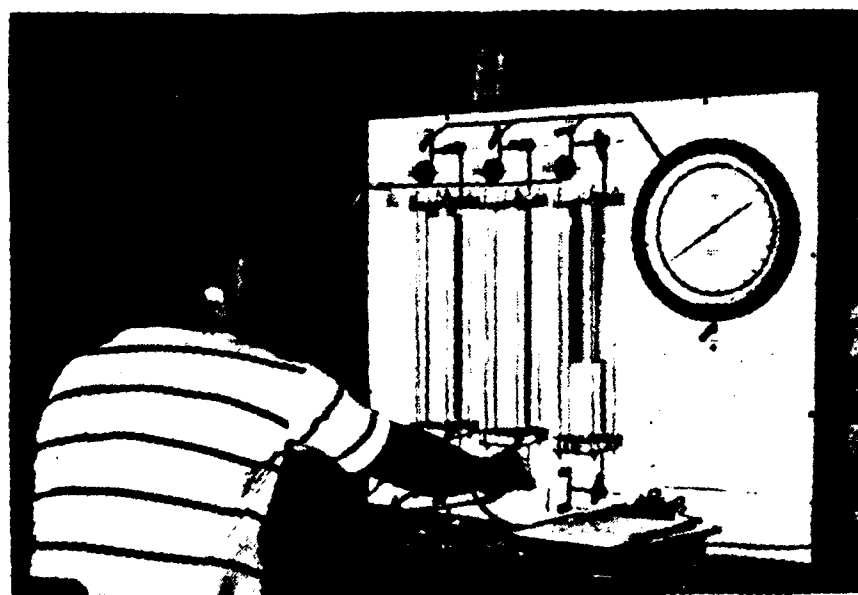


Fig. 3.4 - Panel Board Used to Pressurize Membranes
in Large-Scale Triaxial Device

When the membranes are full of water, air pressure from the building air supply is used to pressurize the membranes. The air pressure is monitored using air regulators together with a 12-in (30.5 cm) diameter, Heise type CM pressure gauge (accurate to within ± 0.1 percent of the full-scale reading). A picture of the control panel is shown in Fig. 3.4 and a schematic drawing of the pressurizing system is shown in Fig. 3.5.

3.2.2 RAINER USED TO PLACE SAND

To place sand into the LSTD in a more uniform state, a new raining device was designed and constructed. The rainer is simply a plywood box about 7.25 ft (2.18 m) long, 1.75 ft (0.53 m) wide and 1.5 ft (0.45 m) deep which can be rolled back and forth across the top of the device. Four rows of 0.75-in. (1.91-cm) diameter holes and four trap doors have been constructed as shown in Fig. 3.6. A steel frame, welded with two 3.42-ft (1.04-m) long angle iron (L 3 x 3) which are fixed with four heavy-duty castors, was used to support the box while moving along rails on a wooden collar around the LSTD as shown in Fig. 3.7. A level-arm system controls the flow rate of sand through the trap doors as illustrated in Fig. 3.8. A 0.25-in. x 0.25-in. (6.4 mm x 6.4 mm) wire mesh screen was hung below the rainer to act as a dispersing screen to help make the placing of sand particles as random a process as possible. Foreign materials like grass and gravel are also kept from becoming part of the sand sample by the screen.

A uniform sand sample was obtained by controlling the drop height of the sand particles (Kilbuszewski, 1948; and Beiganousky and Marcusson, 1976). This was accomplished with the same wooden collar made by Knox and Kopperman. However, the collar was reinforced with angle iron (L 2 x 2) along the four vertical edges (see Fig. 3.7). The height of the collar is 3 ft (0.9 m). Hence, the drop height of the sand ranged from 9.5 ft (2.9 m) at the start of raining to 2.5 ft (0.76 m) at the conclusion.

With the new rainer, the density of the sand specimen increased by about 6 percent relative to the earlier test (see Section 4.2), and the specimen was more uniform with a maximum variation in density of less than 6.3 percent.

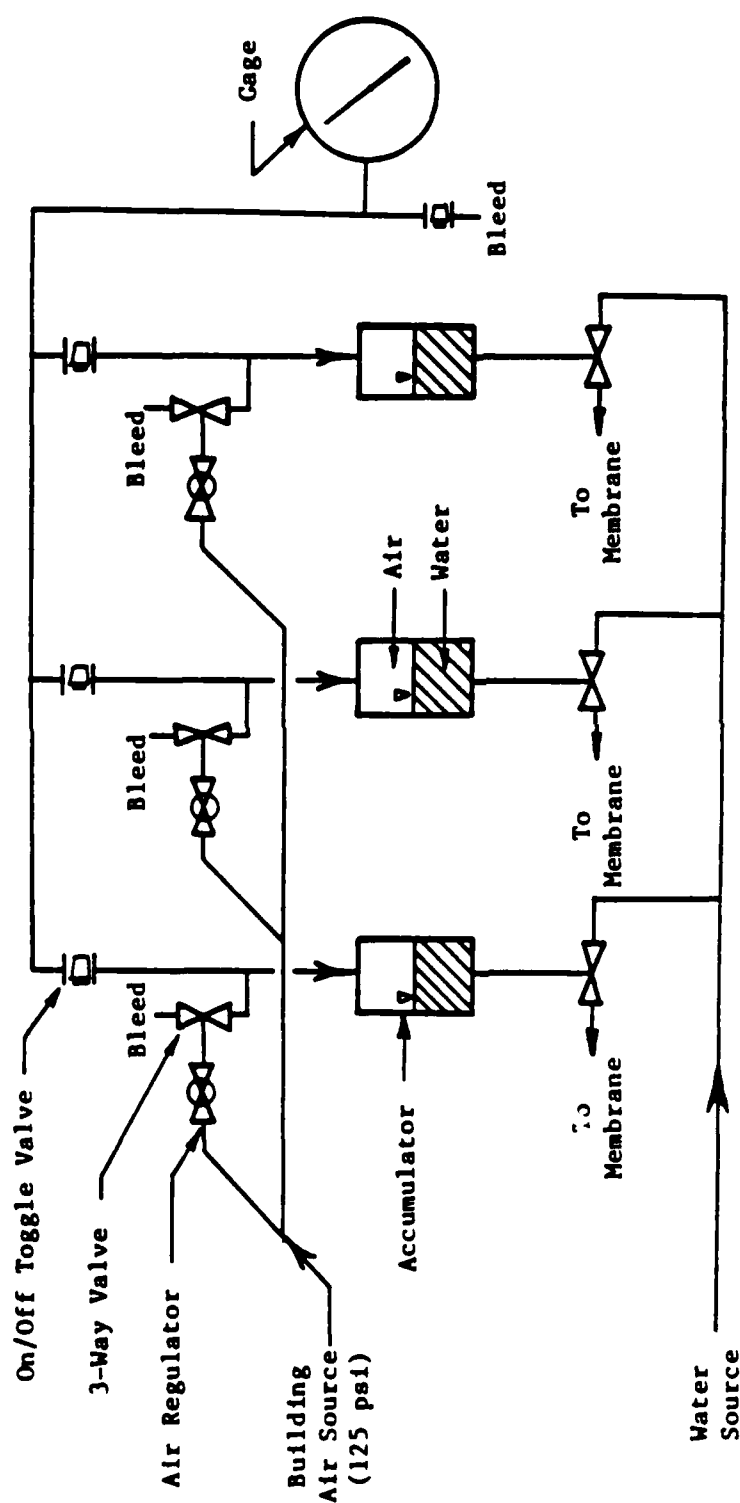


Fig. 3.5 - Schematic Diagram of Air/Water System Used to Pressurize Membranes (from Kopperman et al, 1982)

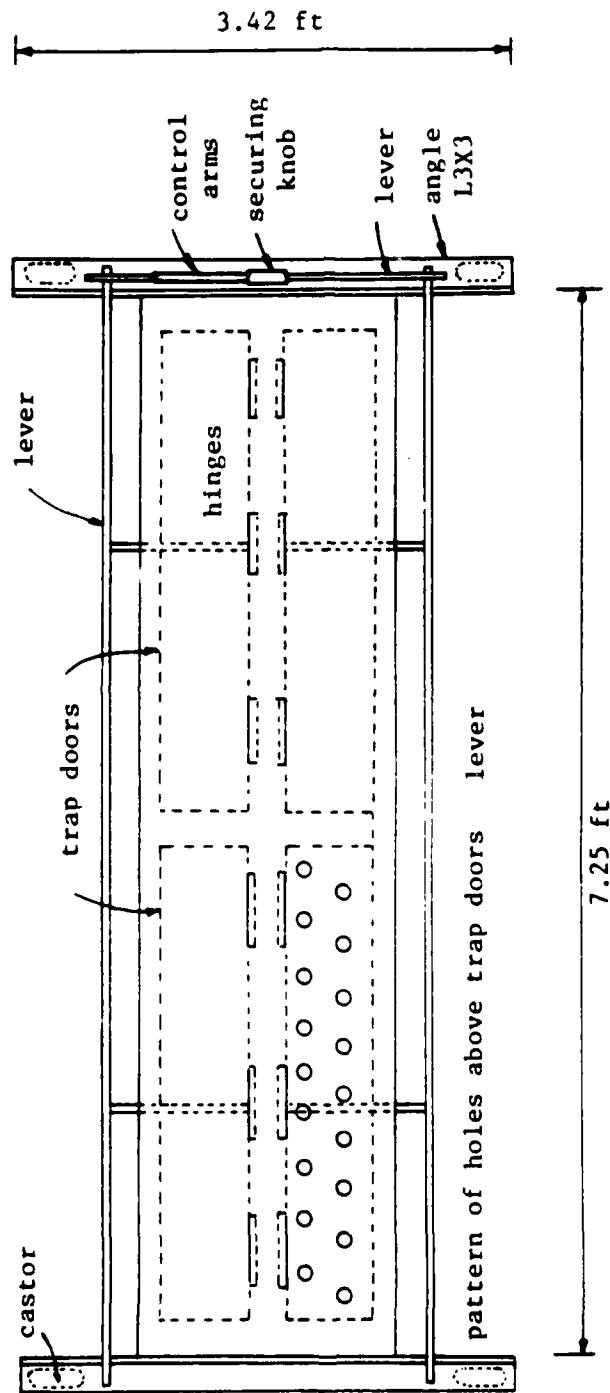
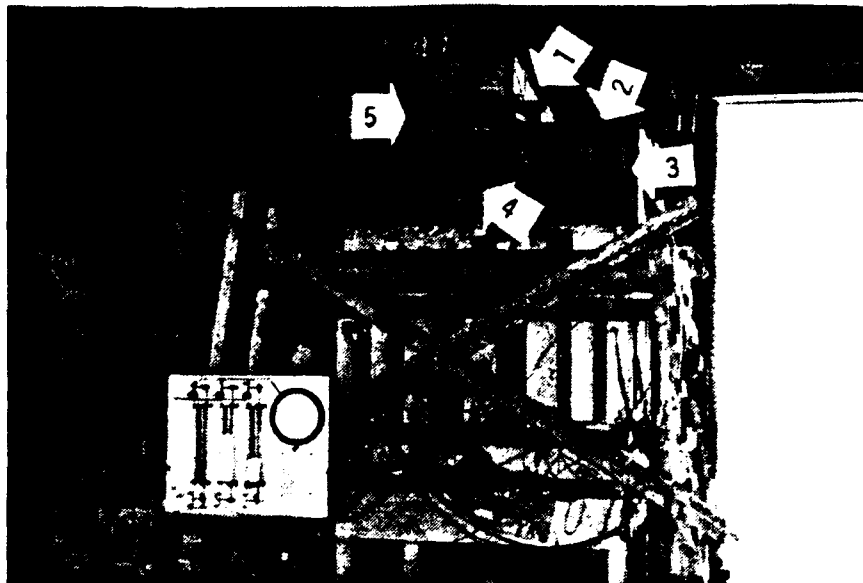


Fig. 3.6 - Top View of New Rainer (from Chu et al, 1984)



- Legend:
1. Steel framework of the new rainer
 2. Rail along which rainer travels
 3. Angle irons (L2x2) along the corners of the wooden collar
 4. Wooden collar
 5. Castor of rainer

Fig. 3.7 - View of New Rainer Loaded with Sand and Ready for Raining Process



- Legend:
1. New rainer
 2. Control arm (see Fig. 3.6)
 3. Lever connection to trap doors
 4. Wire mesh used as dispersing screen

Fig. 3.8 - Raining Sand into the LSTD Using New Rainer

3.2.3 EXCITATION PORTS

To generate body waves in the sand, excitation ports were constructed on three sides of the LSTD (south, east and bottom). A typical port is shown in Fig. 3.9. Compression waves were generated by striking the top surface of the anvil. Shear waves were generated by either horizontally or vertically striking the anvil shaft. The striking locations are shown in Fig. 3.9b. A clamping tool was added to each excitation port as shown in Fig. 3.9 so that the anvil would be firmly fixed to the external frame in the wall of the LSTD during construction of the sample in order that the anvil would be kept properly aligned and a sand leakage would be prevented. A completed port during sample construction is shown in Fig. 3.10. Once the sample was constructed, the clamping tool was removed, and body waves were generated by striking the anvil as illustrated in Fig. 3.11 for an SV-wave.

Strain gages mounted to the thin plate of the external frame of the excitation port (at locations "a" and "b" in Fig. 3.9) were used to adjust the contact pressure of the anvil. These strain gages (type EA-06-500BL-350) and associated installation aids were made by the Micro-Measurements Division of the Measurements group of Rayleigh, North Carolina. The strain gages were arranged as a potentiometer circuit with temperature compensation (Dolly and Riley, 1978). The relation between strain and resistance change for these gages is:

$$\epsilon = (1/F) \cdot (\Delta R/R) \quad (3.1)$$

where:

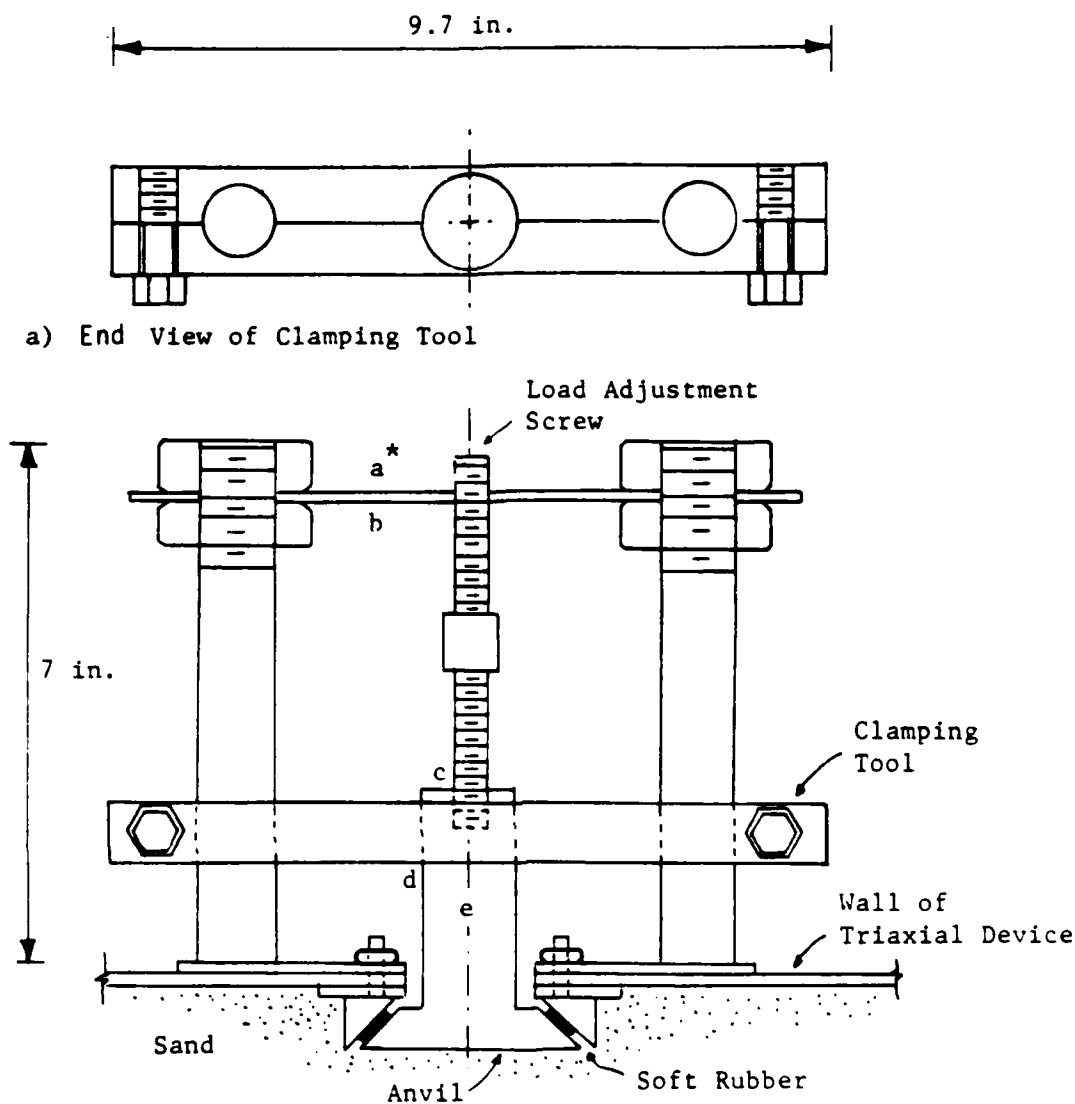
ϵ = strain in microstrains (10^{-6} cm/cm),

F = gage factor,

ΔR = change in resistance in ohms, and

R = gage resistance in ohms.

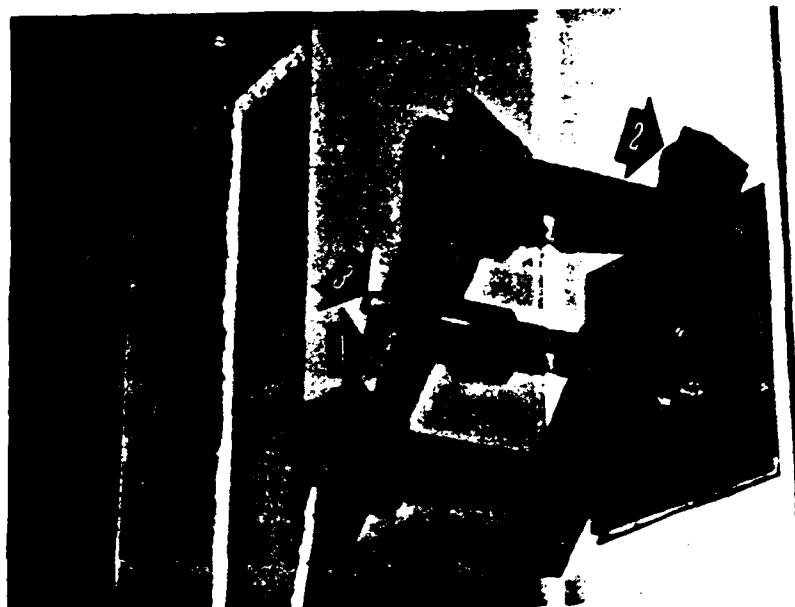
A strain indicator was used to read off the resulting strains. Silicone rubber was placed over the gages to protect them from environmental moisture and dirt. The strain gages were calibrated in terms of pressure with the calibration set-up shown in Fig. 3.12. Final calibration curves for two ports are shown in Fig. 3.13 and 3.14. The reading for 40 psi (metric) was obtained by linear extrapolation since only a 300-lb (136.4 kg) load cell was available and the calibration curve appeared linear.



Note:

1. *a and b are locations where strain gages are mounted on the surface of the thin plate
 2. c is location of striking for compression waves
 3. d and e are locations of striking for shear waves
- b) Top View of Excitation Port with Clamping Tool in Place

Fig. 3.9 - Excitation Port with Clamping Tool
(from Chu et al, 1984)

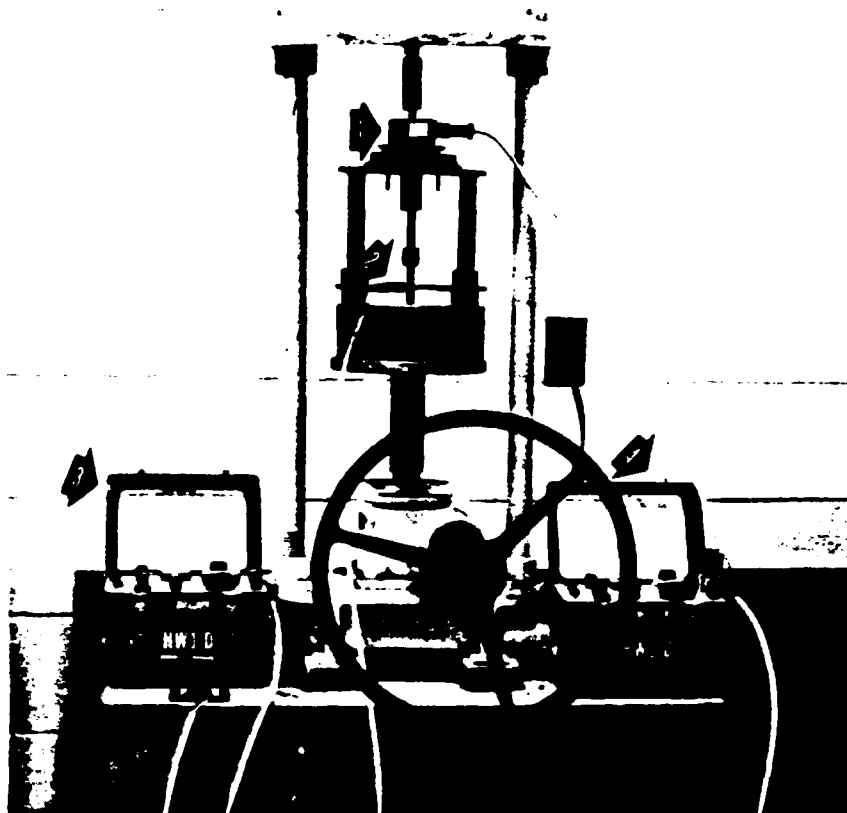


- Legend: 1. Strain gage
2. Clamping tool
3. Load adjustment screw
4. Location of striking for P-Waves

Fig. 3.10 - Completed Excitation Port in Place
(from Chu et al, 1984)



Fig. 3.11 - Generation of SV-Wave at North Excitation Port



- Legend:
- 1. 300-lb load cell
 - 2. Strain gages
 - 3. Strain Indicator for strain gages
 - 4. Strain Indicator for load cell

Fig. 3.12 - Set-Up for Calibrating Strain Gages on Each Excitation Port
(from Chu et al, 1984)

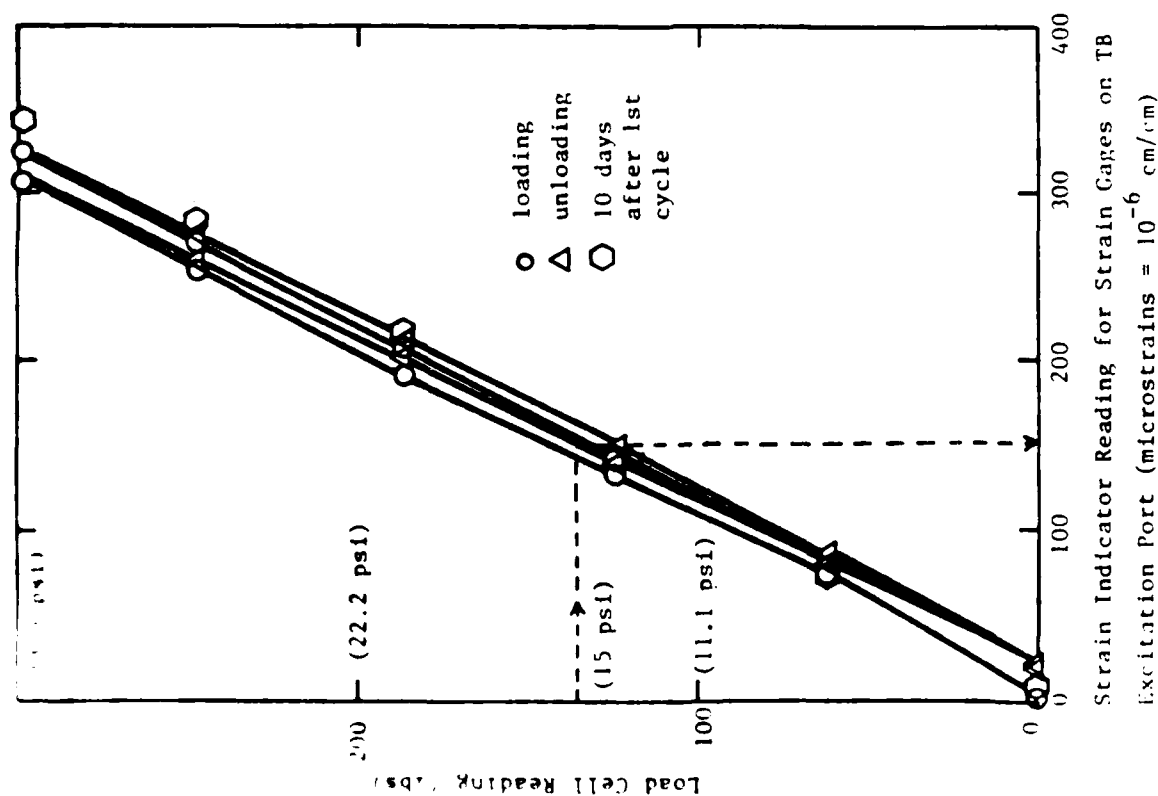


Fig. 3.13 - Calibration Curve for Strain Gages on the Excitation Port along the Z-Direction (from Chu et al, 1984)

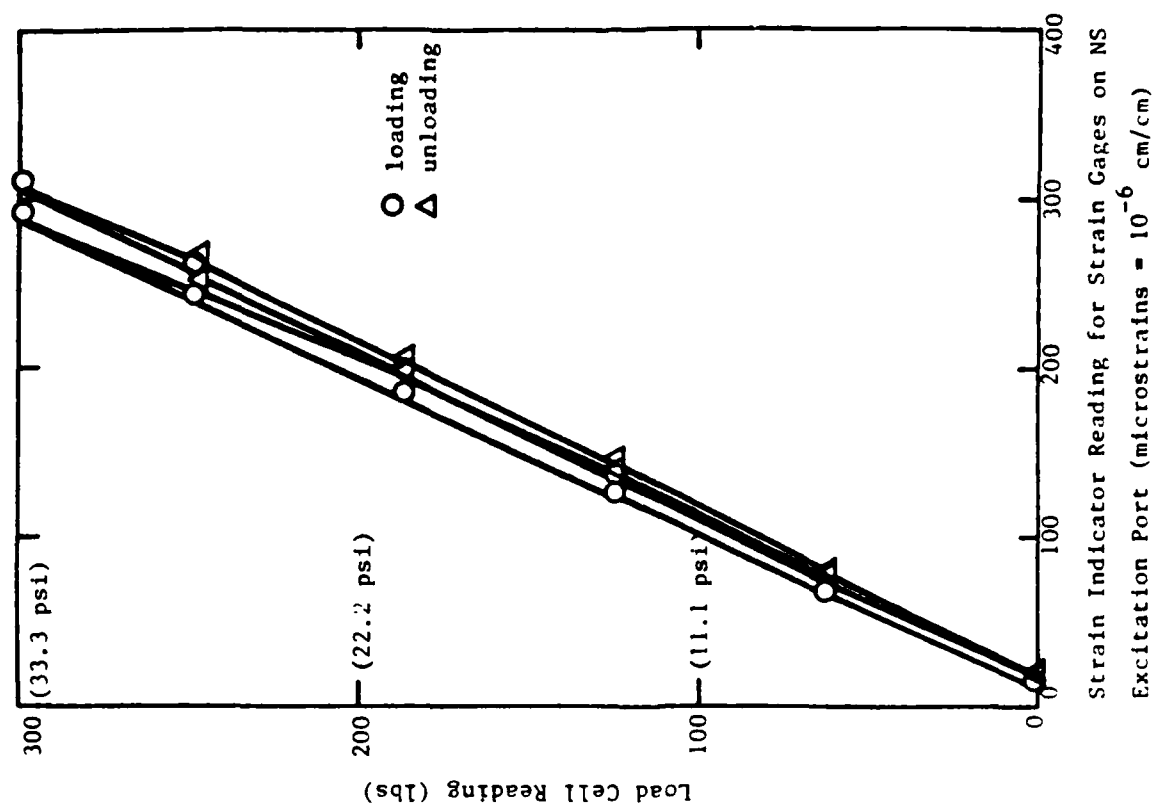


Fig. 3.14 - Calibration Curve for Strain Gages on the Excitation Port along the X-Direction (from Chu et al, 1984)

To study the influence of creep on the strain gages, loads were held for a maximum of ten days as shown in Fig. 3.13. No influence of creep in the strain gages was observed, and, therefore, any creep was neglected in the study.

By tightening or loosening the adjustment screw in each excitation port, the pressure around the anvil was kept equal to the pressure of the membrane. One example is shown that a reading of 152 microstrains in the strain indicator means a 15 psi (103.4 kPa) contact pressure between soil and the port can be reached from the calibration curve in Fig. 3.13.

3.3 MONITORING AND RECORDING SYSTEMS

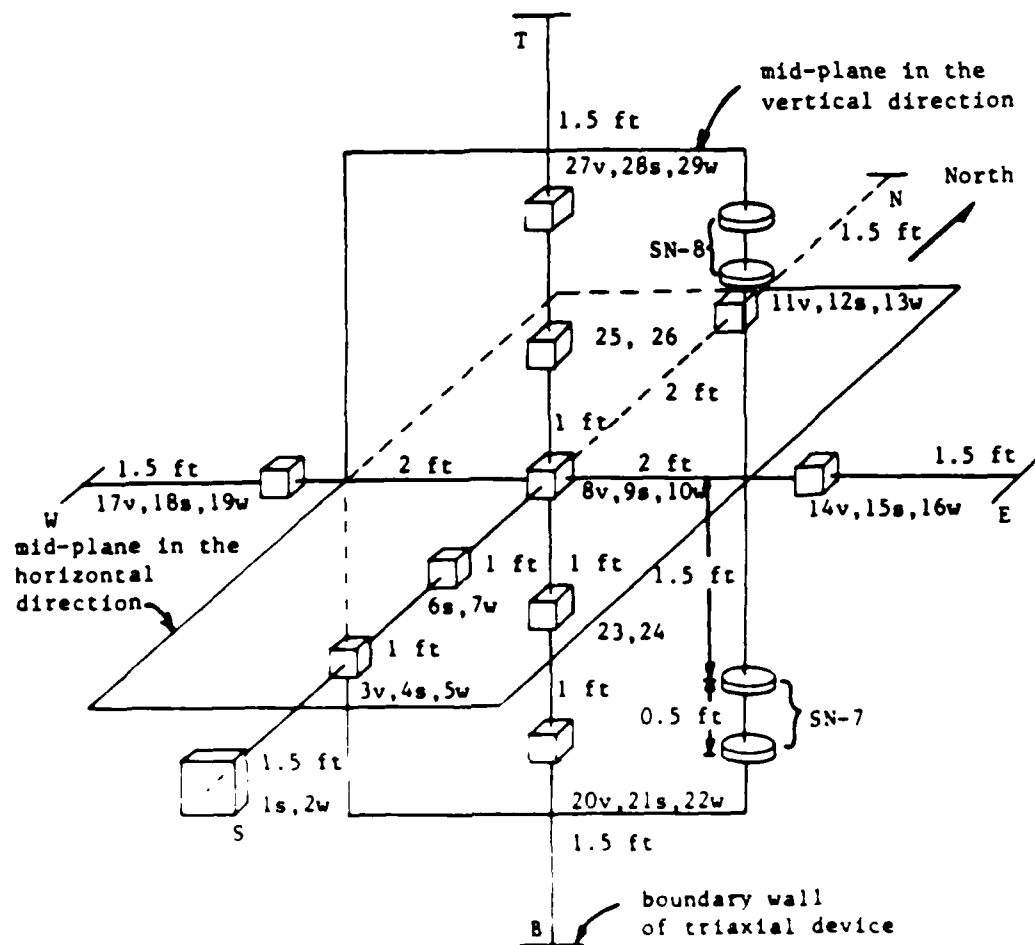
The monitoring and recording systems consisted of 29 accelerometers, 9 charge amplifiers, 8 strain cells, 3 stress cells, and 3 oscilloscopes. All instruments were calibrated before using them.

3.3.1 ACCELEROMETERS

Twenty three Endevco accelerometers, model 7701-100, and six Endevco accelerometers, model 7701-50, were used in this research. The model 7701-100 accelerometers have a typical charge sensitivity of 100 pc/g (10^{-12} coulombs per gravitational acceleration). The model 7701-50 accelerometers have half the charge sensitivity of a model 7701-100, namely 50 pc/g. This variation in charge sensitivity did not affect collection of data since the same full-scale output could be obtained simply by changing the sensitivity dial and full-scale range switch on the charge amplifiers. The six, 7701-50 accelerometers were used in the locations of the first and last 3-D accelerometer packages in the y-axis (east-west direction) shown in Fig. 3.15. From the calibration results, it was found that all accelerometers were functioning satisfactorily with differences between each output less than ± 0.05 percent.

Since the frequency range of the wave signals that could be generated with the hammer taps was generally less than 3000 Hz, both selected accelerometers (7701-100 and 7701-50) with mounted resonance frequency, of 20,000 Hz and 26,000 Hz, respectively, exhibited satisfactorily linear responses (Drantz and Ortiacchio, 1976).

To monitor body waves in principal directions, 3-D accelerometer blocks were designed as shown in Figs. 3.16 and 3.17. The blocks are are 1.5 in



- Legend:
1. NS = north-south principal axis
EW = east-west principal axis
TB = vertical (top-bottom) principal axis
 2. Letter following accelerometer number indicates direction of sensitivity for that particular accelerometer (v=vertical, s=south and w=west)
 3. Accelerometers 23, 25 are 45° to N-S axis
Accelerometers 24, 26 are 22.5° to N-S axis
 4. SN-7, SN-8 are two pairs of $\frac{1}{4}$ in.-diam. strain sensors for vertical strain measurement

Fig. 3.15 - Schematic view of instrumented structure
(from [1], p. 41, 1974)

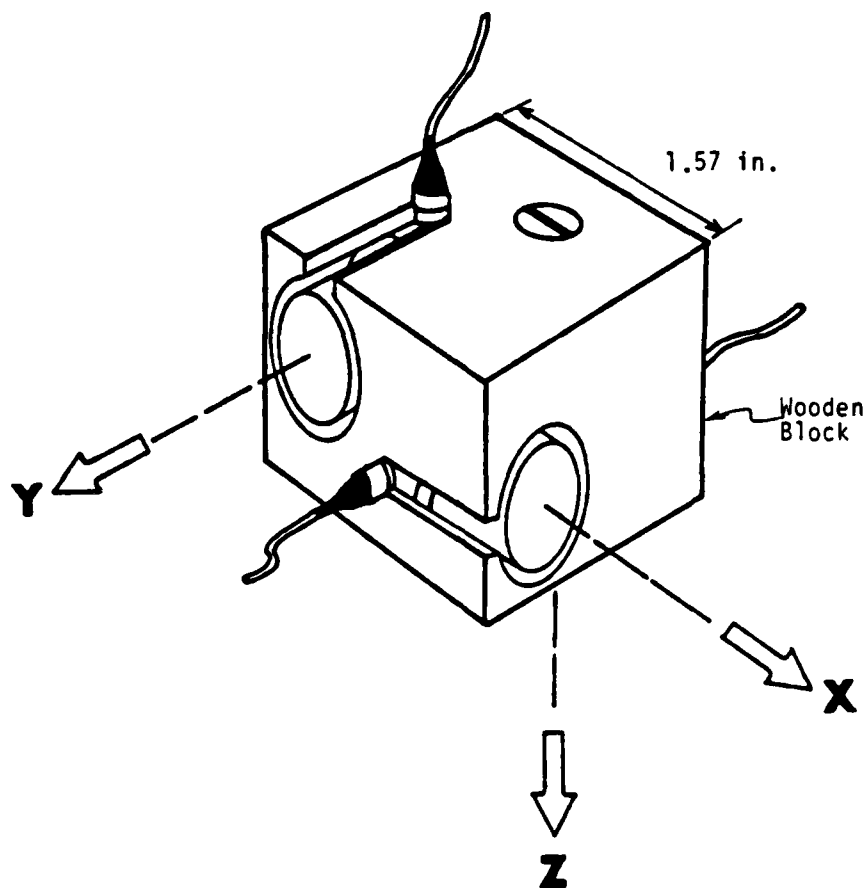


Fig. 3.16 - Isometric View of 3-D Accelerometer Package
(from Kopperman et al, 1982)

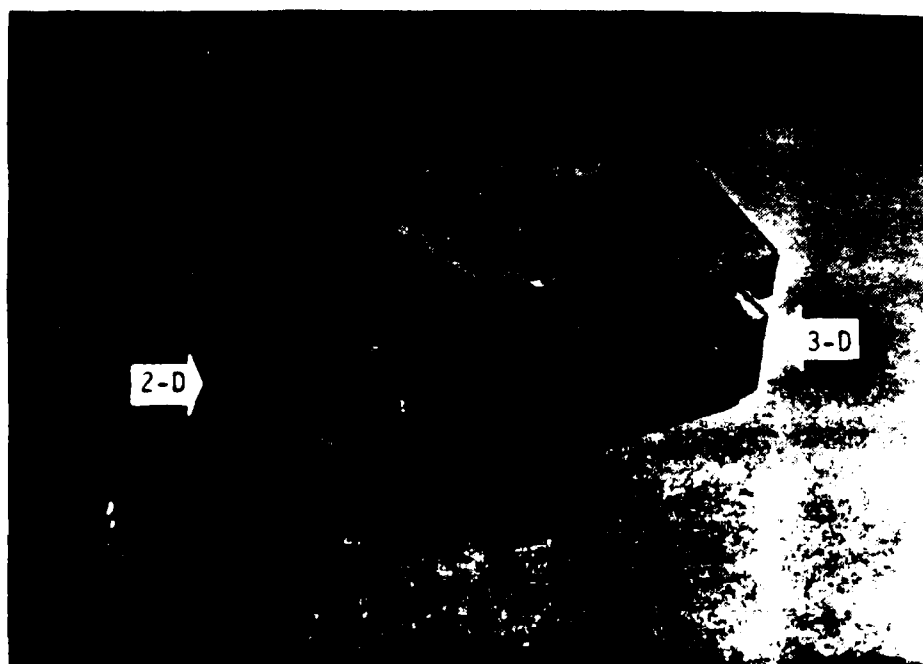


Fig. 3.17 - Two-Dimensional and Three-Dimensional Accelerometer Blocks

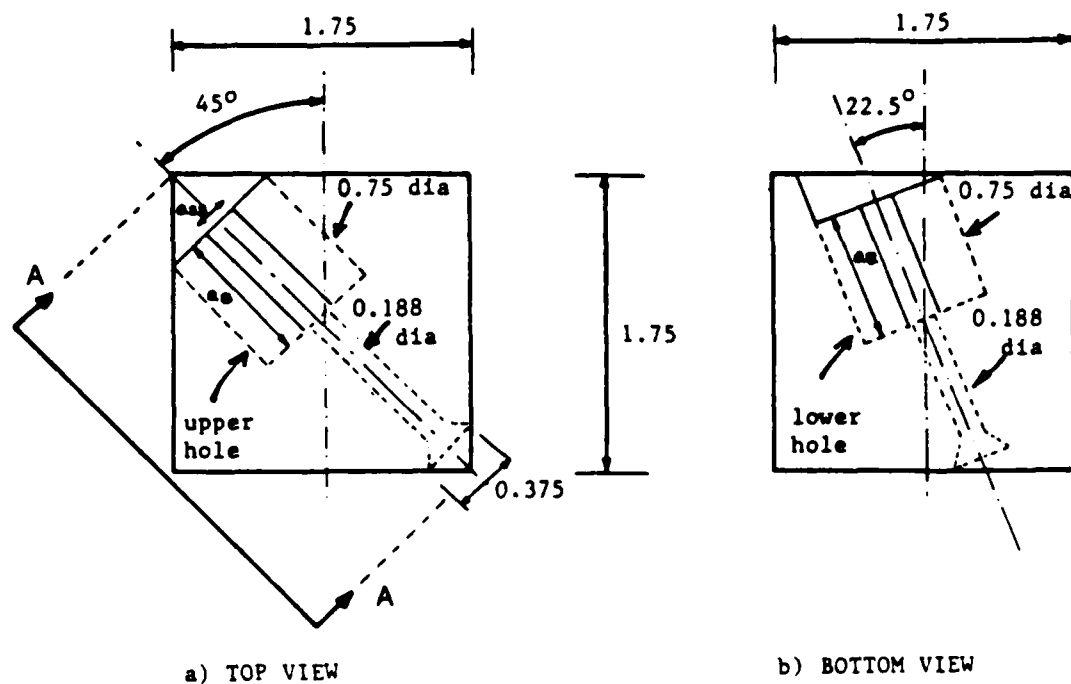
(44-mm) cubical wooden blocks in which three single accelerometers are rigidly attached. These 3-D accelerometer blocks were designed to make the overall unit weight of the block equivalent to that of the sand sample to minimize any impedance mismatch between the sand and the block (Eller and Conrad, 1976). Since the size of the block is generally less than 0.3 times the minimum wavelength of the body waves, the amount of reflected waves and the shadow cast by the inclusion is negligible (Olson, 1967; Suddhiprakarn and Roesset, 1984).

In addition to the 3-D accelerometers, 2-D accelerometers were also constructed. The 2-D accelerometer package is composed of two single accelerometers, at 45- and 22.5-degrees respectively, and is shown in Fig. 3.18. Two, 2-D accelerometer blocks were located in the vertical principal axis to monitor vertically propagating shear waves with particle motions polarized along two planes inclined with respect to the y-axis (east-west direction), a 45-degree plane (numbered 23 and 25 in Fig. 3.15) and a 22.5-degree plane (numbered 24 and 26 in Fig. 3.15). These shear waves are referred to as oblique shear waves hereafter.

A picture of the 3-D and 2-D accelerometer blocks is shown in Fig. 3.17.

One of the 2-D accelerometer blocks was machined from aluminum while the other two were made of Birchwood (the same material as that of the 3-D blocks). The aluminum block is shown in Fig. 3.19. The aluminum block was attached to the excitation port on the south wall of the triaxial device. One accelerometer inside the block was oriented in the north-south direction and the other east-west (accelerometers 1s and 2w, respectively, in Fig. 3.15). Two more accelerometers oriented in the same relative directions (accelerometers 6S and 7W in Fig. 3.18) rigidly attached to a 3-D wooden block, were located 2.5-ft (1.07 m) away from the aluminum block along the north-south principal direction. These accelerometers were also included for use in an attenuation study. Based on the finite element model analysis, the influence of the block is negligible at this distance (Suddhiprakarn and Roesset, 1984).

The location of all 2-D and 3-D accelerometer blocks with the associated numbers and part of strain sensors are shown in Fig. 3.15. This arrangement is designed to monitor compression and shear waves propagating in the three principal directions and oblique shear waves propagating in the vertical direction.



Note: All dimensions are in inches

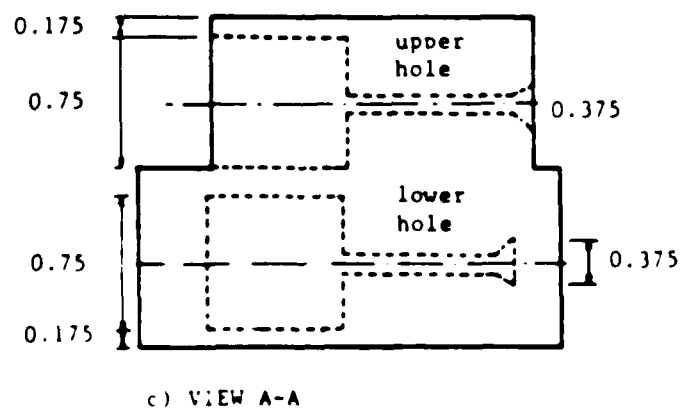


Fig. 3.18 - A piezometer Block Used to Monitor Oblique Shear
Wells (from Chu et al., 1984)

A complete list of distances between each pair of receivers is summarized in Table 3.1.

3.3.2 CHARGE AMPLIFIERS

Since only nine Endevco charge amplifiers, model 2735, were purchased earlier, the accelerometers were switched among them before the signals were displayed on the digital oscilloscopes. These nine charge amplifiers were calibrated to make sure that they provided the same system gain. The charge amplifiers were calibrated using the full-scale sensitivity test described in the instruction manual. A schematic drawing for the electrical set-up is shown in Fig. 3.20. The system gain had an accuracy of better than ± 1.5 percent on all full-scale ranges which means that the output from any two accelerometers should be within about 3 percent for the same input.

3.3.3 DIGITAL OSCILLOSCOPES

Two digital oscilloscopes with magnetic storage capabilities, series 2090, were purchased earlier from the Nicolet Instrument Corporation at Madison, Wisconsin. These units were used to monitor and record the outputs from the accelerometers.

A microcomputer-based instrument, namely the DATA 6000, was purchased from the Analogic Corporation of Danvers, Massachusetts, and was used in analyzing the wave records of the second sample reported in Lee and Stokoe, 1985. Three subsystems were installed in the DATA 6000: (1) data acquisition and signal conditioning systems, (2) a microprocessor-controlled digital storage and display system, and (3) keypad-selectable microcomputer signal processing. With these functions, the wave signals can be analyzed in the frequency domain.

3.3.4 STRESS CELLS

In an attempt to measure the response of static pressure inside the specimen, three total stress cells, model TE-9010, and a control unit, model C-9001, were purchased earlier from Terra Technology of Redmond, Washington (See Fig. 3.21a)

Each stress cell was calibrated before it was placed in the sand. The set-up for calibrating the stress cells was basically the same as that used for calibrating the strain gages on the excitation ports (Section 3.2.3).

Table 3.1 - Distances Between Accelerometers Inside the Triaxial Device (from Chu et al, 1984)

Accelerometer <u>From</u>	Labels* <u>To</u>	<u>Distance (ft)</u>
1S	4S	1.13
4S	6S	0.99
6S	9S	0.99
9S	12S	2.00
16W	10W	2.07
10W	19W	2.06
20V	8V	2.00
8V	27V	2.00
2W	5W	1.13
5W	7W	0.99
7W	10W	0.99
10W	13W	2.00
3V	8V	1.98
8V	11V	2.00
15V	9S	2.07
9S	18S	2.06
14V	8V	2.07
8V	17V	2.06
21S	9S	2.00
9S	28S	2.00
22W	10W	2.00
10W	29W	2.00
23	25	2.00
24	26	2.00

*See Fig. 3.15 for Accelerometer Locations



Fig. 3.19 - Accelerometer Being Assembled in Aluminum Accelerometer Block which is Part of NS Excitation Port
(from Chu et al, 1984)

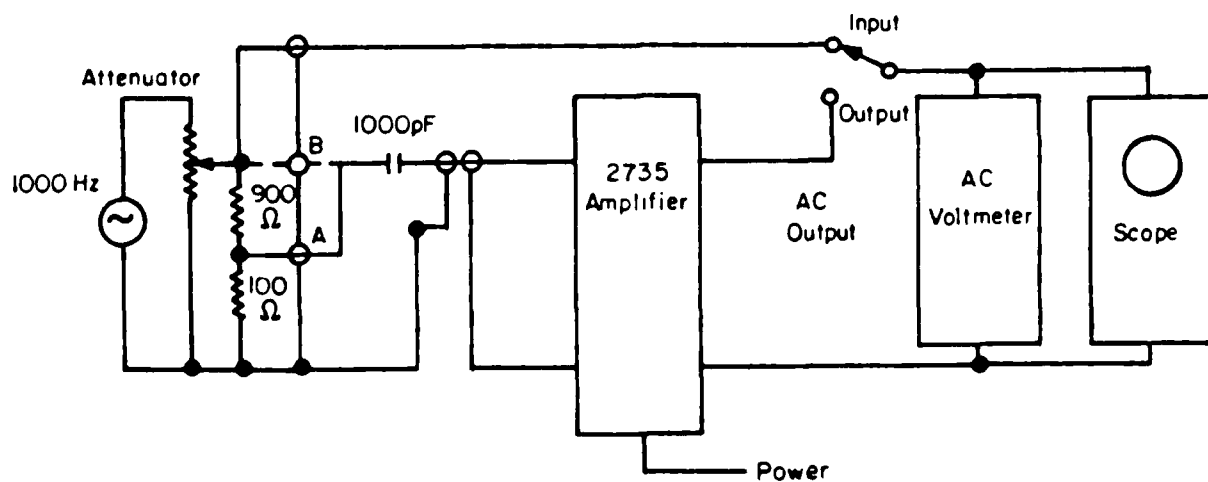
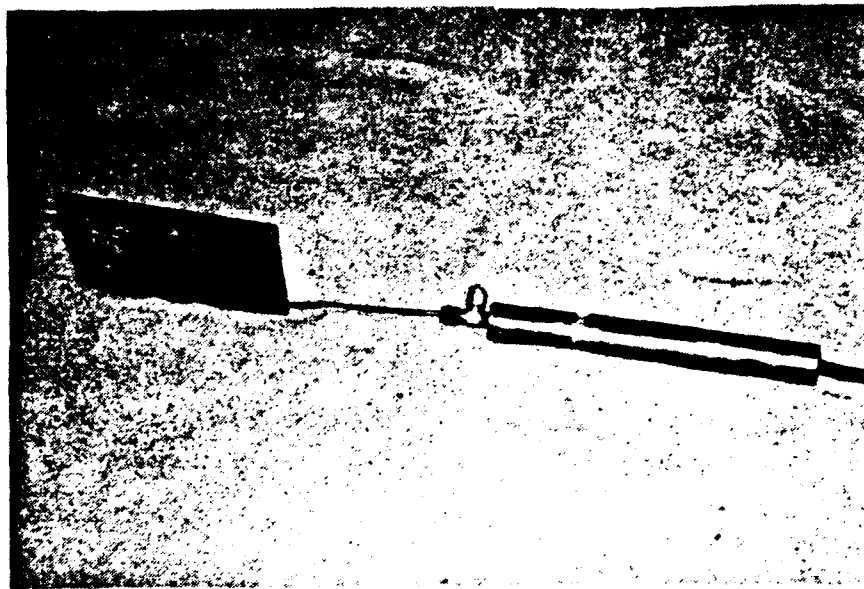
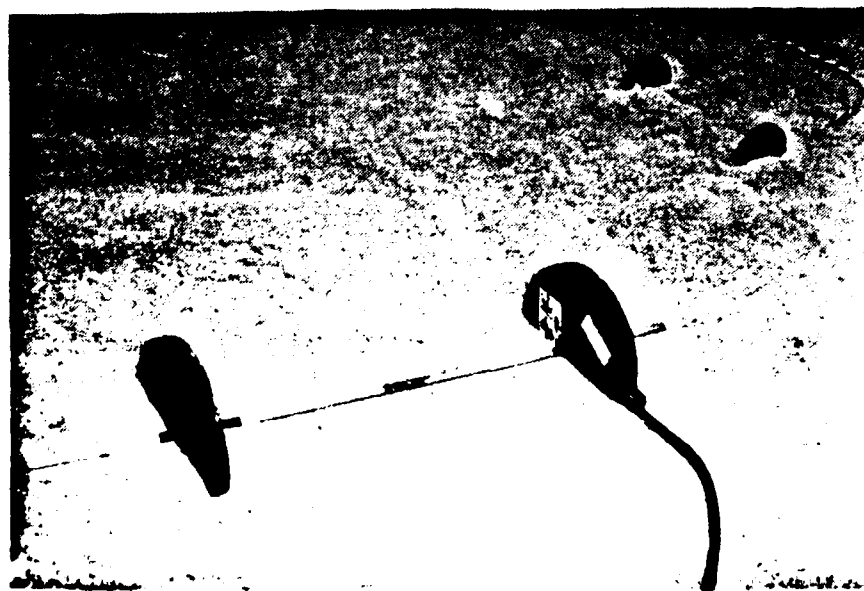


Fig. 3.20 - Electric Set-Up Used in Calibrating Endevco Model 2735 Charge Amplifiers (from Chu et al, 1984)



(a) Stress Cell



(b) Strain Sensors

Fig. 3.21 - Stress Cell and Strain Sensors

However, this time a larger capacity load cell [1000-lb (4450 N)] was used to monitor the applied load. Each stress cell was covered with 0.25-in. (0.64 mm) thick rubber pad on both faces before it was placed between the top and bottom 6-in (15.2 cm) square platens. The loading frame was then used to load the stress cell to known pressures and readings from the control unit of the stress cells were recorded. Calibration curves and sample output readings are shown in Appendix A. The curves are essentially straight lines above an applied pressure of 5 psi (34.5 kPa), with values of the ratio of reading to applied pressure of 0.57, 0.62, and 0.69 for the three cells. There is no hysteresis effect upon load cycling.

3.3.5 STRAIN SENSORS

Strain sensors were also placed in the sample. The sensors were purchased from Bison Instruments of Minnesota. The strain sensors were calibrated using the calibration fixture and control unit purchased from the manufacturer. The strain sensors are the model 4000 series of Bison soil strain gages (shown in Fig. 3.21b). There are four pairs of 2-in. (5.1-cm) diameter strain sensors and four pairs of 4-in. (10.2-cm) diameter strain sensors. Dial calibration curves were generated following procedures recommended in the manufacturer's manual for each pair of strain sensors. One of the calibration curves is shown in Fig. 3.22, and the remainder are included in Appendix B.

An example of using the calibration curve is illustrated in Fig. 3.22 for a pair of strain sensors shown as SN-1 in Fig. 3.23 with spacing of 4.5 in. (11.4 cm) and an initial null reading of 600. For these sensors, the corresponding calibration factor is 0.0505 percent. If a null reading is 598 was obtained after a pressure of 10 psi (68.9 kPa) was added, the equivalent change of strain is -2 ($598 - 600$) multiplied by 0.0505 or -0.101 percent (negative for compression). A schematic drawing of the locations of the stress cells and strains sensors is given in Fig. 3.23.

3.4 SAMPLE CONSTRUCTION AND DYNAMIC TESTING

A step-by-step procedure of sample construction and dynamic testing is presented below:

1. Clean the interior of the LSTD.

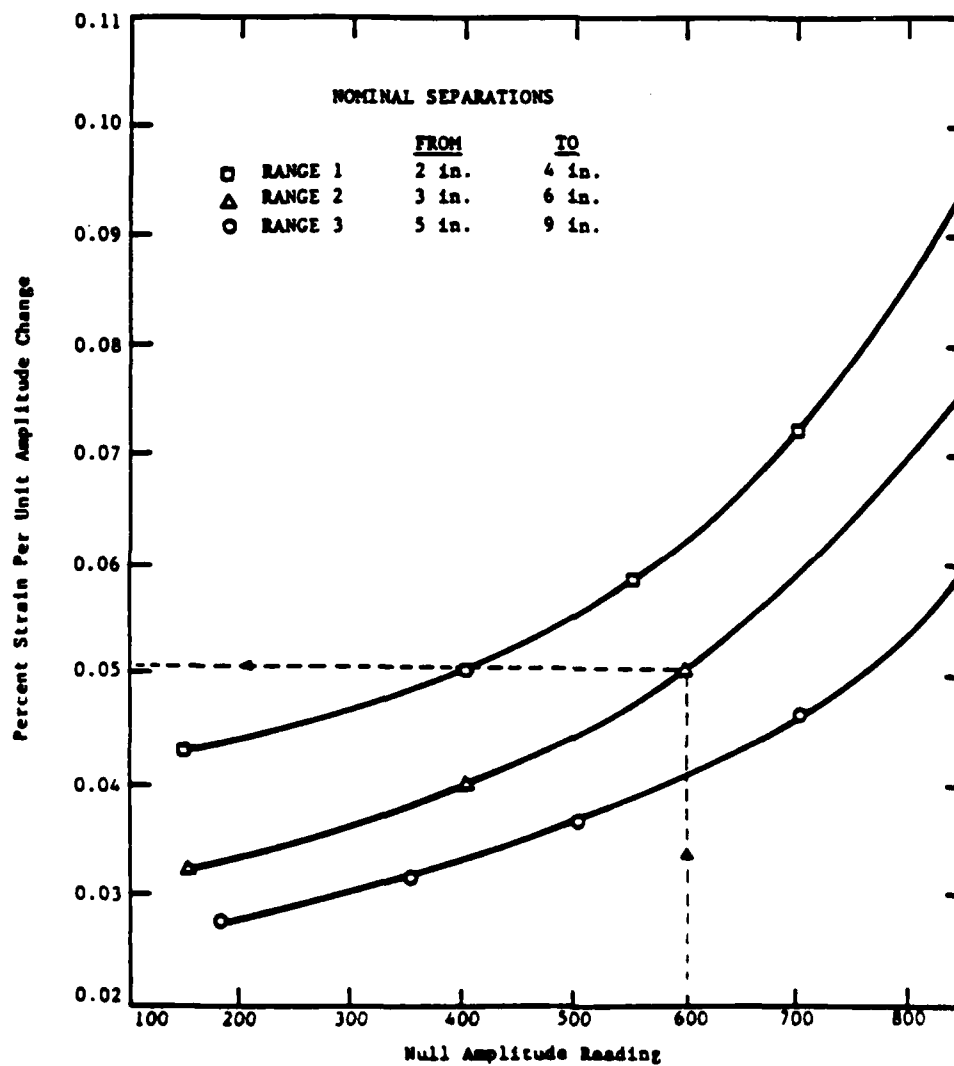
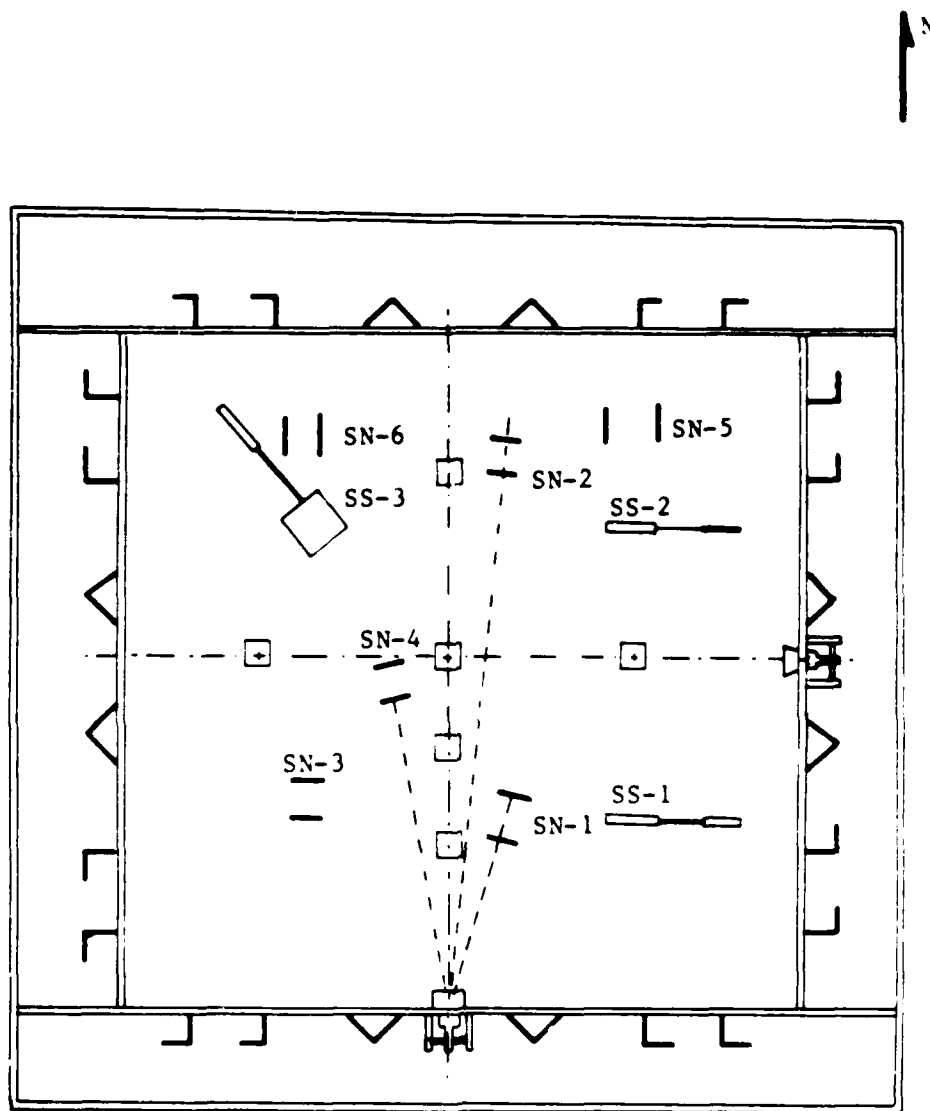


Fig. 3.22 - Strain Calibration Curve for Strain Sensor SN-1 (from Chu et al, 1984)




- Legend:
1.  2-D or 3-D Accelerometers
 2. SS-1 to SS-3 stress cells (which are actually 6 in. above the mid-depth plane)
 3. SN-1 to SN-4: 2-in. strain sensors
 4. SN-5 to SN-6: 4-in. strain sensors

Fig. 3.23 - Instrumentation at Mid-Depth Plane in the LSTD (from Chu et al, 1984)

2. Suspend two loading membranes on adjacent vertical sides of the LSTD (see Fig. 3.24).
3. Place two greased sheets in the form of a plastic bag on the four sides and bottom of the LSTD to minimize shear stresses on the sides (see Fig. 3.24) and put a plastic sheet as a cover on each side.
4. Tie nylon lines at various elevations on the interior corners of the LSTD to prevent the plastic sheets from being blown up due to air currents from the sand raining.
5. Put a small amount of sand by hand at the interior corner of the bottom so that the plastic sheets would not be blown up during sand raining.
6. Bolt collar of rainer on top of device (see Fig. 3.25).
7. Attach raining device to the rails on the collar.
8. Fill the side-membranes with water to a point about 3 in. (7.6 cm) above the present level of the sand inside the LSTD.
9. Use concrete bucket and overhead crane to fill raining device with dry sand (Fig. 3.26).
10. Carefully adjust control arm and move raining device along the rails at a constant rate so that dry sand flows uniformly into the LSTD (see Fig. 3.8).
11. Stop raining sand when the nylon lines touch the sand level or the designated level is reached.
12. Remove nylon lines just before they are going to be buried.
13. Lower working platform into the LSTD so that accelerometers, stress sensors, and strain sensors can be loaded at the designated locations inside the sand sample without disturbing the sand (see Fig. 3.27 through 3.29).
14. Place the density sampler on top of sand at designated locations during filling (Fig. 3.30).
15. Perform step 10 again and remember to remove density sampler when full. Carefully fill hole left by density sampler upon removal.
16. Repeat steps 8 to 15 until the top of the sand is 2 in. (5.08 cm) from top of the LSTD.
17. Level top of sand sample.
18. Put greased plastic sheets and then third membrane on top of sand sample.
19. Place steel top on LSTD and bolt tightly.

NO-A179 363

INVESTIGATION OF LOW-AMPLITUDE SHEAR WAVE VELOCITY IN
ANISOTROPIC MATERIAL. (U) TEXAS UNIV AT AUSTIN
GEOTECHNICAL ENGINEERING CENTER S H LEE ET AL. AUG 86

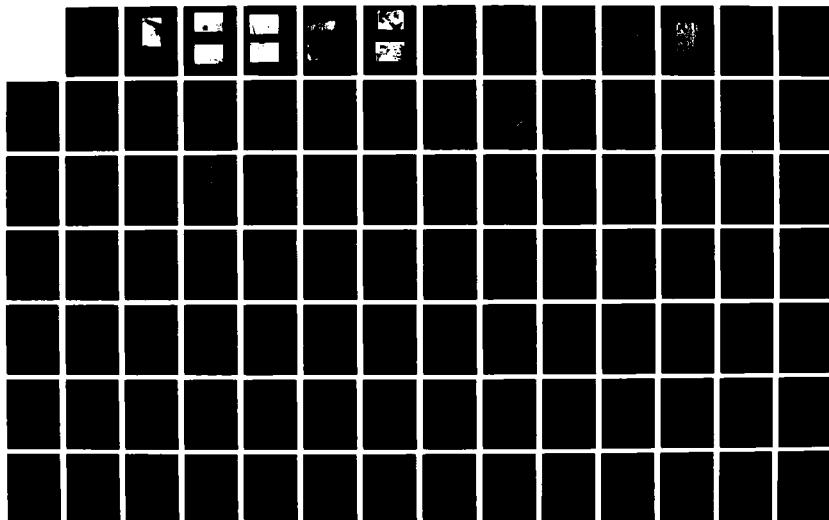
2/4

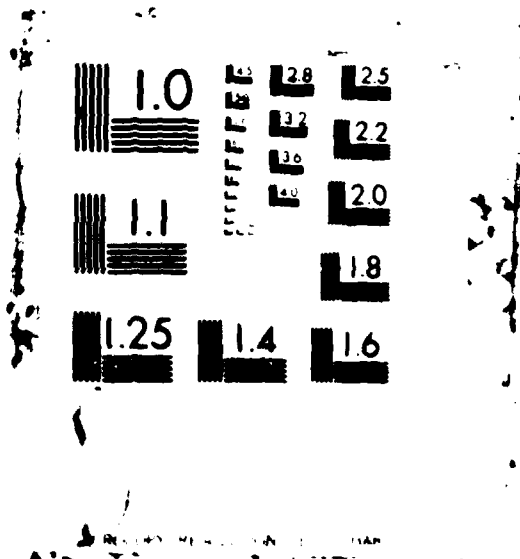
UNCLASSIFIED

AFOSR-TR-87-0483 AFOSR-83-0062

F/G 8/13

NL







Legend: 1. Greased sheets of plastic
2. Nylon line
3. Cover sheet

Fig. 3.24 - Membranes Hung on Adjacent Vertical
Sides of LSTC and Covered with
Greased Plastic Sheets



Fig. 3.25 - Raining Device on Top of Elevation Collar that is Bolted to LSTD



Fig 3.26 - Overhead Crane Used to Fill Rainier with Sand

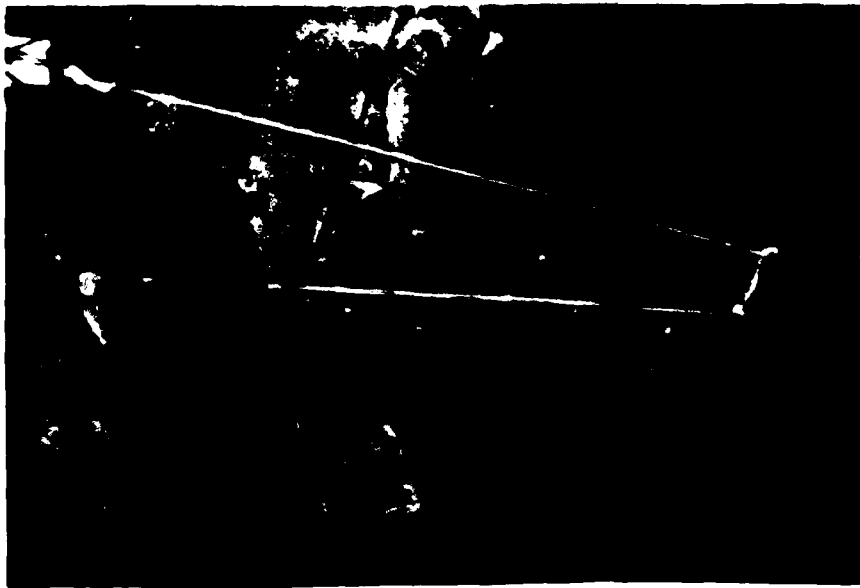


Fig. 3.27 - Working Platform Hanging
from Rainer



Fig. 3.28 - Placement of Accelerometers
at Desired Locations and
Elevations



- Legend: 1. 1S to 13W: accelerometer levels; letter following accelerometer number indicates direction of sensitivity (see Fig. 2.11)
2. SN-1 to SN-4: 2-in. strain sensors
3. SN-6 : 4-in. strain sensors

Fig. 3.29 - Instruments Being Placed at the Mid-Depth Plane
(from Chu et al, 1984)



Fig. 3.30 - Placement of Density Sampler at Designated Elevation and Location

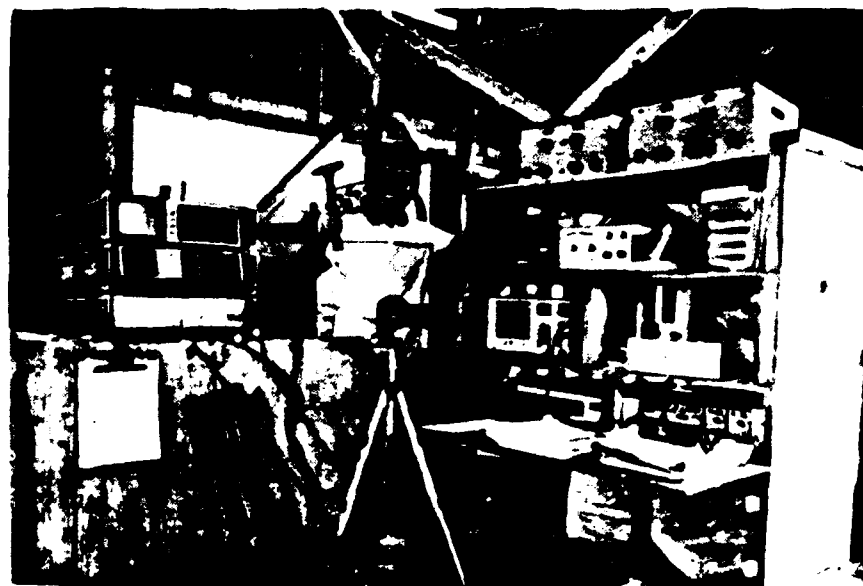


Fig. 3.31 - Data Acquisition System

20. Use hydraulic pressure system to add water to each membrane until the expected pressure is achieved.
21. Control the pressure of the excitation port by manually adjusting the reading of the strain gage on the port while adding air pressure to membrane.
22. Record the readings of the stress and strain sensors inside the sample (see Fig. 3.23).
23. Perform dynamic testing.
 - a. Use hand-held hammer to generate compression waves by striking point c of anvil as shown in Fig. 3.9.
 - b. Strike points d and e (see Fig. 3.9) parallel to the side of the device to excite shear waves.
 - c. Repeat step b but strike on opposite side of anvil to points d and e to generate a reversed shear wave (see Fig. 3.11).
 - d. Check the received signals on the screen of the oscilloscope and adjust the range of the amplifiers and the scale of the screen to obtain an adequate waveform.
 - e. Record the wave signals on the floppy disc.
24. Repeat steps 20 through 23 for dynamic testing with different confinements.
25. Determine wave velocities by methods indicated in Section 3.5.

Figure 3.31 shows the data acquisition system. Appendix C depicts a series of typical wave signals.

3.5 DETERMINATION OF WAVE VELOCITY

In a linear source-receiver array, shear waves are generated in the source and propagate past two (or more) receivers. The time difference between the initial arrivals of the wave signals (T) can be measured from the wave forms recorded at the first and second receivers as shown in Fig. 3.32. The wave velocity V can then be calculated from the time difference and the known distance (d) between the two receivers as follows:

$$V = d/t \quad (3.2)$$

when V is in fps, d is in ft, and t is in sec. This procedure is referred to as the initial arrival method (IAM) for determination of wave velocity.

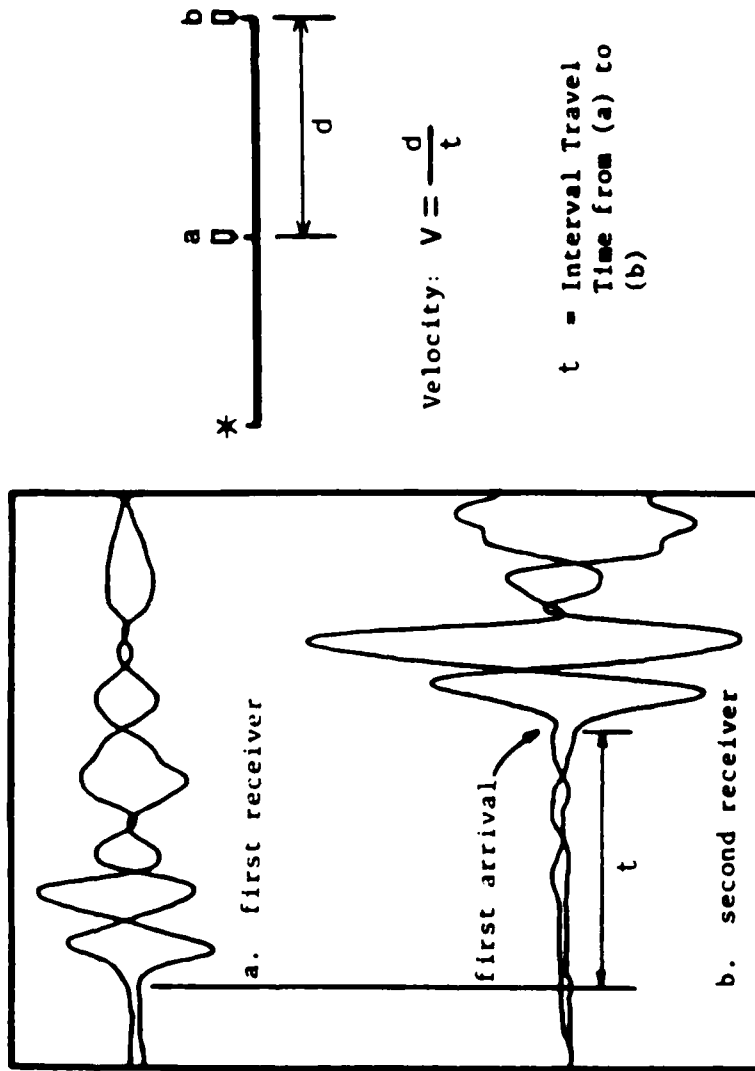


Fig. 3.32 - Determination of Shear Wave Velocity from a Linear Source-Receiver System

CHAPTER FOUR

MATERIAL AND TESTING PROCEDURES

4.1 INTRODUCTION

A locally available washed mortar sand was selected as the sand with which to build the sample because it is easy to handle and place. When dried and placed with the raining device described in Section 3.2.2, uniform medium-dense sand samples can be obtained and duplicated from one test to the next. The static and dynamic properties of the dry sand are essentially independent of time of loading, frequency, and number of loading cycles in the small-strain range. As such, a consistent data set can be obtained by stage testing one sample, and testing can proceed as rapidly as data can be gathered. Various loading sequences can be added with little influence of stress history (as shown in Chapters Five through Seven).

4.2 SAND CLASSIFICATION

The sand is a medium dense, washed mortar sand which is classified as SP in the Unified Soil Classification System. An average gradation curve for the sand is shown in Fig. 4.1. The sand has a mean grain diameter, D_{50} of about 0.45 mm, an effective grain size, D_{10} , of 0.28 mm, and a uniformity coefficient, C_u , of 1.71 as shown in Fig. 4.1. Less than one percent of the material passes the #200 sieve (0.074 mm). The grain shape is subangular to subrounded as shown in Fig. 4.2. The sand has a specific gravity of 2.67.

Rix (1984) performed maximum and minimum density tests on the sand in accordance with ASTM D 2049-69. He obtained a minimum dry density of 90.6 pcf (14.2 kN/m³) and a maximum dry density of 106.6 pcf (16.7 kN/m³). The corresponding maximum and minimum void ratios are 0.839 and 0.563, respectively (see Table 4.1).

Densities and corresponding void ratios were measured while the sand sample was constructed, and the resulting values are listed in Table 4.2. Measured densities of the sample ranged from 98.6 to 104.8 pcf, and corresponding void ratios ranged from 0.62 to 0.70. The relative densities, D_r , of the sample, therefore, ranged from 79.3 percent to 50.4 percent and had an average value of 72.1 percent.

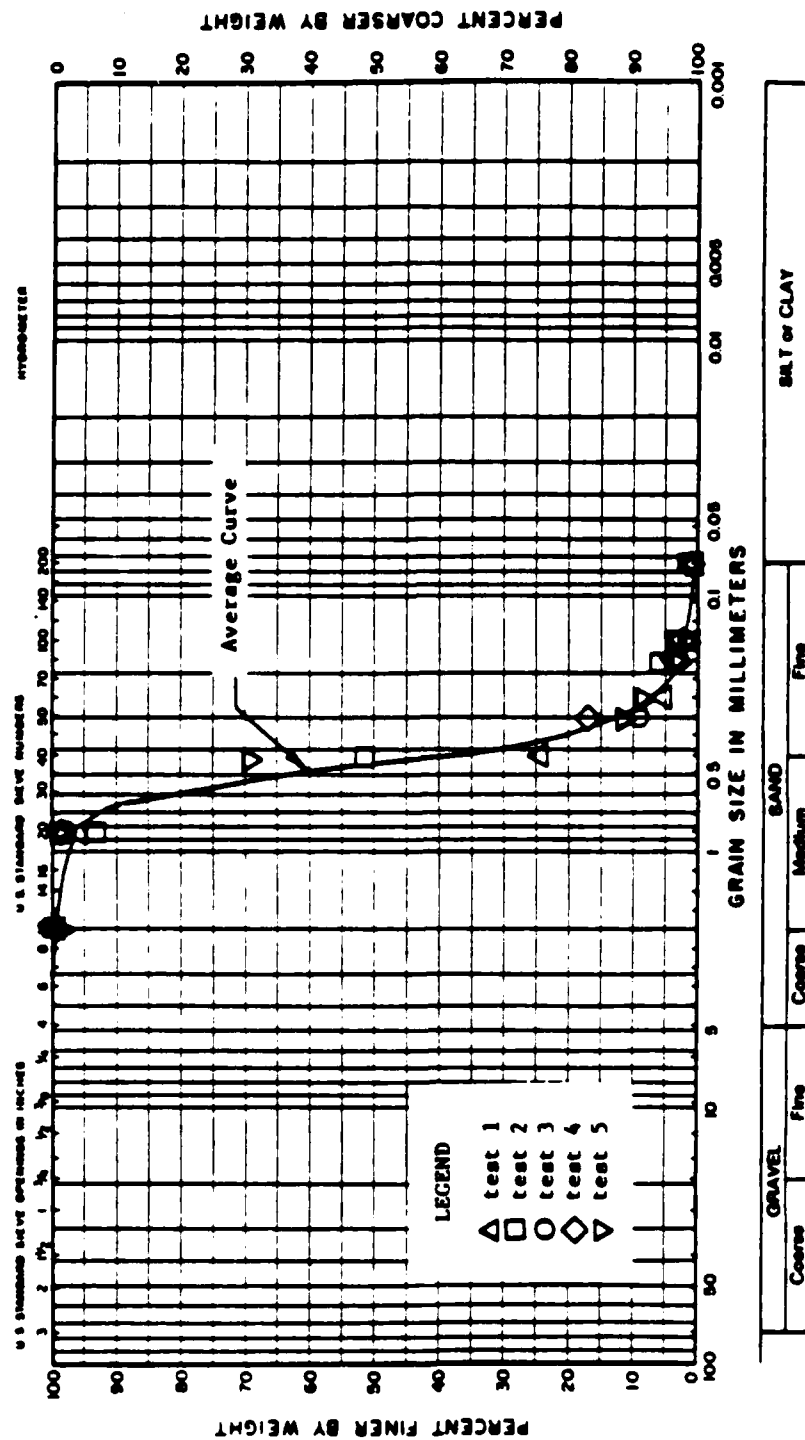


Fig. 4.1 - Grain Size Analysis of Washed Mortar Sand (from Knox et al, 1982)



Fig. 4.2 - Photomicrograph of Washed Mortar Sand
(from Rix, 1984)

Table 4.1 - Summary of Soil Characteristics (a) and Properties (b) of Washed Mortar Sand (from Rix, 1984)

Soil Type:	Washed Mortar Sand
Unified Soil Classification:	SP
Mean Grain Diameter, D_{50} :	0.35 mm
Percent Passing #200 Sieve:	<1%
Specific Gravity:	2.67
Maximum Dry Density:	106.6 pcf
Minimum Dry Density:	90.6 pcf
Maximum Void Ratio:	0.839
Minimum Void Ratio:	0.563
Grain Shape:	subangular to subrounded

(a)

Relative Density, %	Angle of Internal Friction, $\bar{\phi}$
5.7	34.5
10.2	34.5
12.3	36.5
17.5	37.2
22.4	38.5
114.0	44.0

(b)

Table 4.2 - Densities and Void Ratios of Sand at Various Elevations in the Large-Scale Triaxial Device (from Chu et al, 1984)

Height Above the Bottom (in.)	Location (see Fig. 3.5)	Density γ (pcf)	Void Ratio e^*
12	A	103.1	0.62
12	E	99.7	0.68
12	C	101.8	0.64
36	D	103.5	0.62
36	B	100.8	0.66
36	F	104.8	0.60
60	A	102.6	0.63
60	B	98.8	0.69
60	F	103.3	0.62
78	D	103.3	0.62
78	E	98.6	0.70
78	C	101.3	0.65
Average		101.8	0.64
Std. Deviation		2.0	0.03

$$* e = \frac{w \cdot G_s}{\gamma_d} - 1 \quad \text{where } G_s = 2.68 ; \quad \gamma_d = \frac{\gamma}{1+w}, \quad \text{and } w = 0.05\%$$

4.3 STATIC SHEAR STRENGTH AND STRESS-STRAIN BEHAVIOR

The angle of internal friction, ϕ , determined by consolidated drained and undrained triaxial tests ranged from 34.5 degrees for loose sand to 44 degrees for dense sand (see Table 4.1).

Two stress-strain curves for dense sand samples loaded under consolidated drained conditions with different confining pressures, 10 psi and 45 psi (68.9 to 310.1 kPa), are shown in Fig. 4.3. The stress-strain curves seem to be reasonably linear at small stresses, when the principal stress differences are less than 25 psi (172.3 kPa) in both cases. Since stress-path dependent behavior may happen mainly in the plastic range of a material (Chen, 1975), it was decided that all stress differences employed in the large-scale triaxial device would not exceed 25 psi (172.3 kPa). The axial strains under such loading conditions will be less than 0.5 percent. Accordingly, a step load of only 5 or 10 psi (34.5 or 68.9 kPa), results in a corresponding variation in axial strain of less than 0.1 to 0.2 percent. This small variation in axial strain does not allow the strain sensors to pick up a very clear reading as they are not sensitive enough. Figure 4.4 shows the measured strains corresponding to the applied pressures. The axial strain value may be even smaller (about 0.03 to 0.05 percent) if the calculated maximum Young's moduli from dynamic testing (see Chapter Nine) are used. These strain sensors were designated to measure static strains of the specimen so that static stiffnesses could be compared with dynamic results. However, because the strains were so small, accurate strain measurements could not be made, and thus the strains were only used as rough references.

The readings of stress cells buried inside the sand sample are presented in Appendix A. The distances between the stress cells, SS-1, SS-2 and SS-3 and the nearest membranes parallel to the face of each cell are 2, 5, and 3 ft (60 cm, 150 cm and 90 cm), respectively. One can see (from Table 4.3) that, at a given isotropic pressure, the vertically oriented stress cell closer to the membrane, SS-2, exhibited the smaller readings of stresses of the two vertically oriented stress cells. However, the horizontally oriented stress cell, SS-3, exhibited smaller readings of stresses than either of the vertically oriented cells. The ratio of stress cell readings to applied loadings changed from low to high confinements, except for cell SS-2. Many factors, such as stress concentration or stress relief (in terms of soil arching; Ingram, 1965), lateral stress rotation (Stewart and Kulhawy, 1981),

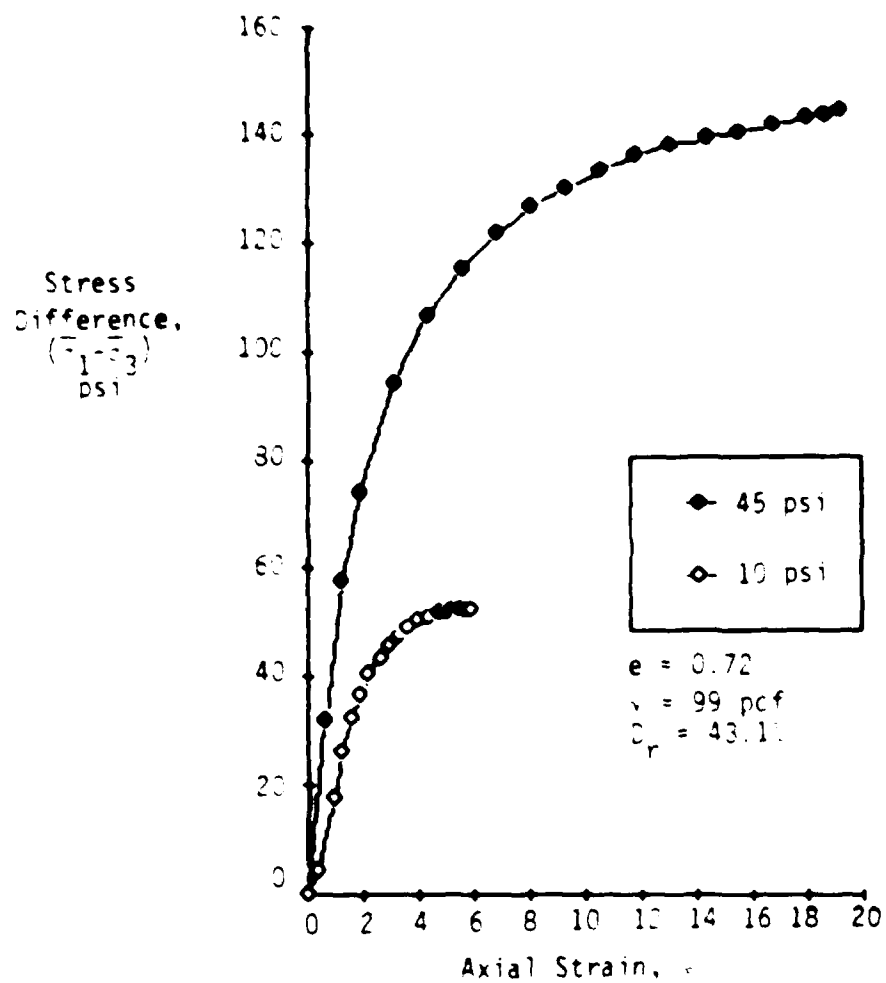


Fig. 4.3 - Stress-Strain Relationship from Consolidated-Drained Triaxial Tests on Washed Mortar Sand

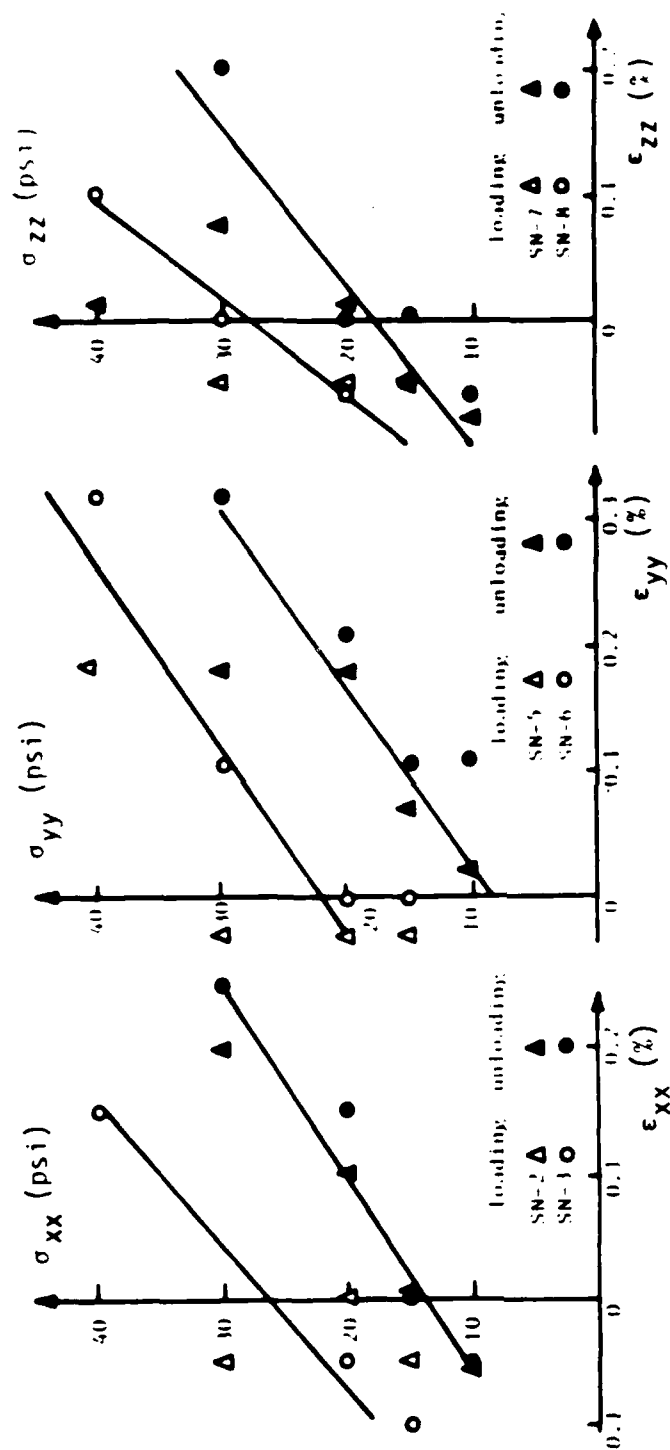


Fig. 4.4 - Stress-Strain Behavior Along Each Principal Direction Under Isotropic Confinement
(from Chu et al, 1984)

Table 4.3 - Ratios of Calibrated Readings of Stress Cells to Applied Confining Pressures

Stress Cell No.	Applied Confining Pressure*, $\bar{\sigma}$, psi					Distance** (ft)
	10	15	20	30	40	
SS-1 ⁺	0.72	0.78	0.71	0.63	0.63	5
SS-2 ⁺	0.53	0.53	0.53	0.52	0.53	2
SS-3 ⁺⁺	0.32	0.20	0.25	0.43	0.40	3

* applied confining pressures in the membrane parallel to the face of each stress cell

** distances between the stress cells and the membranes parallel to the face of each cell

+ placed vertically

++ placed horizontally

and nonuniform stress distribution (Januskevicius and Vey, 1965), may cause a scattering in stress readings. Further study on interpreting the stress cells is necessary. Therefore, stress readings from the pressure gages in the air/water system were used in all subsequent analyses.

4.4 DYNAMIC PARAMETERS

Shear moduli and damping ratios determined with resonant column tests on isotropically loaded specimens are presented in Figs. 4.5 through 4.8 (Knox, 1982). These results were used to make a preliminary examination of the effect of stress history, and, thereafter, used to compare with the results from the LSTD.

Recently, a series of resonant column tests using biaxial loading was conducted by Stokoe and Ni (1985). Results from these tests are shown in Figs. 4.9 through 4.12, and the tests are discussed in the following chapters where appropriate.

A relationship between cone penetration resistance, q_c , and shear wave velocity for this sand under normally consolidated conditions was developed by Rix (1984), and these results are presented in Fig. 4.13 for completeness.

4.5 PREDOMINANT FREQUENCY, STRAIN AMPLITUDE AND WAVELENGTH

Waveforms of both P- and S-waves were recorded on magnetic disks using two Nicolet oscilloscopes. These records were used to determine propagation velocities, frequencies, particle motions, and strain amplitudes. Evaluation of these parameters was conducted in both the time and frequency domains.

In the time domain, two fractional values of the period, 0.25 T and 0.5 T, were measured from each accelerometer record as shown in Fig. 4.14. These periods were then used to estimate predominant frequencies. Wavelengths were calculated from:

$$\lambda = V/f \quad (4.1)$$

where V is the wave velocity in fps, f is the frequency in Hz, and λ is the wavelength in ft. The predominant frequencies of P- and S-waves ranged from 1000 Hz to 2500 Hz and 1000 Hz to 1500 Hz, respectively. Wavelengths of the

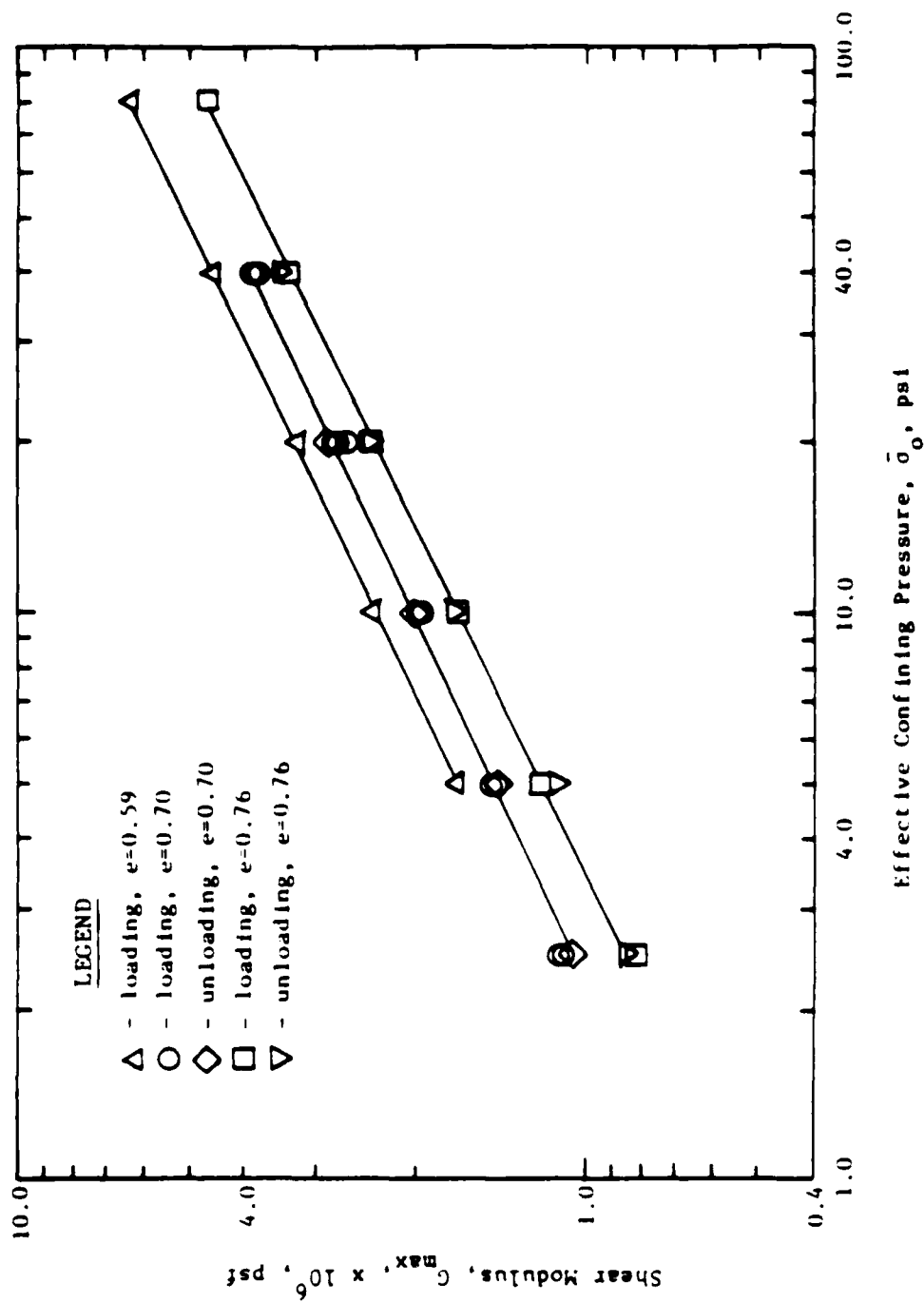


Fig. 4.5 - Variation in Low-Amplitude Shear Modulus with Effective Confining Pressure (from Knox, 1982)

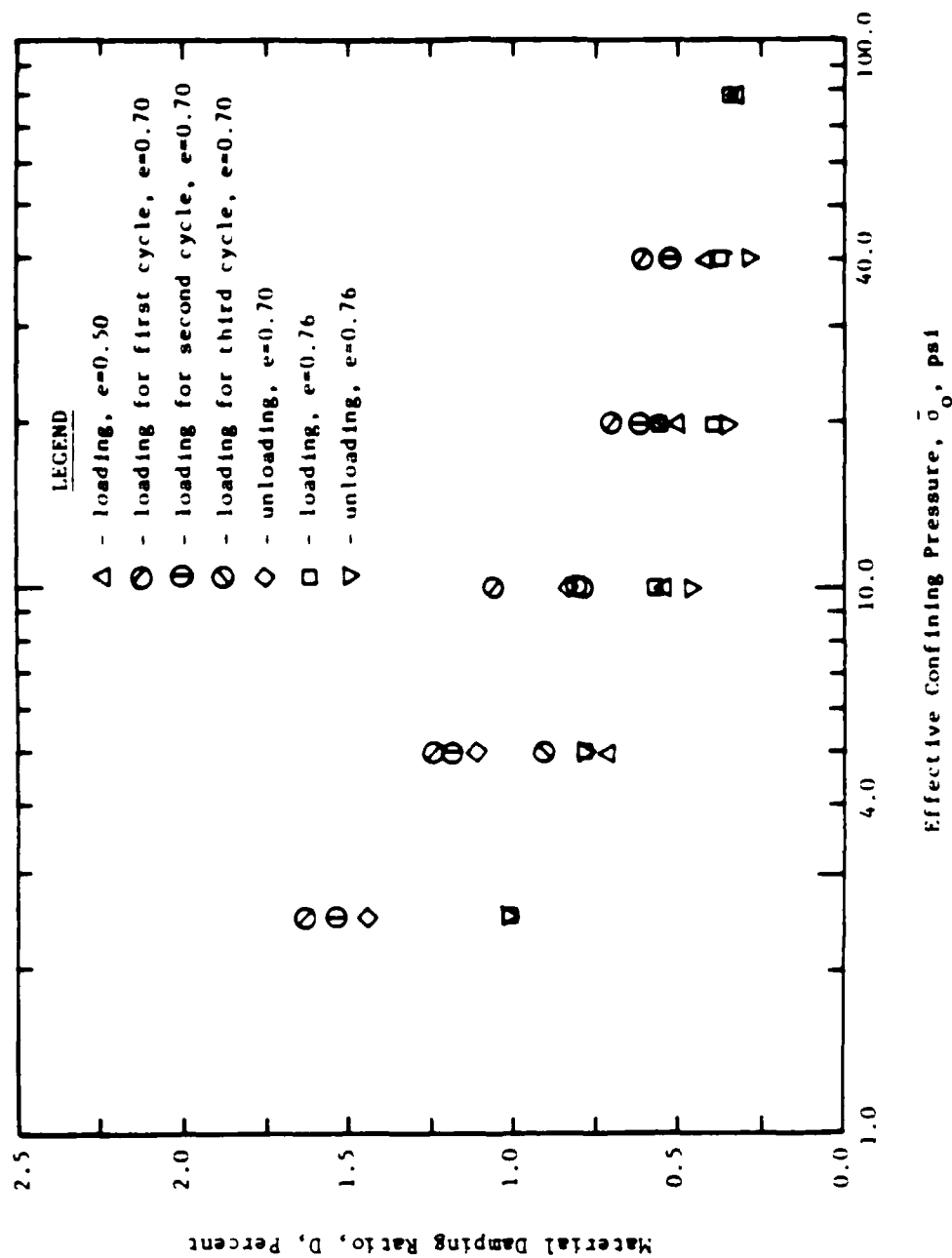


Fig. 4.6 - Variation in Low-Amplitude Material Damping Ratio with Effective Confining Pressure (from Knox, 1982)

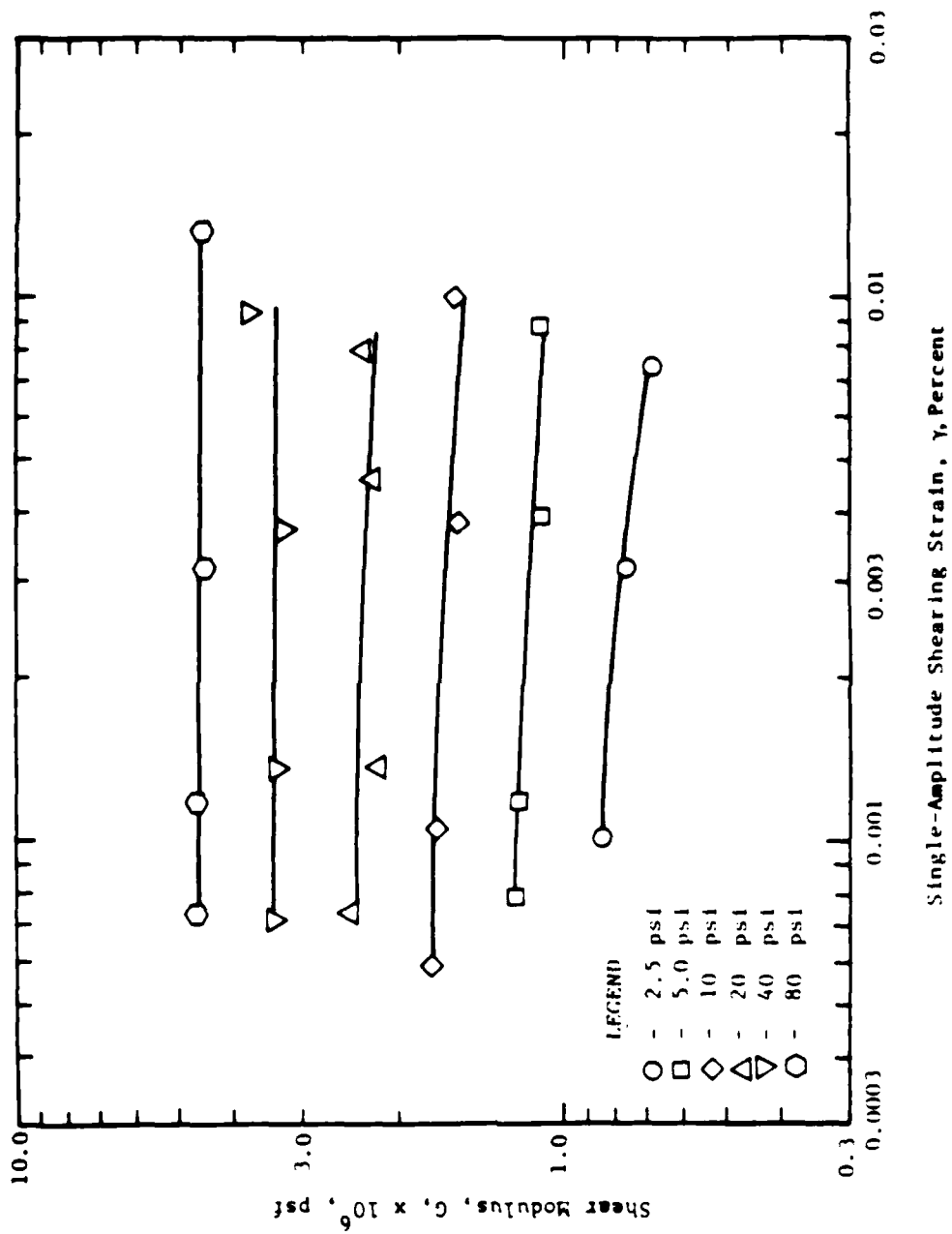


Fig. 4.7 - Variation in Shear Modulus with Shearing Strain
(from Knox, 1982)

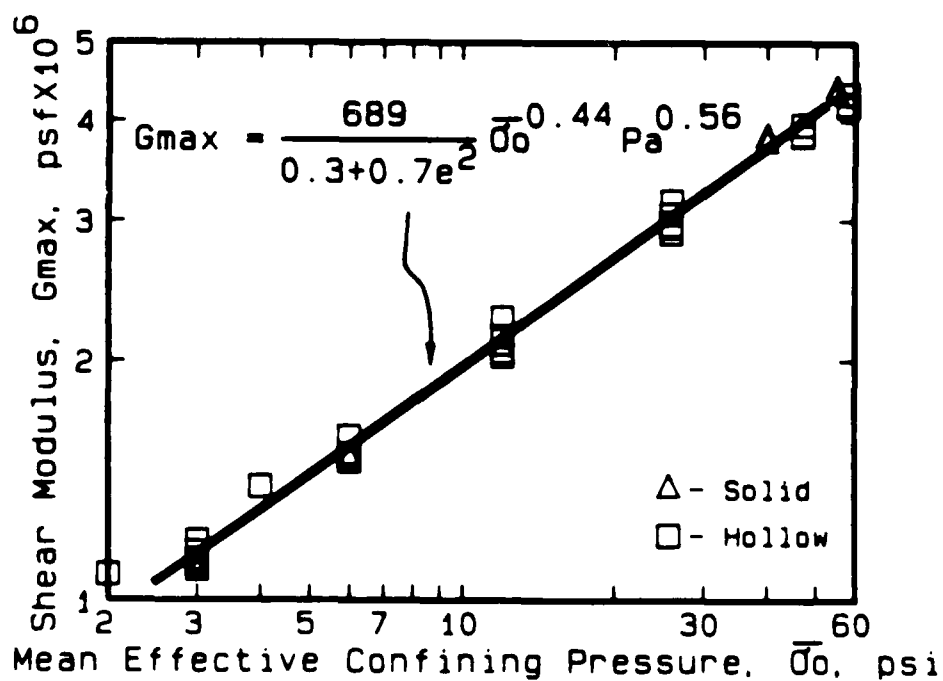


Fig. 4.11 - Relationship between Shear Modulus and Isotropic Stress State

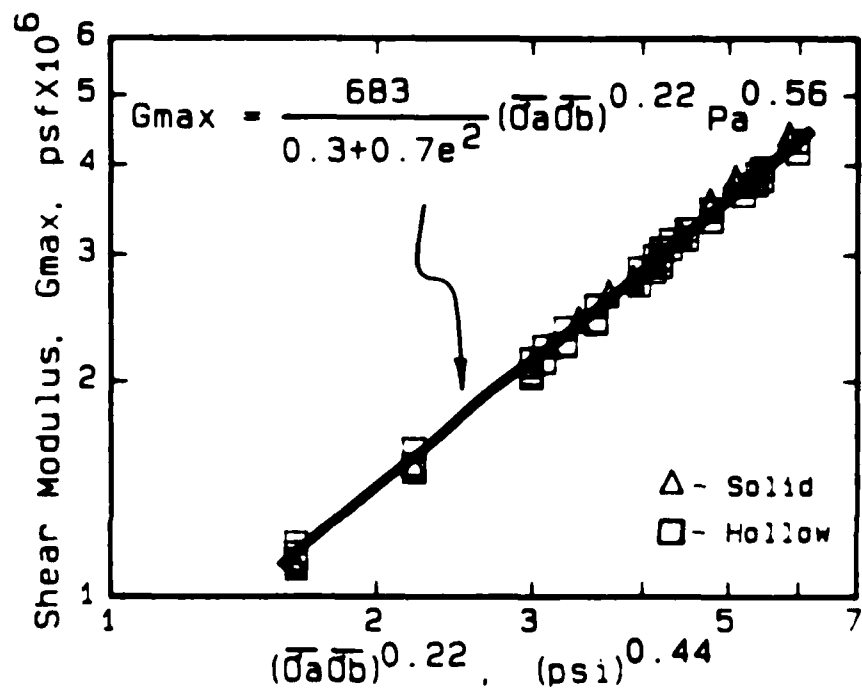


Fig. 4.12 - Relationship between Shear Modulus and Anisotropic Stress State

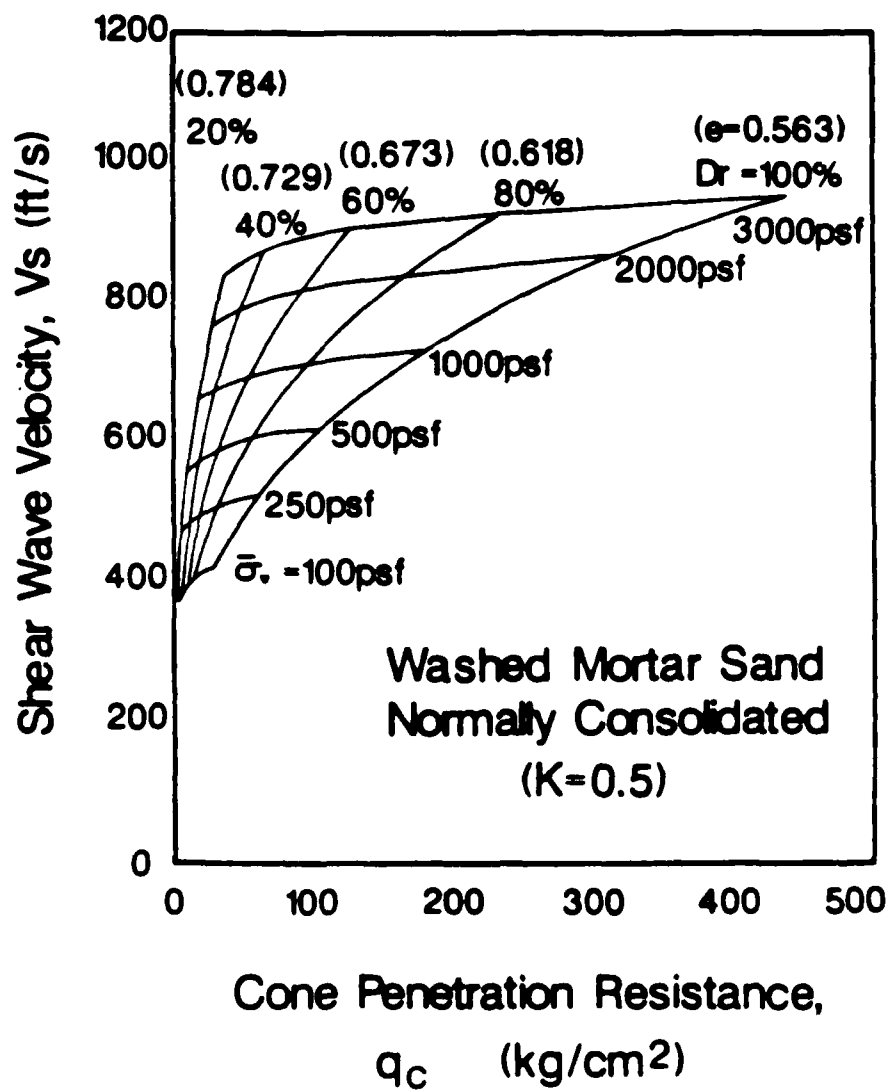


Fig. 4.13 - Relationship between q_c and V_s for Washed Mortar Sand Confined Under Normally Consolidated Conditions (from Rix, 1984)

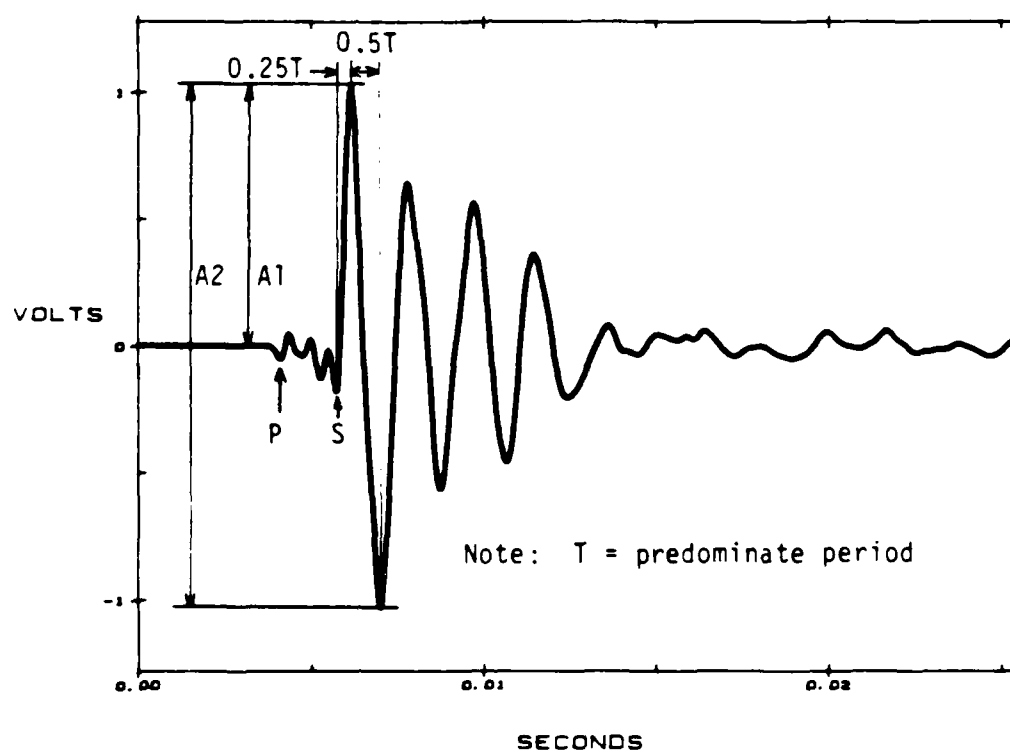


Fig. 4.14 - Determination of Particle Amplitudes and Predominant Periods from a Typical S-Wave Accelerometer Record

P- and S-waves ranged from 0.4 to 1.5 ft (12 to 45 cm) and 0.5 to 1.0 ft (45 to 30 cm), respectively.

The maximum (peak) acceleration was determined from either the first peak in the waveform or the average of the first peak-to-peak motion (A_1 and A_2 in Fig. 4.14, respectively). A calibration factor of 10 volt/g was used to calculate the acceleration amplitude. There are not distinct patterns of acceleration amplitude for different kinds of shear waves. The value of acceleration amplitude ranged from about 1 to 20 ft/sec² (0.3 to 6.0 m/sec²).

By using a harmonic approximation, peak particle amplitude, Z can be related to peak acceleration, \ddot{Z} , as:

$$\ddot{Z} = (2\pi f)^2 Z, \quad (4.2)$$

and peak particle velocity, \dot{Z} , as:

$$\dot{Z} = (2\pi f) Z. \quad (4.3)$$

Strain amplitudes, ϵ and γ , for plane P- and S waves, respectively, can then be determined from particle velocities (\dot{Z}) and propagation velocities (V) as:

$$\epsilon = \dot{Z}/V_P \quad (4.4.a)$$

or

$$\gamma = \dot{Z}/V_S \quad (4.4.b)$$

The sources in this study tend to generate spherical waves rather than plane waves. Therefore, particle amplitudes and strain amplitudes determined from Eqs. 4.2 through 4.4 can only be used as approximations to reflect the order of the magnitude of the strain amplitudes in the sand. Peak particle amplitudes and strain amplitudes for both P- and S-waves ranged from 1×10^{-7} to 6×10^{-6} in. (2.54×10^{-7} to 1.52×10^{-5} cm) and from 0.0001 percent to 0.001 percent, respectively. Since peak strain amplitude is less than 0.001 per cent, testing may be considered to be low amplitude and the effect of strain amplitude can be ignored (see Figs. 4.9 and 4.10).

In the frequency domain, the range of the frequencies for each wave type can be examined in detail. The spectrum of the typical waveforms in Appendix C are shown in Appendix D. The full frequency ranges for P- and S-waves is in 200 Hz to 3000 Hz and 100 Hz to 2000 Hz, respectively, from the combination of the trigger device, hammer, inclusion, and sand sample. The predominant frequencies of the P-wave in the isotropic plane (V_{pI}) and in the anisotropic plane (V_{pA}) are 900 Hz to 1250 Hz and 500 Hz to 900 Hz, respectively. An oblique P-wave falls in the range of 450 Hz to 1250 Hz. Two predominant frequencies occurred in the S-wave signals. They ranged from 150 Hz to 250 Hz and 450 Hz to 700 Hz for both V_{SI} and V_{SA} (shear wave velocity in isotropic and anisotropic planes, respectively). However, there is less energy in the frequencies ranging from 250 Hz to 450 Hz for the S-waves. The same phenomenon was also noticed in the oblique shear waves but with a wider frequency range (150 Hz to 300 Hz and 450 Hz to 800 Hz).

Differences between predominant frequency ranges for measurements analyzed in the time or frequency domain (except for V_{pI}) are clearly shown in this data. Determination of displacement or strain from time-domain records always results in larger displacement or strain values (unless one pure harmonic waveform exists). That is, the maximum amplitude of displacement (or acceleration) is the superposition of the magnitudes of a number of frequencies rather than one, and the equivalent frequency (or more generally called the predominant frequency) to this peak amplitude may not be coincident with the individual predominant frequencies. For instance, the predominant frequency of the P-wave in the anisotropic plane is from 1000 Hz to 2500 Hz obtained in the time domain, but it is only from 500 Hz to 900 Hz when obtained in the frequency domain.

4.6 TESTING PROGRAM

The testing program was composed of three sequences of pressure variation. The first step was to perform tests with isotropic confinement ($\bar{\sigma}_1 = \bar{\sigma}_2 = \bar{\sigma}_3$). This state of stress is the simplest one that can be applied with the LSTD, and it is the easiest one to compare with other research conducted with other devices. Moreover, structural anisotropy (or inherent anisotropy) can easily be detected under this state of stress.

To understand stress-induced anisotropy and the effect of individual principal stresses on S-wave velocity, a complete set of biaxial tests was

performed on the sample. Two series of biaxial confinement tests were examined: the first series consisted of tests with confining stress varying in only one principal direction (named BIA1), while the second series consisted of tests with confining stresses varying in two principal directions (named BIA2). Both series of tests were conducted with the major principal stress oriented along each of the three principal stress axes to check the possible difference due to anisotropy of the sample. To check the influence of intermediate principal stress on the stiffness of the sample, the first series of tests contained two subsets: the first subset was composed of tests with the intermediate principal stress always equal to the minor principal stress, while the second subset was composed of tests where the intermediate principal stress ranged in value from the minor to the major principal stress. "BIAR" was the name given the second subset while "BIA1" was still kept for the first subset. Test numbers from 10 to 22 and 32 to 60 represented the series BIA1 while numbers 23 to 31 represent the subset of BIAR (Test numbers are given in Table 4.4.)

The loading sequence of biaxial confinement all started with an isotropic state of stress of 15 psi (103 kPa) in BIA1. The stress in the vertical direction (z-direction) was then increased from 15 psi to 20, 30, and 40 psi (103, 138, 207, and 276 kPa) as shown in Fig. 4.15a (named BIA1Z). With the stress of 40 psi (275.6 kPa) being held constant in the z-direction, stresses in the x- and y-directions were then increased from 15 to 40 psi (103.4 to 275.6 kPa) in the same increments as before as shown in Fig. 4.16a (named BIA2Z). After the loading sequence, unloading tests were employed with the horizontal stresses being reduced from 40 to 15 psi (275.6 to 103.4 kPa) while the vertical stress remained constant at 40 psi (275.6 kPa). Then, the vertical stress was unloaded from 40 to 15 psi (275.6 to 103.4 kPa) in the reverse sequence with the horizontal stresses being kept at 15 psi (103.4 kPa). The same loading and unloading sequences were also repeated in the x- and y-directions as shown in Figs. 4.15b, 4.16b, 4.15c, and 4.16c, respectively.

The BIAR biaxial confinement tests were started from two different initial conditions: the first one was from the isotropic confinement of test number 23 and the second one was from the biaxial confinement of test number 28 (see Table 4.4). The intermediate principal stress was varied from the minor to the major principal stress in the first subset while it was varied

Table 4.4 - Loading Pressure Sequences (from Chu et al, 1984)

Test No.	Date of Test	Vertical Effective Stress σ_z (psi)*	Horizontal Effective Stresses	
			σ_x (psi)*	σ_y (psi)*
1	10/08/82	10	10	10
2	10/13/82	15	15	15
3	10/16/82	20	20	20
4	10/16/82	30	30	30
5	10/20/82	40	40	40
6	10/23/82	30	30	30
7	10/23/82	20	20	20
8	10/23/82	15	15	15
9	10/23/82	10	10	10
10	11/08/82	15	15	15
11	11/10/82	20	15	15
12	11/12/82	30	15	15
13	11/13/82	40	15	15
14	11/13/82	40	20	20
15	11/15/82	40	30	30
16	11/28/82	40	40	40
17	12/17/82	40	30	30
18	12/17/82	40	20	20
19	12/17/82	40	15	15
20	12/18/82	30	15	15
21	12/18/82	20	15	15
22	12/18/82	15	15	15
23	12/18/82	20	20	20
24	12/20/82	30	20	20
25	12/20/82	40	20	20
26	12/20/82	15	20	20
27	12/21/82	10	20	20
28	12/21/82	20	10	20
29	12/21/82	20	15	20
30	12/22/82	20	30	20
31	12/22/82	20	40	20

Table 4.4 (continued) - Loading Pressure Sequences (from
Chu et al, 1984)

Test No.	Date of Test	Vertical Effective Stress $\bar{\sigma}_z$ (psi)*	Horizontal Effective Stresses	
			$\bar{\sigma}_x$ (psi)*	$\bar{\sigma}_y$ (psi)*
32	12/22/82	30	30	30
33	01/05/83	40	40	40
34	01/06/83	20	30	20
35	01/06/83	20	20	20
36	01/06/83	20	15	20
37	01/07/83	20	10	20
38	01/07/83	15	15	15
39	01/07/83	15	20	15
40	01/08/83	15	30	15
41	01/08/83	15	40	15
42	01/08/83	20	40	20
43	01/10/83	30	40	30
44	01/10/83	20	40	20
45	01/10/83	15	40	15
46	01/11/83	15	30	15
47	01/11/83	15	20	15
48	01/11/83	15	15	20
49	01/11/83	15	15	30
50	01/12/83	15	15	40
51	01/12/83	20	20	40
52	01/12/83	30	30	40
53	05/19/83	30	30	30
54	05/20/83	40	40	40
55	05/20/83	30	30	40
56	05/20/83	20	20	40
57	05/21/83	15	15	40
58	05/23/83	15	15	30
59	05/23/83	15	15	20
60	05/24/83	15	15	15

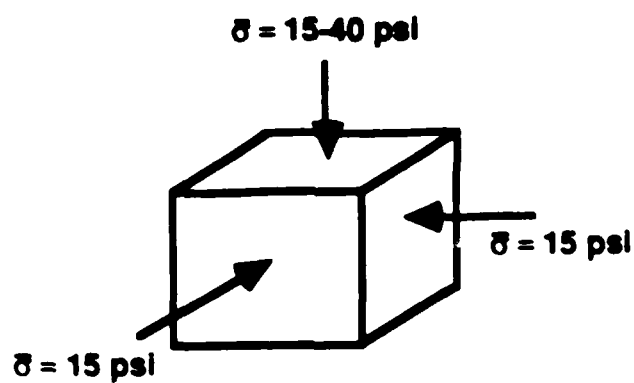
Table 4.4 (continued) - Loading Pressure Sequences (from Chu et al, 1984)

Test No.	Date of Test	Vertical Effective Stress	Horizontal Effective Stresses	
		$\bar{\sigma}_z$ (psi)*	$\bar{\sigma}_x$ (psi)*	$\bar{\sigma}_y$ (psi)*
61	05/24/83	40	25	20
62	05/24/83	40	15	25
63	05/24/83	40	15	30
64	05/24/83	40	15	35
65	05/25/83	28	28	28
66	05/25/83	32	28	24
67	05/25/83	36	28	20
68	05/25/83	40	28	16
69	05/26/83	28	28	28
70	05/26/83	32	31	24
71	05/26/83	36	34	20
72	05/26/83	40	37	16
73	06/01/83	40	40	40
74	06/01/83	40	40	40
75	06/01/83	40	40	40
76	06/02/83	40	40	40
77	06/05/83	40	15	15
78	06/05/83	40	15	15
79	06/05/83	40	15	15
80	06/06/83	40	15	15
81	06/10/83	32	28	24
82	06/10/83	32	28	24
83	06/10/83	32	28	24
84	06/11/83	32	28	24

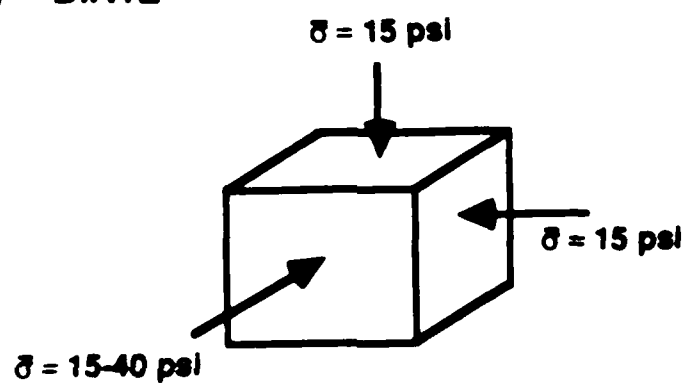
* $\bar{\sigma}_z$ = Vertical (top-bottom) effective stress

$\bar{\sigma}_x$ = Horizontal (north-south) effective stress

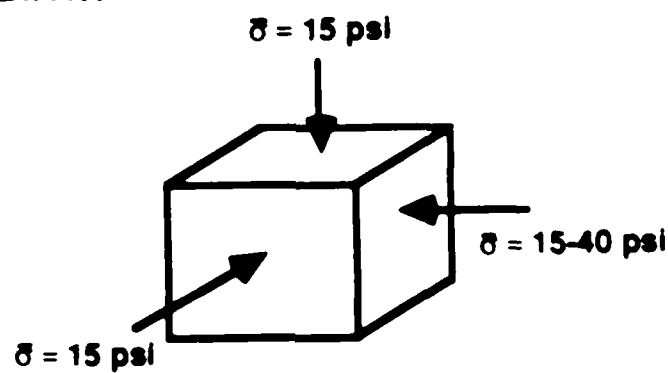
$\bar{\sigma}_y$ = Horizontal (east-west) effective stress



(a) BIA1Z

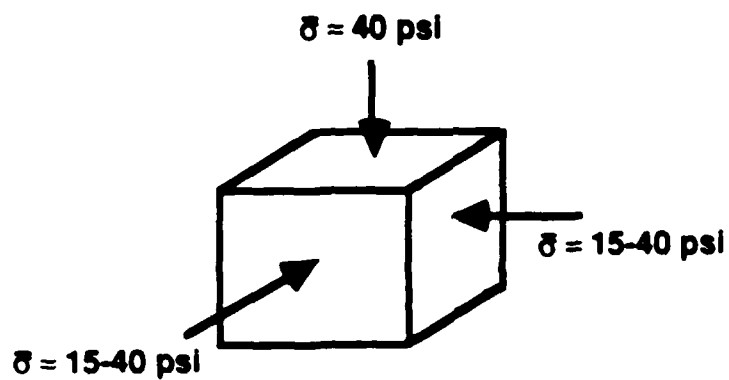


(b) BIA1X

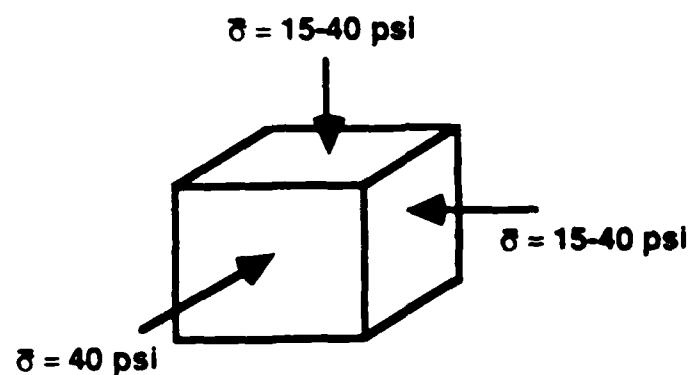


(c) BIA1Y

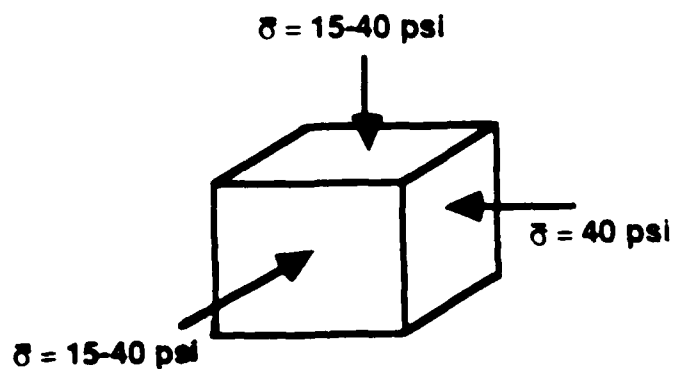
Fig. 4.15 - Initial Subset of First Series of Biaxial Confinement Tests with Variation of Stress in One Principal Direction (BIA1)



(a) BIA2Z



(b) BIA2X



(c) BIA2Y

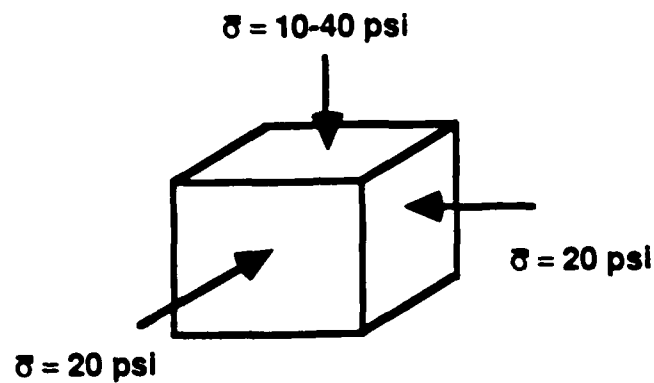
Fig. 4.16 - Second Series of Biaxial Confinement Tests with Variations of Stresses in Two Principal Directions (BIA2)

from major to minor principal stress in the second subset. The principal stress varied from 10 psi (68.9 kPa) to 40 psi (275.6 kPa), while the other two principal stresses were held constant at 20 psi (137.8 kPa) as shown in Fig. 4.17.

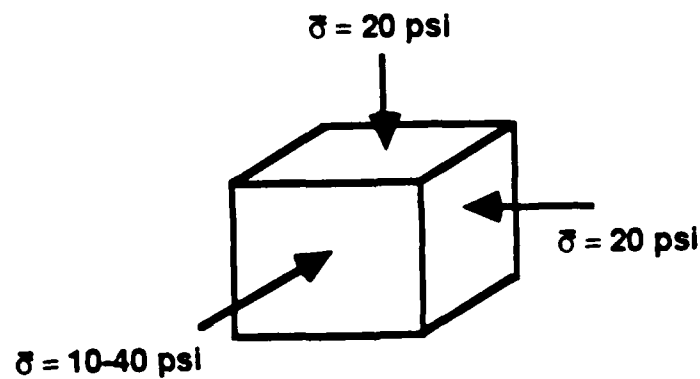
For biaxial confinement, all principal stresses were no longer the same as in isotropic confinement so the effect of each stress component on shear wave velocity could be investigated. The orientation of the principal stress in both series of tests (BIA1 and BIA2) was never changed, i.e., no matter whether one or two principal stresses were varied, the directions of major, intermediate, and minor principal stresses never changed.

Triaxial confinement states represented the last step in using the LSTD to study the effect of stress state on S-wave velocity. This stress state was examined after the effects of isotropic and biaxial confinements had been examined. Three series of tests were performed in the triaxial tests: (1) the first series consisted of tests in which confining stress was varied in only one principal direction, (2) the second series consisted of tests in which confining stress was varied in two principal directions, and (3) the third series consisted of tests in which confining stresses were varied in all three principal directions. These three series were named TRI1, TRI2 and TRI3, respectively. The loading conditions for each series of tests are shown in Fig. 4.18.

A complete listing of the tests is given in Table 4.4. Interruptions caused by the rupture of the membrane on top of the LSTD are noted (January 12, 1983) in the table.



(a) BIARZ



(b) BIARX

Fig. 4.17 - Second Subset of First Series of Biaxial Confinement Tests with Variation of Stress in One Principal Direction (BIAR)

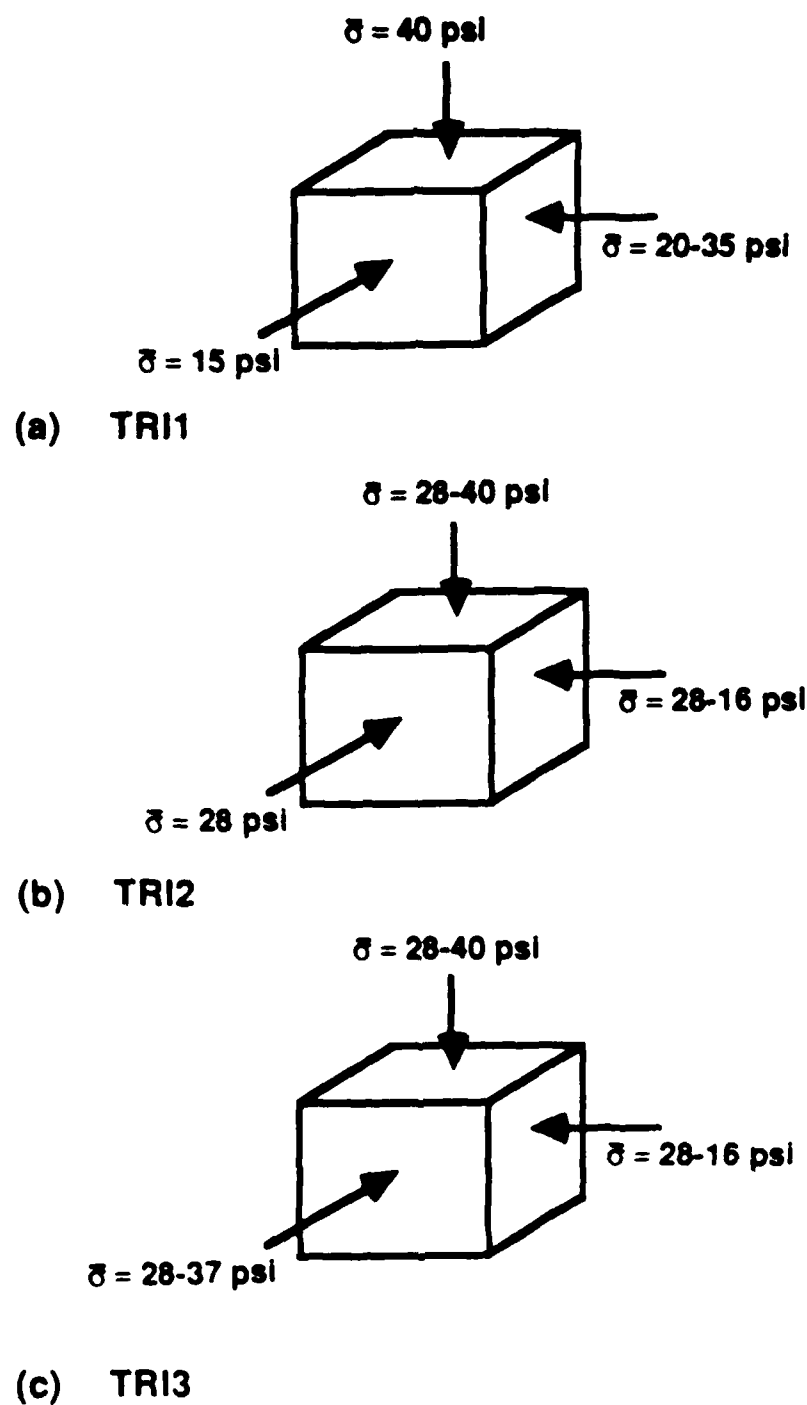


Fig. 4.18 - Loading Conditions for Triaxial Confinement Tests

CHAPTER FIVE

ISOTROPIC CONFINEMENT

5.1 INTRODUCTION

Six shear waves, four SV and two SH, were studied under isotropic states of stress. These waves always had their directions of propagation and particle motion polarized along principal stress directions. Nomenclature used to discuss these waves is shown in Fig. 2.4. Shear wave velocities presented herein are based on the initial arrival method (IAM) described in Section 3.5, and only average values of interval velocities are presented.

In a medium where stiffness increases as depth increases, wave travel paths will tend towards concave ray paths (Slotnick, 1959). Since the receivers are closely spaced when compared to the vertical variation in soil stiffness, the effect of curved ray paths was considered negligible (Haupt, 1973). Therefore, the horizontal plane at the mid-height of the cubical sample resulted in nearly isotropic conditions, with essentially no pressure gradient in the vertical direction.

Testing under conditions of isotropic confinement was first performed, and the results are presented in this chapter. This work was performed to understand the effect of the simplest stress state, isotropic confinement, on shear wave velocity. Moreover, shear wave velocity from these tests can be used: (1) to evaluate the effect of the mean effective stress on V_s , (2) to compare with other available data, and (3) to study structural anisotropy of the specimen (also called inherent anisotropy). As the idealized condition of isotropic confinement is impossible to attain perfectly (Section 3.2), all three effective principal stresses reported herein are those values which were applied to the horizontal plane at the mid-height of the cubical sample.

The effective major principal stress ($\bar{\sigma}_1$), the effective intermediate principal stress ($\bar{\sigma}_2$), and the effective minor principal stress ($\bar{\sigma}_3$) are all the same in isotropic confinement tests. All tests were performed at confining pressures ranging from 10 to 40 psi (68.9 to 275.6 kPa) measured at the center of the sample. Due to the weight of sand in the sample, the variation in vertical stress between the vertical monitoring accelerometers was ± 1.4 psi (± 9.6 kPa), which resulted in a ± 14 to ± 3.5 percent variation in confinement when the isotropic pressure varied from 10 to 40 psi (68.9 to 275.6 kPa), respectively.

5.2 EFFECTS OF STRESS STATE AND STRESS HISTORY

Tests with isotropic confinement afforded an opportunity to study the effect of stress state together with the effect of stress history on shear wave velocity. In addition, such tests permit direct comparison with available results, mostly from resonant column tests. To study the effect of stress history, a continuous sequence of loading and unloading tests was conducted with isotropic pressures ranging from 10 to 40 psi (68.9 to 275.6 kPa). Also, some tests at similar pressures were repeated during loading sequences using biaxial and triaxial states of stress.

5.2.1 CONTINUOUS SEQUENCE OF LOADING AND UNLOADING

The variation of shear wave velocity with isotropic confinement for the first continuous loading and unloading sequence is given in Tables 5.1 and 5.2. A linear variation in the $\log V_s - \log \bar{\sigma}_0$ relationship was assumed for each shear wave, and a least-squares straight line was fit through the data as illustrated in Figs. 5.1 to 5.3. The regression line for the $\log V_s - \log \bar{\sigma}_0$ relationship can be expressed as (Hardin and Richart, 1963):

$$V_s = C_2 \bar{\sigma}_0^{nm} \quad (5.1)$$

where:

V_s = shear wave velocity in fps,

C_2 = constant,

$\bar{\sigma}_0$ = mean effective principal stress in psf, and

nm = slope of $\log V_s - \log \bar{\sigma}_0$ relationship.

Values of C_2 and nm shown in Tables 5.1 and 5.2 were computed for each of the six shear waves.

As shown in Figs. 5.1 through 5.3, the regression lines for the unloading data have slightly flatter slopes than those for the loading data which results in the values of nm being slightly greater and the values of C_2 being slightly less upon loading. The largest variation in shear wave velocity for any shear wave upon loading and unloading is only 5 percent for V_{xz} at 10 psi (68.9 kPa), and the least variation is zero percent difference for V_{xy} at 10 psi (68.9 kPa). As a result, the hysteresis effect (stress history effect) upon shear wave velocity was not significant, and the general $\log V_s - \log \bar{\sigma}_0$ relationship for loading and unloading remained the same.

Table 5.1 - Shear Wave Velocities Measured During First Continuous Loading Sequence under Isotropic Confinement

Shear Wave Type	Isotropic Confining Pressures, psi					nm*	C ₂ *
	10	15	20	30	40		
V _{xy}	859	941	998	1079	1123	0.19	236
V _{xz}	789	857	890	990	1040	0.20	182
V _{yx}	861	924	991	1081	1154	0.21	166
V _{yz}	803	857	921	975	1032	0.18	212
V _{zx}	744	805	846	926	990	0.21	157
V _{zy}	773	815	873	957	988	0.19	177

*Eq. 5.1; $V_s = C_2 \bar{\sigma}_o^{nm}$ (with V_s in fps and $\bar{\sigma}_o$ in psf)

Table 5.2 - Shear Wave Velocities Measured During First Continuous Unloading Sequence under Isotropic Confinement

Shear Wave Type	Isotropic Confining Pressures, psi					nm*	C ₂ *
	10	15	20	30	40		
V _{xy}	859	940	976	1093	1123	0.20	182
V _{xz}	828	888	914	992	1041	0.16	259
V _{yx}	848	967	1023	1076	1154	0.21	181
V _{yz}	807	871	925	950	1032	0.17	271
V _{zx}	760	836	884	945	990	0.19	181
V _{zy}	787	828	876	958	988	0.17	211

*Eq. 5.1; $V_s = C_2 \bar{\sigma}_o^{nm}$ (with V_s in fps and $\bar{\sigma}_o$ in psf)

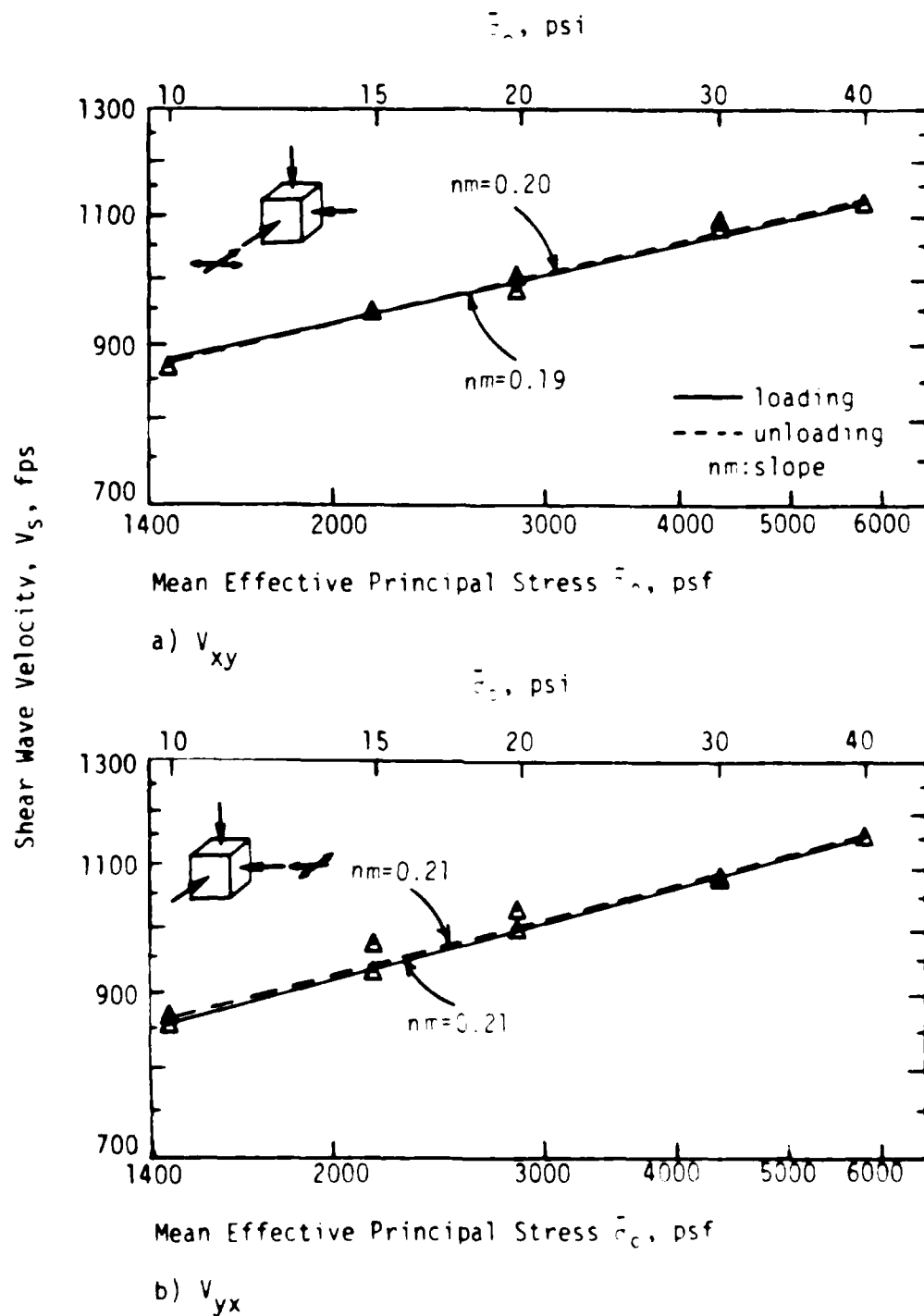


Fig. 5.1 - Effect of Stress History on Variation of S-Wave Velocities, V_{xy} and V_{yx} , with Isotropic Confining Pressure

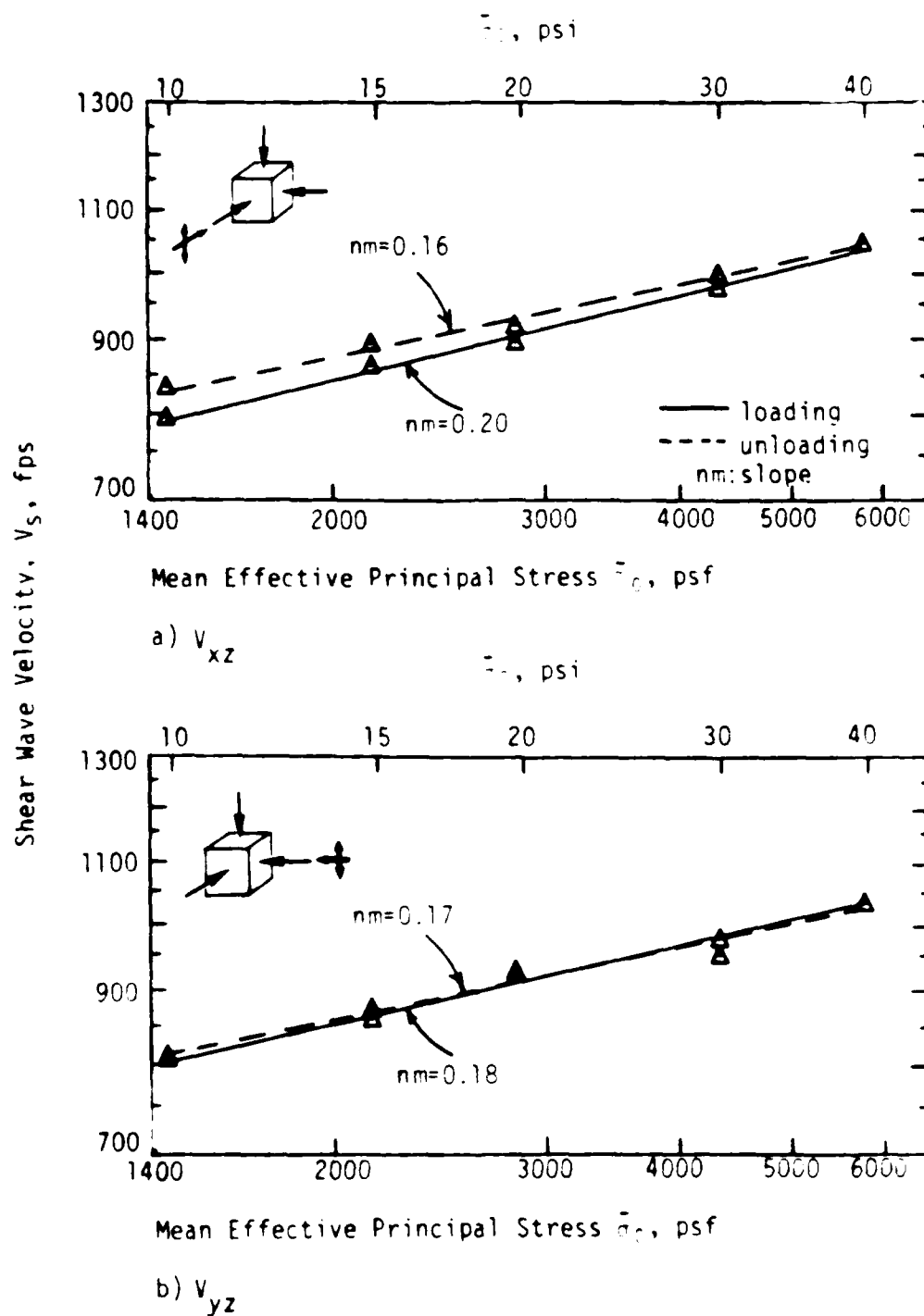


Fig. 5.2 - Effect of Stress History on Variation of S-Wave Velocities, V_{xz} and V_{yz} , with Isotropic Confining Pressure

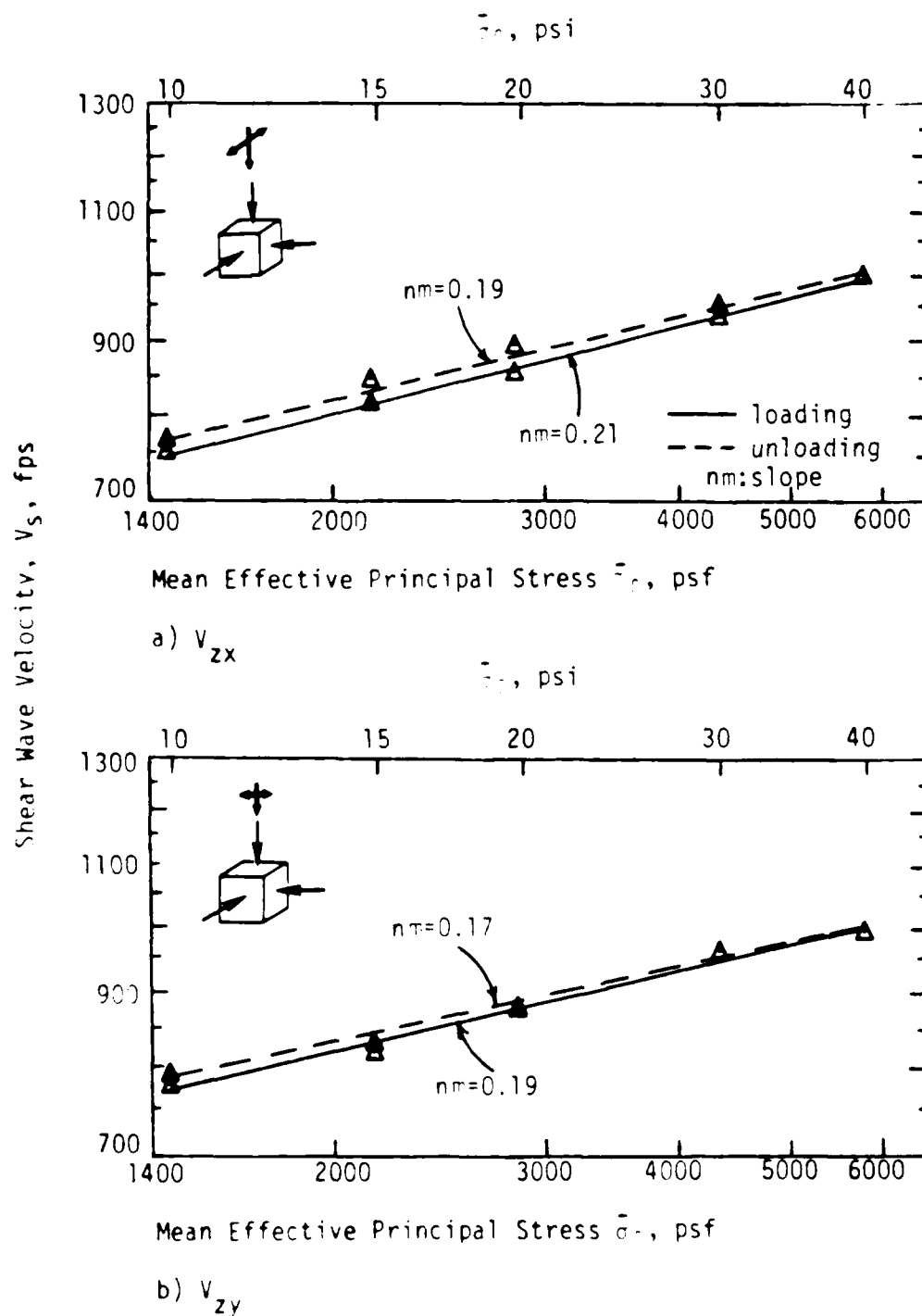


Fig. 5.3 - Effect of Stress History on Variation of S-Wave Velocities, V_{zx} and V_{zy} , with Isotropic Confining Pressure

5.2.2 REPEATED TESTS AT SIMILAR PRESSURES

Throughout the complete series of tests (summarized in Table 4.4), some shear wave velocities measured during the anisotropic confinement series were actually under isotropic states of stress as listed in Table 5.3. Average and standard deviations of velocities at each isotropic state of stress were determined for each shear wave and are summarized in Table 5.4. As can be seen in the table, shear wave velocities at each confining pressure are nearly the same. Standard deviations are less than 5.8 percent of the average velocities for all cases (124 tests for 30 cases), and less than 4 percent for 24 cases. The effect of repeated isotropic confinement on each of the six shear waves is shown in Figs. 5.4 to 5.6.

The 95-percent confidence intervals are also shown as dashed lines in Figs. 5.4 through 5.6. The probability of the value of shear wave velocity at a certain confining pressure falling between the interval constrained by the dashed lines is 95 percent (Ang and Tang, 1975; and Mandel, 1984). Therefore, the narrower the 95-percent interval, the better the test results. Figures 5.4 through 5.6 show fairly good results as expected, and the effect of stress history on shear wave velocity through repeated tests at similar pressures is negligible.

5.2.3 EFFECT OF CONFINEMENT PERIOD AT ONE PRESSURE

Age of soil has been shown to be an important consideration when comparing field and laboratory shear wave velocities (Stokoe and Lodde, 1978). The period of confinement at a single pressure is especially important in a laboratory test (Hardin and Black, 1968; Hardin and Drnevich, 1970; and Anderson and Stokoe, 1978). Test numbers 73 through 76 were conducted under isotropic confining pressure of 40 psi (275.6 kPa) for 47 hours. Pulse testing was done at 0.5, 1.5, 2.0, and 46.5 hours after the confining pressure was added. (Usually it took about three hours for added confining pressures to become completely stable.) The test results are listed in Table 5.5 and are shown in Fig. 5.7. Because shear wave velocities in this research are generally depicted with log-log scales, Fig. 5.7 is drawn on a scale of $\log V - \log t$.

Although there is a slight amount of scattering in shear wave velocities at one pressure, the linear regression lines of shear wave velocities in this test are found to be parallel and have zero slopes. The largest difference

Table 5.3 - Shear Wave Velocities Measured from Repeated Tests Under Isotropic Confinement

Test No.	10	16	22	23	32	33	35	38	53	54	60	63
Isotropic Confining Pressure, psi	15L*	40L	15U**	20L	30L	40L	20U	15L	30L	40L	15U	40L
Shear Wave Type	V _{xy}	1110	940	978	997	1101	1001	927	1013	1104	917	1124
	V _{xz}	1030	880	923	976	1051	916	843	976	1050	***	-
	V _{yx}	1135	939	983	1161	1192	1115	929	1105	1171	936	1164
	V _{yz}	1032	943	984	1047	1077	947	929	1047	1100	913	1040
	V _{zx}	821	854	890	951	1025	896	835	921	979	843	1023
	V _{zy}	828	847	882	925	970	891	830	922	960	804	1004

* L: Loading sequence

** U: Unloading sequence

*** : Malfunction of Accelerometers

Table 5.4- Average Value of Shear Wave Velocities from All Tests
under Isotropic Confining Pressures

Shear Wave Type	Isotropic Confining Pressures, psi					nm*	C ₂ **
	10	15	20	30	40		
V _{xy}	860+0*	953+11	988+14	1046+47	1112+10	0.18	238
V _{xz}	809+28	861+23	911+15	978+9	1043+9	0.19	206
V _{yx}	855+9	933+33	1028+60	1106+39	1164+21	0.23	167
V _{yz}	806+3	898+37	944+29	999+59	1057+31	0.18	224
V _{zx}	752+11	833+17	889+33	936+14	1001+22	0.19	187
V _{zy}	781+10	825+15	881+8	941+19	984+15	0.17	219

* Standard deviation

** Eq. 5.1; $V_s = C_2 \bar{\sigma}_0^{nm}$ (with V_s in fps and $\bar{\sigma}_0$ in psf)

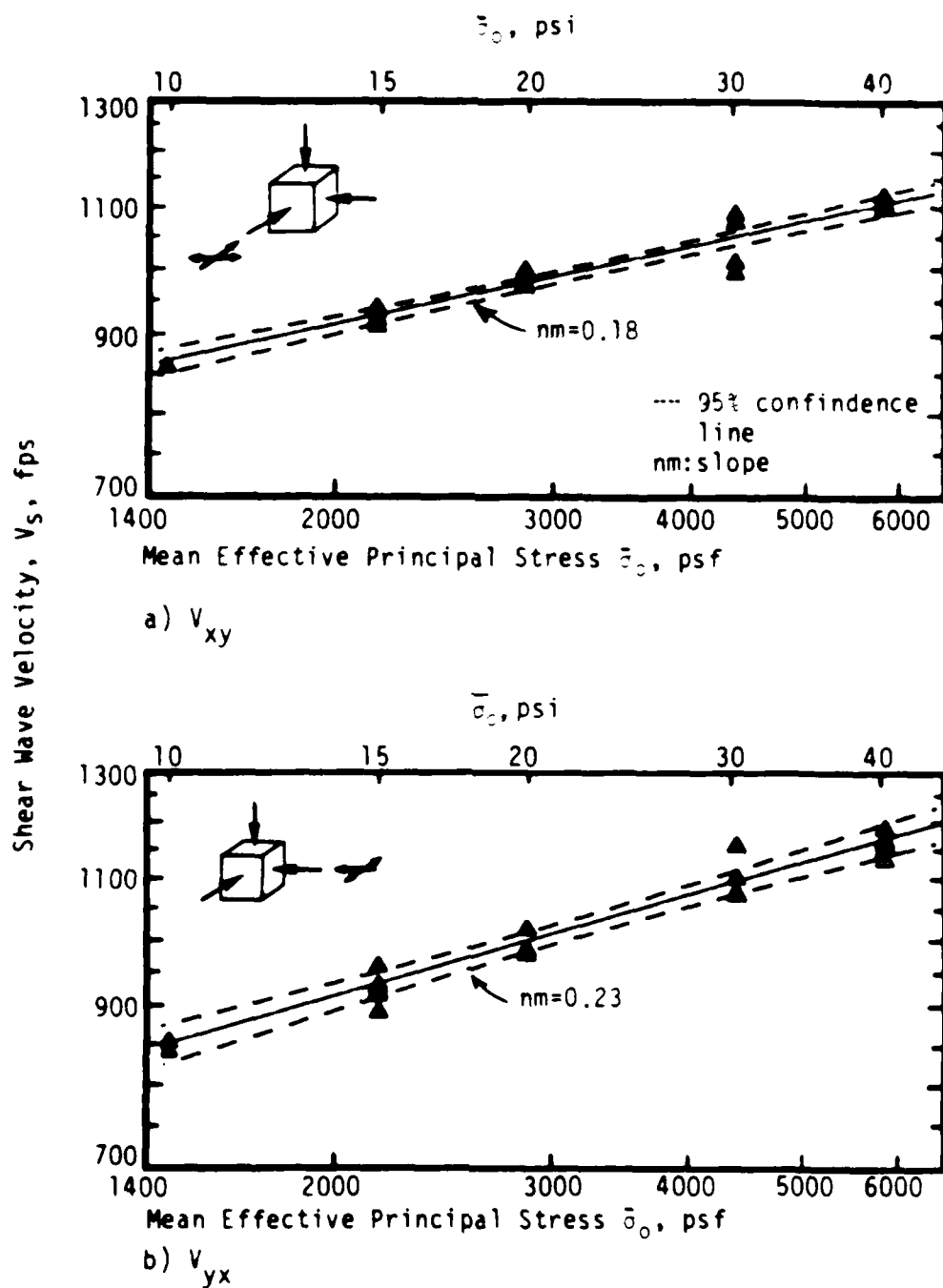


Fig. 5.4 - Effect of Repeated Loading on Variation of S-Wave Velocities, V_{xy} and V_{yx} , with Isotropic Confinement

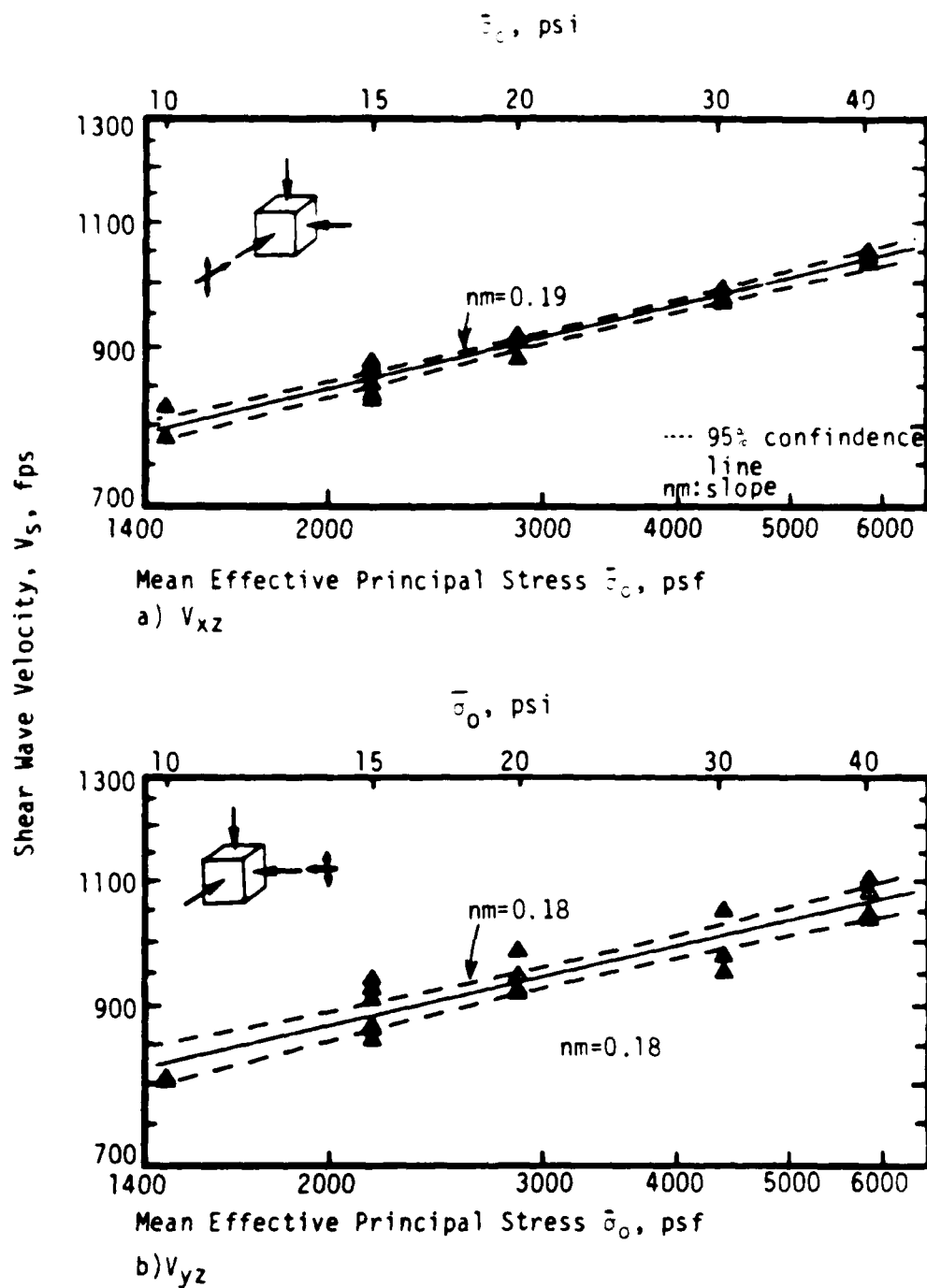


Fig. 5.5 - Effect of Repeated Loading on Variation of S-Wave Velocities, V_{xz} and V_{yz} , with Isotropic Confinement

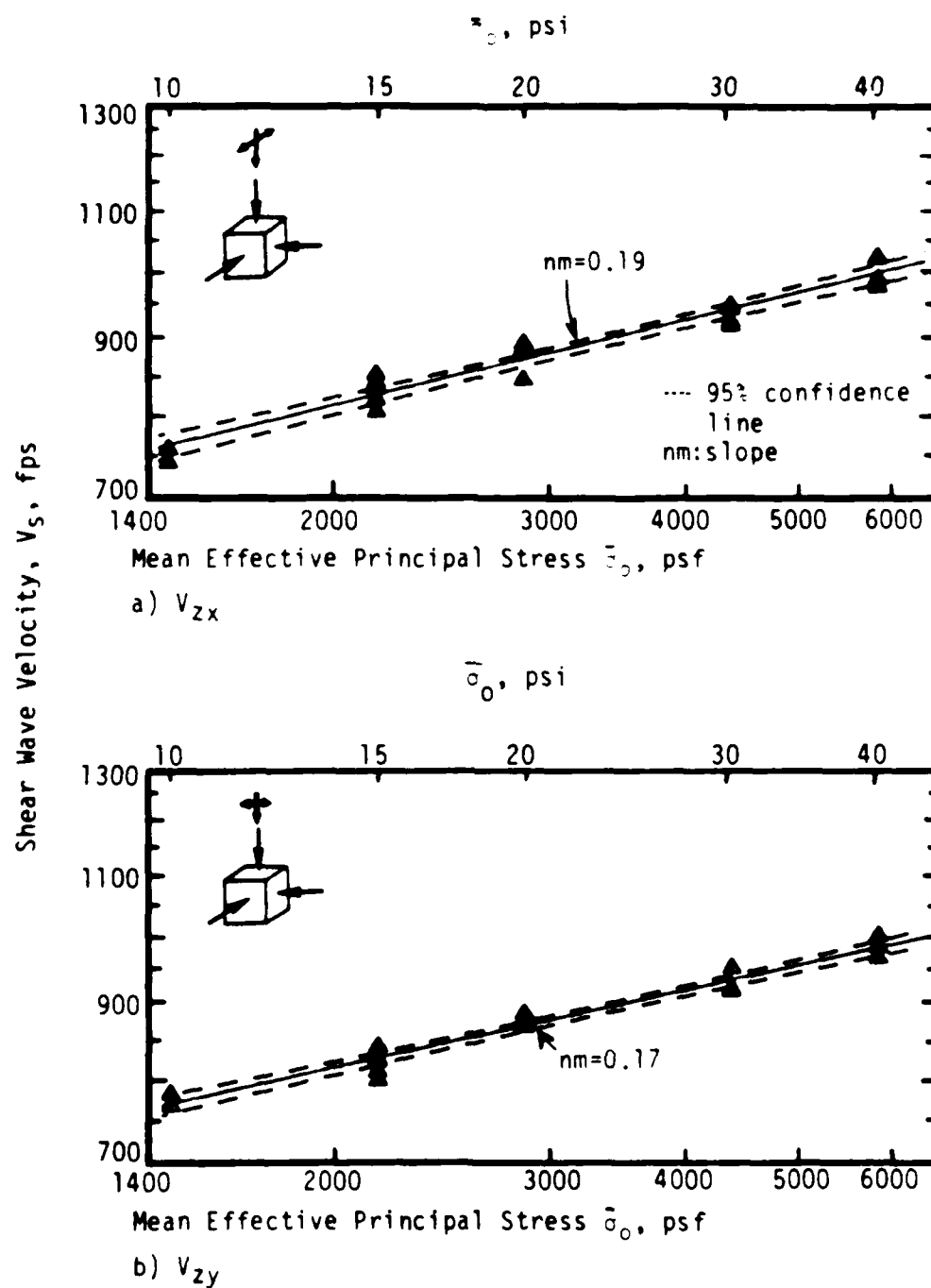


Fig. 5.6 - Effect of Repeated Loading on Variation of S-Wave Velocities, V_{zx} and V_{zy} , with Isotropic Confinement

Table 5.5 - Shear Wave Velocities at Different Times under an Isotropic Pressure of 40 psi

Shear Wave Type	Time, T, hours				Slope* nt
	0.5	1.5	2.0	46.5	
V_{xy}	1123	1119	1116	1114	0.00
V_{xz}^{**}	---	---	---	---	---
V_{yx}	1164	1149	1154	1143	0.00
V_{yz}	1040	1043	1043	1053	0.00
V_{zx}	1023	1023	1026	1022	0.00
V_{zy}	1004	1005	1006	1008	0.00

* nt = the slope of $\log V - \log T$ curve

V = shear wave velocity

T = period of isotropic confinement

** Accelerometers in the direction of V_{xz} were out of order.

ISOTROPIC CONFINEMENT

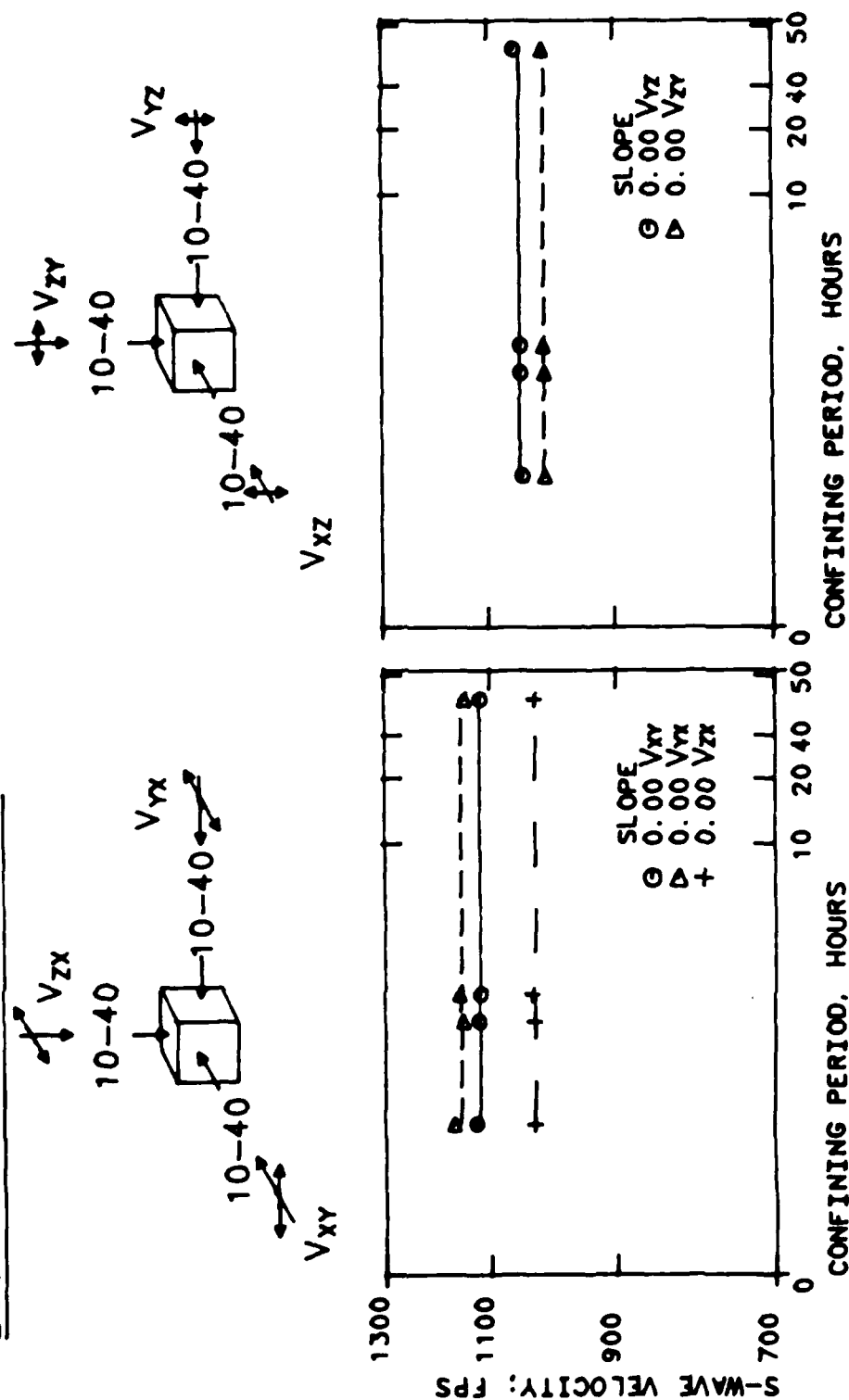


Fig. 5.7 - Effect on V_s of Confining Period at an Isotropic Pressure of 40 psi

in shear wave velocities for any direction (Table 5.5) is only 1.8 percent which was measured for V_{xy} . Afifi and Richart (1973) concluded from isotropic resonant column tests that the influence of confining period on shear modulus of a sample with $D_{50} \gg 0.04$ mm is not significant. The value of D_{50} of this sand is 0.35 mm (see Section 4.2), and the results of the effect of confining period on shear wave velocity agree with the conclusion from Afifi and Richart. The effect of confining period is, therefore, considered negligible in the range of pressures and time periods used in this study.

As can be seen in Figs. 5.1 through 5.3, shear wave velocities in the unloading sequence are a little higher than those in the loading sequence. But there is not much scattering of shear wave velocity under the same isotropic confinement condition throughout the complete series of tests, and most data are located between the 95% confidence lines for loading and unloading tests for all cases (see Figs. 5.4 to 5.6). The standard deviations are always less than 5.8 percent of the average velocities for all cases (Section 5.2.2). Furthermore, the maximum difference of shear wave velocities in first loading and unloading sequence is only +5.7 percent with an average of +1.4 percent for all types of shear waves (see Table 5.6). Also, the maximum difference between the first loading and the average of the complete set is only +3.9 percent, with an average of +1.0 percent for all tests. Consequently, the effects of time of confinement and stress history are considered to be negligible under isotropic confinement, especially if the average of a large number of shear wave velocities measurements can be obtained.

5.3 EFFECT OF STRUCTURAL ANISOTROPY

In Section 4.3 of the report of Chu et al (1984), this sand sample has been shown to behave like a cross-anisotropic medium under isotropic loading. Based on the cross-anisotropic model discussed in Section 2.2, shear waves in the isotropic plane (the horizontal (xy) plane for this sample) should exhibit the same velocities while shear waves in the anisotropic planes (xz and yz planes) should exhibit the same velocities which are different from those in the isotropic plane, or:

$$V_{SI} = V_{xy} = V_{yx}, \text{ and} \quad (5.2.a)$$

Table 5.6 - Comparison of Shear Wave Velocities on First Loading, First Unloading and Complete Set of Tests under Isotropic Confinement

Shear Wave Type	(1) First Loading		(2) First Unloading		(3) Average of Complete Set		(2) - (1) (1), %		(3) - (1) (1), %		No. of Samples
	$\bar{\sigma}_o =$ 10 psi	$\bar{\sigma}_o =$ 40 psi	$\bar{\sigma}_o =$ 10 psi	$\bar{\sigma}_o =$ 40 psi	$\bar{\sigma}_o =$ 10 psi	$\bar{\sigma}_o =$ 40 psi	$\bar{\sigma}_o =$ 10 psi	$\bar{\sigma}_o =$ 40 psi	$\bar{\sigma}_o =$ 10 psi	$\bar{\sigma}_o =$ 40 psi	
V _{xy}	878	1129	857	1151	868	1110	-2.4	+2.0	-1.1	-1.7	21
V _{xz}	783	1033	828	1033	801	1037	+5.7	0	+2.3	+0.4	19
V _{yx}	846	1154	866	1167	859	1174	+2.4	+0.1	+1.5	+1.7	21
V _{yz}	801	1033	816	1007	827	1061	+1.9	-2.5	+3.2	+2.7	21
V _{zx}	735	987	765	1008	764	999	+4.2	+2.1	+3.9	+1.2	21
V _{zy}	757	999	779	1000	775	986	+2.9	+0.1	+2.4	-1.3	21
Average =					+1.4		+1.0				

$$V_{SA} = V_{xz} = V_{yz} = V_{zx} = V_{zy} \quad (5.2.b)$$

A comparison of mean values of V_{xy} and V_{yx} for the overall tests is presented in Table 5.7. The average difference is only 2.7 percent which is nearly the same as the difference of 3 percent in P-wave velocities (V_{xx} and V_{yy}) measured in the horizontal plane (see Sections 4.3 of Chu et al, 1984).

The mean values of shear wave velocities of V_{xz} , V_{yz} , V_{zy} , and V_{zx} are listed in Table 5.8. Since compression wave velocities measured in the xy plane exhibited some scatter, shear wave velocities, V_{xz} , V_{yz} , V_{zx} and V_{zy} also exhibited some scatter as expected. This implies that this sample is a little like an orthotropic medium rather than a perfect cross-anisotropic one. The difference between each shear wave velocity and its mean value at one isotropic confining pressure does not exceed 5.5 percent as shown in Table 5.8, and the maximum average difference between each shear wave type is only 3.6 percent which is close to the value found in the horizontal plane from P-wave velocities and V_{SI} .

Furthermore, the F-test results in Table 5.9 indicate that a linear regression analysis on the group of shear wave velocities of V_{xz} , V_{yz} , V_{zx} , as well as V_{zy} is very significant. Based on the value of adjusted R-square, at least 83 percent of the variation in V_s can be explained by the the $\log V_s - \log \bar{\sigma}_0$ equation used. Compared with an 89-percent explanation factor for the isotropic plane (Table 5.9), the explanation for the group of V_{xz} , V_{yz} , V_{zx} and V_{zy} is quite satisfactory. The results of the F-test for the constant C_2 and slope nm also indicate these values are very significant. Therefore, it seems that this sample can be treated reasonably well as a cross-anisotropic medium, and the shear wave velocities can be simplified as:

$$V_{SI} = 200 \bar{\sigma}_0^{0.20} \quad (5.3.a)$$

$$V_{SA} = 209 \bar{\sigma}_0^{0.18} \quad (5.3.b)$$

where:

V_{SI} = shear wave velocity in horizontal plane (perpendicular to axis of symmetry), fps,

V_{SA} = shear wave velocity propagating in vertical planes with particle motion in horizontal planes, and vice versa, i.e. S-wave in the anisotropic planes.

Table 5.7 - Comparison of Shear Wave Velocities, V_{xy} and V_{yx} , in the Isotropic Plane Measured under Isotropic Confinement

Isotropic Confinement psi	V_{xy} fps	V_{yx} fps	$\frac{(3) - (2)}{(2)}$ %
(1)	(2)	(3)	(4)
10	860	855	-0.5
15	935	833	-0.2
20	988	1028	+4.0
30	1046	1106	+5.7
40	1112	1164	+4.7
Average =			+2.7

Table 5.8 - Comparison of Shear Wave Velocities, V_{xz} , V_{yz} , V_{zx} and V_{zy} , in Anisotropic Planes Measured under Isotropic Confinement

Isotropic Confinement psi	(1) V_{xz} fps	(2) V_{yz} fps	(3) V_{zx} fps	(4) V_{zy} fps	(5) $\frac{(1)+(2)+(3)+(4)}{(4)}$	(6) $\frac{(1)-(5)}{(5)}$ %	(7) $\frac{(2)-(5)}{(5)}$ %	(8) $\frac{(3)-(5)}{(5)}$ %	(9) $\frac{(4)-(5)}{(5)}$ %
10	809	806	752	781	787	+2.8	+2.4	-4.4	-0.8
15	861	902	833	825	855	+0.7	+5.5	-2.6	-3.5
20	911	944	889	881	906	+0.5	+4.1	-1.9	-2.7
30	978	998	936	941	963	+1.5	+3.6	-2.8	-2.3
40	1043	1056	1001	984	1021	+2.2	+3.4	-1.9	-3.6
					Average =	+1.5	+3.6	-2.7	-2.6

Table 5.9 - Results of Linear Regression Analysis of V_S Values Used in Representing Cubical Sample as a Cross-Anisotropic Model

Shear Wave Type	Linear Correlation Coefficient	R-Square	Adjusted R-Square	F-test of Sample		C_2^*			nm^*		
				ratio	α	value	F-test		value	F-test	
							ratio	α		ratio	α
V_{xy} or V_{yx} **	0.945	0.893	0.891	355.5	0	199.6	33629	0	0.201	355.5	0
V_{xz} , V_{yz} V_{zx} or V_{zy} ***	0.912	0.831	0.829	394.2	0	208.9	47185	0	0.183	394.2	0

* Eq. 5.1; $V_S = C_2 \bar{\sigma}_0^{nm}$ (with V_S in fps and $\bar{\sigma}_0$ in psf).

** $V_{SI} = V_{xy} = V_{yx}$

*** $V_{SA} = V_{xz} = V_{zx} = V_{yz} = V_{zy}$

Experimental results using Eq. 5.3 are shown in Fig. 5.8. It is important to note that since the constants in Eq. 5.3 are almost the same, structural anisotropy is caused mainly by the variation in the value of the slope of Eq. 5.3 rather than by general shifting of the line by the value of the constant. In other words, V_{SI} will be equal to V_{SA} at a certain confining pressure [9.033 psf (0.43 kPa)] in this study). It is interesting to note that the same results for P-wave velocities were also found. However, more research is necessary to better understand this behavior.

The difference between V_{SI} and V_{SA} under isotropic loading is caused by structural anisotropy in the sample. Different shear wave velocities measured in situ with crosshole and downhole seismic tests have also been reported by Arango, Moriwaki, and Brown (1978). Structural as well as stress anisotropy can be the cause of these differences (Stokoe, et al 1978). Stress induced anisotropy is discussed in Chapter Six.

5.4 EFFECT OF ISOTROPIC CONFINEMENT

Detailed results of the linear regression analysis of the shear wave velocities from all tests under isotropic confinement are listed in Table 5.10. From the minimum value of R-square (0.857), one can say that at least 86 percent of the variation in V_s can be explained by the linear correlation with mean effective stress (Draper and Smith, 1981). The average value of R-square is 0.93. By considering the number of samples, the minimum value of adjusted R-square is still 85 percent (0.847 in Table 5.10), and the maximum value of adjusted R-square is 96 percent (0.962 in Table 5.10) i.e., about 85 to 96 percent of the variation can be explained by the linear regression results. All the α -values of the F-test equal zero which means that the linear regression analysis is very significant. Equation 5.1 is, therefore, a proper form of expressing the variation of shear wave velocity with isotropic confining pressure.

By substituting the values of the constants and slopes in Table 5.9 into Eq. 5.1, the relationship between the velocities in the isotropic and anisotropic planes is:

$$V_{SI} = 0.566 (V_{SA})^{1.098} \quad (5.4)$$

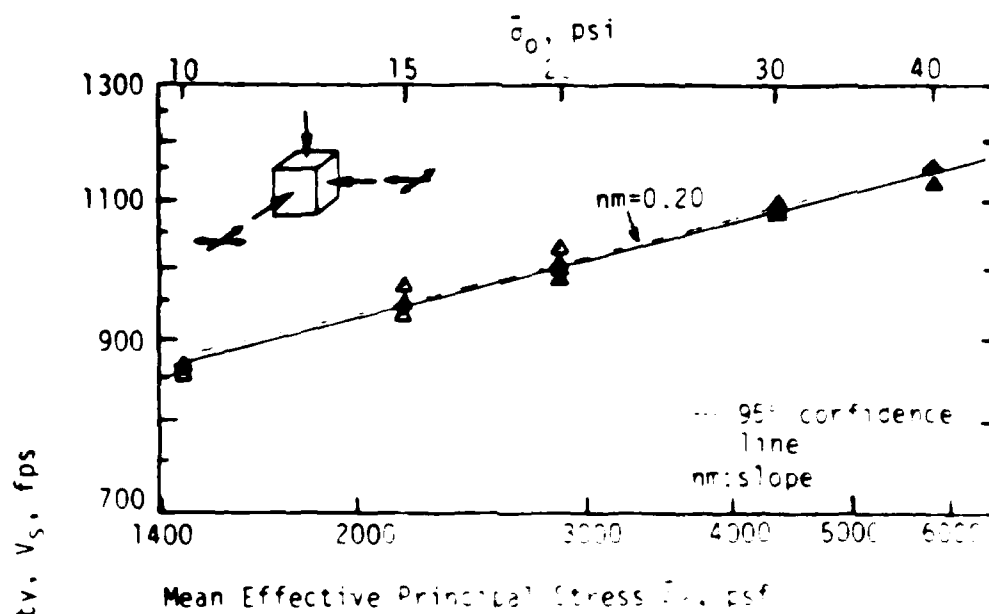
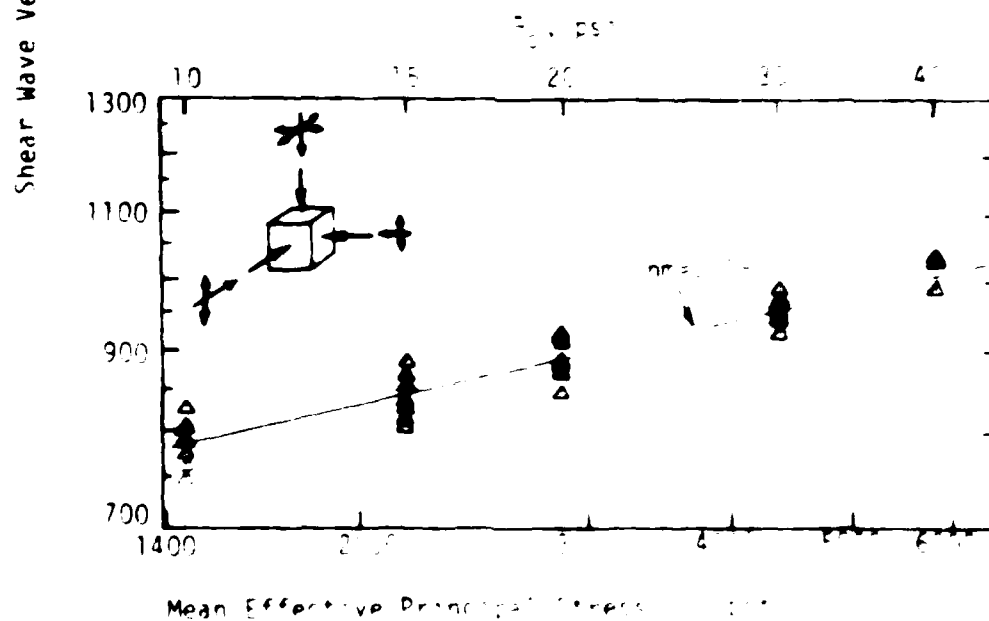
a) V_{S1} b) V_{SA}

Fig. 5. Effect of principal stress on shear wave velocity for interlocking concrete.

Table 4.10 Regression Analysis of Shear Wave Velocities from Complete Set of Tests under Isotropic Confinement

Shear Wave Type	Number of Samples	Linear Correlation Coefficient	R-Square	Adjusted R-Square	F-Test of Sample		C ₂ [*]		nm [*]	
					ratio	n	Value	F-Test ratio	Value	F-Test ratio
V _{xy}	21	0.970	0.941	0.938	304.9	0	238.38 +1.03	40032.7	0.1776 +0.0101	304.9
V _{yx}	21	0.956	0.914	0.909	201.7	0	167.04 +1.64	15874.3	0.2251 +0.0150	201.7
V _{xz}	19	0.979	0.958	0.956	392.6	0	205.89 +1.02	15874.3	0.1867 +0.0094	392.6
V _{yz}	21	0.925	0.857	0.849	113.8	0	223.72 +1.05	45532.8	0.1797 +0.0168	113.8
V _{zx}	21	0.975	0.952	0.949	376.3	0	187.09 +1.03	39531.4	0.1935 +0.0097	376.3
V _{zy}	21	0.982	0.964	0.962	505.3	0	219.02 +1.02	67108.5	0.1737 +0.0077	505.3

* $V_s = C_2 \sqrt{\rho}$ nm

By substituting the values listed in Table 5.8 into Eq. 5.4, the ratio of V_{SI} to V_{SA} is from +8.8 percent to +11.6 percent for confining pressures from 10 to 40 psi (68.9 to 275.6 kPa). On the average, V_{SI} is about 10 percent higher than V_{SA} for this sand sample, i.e.,

$$V_{SI} = 1.10 V_{SA} \quad (5.5)$$

The value of the ratio (1.10) is a little smaller than the ratio (1.17) of V_{PI} to V_{PA} (Chu, et al, 1984).

5.5 SUMMARY

Six types of shear waves were generated to test the influence of isotropic confinement on the structural characteristic as well as the stress history of the sand sample. No significant effects of stress history or time of confinement were found.

The effect of effective isotropic confining pressure, $\bar{\sigma}_0$, on shear wave velocity was found to be well represented by a linear relationship between $\log V_s$ and $\log \bar{\sigma}_0$. Furthermore, a cross-anisotropic model is a good representation of wave velocities in the sample, and Eq. 5.3 can then be used to predict the shear wave velocities. In Eq. 5.3, quite similar values of the constants (C_2) for horizontally and vertically polarized shear waves (200 and 209, respectively) were found while the values for the slopes (η) exhibited somewhat larger variations (0.20 and 0.18, respectively). These results imply that the effect of structural anisotropy in this sand under isotropic loading is more reflected by the slopes in Eqs. 5.3. However, more work is necessary to understand and define this point in greater detail.

Although the equation for shear modulus suggested by Hardin (1978) is well suited for isotropic confining pressures, it was noted that different shear moduli existed for the vertical and horizontal directions in the large sample (as well as in natural soil). At this time, such differences cannot be easily detected with small samples such as those used in resonant column, torsional shear, cyclic shear and cyclic triaxial testing.

CHAPTER SIX

BIAXIAL CONFINEMENT

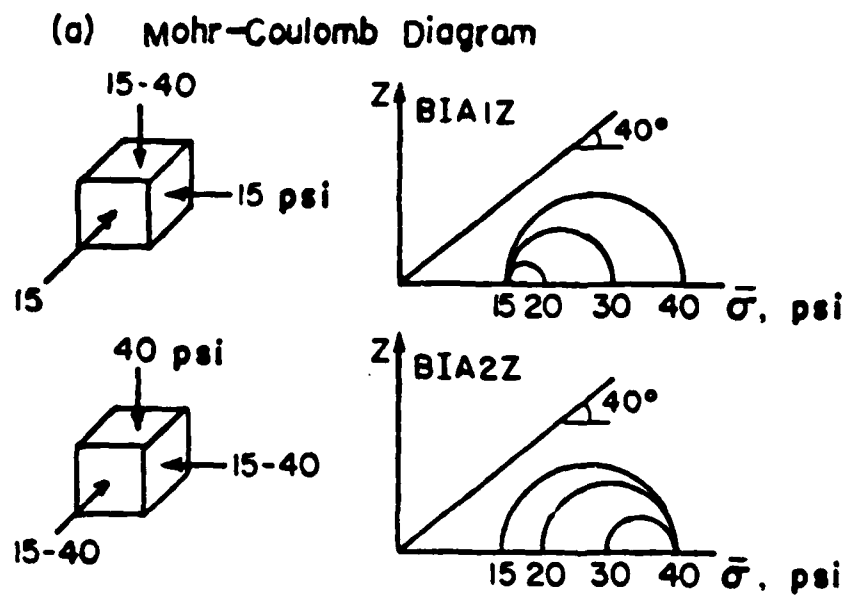
6.1 INTRODUCTION

An extensive set of tests was performed under biaxial confinement as outlined in Section 4.6. Biaxial confinement of the sand sample is defined herein to represent those stress states when two of the three principal stresses are equal. The complete set of biaxial tests can be divided into two basic sets of tests; the first representing those tests when only one principal stress was varied, called BIA1, and the second set when two principal stresses were varied simultaneously called BIA2. A subset of BIA1, called BIAR, was also conducted in which one principal stress was varied and principal stress reorientation occurred.

For biaxial confinement, all principal stresses were no longer the same as in isotropic confinement so that the effect of each stress component on shear wave velocity could be investigated. The orientation of principal stresses in both series of tests (BIA1 and BIA2) was always held constant, i.e., no matter whether one or two principal stresses were varied, the directions of major, intermediate, and minor principal stresses were never changed. On the other hand, the major principal stress of BIAR was varied to be the minor principal stress during testing, and vice versa (see Section 4.6). The Mohr-Coulomb and space diagrams of BIA1, BIAR, and BIA2 are shown in Figs. 6.1 and 6.2. Figure 6.1a illustrates BIA1Z and BIA2Z. (The fifth character in the notation refers to the direction in which the stress was varied for the BIA1 series and the direction in which the stress was not varied for the BIA2 series.) As shown in the Fig. 6.1b, the stress paths of BIA1Z and BIA2Z are drawn with solid lines, whereas BIA1X, BIA2X, BIA1Y and BIA2Y are drawn with dashed lines. For BIAR, the principal stress was varied along the z- and y-directions only as shown in Fig. 6.2b. Figure 6.2a shows the Mohr-Coulomb diagram for BIARZ.

6.2 EFFECT OF STRESS HISTORY

The effect of stress history on the dynamic stiffness of the sand under isotropic confinement is shown to be negligible in Section 5.2.2. The effects of stress history due to unloading-reloading, repeated tests, and confinement time at the same confinement state were also investigated under



(b) Principal Stress Space

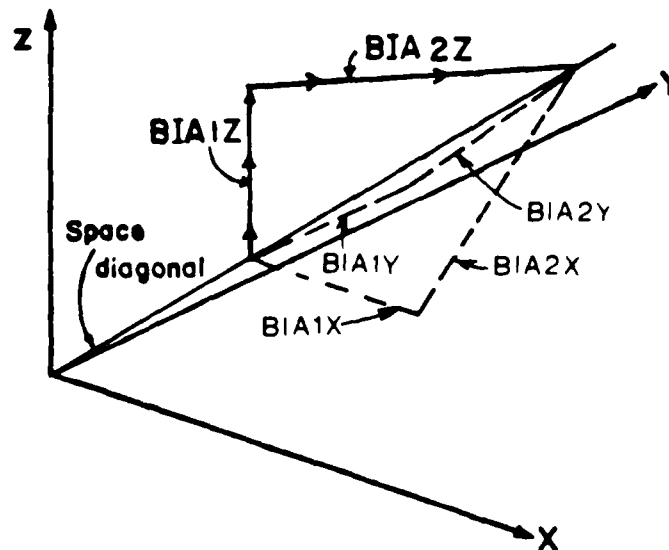
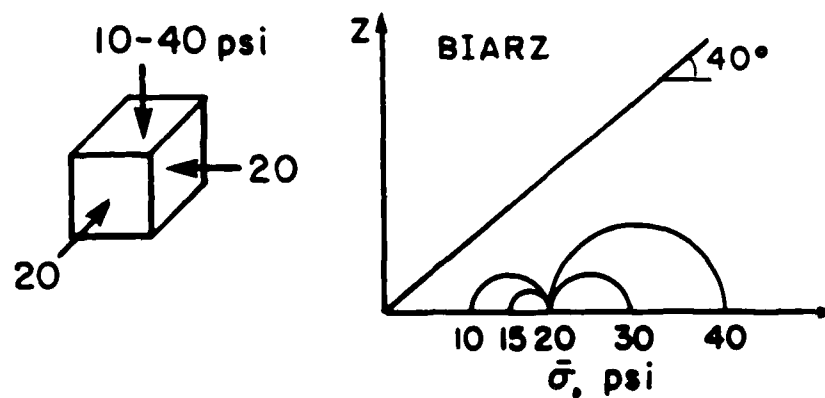


Fig. 6.1 - Biaxial Confinement Tests with Direction of Major Principal Stress Remaining Constant

(a) Mohr - Coulomb Diagram



(b) principal stress diagram

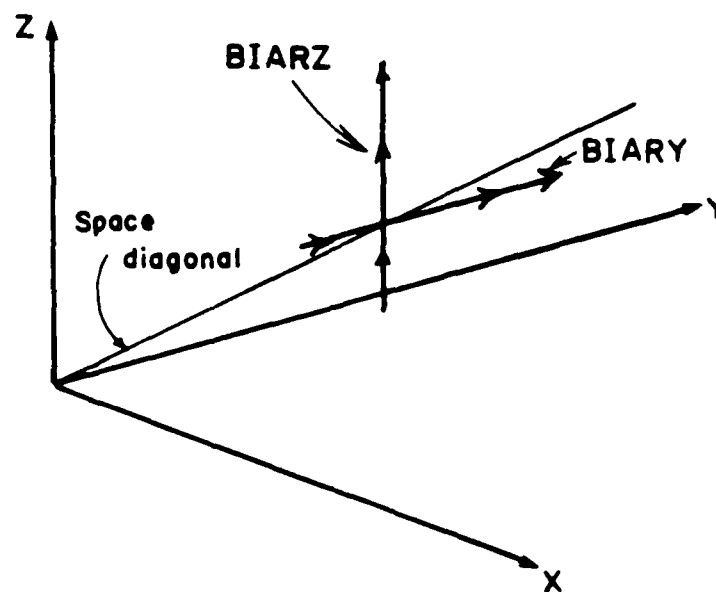


Fig. 6.2 - Biaxial Confinement Tests with Direction of Major Principal Stress Reorienting

biaxial loading. This was done to determine the importance of stress history in testing this sand.

Since plastic material behavior is stress-path dependent, stress history will affect the stress-strain behavior if the stress state exceeds the elastic range (Chen, 1975). A series of consolidated drained tests was performed with traditional static triaxial equipment to evaluate the stress-strain behavior of this sand. Two curves for the dense sand under confining pressures equalling 10 and 45 psi (68.9 and 310 kPa) are shown in Fig. 4.4. The stress-strain behavior seems to be reasonably within the elastic range when the stress difference ($\sigma_1 - \sigma_3$) is less than 25 psi (172.3 kPa). Therefore, the maximum stress difference under biaxial confinement in this study was limited to 25 psi (172.3 kPa) to minimize any stress-path dependency. This limiting condition resulted in the major principal stress equalling 40 psi (275.6 kPa) together with minor principal stress equalling 15 psi (103.4 kPa) as the maximum stress difference throughout the biaxial confinement tests. With this condition, the stress level, $(\sigma_1 - \sigma_3)/(\sigma_1 + \sigma_3)_f$, was always kept below 0.463, and the ratio of major-to-minor effective principal stresses, $K_{13} = \bar{\sigma}_1/\bar{\sigma}_3$, never exceeded 2.67.

6.2.1 CONTINUOUS SEQUENCE OF LOADING AND UNLOADING

Two loading and unloading sequences under biaxial confinement are shown in Figs. 6.3 and 6.4. A small influence, less than 5 percent, on the S-wave velocities measured upon loading and unloading was observed. This was true for both the BIA1 and BIA2 series. These small differences are similar to those noted for the isotropic loading tests presented in Section 5.2.1. As such, these small differences are ignored in subsequent analyses.

As a note, it is obvious by looking at Figs. 6.3 and 6.4 that biaxial stress state has a different effect on Vs than the isotropic stress state. This point is addressed in detail in subsequent sections in this chapter. Between the loading and unloading sequence, tests of BIA2 were performed. Therefore, the regression lines on the loading and unloading sequence in BIA1 are not exactly the same as shown in Figs. 6.3 and 6.4 when the maximum confining pressure of 40 psi (275.6 kPa) was applied.

BIAXIAL CONFINEMENT BIA1Z

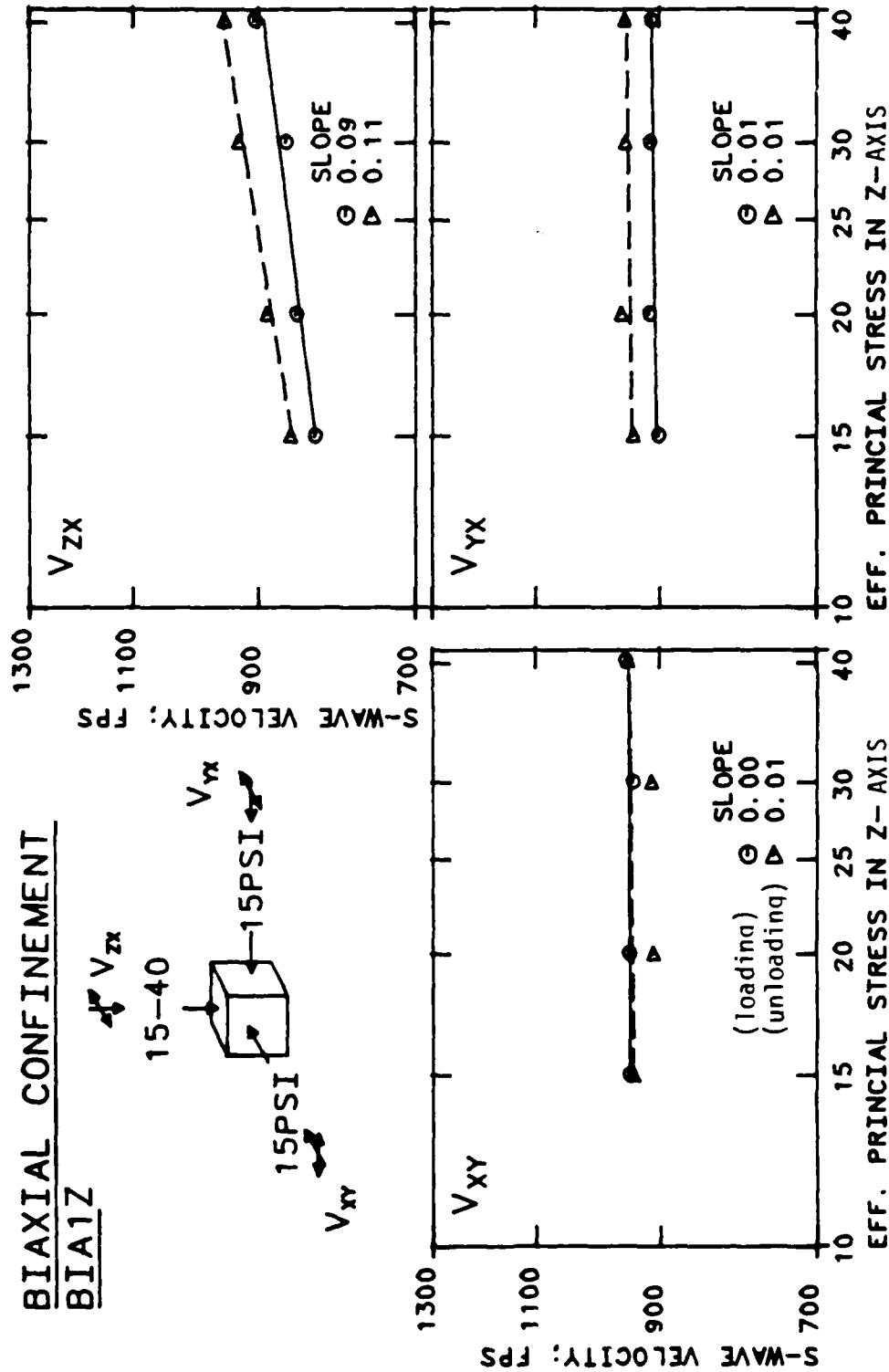
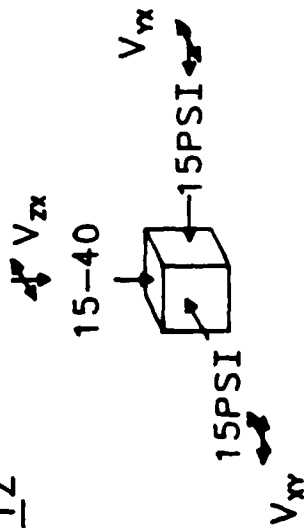


Fig. 6.3 - Shear Wave Velocities, V_{xy} , V_{yx} , and V_{zx} Under BIA1Z Loading

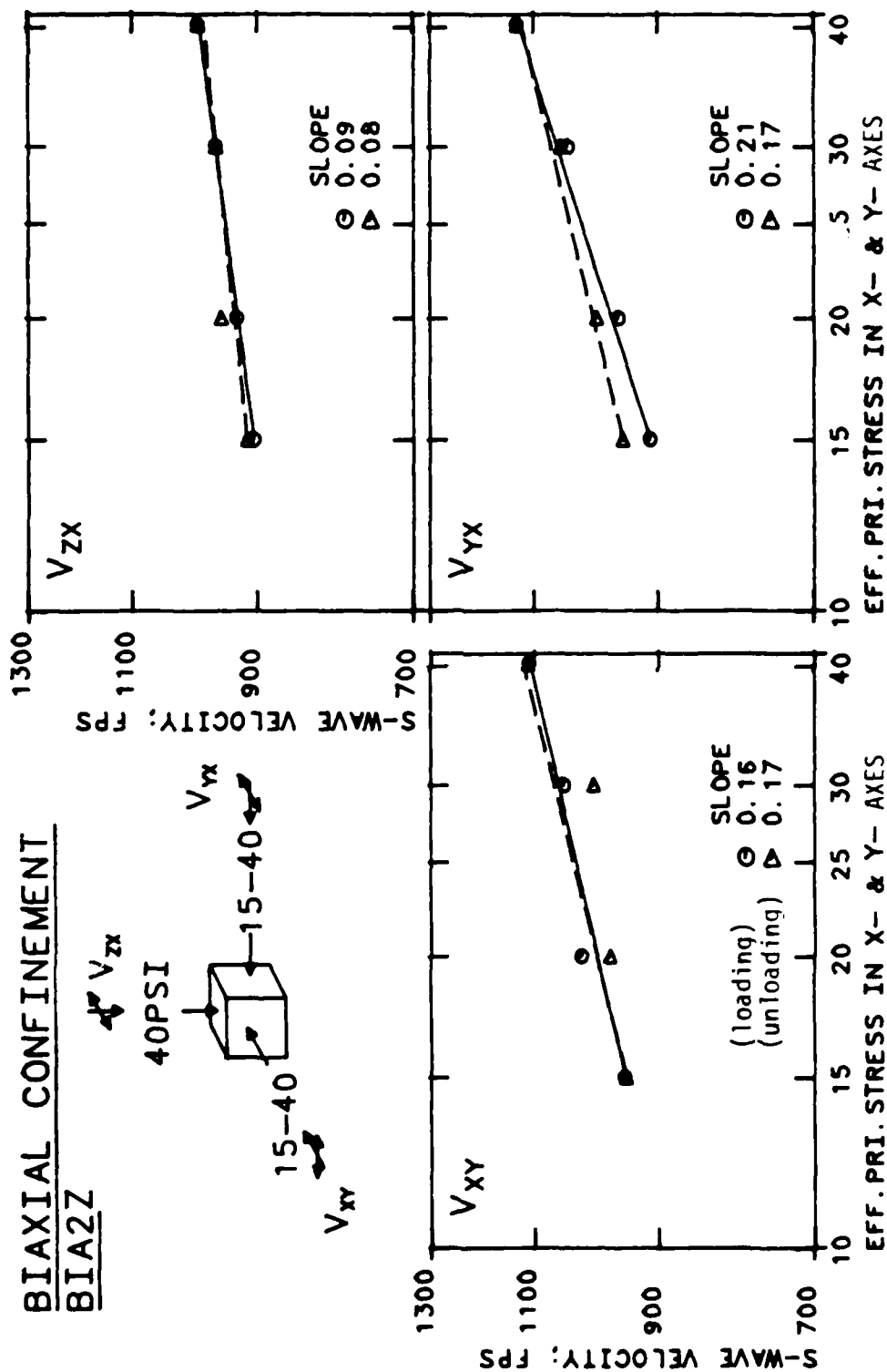


Fig. 6.4 - Shear Wave Velocities, V_{xy} , V_{yx} , and V_{zx} Under BIA2Z Loading

6.2.2 REPEATED TESTS AT SIMILAR PRESSURES

In the complex sequences of loading-unloading-reloading performed with the sand sample, the same stress state occurred several times. For instance, in series BIA2, $\bar{\sigma}_z$ equalled 40 psi (275.6 kPa) and both $\bar{\sigma}_x$ and $\bar{\sigma}_y$ equalled 20 psi (137.8 kPa) in test number 18, and this same stress state occurred in test number 25 in series BIAR. Likewise, the stress state of test number 42 in BIA2 is the same as test number 31 in BIAR, with $\bar{\sigma}_x$ equaling 40 psi (275.6 kPa) and both $\bar{\sigma}_y$ and $\bar{\sigma}_z$ equaling 20 psi (137.8 kPa). Therefore, these four tests were treated as two groups of repeated tests as summarized in Table 6.1.

To compare shear wave velocities measured at different times under the same biaxial confinement state, the ratios of differences between shear wave velocities under the BIA2 and BIAR states divided by the former were defined as DIFF. The values of DIFF listed in Table 6.1 generally range from -1 percent to +5 percent with the average being +3.4 percent in case 1 and +2.4 percent in case 2. Accordingly, the conclusion that the tests are quite repeatable at any given confining pressure under biaxial confinements is correct, just as it was for isotropic confinements (Section 5.2.2). Also, this leads to the conclusion that the effect of stress history is negligible if K_{13} is below 2.67.

Additionally, it should be noted that shear wave velocities in Table 6.1 have been determined for the following cases: (1) stresses varied in two directions with the major principal stress remaining constant, (2) stress varied in one direction with the major principal stress reoriented, (3) principal stress varied in the direction of wave propagation, (4) principal stress varied in the direction of particle motion, (5) principal stress varied in the out-of-plane direction, and (6) principal stress varied in both directions of wave propagation and particle motion. Only three of twelve values of DIFF are larger than +5 percent. The other nine values are less than +2.6 percent. This shows that all kinds of varying stress histories produce a very small influence on the shear wave velocity in the range of this study.

6.2.3 CONFINING PERIOD AT ONE PRESSURE

Test numbers 77 through 80 (described in Section 4.6) were performed with $\bar{\sigma}_1=40$ psi (275.6 kPa) in the z-direction and $\bar{\sigma}_2=\bar{\sigma}_3=15$ psi (103.4 kPa) in

Table 6.1 - Effect of Repeated Tests on Shear Wave Velocity Under Biaxial Confinement

Shear Wave Type	Constant Principal Stress States (1) V_s , fps *	Reorienting Principal Stress States (2) V_s , fps **	DIFF = $\frac{(2)-(1)}{(2)}$ λ	Remark
V_{xy} V_{yx} V_{xz} V_{yz} V_{zx} V_{zy}	996	1011	1.43	Case 1 $\bar{\sigma}_z = 40$ psi $\bar{\sigma}_x = \bar{\sigma}_y = 20$ psi
	979	990	1.11	
	973	983	1.03	
	956	1054	10.23	
	929	976	5.07	
	940	954	1.53	
	Average = +3.40			
V_{xv} V_{yx} V_{xz} V_{yz} V_{zx} V_{zy}	1051	1075	2.23	Case 2 $\bar{\sigma}_x = 40$ psi $\bar{\sigma}_y = \bar{\sigma}_z = 20$ psi
	1086	1181	8.81	
	942	946	0.51	
	931	955	2.59	
	924	936	1.25	
	849	841	-0.97	
	Average = +2.40			

*Constant Principal Stress States with two stress varying

l : in directions of wave propagation and particle motion

a : in directions of wave propagation and out-of-plane

b : in directions of particle motion and out-of-plane

**Reorienting Principal Stress States with only one stress varying

a' : in direction of wave propagation

b' : in direction of particle motion

c' : in out-of-plane direction

both the x- and y-directions for 19.5 hours. These tests were performed to evaluate the effect of confining period at one pressure under biaxial loading. The $\log V_s - \log t$ relationship for five of the six shear waves are listed in Table 6.2 and show that the effect of confining period within 19.5 hours is negligible. Figure 6.5 shows the data presented in Table 6.2.

Based on the results presented in Sections 6.2.1 through 6.2.3, tests under biaxial confinement exhibited no effects of stress history as expected.

6.3 TESTS WITH DIRECTION OF MAJOR PRINCIPAL STRESS REMAINING CONSTANT

In both the BIA1 and BIA2 series of tests, the orientation of principal stresses was held constant during the tests. The only thing varied was the magnitude of either one (BIA1) or two (BIA2) principal stresses. Therefore, the influence on V_s of principal stresses varying in one or two directions could be evaluated and compared. In this discussion, three types of influences are addressed:

- a) the effect of the principal stress in the direction of wave propagation
- b) the effect of the principal stress in the direction of particle motion and
- c) the effect of the principal stress in the out-of-plane direction (the direction perpendicular to the plane made in cases (a) and (b)).

6.3.1 EFFECT OF PRINCIPAL STRESS IN DIRECTION OF WAVE PROPAGATION

The effect on V_s of principal stress varying in the direction of wave propagation is shown in Figs. 6.6 to 6.8. The slopes and constants of the regression analysis, shown by the solid lines in the figures, are listed in Table 6.3. The dashed lines show the 95-percent confidence intervals. The effect on V_s of varying the principal stress in the direction of wave propagation along with varying the principal stress in the out-of-plane direction is shown in Figs. 6.9 to 6.11. Table 6.4 contains the slopes and constants determined from this group of tests assuming that only σ_3 affects V_s . Details and conclusions from these tests are discussed in Section 6.4.

Average values for slopes and constants presented in Tables 6.3 and 6.4 were calculated from the regression line of data from both the loading and unloading series of tests. Therefore, these values are not necessarily the

Table 6.2 - Effect of Confining Period at One Biaxial Stress State

Shear Wave Type	Confining Period, T				Slope*	Coeff.*
	0.5 HR	1.5 HR	2.5 HR	19.5 HR		
V_{xy}	989	976	1007	1003	0.00	966
V_{xz}	---**	---	---	---	---	---
V_{yx}	978	981	982	983	0.00	974
V_{yz}	976	977	981	992	0.00	954
V_{zx}	959	960	961	961	0.00	957
V_{zy}	945	944	945	955	0.00	931

* $V_s = C \cdot T^{n1}$

** = malfunction of accelerometers

BIAXIAL CONFINEMENT

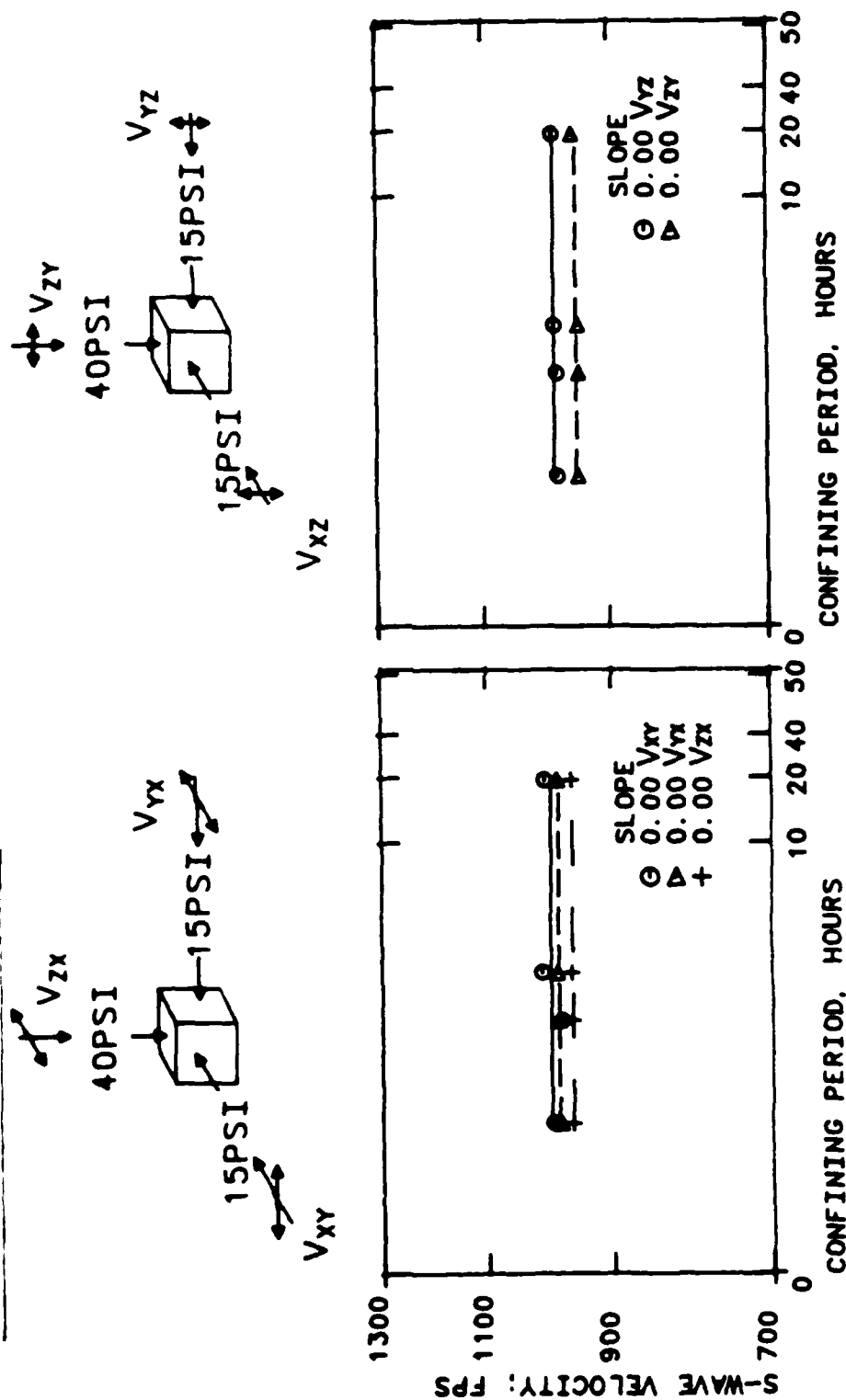
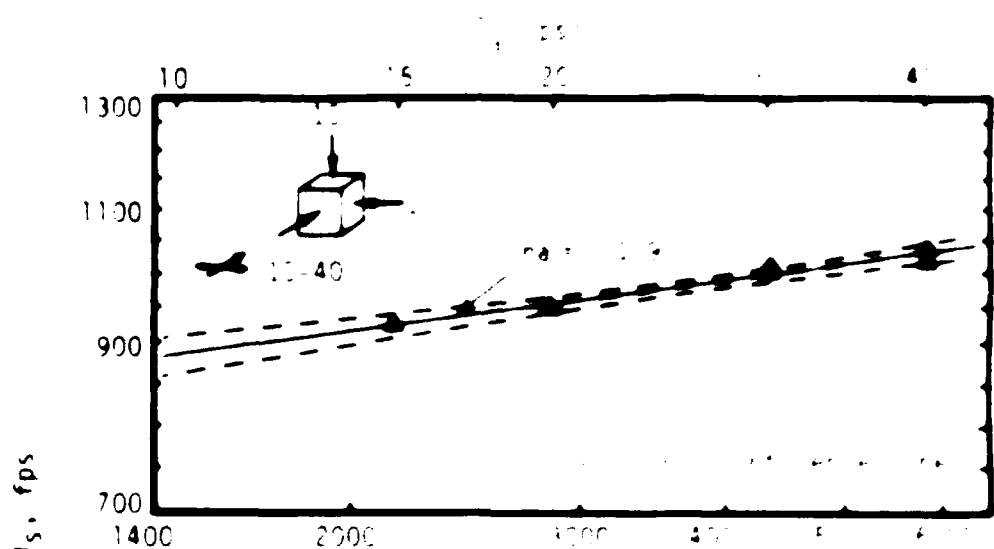
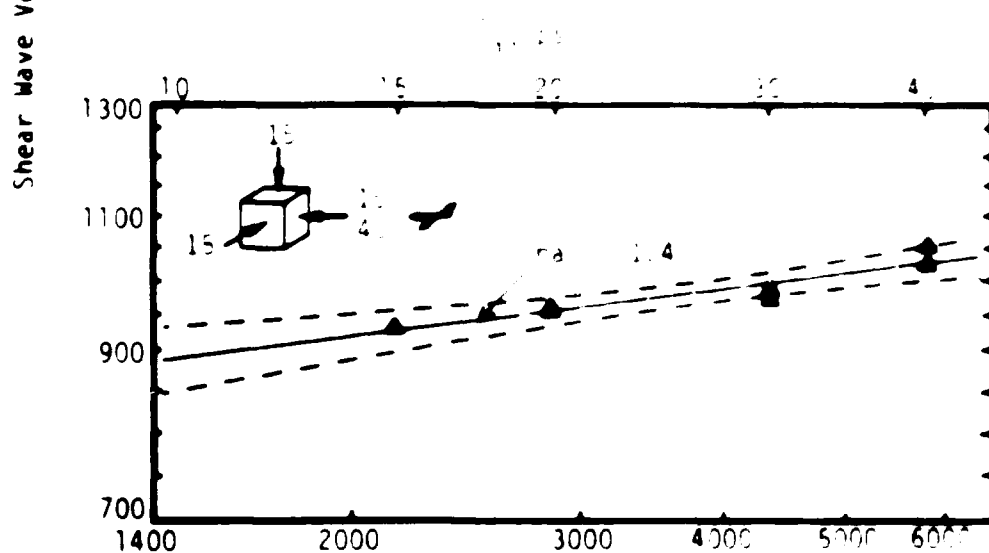


Fig. 6.5 - Effect of Confining Period on S-Wave Velocity Under Biaxial Confinement BIA1



Effective Principal Stress in Direction of Wave Propagation, psf

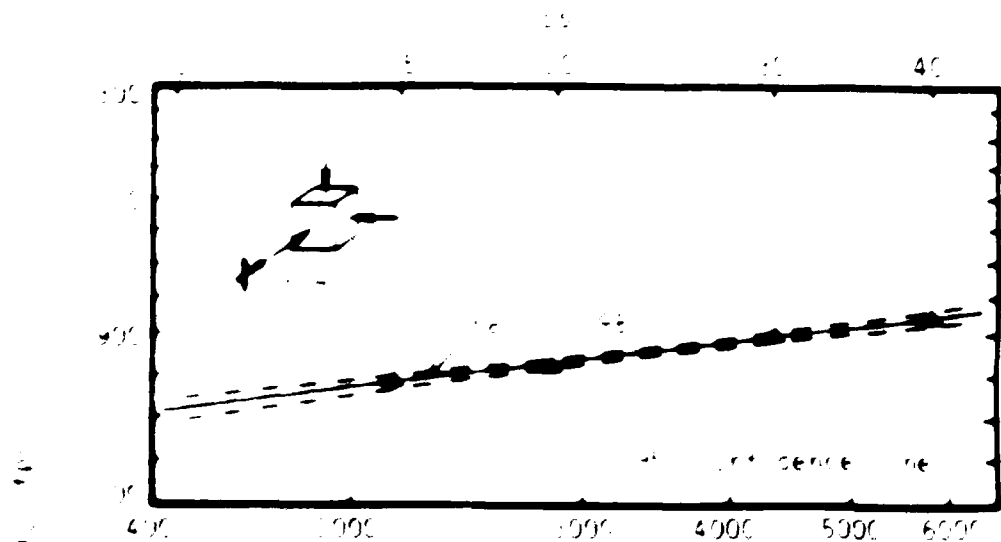
a) V_{xy}



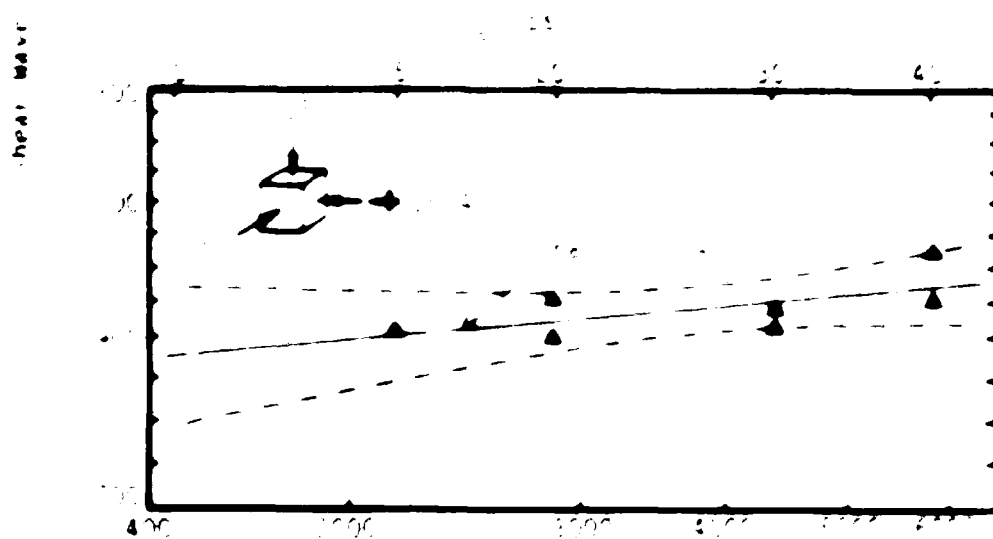
Effective Principal Stress in Direction of Wave Propagation, psf

b) V_{yx}

Fig. 6.6 - Effect on V_{xy} and V_{yx} of Varying Only Principal Stress in Direction of Wave Propagation Under Biaxial Loading



Effective Principal Stress in Direction of wave Propagation, 15°



Effective Principal Stress in Direction of wave Propagation, 30°

Fig. 1. Shear wave velocity vs. effective principal stress in direction of wave propagation, 15° and 30°.

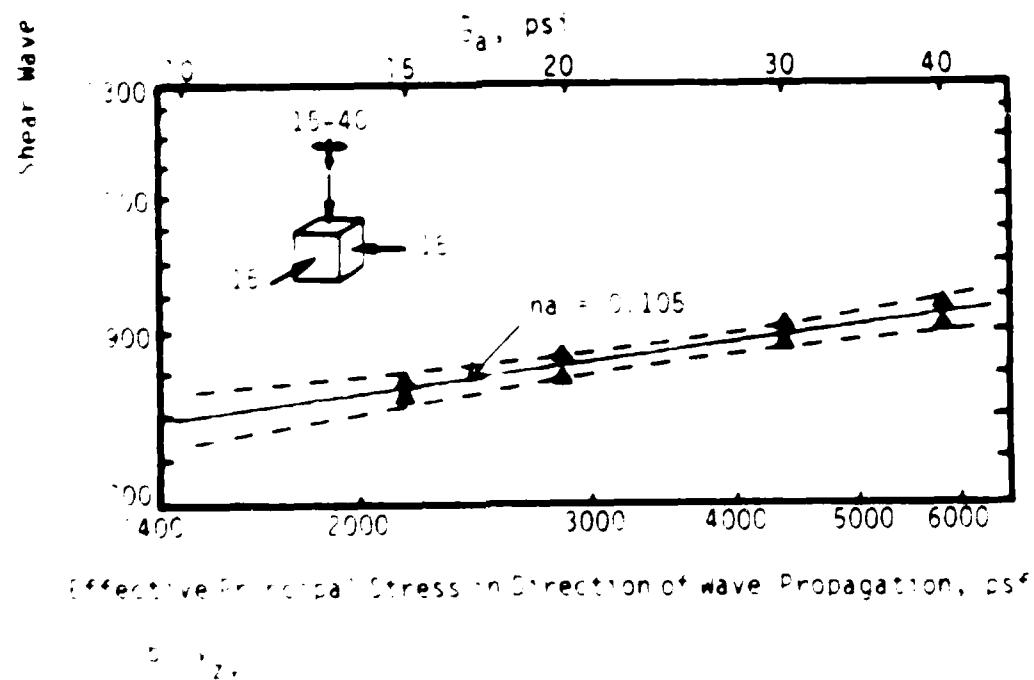
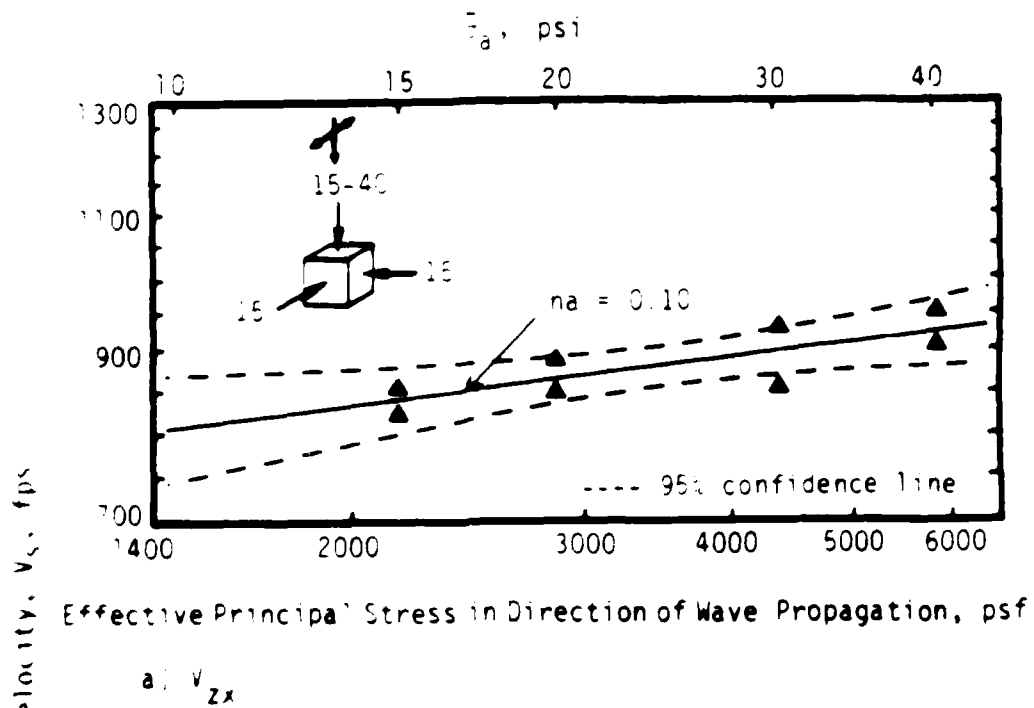


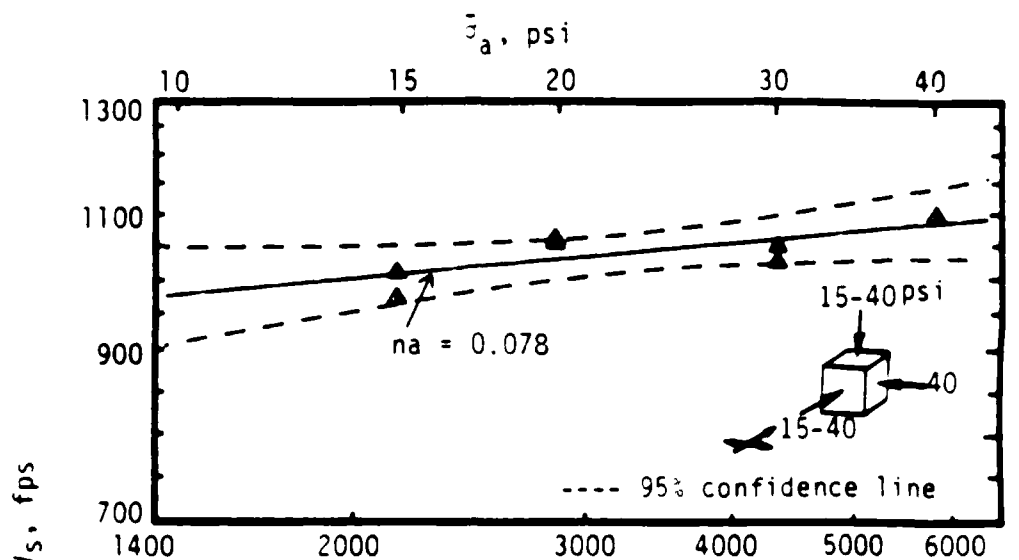
Fig. 6.8 - Effects of σ_1 , and σ_2 , of Varying Only, Principal Stress in Direction of wave Propagation Under Biaxial Loading

Table 6.3 - Effect on V_s of Varying Only Principal Stress in Direction of Wave Propagation Under Biaxial Confinement

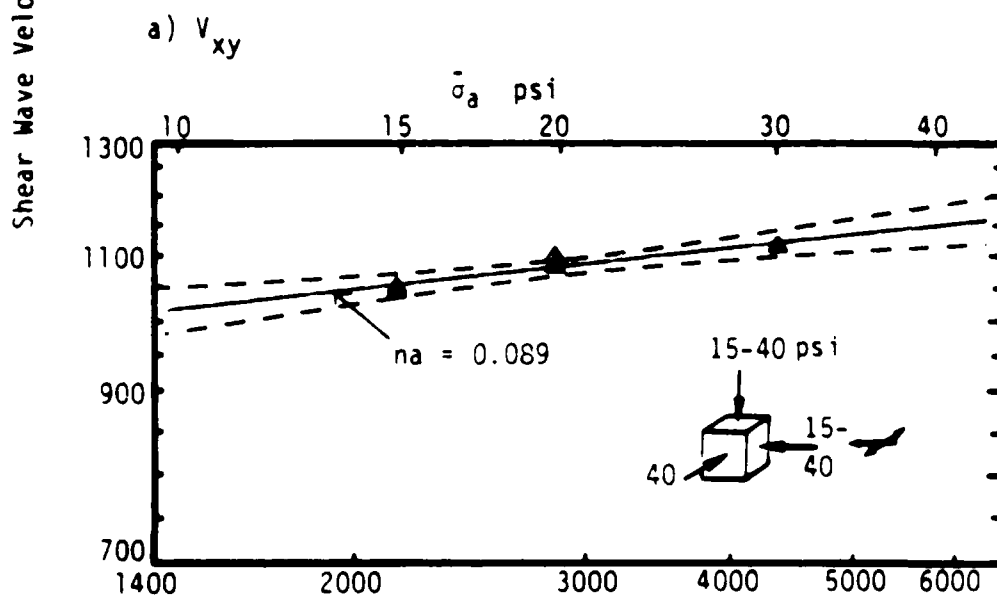
Shear Wave Type	Loading		Unloading		Average		Remark
	na^*	C_a^*	na	C_a	na	C_a	
V_{xy}	0.097	440	0.129	342	0.109	401	Fig. 6.6
V_{yx}	0.095	446	0.115	384	0.104	419	
V_{xz}	0.095	406	**	—	0.095	406	Fig. 6.7
V_{yz}	0.075	495	0.097	436	0.074	515	
V_{zx}	0.087	421	0.110	369	0.100	394	Fig. 6.8
V_{zy}	0.102	409	0.107	372	0.105	375	

** = malfunction of records on floppy disc

* $V_s = C_a/na$



Effective Principal Stress in Direction of Wave Propagation, psf



Effective Principal Stress in Direction of Wave Propagation, psf

b) V_{yx}

Fig. 6.9 - Effect on V_{xy} and V_{yx} of Principal Stress in Direction of Wave Propagation Under Biaxial Loading When $\bar{\sigma}_a$ and $\bar{\tau}_c$ are Varied

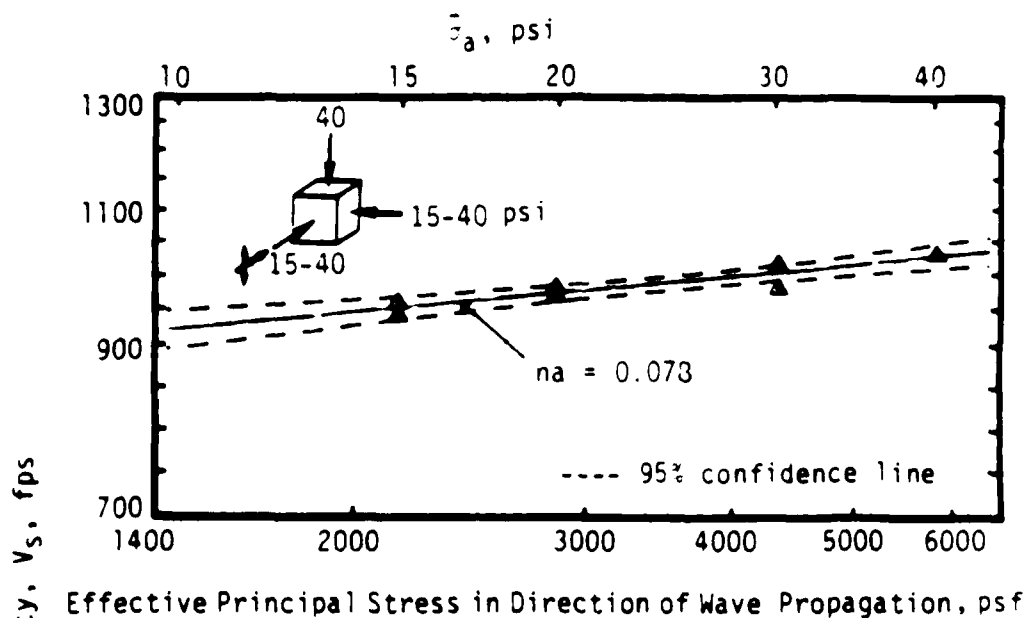
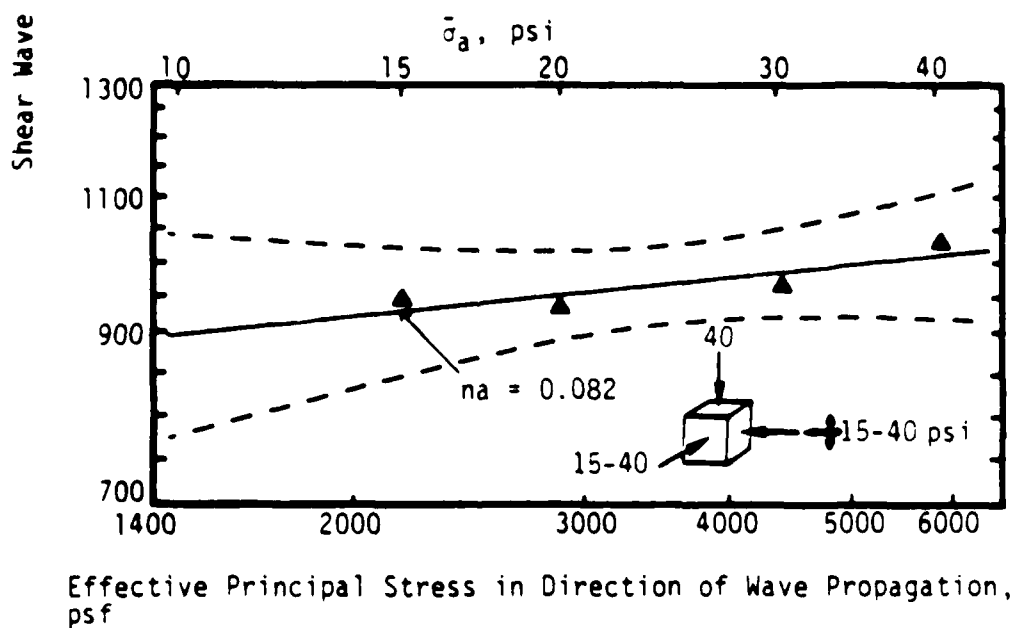
a) V_{xz} b) V_{yz}

Fig. 6.10 - Effect on V_{xz} and V_{yz} of Principal Stress in Direction of Wave Propagation Under Biaxial Loading When $\bar{\sigma}_a$ and $\bar{\sigma}_c$ are Varied

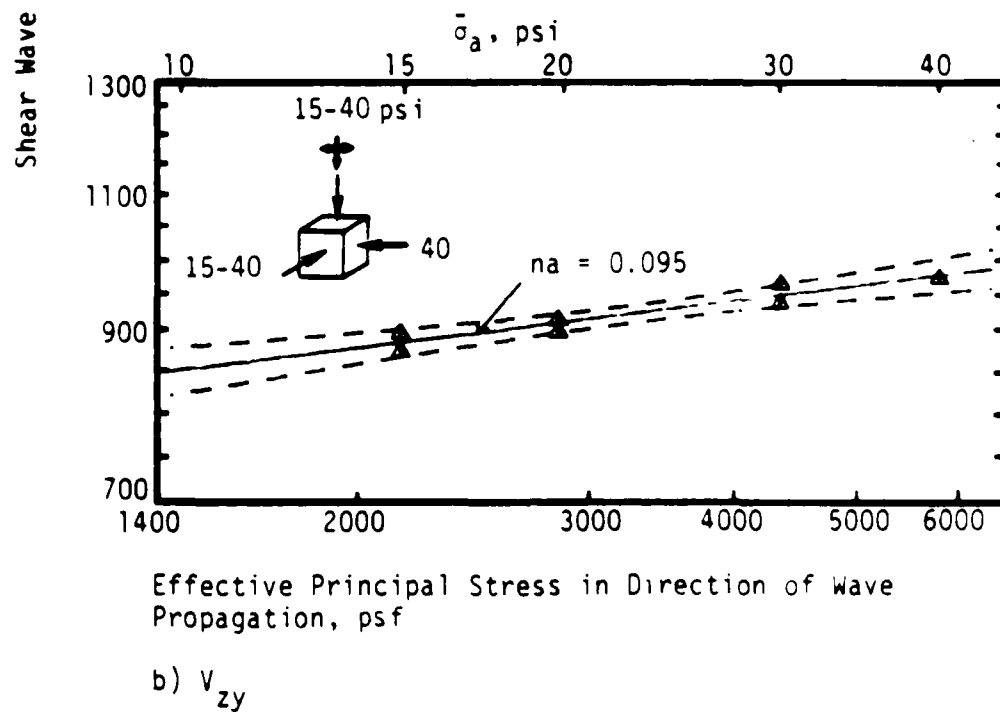
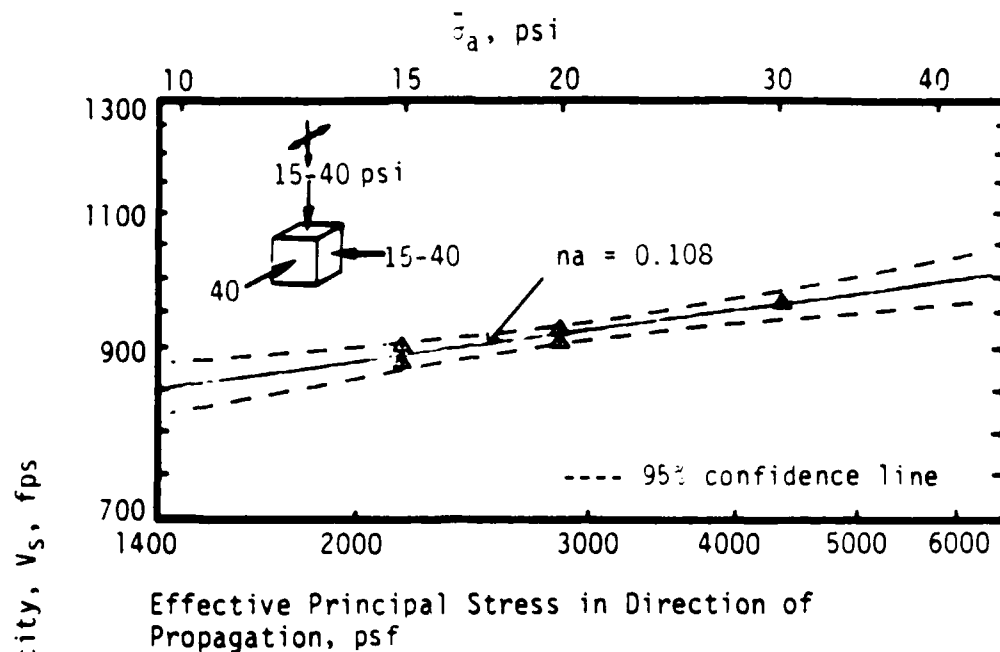


Fig. 6.11 - Effect on V_{zx} and V_{zy} of Principal Stress in Direction of Wave Propagation Under Biaxial Loading When $\bar{\sigma}_a$ and $\bar{\sigma}_c$ are Varied

Table 6.4 - Effect on V_S of P-Principal Stress in Direction of Wave Propagation Under Biaxial Confinement When $\bar{\sigma}_a$ and $\bar{\sigma}_c$ Varied

Shear Wave Type	Loading		Unloading			Average		Remark
	na*	C _a *	na	C _a	na	C _a		
V _{xy}	0.070	585	0.071	596	0.078	554	Fig. 6.9	
V _{yx}	0.095	549	0.092	523	0.089	536		
V _{xz}	0.082	528	0.074	546	0.078	524	Fig. 6.10	
V _{yz}	0.082	496	— **	—	0.082	496		
V _{zx}	0.09	443	0.12	345	0.108	391	Fig. 6.11	
V _{zy}	0.10	408	0.10	395	0.095	426		

** = malfunction of records on floppy disc

* $V_S = C_a \bar{\sigma}_a na$

arithmetic average of values for the loading and unloading series by themselves.

The trends of both groups of data given in Tables 6.3 and 6.4 are the same, i.e., shear wave velocity increases as the principal stress in the direction of wave propagation increases. This is true no matter whether the principal stress in the out-of-plane direction is varied. However, when the stress in the out-of-plane direction is varied, the slopes of the $\log V_s - \log \bar{\sigma}_a$ relationship are slightly smaller and the constants are slightly larger. This point is examined in more detail later in this chapter.

6.3.2 EFFECT OF PRINCIPAL STRESS IN DIRECTION OF PARTICLE MOTION

Variation of the principal stress only in the direction of particle motion was performed to detect the importance of this factor on shear wave velocity. These tests are shown in Figs. 6.12 to 6.14. The relative values of the slopes and constants of the regression analysis of the $\log V_s - \log \bar{\sigma}_b$ relationship for these tests are listed in Table 6.5. The results under the condition that principal stress varied in both the direction of particle motion, $\bar{\sigma}_b$, and the out-of-plane direction, $\bar{\sigma}_c$, are shown in Figs. 6.15 through 6.17 and are listed in Table 6.6. As with the tests with $\bar{\sigma}_a$ varying and then $\bar{\sigma}_a$ and $\bar{\sigma}_c$ both varying, the slope in the first group is higher than the second, while the constant is lower.

By comparing the figures when one principal stress was varied with those when two principal stresses were varied, one can see that shear wave velocity in the case when two stresses were varying was always slightly higher than when only one stress was varied, no matter whether the principal stress was varying in the direction of wave propagation or particle motion. Since a higher mean effective stress occurs when the principal stress in the out-of-plane direction is also varied with one of the other principal stresses, the principal stress in the out-of-plane direction or the mean effective stress may have minor effect on V_s . However, the major effects are due to the principal stresses varying in the direction of wave propagation and particle motion.

Additional research on the influence of the principal stress in the out-of-plane direction is discussed in the next section. The influence of the mean effective stress is re-examined in Section 6.4.

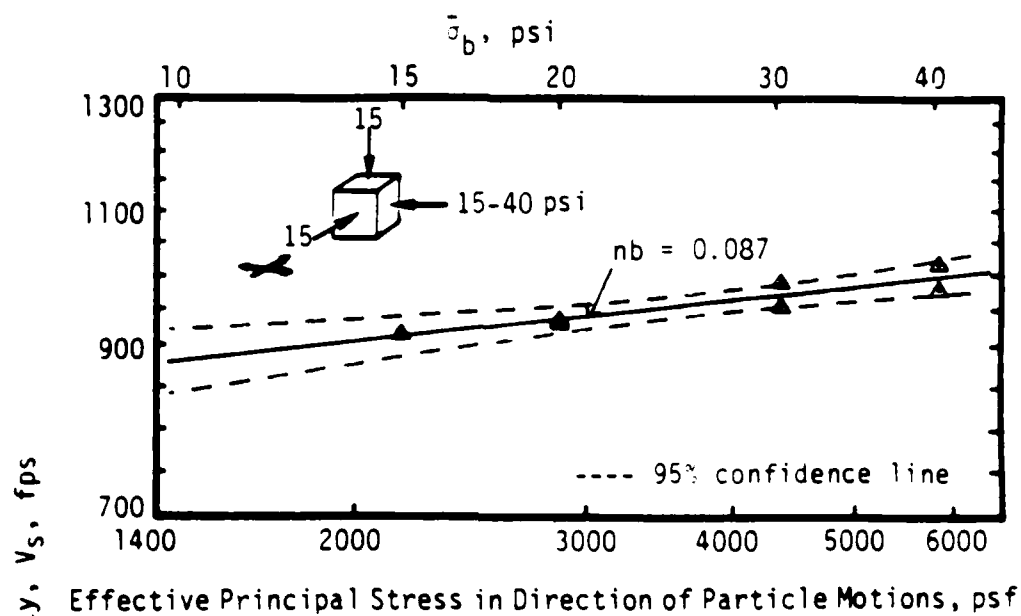
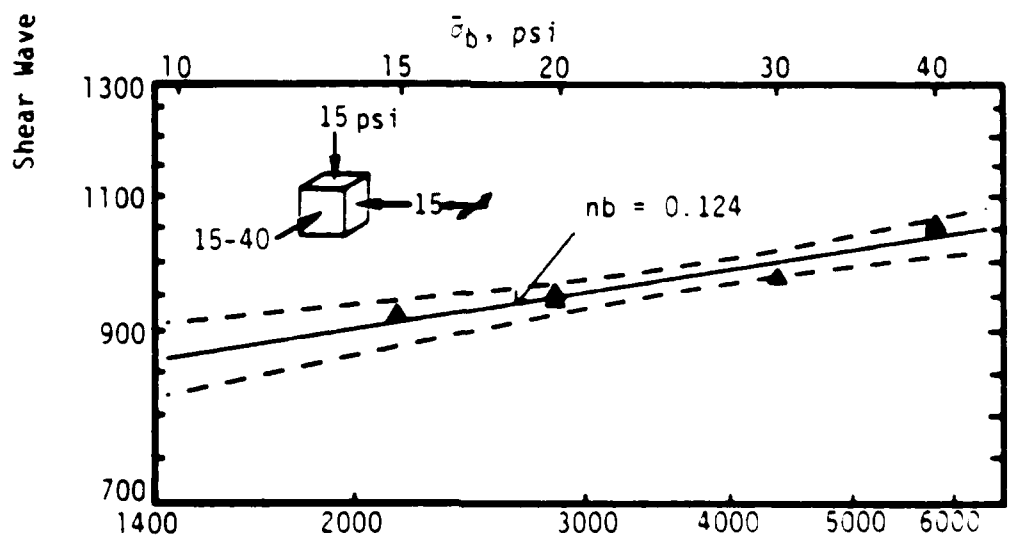
a) V_{xy} b) V_{yx}

Fig. 6.12 - Effect on V_{xy} and V_{yx} of Varying Only Principal Stress in Direction of Particle Motion Under Biaxial Loading

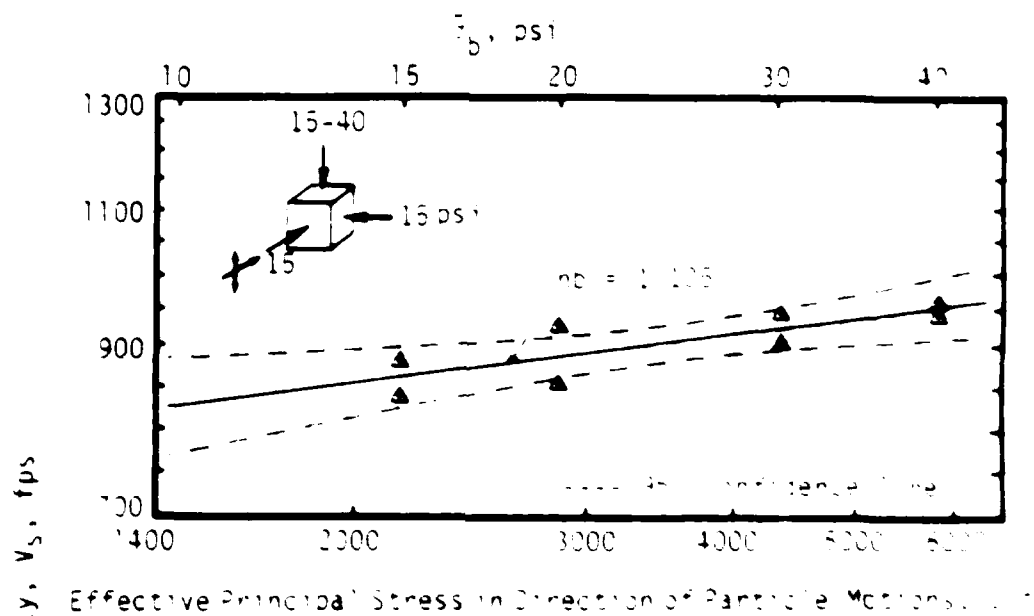
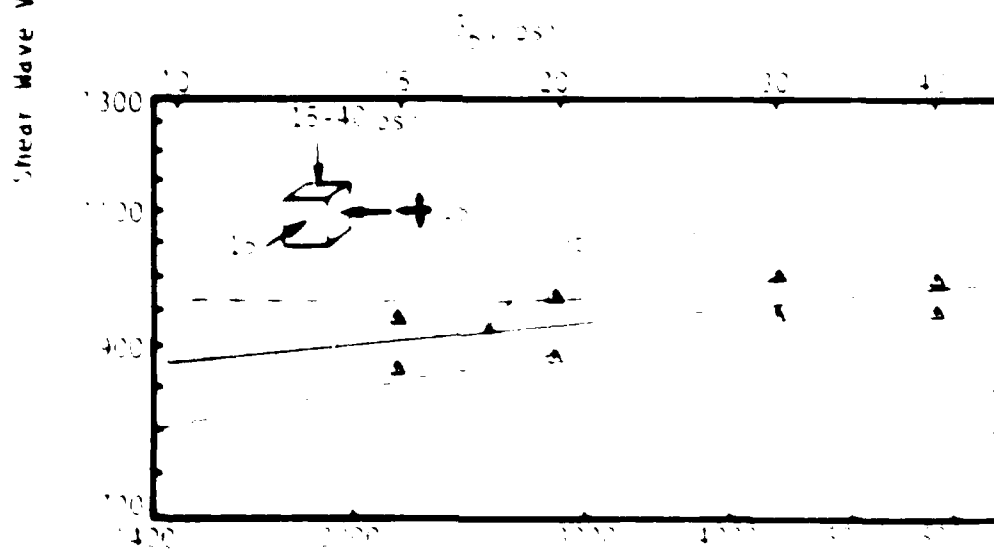
a = x_2 a = x_1

Fig. 12. Shear wave velocity vs. effective principal stress in the direction of particle motion. The data were obtained from the same tests as those shown in Fig. 11.

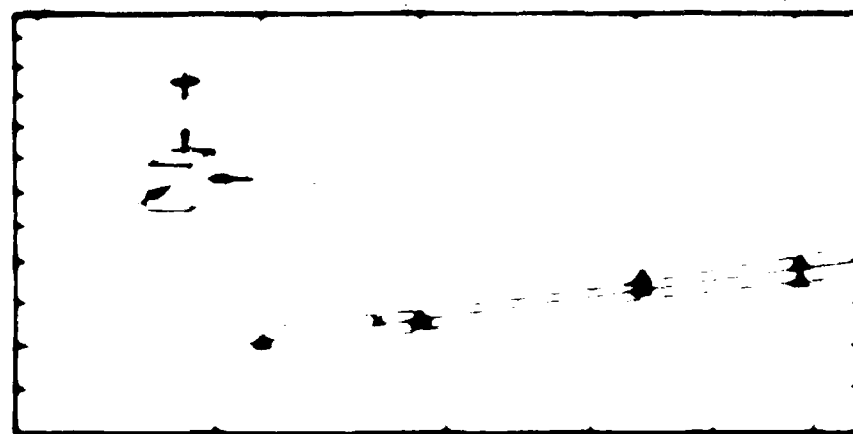
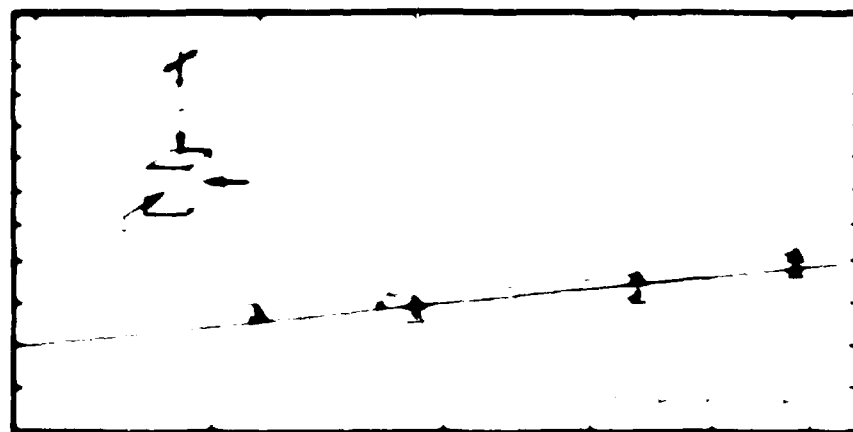
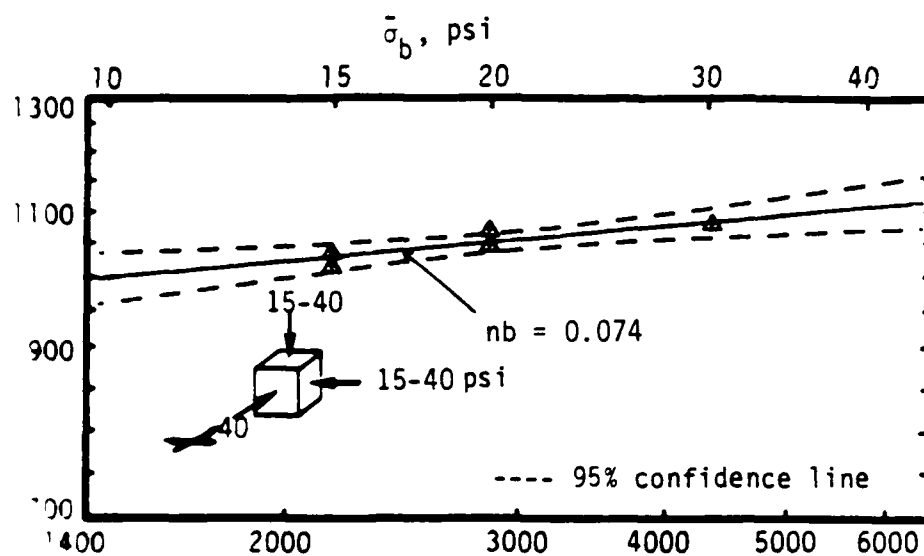


Table 6.5 - Effect on V_s of Varying Only Principal Stress in Direction of Particle Motion Under Biaxial Loading

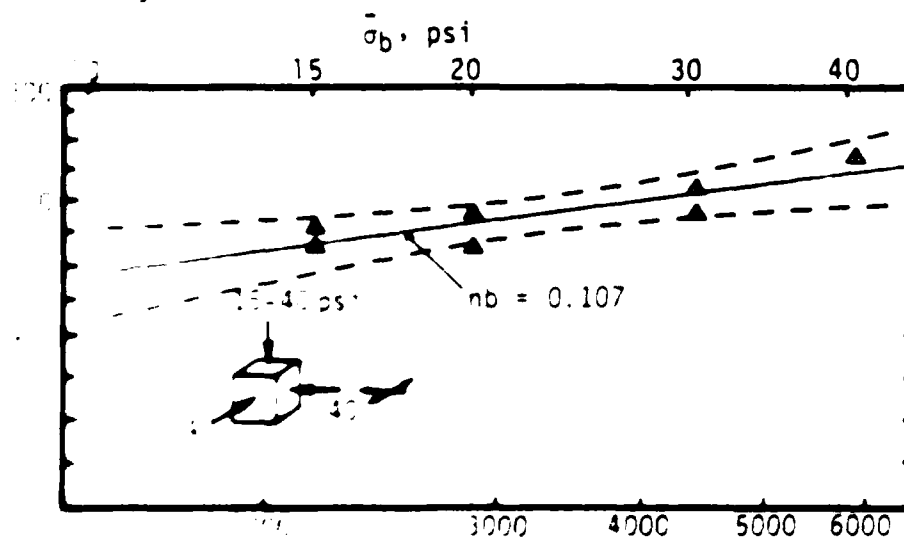
Shear Wave Type	Loading		Unloading		Average		Remark
	nd^*	C_b^*	nb	C_b	nb	C_b	
V_{xy}	0.074	521	0.095	442	0.087	467	Fig. 6.12
V_{yx}	0.120	367	0.143	300	0.124	354	
V_{xz}	0.127	314	0.084	468	0.105	383	Fig. 6.13
V_{yz}	0.094	424	0.061	594	0.078	502	
V_{zx}	0.087	425	0.095	388	0.081	444	Fig. 6.14
V_{zy}	0.121	314	0.096	388	0.104	363	

$$*V_s = C_b^* \frac{nb}{b}$$



Effective Principal Stress in Direction of Particle Motion, psf

(a) v_{xy}



Effective Principal Stress in Direction of Particle Motion, psf

Effective Principal Stress in Direction of Particle Motion, psf

Effective Principal Stress in Direction of Particle Motion, psf

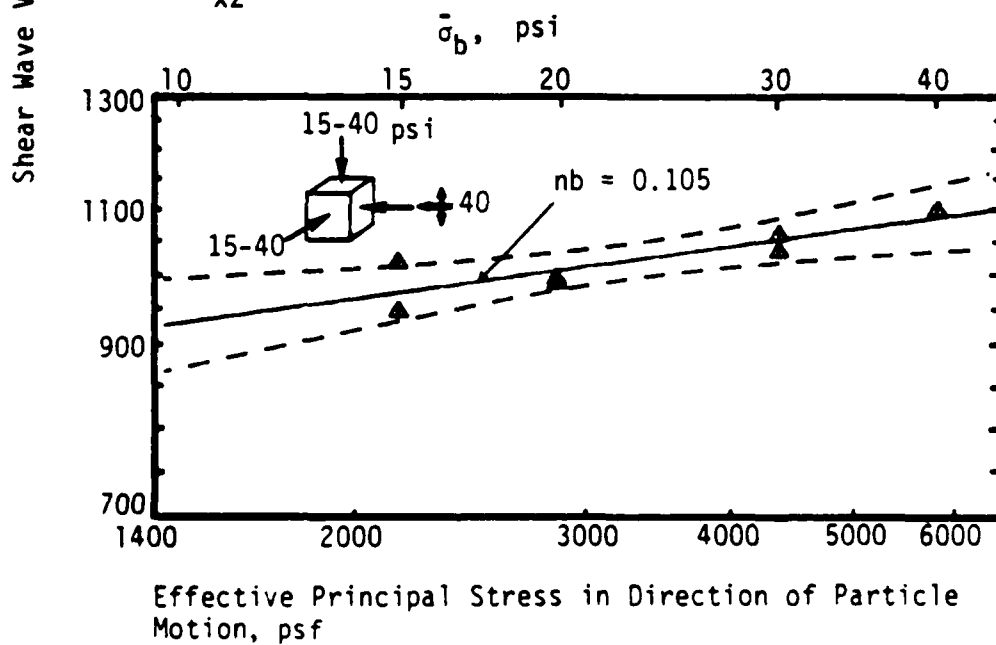
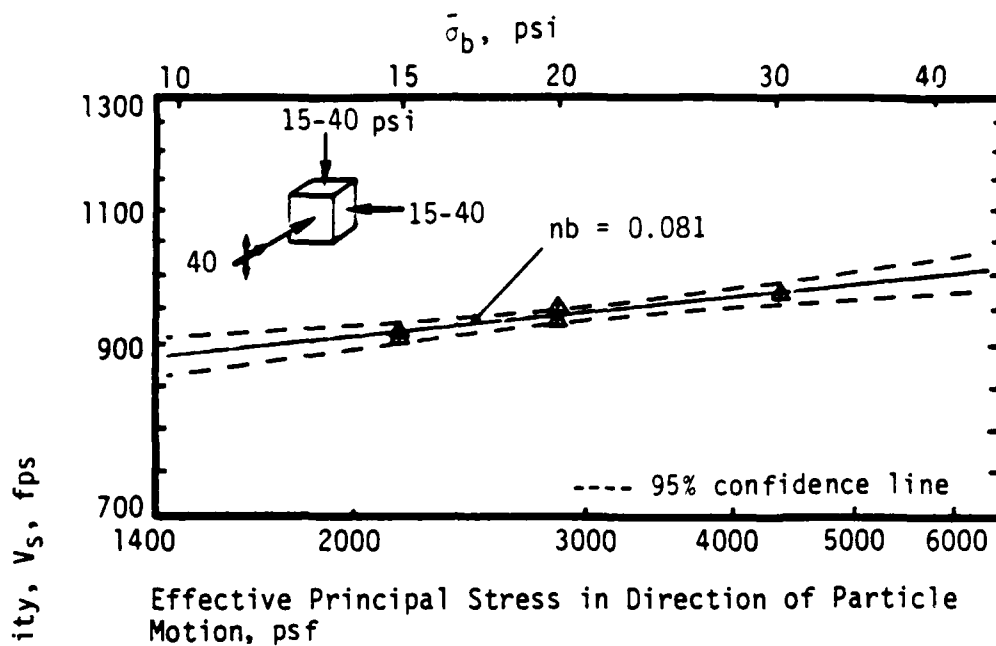


Fig. 6.16 - Effect on V_{xz} and V_{yz} of Principal Stress in Direction of Particle Motion Under Biaxial Loading When $\bar{\sigma}_b$ and $\bar{\sigma}_c$ are Varied

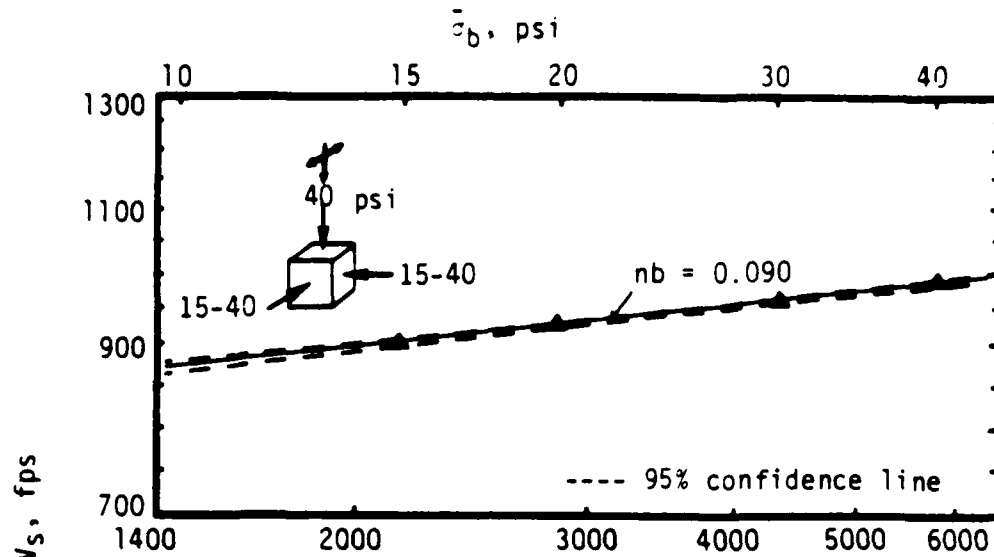
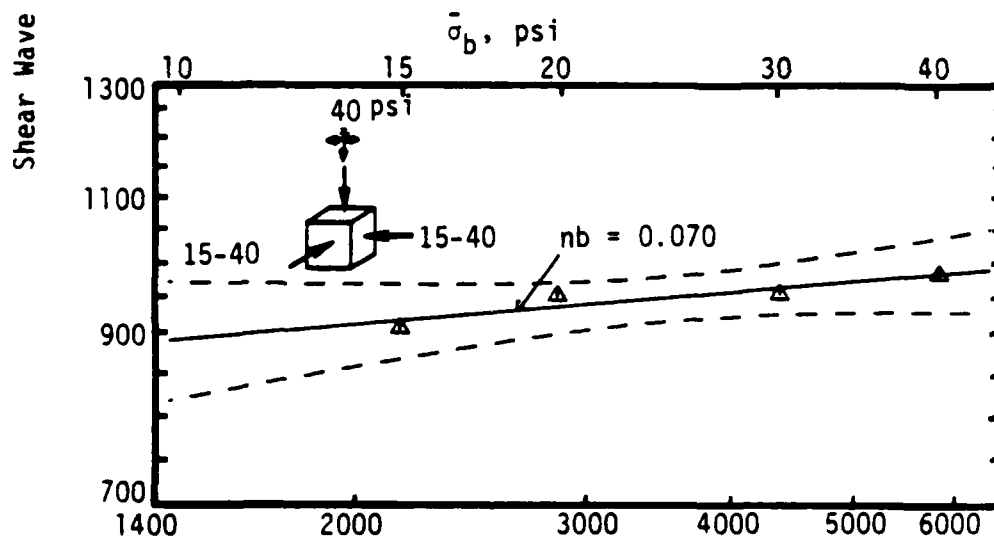
a) V_{zx} b) V_{zy}

Fig. 6.17 - Effect on V_{zx} and V_{zy} of Principal Stress in Direction of Particle Motion Under Biaxial Loading When $\bar{\sigma}_b$ and $\bar{\sigma}_c$ are Varied

Table 6.6 - Effect on V_s of Principal Stress in Direction of Particle Motion Under Biaxial Loading When $\bar{\sigma}_b$ and $\bar{\sigma}_c$ Varied

Shear Wave Type	Loading		Unloading		Average		Remark
	nb*	C_b^*	nb	C_b	nb	C_b	
V_{xy}	0.090	511	0.060	663	0.074	583	Fig. 6.15
V_{yx}	0.072	589	0.102	480	0.107	454	
V_{xz}	0.077	510	0.086	477	0.081	493	Fig. 6.16
V_{yz}	0.119	384	0.083	532	0.105	436	
V_{zx}	0.090	454	—**	—	0.090	454	Fig. 6.17
V_{zy}	0.070	539	—	—	0.070	539	

** = malfunction of records in floppy disc

* $V_s = C_b^{\sigma_b} nb$

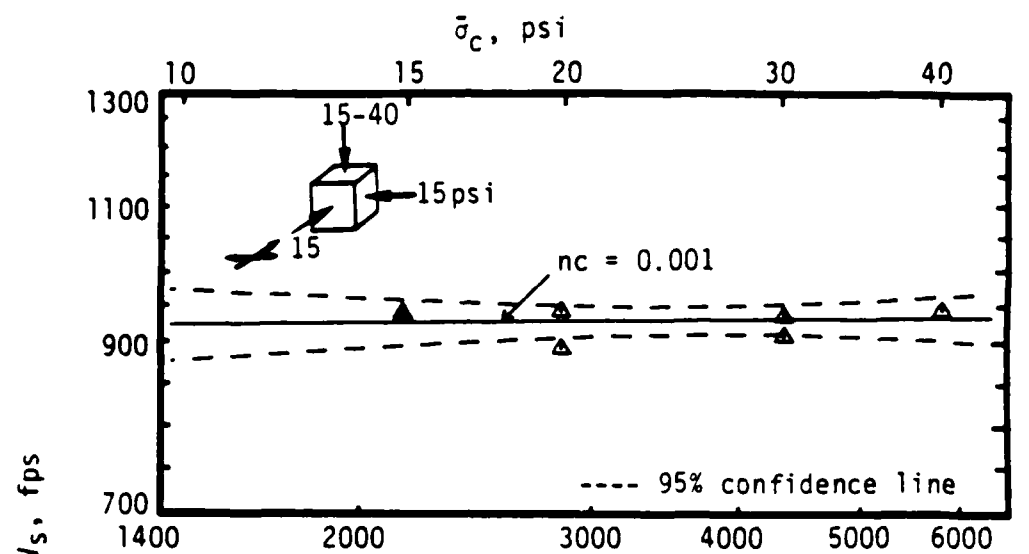
6.3.3 EFFECT OF PRINCIPAL STRESS IN OUT-OF-PLANE DIRECTION

To understand the effect of the principal stress in the out-of-plane direction, the principal stresses in the directions of wave propagation and particle motion were kept constant while the stress in the out-of-plane direction was increased and then decreased. These loading conditions together with the resulting shear wave velocities are presented in Figs. 6.18 to 6.20. The slopes and constants of the regression analysis are listed in Table 6.7.

There are nearly no variations in shear wave velocities when the principal stresses in the out-of-plane direction were changed. Yet, a careful comparison of the values of slopes in Table 6.7 shows that there was a positive slope for only V_{xy} due to the principal stress varying in the out-of-plane direction and negative slopes occurred for all other velocities.

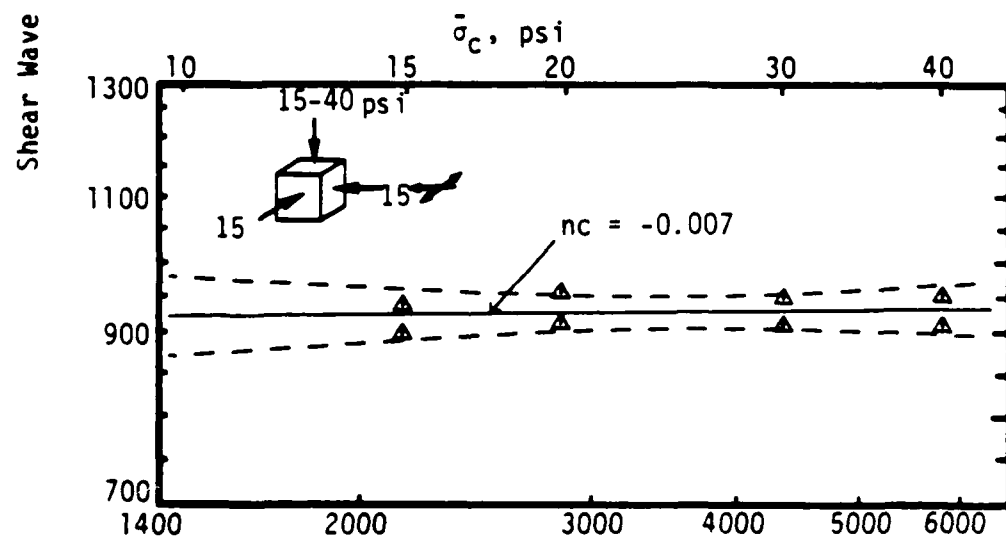
One possible explanation for the very small but generally negative values of nc is as follows. Theoretically, the increasing of compressive stress in one direction causes extension strains in the plane perpendicular to this direction for stress controlled boundaries. These changes, which can be estimated by Poisson's ratio and Young's modulus, may possibly tend to "soften" the stiffness in this plane, because of minute changes in particle contacts. In an isotropic and homogeneous medium, this type of softening would be the same in all three directions. The sand tested in this study is more nearly cross-anisotropic, and the ratio of Poisson's ratio to Young's modulus is smaller in the isotropic plane than in the anisotropic plane (see Sections 9.5 and 9.6). Therefore, the effect of softening by $\bar{\sigma}_c$ on V_{xz} , V_{yz} , V_{zx} , and V_{zy} should be larger than on V_{xy} and V_{yx} as shown in Table 6.7. Values of "nc" due to softening should all be negative theoretically. The test results in column six (average nc) of Table 6.7 verify this conclusion, except for nc associated with V_{xy} . However, the value of nc for V_{xy} , equal to 0.001, is very close to zero. More research into this effect is warranted.

An alternative method for estimating the effect of the principal stress in the out-of-plane direction is suggested when Eq. 2.52 is used with shear wave velocities determined under both one stress varying and two stresses, $\bar{\sigma}_a$ or $\bar{\sigma}_b$ and $\bar{\sigma}_c$, varying. For one stress in the direction of wave propagation varying (i.e. BIA1), Eq. 2.52 can be expressed as:



Effective Principal Stress in Direction of Out-of-Plane, psf

a) V_{xy}



Effective Principal Stress in Direction of Out-of-Plane, psf

b) V_{yx}

Fig. 6.18 - Effect on V_{xy} and V_{yx} of Principal Stress in Out-of-Plane Direction Under Biaxial Loading

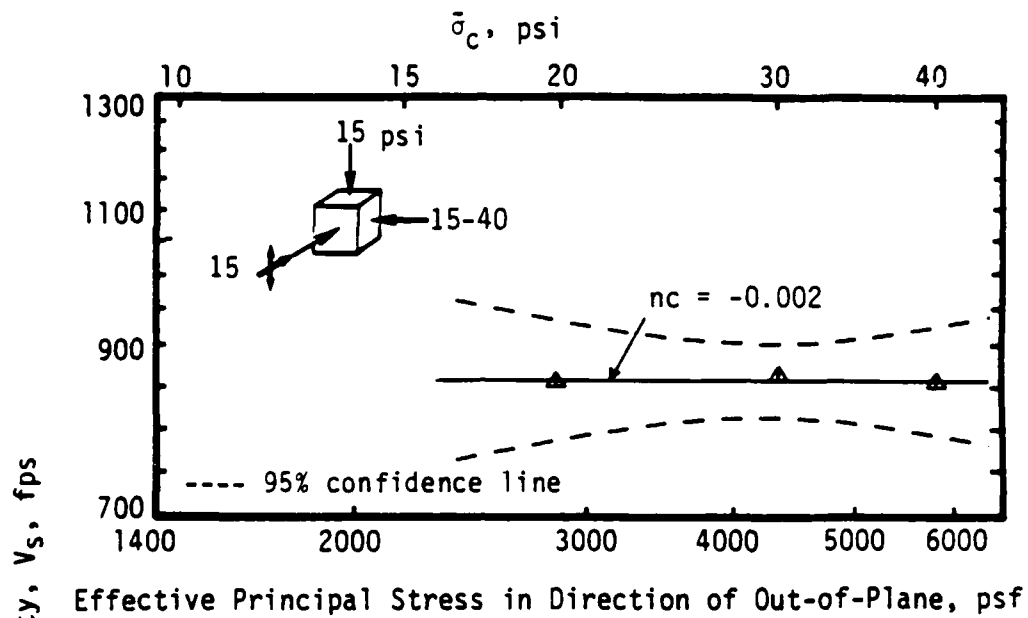
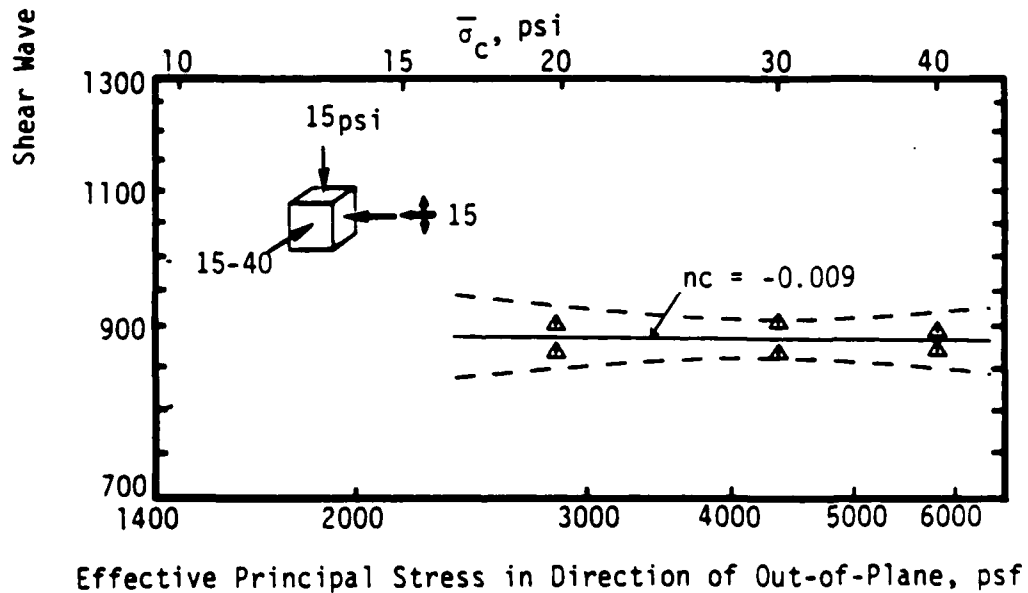
a) V_{xz} b) V_{yz}

Fig. 6.19 - Effect on V_{xz} and V_{yz} of Principal Stress in Out-of-Plane Direction Under Biaxial Loading

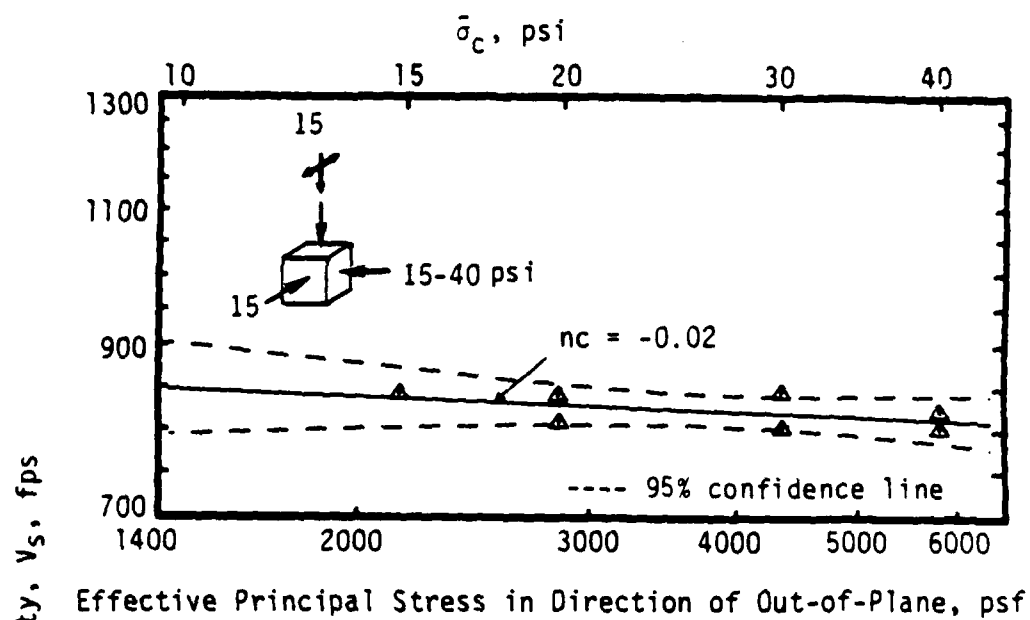
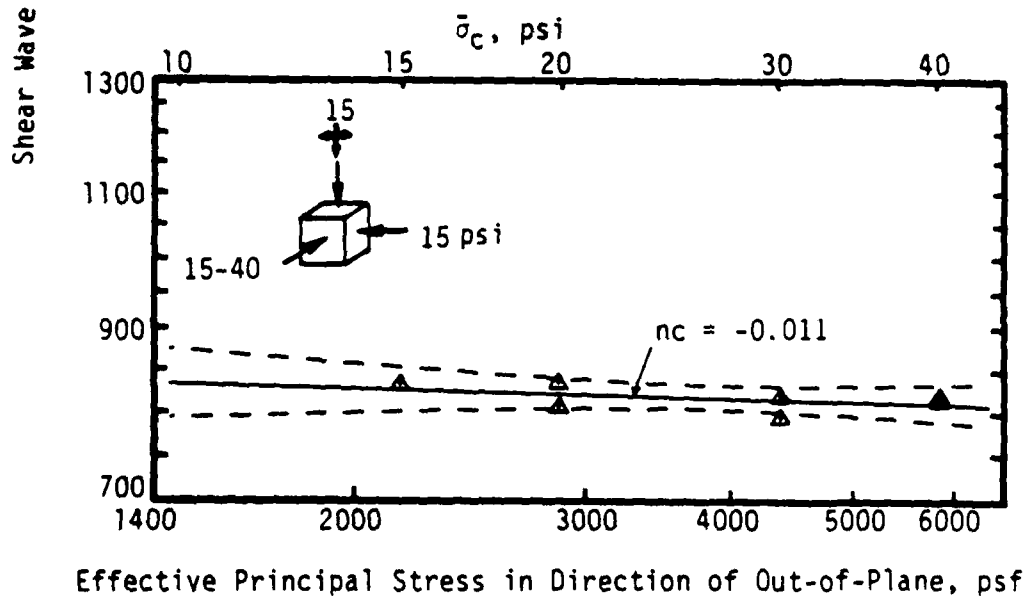
a) V_{zx} b) V_{zy}

Fig. 6.20 - Effect on V_{zx} and V_{zy} of Principal Stress in Out-of-Plane Direction Under Biaxial Loading

Table 6.7 - Effect on V_s of Varying Principal Stress in the Out-of-Plane Direction Under Biaxial Loading

Shear Wave Type	Loading		Unloading		Average		Remark
	nc*	C_c^*	nc	C_c	nc	C_c	
V_{xy}	0.003	922	0.015	818	0.001	868	Fig. 6.18
V_{yx}	0.010	838	0.010	875	-0.007	856	
V_{xz}	-0.002	872	—	—	-0.002	872	Fig. 6.19
V_{yz}	-0.030	1160	-0.001	879	-0.009	960	
V_{zx}	-0.016	913	-0.022	1000	-0.020	1075	Fig. 6.20
V_{zy}	-0.023	996	0.009	742	-0.011	974	

$$* V_s = C_c \bar{\sigma}_c^{nc}$$

$$V_{s1} = C_1 \bar{\sigma}_a^{na} (2160)^{nb} (2160)^{nc} \quad (6.1)$$

For two stresses varying, $\bar{\sigma}_a$ and $\bar{\sigma}_c$, Eq. 2.52 can be expressed as:

$$V_{s2} = C_2 \bar{\sigma}_a^{na} (5760)^{nb} \bar{\sigma}_c^{nc} \quad (6.2)$$

where V_s is in fps and $\bar{\sigma}$ is in psf. Equation 6.2 can be divided by Eq. 6.1 giving:

$$V_{s2}/V_{s1} = (C_2/C_1) (5760/2160)^{nb} (\bar{\sigma}_c/2160)^{nc} \quad (6.3)$$

Equation 6.4 is obtained by taking the logarithm of both sides of Eq. 6.3 yielding:

$$nc = \log [(C_1 \cdot V_{s2}/V_{s1} \cdot C_2)/(2.667)^{nb}] / \log [\bar{\sigma}_c/2160] \quad (6.4)$$

A similar procedure can be applied to the case of shear wave velocity determined under conditions with only the principal stress varying in the direction of particle motion and with $\bar{\sigma}_b$ and $\bar{\sigma}_c$ both varying. The resulting equation is:

$$nc = \log [(C_1 \cdot V_{s2}/V_{s1} \cdot C_2)/(2.667)^{na}] / \log [\bar{\sigma}_c/2160] \quad (6.5)$$

By substituting the data in Tables 6.3 through 6.6 into Eqs. 6.4 and 6.5, average values of nc were calculated and are summarized in Table 6.8. Two positive values of the slope and four negative of the slope were obtained which nearly fall in the same ranges as the test results in Table 6.7. By using +0.10 for nb and -0.01 for nc in Eq. 6.3, the ratio of V_{s2} to V_{s1} (which is V_s in the series of BIA2 to V_s in the series of BIA1) will range from 1.10 to 1.09 as $\bar{\sigma}_c$ varies from 15 to 40 psi (103.4 to 275.6 kPa) in BIA2. This explains why the value of V_s in BIA2 is always larger than in BIA1.

Finally, to keep the importance of all of the values in perspective, it should be noted that the effect on V_s of major principal stress varying in the out-of-plane direction is very small compared to the effect of stress

Table 6.8 - Effect on V_s of Principal Stress in Out-of-Plane Direction Under Biaxial Confinement Calculated from Eqs. 6.4 and 6.5

Shear Wave Type	V_{xy}	V_{yx}	V_{xz}	V_{yz}	V_{zx}	V_{zy}
slope, nc^*	0.014	0.029	-0.045	-0.029	-0.030	-0.004

* average value

varying in either the direction of wave propagation or the direction of particle motion.

6.4 TESTS WITH DIRECTION OF MAJOR PRINCIPAL STRESS REORIENTING

The intermediate principal stress of tests discussed in Section 6.3.1 was equal to the minor principal stress either in BIA1 or BIA2. To examine the influence of the intermediate principal stress on the stiffness of sand, tests BIA3 were controlled in such a way that the intermediate principal stress varied from the major to minor principal stress or from the minor to major principal stress as shown in Fig. 6.2.

Tests in this group can be placed into the following three categories:

- a) ones in which the principal stress in the direction of wave propagation was studied,
- b) ones in which only the effect of the principal stress in the direction of particle motion was studied, and
- c) ones in which the effect of varying principal stresses in two directions was studied.

6.4.1 EFFECT OF PRINCIPAL STRESS IN DIRECTION OF WAVE PROPAGATION

Tests in this series consisted of varying one stress in either the z-direction or the x-direction. Therefore, there are only four types of shear wave velocities in each group. The results of these tests are shown in Figs. 6.21 and 6.22 and are listed in Table 6.9. The trend is obviously similar to the one with one increment varying which is discussed in Section 6.3.1 for the BIA1 series.

The narrow band of 95-percent confidence interval in the figures shows that the relation of $\log V_s - \log \bar{\sigma}_a$ is very significant in this group of tests.

6.4.2 EFFECT OF PRINCIPAL STRESS IN DIRECTION OF PARTICLE MOTION

In a manner similar to that used to study the $\log V_s - \log \bar{\sigma}_b$ relationship in Section 6.3.2, tests in which only $\bar{\sigma}_b$ varied from $\bar{\sigma}_1$ to $\bar{\sigma}_3$ and $\bar{\sigma}_3$ to $\bar{\sigma}_1$ were used to examine the effect of principal stress in the direction of particle motion. The results of the least squares fit to the data are shown in Figs. 6.23 and 6.24 and are summarized in Table 6.10. The

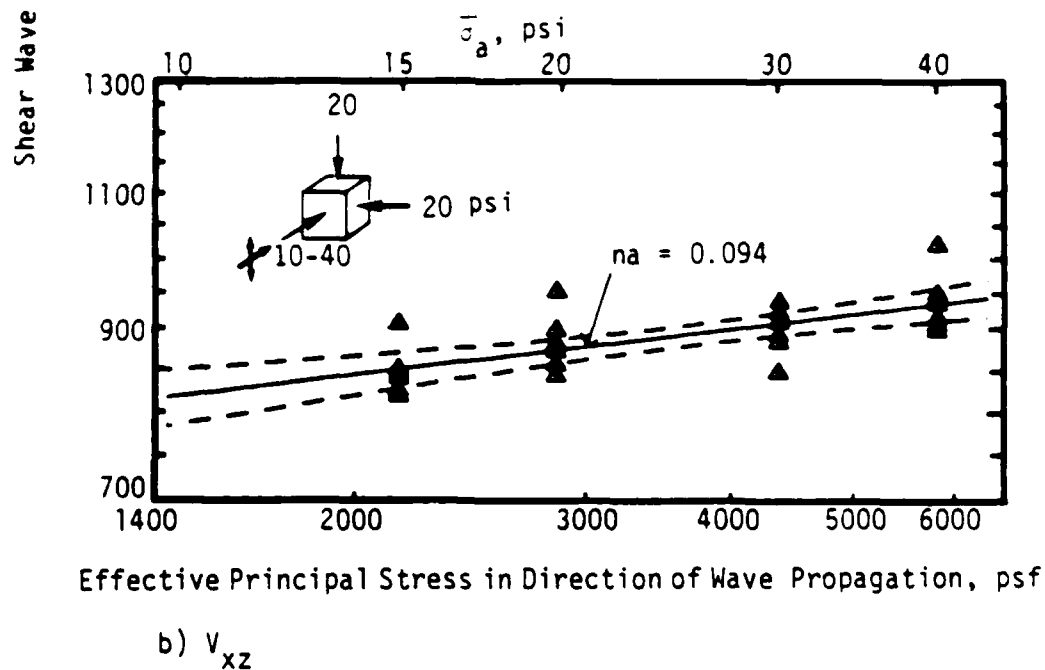
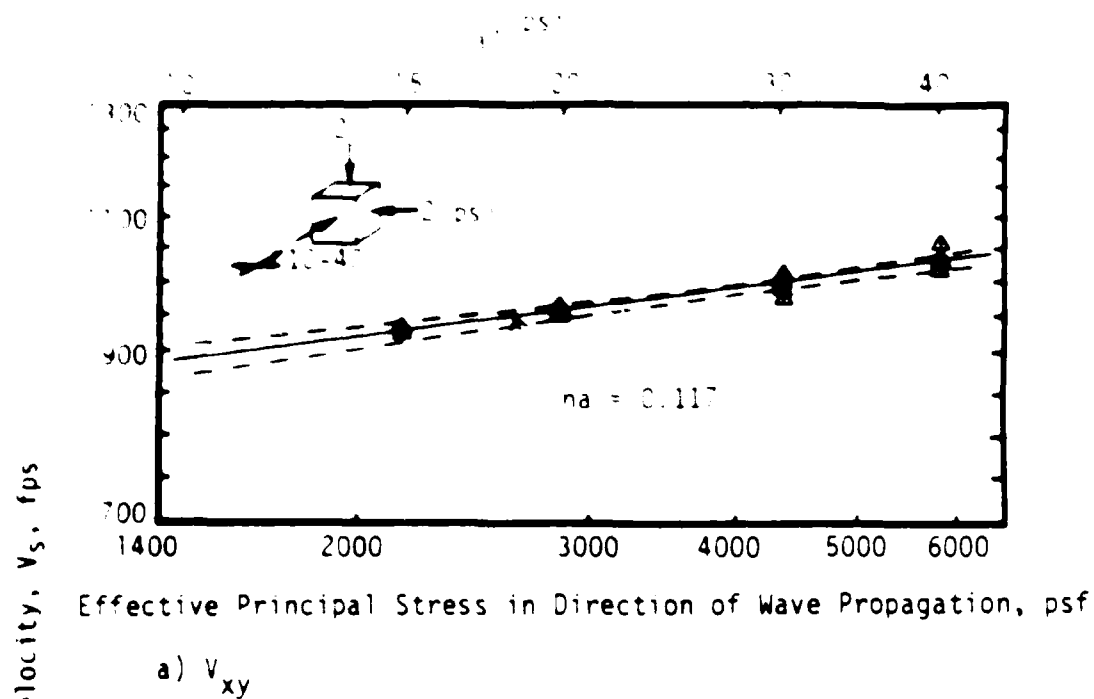
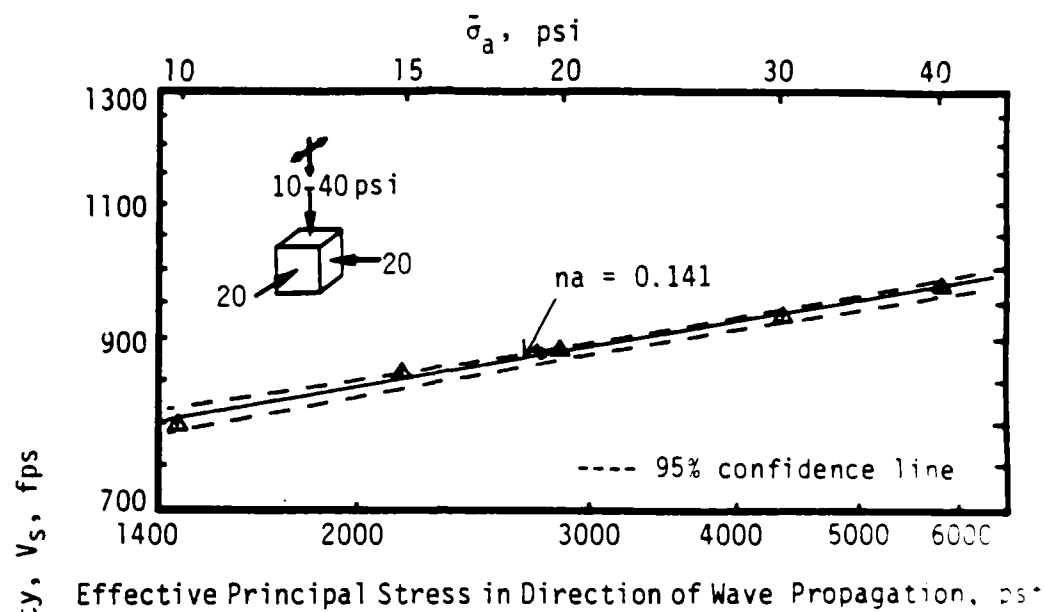
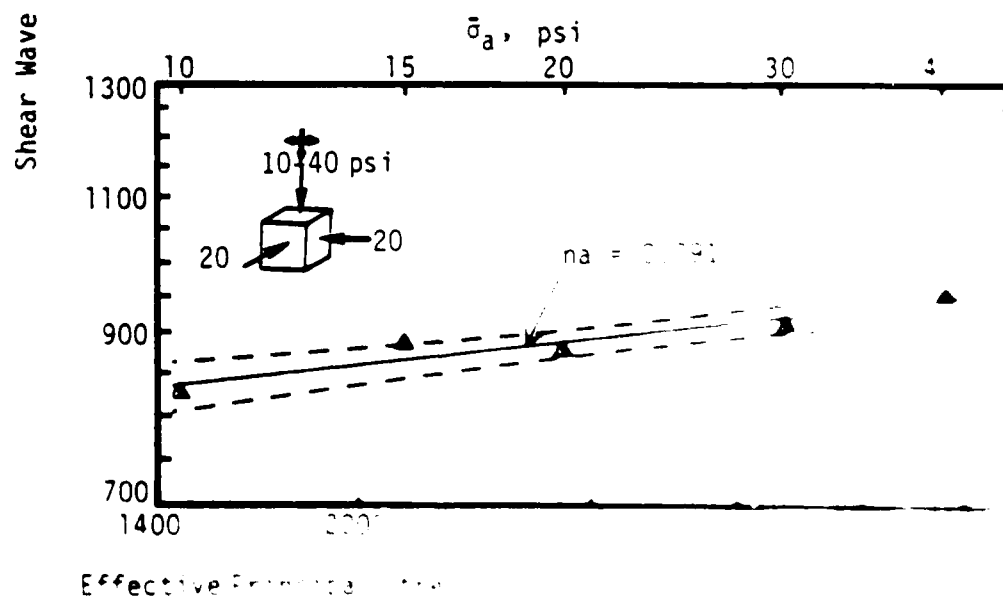


Fig. 6.21 - Effect on V_{xy} and V_{xz} of Varying Only Principal Stress in Direction of Wave Propagation Under Biaxial Loading for BIAR Series

a) V_{zx} 

Effective Principal Stress, psi

NO-A179 563

INVESTIGATION OF LOW-AMPLITUDE SHEAR WAVE VELOCITY IN
ANISOTROPIC MATERIAL. (U) TEXAS UNIV AT AUSTIN
GEOTECHNICAL ENGINEERING CENTER S H LEE ET AL. AUG 86

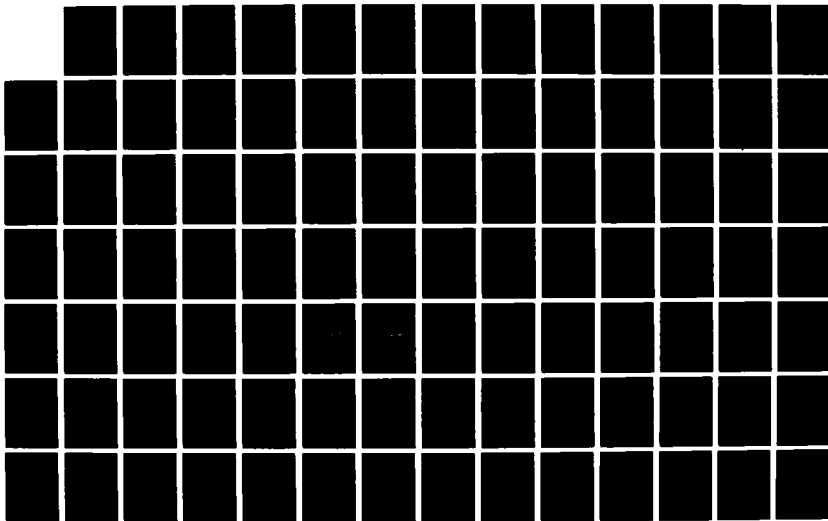
3/4

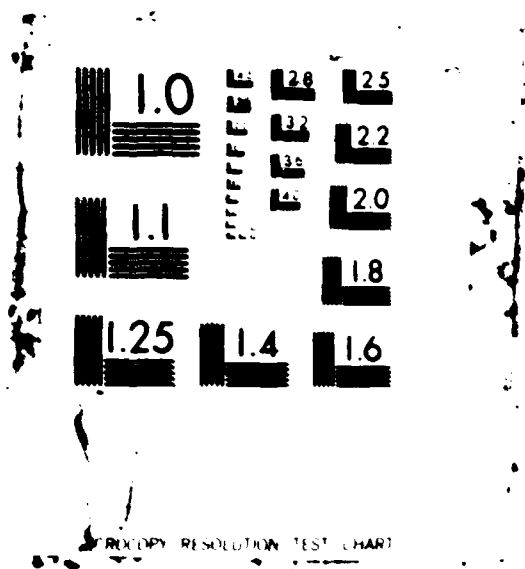
UNCLASSIFIED

AFOSR-TR-87-0403 AFOSR-83-0062

F/8 8/13

NL





RESOLUTION TEST CHART

Table 6.9 - Effect on V_s of Varying Only Principal Stress in Direction of Wave Propagation Under Biaxial Loading for BIAR Series

Shear Wave Type	Loading		Unloading		Average		Remark
	na^*	C_a^*	na	C_a	na	C_a	
V_{xy}	0.113	405	0.127	363	0.117	392	Fig. 6.21
V_{xz}	0.082	463	0.119	345	0.094	419	
V_{zx}	0.134	307	0.143	284	0.141	289	Fig. 6.22
V_{zy}	0.112	360	0.095	423	0.091	434	

$$* V_s = C_a \frac{na}{a}$$

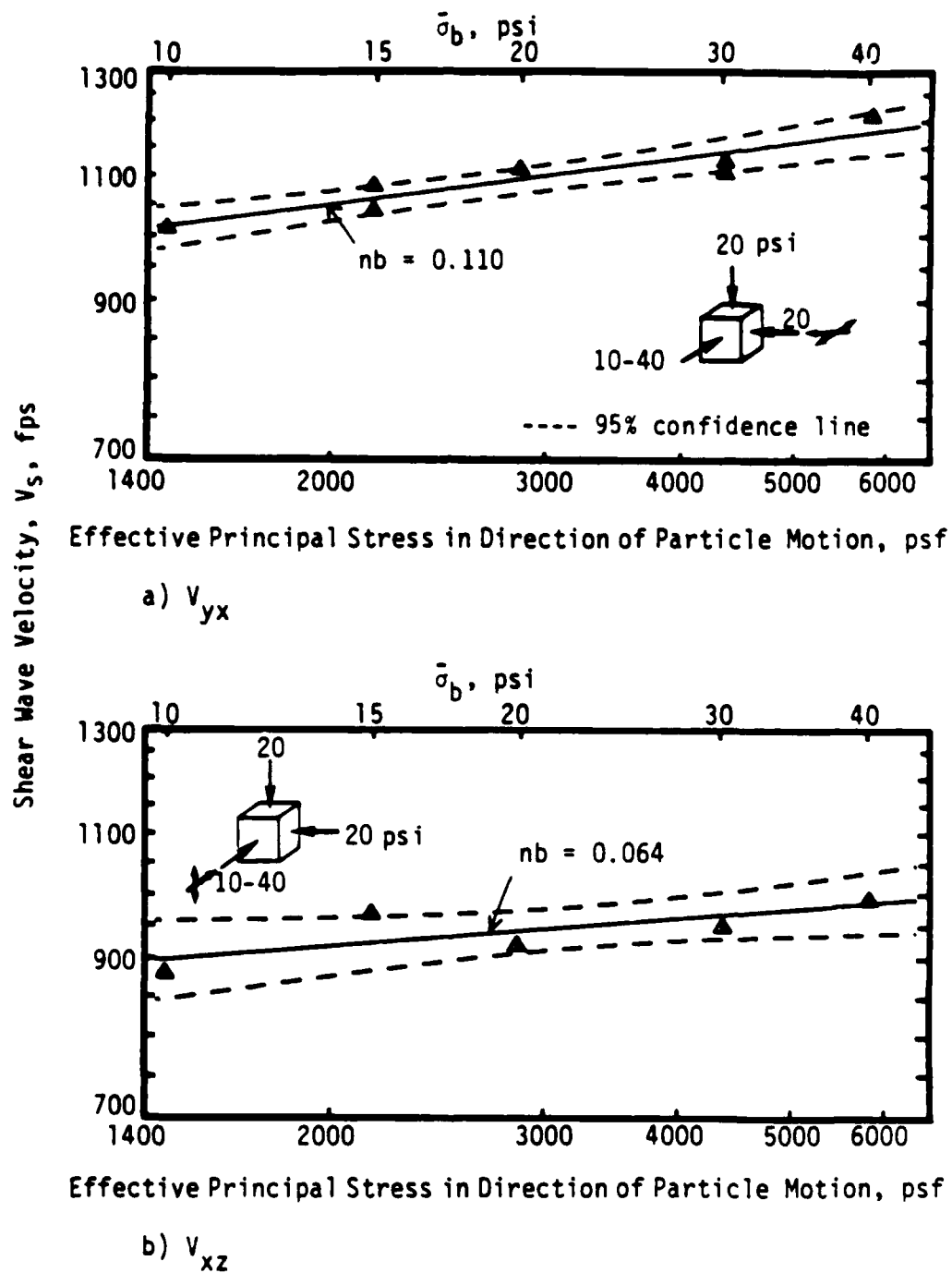


Fig. 6.23 - Effect on V_{yx} and V_{xz} of Varying Only Principal Stress in Direction of Particle Motion Under Biaxial Loading for BIAR Series

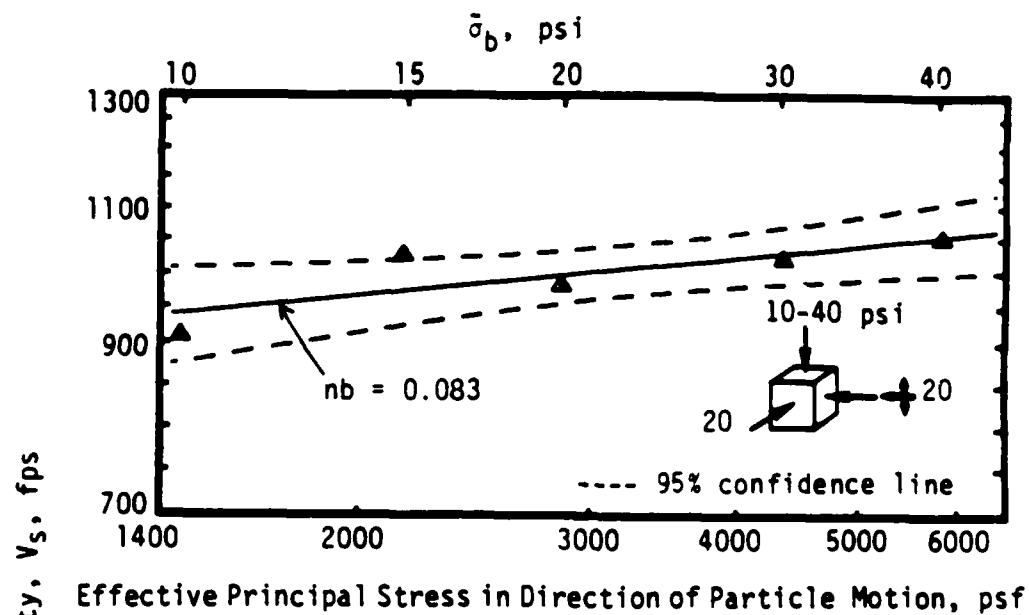
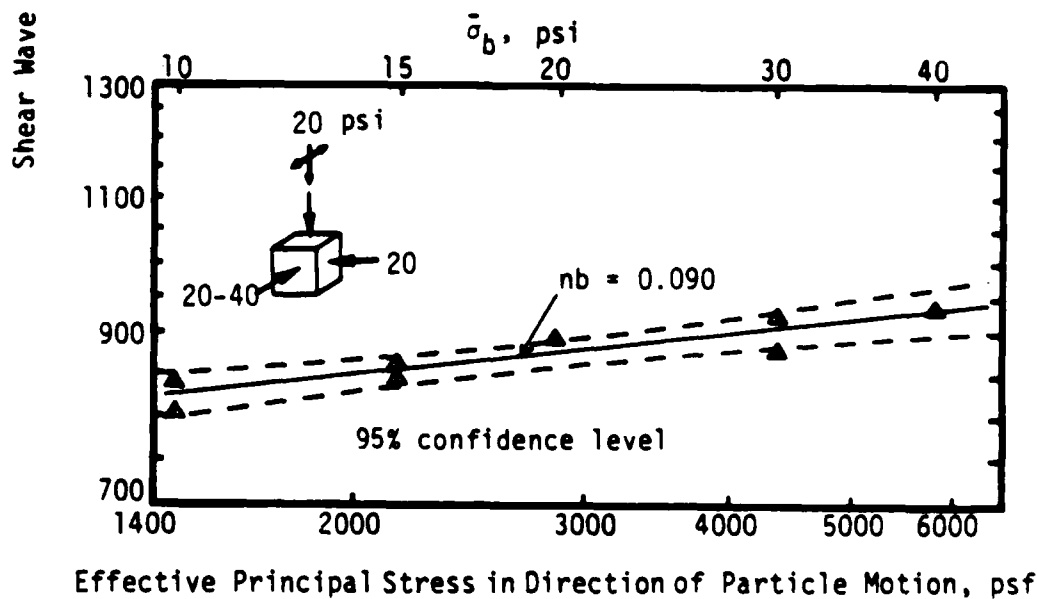
a) V_{yz} b) V_{zx}

Fig. 6.24 - Effect on V_{yz} and V_{zx} of Varying Only Principal Stress in Direction of Particle Motion Under Biaxial Loading for BIAR Series

Table 6.10 - Effect on V_s of Varying Only Principal Stress in Direction of Particle Motion Under Biaxial Loading for BIAR Series

Shear Wave Type	Loading		Unloading		Average		Remark
	nb*	C_b^*	nb	C_b	nb	C_b	
V_{yx}	0.120	419	0.099	501	0.110	455	Fig. 6.23
V_{xz}	0.100	414	0.071	542	0.064	564	
V_{yz}	0.100	445	0.089	494	0.083	545	Fig. 6.24
V_{zx}	0.099	393	0.091	433	0.090	430	

$$* V_s = C_b^* \sigma_b^{nb}$$

trend is similar to the one discussed in Section 6.3.2 for the BIA1 series with the values of n_b ranging from 0.08 to 0.12.

6.4.3 EFFECT OF PRINCIPAL STRESS IN OUT-OF-PLANE DIRECTION

As the effect of principal stress in this direction is a minor factor, the variation of shear wave velocity with stress is very small. The results of this effect in the BIAR series are shown in Figs. 6.25 and 6.26 and are listed in Table 6.11. Only the value of n_c for V_{yx} is the same as measured earlier. The other values of n_c are close to zero but are positive. More advanced research with better equipment is necessary to investigate fully this effect.

6.4.4 COMPARISON OF EFFECTS OF CONSTANT AND REORIENTED MAJOR PRINCIPAL STRESS DIRECTIONS

Average values of the slopes and constants of the $\log V_s - \log \bar{\sigma}_a$, $\log V_s - \log b$, and $\log V_s - \log \bar{\sigma}_c$ relationships under constant and reoriented major principal stress directions are summarized in Table 6.12. The slopes of the $\log V_s - \log \bar{\sigma}_a$, $\log V_s - \log \bar{\sigma}_b$, and $\log V_s - \log \bar{\sigma}_c$ ranged from 0.095 to 0.109, 0.078 to 0.124 and -0.022 to 0.010, respectively, for the constant major principal stress direction; the values ranged from 0.091 to 0.141, 0.064 to 0.110, and -0.006 to 0.021, respectively, for the reoriented major principal stress direction. Thus, the values determined from each test series are in reasonably good agreement.

Since measured shear wave velocities can be considered to reflect the sum total effect of the values of the slope, constant and effective principal stress, shear wave velocities were calculated with $\bar{\sigma}_a$, $\bar{\sigma}_b$, and $\bar{\sigma}_c$ equalling 15 psi (103.4 kPa) and 40 psi (275.6 kPa) and were then compared in the following way:

$$RD = V_s(2) - V_s(1) / V_s(1) \quad (6.6)$$

where

RD = ratio of difference of shear wave velocity, %,

$V_s(1)$ = shear wave velocity with constant orientation of the major principal stress, and

$V_s(2)$ = shear wave velocity with reoriented major principal stress.

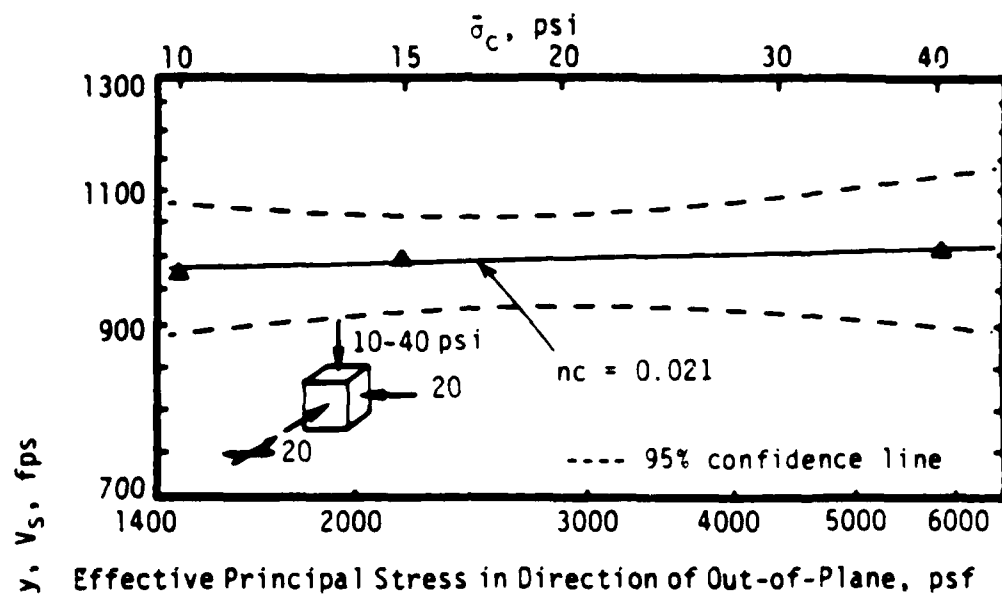
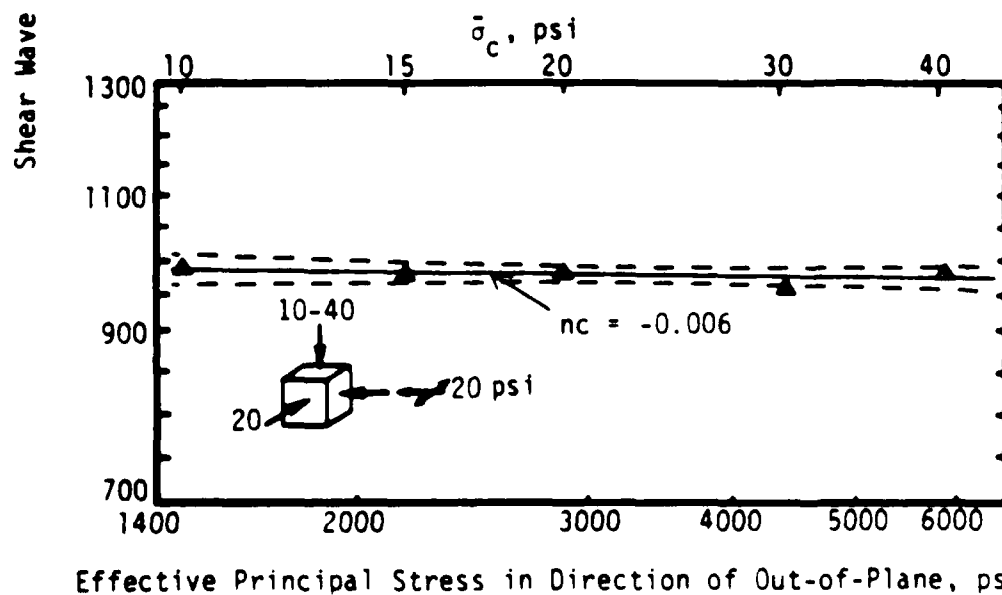
a) V_{xy} b) V_{yx}

Fig. 6.25 - Effect on V_{xy} and V_{yx} of Varying Only Principal Stress in Out-of-Plane Direction Under Biaxial Loading for BIAR Series

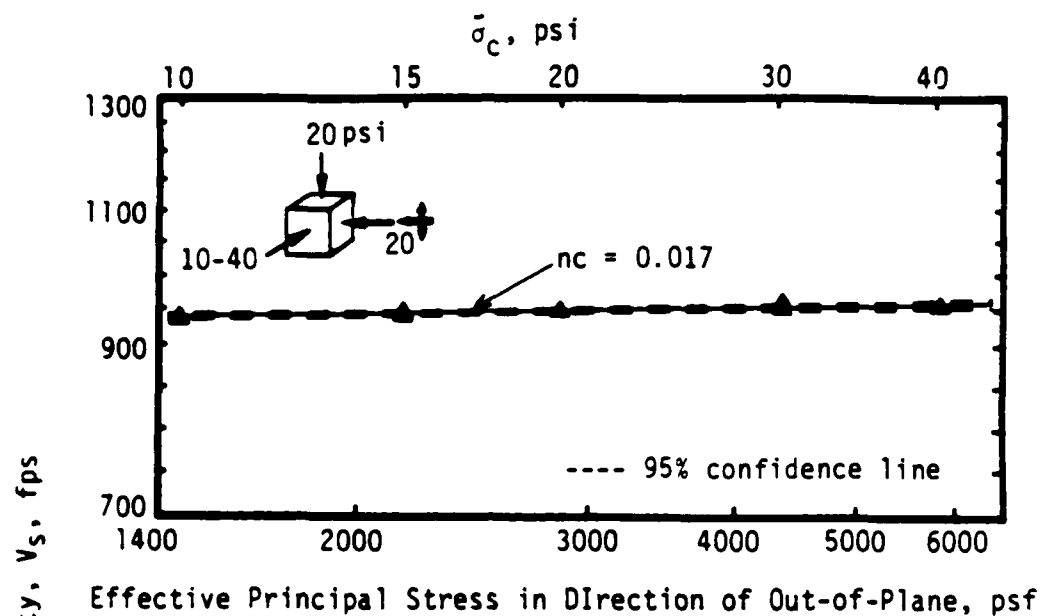
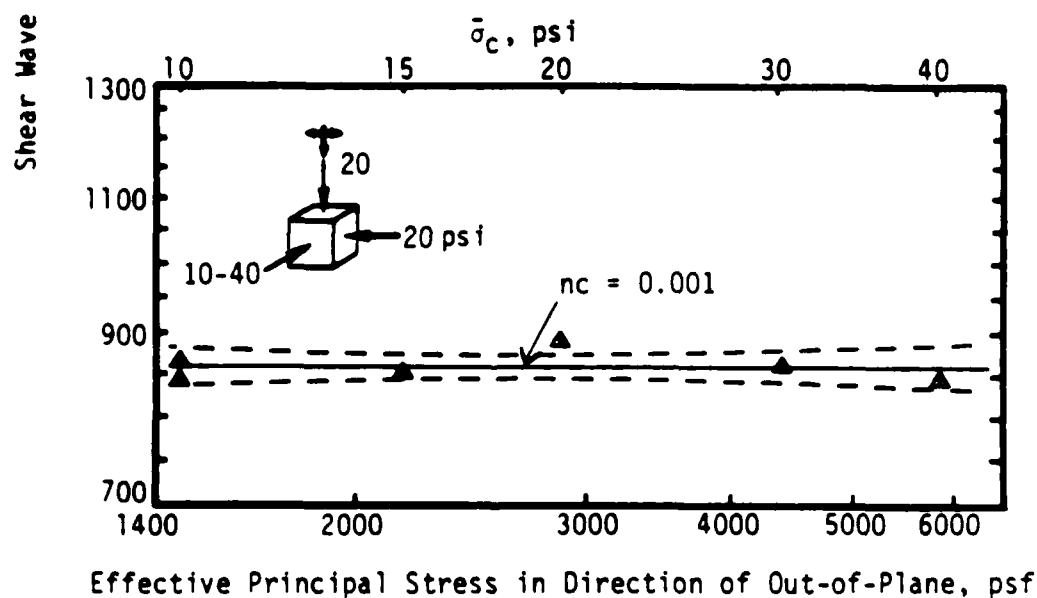
a) V_{yz} b) V_{zy}

Fig. 6.26 - Effect on V_{yz} and V_{zy} of Varying Only Principal Stress in Out-of-Plane Direction Under Biaxial Loading for BIAR Series

Table 6.11 - Effect on V_s of Varying Only Principal Stress in Out-Of-Plane Direction Under Biaxial Loading for BIAR Series

Shear Wave Type	Loading		Unloading		Average		Remark
	nc^*	C_c^*	nc	C_c	nc	C_c	
V_{xy}	—**	—	0.021	842	0.021	842	Fig. 6.25
V_{yx}	-0.003	1002	-0.003	1008	-0.006	1030	
V_{yz}	0.016	829	0.021	897	0.017	828	Fig. 6.26
V_{zy}	0.005	818	0.005	832	0.001	852	

** malfunction of records on floppy disc

* $V_s = C_c \sigma_c / nc$

Table 6.12 - Comparison of Slopes, Constants and S-Wave Velocities Between the State of Constant Principal Stress Directions and the State of Reorientation of Principal Stress Directions Under Biaxial Confinement

case*	Shear Wave Type	Constant Principal Stress States (1)		Reorienting Principal Stress States (2)		RD = $\frac{V_S(2) - V_S(1)}{V_S(1)}$, %
		na**	C _a **	na	C _a	
1	V _{xy}	0.109	401	0.117	392	$\bar{\sigma}_a = 15 \text{ psi}$ $\bar{\sigma}_a = 40 \text{ psi}$ +3.4 +4.6
	V _{xz}	0.095	406	0.094	419	+2.6 +2.6
	V _{zx}	0.098	394	0.141	289	+1.6 +5.9
	V _{zy}	0.105	375	0.091	434	+3.8 +2.4
2	V _{yx}	nb	C _b	nb	C _b	Average 3.4 $\bar{\sigma}_b = 15 \text{ psi}$ $\bar{\sigma}_b = 40 \text{ psi}$ +15.6 +14.0
	V _{xz}	0.124	354	0.110	455	+7.6 +3.3
	V _{yz}	0.105	383	0.064	564	+6.8 +7.4
	V _{zx}	0.078	502	0.083	515	+3.8 +4.7
3	V _{xy}	nc	C _c	nc	C _c	Average 7.9 $\bar{\sigma}_c = 15 \text{ psi}$ $\bar{\sigma}_c = 40 \text{ psi}$ +6.6 +7.9
	V _{yx}	0.009	868	0.021	842	+6.3 +4.6
	V _{yz}	0.010	856	-0.006	1030	+5.5 +8.2
	V _{zy}	-0.009	960	0.017	828	+4.0 +4.1
	V _{zy}	-0.022	974	0.001	852	Average 5.9

*1 = major principal stress in direction of wave propagation ** V_S = C_a^{na}

2 = major principal stress in direction of particle motion V_S = C_a^{na}

3 = major principal stress in out-of-plane direction V_S = C_b^{nb}

V_S = C_c^{nc}

The values of RD are listed in Table 6.12. For case 1 in which only the principal stress in the direction of wave propagation was varied, values of RD ranged from 1.6 percent to 4.6 percent and had an average value of 3.4 percent. For case 2 in which only the principal stress in the direction of particle motion was varied, values of RD ranged from 3.3 to 15.6 percent and had an average value of 7.9 percent. For case 3 in which only the principal stress in the out-of-plane direction was varied, values of RD ranged from 4.0 to 8.2 percent, with an average value of 5.9 percent. These values show that shear wave velocities were always higher in the reoriented principal stress conditions. By employing Eq. 2.52, one can see that for constant major principal stress with one stress varying in the direction of wave propagation [i.e., $\bar{\sigma}_b = \bar{\sigma}_c = 15$ psi (103 kPa)], shear wave velocity can be expressed as:

$$V_s(1) = C_2 \bar{\sigma}_a^{na} (2160)^{nb} (2160)^{nc}; \quad (6.7)$$

and for reoriented major principal stress with one stress varying in the direction of wave propagation [i.e., $\bar{\sigma}_b = \bar{\sigma}_c = 20$ psi (138 kPa)],

$$V_s(2) = C_2 \bar{\sigma}_a^{na} (2880)^{nb} (2880)^{nc} \quad (6.8)$$

Therefore, the value of RD in Eq. 6.6 can be calculated by the following if C_2 in Eqs. 6.7 and 6.8 are assumed equal:

$$RD = V_s(2) - V_s(1) / V_s(1) = (2880/2160)^{nb+nc} - 1 \quad (6.9)$$

The value of RD ranges from 4.4 percent to 10 percent, which includes the range of the ratio (RD) in Table 6.12 and indicates why the S-wave velocities in BIAR are larger than those in BIA1. Consequently, the data from BIA1, BIA2, and IAR must be analyzed separately, although the slopes in the $\log V_s$ - $\log \bar{\sigma}$ relationships are nearly the same.

6.5 COMPARISON OF SHEAR WAVE VELOCITY UNDER ISOTROPIC CONFINEMENT AND BIAxIAL CONFINEMENT

In the series of biaxial tests with two stresses varying (BIA2), some tests were conducted with both major principal stresses in the directions of wave propagation and particle motion varying as shown in Figs. 6.27 through

6.29. One can see that the values of the slope from these tests (listed in Table 6.13) are nearly equal to those in Table 5.9 for isotropic confining pressure conditions, but not entirely.

If Eq. 2.52 is used to analyze and compare these two conditions, Eq. 6.10 can be obtained for the group of tests BIA2 as:

$$V_{BI} = C_{BI} \bar{\sigma}_a^{na} \bar{\sigma}_b^{nb} (5760)^{nc} \quad (6.10)$$

where $\bar{\sigma}_a$ equals $\bar{\sigma}_b$, and for isotropic confinement,

$$V_I = C_I \bar{\sigma}_a^{na} \bar{\sigma}_b^{nb} \bar{\sigma}_c^{nc}, \quad (6.11)$$

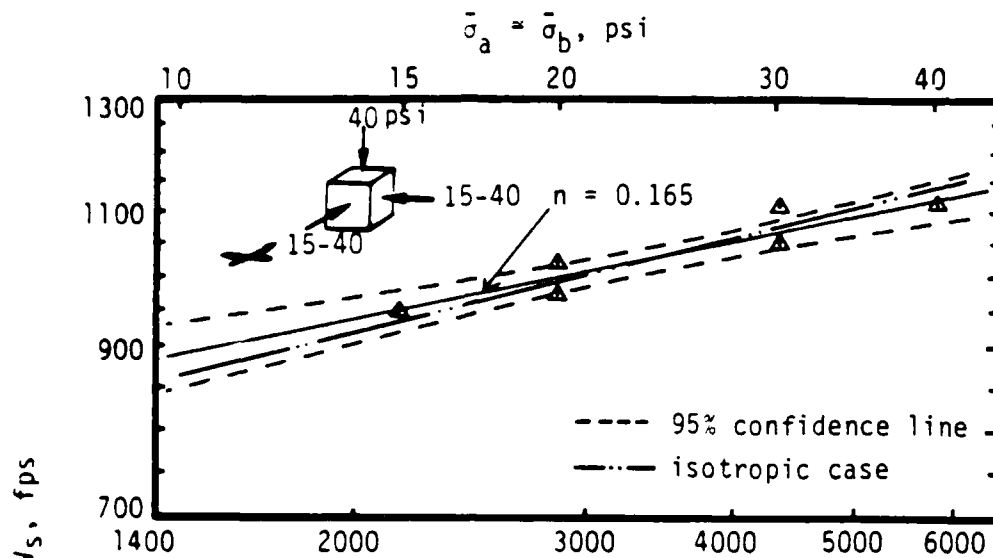
in which case $\bar{\sigma}_a = \bar{\sigma}_b = \bar{\sigma}_c$. By dividing Eq. 6.10 by 6.11,

$$V_{BI}/V_I = (C_{BI}/C_I)(5760/\bar{\sigma}_c)^{nc} \quad (6.12)$$

The units of V_s are fps and $\bar{\sigma}$ are psf.

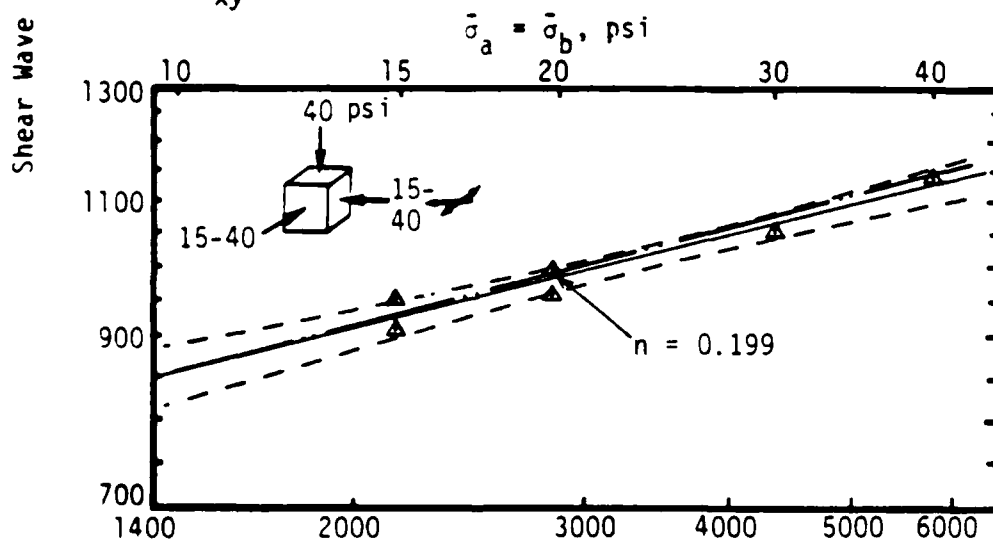
It is obvious that V_{BI} will be the same as V_I once $nc=0$ and $C_{BI}=C_I$ are assumed. However, based on the slopes listed in Table 6.6 and the constants listed in Table 6.13 for V_{BI} and Table 5.9 for V_I , the ratio of V_{BI} to V_I will range from 0.973 to 1.001 as shown in column 8 of Table 6.13 when $\bar{\sigma}_c$ equals 40 psi (275.6 kPa) and agree with those regression results shown in Figs. 6.27 through 6.29. Additionally, the average values of the principal stresses in the directions of wave propagation and particle motion are the same in both series of BIA1 and isotropic confinement. If the "average-stress" method were used to estimate the shear wave velocity, V_{BI} will be the same as V_I regard less of the variation of principal stress in out-of-plane direction. The experimental results in column 8 of Table 6.13 show that the "average-stress" method cannot be used to predict properly the shear wave velocity because they are not all 1.0. Additional study of this method is presented in Chapter Seven.

Since the influence of the effective principal stress in the directions of wave propagation and particle motion and the out-of-plane direction have been examined individually, and the influence of stress history has been found to be quite small (negligible) in the range of this study, Eq. 2.52 with a small value for the slope of the out-of-plane stress (nc) is



Effective Principal Stress in Directions of Wave Propagation and Particle Motion

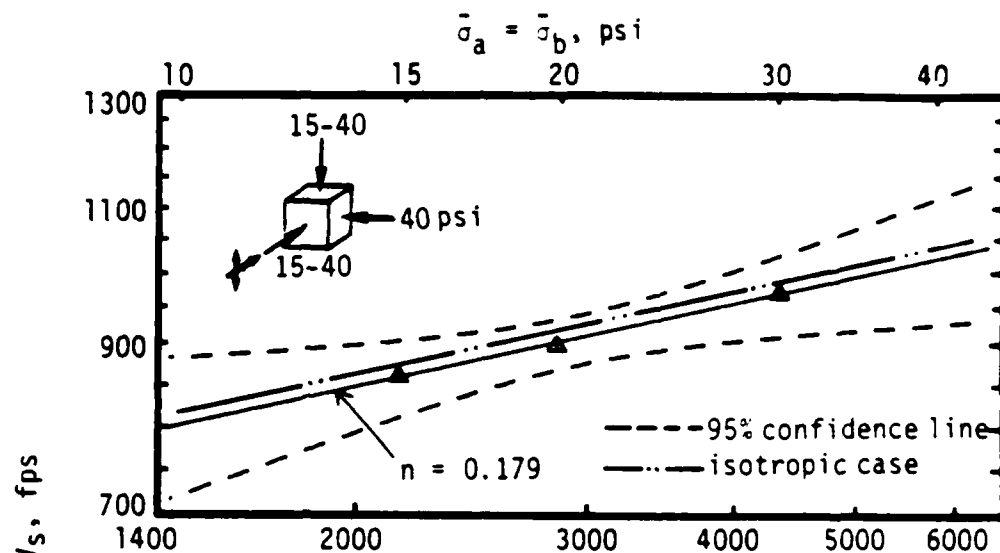
a) V_{xy}



Effective Principal Stress in Directions of Wave Propagation and Particle Motion

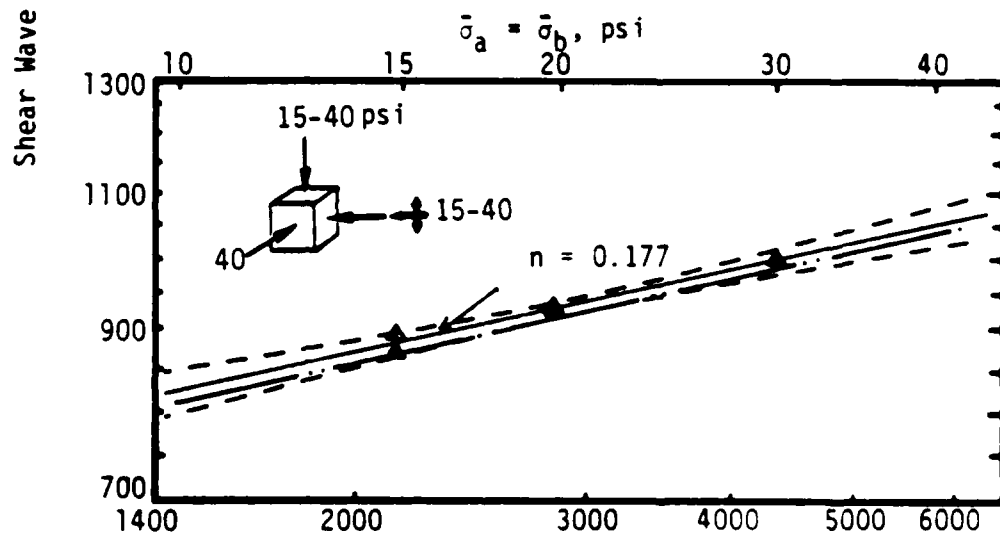
b) V_{yx}

Fig. 6.27 - Effect on V_{xy} and V_{yx} of Varying Principal Stress in Both Directions of Wave Propagation and Particle Motion Under Biaxial Loading for BIA2 Series



Effective Principal Stress in Directions of Wave Propagation and Particle Motion

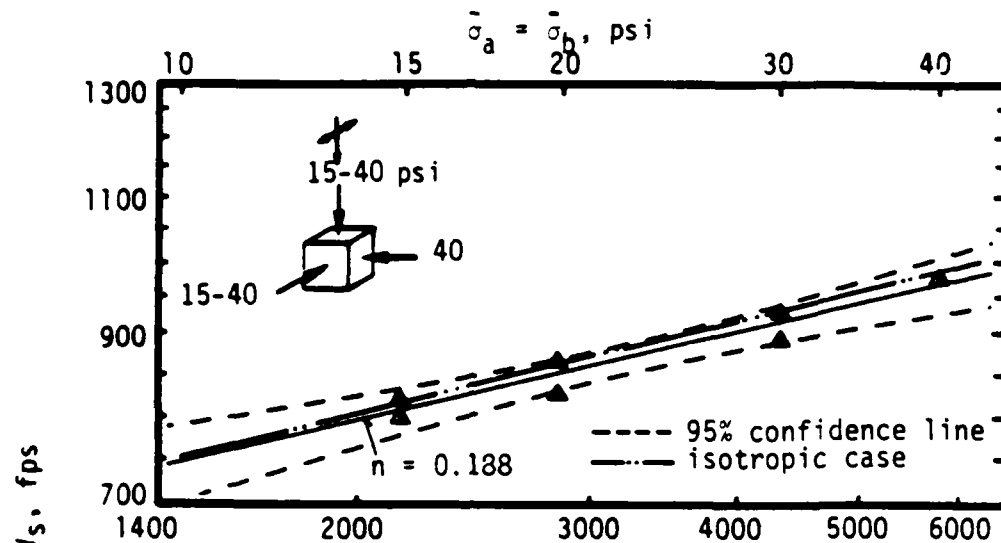
a) V_{xz}



Effective Principal Stress in Directions of Wave Propagation and Particle Motion

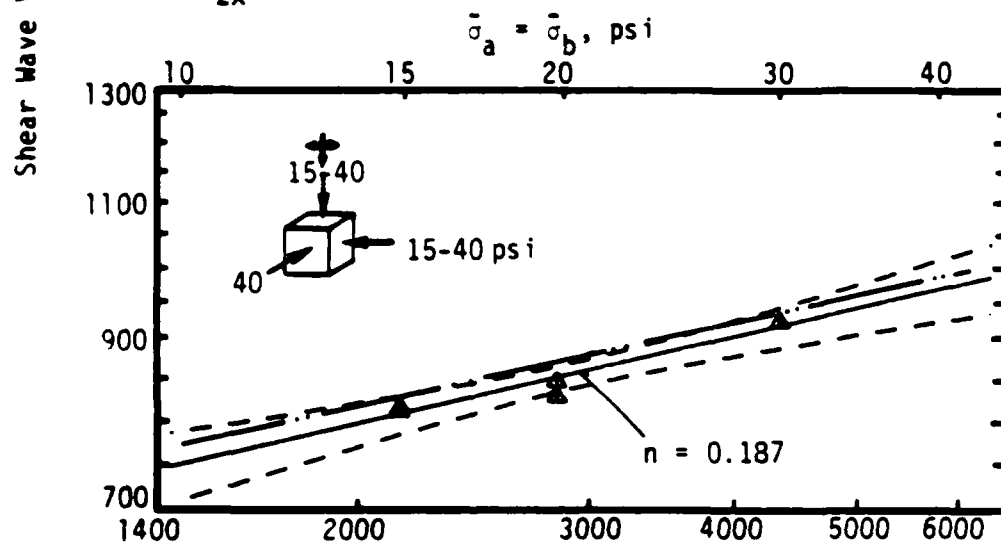
b) V_{yz}

Fig. 6.28 - Effect on V_{xz} and V_{yz} of Varying Principal Stress in Both Directions of Wave Propagation and Particle Motion Under Biaxial Loading for BIA2 Series



Effective Principal Stress in Directions of Wave Propagation and Particle Motion

a) V_{zx}



Effective Principal Stress in Directions of Wave Propagation and Particle Motion

b) V_{zy}

Fig. 6.29 - Effect on V_{zx} and V_{zy} of Varying Principal Stress in Both Directions of Wave Propagation and Particle Motion Under Biaxial Loading for BIA2 Series

Table 6.13 - Effect of Variation of Principal Stresses in Both
Directions of Wave Propagation and Particle
Motion on S-Wave Velocity Under Biaxial Confinement

Shear Wave Type	Loading		Unloading		Average		$\frac{V_{BI}^{**}}{V_I}$	Remark
	n^*	C^*	n	C	n	C		
V_{xy}	0.146	314	0.184	230	0.165	269	1.00	Fig. 6.27
V_{yx}	0.224	152	0.174	249	0.199	201	0.980	
V_{xz}	0.178	316	0.187	206	0.179	216	0.977	Fig. 6.28
V_{yz}	0.157	268	0.196	194	0.177	228	0.994	
V_{zx}	0.166	222	0.178	208	0.188	191	0.973	Fig. 6.29
V_{zy}	0.184	195	1.190	188	0.187	192	0.985	

** Shear wave velocities under condition of $\bar{\sigma}_a = \bar{\sigma}_b = \bar{\sigma}_c = 40$ psi

* $V_s = C(\bar{\sigma}_a \bar{\sigma}_b)^{n/2}$; in which $\bar{\sigma}_a = \bar{\sigma}_b$

preferred. From the results of this study, listed in Tables 6.3 through 6.7, the constants and slopes for each type of shear wave with one and two stresses varying under biaxial confinement are summarized in Table 6.14. The new constants are the arithmetic average from Eq. 6.13:

$$C_2 = \sum_{n=1}^N (V_s(n)/N) / (\bar{\sigma}_a^{na} \bar{\sigma}_b^{nb} \bar{\sigma}_c^{nc}) \quad (6.13)$$

C_2 = new constants in column 2 of Table 6.14,

N = total number of tests of each type of shear wave,

V_s = test result of velocity of each type of shear wave,

na, nb, nc = slopes shown in Table 6.3 through 6.7, and

$\bar{\sigma}_a, \bar{\sigma}_b, \bar{\sigma}_c$ = effective principal stresses as the test conditions listed in Table 4.4.

As discussed in Section 6.3.3, the possible "softening" induced by extension strains from static confining pressures is larger in BIA2 than in BIA1. Therefore, the slopes in BIA2 will be smaller than in BIA1. Because na and nb are defined as slopes caused by the variation of one principal stress, na^* and nb^* are defined as "apparent slopes" caused by two stresses varying in the series of BIA2. Since more extension strain (softening) occurs in BIA2 than in BIA1, the "apparent slope" should be slightly less than the values determined from BIA1. Table 6.14 shows the experimental results for the slopes and apparent slopes which agree with the postulate of "strain softening". The slope nc cannot be measured in BIA2 tests. Since the effect of nc has been included in both na^* and nb^* , $nc^* = -nc$ was used to reduce the influence of stress in the out-of-plane direction to one time only. From the conclusion in Section 6.4.4, the regression equation for BIA1 could be used for BIAR. A comparison between shear wave velocity predicted by Eq. 2.52 with values listed in Table 6.14 and test results of BIA1 and BIA2 is summarized in Table 6.15. The range of the ratio falls between 0.966 and 1.036 (-3.4 percent to +3.6 percent) and reflects good correlation between predicted and measured shear wave velocity.

However, shear wave velocities of BIA2 are always larger than those in BIA1 due to the larger principal stresses in the BIA2 tests (see Section 6.3.3). Table 6.16 summarizes the ratio of test results of BIA1 to BIA2. If one assumes that Eq. 2.52 is a proper way of relating shear wave velocity and stress state, shear wave velocities predicted by Eq. 2.52 with constants and

Table 6.14 - Values of Constants and Slopes of Eq. 2.52 for each Type of Shear Wave Velocity Under Biaxial Confinement

(a) for the case of one increment under biaxial confinement (BIA1)⁺:

Shear Wave	Constant	na	nb	nc	Remark
V _{xy}	202	0.109	0.087	0.001	na = from Table 6.1
V _{yx}	169	0.104	0.124	-0.007	nb = from Table 6.3
V _{xz}	186	0.095	0.105	-0.002	nc = from Table 6.5
V _{yz}	305	0.074	0.078	-0.009	
V _{zx}	243	0.100	0.081	-0.020	
V _{zy}	180	0.105	0.104	-0.011	

(b) for the case of two increments under biaxial confinement (BIA2)⁺⁺:

Shear Wave	Constant	na*	nb*	nc*	Remark
V _{xy}	292	0.078	0.074	-0.001	na* = from Table 6.2
V _{yx}	224	0.089	0.107	0.007	nb* = from Table 6.4
V _{xz}	259	0.078	0.081	0.002	nc* = -nc
V _{yz}	224	0.082	0.105	0.009	* = apparent slope
V _{zx}	211	0.108	0.090	0.020	
V _{zy}	257	0.095	0.070	0.011	

na and nb = slopes due to one increment

na* and nb* = slopes due to two increments; or apparent slope

$$+ V_s = C_2 \frac{na}{\sigma_a} \frac{nb}{\sigma_b} \frac{nc}{\sigma_c}$$

$$++ V_s = C_2 \frac{na^*}{\sigma_a} \frac{nb^*}{\sigma_b} \frac{nc^*}{\sigma_c}$$

Table 6.15 - Ratio of Shear Wave Velocity Predicted by Eq. 2.52 with Constants and Slopes Listed in Table 6.14 to the Test Results of BIA1 and BIA2

$\bar{\sigma}_1$ or $\bar{\sigma}_3$, *psf	Shear Wave Type	R1(MA)	R2(MA)	R1(MB)	R2(MB)
2160	V_{xy}	.993	1.008	1.007	.988
	V_{yx}	.993	.995	1.007	1.023
	V_{xz}	1.009	.983	.991	1.020
	V_{yz}	1.002	1.036	.998	.988
	V_{zx}	.987	.997	1.014	.985
	V_{zy}	.981	1.009	1.020	.967
2880	V_{xy}	.993	1.008	1.014	.990
	V_{yx}	.993	.994	1.001	1.017
	V_{xz}	1.009	.983	.998	1.019
	V_{yz}	1.002	1.035	.997	.980
	V_{zx}	.987	.994	1.019	.987
	V_{zy}	.981	1.008	1.020	.972
4320	V_{xy}	.993	1.008	1.023	.992
	V_{yx}	.993	.992	.993	1.008
	V_{xz}	1.009	.983	.984	1.018
	V_{yz}	1.002	1.033	.995	.969
	V_{zx}	.987	.990	1.027	.990
	V_{zy}	.981	1.005	1.021	.980
5760	V_{xy}	.993	1.008	1.029	.993
	V_{yx}	.993	.992	.987	1.002
	V_{xz}	1.009	.982	.981	1.016
	V_{yz}	1.002	1.032	.994	.962
	V_{zx}	.987	.988	1.033	.993
	V_{zy}	.981	1.004	1.021	.986

R = Ratio of predicted shear wave velocity to test results

R1 = Ratios for the tests of BIA1, i.e. one increment only, and Eq. 2.52 was used to predict shear wave velocity

R2 = Ratios for the tests of BIA2, i.e. two increments, and Eq. 2.52 was used to predict shear wave velocity

MA = Test data from the group of principal stress varying in the direction of wave propagation

MB = Test data from the group of principal stress varying in the direction of particle motion

* = in case of BIA1, $\bar{\sigma}_1$ is shown in the column;

in case of BIA2, $\bar{\sigma}_3$ is shown in the column

Table 6.16 - Ratio of Shear Wave Velocities Measured
in BIA1 to BIA2

Shear Wave Type	$\bar{\sigma}_1$ or $\bar{\sigma}_3^*$, psf				Remark
	2160	2880	4320	5760	
V_{xy}	0.90	0.91	0.92	0.93	* $\bar{\sigma}_1$ in BIA1 with $\bar{\sigma}_2 = \bar{\sigma}_3 = 2160$ psf
V_{yx}	0.88	0.90	0.89	0.89	
V_{xz}	0.91	0.91	0.92	0.92	
V_{yz}	0.94	0.94	0.94	0.94	* $\bar{\sigma}_3$ in BIA2 with $\bar{\sigma}_1 = 5760$ psf and $\bar{\sigma}_2 = \bar{\sigma}_3$
V_{zx}	0.94	0.94	0.94	0.94	
V_{zy}	0.92	0.93	0.93	0.94	

slopes from BIA1 and BIA2 should be the same, once the same confining pressures are employed. Ratios of these two shear wave velocities listed in Table 6.17 ranging from 0.971 to 1.047 (-2.9 percent to +4.7 percent) verify that the "three-individual-stresses" method, Eq. 2.52, predicts very well the shear wave velocities for both BIA1 and BIA2.

In previous research on sand, values of the slope generally ranged from 0.06 to 0.15 for n_a and from 0.08 to 0.14 for n_b (see Table 2.3). The values of n_a , ranging from 0.07 to 0.11, and n_b , ranging from 0.08 to 0.12, were measured in this study which agrees closely with previous work. Also the value of n_c measured in this research is nearly zero which agrees well with the work by Roesler (1979).

6.6 EFFECT OF STRUCTURAL ANISOTROPY

Based on the discussion in Section 5.3, structural anisotropy should result in V_{SI} being equal to V_{xy} and V_{yx} , and V_{SA} being equal to V_{xz} , V_{yz} , V_{zx} , and V_{zy} . A detailed regression analysis of the BIA1 tests for each parameter in Eq. 2.52 based on this cross-anisotropic model is given in Table 6.18 and is shown in Figs. 6.30 and 6.31. The ratio of shear wave velocity in the isotropic plane (V_{SI}) to that in the anisotropic plane (V_{SA}) is

$$V_{SI}/V_{SA} = 0.9435 \pm 0.003 \pm 0.009 \pm 0.007 \quad (6.14)$$

In an isotropic confinement condition, Eq. 6.14 can be expressed as:

$$V_{SI}/V_{SA} = 0.9435 \pm 0.019 \quad (6.15)$$

If the mean effective stress was varied from 15 to 40 psi (103.4 to 275.6 kPa), the value of Eq. 6.15 would range between 1.092 and 1.112. So, an average value of the ratio of V_{SI} to V_{SA} under isotropic confinement in this study is:

$$V_{SI} = 1.10 V_{SA} \quad (6.16)$$

Equation 6.19 is precisely the same as Eq. 5.5 obtained in this study under isotropic confining pressure conditions. Consequently, the existence of the

Table 6.17 - Ratio of Shear Wave Velocity Predicted by Eq. 2.52
with Constant and Slopes of BIA1 to BIA2 Under Same
Biaxial Confining Pressures

Shear Wave Type	$\bar{\sigma}_1$, psf				Remark
	2160	2880	4320	5760	
V_{xy}	0.97	0.98	1.00	1.02	$\bar{\sigma}_2 = \bar{\sigma}_3 = 2160$ psf for both BIA1 and BIA2
V_{yx}	0.97	0.98	0.99	1.00	
V_{xz}	0.98	0.99	1.01	1.02	
V_{yz}	1.05	1.04	1.02	1.01	
V_{zx}	1.02	1.02	1.01	1.00	
V_{zy}	0.99	1.00	1.02	1.03	

Table 6.18 - Results of Regression Analysis of the Sand Sample Based on an Idealized Cross-Anisotropic Model and BIAI Test Series

Shear* Wave Type	Slope	Linear Correlation Coefficient	R-square	Adjusted R-square	F-Test of Sample		Constant, C ₂		Slope, n	
					Ratio	α	Value	Ratio	Value	Ratio
V _{SI} **	na	0.941	0.895	0.887	119.3	0	484.8	7594.4	0	0.095
	nb	0.892	0.796	0.782	54.7	0	473.8	3158.4	0	0.098
	nc	0.072	0.005	0.000	0.07	0.79	934.3	5780.8	0	-0.003
V _{SA} ***	na	0.783	0.612	0.599	47.4	0	369.9	3128.5	0	0.092
	nb	0.722	0.521	0.505	32.6	0	378.1	2248.5	0	0.089
	nc	0.116	0.013	0.000	0.41	0.53	850.7	2581.9	0	-0.010

$$* V_s = C_2 \frac{na}{\sigma_a} - \frac{nb}{\sigma_b} - \frac{nc}{\sigma_c}$$

$$** V_{SI} = V_{xy} = V_{yx}, C_2 = 218 \quad \text{from the regression analysis}$$

$$*** V_{SA} = V_{xz} = V_{yz} = V_{zx} = V_{zy}, C_2 = 230 \quad \text{from the regression analysis}$$

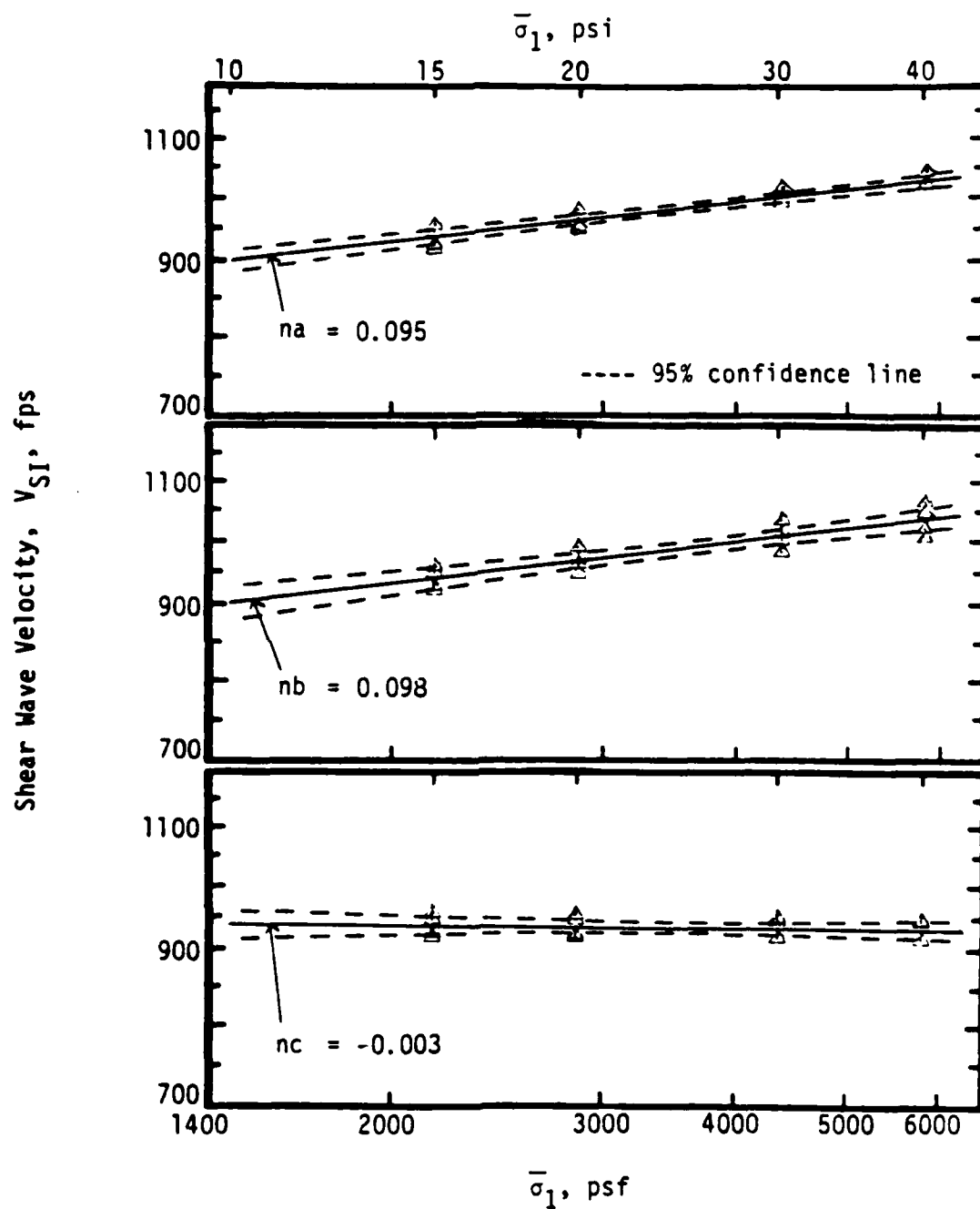


Fig. 6.30 - Regression Analysis of Slopes of Shear Wave Velocity (V_{SI}) with Idealized Cross-Anisotropic Model

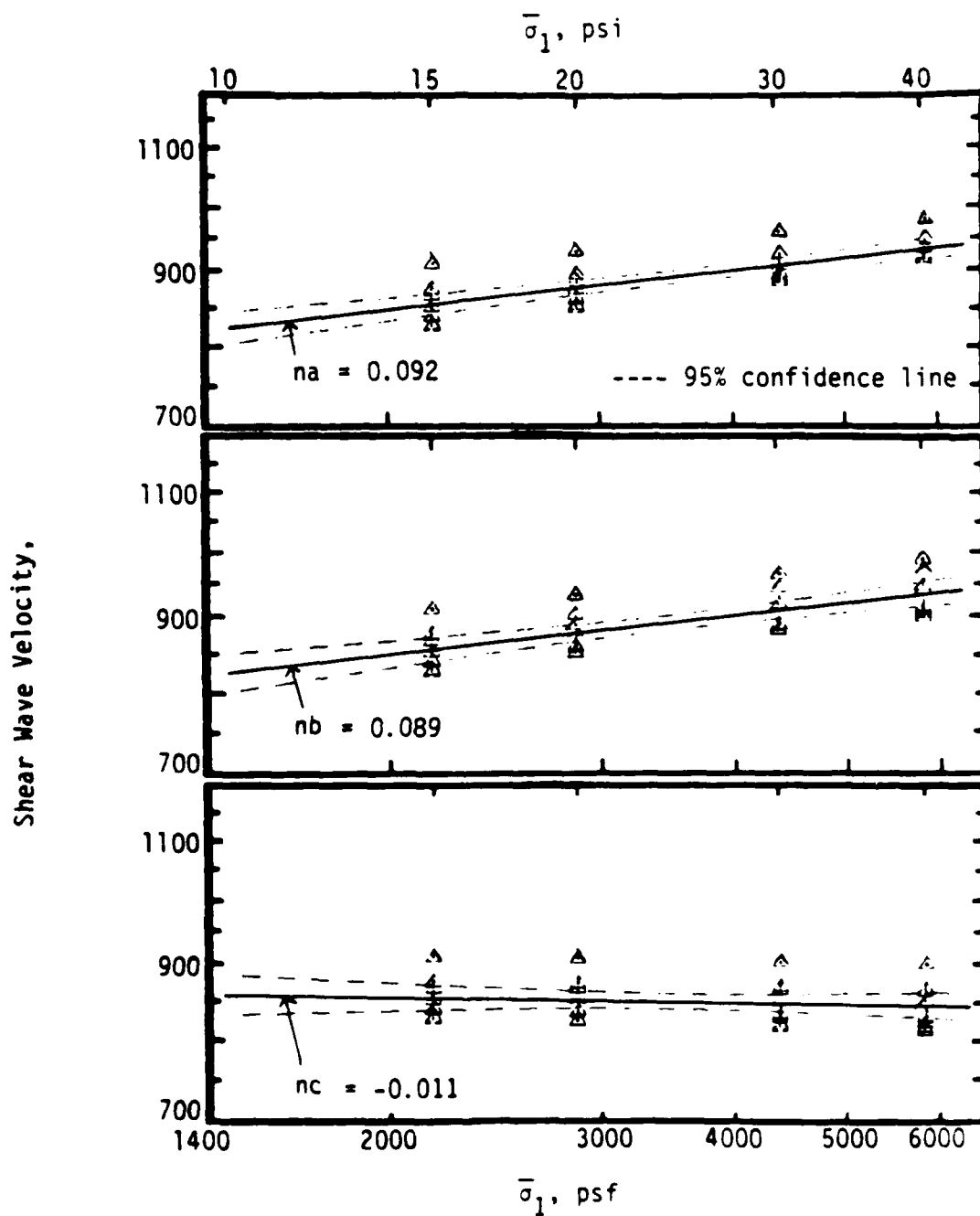


Fig. 6.31 - Regression Analysis of Slopes of Shear Wave Velocity (V_{SA}) for Idealized Cross-Anisotropic Model

structural anisotropy of this sand sample is independent of the stress state applied in this study.

The effect of structural anisotropy caused by the ratio of P-wave velocities, the ratio of V_{pI} to V_{pA} (Chu, et al, 1984), to be 1.17 which is about 7 percent higher than the ratio of the S-wave velocities. It is understood that shear wave velocity is mainly a function of both $\bar{\sigma}_a$ and $\bar{\sigma}_b$ (confining pressures in the directions of wave propagation and particle motion) while compression wave velocity is (almost) only a function of $\bar{\sigma}_a$. This dependency of V_s on two directions may cause the ratio of V_{SI} to V_{SA} to be different and slightly lower than found for the ratio of V_{pI} to V_{pA} .

For the parameters n_a and n_b , the linear correlation coefficients ranged from 0.72 to 0.94 as shown in Table 6.18 and indicate that the analysis based on Eq. 2.52 together with a cross-anisotropic model is adequate in this study. The value of adjusted R-square indicates that at least 78 percent of the test results for V_{SI} could be explained by Eq. 2.52 from a cross-anisotropic model. The α values of the F-test for parameters C_2 , n_a , and n_b are all zero, which means the relationship between shear wave velocity and effective principal stress expressed by Eq. 2.52 is significant.

In contradiction, the small values for the linear correlation coefficient and zero for adjusted R-square for the parameter of n_c suggest that it is almost independent of varying confining pressure, or the precision of this test is not good enough to detect such a small slope. The smaller value of adjusted R-square (0.51 at minimum) reflects that the regression result for V_{SA} is poorer than the one for V_{SI} .

Velocities of shear waves propagating along each principal axis under biaxial confinements (BIA1, BIA2 and BIAR) are plotted versus increasing stress in Figs. 6.3 and 6.4, respectively. For V_{xy} in Fig. 6.3, one can see that shear wave velocity remains almost constant when the confining stresses in the directions of wave propagation and particle motion do not change (see also Sections 6.3.3 and 6.4.3). However, V_{xy} (Fig. 6.4) increases nearly at the same rate as in isotropic confinement tests since the confining pressures increased in both directions of wave propagation and particle motion (see also Section 6.5). The remaining shear wave velocities, such as V_{xz} and V_{zx} in these figures, increase at a slope of about half ($= 0.10$) of the slope when compared to isotropic confinement conditions ($= 0.20$) because confining stress in only one direction of either wave propagation or particle motion

increased (see Sections 6.3.1, 6.3.2, 6.4.1, and 6.4.2). Therefore, Eq. 6.17 is recommended to exhibit the characteristics of shear wave velocity under biaxial confinement:

$$V_s = C_2 \bar{\sigma}_a^{na} \bar{\sigma}_b^{nb} \bar{\sigma}_c^{nc} \quad (6.17)$$

In Eq. 6.17, the slope na is nearly equal to nb , and the slope nc is about zero. Therefore, shear wave velocity will be almost constant when only the principal stress in the out-of-plane direction ($\bar{\sigma}_c$) varies. For practical purposes, Eq. 6.17 can be well represented by:

$$V_s = C_2 \bar{\sigma}_a^{na} \bar{\sigma}_b^{nb} \quad (6.18)$$

When biaxial confinement was applied, the summation of the slopes na and nb nearly equaled nm , the slope when isotropic confinement is applied. Since na is about equal to nb , the values of na and nb are about half of the value of nm . Consequently, the increasing rate of V_{xz} under biaxial confinement is about a half of the rate under isotropic confinement, when only one stress in either the direction of wave propagation or particle motion is varied.

The ratio of shear wave velocity predicted by the idealized cross-anisotropic model to best-fit values taken from Table 6.14 are listed in Table 6.19. The ratio ranges between 0.936 to 1.037 (-0.64 percent to +3.7 percent), and, indicates that a cross-anisotropic model is a good model for this study. However, stress-induced anisotropy along with structural anisotropy in the biaxial tests can make the sand sample behave a little more like an orthotropic medium rather than a cross-anisotropic one as found under isotropic confining conditions.

6.7 SUMMARY

Extensive wave velocity measurements were conducted with the sand sample confined under a biaxial state of stress. This stress state is defined as that condition when two of the three principal stresses are equal. Three types of biaxial confinement were employed in the tests. BIA1 was the case in which only one principal stress was varied, BIA2 was the case in which two principal stresses were varied, and BIAR was the case in which the major principal stress was reoriented during testing. The principal stresses used

Table 6.19 - Ratio of Shear Wave Velocity Predicted by Idealized Cross-Anisotropic Model to the Best-Fit Value Predicted by Table 6.14

Shear Wave Type	$\bar{\sigma}_a^*$, psf				Remark
	2160	2880	4320	5760	
V_{xy}	1.02	1.02	1.01	1.01	Parameters from Table 6.14a
V_{yx}	1.01	1.00	0.99	0.98	
V_{xz}	1.00	1.00	0.98	0.98	
V_{yz}	0.94	0.94	0.96	0.96	
V_{zx}	1.02	1.02	1.03	1.03	
V_{zy}	1.04	1.03	1.02	1.01	
V_{xy}	0.99	1.00	1.02	1.03	Parameters from Table 6.14b
V_{yx}	0.98	0.98	0.98	0.98	
V_{xz}	0.99	0.99	1.00	1.00	
V_{yz}	0.98	0.97	0.97	0.97	
V_{zx}	1.03	1.03	1.03	1.03	
V_{zy}	1.02	1.02	1.03	1.04	

* $\bar{\sigma}_b = \bar{\sigma}_c = 2160$ psf

in the BIA2 and BIAR series were higher than those used in the BIA1 series which resulted in shear wave velocities in the BIA2 and BIAR series always being higher than those measured in the BIA1 series.

The effects on shear wave velocity of stress history, repeated tests at similar pressures, confinement time at a given pressure, and principal stress reorientation were investigated. Each of these variables was found to have an essentially negligible effect on V_s . The main variables affecting V_s were the principal stress in the direction of wave propagation ($\bar{\sigma}_a$) and the principal stress in the direction of particle motion ($\bar{\sigma}_b$). These two principal stresses affected V_s about equally. The effect of the principal stress in the out-of-plane direction ($\bar{\sigma}_c$) was very small. Based on these findings, Eq. 6.17 best represents the influence of stress state on shear wave velocity for shear waves with particle motion and propagation direction polarized along principal stress directions. For most practical purposes, the effect of $\bar{\sigma}_c$ can be neglected and Eq. 6.18 can be used to represent the influence of stress state on V_s .

The sand sample was found to be well represented by a cross-anisotropic model when the axis of symmetry for stress-induced anisotropy coincided with the axis of symmetry of structural anisotropy. This condition existed when the z-axis was the axis of symmetry under biaxial loading ($\bar{\sigma}_x = \bar{\sigma}_y$ and $\bar{\sigma}_z \neq \bar{\sigma}_x$). When the stress-induced axis of symmetry of this sample under biaxial confinement was not the z-axis, the sample behaved as an orthotropic medium rather than a cross-anisotropic one.

CHAPTER SEVEN

TRIAXIAL CONFINEMENT

7.1 INTRODUCTION

True triaxial confinement, in which the major, intermediate, and minor principal stresses are all different, was applied to the sand sample. The LSTD was designed specifically so that this type of loading could be applied. With this loading condition, the mean effective stress condition, individual stress components, and average of any two stress components could then be studied in detail.

The complete set of triaxial confinement tests was composed of three series of tests: (1) the first with only one principal stress varying called TRI1, (2) the second with two principal stresses varying called TRI2, and (3) the third with all three principal stresses varying, named TRI3. The loading conditions for each of these series are shown in Table 4.4 and Fig. 4.18. The Mohr-Coulomb diagram of the TRI2 series is shown in Fig. 7.1a. The stress-space diagram for each series is shown in Fig. 7.1b. The test numbers for the triaxial confinement tests are from 61 through 72, and from 81 to 84 as given in Table 4.4.

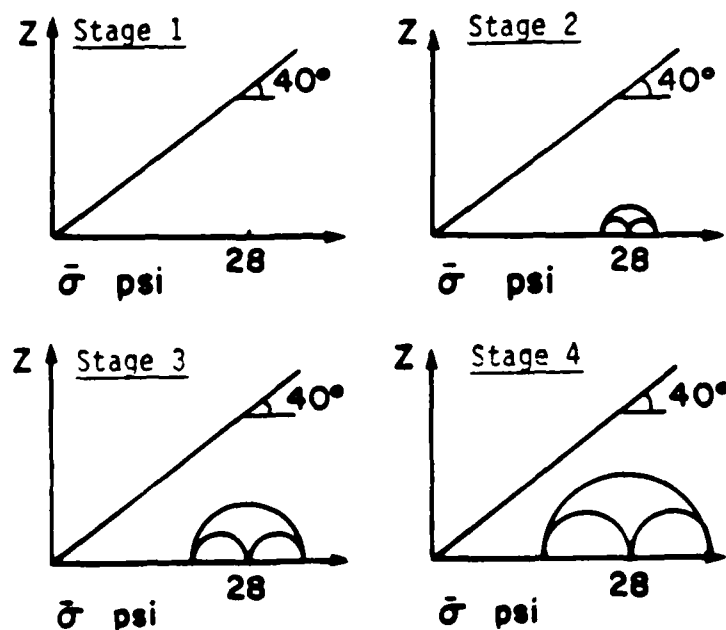
Since a negligible effect of stress history was noted in the previous isotropic and biaxial tests (Sections 5.2 and 6.2), unloading tests were not performed in the triaxial series, and stress history was assumed negligible.

7.2 EFFECT OF CONFINING PERIOD AT ONE PRESSURE

To evaluate the effect of time of confinement under a given stress state, test numbers 81 to 84 were held constant at principal stresses equaling 32 psi (220.5 kPa) in the z-direction, 28 psi (192.9 kPa) in the x-direction, and 24 psi (165.4 kPa) in the y-direction for 24 hours. Shear wave velocities were measured at times of 0.5, 1.0, 2.5, and 24 hours after the stress state was applied. Resulting V_s values are listed in Table 7.1 and are shown in Fig. 7.2. The slope of each regression line for the $\log V_s - \log t$ relationship is almost zero which suggests that the effect of confining period at this triaxial state is negligible. This conclusion is the same as that found for isotropic and biaxial stress states.

One interesting point with regard to time is that it took about one half of the time for the triaxial pressures to be balanced as it did to balance

(a) Mohr-Coulomb Diagram for the TRI2 Series



(b) Principal Stress Space

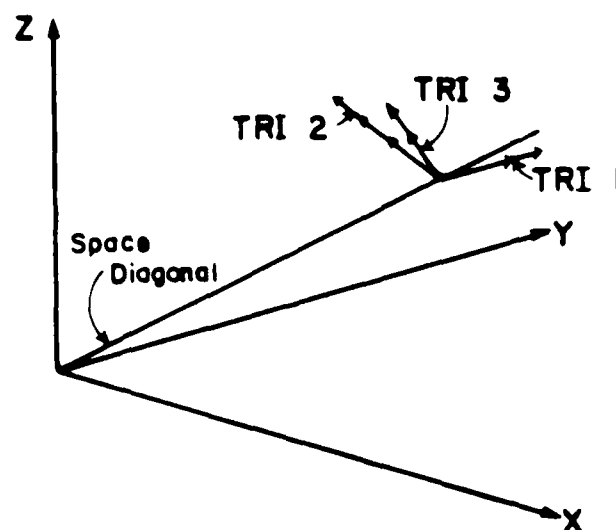


Fig. 7.1 - Mohr-Coulomb and Stress-Space Diagrams for Triaxial Confining Pressure Tests

Table 7.1 - Effect of Confining Period on S-Wave Velocities
Under Triaxial Confinement, TRI3

Shear* Wave Type	Confining Period, T, hour				Slope** n1
	0.5	1.0	2.5	24.0	
V _{xy}	1087	1094	1092	1114	.01
V _{yx}	1006	1007	1004	998	-.00
V _{zx}	972	972	972	978	.00
V _{zy}	932	945	947	947	.00

* accelerometers of V_{xz} and V_{yz} were both malfunctioning

** $V_s = C \cdot T^{n1}$

TRIAXIAL CONFINEMENT

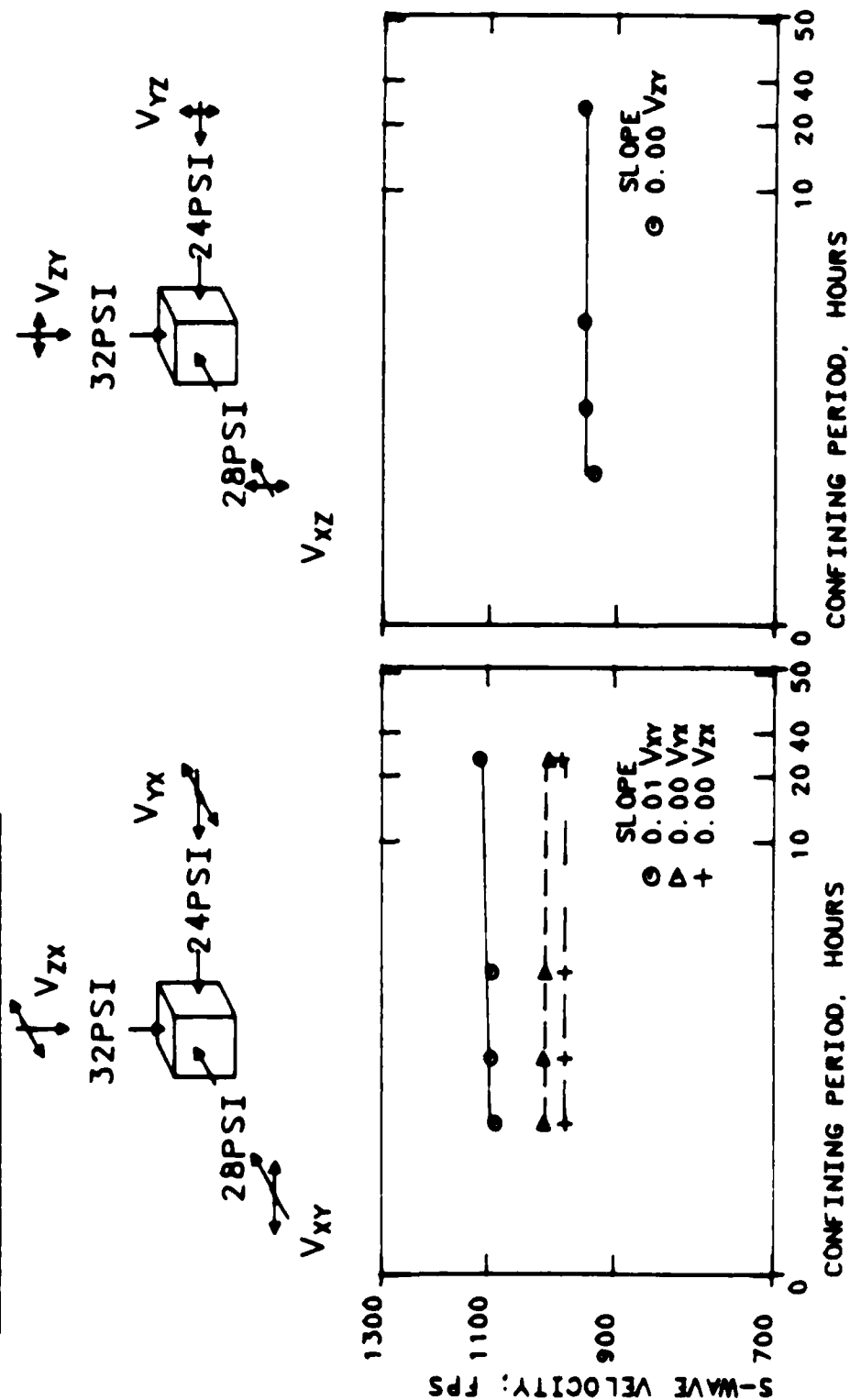


Fig. 7.2 - Effect of Confining Period on S-Wave Velocity Under Triaxial Confinement TRI3

the pressures when applied in the other two conditions (isotropic and BIA2). For instance, balancing the triaxial pressures took about 1.5 hours versus about 3 hours for isotropic loading. The reason for the relatively short time to reach equilibrium is due to the increments in triaxial confinement which were smaller than those used in the other two tests.

7.3 EFFECT OF TRIAXIAL CONFINEMENT

Although the "three-individual-stresses" method is the most appropriate one to predict shear wave velocity based on the biaxial test results given in Chapter Six, the shear wave velocity relationship with its three parameters cannot be shown in a two-dimensional figure. Therefore, the easiest way to evaluate the "three-individual-stresses" method is to compare shear wave velocities measured under triaxial stress states with those predicted by the "three-individual-stresses" method. This comparison is made in Tables 7.2 through 7.4 using values of the constants and slopes from Table 6.18 to predict the velocities.

The trends of measured and predicted wave velocities in the test series TRI1, TRI2 and TRI3 are essentially all the same. For example, V_{zx} is about constant while the measured and predicted values of V_{xy} , V_{yx} , V_{yz} , and V_{zy} all increase as the applied confining pressures changed in the TRI1 test series. The ratio of measured to predicted shear wave velocities ranges from 0.95 to 1.10 for TRI1 with an average of 1.03, from 0.98 to 1.12 for TRI2 with an average of 1.03, and from 0.98 to 1.11 for TRI3 with an average of 1.03. These values give a -5.4 to +11.6 percent range of differences between measured data and predicted values, which is greater than the values of -3.4 percent to +3.6 percent in the case of biaxial confinement (See Section 6.5). One possible reason for this scattering is that the accelerometers exhibited more noise during the final series of tests. This noise made it difficult to determine the initial S-wave arrival, thus increasing the scatter in the data under triaxial confinement. Another reason is that the stress increments used in the triaxial confinement tests were generally smaller than those used in the isotropic and biaxial tests so that smaller velocity changes had to be measured. Finally, interruption in testing caused by the ruptured top membrane also seemed to influence the results by possibly creating some plastic deformation in the sand.

Table 7.2 - Comparison of Measured Shear Wave Velocities* to Values Predicted by "Three-Individual-Stresses" Method in Test Series TR11

Velocities		Confinement $\bar{\sigma}_z =$ $\bar{\sigma}_y =$ $\bar{\sigma}_x =$	40 20 15	40 25 15	40 30 15	40 35 15	Velocity Change
measured V_s , fps	V_{xy}		1053	1082	1092	1110	increasing
	V_{yx}		976	999	1016	1024	increasing
	V_{yz}		1038	1060	1072	1101	increasing
	V_{zx}		931	939	940	941	constant
	V_{zy}		893	910	926	934	increasing
predicted V_s , fps	V_{xy}		959	980	998	1013	increasing
	V_{yx}		958	979	996	1011	increasing
	V_{yz}		982	1000	1015	1028	increasing
	V_{zx}		914	911	908	906	constant
	V_{zy}		941	960	975	988	increasing
$\frac{V_{s, \text{ meas. }} }{V_{s, \text{ pred. }}}$	V_{xy}		1.10	1.10	1.10	1.10	avg. = 1.03
	V_{yx}		1.02	1.02	1.02	1.01	
	V_{yz}		1.06	1.06	1.06	1.07	
	V_{zx}		1.02	1.03	1.03	1.04	
	V_{zy}		0.95	0.95	0.95	0.95	

* accelerometers of V_{xz} were malfunctioning

Table 7.3 - Comparison of Measured Shear Wave Velocities* to Values Predicted by "Three-Individual-Stresses" Method in Test Series TRI2

Velocities		Confinement $\bar{\sigma}_z =$	28	32	36	40	Velocity Change
		$\bar{\sigma}_y =$	28	24	20	16	
		$\bar{\sigma}_x =$	28	28	28	28	
measured V_s , fps	V_{xy}		1078	1065	1060	1031	decreasing
	V_{yx}		1065	1041	1020	1006	decreasing
	V_{yz}		1086	1077	1065	1060	decreasing
	V_{zx}		930	949	962	968	increasing
	V_{zy}		925	921	912	900	decreasing
predicted V_s , fps	V_{xy}		1053	1037	1018	996	decreasing
	V_{yx}		1063	1037	1019	999	decreasing
	V_{yz}		973	973	969	960	decreasing
	V_{zx}		925	940	954	968	increasing
	V_{zy}		925	926	922	915	decreasing
$\frac{V_{s, \text{ meas. }} }{V_{s, \text{ pred. }}}$	V_{xy}		1.02	1.03	1.04	1.04	avg. = 1.03
	V_{yx}		1.00	1.00	1.00	1.01	
	V_{yz}		1.16	1.11	1.10	1.10	
	V_{zx}		1.01	1.01	1.01	1.00	
	V_{zy}		1.00	1.00	1.00	1.00	

* accelerometers of V_{xz} were malfunctioning

Table 7.4 - Comparison of Measured Shear Wave Velocities* to Values Predicted by "Three-Individual-Stresses" Method in Test Series TRI3

<div> <div>Confinement $\bar{\sigma}_z =$</div> <div>$\bar{\sigma}_y =$</div> <div>Velocities $\bar{\sigma}_x =$</div> </div>		28	32	36	40	Velocity Change
measured V_s , fps	V_{xy}	1084	1081	1077	1053	decreasing
	V_{yx}	1045	1037	1028	1008	decreasing
	V_{yz}	1084	1076	1069	1063	decreasing
	V_{zx}	939	962	978	988	increasing
	V_{zy}	920	915	907	900	decreasing
predicted V_s , fps	V_{xy}	1053	1047	1037	1022	decreasing
	V_{yx}	1053	1048	1039	1025	decreasing
	V_{yz}	973	972	968	959	decreasing
	V_{zx}	925	949	971	992	increasing
	V_{zy}	925	924	920	911	decreasing
$\frac{V_s, \text{ meas. }}{V_s, \text{ pred. }}$	V_{xy}	1.03	1.03	1.04	1.03	avg. = 1.03
	V_{yx}	0.99	0.99	0.99	0.98	
	V_{yz}	1.11	1.11	1.11	1.11	
	V_{zx}	1.02	1.01	1.00	1.00	
	V_{zy}	1.00	0.99	0.99	0.98	

* accelerometers of V_{xz} were malfunctioning

An alternative method of showing the trend of the shear wave velocity under triaxial confinement is suggested hereafter. As the effect of principal stress in the directions of wave propagation and particle motion are almost the same and because the stress in the out-of-plane direction has only a minor influence, Eq. 2.52, suggested in Sections 2.36 and 6.7, can be rewritten as follows:

$$V_s = C_2 \bar{\sigma}_a^{ne} \bar{\sigma}_b^{ne} \quad (7.1)$$

where $ne=na=nb=0.10$ for V_{SI} , and $ne=na=nb=0.09$ for V_{SA} (see Table 6.18). Therefore, Eq. 7.1 can be written as:

$$\log V_s = \log C_2 + ne \cdot \log (\bar{\sigma}_a \cdot \bar{\sigma}_b) \quad (7.2)$$

Equation 7.2 can be easily represented with a two-dimensional log-log plot. In this manner, the test results for TRI1, TRI2, and TRI3 are shown in Figs. 7.3 through 7.5, respectively. Since the slopes of na and nb found in this study are not exactly the same and since there is a minor effect of the principal stress in the out-of-plane direction, the slopes in the figures for each shear wave are not any one of the real slopes. Nevertheless, these figures have the advantage that the trend in shear wave velocity with stress state can be visually illustrated. However, if the value of principal stress in the out-of-plane direction is far larger than the other two stresses, the distortion of shear wave velocity represented by Eq. 7.2 and shown in Figs. 7.3 through 7.5 may be distinguishable-(e.g. V_{xy} in TRI2 and TRI3).

7.4 COMPARISON WITH PREVIOUS EMPIRICAL EQUATIONS

Empirical equations used to predict shear wave velocity generally have state of stress in them in some fashion. State of stress can enter in terms of: 1. the average of the principal stresses ("mean-effective-stress" method), 2. the average of the two principal stresses in the directions of wave propagation and particle motion ("average-stress" method), and 3. the principal stress individually ("three-individual-stresses" method). The "average-stress" method has been shown to model poorly V_s measured in the biaxial test series (see Section 6.5). However, velocities measured under biaxial confinement cannot be used to distinguish easily between the

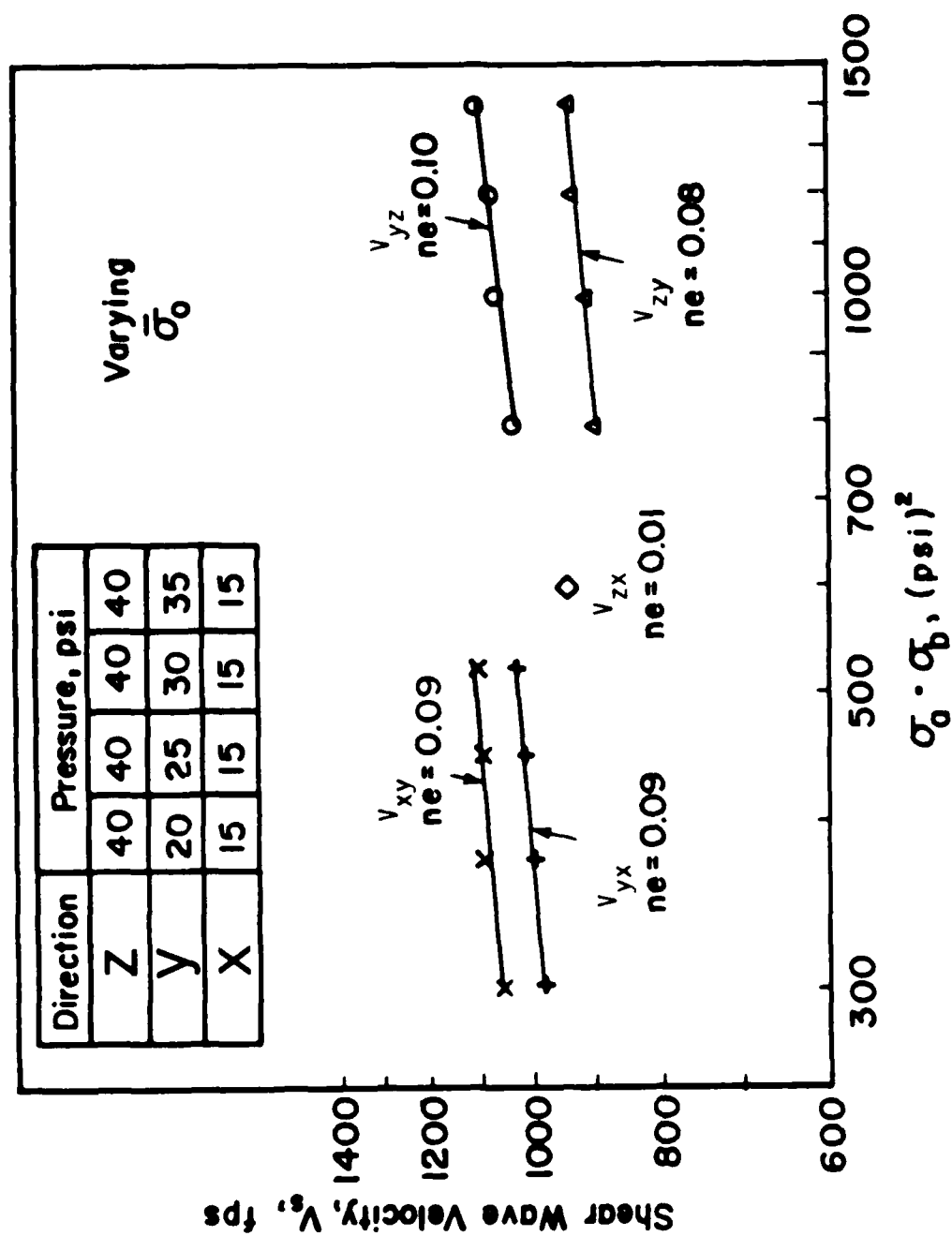


Fig. 7.3 - Variation of S-Wave Velocities Under Triaxial Confinement, TR11,
Based on Eq. 7.1

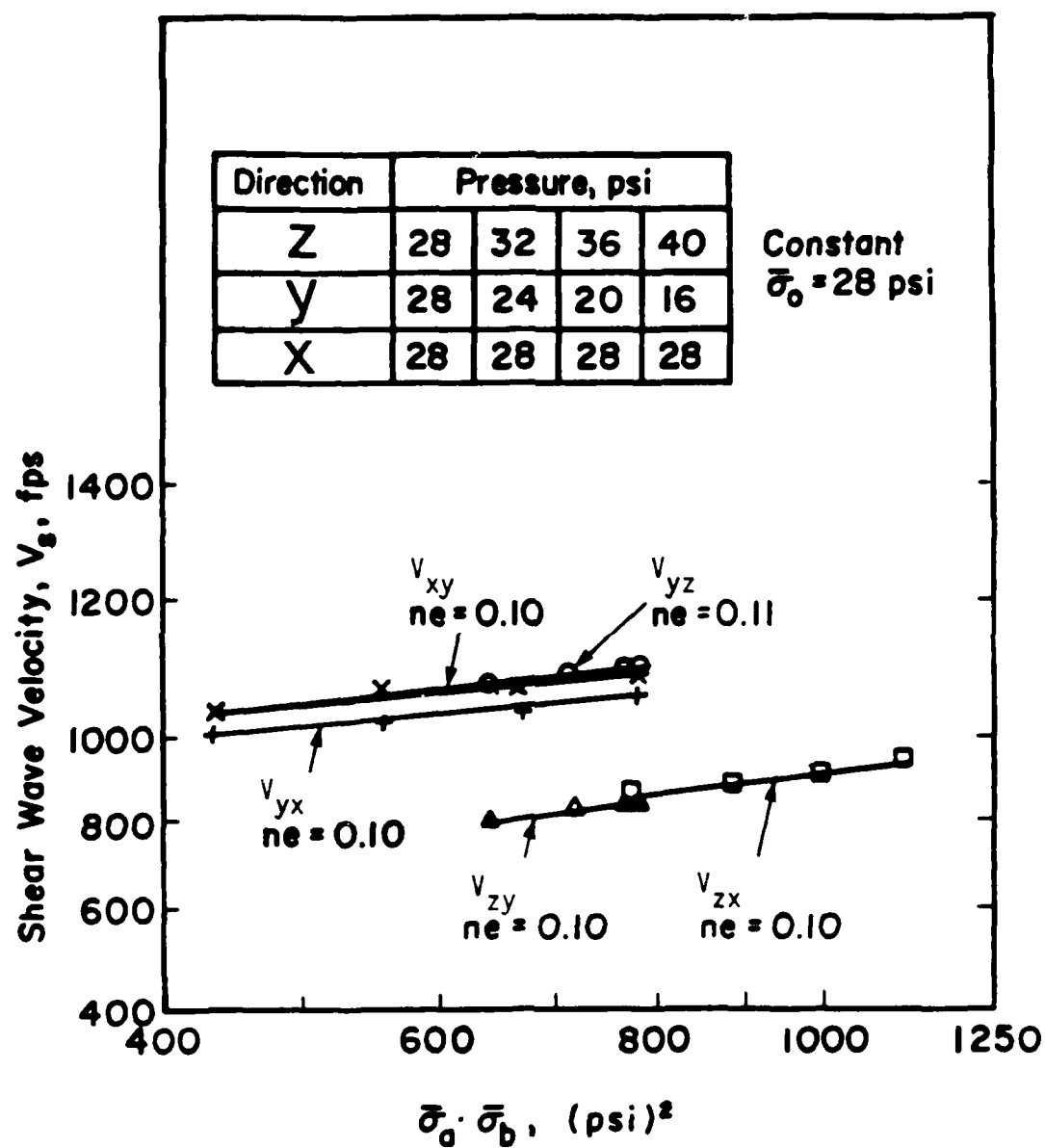


Fig. 7.4 - Variation in S-Wave Velocities Under Triaxial Confinement, TRI2, Based on Eq. 7.1

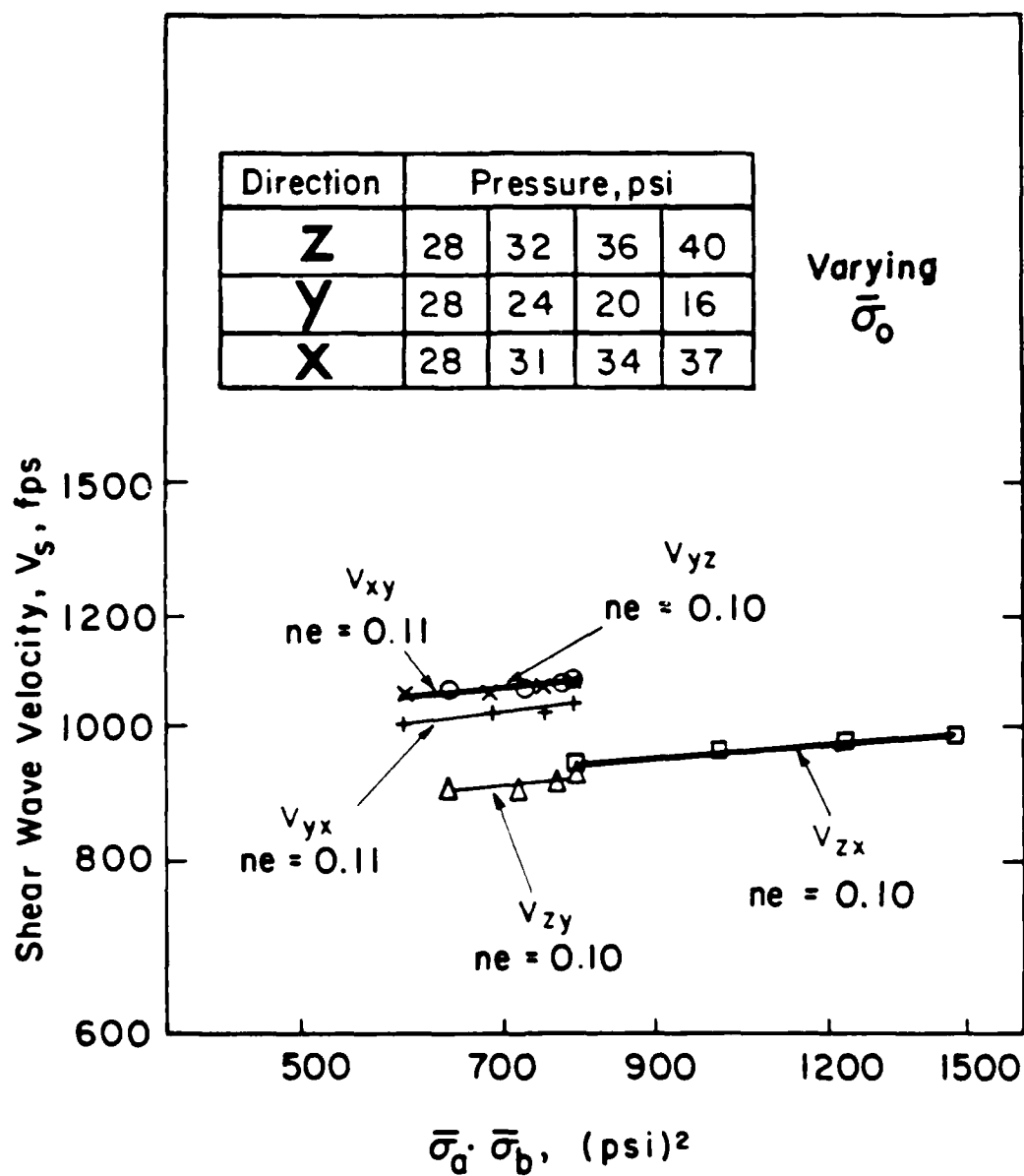


Fig. 7.5 - Variation of S-Wave Velocities Under Triaxial Confinement, TRI3, Based on Eq. 7.1

advantage of the "mean-effective-stress" method and the "three-individual-stresses" method.

Fortunately, shear wave velocities predicted by these three methods can be examined in the tests under triaxial confinement to evaluate which method is most accurate.

In test series TRI2 and TRI3, the average of the two principal stresses in the z- and y-directions was held constant at 28 psi (192.9 kPa) by increasing the principal stress in the z-direction from 28 to 40 psi (192.9 to 275.6 kPa) while simultaneously decreasing the stress in the y-direction from 28 to 16 psi (192.9 to 110.2 kPa). The predicted shear wave velocities for V_{yz} and V_{zy} should be constant in both series TRI2 and TRI3 if the "average-stress" method is used. However, predicted shear wave velocities for V_{yz} and V_{zy} should decrease if the "three-individual-stresses" method is used. The test results listed in Tables 7.5 and 7.6 show both V_{yz} and V_{zy} decrease in these triaxial test series. Therefore, the "average-stress" method is not a proper formulation, while the "three-individual-stresses" method is at least proper for shear waves propagating along principal stress directions.

Additionally, the mean effective stress was held constant at 28 psi (192.9 kPa) in test series TRI2. If the "mean-effective-stress" method is valid, then shear wave velocities in each direction should be constant. However, the values of V_{xz} and V_{zx} should increase while the values of V_{xy} , V_{yx} , V_{yz} , and V_{zy} should decrease if the "three-individual-stresses" method is valid. From the results summarized in Table 7.7, it is obvious that the "mean-effective-stress" method cannot be used to predict V_s values in series TRI2 while the "three-individual-stresses" method can.

Based on these experimental results, there is an effect on V_s of the principal stress in the out-of-plane direction, although a minor one (see Sections 6.3.3, 6.4.3, and 7.3). Therefore, the "three-individual-stresses" method is more complete and satisfactory than the "two-individual-stresses" method suggested by Roesler (1979).

It is interesting to try to understand why the "mean-effective-stress" method has been used as the main empirical equation for about the past two decades if it is not the best indicator of V_s . If the "three-individual-stresses" method and associated constants and slopes listed

Table 7.5 - Loading Sequence and Shear Wave Velocities
Measured under TRI2

Applied Confining Pressure, psi						Remark
Direction	z	28	32	36	40	TRI2
	y	28	24	20	16	
	x	28	28	28	28	
V_s , fps	v_{yz}	1086	1077	1065	1060	decreasing
	v_{zy}	925	921	912	899	decreasing

Table 7.6 - Loading Sequence and Shear Wave Velocities
Measured under TRI3

Applied Confining Pressure, psi						Remark
Direction	z	28	32	36	40	TRI3
	y	28	24	20	16	
	x	28	31	34	37	
V_s , fps	v_{yx}	1084	1076	1069	1063	decreasing
	v_{zy}	920	915	907	900	decreasing

Table 7.7 - Test Results of Shear Wave Velocities*
Measured Under Triaxial Confinement, TRI2

		Applied Confining Pressure, psi				Remark
Direction	Z	28	32	36	40	$\bar{\sigma}_0 = 28$ psi
	X	28	24	20	16	
	Y	28	28	28	28	
V_s , pfs	V_{xy}	1078	1065	1060	1031	decreasing
	V_{yx}	1065	1040	1020	1006	decreasing
	V_{yz}	1086	1077	1070	1060	decreasing
	V_{zx}	930	949	962	968	increasing
	V_{zy}	925	921	910	899	decreasing

* accelerometers for V_{xz} were malfunctioning

in Table 6.18 are adopted to estimate shear wave velocities of this sand sample, then the following equations are obtained:

$$V_{SI} = 218 \bar{\sigma}_a^{0.095} \bar{\sigma}_b^{0.098} \bar{\sigma}_c^{-0.003} \quad (7.3a)$$

and

$$V_{SA} = 230 \bar{\sigma}_a^{0.092} \bar{\sigma}_b^{0.089} \bar{\sigma}_c^{-0.010} \quad (7.3b)$$

If the parameters in Eq. 7.3 are used to obtain similar parameters for use in the the "mean-effective-stress" method for the sample, then the equations become ($nm = na + nb + nc$):

$$V_{SI} = 218 \bar{\sigma}_o^{0.190} \quad (7.4a)$$

$$V_{SA} = 230 \bar{\sigma}_o^{0.171} \quad (7.4b)$$

If the parameters in Eq. 7.4 for the "mean-effective-stress" method were obtained under isotropic confining pressure conditions (see Table 5.9 and Eq. 5.1), these relationships would be expressed as:

$$V_{SI} = 200 \bar{\sigma}_o^{0.201} \quad (7.5a)$$

$$V_{SA} = 209 \bar{\sigma}_o^{0.183} \quad (7.5b)$$

where V_{SI} and V_{SA} are the shear wave velocities based on a cross-anisotropic model. Tables 7.8 through 7.11 present comparisons of the shear wave velocities estimated by Eqs. 7.3, 7.4, and 7.5 under isotropic, biaxial, and triaxial confinement conditions. The range of the ratios of shear wave velocities from Eq. 7.4 and 7.5 are 0.990 to 1.007, 0.997 to 1.002, 0.990 to 0.997, and 0.993 to 0.996 for the cases of isotropic, BIA1, BIA2, and triaxial confinements, respectively. These ratios are all essentially one. Hence, the way in which the exact parameters used with $\bar{\sigma}_o$ are obtained has only a minor effect on the predicted velocities in the pressure ranges over which these tests were performed.

When the maximum principal stress is not in the out-of-plane direction, the range of the ratios of shear wave velocities from Eqs. 7.3 and 7.4 are 1.00 to 1.00, 1.00 to 0.99, 1.00 to 0.99, and 1.02 to 0.95 for the isotropic,

Table 7.8 - Comparison of Shear Wave Velocities Predicted by Eqs. * 7.3, 7.4, and 7.5 Under Isotropic Confinement

(1) Confining Pressure psi	(2) Shear Wave Type	(3) V_S Predicted by Eq. 7.3 fps	(4) V_S Predicted by Eq. 7.4 fps	(5) V_S Predicted by Eq. 7.5 fps	(6) $\frac{V_{S,(4)}}{V_{S,(3)}}$	(7) $\frac{V_{S,(5)}}{V_{S,(3)}}$	(8) $\frac{V_{S,(4)}}{V_{S,(3)}}$
$\bar{\sigma}_a$	V_I	866	866	861	1.00	0.99	1.01
$\bar{\sigma}_b$	V_I	795	796	791	1.00	0.99	1.01
$\bar{\sigma}_c$							
$\bar{\sigma}_a$	V_I	988	988	990	1.00	1.00	1.00
$\bar{\sigma}_b$	V_A	895	896	897	1.00	1.00	1.00
$\bar{\sigma}_c$							
$\bar{\sigma}_a$	V_I	1066	1067	1074	1.00	1.01	0.99
$\bar{\sigma}_b$	V_A	961	961	967	1.00	1.01	0.99
$\bar{\sigma}_c$							
$\bar{\sigma}_a$	V_I	1127	1127	1138	1.00	1.01	0.99
$\bar{\sigma}_b$	V_A	1009	1009	1019	1.00	1.01	0.99
$\bar{\sigma}_c$							

* Eqs.: $V_{SI} = 218 \bar{\sigma}_a^{0.095} \bar{\sigma}_b^{0.098} \bar{\sigma}_c^{-0.003}$ (7.3a) $V_{SA} = 230 \bar{\sigma}_a^{0.092} \bar{\sigma}_b^{0.089} \bar{\sigma}_c^{-0.010}$ (7.3b)

$V_{SI} = 218 \bar{\sigma}_o^{0.19}$ (7.4a) $V_{SA} = 230 \bar{\sigma}_o^{0.171}$ (7.4b)

$V_{SI} = 200 \bar{\sigma}_o^{0.201}$ (7.5a) $V_{SA} = 209 \bar{\sigma}_o^{0.183}$ (7.5b)

Table 7.9 - Shear Wave Velocities Predicted by Eqs. 7.3, 7.4, and 7.5 Under Biaxial Confining Pressure Conditions of BIA1

Confining Pressure, psi			V_s Predicted by Eq. 7.3 fps (1)	V_s Predicted by Eq. 7.4 fps (2)	V_s Predicted by Eq. 7.5 fps (3)	(2) (1)	(3) (1)	(2) (3)
$\bar{\sigma}_a$	$\bar{\sigma}_b$	$\bar{\sigma}_c$						
15	15	15	935	935	934	1.00	.99	1.00*
15	15	15	853	853	851	1.00	.99	1.00**
20	15	15	961	954	954	.99	.99	1.00*
20	15	15	876	869	868	.99	.99	1.00**
30	15	15	999	988	990	.98	.99	.99*
30	15	15	910	896	897	.98	.98	.99**
40	15	15	1027	1017	1021	.99	.99	.99*
40	15	15	934	920	923	.98	.98	.99**
15	15	15	935	935	934	1.00	.99	1.00*
15	15	15	853	853	851	1.00	.99	1.00**
15	20	15	962	954	954	.99	.99	1.00*
15	20	15	876	869	868	.99	.99	1.00**
15	30	15	1001	988	990	.98	.98	.99*
15	30	15	908	896	897	.98	.98	.99**
15	40	15	1030	1017	1021	.98	.99	.99*
15	40	15	931	920	923	.98	.99	.99**
15	15	15	935	935	934	1.00	.99	1.00*
15	15	15	853	853	851	1.00	.99	1.00**
15	15	20	934	954	954	1.02	1.02	1.00*
15	15	20	851	869	868	1.02	1.02	1.00**
15	15	30	933	988	990	1.05	1.06	.99*
15	15	30	847	896	897	1.05	1.05	.99**
15	15	40	933	1017	1021	1.09	1.09	.99*
15	15	40	845	920	923	1.09	1.09	.99**

* V_{SI}

** V_{SA}

Table 7.10 - Shear Wave Velocities Predicted by Eqs. 7.3, 7.4, and 7.5 Under Biaxial Confining Pressure Conditions of BIA2

Confining Pressure, psi			Predicted by Eq. 7.3	Predicted by Eq. 7.4	Predicted by Eq. 7.5	(2) (1)	(3) (1)	(2) (3)
$\bar{\sigma}_a$	$\bar{\sigma}_b$	$\bar{\sigma}_c$	fps (1)	fps (2)	fps (3)			
40	15	15	1027	1017	1021	.99	.99	.99*
40	15	15	934	920	923	.98	.98	.99**
40	20	20	1055	1043	1049	.98	.99	.99*
40	20	20	955	941	946	.98	.99	.99**
40	30	30	1096	1088	1097	.99	1.00	.99*
40	30	30	986	978	985	.99	.99	.99**
40	40	40	1127	1127	1138	1.00	1.01	.99*
40	40	40	1009	1009	1019	1.00	1.01	.99**
15	40	15	1030	1017	1021	.98	.99	.99*
15	40	15	931	920	923	.98	.99	.99**
20	40	20	1057	1043	1049	.98	.99	.99*
20	40	20	954	941	946	.98	.99	.99**
30	40	30	1097	1088	1097	.99	.99	.99*
30	40	30	986	978	985	.99	1.00	.99**
40	40	40	1127	1127	1138	1.00	1.01	.99*
40	40	40	1009	1009	1019	1.00	1.01	.99**
15	15	40	933	1017	1021	1.09	1.09	.99*
15	15	40	845	920	923	1.09	1.09	.99**
20	20	40	986	1043	1049	1.05	1.06	.99*
20	20	40	890	941	946	1.05	1.06	.99**
30	30	40	1066	1088	1097	1.02	1.02	.99*
30	30	40	958	978	985	1.02	1.02	.99**
40	40	40	1127	1127	1138	1.00	1.01	.99*
40	40	40	1009	1009	1019	1.00	1.01	.99**

*V_{SI}

**V_{SA}

Table 7.11 - Shear Wave Velocities Predicted by Eqs. 7.3, 7.4 and 7.5 Under Triaxial Confining Pressure Conditions of TRI1

Confining Pressure, psi			V_s Predicted by Eq. 7.3 fps (1)	V_s Predicted by Eq. 7.4 fps (2)	V_s Predicted by Eq. 7.5 fps (3)	$\frac{(2)}{(1)}$	$\frac{(3)}{(1)}$	$\frac{(2)}{(3)}$
$\bar{\sigma}_a$	$\bar{\sigma}_b$	$\bar{\sigma}_c$						
40	20	15	1056	1031	1035	.97	.98	.99*
40	20	15	958	931	935	.97	.97	.99**
40	25	15	1079	1043	1049	.96	.97	.99*
40	25	15	978	941	946	.96	.96	.99**
40	30	15	1099	1055	1062	.96	.96	.99*
40	30	15	994	951	957	.95	.96	.99**
40	35	15	1115	1067	1074	.95	.96	.99*
40	35	15	1007	961	967	.95	.96	.99**
28	28	28	1053	1053	1059	1.00	1.00	.99*
28	28	28	949	949	954	1.00	1.00	.99**
32	24	28	1050	1053	1059	1.00	1.00	.99*
32	24	28	948	949	954	1.00	1.00	.99**
36	20	28	1043	1053	1059	1.00	1.01	.99*
36	20	28	943	949	954	1.00	1.01	.99**
40	16	28	1031	1053	1059	1.02	1.02	.99*
40	16	28	933	949	954	1.01	1.02	.99**
28	28	28	1053	1053	1059	1.00	1.00	.99*
28	28	28	949	949	954	1.00	1.00	.99**
32	24	31	1050	1060	1066	1.00	1.01	.99*
32	24	31	947	955	961	1.00	1.01	.99**
36	20	34	1043	1067	1074	1.02	1.03	.99*
36	20	34	941	961	967	1.02	1.02	.99**
40	16	37	1030	1074	1081	1.04	1.04	.99*
40	16	37	931	966	972	1.03	1.04	.99**

* V_{SI}

** V_{SA}

B2A1, B2A2, and triaxial confinements, respectively. That is, the maximum difference between V_s values predicted by the "three-individual-stresses" method and the "mean-effective-stress" method are zero percent for isotropic confinement, -1.5 to 0.0 percent for biaxial confinements, and -4.6 to +2.1 percent for triaxial confinements. Therefore, shear moduli estimated from shear wave velocities measured with resonant column tests under biaxial confining conditions will then be within -2.3 to 0.0 percent in a scattered range of the regression line determined with the "mean-effective-stress" method. This discrepancy is acceptable for most problems and, hence, would normally not be considered worthy of further study. Moreover, the non-uniformity of shear strain inside a resonant column sample combined with the difficulty of measuring the change of volume of the sample make the scattering indistinguishable in the resonant column test.

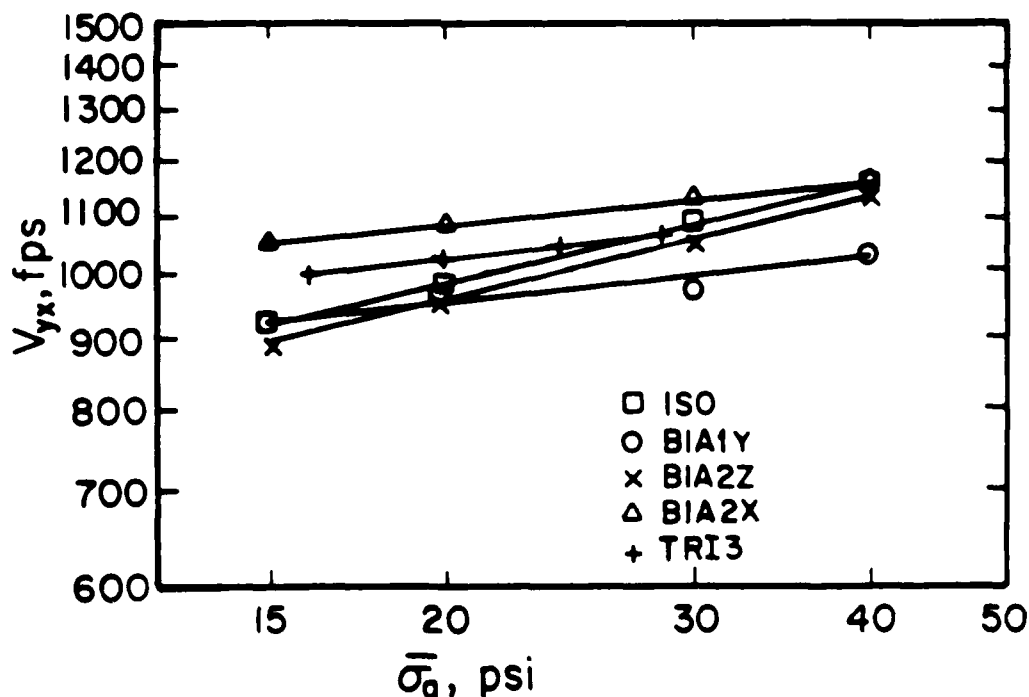
It is interesting to note that Hardin and Black (1966) reported discrepancies between shear moduli of a sand predicted by the "mean-effective-stress" method and data measured from biaxial resonant column tests ranging from -2.4 to +8.9 percent. Discrepancies ranging from +10 to -20 percent for maximum shear moduli determined under isotropic and biaxial confinement states with the same mean effective stress in resonant column tests have been reported by Yanagisawa and Yan (1977). Higher discrepancies have been noticed when the stress level $[(\sigma_1 - \sigma_3)/(\sigma_1 - \sigma_3)_f]$ is large (Kuribayashi, Iwasaki, and Tatsuoka, 1975; Yanagisawa and Yan, 1977; Yu and Richart, 1984). This behavior has also been found in cyclic torsional shear tests (Tatsuoka, Iwasaki, Fukushima and Sudo, 1979). Therefore, researchers have found the "mean-effective-stress" method to be less than perfect, but little has been done to try to reconcile these discrepancies.

In an attempt to compare the three empirical methods and the experimental results at one time, part of the loading sequence and resulting shear wave velocities are shown in Fig. 7.6. The trend of shear wave velocity, V_{yx} , predicted by the "three-individual-stresses" method, the "average-stress" method, and the "mean-effective-stress" method under the same isotropic, BIA1, BIA2 and TRI2 confinements given in Fig. 7.6 are drawn in Fig. 7.7.

The same value of shear wave velocity for series BIA2Z and BIA2X is predicted by the "mean-effective-stress" method as shown in Fig. 7.7.c. If the "average-stress" method is used, the value of V_{yx} is predicted to be the

Shear Wave Type	Type of Confinement	Applied Confining Presures, psi			No. of Test Series	Remark
		$\bar{\sigma}_a$	$\bar{\sigma}_b$	$\bar{\sigma}_c$		
V_{yx}	ISO	15-40	15-40	15-40	2- 5	□
V_{yx}	BIA1Y	15-40	15	15	48-50	○
V_{yx}	BIA2Z	15-40	15-40	40	13-16	×
V_{yx}	BIA2X	15-40	40	15-40	41-43	△
V_{yx}	TRI3	28-16	28-37	28-40	69-72	+

a. Load History



b. Measured Shear Wave Velocities

Fig. 7.6 - Shear Wave Velocities Measured During Loading Sequence of ISO, BIA1, BIA2, and TRI2

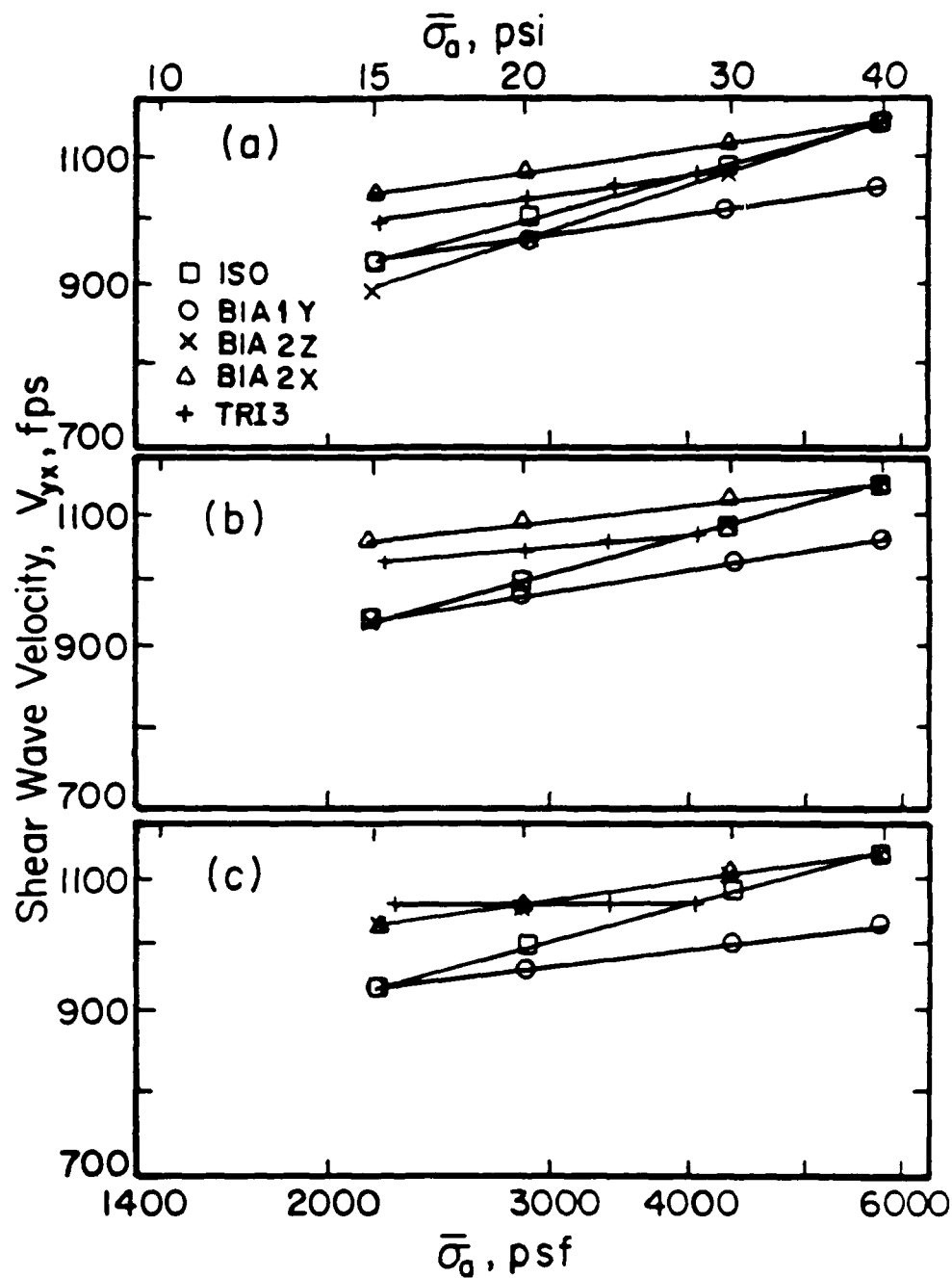


Fig. 7.7 - Trend in Shear Wave Velocities Predicted by Different Methods:
 (a) Three-Individual-Stresses Method,
 (b) Average-Stress Method, and
 (c) Mean-Effective-Stress Method

same in series ISO and BIA2Z. However, the test results in this study, as shown in Fig. 7.6, gave different trends for both cases, and these trends are correctly predicted by the "three-individual-stresses" method. Furthermore, the values of V_{yx} listed in Tables 7.5 and 7.6 are also shown to decrease in Fig. 7.6 for TRI3. But, both trends from the "average-stress" method and the "mean-effective-stress" method are horizontal lines in Fig. 7.7. Again, only the "three-individual-stresses" method gives the correct prediction of V_{yx} in TRI3.

Consequently, it is fair to say that the "three-individual-stresses" method is better than other two methods in predicting experimental results as well as in theory, and Eq. 2.52 can be treated as a general form for all states of stress.

Only a few tests has been done under biaxial or triaxial conditions. Knox, et al (1982) reported tests with a similar sand sample with an average unit weight equaling 96.6 pcf (1547 kg/m³) in the same large-scale device triaxial. Constants and slopes for Eqs. 2.52 and 7.1 from their results and this study are listed in Table 7.12. One can see that the value of n_a is equal to n_b when rounded to two decimal points, thus resulting in one value, n_e , in both studies. Values of the slope in Eq. 5.1 were derived from different laboratory testing devices under isotropic confinement or from in situ tests, and ranged from 0.15 to 0.33 as shown in Table 2.2. In this study, all values of the slopes ranged between 0.17 and 0.23.

7.5 SUMMARY

Tests under true triaxial stress states, TRI2 and TRI3, were used to compare measured values of V_s with those predicted by three empirical equations: the "mean-effective-stress" method, the "average-stress" method, and the "three-individual-stresses" method. Equation 2.52 based on the "three-individual-stresses" method was found to predict most correctly the experimental results. This equation is:

$$V_s = C_2 \bar{\sigma}_a^{n_a} \bar{\sigma}_b^{n_b} \bar{\sigma}_c^{n_c} \quad (7.6)$$

However, the confining pressure in the out-of-plane direction, $\bar{\sigma}_c$, has only a minor effect on shear wave velocity. For practical engineering purposes, Eq. 7.6 can be simplified to:

Table 7.12 - Comparison of Constants and Slopes for Eq. 2.52⁺
 Relating V_s to $\bar{\sigma}_a$, $\bar{\sigma}_b$, and $\bar{\sigma}_c$ with Those Reported
 by Knox et al (1982)

Reference	Shear Wave Type	Isotropic		Biaxial				Triaxial	
		C_2	n	C_2	na	nb	nc	C_2	ne
1*	V_{xy}	238	0.18	202	0.11	0.09	0.001	210	0.09
	V_{yx}	167	0.23	169	0.10	0.12	-0.007	224	0.10
	V_{xz}	206	0.19	186	0.10	0.11	-0.002	-	-
	V_{yz}	224	0.18	305	0.07	0.08	-0.009	260	0.10
	V_{zx}	187	0.19	243	0.10	0.08	-0.02	250	0.09
	V_{zy}	219	0.17	180	0.11	0.10	-0.01	165	0.09
	V_{SI}	200	0.20	218	0.10	0.10	-0.00	217	0.10
	V_{SA}	210	0.18	230	0.09	0.09	-0.01	225	0.09
2**	V_{xy}	201	0.19	201	0.09	0.09	0.01	146 ⁺⁺	0.11 ⁺⁺
	V_{yx}	224	0.18						
	V_{xz}	210	0.18	180	0.10	0.10	-	182 ⁺⁺	0.10 ⁺⁺
	V_{zx}	188	0.19						
	V_{yz}	140	0.22	132	0.12	0.11	-0.01	149 ⁺⁺	0.11 ⁺⁺
	V_{zy}	141	0.22						
	V_{SI} ^{††}	217	0.18	201	0.09	0.09	0.01	146	0.10
	V_{SA} ^{††}	171	0.21	156	0.11	0.11	-0.01	154	0.11

$$+ V_s = C_2 \bar{\sigma}_a^{na} \bar{\sigma}_b^{nb} \bar{\sigma}_c^{nc}$$

++ data reduced in this study

* this study

** Knox, Stokoe, and Kopperman (1982)

$$V_s = C_2 (\bar{\sigma}_a \cdot \bar{\sigma}_b)^{n_e} \quad (7.7)$$

in which case $n_e = (n_a + n_b)/2$. This expression results in a scattering of less than ± 5 percent when compared with the experimental data.

The empirical equation based on the "mean-effective-stress" method (Eq. 5.1) may also be used to fit a curve to the experimental data which exhibits discrepancies in the range of ± 5 percent. However, only Eq. 7.7 properly reflects the influence of stress path on S-wave velocity.

CHAPTER EIGHT

OBLIQUE SHEAR WAVES

8.1 INTRODUCTION

A preliminary study of oblique shear waves was conducted as described in Section 3.3.1. For the purpose of this study, oblique shear waves are considered to be those shear waves propagating along a principal stress direction but with particle motion at some angle $\bar{\theta}$ to the principal stress direction. The angle $\bar{\theta}$ will be used to identify and distinguish the particular oblique waves.

Testing was conducted with shear waves propagating only the z-direction under isotropic, biaxial, and triaxial confinement states. These shear waves were generated at the excitation port at the bottom of the LSTD as shown in Fig. 3.16. Only two different oblique shear waves were studied; one with $\bar{\theta} = 22.5$ degrees and a second with $\bar{\theta} = 45$ degrees. The motions of these waves were detected by accelerometers numbered 23 and 25 for the 45-degree oblique shear waves and accelerometers numbered 24 and 26 for the 22.5-degree oblique shear waves.

8.2 CROSS-ANISOTROPIC CONDITION

In Sections 5.3 and 6.6, structural anisotropy of the sand sample was measured and was shown to be well represented by a cross-anisotropic material when an isotropic confining pressure is applied or when a biaxial confining pressure is applied in which the axis of symmetry coincides with the axis of symmetry for structural anisotropy. Shear wave velocities, V_{zx} , V_{zy} , V_{xz} , and V_{yz} , are all the same in a cross-anisotropic medium in which the axis of symmetry is in the z-direction as is the case for the sand sample.

The waveforms of oblique shear waves propagating along the axis of symmetry (z-axis) of the cross-anisotropic material look like the other shear waves propagating in the principal stress directions as shown in Figs. 8.1 through 8.4. Hence, it is simple to determine shear wave velocity in this condition by the initial arrival method (IAM) described in Section 3.5.

The results of oblique shear wave velocities, V_{SH45} and $V_{SH22.5}$, measured under isotropic confinement and under biaxial confinement with only one stress varying in the z-direction are presented in Figs. 8.5 and 8.6, respectively. The measured shear wave velocities are also compared to shear

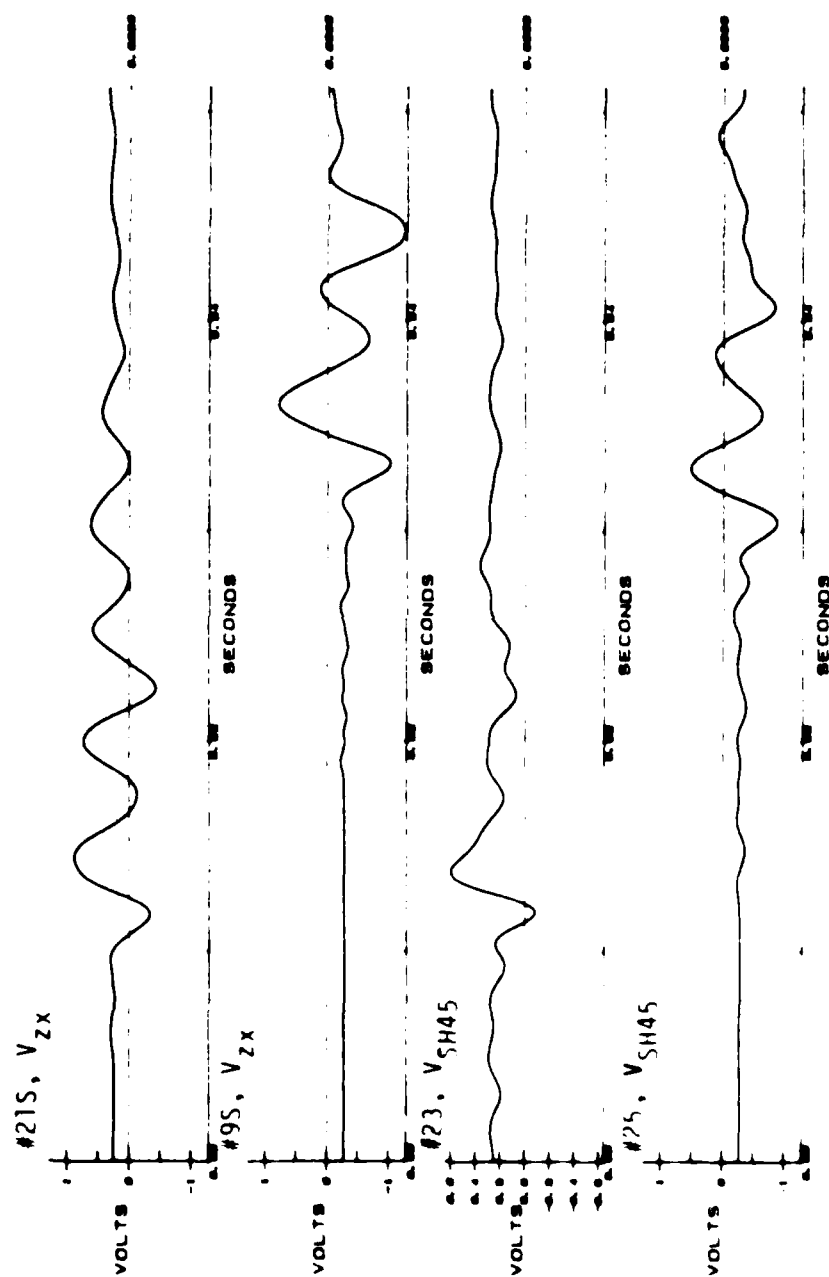


Fig. 8.1 - Waveforms of Shear Wave V_{ZX} and Oblique Shear Wave V_{SH45} Under Isotropic Confinement with $\sigma_0 = 40$ psi

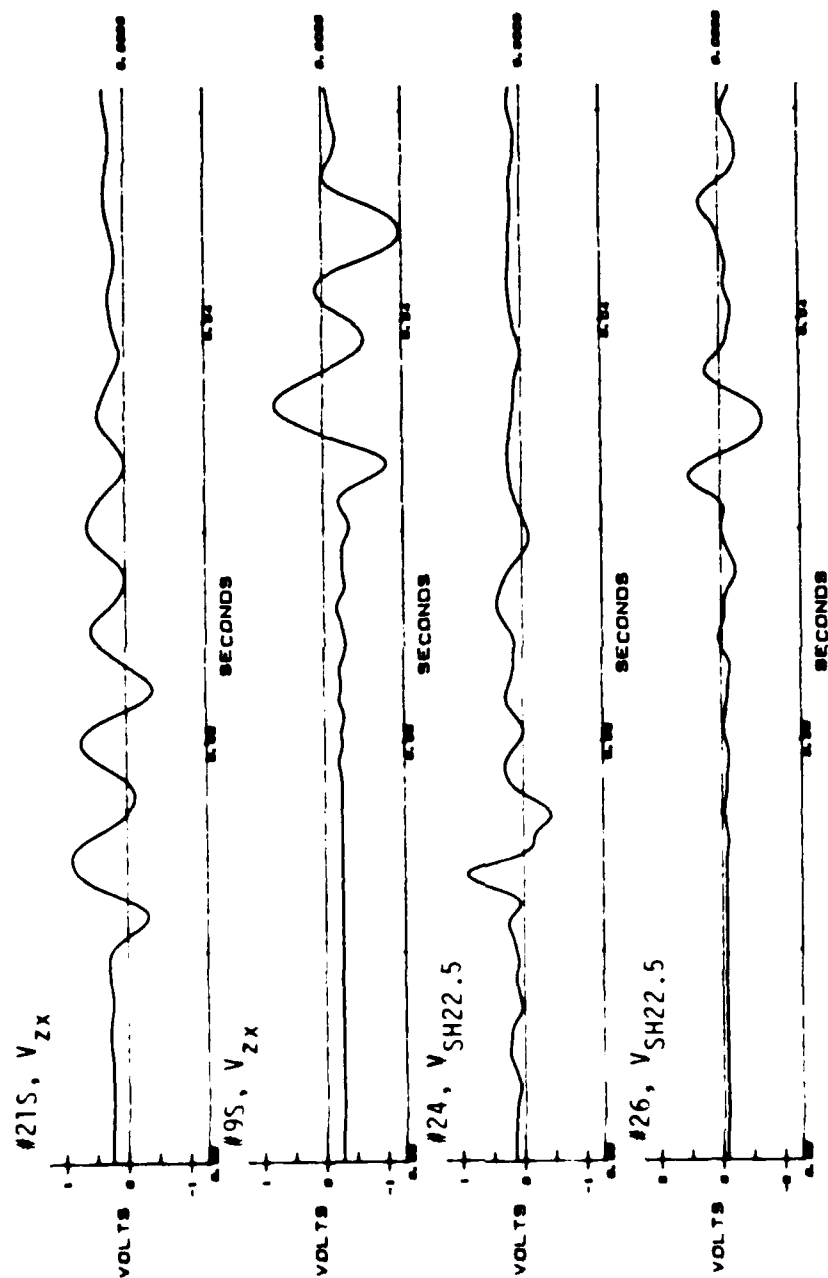


Fig. 8.2 - Waveforms of Shear Wave V_{zx} and Oblique Shear Wave $V_{SH22.5}$ Under Isotropic Confinement with $\bar{\sigma}_0 = 40$ psi

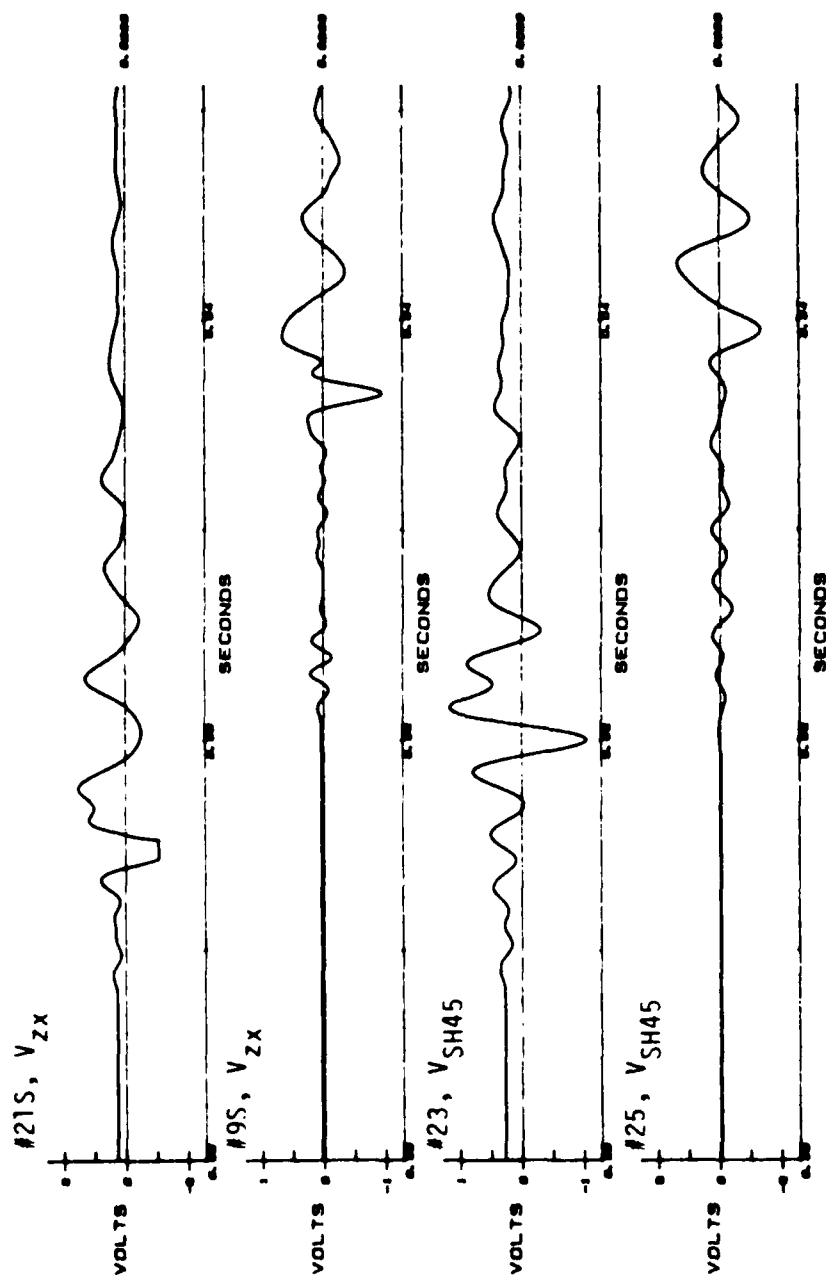


Fig. 8.3 - Waveforms of Shear Wave V_{zx} and Oblique Shear Wave V_{SH45} Under Biaxial Confinement BIA1Z with $\bar{\sigma}_x = \bar{\sigma}_y = 15$ psi, and $\bar{\sigma}_z = 40$ psi

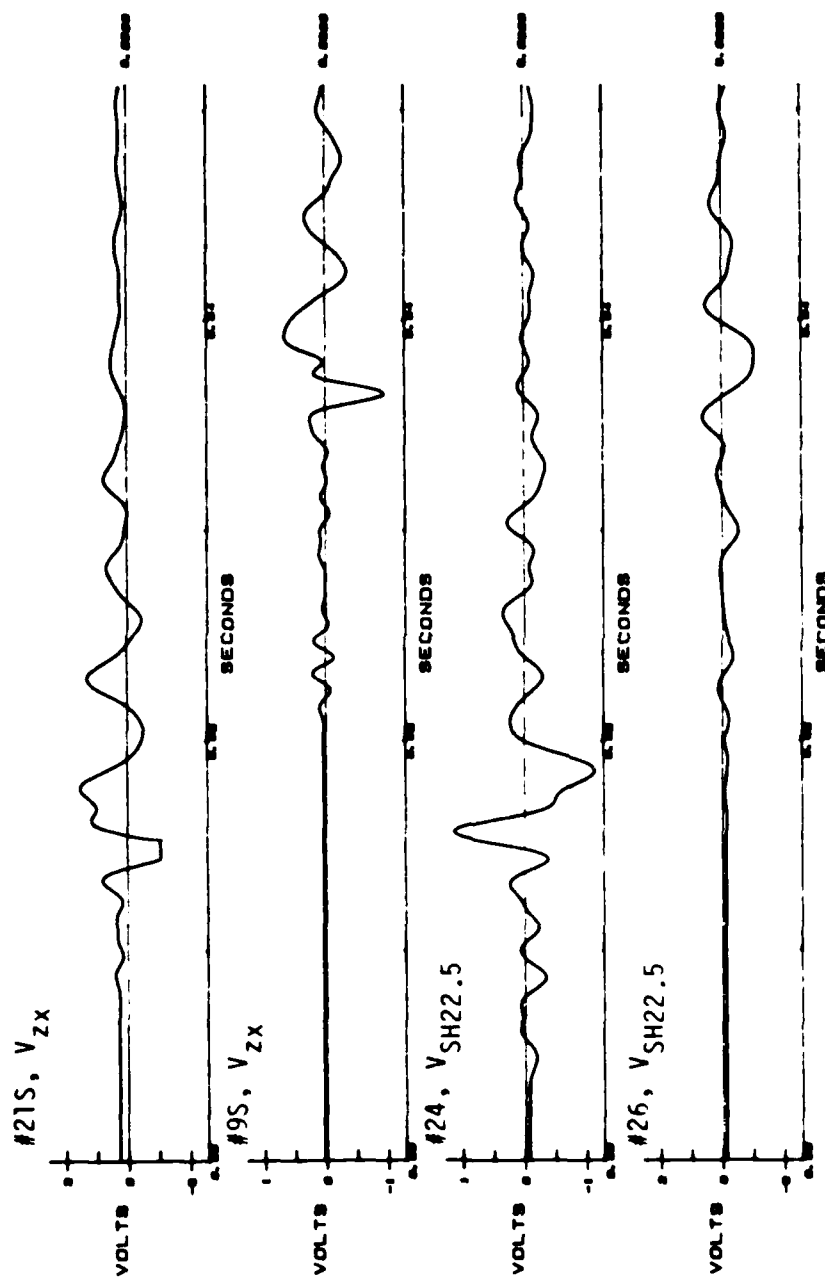


Fig. 8.4 - Waveforms of Shear Wave V_{zx} and Oblique Shear Wave $V_{SH22.5}$ Under Biaxial Confinement BIA1Z with $\bar{\sigma}_x = \bar{\sigma}_y = 15$ psi, and $\bar{\sigma}_z = 40$ psi

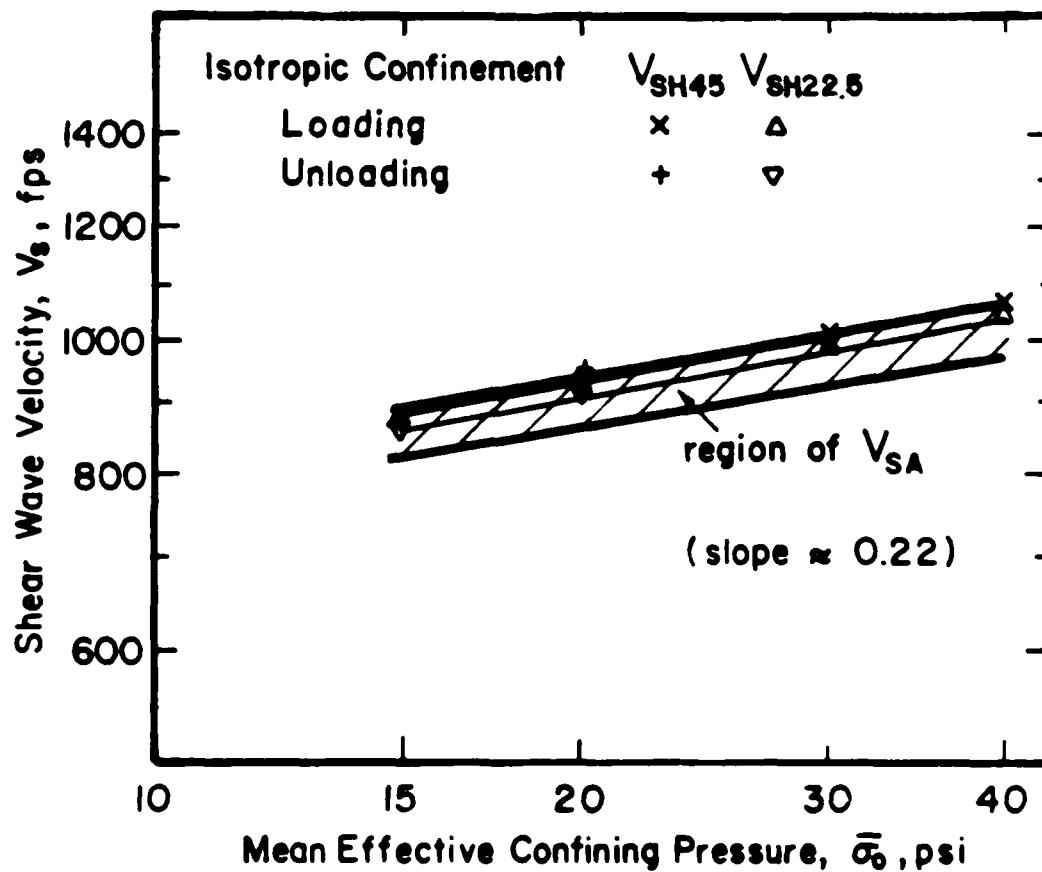


Fig. 8.5 - Velocities of Oblique Shear Waves, V_{SH45} , and $V_{SH22.5}$ Under Isotropic Confining Pressures

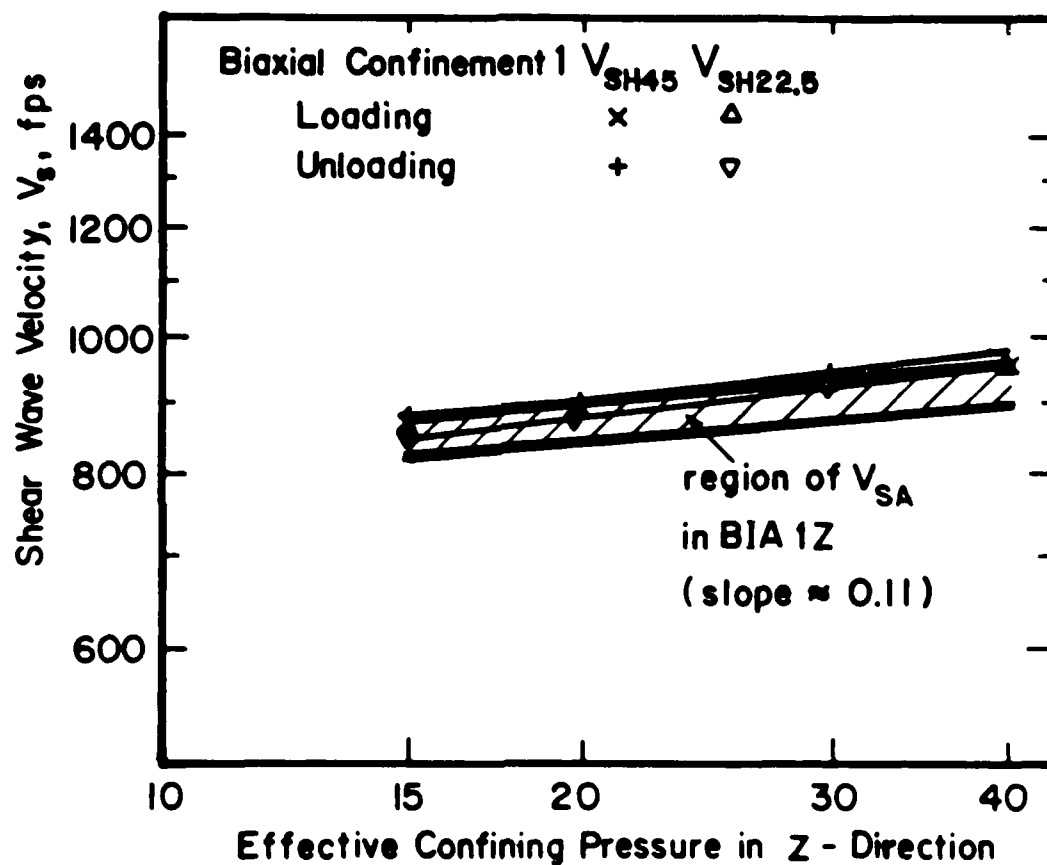


Fig. 8.6 - Velocities of Oblique Shear Waves, V_{SH45} and $V_{SH22.5}$. Under Biaxial Confinement with Only One Stress in the Z-Direction Varying, BIA1Z

wave velocities of V_{SA} (i.e. V_{xz} , V_{yz} , V_{zx} , and V_{zy}) in the figures. Since the direction of propagation of the oblique shear waves coincides with the axis of symmetry, the velocity should be the same as either V_{zx} or V_{zy} no matter whether the direction of particle motion is 45 or 22.5 degrees from the principal stress axis (White, 1965). An acceptable agreement is shown in both cases. Additionally, scattering in oblique shear wave velocities is less than the scatter in the four shear wave velocities (V_{SA}) in the principal planes.

8.3 ORTHOTROPIC CONDITION

An isotropic medium will become anisotropic once an anisotropic stress state is applied. Once the stress state causes the sample to become orthotropic, the waveforms appear to change. In addition, the signals of the oblique shear waves turn out to be more complex as the distance of travel increases as shown in Figs. 8.7 and 8.8 because the P-wave component seems to increase. No obvious wave peak can be selected in this condition. Different frequency components caused by different stiffnesses in each principal plane may force the oblique shear wave to no longer be a monochromatic wave (French, 1971; and Pain 1976). Additional study of oblique shear waves under orthotropic conditions, especially in the frequency domain, is necessary. Unfortunately, this work is beyond the scope (and instrumentation) of the present study.

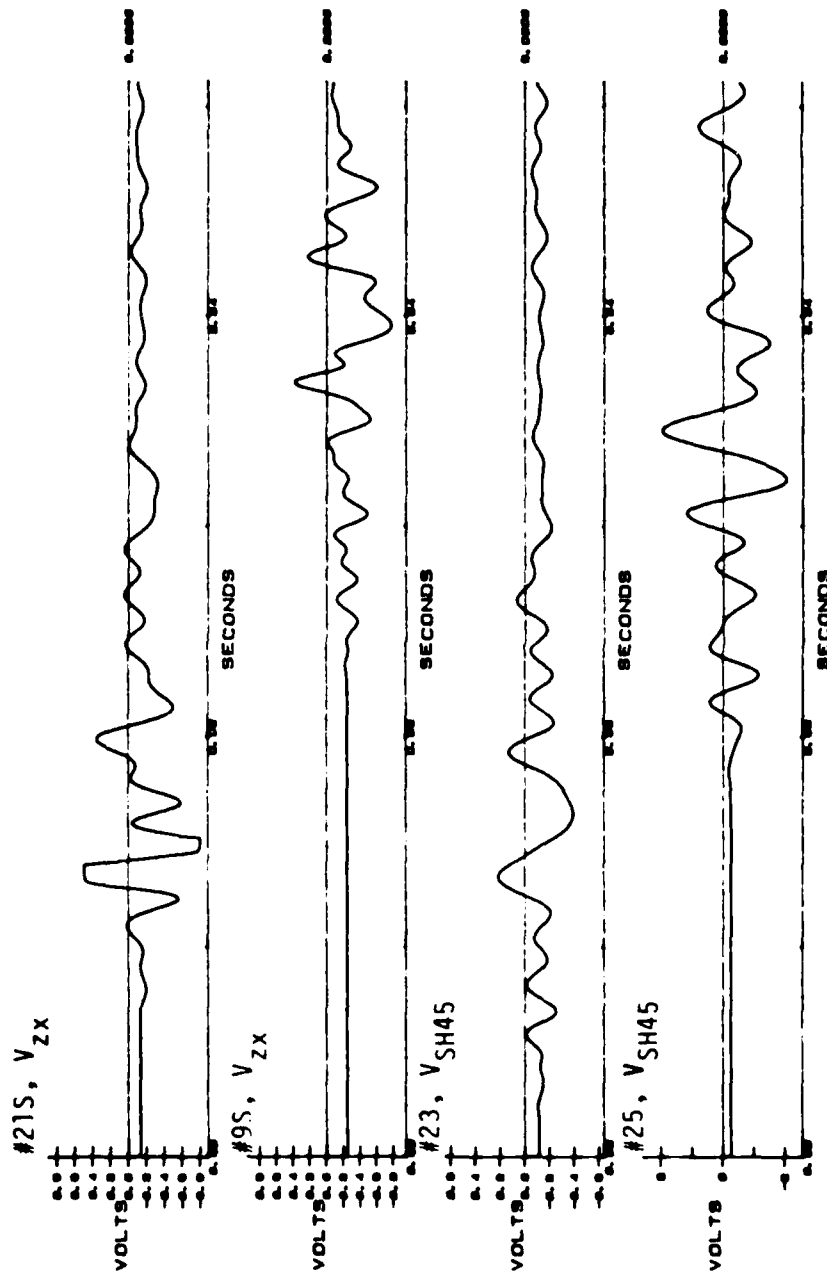


Fig. 8.7 - Waveforms of Oblique Shear Wave, V_{SH45} , in the Orthotropic Condition
BIAIX with $\sigma_x = 40$ psi and $\sigma_y = \sigma_z = 15$ psi

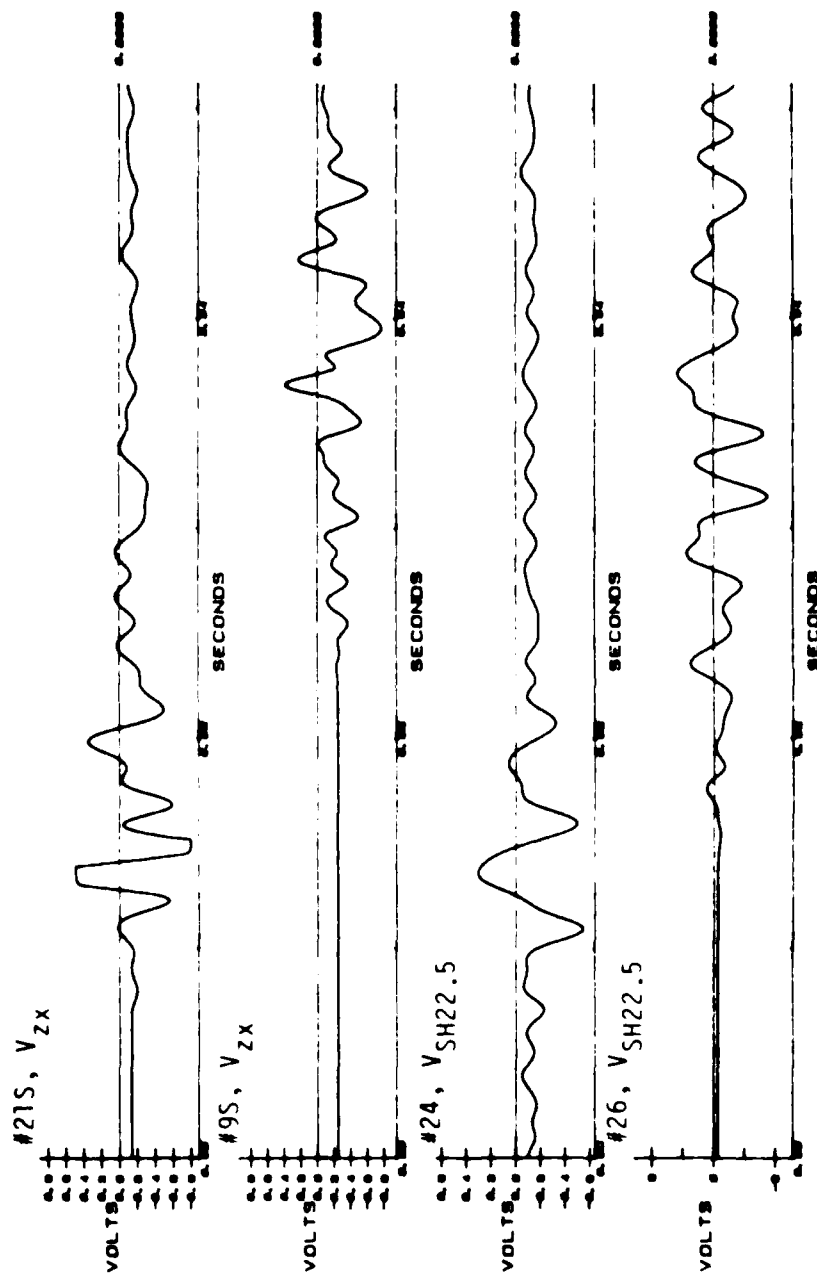


Fig. 8.8 - Waveforms of Oblique Shear Wave, $V_{SH22.5}$, in the Orthotropic Condition
BIAIX with $\bar{\sigma}_x = 40$ psi and $\bar{\sigma}_y = \bar{\sigma}_z = 15$ psi

CHAPTER NINE

CROSS-ANISOTROPIC MODEL AND BODY WAVE PROPAGATION

9.1 INTRODUCTION

Natural soils are often assumed to be isotropic, homogeneous and elastic materials for the purposes of conducting and analyzing seismic wave propagation tests in geotechnical engineering. With this simplified model, the velocities of only one P-wave and one S-wave need to be measured to describe soil behavior in the small-strain range (see Eqs. 2.1 and 2.2). Single values for the constrained modulus, shear modulus, Young's modulus, and Poisson's ratio can then be obtained from the wave velocities using Eqs. 2.4, 2.3, 2.6 and 2.5, respectively. Although this simple model has many shortcomings, its use continues because of reasons such as ease in application, minimum amount of computational time necessary in numerical calculations, and ability to achieve analytical solutions for many complex boundary conditions.

In fact, essentially all natural soils behave in a more complicated fashion than described by an isotropic model, especially for body wave propagation. However, the complexity of the model is limited in practical terms. For instance, no analytical solutions for the wave equations in an orthotropic soil seem to exist. Fortunately, level deposits of natural soil are reasonably approximated by a cross-anisotropic model in which five independent constants are necessary. These constants can be evaluated with body waves propagated along principal stress and inclined directions. Equations 2.12 through 2.31 give four of the five constants as follows:

$$C_{11} = \rho V_{PI}^2 = \rho (V_{P90})^2 \quad (9.1)$$

$$C_{33} = \rho V_{PA}^2 = \rho (V_{P0})^2 \quad (9.2)$$

$$C_{44} = \rho V_{SA}^2 = \rho (V_{SA90})^2 \quad (9.3)$$

$$C_{66} = \rho V_{SI}^2 = \rho (V_{SI90})^2 \quad (9.4)$$

where

$$V_{PI} = V_{xx} = V_{yy}, \quad (9.5)$$

$$V_{PA} = V_{zz}, \quad (9.6)$$

$$V_{SI} = V_{xy} = V_{yx}, \quad (9.7)$$

$$V_{SA} = V_{xz} = V_{yz} = V_{zx} = V_{zy}, \text{ and} \quad (9.8)$$

ρ = mass density.

The fifth elastic constant, C_{13} , is more difficult to evaluate. The easiest way is to use an oblique P-wave velocity measured at an angle θ ($0 \leq \theta \leq 90^\circ$) as follows:

$$V_{p,\theta} = \{[(C_{11}\sin^2\theta + C_{33}\cos^2\theta + C_{44} + \Delta)/(2\rho)]^{1/2} \quad (9.9)$$

where

$$\Delta = [(C_{11} - C_{44})\sin^2\theta - (C_{33} - C_{44})\cos^2\theta]^2 + 4(C_{13} + C_{44})^2\sin^2\theta\cos^2\theta, \text{ and}$$

θ = the angle between the direction of propagation of the plane wave and the axis of symmetry (z-axis) as shown in Fig. 2.5.

To illustrate the use of a cross-anisotropic model for soil, shear wave velocities measured and discussed in Chapter Five, Six and Seven are converted to shear moduli according to the relationships shown in Sections 2.3.1 to 2.3.4. Constrained moduli are calculated from P-wave velocities measured in this sand and reported by Chu et al, 1984. The effects on body wave propagation are then discussed and compared with an isotropic model in the following sections.

9.2 CONSTRAINED MODULUS

A general equation relating P-wave velocity and principal stress was recommended by Chu et al (1984) in the following form:

$$V_p = C_p \bar{\sigma}_a^{mm} \quad (9.10)$$

where $\bar{\sigma}_a$ is the effective principal stress in the direction of wave propagation and C_p is a constant. By substituting Eq. 9.10 into Eq. 9.1 with $V_{xx} = V_{PI}$ for the isotropic plane, one obtains:

$$C_{11} = M_I = \rho C_{xx}^2 \bar{\sigma}_a^{2mm} \quad (9.11)$$

and

$$C_{11} = C_{22} = \rho C_{yy}^2 \bar{\sigma}_a^{2mm} \quad (9.12)$$

in which the constrained modulus has the same units as the normal stress $\bar{\sigma}_a$ (psf in this study) and C_{xx} and C_{yy} are the values of the P-wave velocities V_{xx} and V_{yy} under a confining stress of unity with units of $\bar{\sigma}_a$ (and $V_{xx} = V_{yy}$).

For the anisotropic plane, the constrained modulus can be expressed as:

$$C_{33} = M_A = \rho C_{zz}^2 \bar{\sigma}_a^{2mm} \quad (9.13)$$

where C_{zz} is the value of V_{zz} under a confining stress of unity with units of $\bar{\sigma}_a$.

Consequently, low-amplitude constrained moduli can be estimated with Eqs. 9.11 through 9.13 as:

$$M = C_M \bar{\sigma}_a^{Mm} \quad (9.14)$$

where

M = constrained modulus

C_M = constant which equals $\rho \cdot (C_p^2)$ with C_p equal to C_{xx} , C_{yy} or C_{zz} ,

Mm = slope of the $\log M - \log \bar{\sigma}_a$ relationship, which equals 2mm.

and

$\bar{\sigma}_a$ = effective principal stress in the direction of P-wave propagation.

The constant and slopes of low-amplitude constrained moduli versus confining pressure relationship for isotropic (M_I) and anisotropic (M_A) planes are summarized in Table 9.1 for each confining pressure condition. The values were taken from Chu et al, 1984.

9.3 SHEAR MODULUS

A general equation relating shear wave velocity and principal stress state as shown in Sections 4.6 and 5.2 is:

$$V_S = C_2 \bar{\sigma}_a^{na} \bar{\sigma}_b^{nb} \bar{\sigma}_c^{nc} \quad (9.15)$$

Table 9.1 - Constants and Slopes of the Log M - Log $\bar{\sigma}_a$ Relationship for This Sand Sample

Stress State	M_I ,* psf		M_A ,** psf	
	C_I	Mm	C_A	Mm
ISOTROPIC	285,351	0.430	255,610	0.412
BIA1	311,031	0.420	376,642	0.370
BIA2	286,871	0.438	199,790	0.420
OVERALL	295,034	0.430	309,506	0.380

$$* M_I = C_I \cdot \bar{\sigma}_a^{Mm}$$

$$** M_A = C_A \cdot \bar{\sigma}_a^{Mm}$$

From Eqs. 2.3 and 8.16, the low-amplitude shear modulus, G , can be expressed as:

$$G = C_G \bar{\sigma}_a^{Na} \bar{\sigma}_b^{Nb} \bar{\sigma}_c^{Nc} \quad (9.16)$$

where

C_G = constant which equals $\rho \cdot (C_S)^2$ at a pressure of unity,

Na = slope of $\log G - \log \bar{\sigma}_a$ relationship and equals $2na$,

Nb = slope of $\log G - \log \bar{\sigma}_b$ relationship and equals $2nb$,

Nc = slope of $\log G - \log \bar{\sigma}_c$ relationship and equals $2nc$,

$\bar{\sigma}_a$ = effective principal stress in direction of S-wave propagation,

$\bar{\sigma}_b$ = effective principal stress in direction of S-wave particle motion, and

$\bar{\sigma}_c$ = effective principal stress in out-of-plane direction.

Under isotropic confinement ($\bar{\sigma}_a = \bar{\sigma}_b = \bar{\sigma}_c = \bar{\sigma}_0$), the shear modulus can be related to stress state as:

$$G = C_G \bar{\sigma}_0^{Nm} \quad (9.17)$$

where

$\bar{\sigma}_0$ = mean effective stress, and

Nm = slope of $\log G - \log \bar{\sigma}_0$ relationship.

For practical engineering purposes, as discussed in Sections 6.7 and 7.3, the general form of the relationship relating shear modulus and anisotropic stress state can be presented as:

$$G = C_G (\bar{\sigma}_a \cdot \bar{\sigma}_b)^{Ne} \quad (9.18)$$

where

$Ne = 2ne$ in Eq. 7.2.

By substituting Eq. 9.16 into Eqs. 9.3 and 9.4, C_{44} and C_{66} can be obtained, respectively. For the isotropic plane:

$$C_{66} = G_I = C_G \bar{\sigma}_a^{Na} \bar{\sigma}_b^{Nb} \bar{\sigma}_c^{Nc} \quad (9.19)$$

where

$$C_6 = \rho(C_{xy})^2$$

C_{xy} = the value of V_{xy} under a confining stress of unity with units of $\bar{\sigma}_a$, $\bar{\sigma}_b$, and $\bar{\sigma}_c$.

For the anisotropic plane, low-amplitude shear moduli may be expressed with Eqs. 9.7 and 9.8 as follows:

$$C_{44} = G_A = C_4 \bar{\sigma}_a^{Na} \bar{\sigma}_b^{Nb} \bar{\sigma}_c^{Nc} \quad (9.20)$$

where

$$C_4 = \rho(C_{xz})^2$$

C_{xz} = the value of V_{xz} under a confining stress of unity with units of $\bar{\sigma}_a$, $\bar{\sigma}_b$ and $\bar{\sigma}_c$, and

$$G_A = C_{44} = C_{55} \quad (9.21)$$

Based on the results given in Table 6.18, the constants and slopes of the $\log G - \log \bar{\sigma}$ relationship for the anisotropic (G_A) and isotropic (G_I) planes are listed in Table 9.2.

9.4 C_{13} IN A CROSS-ANISOTROPIC MODEL

Measurement of the velocities of oblique P-waves is the easiest way of evaluating the constant C_{13} required in a cross-anisotropic model for soil. This was done between July and October 1984 for the sand sample constructed with accelerometers buried at inclined angles to the principal stress directions. (These results are presented in a report by Lee and Stokoe, 1986.) The measured values of C_{13} are given in Table 9.3. They were calculated using P-waves propagating at angles to the z-axis with 15, 24, and 35 degrees under isotropic, BIA1Z and BIA2Z confinements.

First of all, the limit of C_{13} estimated by substituting Eqs. 9.14, 9.15, and 9.23 into Eq. 2.43 gives the upper limit for values of C_{13} for each confining pressure condition. Table 9.3 lists the upper limit of C_{13} for isotropic and biaxial (BIA1 and BIA2) conditions. BIA1 and BIA2 conditions listed in Table 9.3 are only for those cases in which the axes of symmetry of the anisotropic stress state and structure anisotropy coincided. The values of C_{13} back-calculated with measured oblique P-wave velocities and Eq. 9.9 are also listed in column four of Table 9.3. These measured values are all less than the upper limit values of C_{13} (in agreement with theory). An equation for an approximate value of C_{13} was given by Drnevich (1974) as:

Table 9.2 - Constants and Slopes of the $\log G - \log \bar{\sigma}$ Relationship for This Sand Sample

Stress State	$G_I,^* \text{ psf}$					$G_A,^{**} \text{ psf}$				
	C_{GI}	Nm	Na	Nb	Nc	C_{GA}	Nm	Na	Nb	Nc
ISOTROPIC	145,636	0.360	---	---	---	162,550	0.34	---	---	---
BIA1	100,904	0.432	0.214	0.212	0.006	139,737	0.366	0.200	0.172	-0.006
BIA2	107,705	0.416	0.200	0.195	0.006	141,052	0.360	0.198	0.174	-0.004
OVERALL	123,200	0.40	0.20	0.20	0.00	135,928	0.36	0.18	0.18	0.00

$$^* G_I = C_{GI} \frac{Nm}{\sigma_0} \text{ or } C_{GI} \frac{Na}{a} \frac{Nb}{b} \frac{Nc}{c}$$

$$^{**} G_A = C_{GA} \frac{Nm}{\sigma_0} \text{ or } C_{GA} \frac{Na}{a} \frac{Nb}{b} \frac{Nc}{c}$$

Table 9.3 - Comparison of Values of C_{13} for the Sand Sample from Theoretical Limits**, Measured Results, and Values Suggested by Drnevich (1974)

Test Type	Confinement, psi			Limit of C_{13} psf	Measured C_{13} psf	Drnevich's C_{13} psf
	$\bar{\sigma}_x$	$\bar{\sigma}_y$	$\bar{\sigma}_z$			
ISO*	15	15	15	4147364.1	2065838.9	1880514.3
	20	20	20	4664400.3	2447630.8	2124918.3
	25	25	25	5109196.0	3101176.8	2337472.2
	30	30	30	5503765.3	3698173.0	2527731.9
BIA1	15	15	15	4330255.7	694630.9	2141581.4
	15	15	20	4566960.0	906252.3	2503890.9
	15	15	25	4759436.8	1260481.5	2812715.4
	15	15	30	4922708.2	1743217.6	3084673.1
BIA2	15	15	30	4841428.3	1851743.3	2989490.0
	20	20	30	5158366.8	1948699.2	2841510.5
	25	25	30	5410419.1	1938557.7	2714106.7
	30	30	30	5640597.3	2051097.7	2601018.8

* Isotropic confinement

** Eq. 2.43: $C_{13} < \left[\frac{(C_{11} + C_{12})C_{33}}{2} \right]^{1/2}$, where $C_{12} = C_{11} - 2 \cdot C_{66}$

$$C_{13} = (C_{11} + C_{33})/2 - 2 \cdot C_{66} \quad (9.22)$$

Values of C_{13} obtained with this equation are listed in the last column of Table 9.3. One can see that these values of C_{13} are always less than the upper limit values. In fact, these values are on the order of half of the limit values. Unfortunately, these values are about 0.7 to 3.1 times the measured values, indicating the approximate nature of Eq. 9.22.

9.5 YOUNG'S MODULUS

For cross-anisotropic material, there are two values of Young's modulus; one for the isotropic plane (E_I) and one for the anisotropic plane (E_A). These two theoretical moduli have been calculated for the sand sample using Eqs. 2.39 and 2.41, and the results are summarized in Table 9.4. If the theoretical values of C_{13} shown in Table 9.3 (which represent an upper limit for C_{13}) are used to calculate theoretical values for E_I and E_A , these theoretical values represent a lower limit for E_I and E_A . Young's moduli equivalent to the measured body waves should always be greater than these theoretical limits. Columns five and six in Table 9.4 show the equivalent and measured Young's moduli which all agree with the theoretical limitation.

9.6 POISSON'S RATIO

Poisson's ratios associated with the isotropic and anisotropic planes (ν_I and ν_A) obtained with Eqs. 2.40 and 2.42, respectively, are listed in Table 9.5. Unlike Young's moduli, if the theoretical upper limit of C_{13} is used to calculate values for Poisson's ratio, ν_I represents the lower limit and ν_A represents the upper limit of Poisson's ratios from these calculations. Therefore, the measured value of ν_I should be greater than the limit while the measured value of ν_A should be smaller than the limit. The measured values of Poisson's ratio under three confining pressure conditions, listed in columns six and seven of Table 9.5, all satisfy this requirement. Values of ν_{31} obtained from Eq. 2.33 are also presented in Table 9.5. In this sand sample, values of ν_{31} are always less than ν_A .

9.7 WAVE SURFACES IN A CROSS-ANISOTROPIC MEDIUM

In 1968, Woods published a diagram showing the wave fronts of all seismic waves at a relatively large distance from a vertically vibrating

Table 9.4 - Limits and Measured Values of Young's Moduli for a Cross-Anisotropic Material

Test Types	Confinement, psi			Limit of Young's Modulus, **		Measured Young's Modulus, psf	
	$\bar{\sigma}_x$	$\bar{\sigma}_y$	$\bar{\sigma}_z$	E_I	E_A	E_I	E_A
ISO*	15	15	15	5533307.2	2980277.4	6932468.1	5170828.9
	20	20	20	6270401.5	3290300.9	7717513.1	5527886.5
	25	25	25	6908283.4	3552815.6	8240182.9	5590120.6
	30	30	30	7476783.4	3782779.4	8822650.9	5734019.6
BIA1	15	15	15	5555938.2	3225868.2	7264772.3	6353214.6
	15	15	20	5555938.2	3588177.9	7253807.3	7032580.8
	15	15	25	5555938.2	3897002.4	7213634.7	7507710.4
	15	15	30	5555938.2	4168960.1	7142357.3	7792492.7
BIA2	15	15	30	5467466.8	4168960.0	7036497.1	7704624.7
	20	20	30	6198635.3	4168960.0	7979912.6	7720027.6
	25	25	30	6832450.4	4168960.0	8819582.2	7787693.0
	30	30	30	7398123.6	4168960.0	9541537.5	7772743.2

* Isotropic confinement

** Lower limit

Table 9.5 - Limits and Measured Values of Poisson's Ratio for a Cross-Anisotropic Material

Test Type	Confinement, psi				Limit of Poisson's Ratio				Measured Poisson's Ratio			
	$\bar{\sigma}_x$	$\bar{\sigma}_y$	$\bar{\sigma}_z$		ν_I^+	ν_A^{\dagger}	ν_{31}^{\ddagger}		ν_I	ν_A	ν_{31}	
ISO*	15	15	15		.04127	.66709	.35930		.30456	.24450	.17897	
	20	20	20		.05171	.67216	.35270		.29443	.27332	.18508	
	25	25	25		.05976	.67606	.34769		.26408	.34016	.21104	
	30	30	30		.06630	.67924	.34365		.25824	.37394	.23091	
BIA1	15	15	15		.04418	.64153	.37248		.36533	.06859	.05975	
	15	15	20		.04418	.60828	.39284		.36327	.08044	.07795	
	15	15	25		.04418	.58368	.40940		.35572	.10444	.10842	
	15	15	30		.04418	.56432	.42344		.34233	.13800	.14995	
BIA2	15	15	30		.02755	.56465	.43055		.32243	.15104	.16468	
	20	20	30		.02882	.60083	.40410		.32447	.15847	.15266	
	25	25	25		.02981	.63048	.38470		.32931	.15635	.13764	
	30	30	30		.03061	.65579	.36955		.32920	.16540	.13438	

* Isotropic confinement

+ Lower limit

‡ Upper limit

footing on the surface of a homogeneous, isotropic, elastic half-space. This diagram is shown in Fig. 9.1. The wave fronts are based upon equations derived by Miller and Pursey (1955). The body waves propagate radially outward from the source along hemispherical wave fronts while the Rayleigh wave propagates radially outward along a cylindrical wave front. This diagram has come to be widely referenced in geotechnical engineering.

In cross-anisotropic material, the diagram presented by Woods (1968) becomes more complex for two reasons. First there are two types of shear waves, SV and SH, which can propagate with different velocities. As a result, there are three wave fronts (P, SV and SH) for the body waves as discussed in Section 2.3.1. Second, the wave surface is different from the velocity surface because of the difference between the ray and wave normals (see Section 2.3.1). The velocity surface represents the planes of equal phase for a plane wave, while the wave surface is the wave front based on ray velocity. Measured body wave velocities represent ray velocities which are used to calculate the wave front. However, ray velocities must be converted to the velocities of the wave normal to calculate the velocity surface (Wooster, 1938; and Postma, 1955).

To illustrate these points, Figs. 9.2 and 9.3 show the velocity surface and wave surface, respectively, for the sand sample under an isotropic confining pressure of 15 psi (103.4 kPa). (No Rayleigh wave front exists in these diagrams because we are dealing with a full space.) Obviously, there is little difference between velocity and wave surfaces in this case, and the wave fronts of body waves are elliptical as expected (Love, 1937; Levin, 1979). Values of C_{13} based on best-fits of measured oblique P-wave velocities were used as discussed in Lee and Stokoe (1986).

Structural anisotropy may result from preferential orientation of soil grains, stress field orientation, and thin bedding and cracks (Jones and Wang, 1981; Bachman, 1983; Melia and Carlson, 1984; and Helbig, 1985). Therefore, C_{13} can be expected to vary from its upper limit value to arbitrary smaller values. To examine the influence of C_{13} on the wave fronts only, C_{13} was varied while C_{11} , C_{33} , C_{44} , and C_{66} were held constant. The velocity and wave surfaces in Figs. 9.2 and 9.3 are changed to those shown in Figs. 9.4 through 9.6 and Figs. 9.7 through 9.9, respectively. One can see that the velocity surface of the P-wave contracts while the SV-wave surface expands when C_{13} is varied from the upper limit value to a smaller value. On

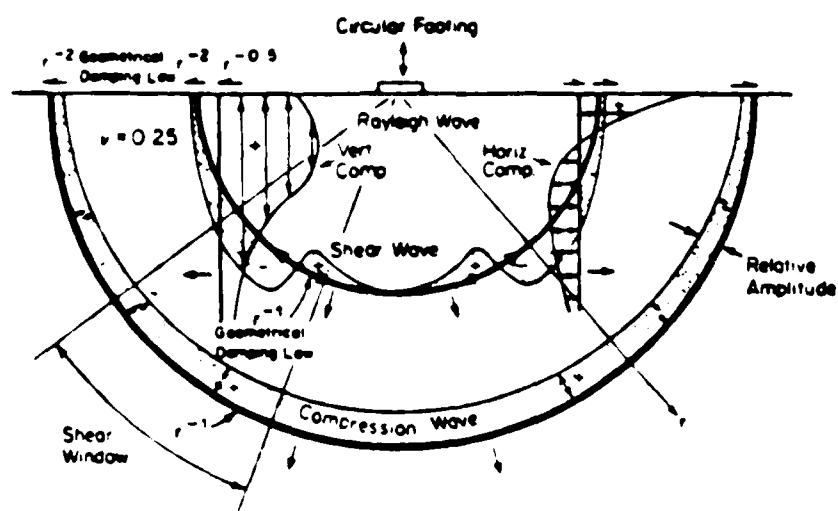


Fig. 9.1 - Distribution of Particle Displacements Associated with Seismic Waves from a Circular Footing on a Homogeneous, Isotropic, Elastic Half-Space (from Woods, 1968)

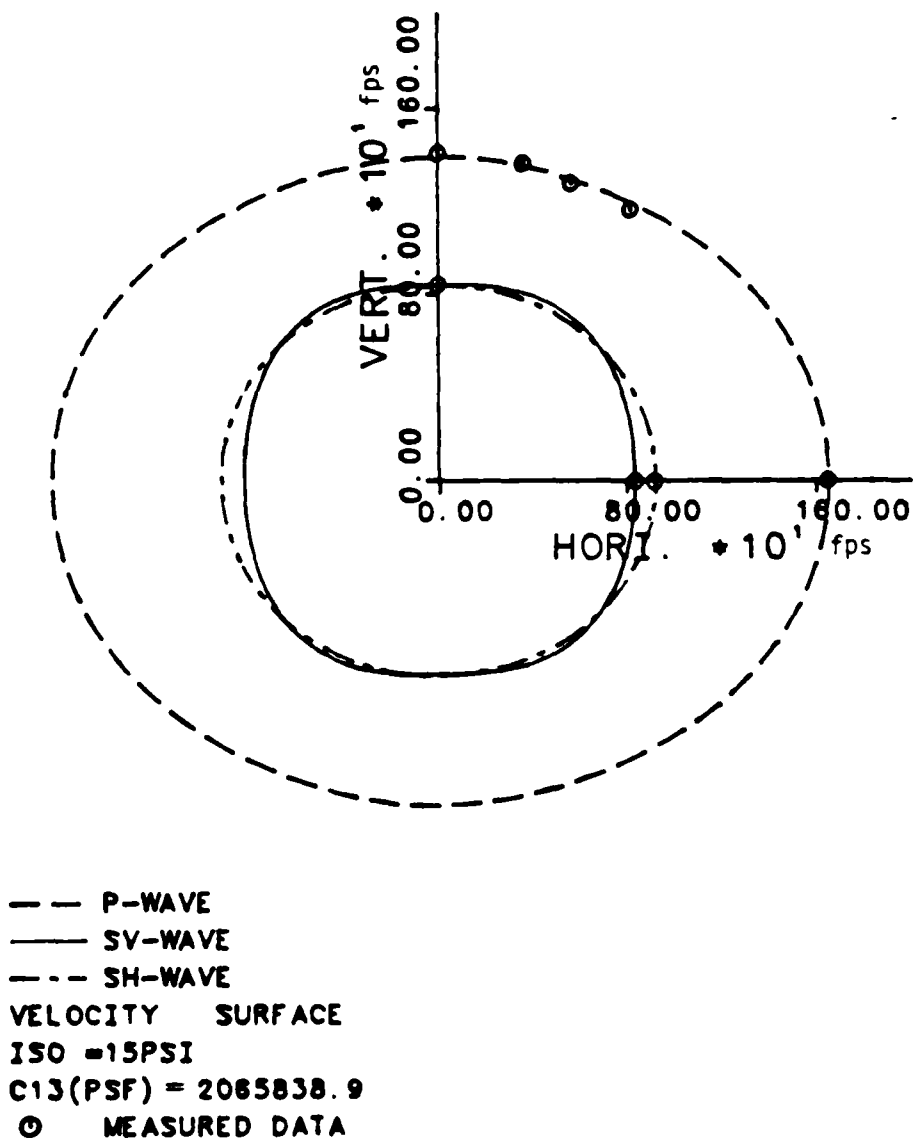


Fig. 9.2 - Comparison of Velocity Surfaces with Measured S-Wave, P-Wave, and Oblique P-Wave Velocities Under Isotropic Confinement with $\bar{\sigma}_0 = 15$ psi

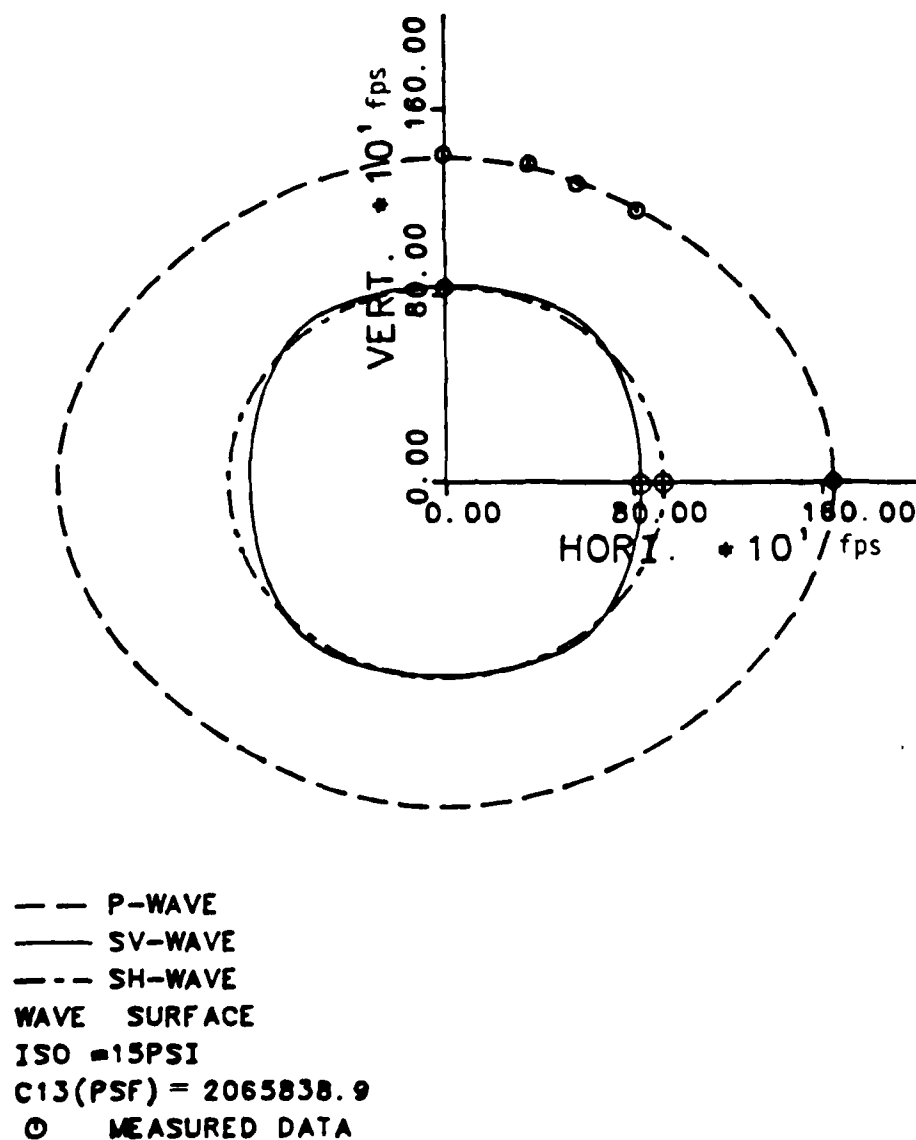


Fig. 9.3 - Comparison of Wave Surfaces with Measured S-Wave, P-Wave, and Oblique P-Wave Velocities Under Isotropic Confinement with $\bar{\sigma}_0 = 15$ psi

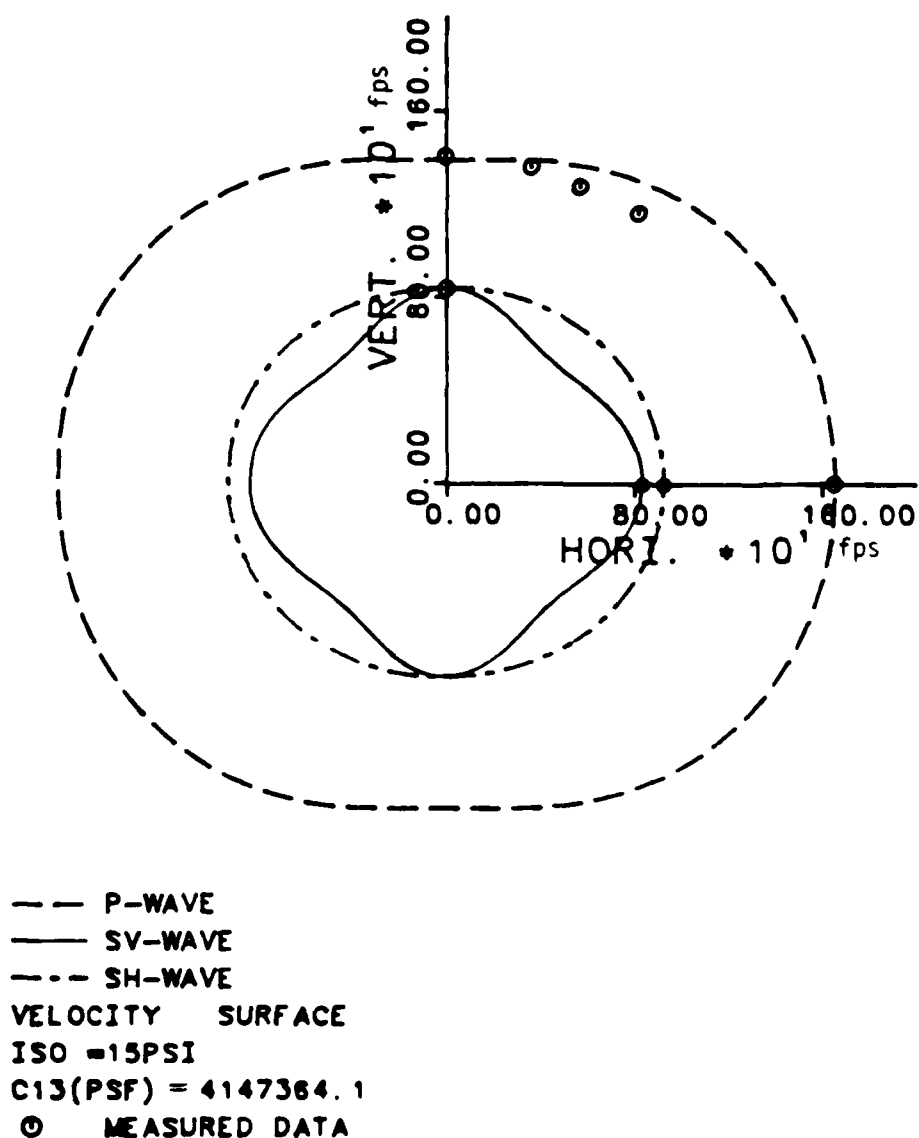
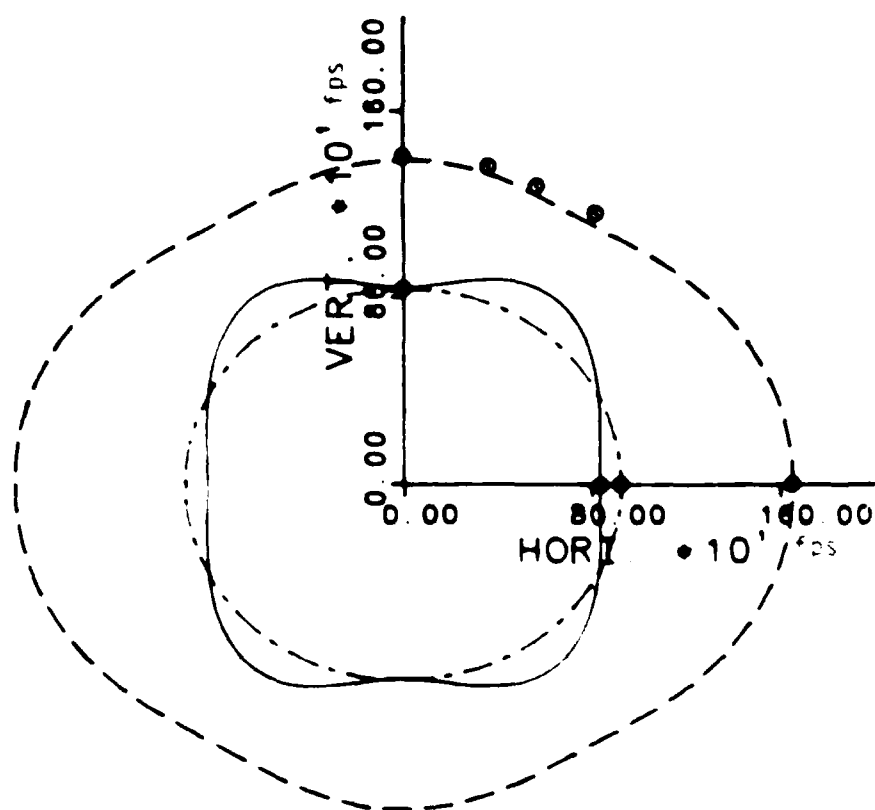


Fig. 9.4 - Comparison of Velocity Surfaces with Measured S-Wave, P-Wave, and Upper Limit of C_{13} Under Isotropic Confinement with $\bar{\sigma}_0 = 15$ psi



--- P-WAVE
 — SV-WAVE
 --- SH-WAVE
 VELOCITY SURFACE
 ISO = 15 PSI
 C13 (PSF) = 992480.6
 ⊙ MEASURED DATA

Fig. 4. Velocity surfaces with measured data. The upper limit of the data is isotropic confinement with 15 psi.

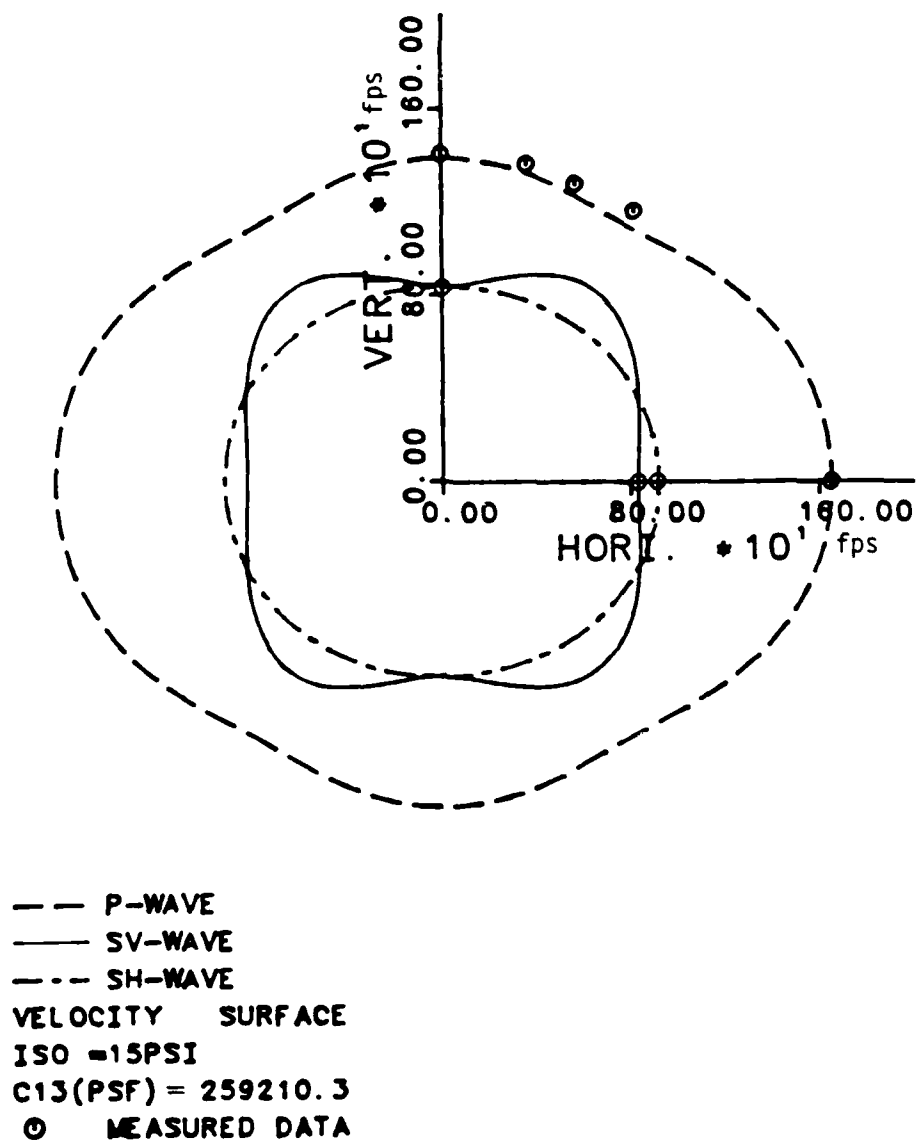


Fig. 9.6 - Comparison of Velocity Surfaces with Measured S-Wave, P-Wave, and 1/16 of Upper Limit of C_{13} Under Isotropic Confinement with $\bar{\sigma}_0 = 15$ psi

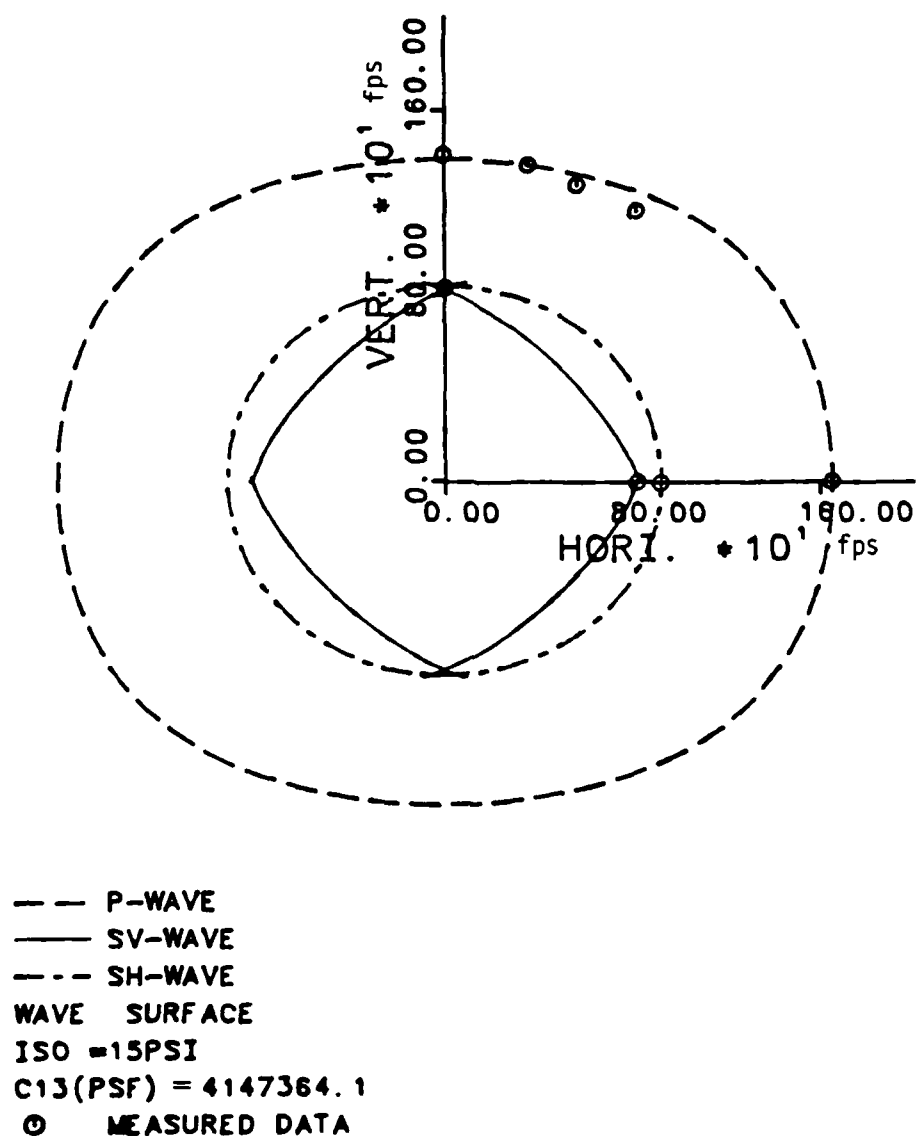


Fig. 9.7 - Comparison of Wave Surfaces with Measured S-Wave, P-Wave, and Upper Limit of C_{13} Under Isotropic Confinement with $\bar{\sigma}_0 = 15$ psi

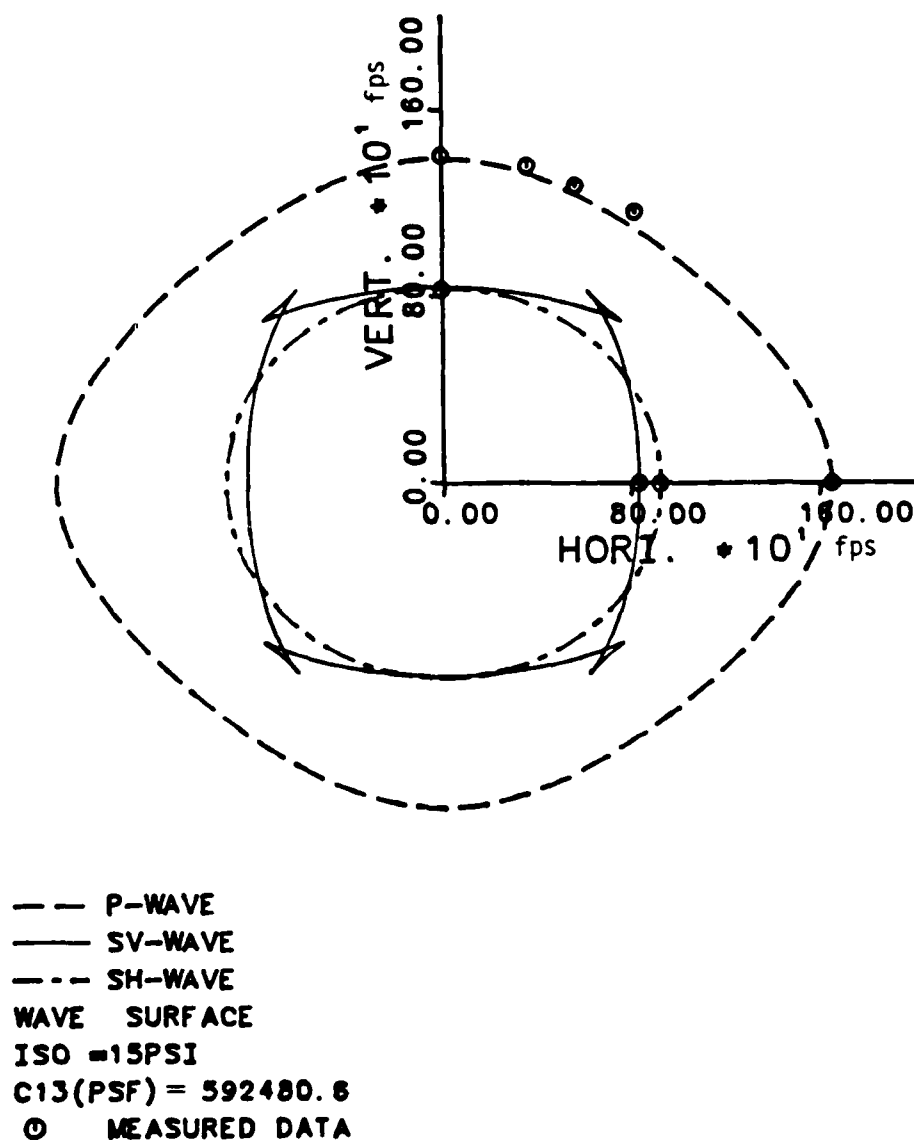


Fig. 9.8 - Comparison of Wave Surfaces with Measured S-Wave, P-Wave, and 1/7 of Upper Limit of C_{13} Under Isotropic Confinement with $\sigma_0 = 15$ psi

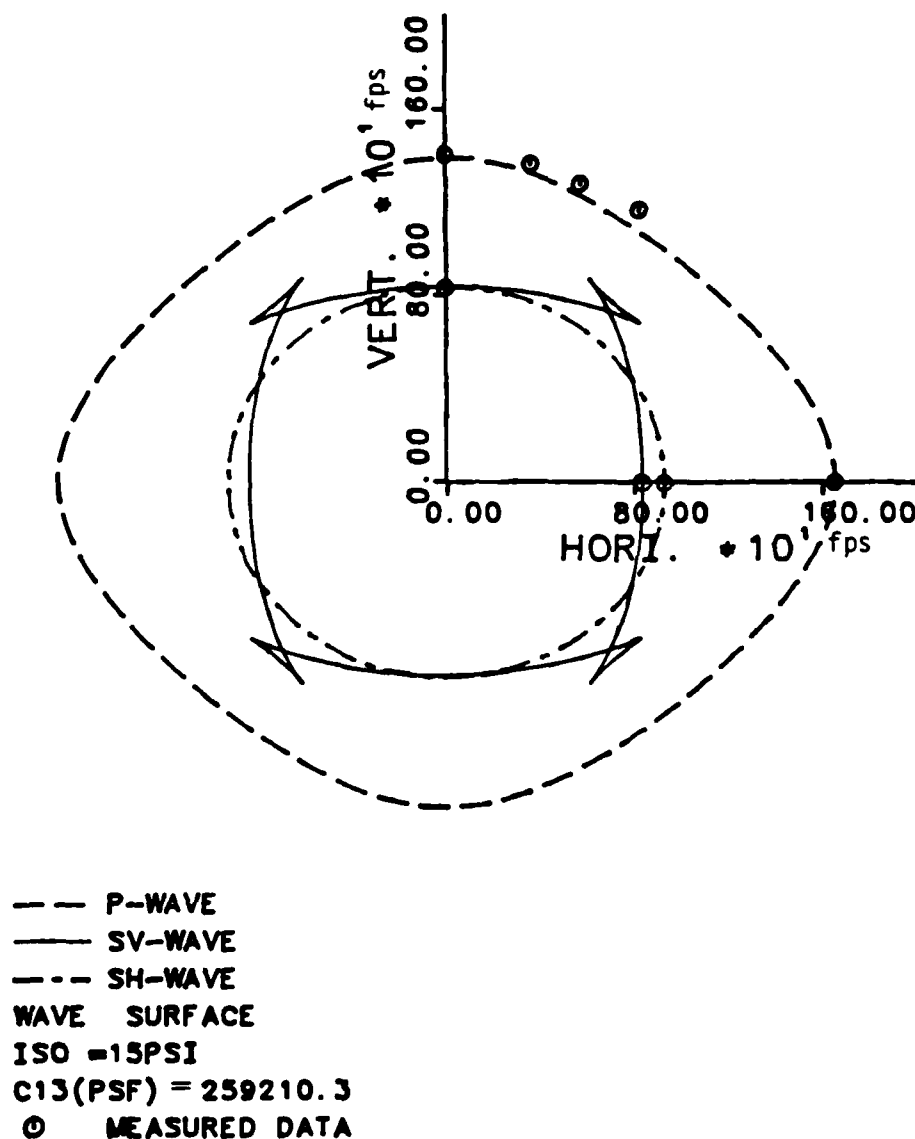


Fig. 9.9 - Comparison of Wave Surfaces with Measured S-Wave, P-Wave, and 1/16 of Upper Limit of C_{13} Under Isotropic Confinement with $\bar{\sigma}_0 = 15$ psi

the wave surface, both the P- and SV-waves behave similarly to that for the velocity surface except for the formation of cusps on the wave front of the SV-wave. Cusps for SV-waves have been reported by Musgrave (1970) for a hexagonal crystal, Banerjee and Pao (1974) for dielectric crystals, Brodov et al (1984) for rocks, and Jolly (1956), Levin (1980), and White et al (1983) for soils. Either cusps, curved ray paths, or inclined soil layers may cause difficulty in determining SV-wave velocity from seismic data (Jolly, 1956; Ludeling, 1977; Helbig, 1983; Byun, 1984; and Jones, 1985).

It is also clear that measured oblique P-wave velocities cannot fit the P-wave surface once an arbitrary C_{13} is used along with the constant values of C_{11} , C_{33} , C_{44} , and C_{66} .

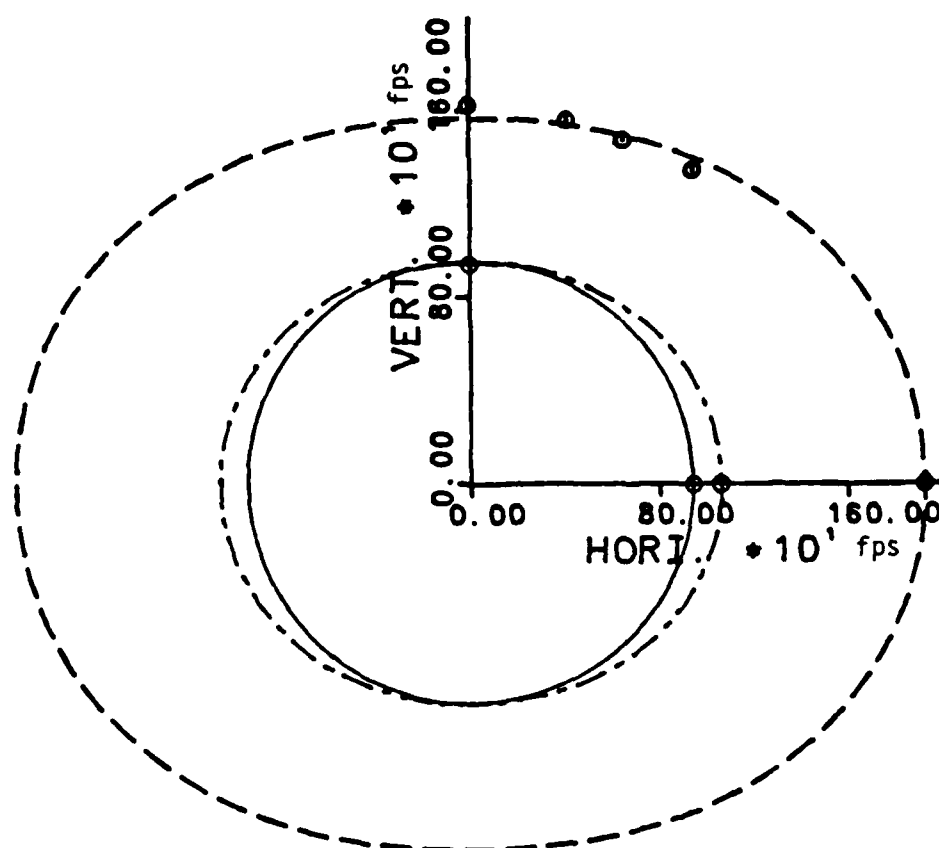
Wave fronts of the SH-wave are ellipsoids for both velocity and wave surfaces.

The effect of stress-induced anisotropy can be seen in Figs. 9.10 through 9.19. Figures 9.10 and 9.11 show the wave fronts for an isotropic pressure of 30 psi (206.7 kPa). As can be seen, structural anisotropy does not cause cusps in the SV-wave front under isotropic pressures from 15 to 30 psi (103.4 to 206.7 kPa) in this study. However, when both structural and stress-induced anisotropies are involved as in the BIA1Z and BIA2Z series of tests, cusps appear in SV-wave fronts for the wave surface as shown in Figs. 9.14 and 9.15 for BIA1Z and in Figs. 9.16 and 9.17 for BIA2Z. Consequently, one can see that cusps in the SV-wave front only appear in some types of cross-anisotropic material, but not all. The effect depends on the amount of the structural and stress-induced anisotropies.

9.8 COMPARISON WITH ISOTROPIC MODEL FOR NATURAL SOIL

In situ crosshole and downhole seismic tests are the methods most often employed to obtain wave velocities in geotechnical engineering. In the crosshole test, P- and SV-waves propagating horizontally are used. Velocities of these waves correspond to V_{PI} and V_{SA} (or V_{XX} , and V_{XZ}). V_{SI} is obtained if a mechanical torsional source is employed. V_{PA} and V_{SA} are obtained in the downhole test if true vertical wave propagation occurs.

To compare true values of Poisson's ratio and Young's modulus with those determined in a crosshole test with a torsional source, a pseudo-Poisson's ratio ν_1' is defined as:



--- P-WAVE
 — SV-WAVE
 --- SH-WAVE
 VELOCITY SURFACE
 ISO = 30 PSI
 C13(PSF) = 3698173.0
 ○ MEASURED DATA

Fig. 9.10 - Comparison of Velocity Surfaces with Measured
 S-Wave, P-Wave, and Oblique P-Wave Velocities
 Under Isotropic Confinement with $\bar{\sigma}_0 = 30$ psi

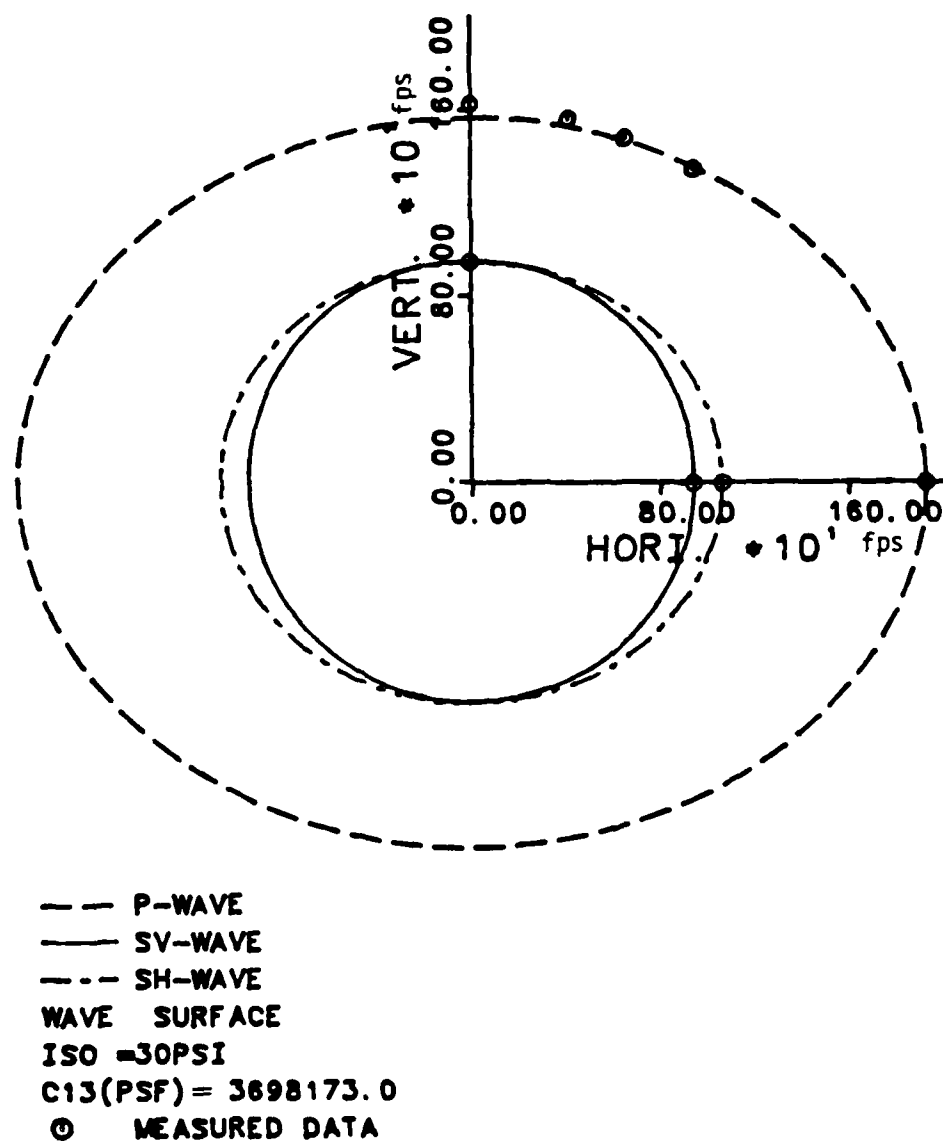


Fig. 9.11 - Comparison of Wave Surfaces with Measured S-Wave, P-Wave, and Oblique P-Wave Velocities Under Isotropic Confinement with $\bar{\sigma}_0 = 30$ psi

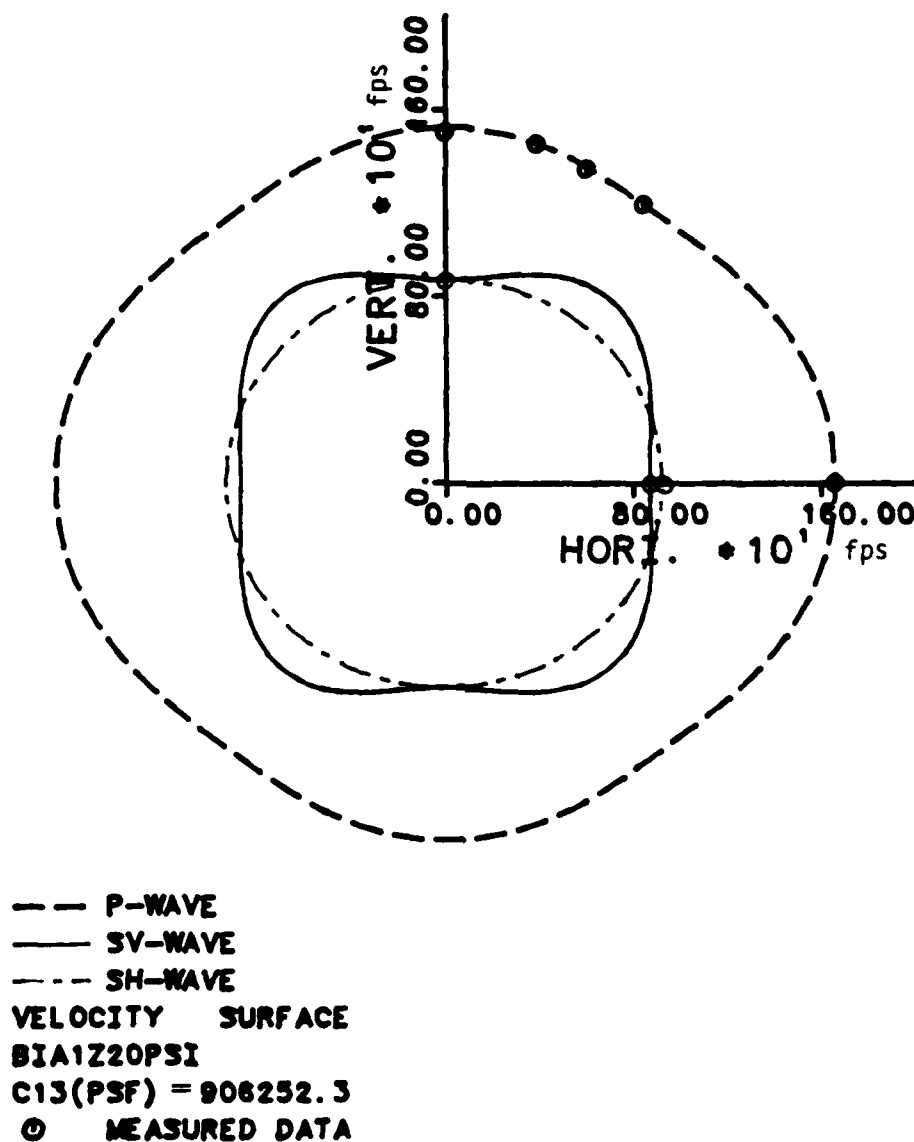


Fig. 9.12 - Comparison of Velocity Surfaces with Measured S-Wave, P-Wave, and Oblique P-Wave Velocities Under Biaxial Confinement BIA1Z with $\bar{\sigma}_z = 20$ psi

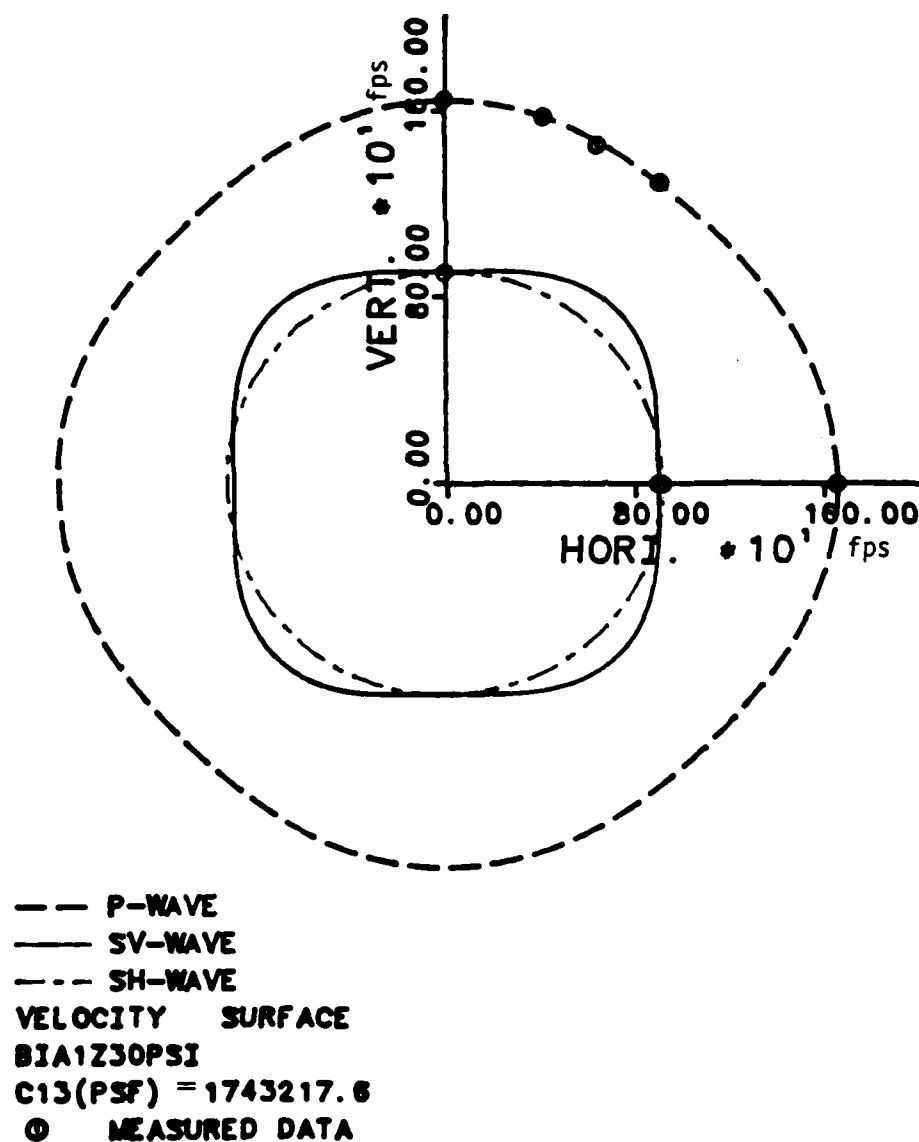


Fig. 9.13 - Comparison of Velocity Surfaces with Measured S-Wave, P-Wave, and Oblique P-Wave Velocities Under Biaxial Confinement BIA1Z with $\bar{\sigma}_z = 30$ psi

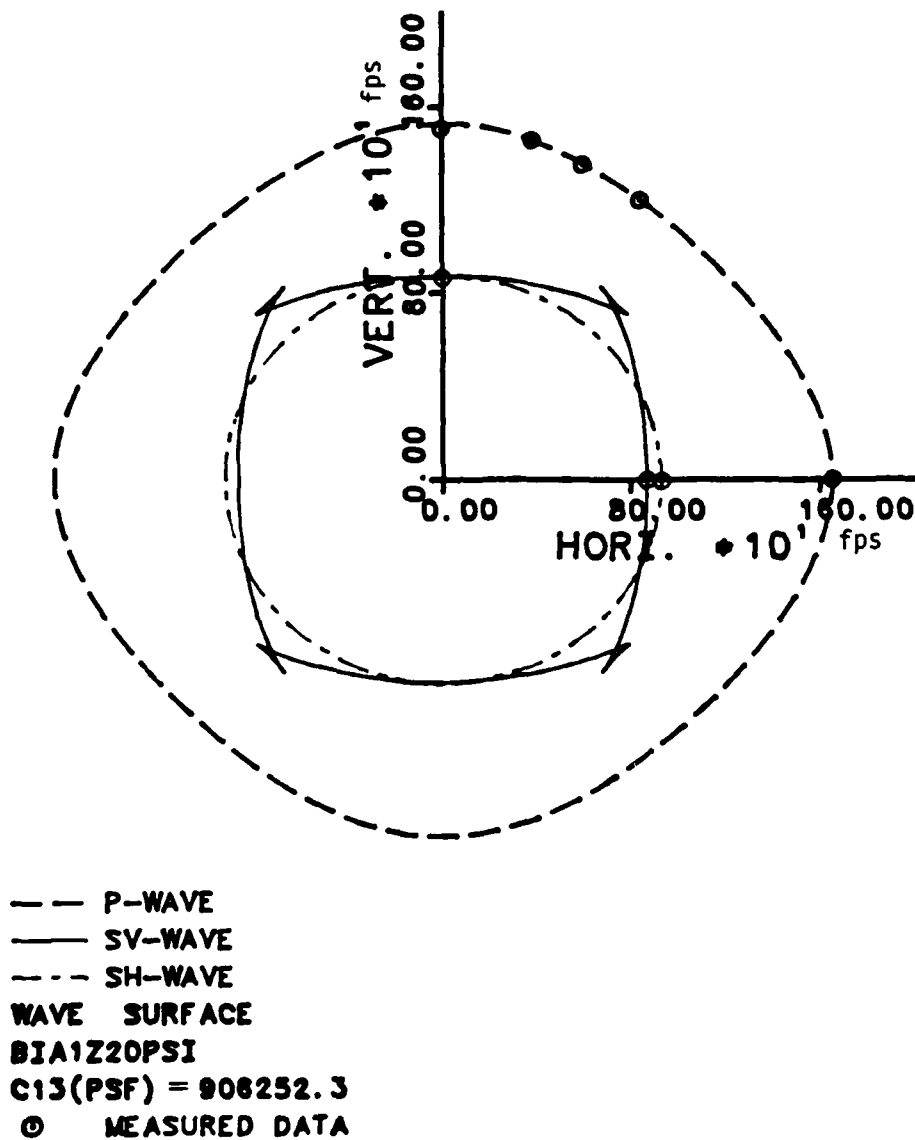


Fig. 9.14 - Comparison of Wave Surfaces with Measured S-Wave, P-Wave, and Oblique P-Wave Velocities Under Biaxial Confinement BIA1Z with $\bar{\sigma}_z = 20$ psi

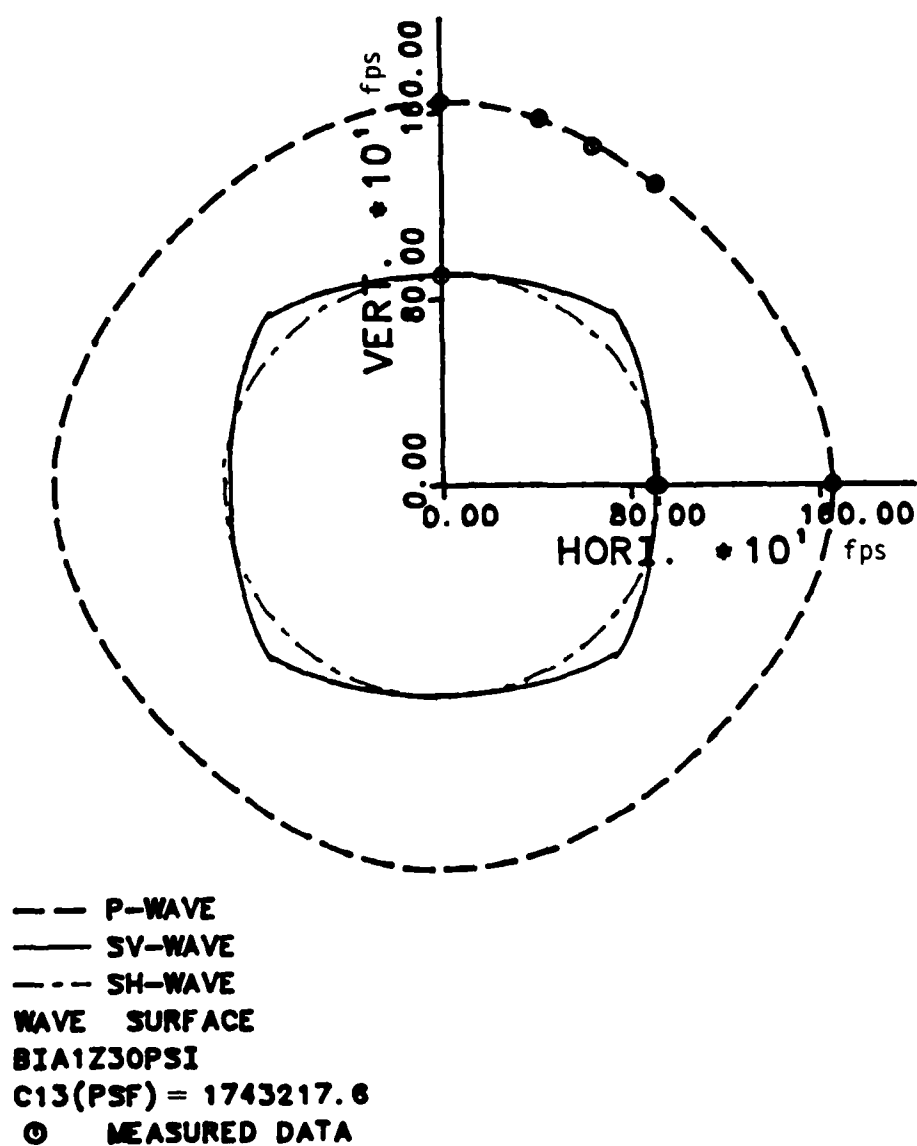


Fig. 9.15 - Comparison of Wave Surfaces with Measured S-Wave, P-Wave, and Oblique P-Wave Velocities Under Biaxial Confinement BIA1Z with $\bar{\sigma}_2=30$ psi

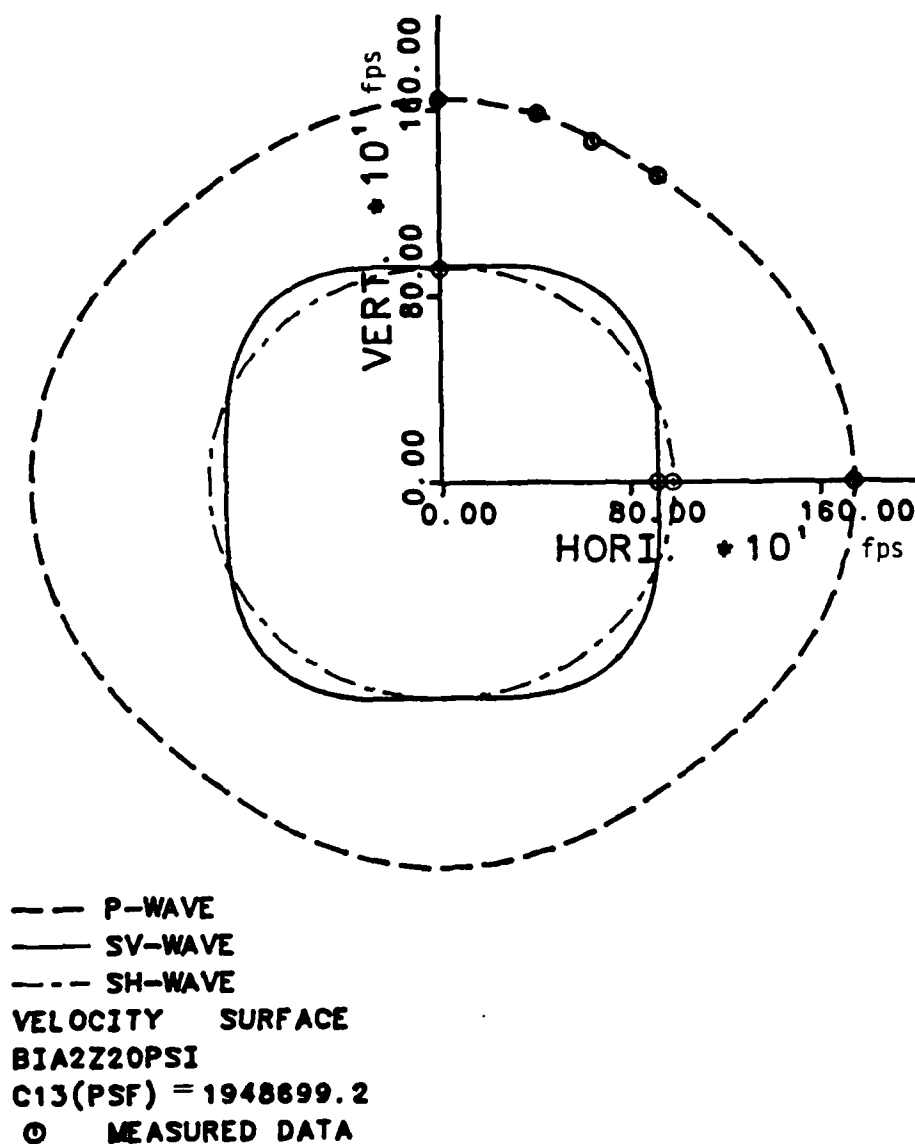


Fig. 9.16 - Comparison of Velocity Surfaces with Measured
 S-Wave, P-Wave, and Oblique P-Wave Velocities
 Under Biaxial Confinement BIA2Z with $\bar{\sigma}_x = \bar{\sigma}_y = 20$ psi

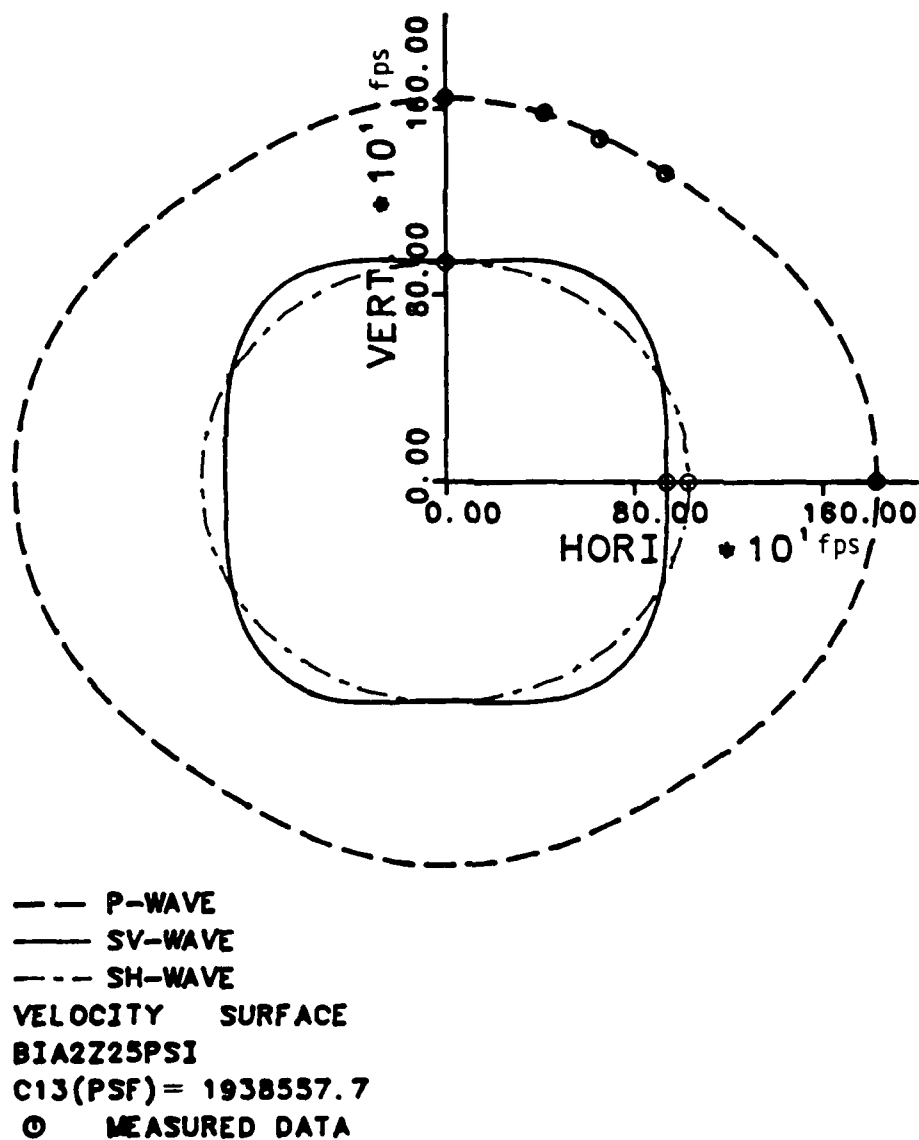


Fig. 9.17 - Comparison of Velocity Surfaces with Measured S-Wave, P-Wave, and Oblique P-Wave Velocities Under Biaxial Confinement BIA2Z with $\bar{\sigma}_x = \bar{\sigma}_y = 25$ psi

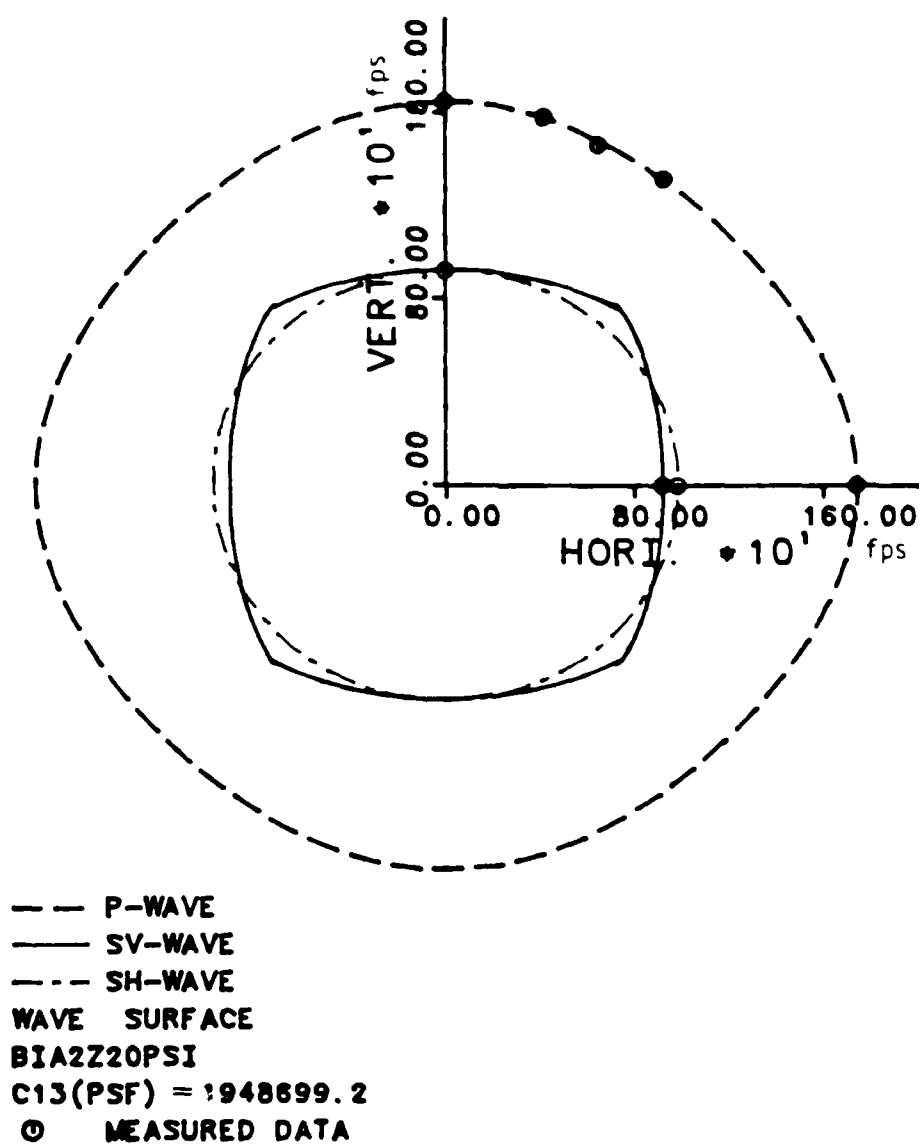


Fig. 9.18 - Comparison of Wave Surfaces with Measured
 S-Wave, P-Wave, and Oblique P-Wave Velocities
 Under Biaxial Confinement BIA2Z with $\bar{\sigma}_x = \bar{\sigma}_y = 20$ psi

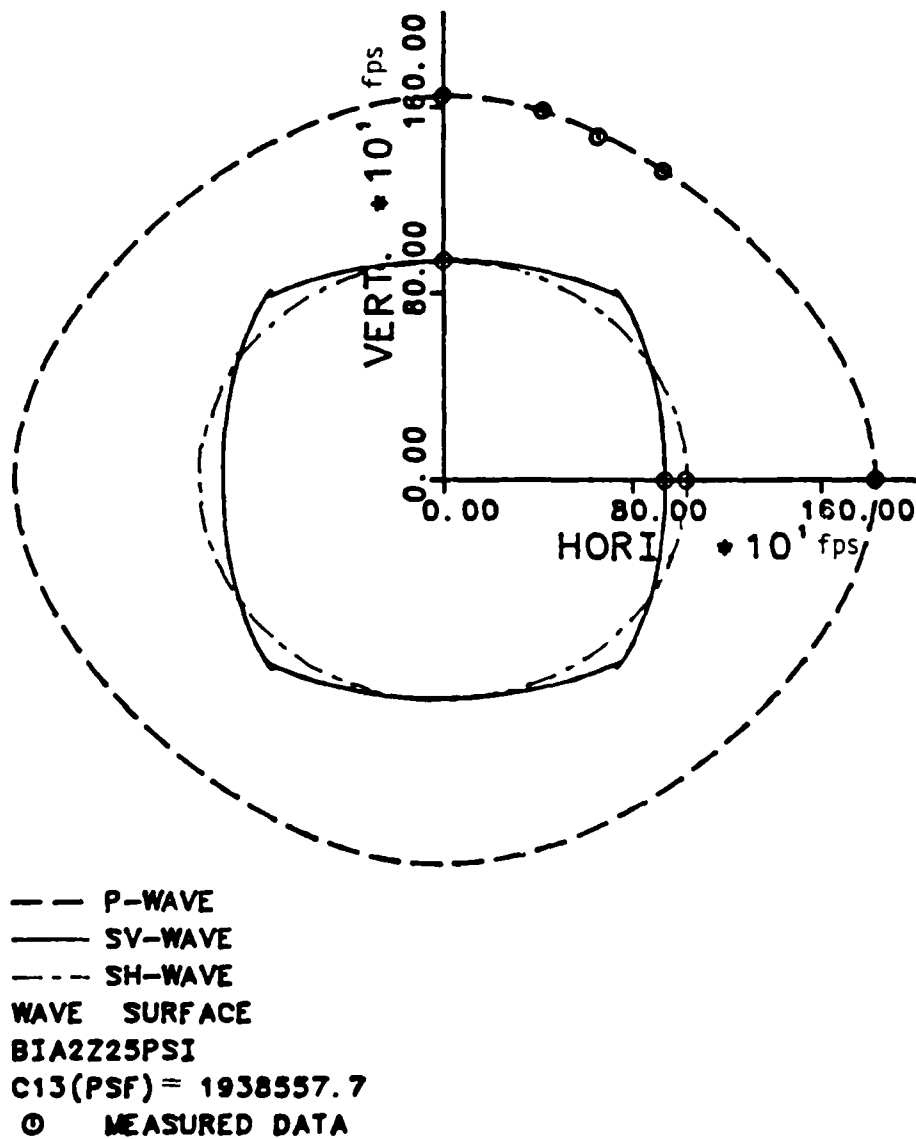


Fig. 9.19 - Comparison of Wave Surfaces with Measured
 S-Wave, P-Wave, and Oblique P-Wave Velocities
 Under Biaxial Confinement BIA2Z with $\bar{\sigma}_x = \bar{\sigma}_y = 25$ psi

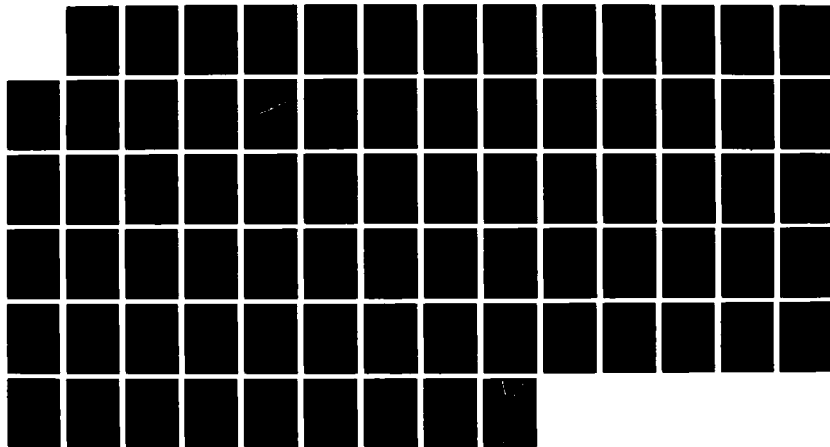
AD-A179 563

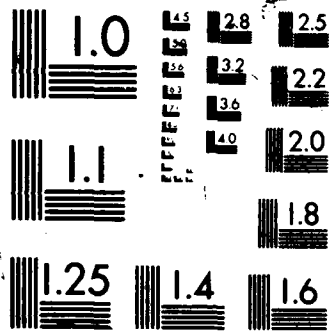
INVESTIGATION OF LOW-AMPLITUDE SHEAR WAVE VELOCITY IN
ANISOTROPIC MATERIAL. (U) TEXAS UNIV AT AUSTIN
GEOTECHNICAL ENGINEERING CENTER S H LEE ET AL. AUG 86
AFOSR-TR-87-0483 AFOSR-83-0062 F/G 8/13

4/4

UNCLASSIFIED

ML





XEROCOPY RESOLUTION TEST CHART

$$\nu_I' = [0.5(V_{PI}/V_{SA})^2 - 1]/[(V_{PI}/V_{SA})^2 - 1] \quad (9.23)$$

and a pseudo-Young's modulus, E_I' , is defined as:

$$E_I' = 2G(1 + \nu_I') \quad (9.24)$$

where G equals $\rho \cdot V_{SI}^2$. Likewise, a pseudo-Poisson's ratio, ν_A' , and a pseudo-Young's modulus, E_A' , can be obtained by substituting V_{PI} and V_{SA} (which are obtained from traditional crosshole tests with a vertical striking source) into Eqs. 2.5 and 2.6 to give:

$$\nu_A' = [0.5(V_{PI}/V_{SA})^2 - 1]/[(V_{PI}/V_{SA})^2 - 1] \quad (9.25)$$

$$E_A' = 2G(1 + \nu_A') \quad (9.26)$$

where $G = \rho V_{SA}^2$.

Pseudo-Young's moduli calculated by Eqs. 9.24 and 9.26 are listed in Table 9.6, while pseudo-Poisson's ratios from Eqs. 9.23 and 9.25 are listed in Table 9.7. The ratio of the pseudo-Young's modulus to the measured value ranges from 0.93 to 0.96 for E_I and 0.83 to 0.92 for E_A . The ratio of the pseudo-Poisson's ratio to the measured value varies from 0.74 to 0.82 for ν_I and 1.88 to 4.71 for ν_A . If Poisson's ratio is an important factor in a particular analysis, the assumption of an isotropic model for natural soil can give a fairly large error as shown by these results.

9.9 SUMMARY

For level soil deposits in which the vertical normal stress is a principal stress, a cross-anisotropic model is a more correct representation of the soil deposit than the often-used isotropic model. Five elastic constants are needed to describe such a cross-anisotropic medium. Four constants, C_{11} , C_{33} , C_{44} , and C_{66} , can be estimated by measuring P- and S-wave velocities along principle stress (x-, y-, and z-) directions. The fifth constant, C_{13} , is most easily evaluated by measuring the velocity of oblique P-waves. It is interesting to note that the upper limit of C_{13} generally increases with the mean effective stress.

Table 9.6 - Comparison of Young's Modulus Estimated by Cross-Anisotropic and Isotropic Models

Test Type	Confinement, psi			Measured Young's Modulus, psf		Young's Modulus by Isotropic Equation, psf	
	$\bar{\sigma}_x$	$\bar{\sigma}_y$	$\bar{\sigma}_z$	E_I	E_A	E'_I	E'_A
ISO*	15	15	15	6932468.1	5170828.9	6747813.9	5724143.3
	20	20	20	7717513.1	5527886.5	7599179.4	6376691.9
	25	25	25	8240182.9	5590120.6	8332190.3	6932680.4
	30	30	30	8822650.9	5734019.6	8982844.4	7422112.3
BIA1	15	15	15	7264771.3	6353214.6	6763650.4	5865253.4
	15	15	20	7253807.3	7032580.8	6763650.4	6130353.1
	15	15	25	7213634.7	7507710.4	6763650.4	6339083.1
	15	15	30	7142357.3	7792492.7	6763650.4	6511046.5
BIA2	15	15	30	7036497.1	7704624.7	6722422.2	6392825.7
	20	20	30	7979912.6	7720027.6	7615628.2	6847126.0
	25	25	30	8819582.2	7787693.0	8389390.7	7210474.8
	30	30	30	9541537.5	7772743.2	9079600.5	7515195.3

* Isotropic confinement

Table 9.7 - Comparison of Poisson's Ratio Estimated by Cross-Anisotropic and Isotropic Models

Test Type	Confinement, psi			Measured Poisson's Ratio		Poisson's Ratio by Isotropic Equation	
	$\bar{\sigma}_x$	$\bar{\sigma}_y$	$\bar{\sigma}_z$	ν_I	ν_A	ν_I'	ν_A'
ISO	15	15	15	.30456	.24450	.26982	.32827
	20	20	20	.29443	.27334	.27459	.33412
	25	25	25	.26408	.34016	.27820	.33848
	30	30	30	.25824	.37394	.28109	.34194
BIA1	15	15	15	.36533	.06859	.27115	.32282
	15	15	20	.36327	.08044	.27115	.30906
	15	15	25	.35572	.10444	.27115	.29745
	15	15	30	.34233	.13800	.27115	.28727
BIA2	15	15	30	.32243	.15104	.26341	.28551
	20	20	30	.32447	.15847	.26401	.30663
	25	25	30	.32931	.15638	.26447	.32121
	30	30	30	.32920	.16540	.26485	.33210

The variation of C_{13} influences the shape of both the velocity and wave surfaces, especially in the principal stress directions and at 45 degrees to the principal axes. Measured body wave velocities represent ray velocities. Ray velocities have to be converted to phase velocities to calculate the velocity surface for a cross-anisotropic medium. The greatest distinction between ray and phase velocities generally appears at 45-degree angles from the principal axes where cusps in the velocity surface may form.

Variations in C_{13} also affect the relationship between shear wave velocities in isotropic and anisotropic planes. As shown in Figs. 9.7 to 9.9, V_{SA} was changed from being less than V_{SI} to being larger than V_{SI} as C_{13} varied. This influence indicates that one should not try to estimate the oblique P- or S-wave velocities with only the four constants (C_{11} , C_{33} , C_{44} , and C_{66}) of a cross-anisotropic material.

In a cross-anisotropic medium, Young's moduli (E_I and E_A) and Poisson's ratios (ν_I and ν_A) for isotropic and anisotropic planes, respectively, can be estimated with the five constants as discussed in Sections 9.5 and 9.6. It is interesting to note that the value of Poisson's ratio in the isotropic plane (ν_I) was generally smaller than the value in the anisotropic plane (ν_A) for this sand sample. It is also interesting to note that ν_A may be greater than 0.5 for a cross-anisotropic material.

CHAPTER TEN

APPLICATIONS

10.1 INTRODUCTION

The "three-individual-stresses" method developed in Chapters Six and Seven for shear wave velocity is applied to the estimation of the coefficient of earth pressure at rest (K_0) in this chapter. In addition, this method is used to understand better wave velocity measurements in the crosshole and downhole tests and stiffness values determined in biaxial resonant column tests. Dynamic stiffnesses used in geotechnical earthquake engineering estimated through the "three-individual-stresses" method and the "mean-effective-stress" method are also compared and discussed herein.

10.2 ESTIMATION OF COEFFICIENT OF EARTH PRESSURE AT REST

Field measurements of the coefficient of earth pressure at rest (K_0) have been extremely difficult and expensive to conduct. The conventional pressuremeter (Menaud, 1967), the hydraulic fracturing method (Bjerrum and Andersen, 1972), the self-boring pressuremeter (Jezequel, 1972; and Wroth and Hughes, 1972), the camkometer (Baguelin, et al., 1974), and the total stress cell (Massarsch, 1974) have been developed for the in situ measurement of K_0 . Limitations of these five methods are mostly due to disturbance of soil around the instruments (Massarsch, et al., 1975; and Massarsch, et al., 1976).

Since interval P- and S-wave velocities can be measured between boreholes, the influence of locally disturbed soil around the boreholes has a minor effect on velocities (Hoar, 1982). Therefore, soil disturbance adjacent to the borehole would have a smaller effect on the estimation of K_0 if seismic methods could be employed for such a use.

10.2.1 P-WAVE METHOD

Because compression wave velocity is a function of the effective principal stress in the direction of wave propagation ($\bar{\sigma}_a$), compression wave velocity measured in the horizontal direction (V_{PI}) in a crosshole test can be expressed as:

$$V_{PI} = C_1 \bar{\sigma}_a^{m_a} \quad (10.1)$$

where $\bar{\sigma}_a (= K_0 \bar{\sigma}_v)$. Therefore, the earth pressure at rest, K_0 , can be obtained, in principle, simply by rearranging Eq. 10.1 as:

$$K_0 = [(V_{PI}/C_1)^{1/ma}] / \bar{\sigma}_v \quad (10.2)$$

The tests in this study were all conducted after the applied confining pressures were balanced. Therefore, the ratio of applied horizontal to vertical pressure was equal to K_0 . As such, the use of Eq. 10.2 was examined by calculating values of K_0 from measured P-wave velocities. These results are presented in Table 10.1. Values of C_1 and ma used for P-wave velocities in the x-direction (V_{xx}) under biaxial confinement with one increment only (BIA1) were 369 and 0.20 (rounded from 0.195), respectively, from Chu et al (1984), whereas $C_1 = 336$ and $na = 0.20$ (rounded from 0.203) were used for V_{xx} in BIA2 (biaxial confinement with two increments).

Although scattering exists in the values of K_0 estimated from Eq. 10.2, the average values of estimated K_0 listed in Table 10.1 (0.34, 0.47, 0.72, 0.97, 1.49, 2.09, and 2.57) are close to the value of applied K_0 (0.38, 0.50, 0.75, 1.00, 1.33, 2.00, and 2.67) as expected. (This really represents a "circular" comparison since measured P-wave velocities were used to determine Eq. 10.1. However, the comparisons do illustrate the general point.) This suggests that a regression equation of P-wave velocity could be used to estimate K_0 if enough data points are obtained for the regression analysis and if the soil deposit is reasonably uniform and uncemented.

10.2.2 SHEAR WAVE METHOD

Since most sedimentation results in developing a cross-anisotropic material, the horizontal plane in sedimented deposits can often be treated as the isotropic plane, and the vertical axis is the axis of symmetry. Let the xy-plane be the isotropic plane, the z-axis be the axis of symmetry as shown in Figs. 2.4 and 2.5, and K_0 be the coefficient of earth pressure at rest. Then $\bar{\sigma}_x$ will be the same as $\bar{\sigma}_y$, and both will be equal to $K_0 \bar{\sigma}_z$. Therefore Eq. 6.20 can be expressed as Eq. 10.3 below for the velocity of the SV-wave generated in the crosshole test by a vertical impulsive source:

$$V_{SA} = C_A (K_0 \bar{\sigma}_z)^{na} (\bar{\sigma}_z)^{nb} (K_0 \bar{\sigma}_z)^{nc} \quad (10.3a)$$

or

Table 10.1 - Comparison Between Applied and Calculated Coefficient of Earth Pressure at Rest, K_0 , from Compression Wave Velocity, V_{xx}

Effective Horizontal Confining Pressure $\bar{\sigma}_H$, psi	Effective Vertical Confining Pressure $\bar{\sigma}_V$, psi	Compression Wave Velocity V_{xx} , fps	Applied $K_0 = \frac{\bar{\sigma}_H}{\bar{\sigma}_V}$	Calculated K_0 by Eq. 10.2	Test No.
15	40	1614	0.38	0.34	13
15	40	1615	0.38	0.34	19
			** AVG = 0.34		
15	30	1619	0.50	0.45	12
15	30	1614	0.50	0.45	20
20	40	1659	0.50	0.46	14
20	40	1698	0.50	0.51	18
			** AVG = 0.47		
15	20	1627	0.75	0.70	11
30	40	1815	0.75	0.71	15
30	40	1837	0.75	0.75	17
			** AVG = 0.72		
15	15	1624	1.00	0.92	10
15	15	1642	1.00	0.98	48
15	15	1614	1.00	0.89	49
15	15	1625	1.00	0.93	57
15	15	1615	1.00	0.89	58
15	15	1607	1.00	0.87	60
40	40	1986	1.00	1.10	16
15	15	1604	1.00	1.03	50
20	20	1631	1.00	0.84	51
30	30	1781	1.00	0.86	52
40	40	1968	1.00	1.06	54
30	30	1857	1.00	1.06	55
20	20	1744	1.00	1.16	56
15	15	1625	1.00	1.10	57
			** AVG = 0.97		
20	15	1781	1.33	1.48	39
20	15	1776	1.33	1.46	47
40	30	1999	1.33	1.52	43
			** AVG = 1.49		
30	15	1906	2.00	2.09	40
30	15	1892	2.00	2.02	46
40	20	1977	2.00	2.16	42
			** AVG = 2.09		
40	15	1995	2.67	2.65	41
40	15	1971	2.67	2.49	45
			** AVG = 2.57		

$$V_{SA} = C_A(\bar{\sigma}_z)^{na+nb+nc} (K_o)^{na+nc} \quad (10.3b)$$

The coefficient of earth pressure at rest can, in principle, be estimated from:

$$K_o = [(V_{SA}/C_A)(\bar{\sigma}_z)^{-(na+nb+nc)}]^{1/(na+nc)} \quad (10.4)$$

With the values for the parameters of the constants and slopes listed in Table 6.41, Eq. 10.4 can be rewritten for the tests under biaxial confinements with either one principal stress or two principal stresses varying as:

$$K_o = [(V_{xz}/185.6)(\bar{\sigma}_z)^{-0.198}]^{10.753} \quad \text{for BIA1Z} \quad (10.5a)$$

$$K_o = [(V_{yz}/304.7)(\bar{\sigma}_z)^{-0.143}]^{15.385} \quad \text{for BIA1Z} \quad (10.5b)$$

$$K_o = [(V_{xz}/258.8)(\bar{\sigma}_z)^{-0.156}]^{13.158} \quad \text{for BIA2Z} \quad (10.5c)$$

$$K_o = [(V_{yz}/223.6)(\bar{\sigma}_z)^{-0.187}]^{13.699} \quad \text{for BIA2Z} \quad (10.5d)$$

$$K_o = [(V_{xz}/185.6)(\bar{\sigma}_z)^{-0.198}]^{13.158} \quad \text{for BIA1X} \quad (10.5e)$$

$$K_o = [(V_{yz}/304.7)(\bar{\sigma}_z)^{-0.143}]^{12.658} \quad \text{for BIA1Y} \quad (10.5f)$$

The notation after BIA1 (X, Y or Z) indicates the direction in which the confining pressure was varied. For BIA2, the notation after BIA2 indicates the direction in which the confining pressure remained constant.

The values of estimated K_o (0.36, 0.47, 0.74, 1.02, 1.36, 1.65, and 2.80) calculated by Eq. 10.5 for each test condition are compared with the applied K_o conditions in Table 10.2. Significant scattering in calculated values of K_o occurs, but the scatter is somewhat random since Eq. 10.5 is a regression result. Nevertheless, average values of calculated K_o are nearly the same as the applied values (as expected because of the "circular" loop in this comparison). Consequently, shear wave velocity can be used to estimate in-situ K_o by a crosshole test once the values of C_A , na , nb , and nc for the given soil are known. Of course, this is the key point which often times is impossible to determine.

Table 10.2 - Comparison Between Applied and Calculated Coefficient of Earth Pressure at Rest, K_0 , by Shear Wave Velocities, V_{xz} and V_{yz}

Effective Horizontal Confining Pressure $\bar{\sigma}_H$, psi	Effective Vertical Confining Pressure $\bar{\sigma}_V$, psi	Shear Wave Velocity V_{HV} fps	Applied $K_0 = \frac{\bar{\sigma}_H}{\bar{\sigma}_V}$	Calculated K_0 by Eq. 10.5	Test No.
15	40	942	0.38	0.38	13*
15	40	952	0.38	0.22	13**
15	40	961	0.38	0.47	19*
			*** AVG = 0.36		
15	30	906	0.50	0.46	12*
15	30	948	0.50	0.38	12**
15	30	946	0.50	0.73	20*
20	40	970	0.50	0.60	14*
20	40	940	0.50	0.08	14**
20	40	982	0.50	0.71	18*
20	40	964	0.50	0.12	18**
			*** AVG = 0.47		
15	20	852	0.75	0.57	11*
15	20	892	0.75	0.37	11**
15	20	927	0.75	1.40	21*
15	20	974	0.75	1.43	21**
30	40	982	0.75	0.71	15*
30	40	971	0.75	0.13	15**
30	40	1017	0.75	1.13	17*
30	40	994	0.75	0.18	17**
			*** AVG = 0.74		
15	15	835	1.00	0.84	10*
15	15	876	1.00	0.52	10**
15	15	880	1.00	1.47	22*
15	15	943	1.00	1.63	22**
40	40	1030	1.00	1.34	16*
40	40	1032	1.00	0.29	16**
			*** AVG = 1.02		
20	15	861	1.33	1.16	40*
20	15	884	1.33	1.53	46*
20	15	905	1.33	0.88	49**
20	15	957	1.33	1.88	58**
			*** AVG = 1.36		
30	15	899	2.00	1.82	40*
30	15	912	2.00	2.13	46*
30	15	918	2.00	1.07	49**
30	15	944	2.00	1.56	58**
			*** AVG = 1.65		
40	15	923	2.67	2.41	40*
40	15	914	2.67	2.18	46*
40	15	955	2.67	1.83	49**
40	15	1026	2.67	4.77	58**
			*** AVG = 2.80		

* V_{xz} ** V_{yz}

From Eq. 10.3b, V_{xz} (or V_{yz}) will increase in a power function as depth increases in a uniform soil layer in which there is a constant K_o . On the other hand, a change in the $V_{xz} - \bar{\sigma}_V$ curve will reflect a variation in the soil layer which may be due to either the same soil material with different K_o 's or a new soil layer with different stiffness reflected by the constant C_A .

By adding a mechanical torsional source to the crosshole test, the shear wave velocity V_{SI} as well as V_{SA} (which is obtained by a regular vertical impulse source) can be measured (Hoar, 1982). The equation for shear wave velocity in the isotropic plane for this case is:

$$V_{SI} = C_I \bar{\sigma}_a^{na} \bar{\sigma}_b^{nb} \bar{\sigma}_c^{nc} \quad (10.6)$$

which can be rewritten as:

$$V_{SI} = C_I (K_o \bar{\sigma}_V)^{na} (K_o \bar{\sigma}_V)^{nb} (\bar{\sigma}_V)^{nc} \quad (10.7)$$

or

$$V_{SI} = C_I (\bar{\sigma}_V)^{na+nb+nc} (K_o)^{na+nb} \quad (10.8)$$

By substituting the values in Tables 6.4 through 6.6 into the ratio of V_{SI} to V_{SA} , the following is obtained:

$$R = V_{SI}/V_{SA} = 0.91(\bar{\sigma}_V)^{0.022} (K_o)^{0.12} \quad (10.9)$$

or

$$K_o = [R/(0.91\bar{\sigma}_V^{0.022})]^{1/0.12} \quad (10.10)$$

For estimating K_o , Eq. 10.10 has no advantage over Eqs. 10.5 or 10.8. In addition, it contains an additional term (R). But, Eq. 10.10 can be used to check one of the shear wave velocities once the other shear wave velocity, K_o and $\bar{\sigma}_V$ are obtained. For instance, a normally consolidated clay with $K_o = 0.35$ will result in a relationship between R and $\bar{\sigma}_V$ as follows:

$$R = 0.80(\bar{\sigma}_V)^{0.022} \quad (10.11)$$

An overconsolidated clay with $K_o = 3$ will yield a trend as shown:

$$R = 1.04(\bar{\sigma}_v)^{0.022} \quad (10.12)$$

Hoar and Stokoe (1980) have shown a variation of R from 0.83 to 1.16 for depths ranging from 3 to 10 ft in a soft clay (Fig. 10.1). These values of R give values of K_o from 0.16 to 3.4 at depths from 3 to 10 ft by using Eq. 10.10. However, it is necessary to point out that the values of n_a , n_b , n_c , C_I and C_A in clay are most likely different from those in this study. The values 0.16 to 3.4 for K_o are only examples to show the application of Eq. 10.10. In addition, the variation of R in Eq. 10.9 is very sensitive to K_o . Consequently, Eqs. 10.4 or 10.10 are only general equations for estimating K_o in soils. The parameters must be measured directly for the soils being studied.

With the same algorithm used for crosshole test, the shear wave velocities, V_{zx} and V_{zy} which are obtainable from a downhole test, can be used to estimate the coefficient of earth pressure at rest, K_o , as well. However, it is assumed that the waves are propagating vertically, not at some inclined angle.

From Eq. 6.20 and Table 6.41, the following equations are employed for this purpose:

$$K_o = [V_{zx}/243.3 (\bar{\sigma}_z)^{-0.161}]^{16.3934} \dots \text{for BIA1Z} \quad (10.13a)$$

$$K_o = [V_{zy}/180.0 (\bar{\sigma}_z)^{-0.198}]^{10.7527} \dots \text{for BIA1Z} \quad (10.13b)$$

$$K_o = [V_{zx}/210.5 (\bar{\sigma}_z)^{-0.178}]^{14.2857} \dots \text{for BIA2Z} \quad (10.13c)$$

$$K_o = [V_{zy}/256.6 (\bar{\sigma}_z)^{-0.154}]^{16.9492} \dots \text{for BIA2Z} \quad (10.13d)$$

$$K_o = [V_{zx}/210.5 (\bar{\sigma}_z)^{-0.178}]^{12.3457} \dots \text{for BIA1X} \quad (10.13e)$$

$$K_o = [V_{zy}/256.6 (\bar{\sigma}_z)^{-0.154}]^{9.6154} \dots \text{for BIA1X} \quad (10.13f)$$

The calculated and applied values of K_o are compared in Table 10.3. The scattering is shown in the calculated results, and, again, the average calculated results are nearly the same as the applied conditions. A detailed examination reveals that the shear wave measurements of V_{xz} and V_{yz} are better than V_{zx} and V_{zy} in this study since less scattering and more usable data were found in the former tests.

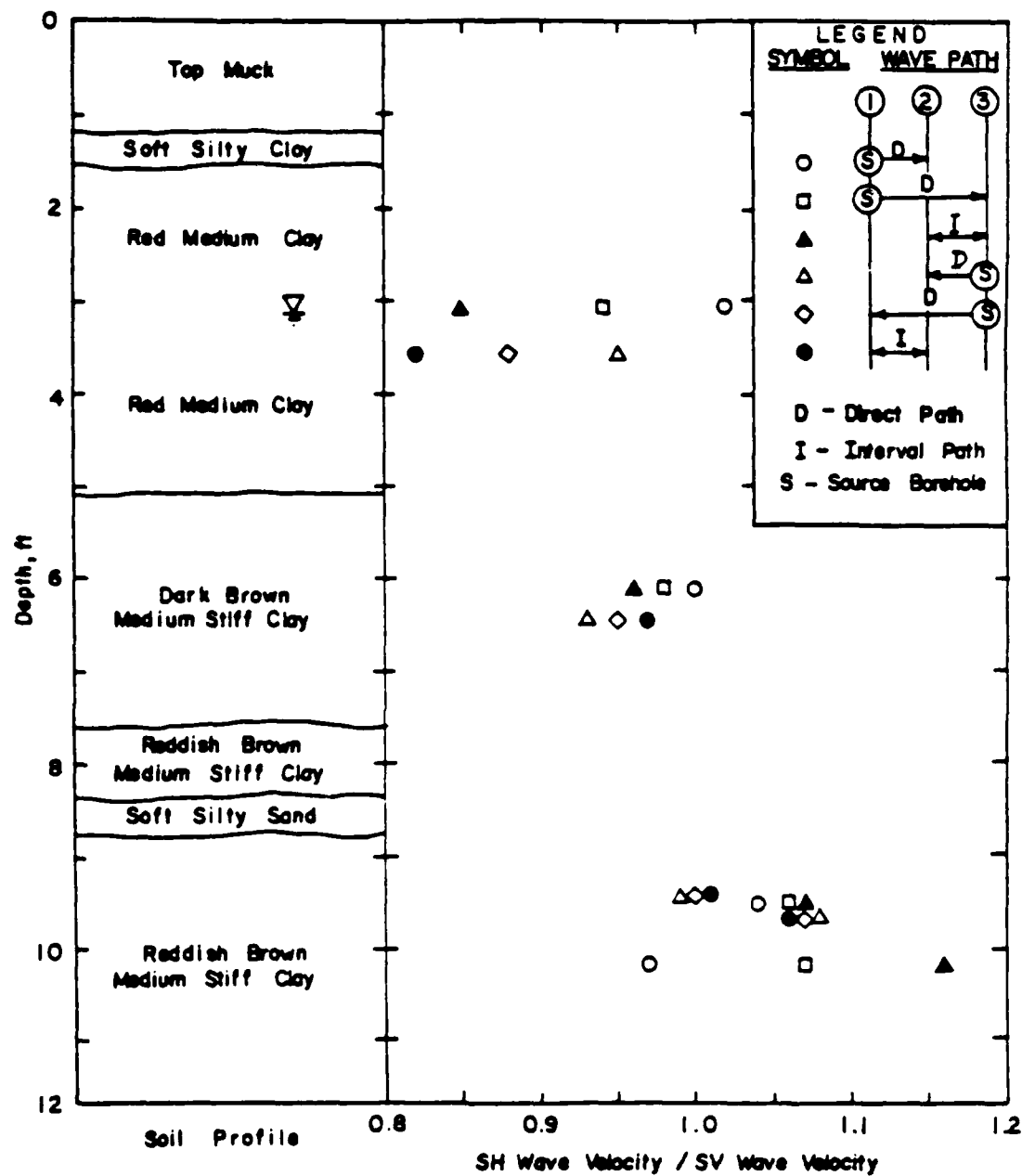


Fig. 10.1 - Ratio of SH- to SV-Wave Velocities at a Soft Clay Site
 (from Hoar and Stokoe, 1980b)

Table 10.3 - Comparison Between Applied and Calculated Coefficient of Earth Pressure at Rest, K_0 , from Shear Wave Velocities, V_{zx} and V_{zy}

Effective Horizontal Confining Pressure $\bar{\sigma}_H$, psi	Effective Vertical Confining Pressure $\bar{\sigma}_V$, psi	Shear Wave Velocity V_{VH} fps	Applied $K_0 = \frac{c_H}{\bar{\sigma}_V}$	Calculated K_0 by Eq. 10.13	Test No.
15	40	905	0.38	0.27	13*
15	40	913	0.38	0.38	13**
15	40	942	0.38	0.53	19**
			*** AVG = 0.39		
15	30	851	0.50	0.21	12*
15	30	890	0.50	0.53	12**
15	30	916	0.50	0.72	20**
20	40	930	0.50	0.46	14*
20	40	957	0.50	0.74	14**
20	40	955	0.50	0.66	18*
			*** AVG = 0.55		
15	20	846	0.75	0.56	11*
15	20	848	0.75	0.74	11**
15	20	878	0.75	1.08	21**
30	40	962	0.75	0.74	15*
30	40	959	0.75	0.78	15**
30	40	956	0.75	0.67	17*
30	40	955	0.75	0.72	17**
			*** AVG = 0.76		
15	15	821	1.00	0.72	10*
15	15	828	1.00	1.06	10**
40	40	990	1.00	1.10	16*
40	40	988	1.00	1.28	16**
			*** AVG = 1.04		
20	15	846	1.33	1.36	39*
20	15	829	1.33	1.05	47**
			*** AVG = 1.21		
30	15	878	2.00	2.14	40*
30	15	877	2.00	1.57	56**
			*** AVG = 1.86		
40	15	909	2.67	3.28	41*
40	15	886	2.67	2.40	45**
40	15	898	2.67	1.97	50*
			*** AVG = 2.55		

* V_{zx}

** V_{zy}

10.2.3 K_0 FROM A COMBINATION OF BODY WAVE VELOCITIES

In the previous two sections, the coefficient of earth pressure at rest has been estimated from velocity measurements of only one body wave, P or S. In addition, the implicit assumptions have been made that: the body wave is polarized along principal stress directions, the horizontal stress is one of the principal stresses, a cross-anisotropic model is a good representation of the site and little or no cementation exists in the soil. Obviously, a better picture of the stress state can be obtained if a combination of P- and S-waves is used and if polarized and oblique waves are measured. For instance, if one could develop a combination of velocity surfaces for P- SV- and SH-waves like the ones shown in Fig. 9.12, then a better picture of the stress state could be developed in comparison with that developed from a single body wave. In addition, a complete picture of the velocity surfaces also permits orientation of the stress state to be determined.

Many problems will occur in applying this approach in the field. Variability in the soil, in the stress state and in structural anisotropy will cause complications. Elimination of measurement of the P-wave in the soil skeleton in saturated soils will also compound such an application. However, seismic wave velocities do have the potential to help evaluate stress state, and further investigations are warranted.

10.3 IN-SITU SEISMIC SURVEYS

Because of the cost of seismic testing, one-borehole tests such as the downhole, in-hole, bottom-hole, or up-hole tests are often preferred by engineers and geophysicists. As such, wave velocities are measured for waves travelling in (essentially) the vertical plane. Wave velocities from one-borehole tests are then assumed implicitly to be equal to those from multi-borehole tests, like the crosshole test, because an isotropic model is used. In some cases, attempts have been made to correlate wave velocities from one-borehole tests to multi-borehole (crosshole) tests (Robertson et al, 1985; and Bachman, 1983), and from downhole tests to refraction surveys (Feng et al, 1976). From the cross-anisotropic model discussed in Chapter Nine, an improved understanding of how to analyze and compare these test results can be developed. Several important considerations are as follows:

1. A directional source is important in a seismic survey, i.e., a polarized wave signal is necessary. One should then attempt to keep the

directions of particle motion and wave propagation parallel to principal stress directions as much as possible unless specifically trying to measure oblique waves.

2. The angle between the borehole and the ray path (θ) is an important variable which must be considered when propagating body waves through natural soil.
3. The body wave velocities of most concern are V_{PI} , V_{PA} , V_{SI} , and V_{SA} , and these velocities relate to only four of the five independent constants used to describe a cross-anisotropic medium.
4. If a polarized wave source is used, V_{SA} and V_{PA} can be obtained from one-borehole tests with vertical boreholes. For multi-borehole tests, V_{SI} , V_{SA} , and V_{PI} can be measured. Oblique P- or S-waves can also be detected in both types of tests.
5. Oblique P- or SV-wave velocities can be used for estimating the fifth independent constant of a cross-anisotropic material. The value of the angle (θ) between the borehole and the ray path must be carefully controlled.
6. Since V_{PI} , V_{PA} , V_{SI} , and V_{SA} are all independent variables, the ratio of the pair of P-wave velocities (V_{PI} and V_{PA}) and the ratio of the pair of S-wave velocities (V_{SI} and V_{SA}) are not necessarily the same and vary from site to site. The scattering in the crosshole and downhole test data may, hence, be a real characteristic of the soils.
7. When an earthquake is used as a source, reflection and refraction prospecting can be employed to measure wave velocities of soil layers on a very large scale (Yu and Tsai, 1981; and Liaw and Yeh, 1983). Waves which propagate in isotropic or anisotropic planes should be measured and analyzed separately using 3-D sensors.

10.4 RESONANT COLUMN TESTS

10.4.1 STRUCTURAL ANISOTROPY

From Eqs. 9.22 and 9.23 and Table 9.2 (with a value of mass density of the sand of 3.16 slugs/ft^3), shear moduli for isotropic and anisotropic planes under isotropic confinement in this sand are:

$$G_I = 126,460 \bar{\sigma}_0^{0.40} \quad (\text{psf}) \quad (10.14a)$$

$$G_A = 138,032 \bar{\sigma}_o^{0.37} \quad (\text{psf}) \quad (10.14b)$$

A series of resonant column tests performed on this sand by Knox et al (1982) and Stokoe and Ni (1985) resulted in Eqs. 10.15 and 10.16, respectively, for isotropic confining pressure conditions as follows:

$$G_{OS} = 58,794 \bar{\sigma}_o^{0.48} \quad (\text{psf}) \quad (10.15)$$

$$G_{OS} = 63,757 \bar{\sigma}_o^{0.45} \quad (\text{psf}) \quad (10.16a)$$

$$G_{OH} = 81,569 \bar{\sigma}_o^{0.44} \quad (\text{psf}) \quad (10.16b)$$

where G_{OS} is the maximum shear modulus determined with solid samples, and G_{OH} is for hollow samples.

The maximum shear modulus for sand under isotropic confinement can be estimated with Eq. 2.51 (suggested by Hardin, 1978) as follows:

$$G_{\max} = [C \cdot OCR^k] / (0.3 + 0.7 e^2) P_a^{1-n} \bar{\sigma}_o^n \quad (10.17)$$

where:

G_{\max} = shear modulus in desired units,

C = dimensionless constant,

OCR = overconsolidation ratio,

k = factor related to soil plasticity,

P_a = atmospheric pressure in same units as G_{\max} ,

e = void ratio,

$\bar{\sigma}_o$ = mean effective principal stress in same units as G_{\max} , and

n = slope of $\log G - \log \bar{\sigma}_o$ relationship.

With values of $k = 0$, $e = 0.64$, $P_a = 2116.8$ psf, $C = 625$, and $n = 0.5$ as suggested by Hardin (1978) for dry sand, Eq. 10.17 becomes:

$$G_{\max} = 49,010 \bar{\sigma}_o^{0.5} \quad (\text{psf}) \quad (10.18)$$

Values of shear moduli from Eqs. 10.14 through 10.18 with mean effective stresses equaling 1440, 2160, 2880, 4320, and 5760 psf (68.9, 103.4, 137.8, 206.7, and 275.6 kPa) are shown in Fig. 10.2 in order to compare these values

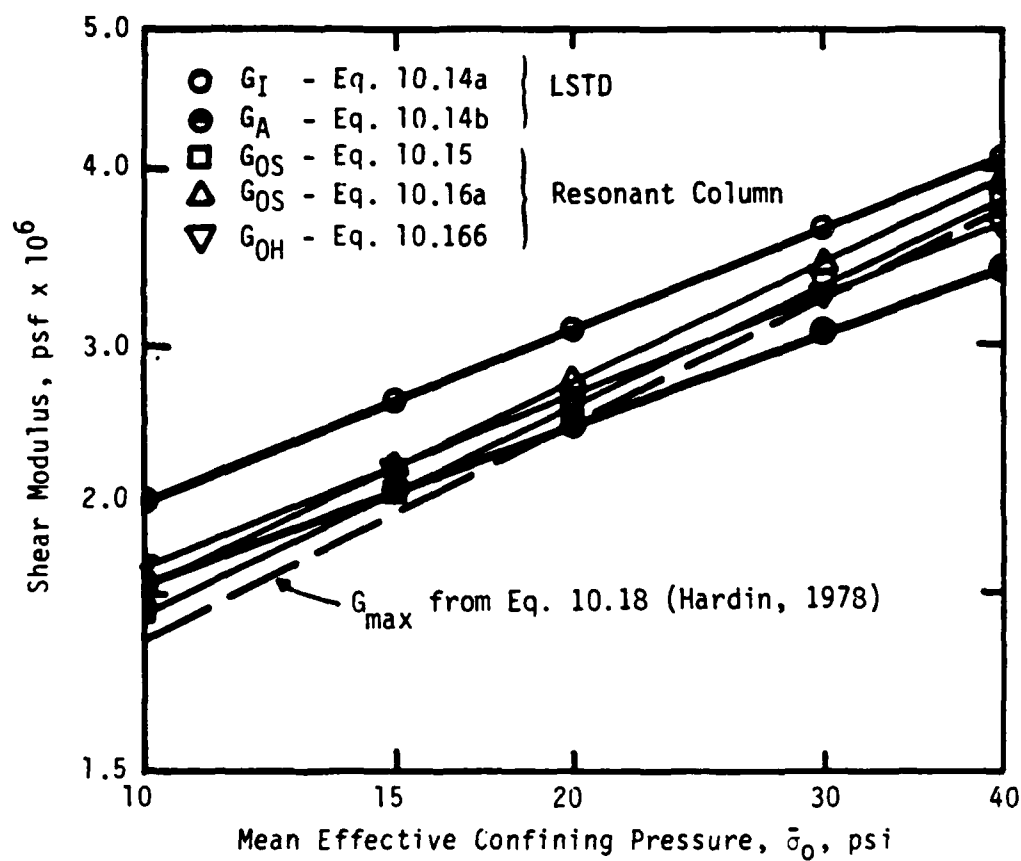


Fig. 10.2 - Comparison of Low-Amplitude Shear Moduli of Dry Sand Determined from Relationships Developed with Different Testing Devices

with the shear moduli (Eqs. 9.22 and 9.23 or Eq. 10.14) listed in Section 9.2 for the LSTD.

Under isotropic confinement, the shear wave velocities measured in the large-scale triaxial device will reflect the structural anisotropy of the sample. However, the small sample in the resonant column test was used to measure only one shear modulus; which is close to the shear modulus for the anisotropic plane (G_A). The values of G_A are smaller than the values of moduli for the isotropic plane (G_I) at low confining pressures and tend towards the values of G_I at high confining pressures. This seems to show that the relative effect of structural anisotropy is most important for this sand at low confining pressures.

10.4.2 VOID RATIO

In most resonant column tests, the displacement of the sample is measured only in the vertical direction after the confinement is changed. The equivalent void ratio is then estimated either by assuming a value of Poisson's ratio for that particular sample or by assuming hydrostatic strain if the loading is isotropic. Although the exact value of Poisson's ratio is rather unimportant when calculating shear moduli, this variation is not negligible in calculating the other independent constants (Drnevich, 1975), and for estimating strain under biaxial loading (see Section 9.7). In a biaxial resonant column test, stress-induced anisotropy will result in three Poisson's ratios (ν_{12} , ν_{13} and ν_{31}) for the sample. Using one unique value of Poisson's ratio for estimating void ratio can, therefore, lead to improper results.

10.4.3 VARIATION OF SHEAR MODULUS DUE TO INITIAL STRESS

The maximum shear modulus estimated using the "mean effective stress" method (Eq. 10.17) does not change when the initial stress ratio, $\bar{\sigma}_1/\bar{\sigma}_3$, $\bar{\sigma}_2/\bar{\sigma}_3$, or $\bar{\sigma}_1/\bar{\sigma}_2$, is varied as long as $\bar{\sigma}_0$ remains constant. However, the variation of shear modulus due to the initial stress state in either static triaxial tests (Ladd, 1964) or in resonant column tests (Kuribayashi, Iwasaki, and Tatsuoka, 1974; Shibata and Tai, 1976; Yanagisawa and Yan, 1977; and Tatsuoka et al, 1979) has been noticed.

Because isotropic or biaxial resonant column tests cannot detect the influence on shear wave velocity of stress in the out-of-plane direction, Eq.

10.19 below (from Eq. 9.17 in Section 9.3) is used to simulate the results of the resonant column tests from data in this study:

$$G = C_G(\bar{\sigma}_a \cdot \bar{\sigma}_b)^{Ne} \quad (10.19)$$

In the resonant column test, waves propagate along the vertical direction and particles vibrate in the direction perpendicular to the radial direction. The stress in the radial direction is equal to the stress in the direction perpendicular to the radial direction under biaxial confinement in the resonant column device. Therefore, Eq. 10.19 is used as follows:

$$G = C_G(\bar{\sigma}_a \cdot \bar{\sigma}_r)^{Ne} \quad (10.20)$$

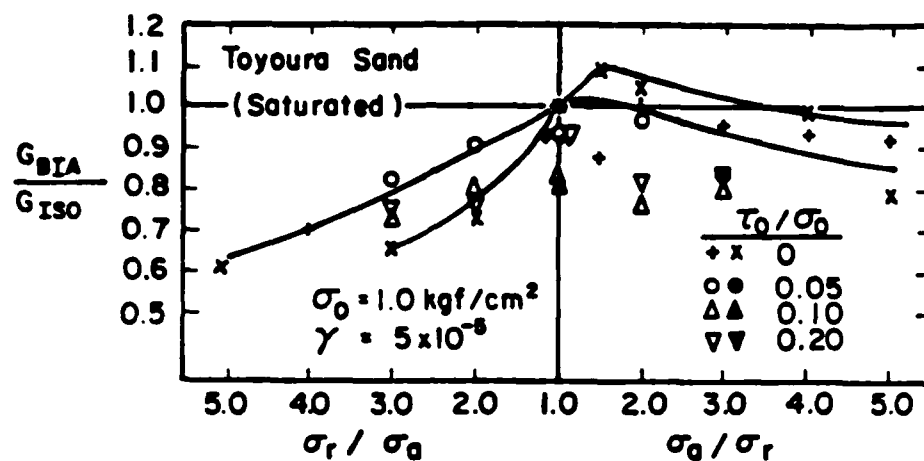
where $\bar{\sigma}_a$ is the effective stress in the axial direction, and $\bar{\sigma}_r$ is in the radial direction, ($\bar{\sigma}_a = \bar{\sigma}_r = \bar{\sigma}_o$ under isotropic confinement). The ratio of maximum shear modulus under biaxial and isotropic confining pressures (G_{BIA} and G_{ISO} , respectively) can then be expressed as:

$$G_{BIA}/G_{ISO} = [(\bar{\sigma}_a \cdot \bar{\sigma}_r)/\bar{\sigma}_o]^{Ne} \quad (10.21)$$

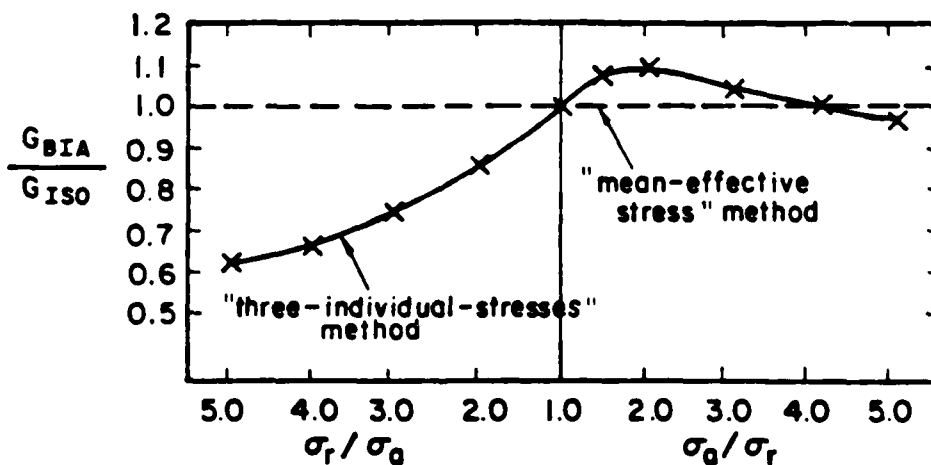
Figure 10.3a shows results from biaxial resonant column tests performed by Tatsuoka et al (1979) with and without an initial shear stress (τ_o). Figure 10.3b shows the trends of the ratio predicted by Eq. 10.21. One can see the agreement between the test results and values predicted by Eq. 10.2 is very good while the test results do not agree with values predicted by Eq. 10.17. The values predicted by the "mean-effective-stress" method (Eq. 10.17) are shown as the (straight) dashed line in Fig. 10.3b. The values predicted by the "three-individual-stresses" method reflect the measured results which may either be larger or smaller than the values from the "mean-effective-stress" method.

10.5 EARTHQUAKE ENGINEERING ANALYSIS

In geotechnical earthquake engineering, upward propagating S-waves are often assumed to be the waves creating the critical ground motion. If the "mean-effective-stress" method is used to estimate the maximum shear modulus associated with these ground motions, Eq. 10.22 is obtained:



(a) from Tatsuoka et al (1979)



(b) from this study (Eq. 10.20)

Fig. 10.3 - Variations of Maximum Shear Modulus Under Constant Mean Effective Stress with Initial Stress

$$G_{\max} = C \bar{\sigma}_o^{0.5} \quad (10.22a)$$

or

$$G_{\max} = C[(1+2K_o)/3]^{0.5} \bar{\sigma}_v^{0.5} \quad (10.22b)$$

From Eq. 10.19 for the simplified "three-individual-stresses" method, the maximum shear modulus is given as (assuming $n = 0.5$):

$$G_{\max} = C \bar{\sigma}_a^{0.25} \bar{\sigma}_b^{0.25} \quad (10.23a)$$

or

$$G_{\max} = C(K_o)^{0.25} (\bar{\sigma}_v)^{0.5} \quad (10.23b)$$

Since $\bar{\sigma}_a = \bar{\sigma}_v$ and $\bar{\sigma}_b = K_o \bar{\sigma}_v$, the ratio of maximum shear moduli between Eqs. 10.22b and 10.23b ranges from 0.99 to 1.16 for K_o equaling 0.3 to 3.0. Therefore, for this condition the "mean-effective-stress" method gives an error no larger than +16 percent for maximum shear modulus in overconsolidated soil with $K_o = 3$, and -1.0 percent for normally consolidated soil with $K_o = 0.3$. This error can be evaluated by:

$$R_G = [(1+2K_o)/3]^{0.5} / (K_o)^{0.25} \quad (10.24)$$

where R_G is the variation of maximum shear moduli between Eqs. 10.22b and 10.23b. In reality, this error is quite small and of little or no consequence given the other unknowns in such problems. However, knowledge of this result is still beneficial to a complete understanding of the dynamic response and to properly modeling the response.

10.6 SUMMARY

Both P- and S-wave velocities can be used to estimate the coefficient of earth pressure at rest, K_o . To do so, measurements must be made with waves polarized along principal stress directions and significant cementation should not exist in the soils. The typical equation used to estimate K_o from P-wave velocities in the horizontal direction (or isotropic plane in a cross-anisotropic medium) from crosshole tests is:

$$K_o = [(V_{p1}/C_1) (\bar{\sigma}_v)^{-na}]^{1/na} \quad (10.25)$$

Typical equations used to estimate for K_o from measurements of V_{SI} and V_{SA} from crosshole and downhole tests are:

$$K_o = [(V_{SI}/C_I) (\bar{\sigma}_V)^{-(na+nb+nc)}]^{1/(na+nb)} \quad (10.26)$$

$$K_o = [(V_{SA}/C_A) (\bar{\sigma}_V)^{-(na+nb+nc)}]^{1/(na+nc)} \quad (10.27)$$

The best opportunity of estimating K_o exists, however, from a "best-fit" model in which velocity measurements of polarized P- and S-waves and velocity measurements of oblique P-waves are combined to give a stress state which best represents all of the velocity measurements.

Based on the "three-individual-stresses" method, in situ seismic measurements should carefully consider:

1. polarization of the source (or wave signal),
2. the angle between the ray direction and the borehole axis (θ) for oblique P- or S-waves, and
3. an understanding of the type of wave velocity (V_{PI} , V_{PA} , V_{SI} , and V_{SA}) measured in a cross-anisotropic medium.

In resonant column tests, three Poisson's ratios (ν_{12} , ν_{13} , and ν_{31}) have to be considered in evaluating the void ratio for a sample under biaxial confinement. Variation of shear modulus under biaxial confinement can be estimated from Eq. 10.21. The maximum shear modulus measured by resonant column tests varies from a value associated with the anisotropic plane to one associated with the isotropic plane. As a result, the slope of $\log G - \log \bar{\sigma}_o$ (or $\log V_S - \log \bar{\sigma}_o$) relationship is a little larger than the one evaluated from measurements of the sand sample in the LSTD.

The error in predicting the maximum shear modulus by the "mean-effective-stress" method for an overconsolidated soil can be as large as +16 percent (for $K_o = 3$) when it is compared with a value estimated by the "three-individual-stresses" method. Equation 10.24 can be used for estimating this error.

CHAPTER ELEVEN

SUMMARY, CONCLUSIONS AND RECOMMENDATIONS

11.1 SUMMARY

A large-scale triaxial device (LSTD) was designed and constructed during 1980 and 1981 under the sponsorship of a grant from the United States Air Force Office of Scientific Research (USAFOSR) (Kopperman et al, 1982). The LSTD is a reinforced steel box with interior dimensions of 7 ft (2.1 m) on a side. A locally available washed mortar sand was selected as the sand with which to build the sample. This sand was used because it is easy to handle and place, and when placed with a raining device, uniform medium-dense sand samples can be obtained and duplicated from one test to the next.

The results of shear wave propagation tests with one sand sample in the LSTD are presented in this report. The testing program was composed of three sequences of pressure variation. The first step was to perform tests with isotropic confinement ($\bar{\sigma}_1 = \bar{\sigma}_2 = \bar{\sigma}_3$). This state of stress is the simplest one that can be applied with the LSTD and is the easiest one to compare with other research conducted with other devices. Moreover, structural anisotropy (or inherent anisotropy) can easily be detected under this stress state.

To understand stress-induced anisotropy and the effect of individual principal stresses on S-wave velocity, a complete set of biaxial tests was performed on the sample. Two series of biaxial confinement tests were examined: the first series consisted of tests with confining stresses varying in only one principal direction (named BIA1), while the second series consisted of tests with confining stresses varying in two principal directions (named BIA2). Both series of tests were conducted with the major principal stress oriented along each of the three principal stress axes of the LSTD to check for possible differences due to structural anisotropy in the sample.

Triaxial confinement states represented the last step in using the LSTD to study the effect of stress state on S-wave velocity. This stress state was examined after the effects of isotropic and biaxial confinements had been examined. Three series of tests were performed in the triaxial tests: (1) the first series consisted of tests in which confining stress was varied in only one principal direction, (2) the second series consisted of tests in which confining stresses were varied simultaneously in two principal

directions, and (3) the third series consisted of tests in which confining stresses were varied in all three principal directions.

Considerable effort was expended on this project to create a homogeneous specimen and to develop a uniform pressurizing system. A new raining device was designed and constructed to build homogeneous samples. Strain gages were attached to each excitation port to control the pressure applied to the sand at the inner side of the ports. Finally, additional accelerometers were embedded in the sample so that a limited number of oblique shear waves could be measured.

11.2 CONCLUSIONS

Based on the measurements of shear wave velocities in this sand sample confined under various states of isotropic, biaxial and triaxial confinements, the following conclusions are made.

1. Stress history has little effect on shear wave velocity of the sand under isotropic, biaxial and triaxial confining pressures if: the stress level (b) is held below 0.46, the principal stress ratio (K_{13}) does not exceed 2.67, the OCR is less than 4.0, and the confining period before measurement at any one stress state is more than 0.5 hours after the applied pressures are balanced.
2. Under isotropic, biaxial and triaxial states of stress, the relationship between shear wave velocity along principal stress directions and the principal stresses may be expressed in a general form as:

$$V_s = C_2 \bar{\sigma}_a^{na} \bar{\sigma}_b^{nb} \bar{\sigma}_c^{nc} \quad (11.1)$$

where

V_s = shear wave velocity (in fps in this study),

C_2 = constant,

$\bar{\sigma}_a$ = effective principal stress in the direction of wave propagation (in psf in this study),

na = slope of $\log V_s - \log \bar{\sigma}_a$ relationship,

$\bar{\sigma}_b$ = effective principal stress in the direction of particle motion (in psf),

nb = slope of $\log V_s - \log \bar{\sigma}_b$ relationship,

$\bar{\sigma}_c$ = effective principal stress in the out-of-plane direction (in psf), and

nc = slope of $\log V_s - \log \bar{\sigma}_c$ relationship.

The last term, $\bar{\sigma}_c^{nc}$, exerts a minor influence on shear wave velocity in that slope nc is nearly zero. However, it was shown not to be zero because of an apparent "strain softening" mechanism.

3. The shear modulus at very small strains is a function of mass density multiplied by the square of the shear wave velocity and can be expressed as:

$$G_{\max} = C_G \bar{\sigma}_a^{Na} \bar{\sigma}_b^{Nb} \bar{\sigma}_c^{Nc} \quad (11.2)$$

where

G_{\max} = shear modulus in desired units,

C_G = constant, equaling (ρC_1^2) , in which ρ is the mass density of soil and C_1 is the constant in Eq. 8.1,

Na = slope of $\log G_{\max} - \log \bar{\sigma}_a$ relationship, equaling $2na$ in Eq. 11.1,

Nb = slope of $\log G_{\max} - \log \bar{\sigma}_b$ relationship, equaling $2nb$ in Eq. 11.1,

Nc = slope of $\log G_{\max} - \log \bar{\sigma}_c$ relationship, equaling $2nc$ in Eq. 11.1.

In Eq. 11.2, $\bar{\sigma}_a$, $\bar{\sigma}_b$, and $\bar{\sigma}_c$ are expressed in the same units as G_{\max} .

4. For practical engineering purposes, the value of nc can be treated as zero, and Eqs. 11.1 and 11.2 can be rewritten as follows:

$$V_s = C_2 \bar{\sigma}_a^{nb} \bar{\sigma}_b^{nb} \quad (11.3)$$

and

$$G_{\max} = C_G \bar{\sigma}_a^{Na} \bar{\sigma}_b^{Nb} \quad (11.4)$$

5. For a preliminary estimation, the values of na and nb may be assumed to be equal, and Eqs. 11.3 and 11.4 can be approximated as:

$$V_s = C_2 (\bar{\sigma}_a \cdot \bar{\sigma}_b)^{ne} \quad (11.5)$$

$$G_{\max} = C_G (\bar{\sigma}_a \cdot \bar{\sigma}_b)^{Ne} \quad (11.6)$$

where

$ne = (na + nb)/2$, and

$Ne = (Na + Nb)/2$.

6. If the sand is confined with an isotropic pressure, Eq. 11.1 can be simplified to:

$$V_s = C_2 \bar{\sigma}_0^{nm} \quad (11.7)$$

where

$$nm = na + nb + nc,$$

$$\bar{\sigma}_0 = \bar{\sigma}_a = \bar{\sigma}_b = \bar{\sigma}_c$$

and Eq. 11.2 can be simplified to:

$$G_{\max} = C_G \bar{\sigma}_0^{Nm} \quad (11.8)$$

where

$$Nm = 2nm.$$

7. Anisotropy arose in the sand sample from both structural and stress induced factors. A cross-anisotropic model can be used to represent the sand under isotropic, BIA1Z, and BIA2Z loading conditions. The constants and slopes for the parameters in Eq. 11.1 for each of these loading conditions are summarized in Table 7.12. Under more complex stress states, the sand behaved as an orthotropic material.
8. In a cross-anisotropic model, P-wave velocities fall into two groups, i.e. V_{pI} and V_{pA} . S-wave velocities also fall into two groups, i.e. V_{sI} and V_{sA} . For a cross-anisotropic material in which the z-axis is the axis of symmetry (hence $\bar{\sigma}_z = \bar{\sigma}_x = \bar{\sigma}_y$), the isotropic plane is the horizontal plane, and V_{pI} and V_{sI} are determined with body waves propagating in this plane. In this same system, vertical planes represent the anisotropic planes in which V_{pA} and V_{sA} are measured.
9. Although the discrepancy between measured shear wave velocities and those predicted by the "mean-effective-stress" method is less than about five percent (see Section 7.4), this method cannot reflect the distinction between the velocities of the different types of P- and S-waves in an anisotropic material.
10. For this sand sample, the shear wave velocity V_{sI} is about 10 percent higher than V_{sA} under isotropic stresses. This difference in wave velocities is assumed to result from structural anisotropy caused by a preferential orientation of the sand grains created during sample construction.

11. Four body wave velocities along principal stress directions, V_{PI} , V_{PA} , V_{SI} , V_{SA} along with the velocity of either an oblique P-wave or an oblique S-wave are required to calculate the five independent constants required in a cross-anisotropic model. Once these constants are calculated, two Young's moduli and three Poisson's ratios can be calculated for the cross-anisotropic material.
12. In an anisotropic material, the velocity surface and the wave surface spread out with different velocities. In addition, these surfaces are not spherical in shape as is the case for an isotropic material and as is typically assumed in most analyses of seismic waves.
13. The coefficient of earth pressure at rest can be estimated from seismic wave velocities with Eq. 10.2, 10.4, or 10.10. If one is to be successful with this method, in principle, body waves polarized along principal stress directions should primarily be used, and the soil should be able to be approximated by a cross-anisotropic model.
14. Variations of shear modulus measured in biaxial resonant column tests, which cannot be estimated by the "mean-effective-stress" method, can be predicted quite accurately by the "three-individual-stresses" method (Eq. 11.2).

11.3 RECOMMENDATIONS

Based on the findings from this study, the following recommendations are made if additional tests are performed with the LSTD.

1. For the measurement of oblique waves, equipment which functions in the time domain as well as the frequency domain should be used. Shear wave velocities calculated by a cross-correlation function or a cross-spectrum analysis may be useful in understanding oblique shear waves.
2. More accelerometers must be installed in the sand sample if shear wave velocities for waves propagating along other than principal stress directions are to be studied in detail.
3. If more samples are tested with different void ratios, the relationship of the constants (C_2) with void ratio could be defined.
4. Clayey samples should be considered in future research.
5. Additional membranes along with internal seismic sources may give a better stress distribution inside the sample.

6. Different types of stress and strain sensors should be considered for measuring static moduli of the sample so that these moduli can be compared with moduli measured under dynamic conditions.

APPENDIX A
CALIBRATION CURVES AND READINGS FOR STRESS CELLS

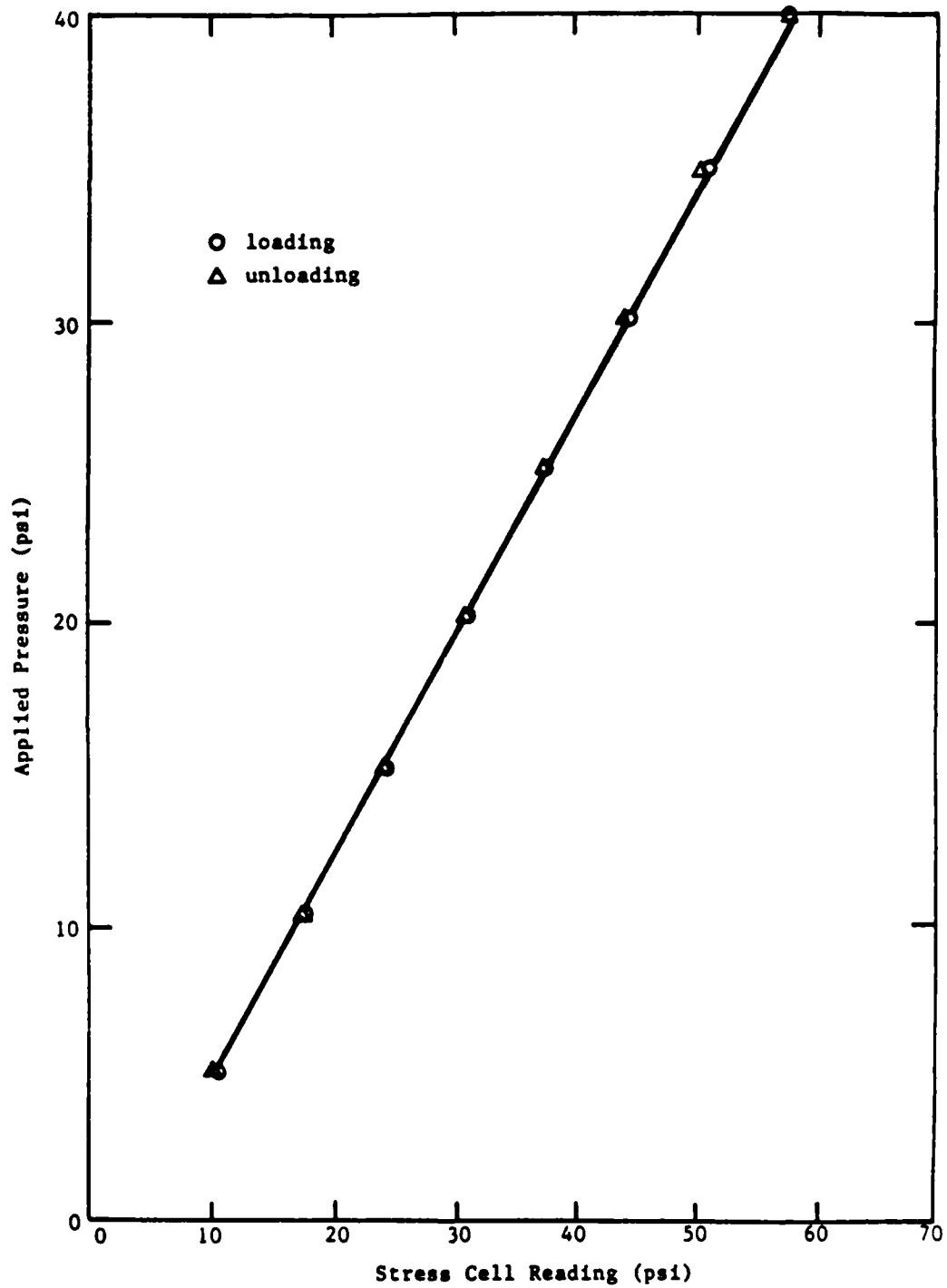


Fig. A.1 - Calibration Curve for Stress Cell SS-1

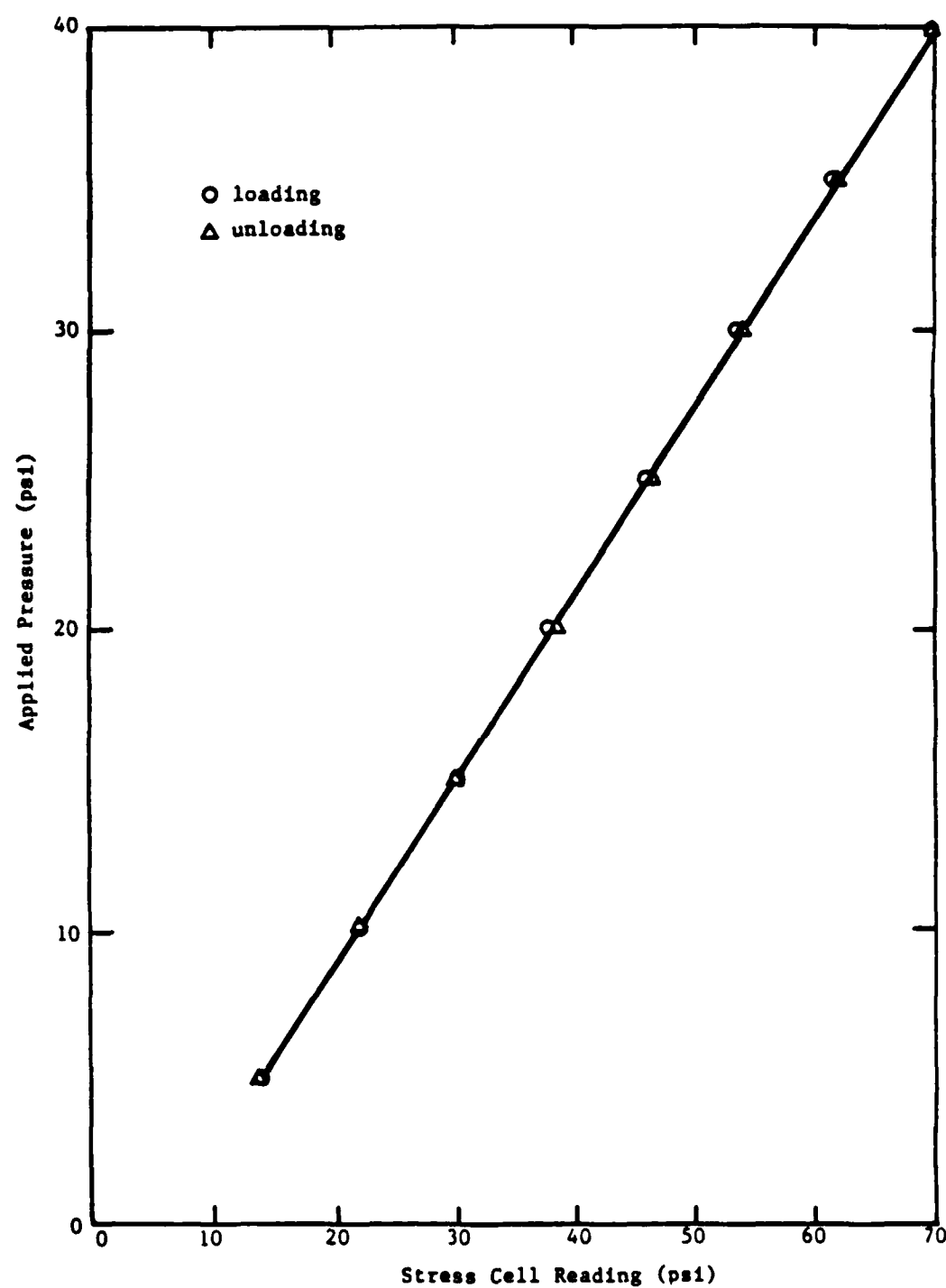


Fig. A.2 - Calibration Curve for Stress Cell SS-2

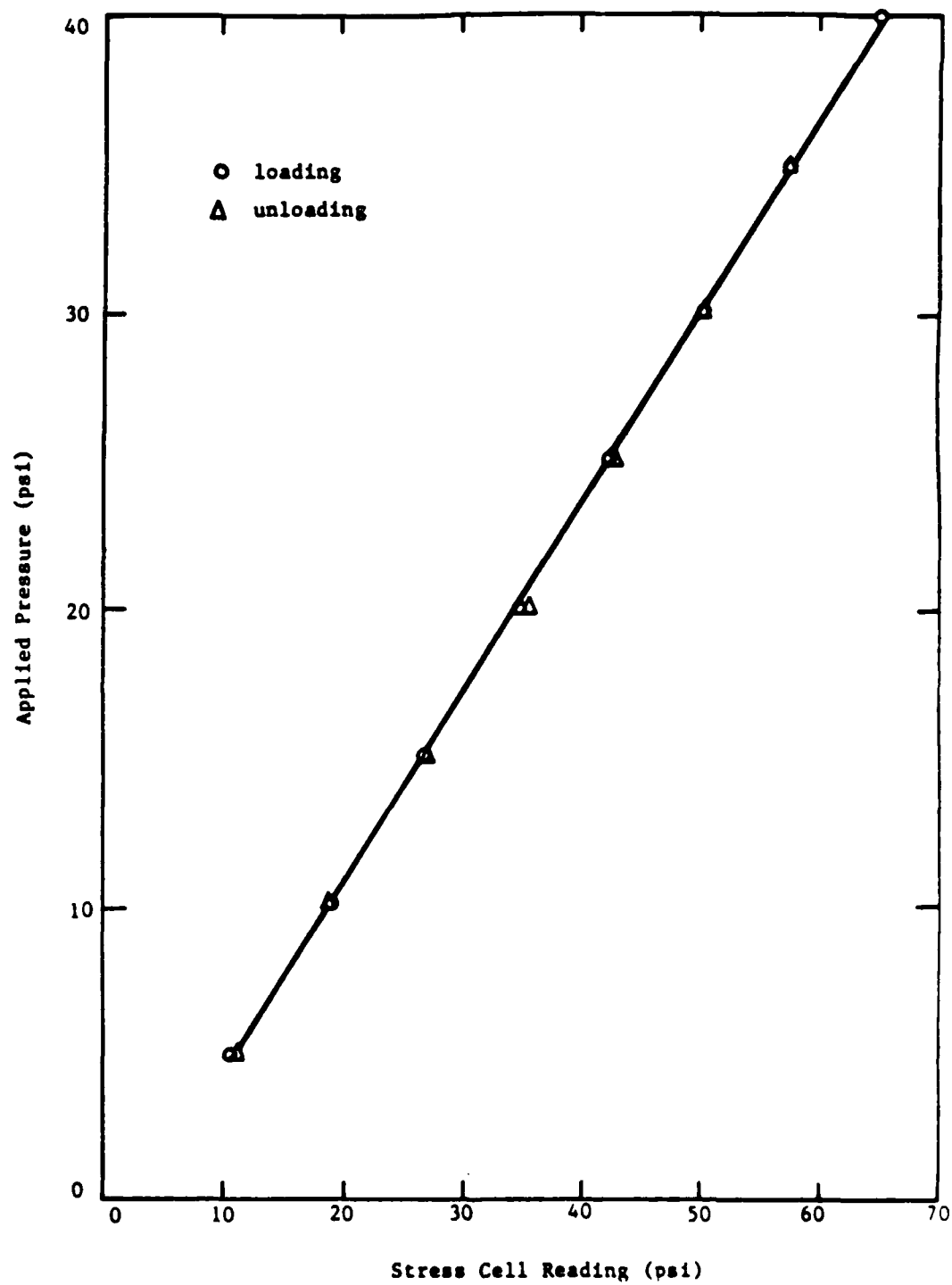


Fig. A.3 - Calibration Curve for Stress Cell SS-3

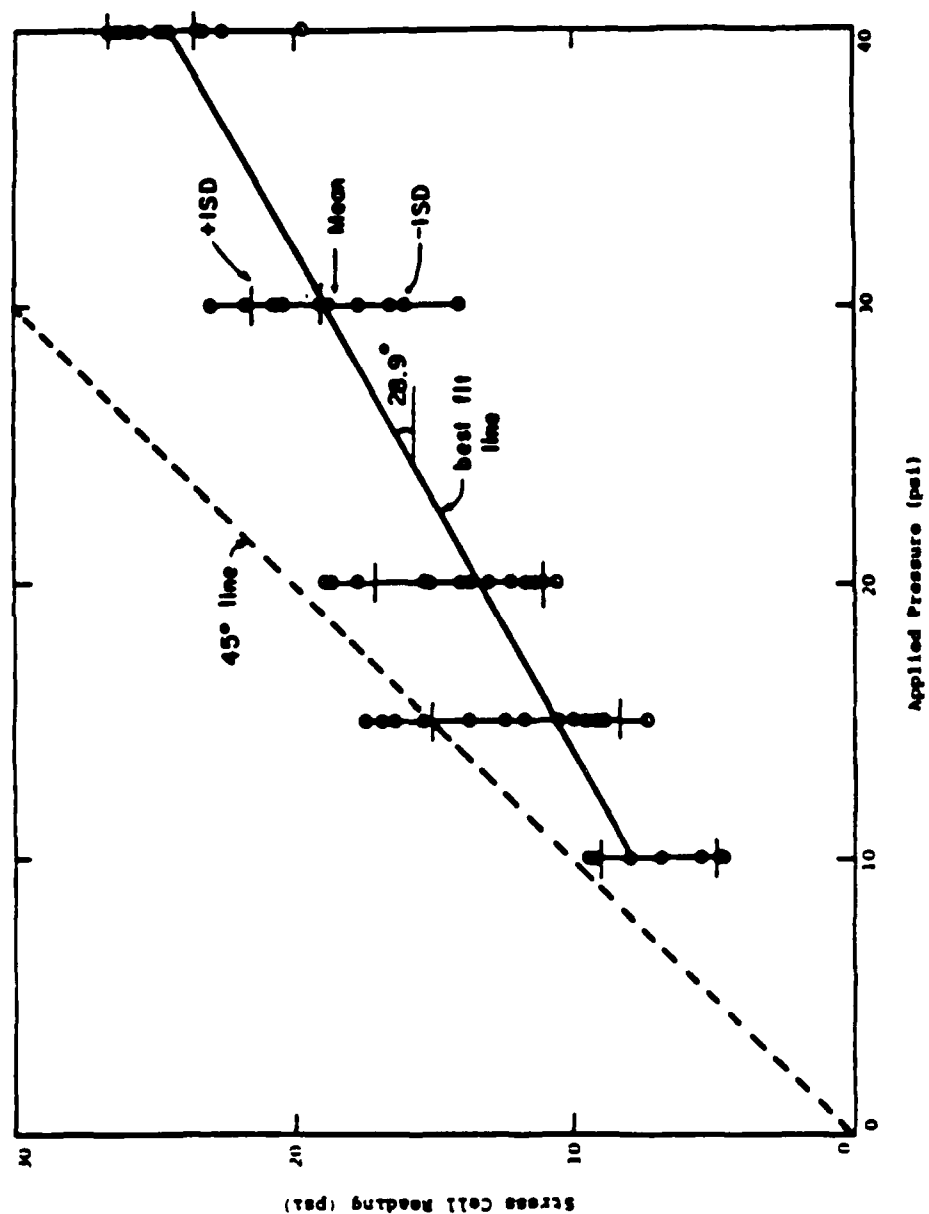


Fig. A.4 - Comparison of Principal Stress Measured by Stress Cell SS-1 with Applied Stress in the Triaxial Device

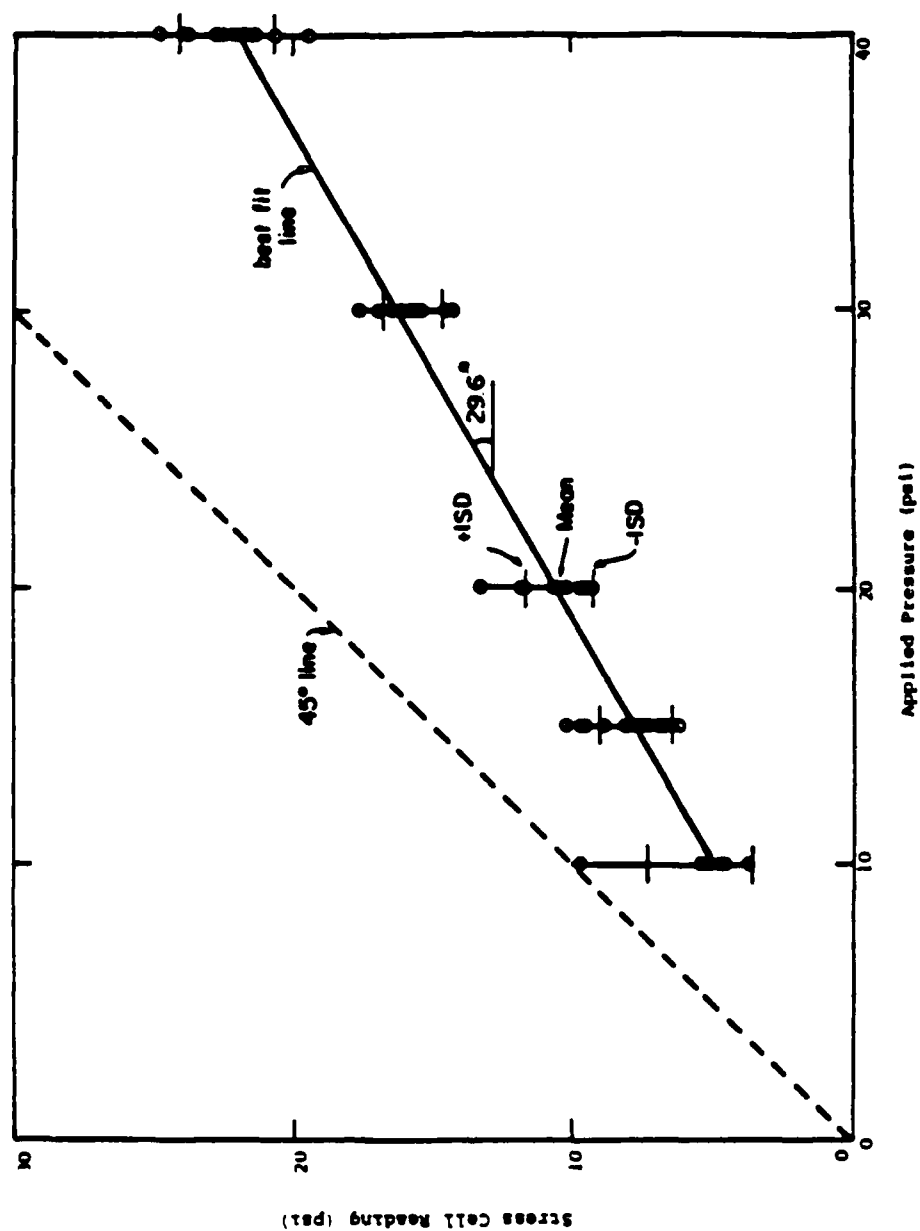


Fig. A.5 - Comparison of Principal Stress Measured by Stress Cell SS-2 with Applied Stress in the Triaxial Device

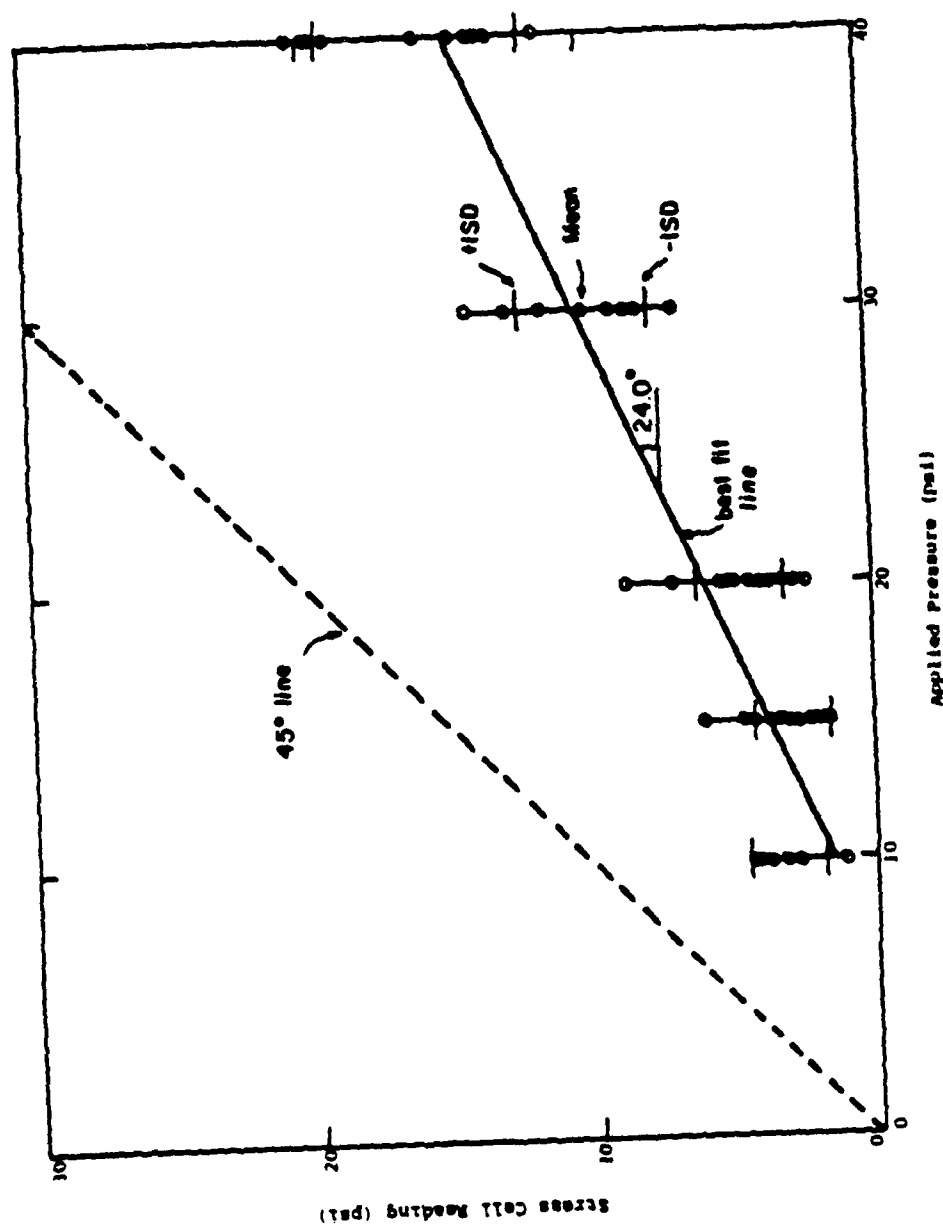


Fig. A.6 - Comparison of Principal Stress Measured by Stress Cell SS-3 with Applied Stress in the Triaxial Device

APPENDIX B
CALIBRATION CURVES FOR STRAIN SENSORS

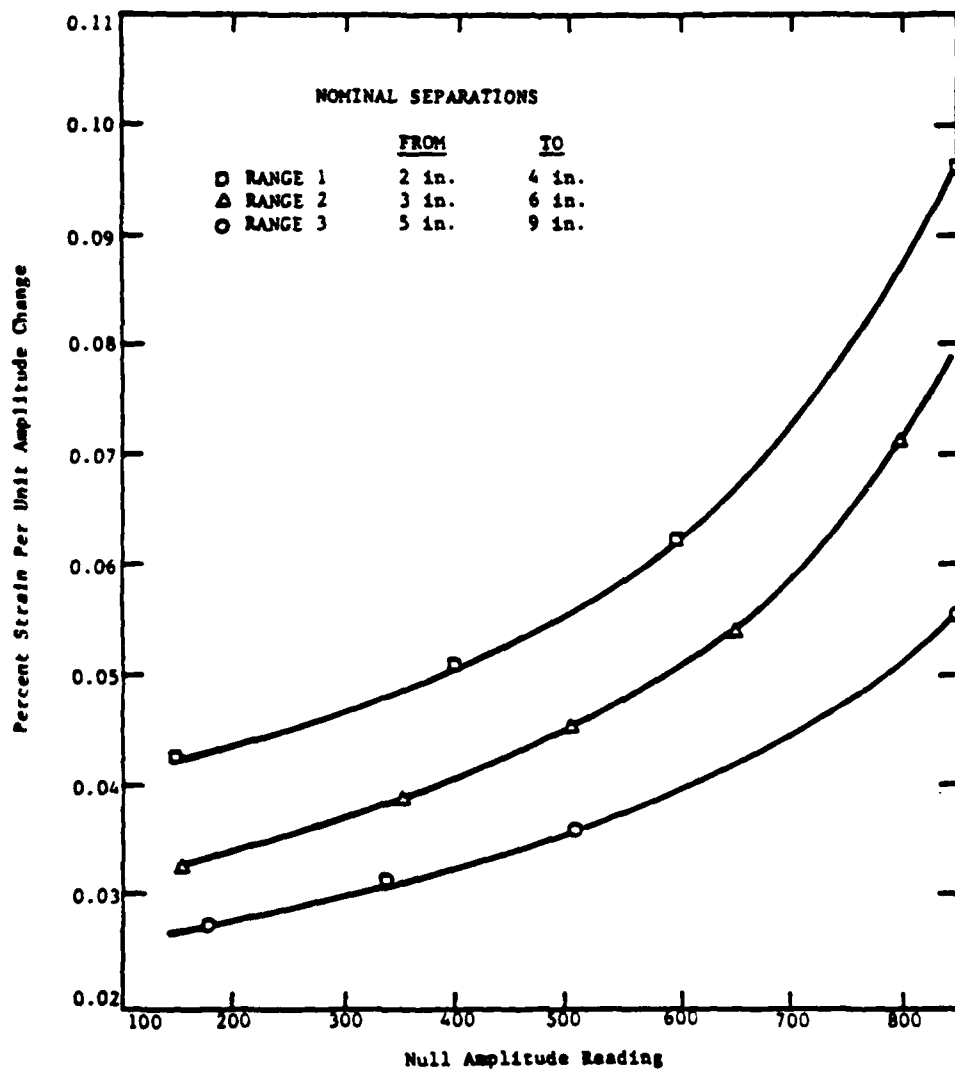


Fig. B.1 - Strain Calibration for Strain Sensor SN-2

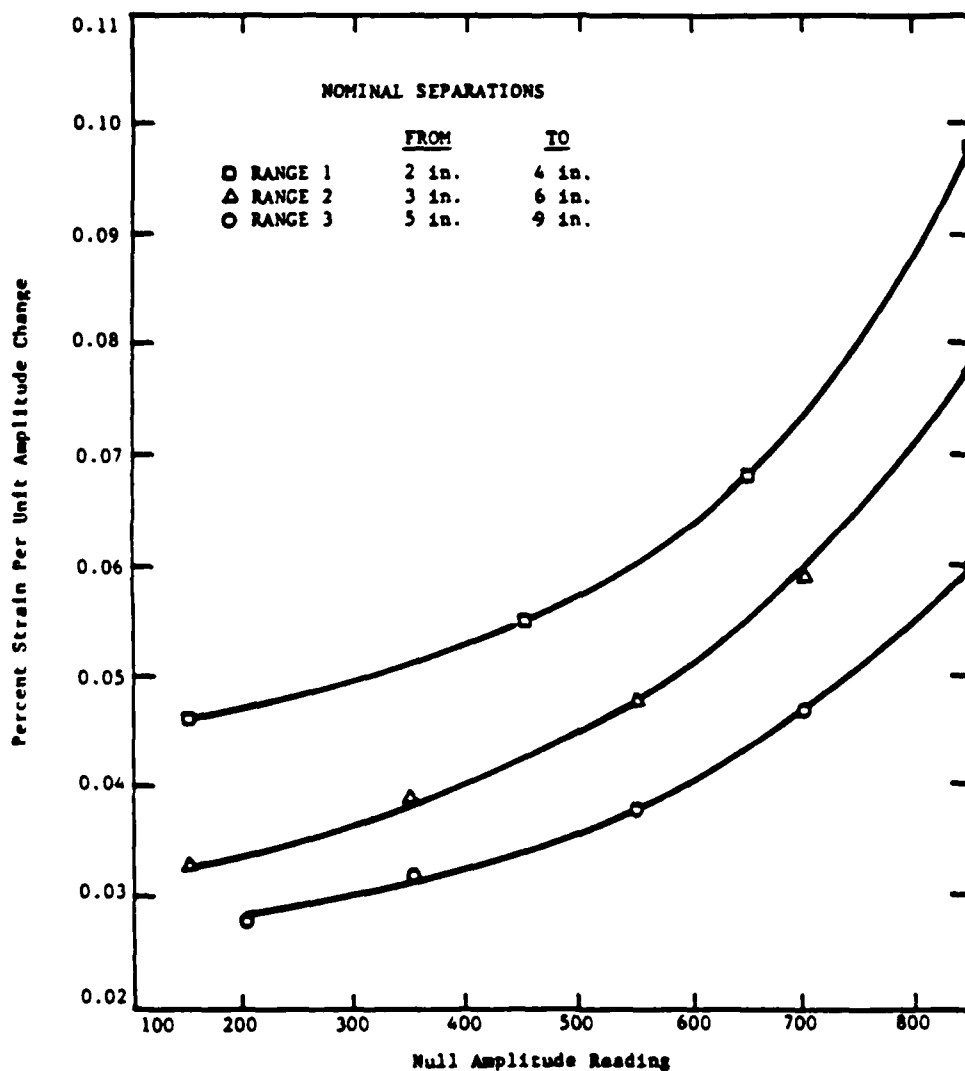


Fig. B.2 - Strain Calibration for Strain Sensor SN-3

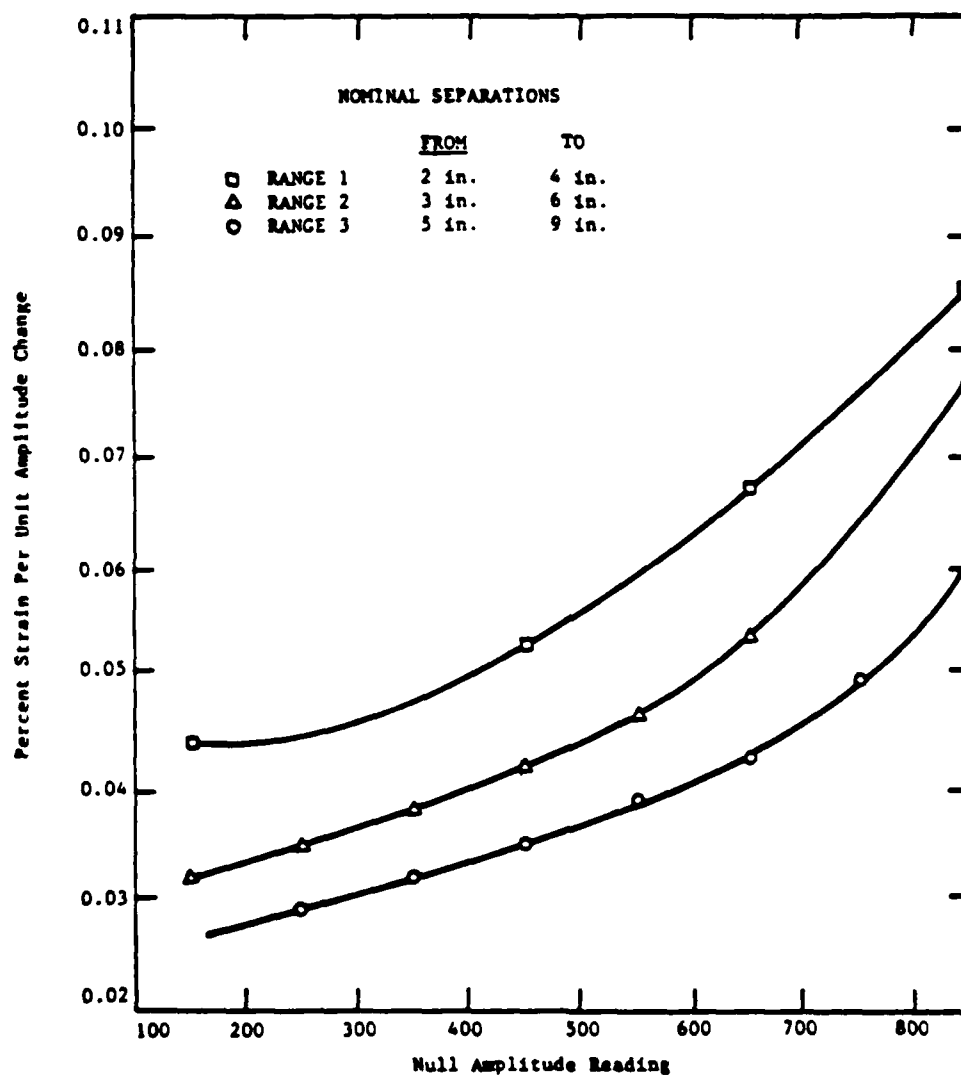


Fig. B.3 - Strain Calibration for Strain Sensor SN-4

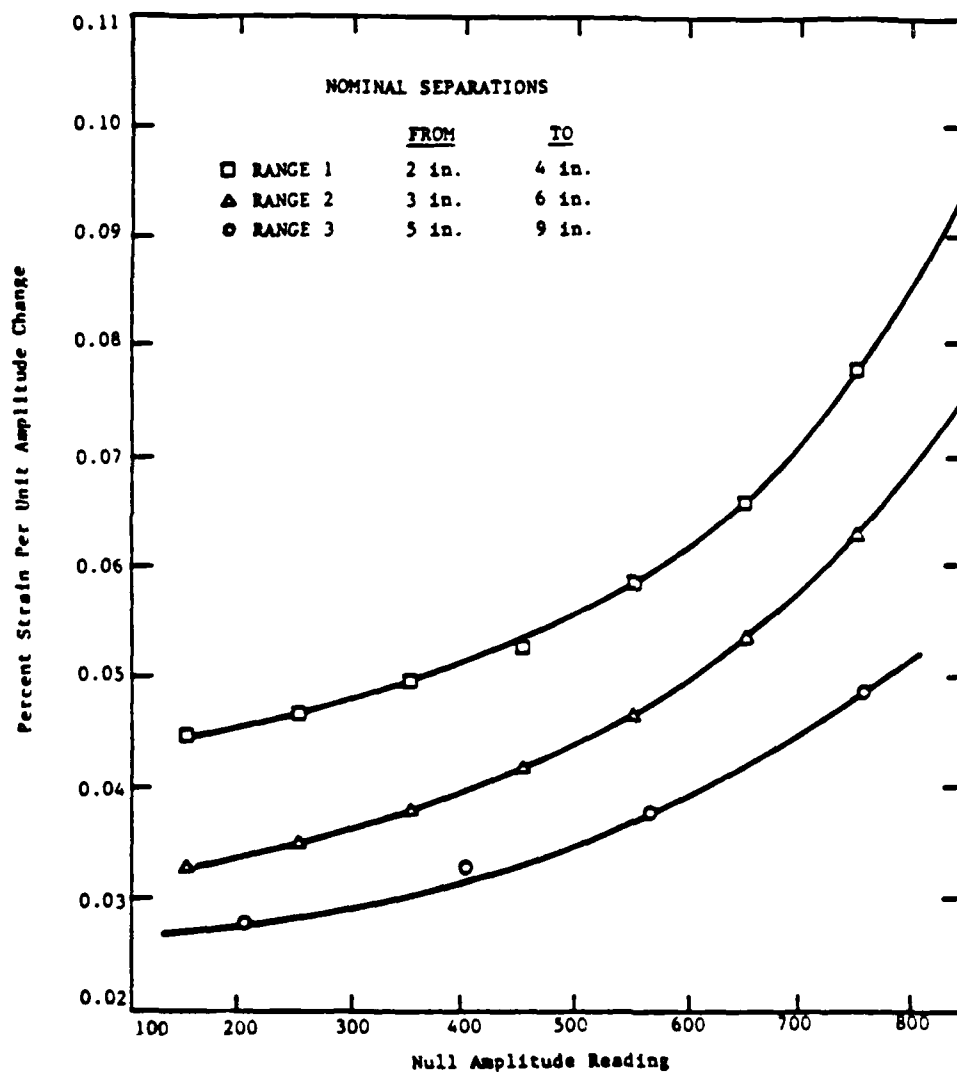


Fig. B.4 - Strain Calibration for Strain Sensor SN-5

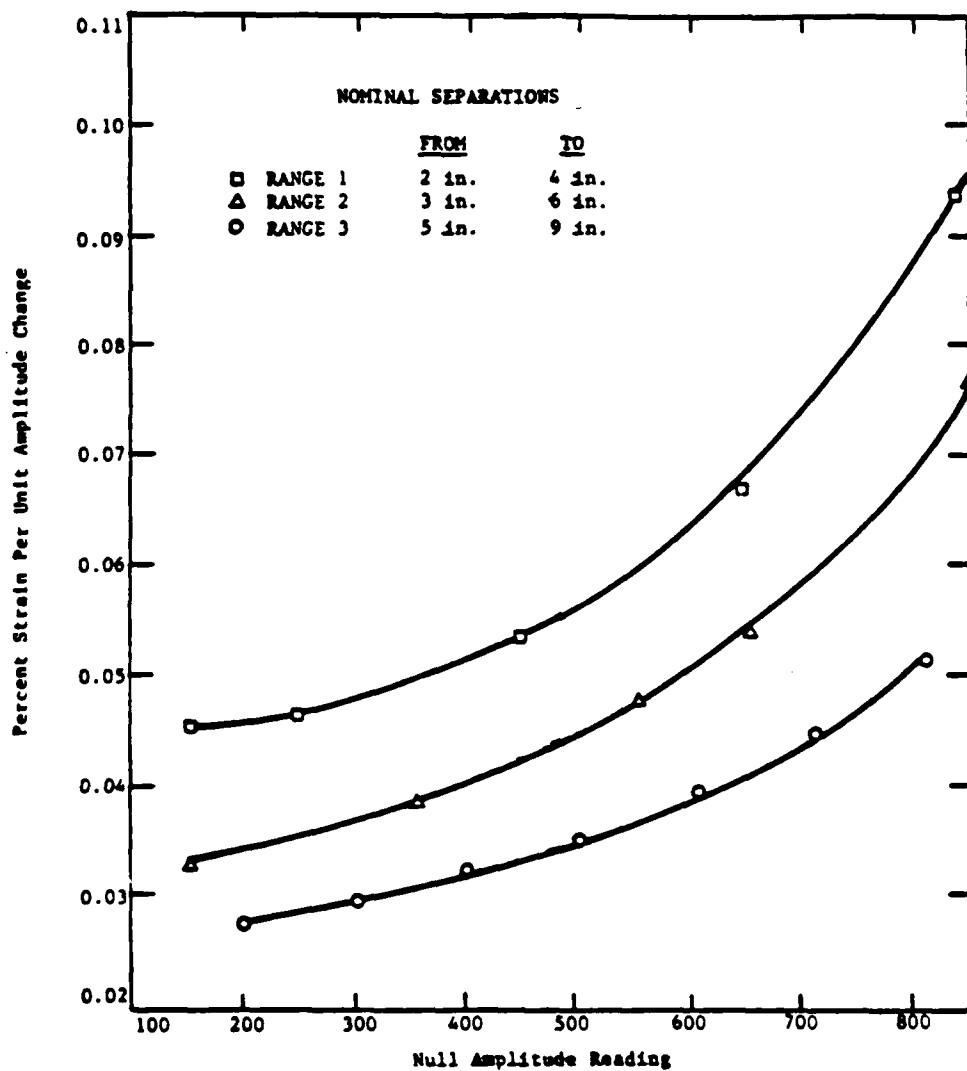


Fig. B.5 - Strain Calibration for Strain Sensor SN-6

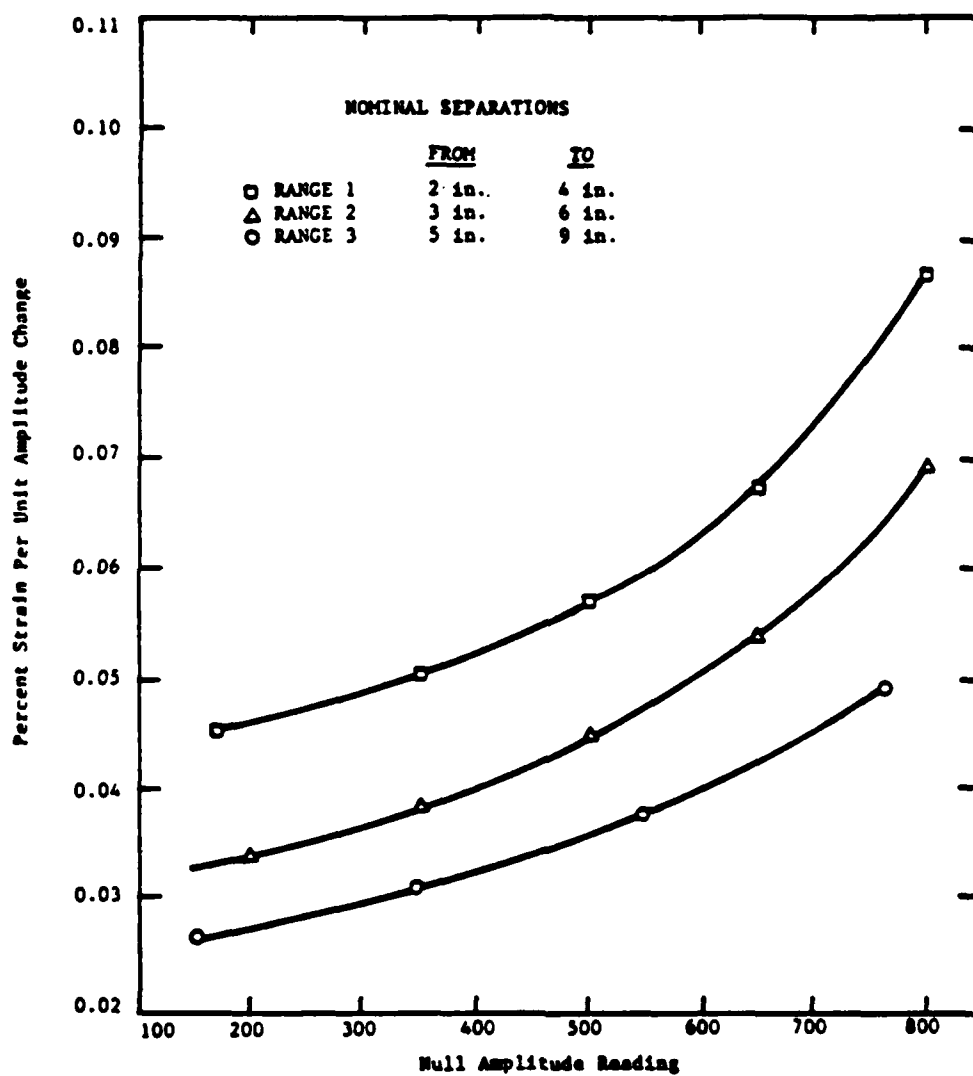


Fig. B.6 - Strain Calibration for Strain Sensor SN-7

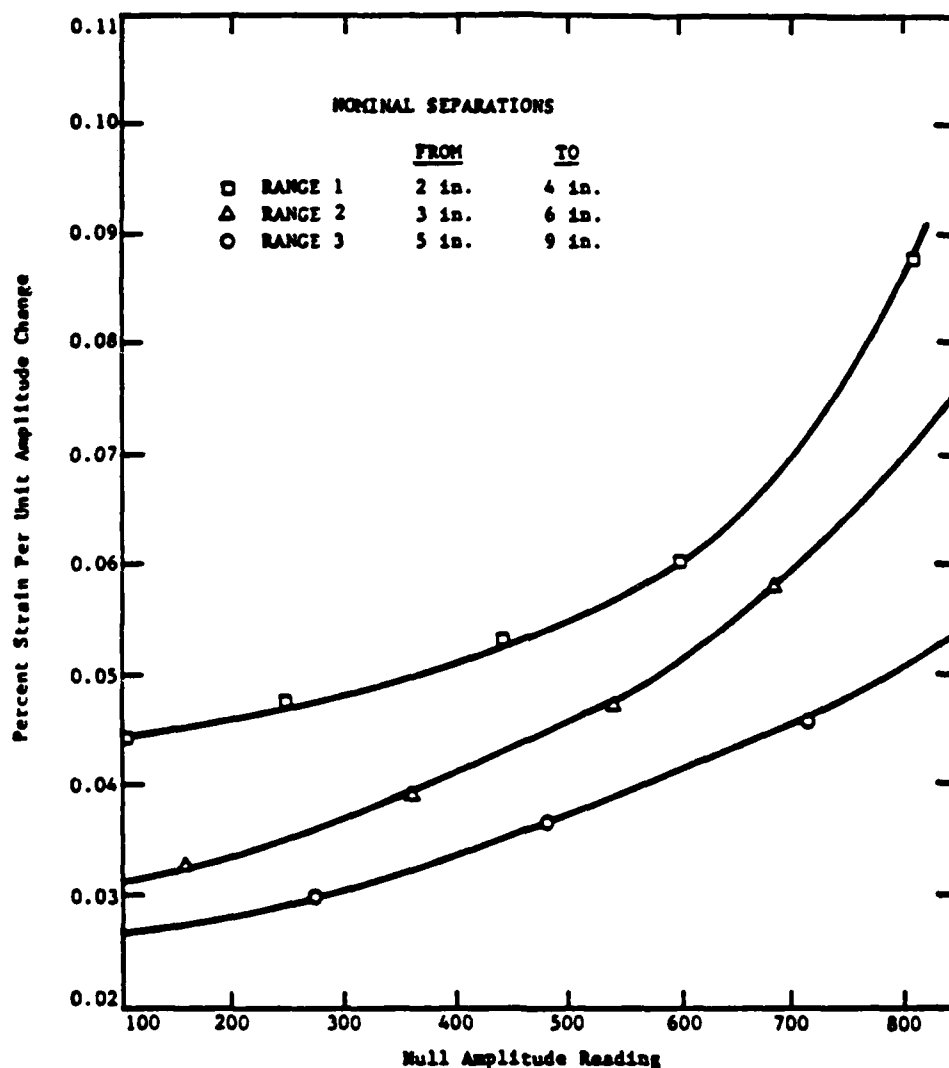


Fig. B.7 - Strain Calibration for Strain Sensor SN-8

APPENDIX C
TYPICAL SHEAR WAVEFORMS

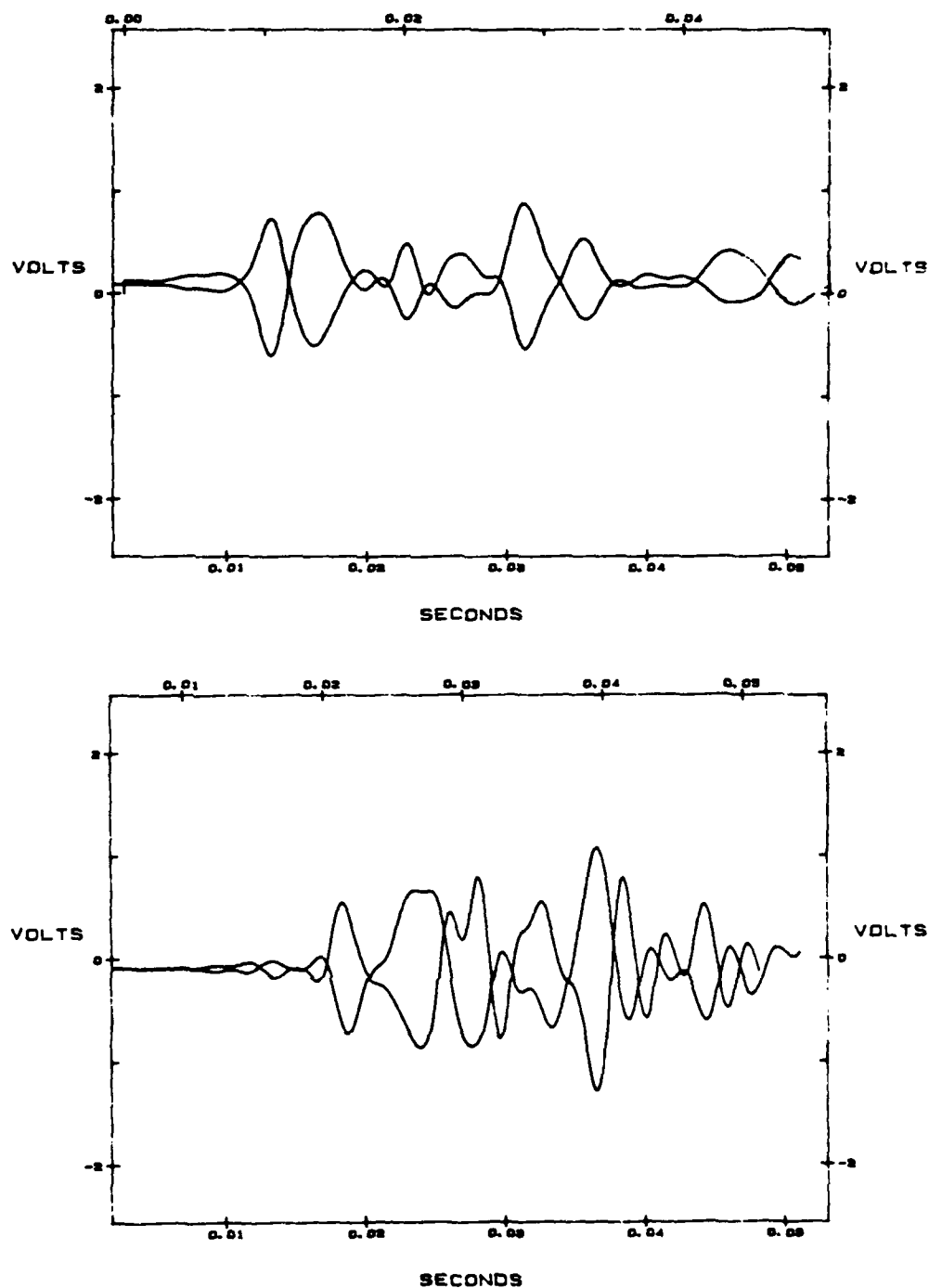


Fig. C.1 - Typical Shear Waveforms from Which V_{xy} Was Determined at $\bar{\sigma}_0 = 40$ psi Under Isotropic Confinement

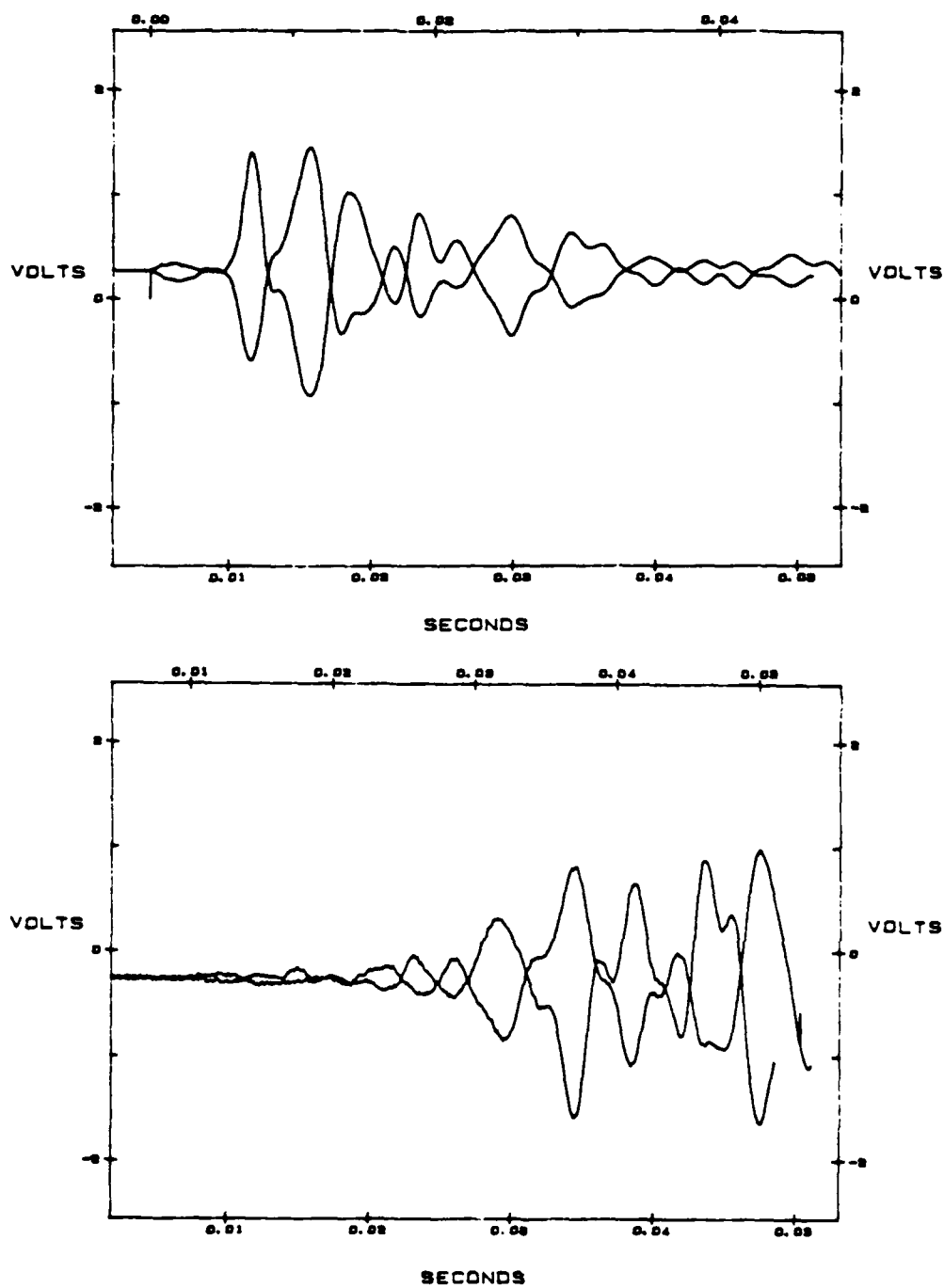


Fig. C.2 - Typical Shear Waveforms from Which V_{yx} Was Determined at $\bar{\sigma}_0 = 40$ psi Under Isotropic Confinement

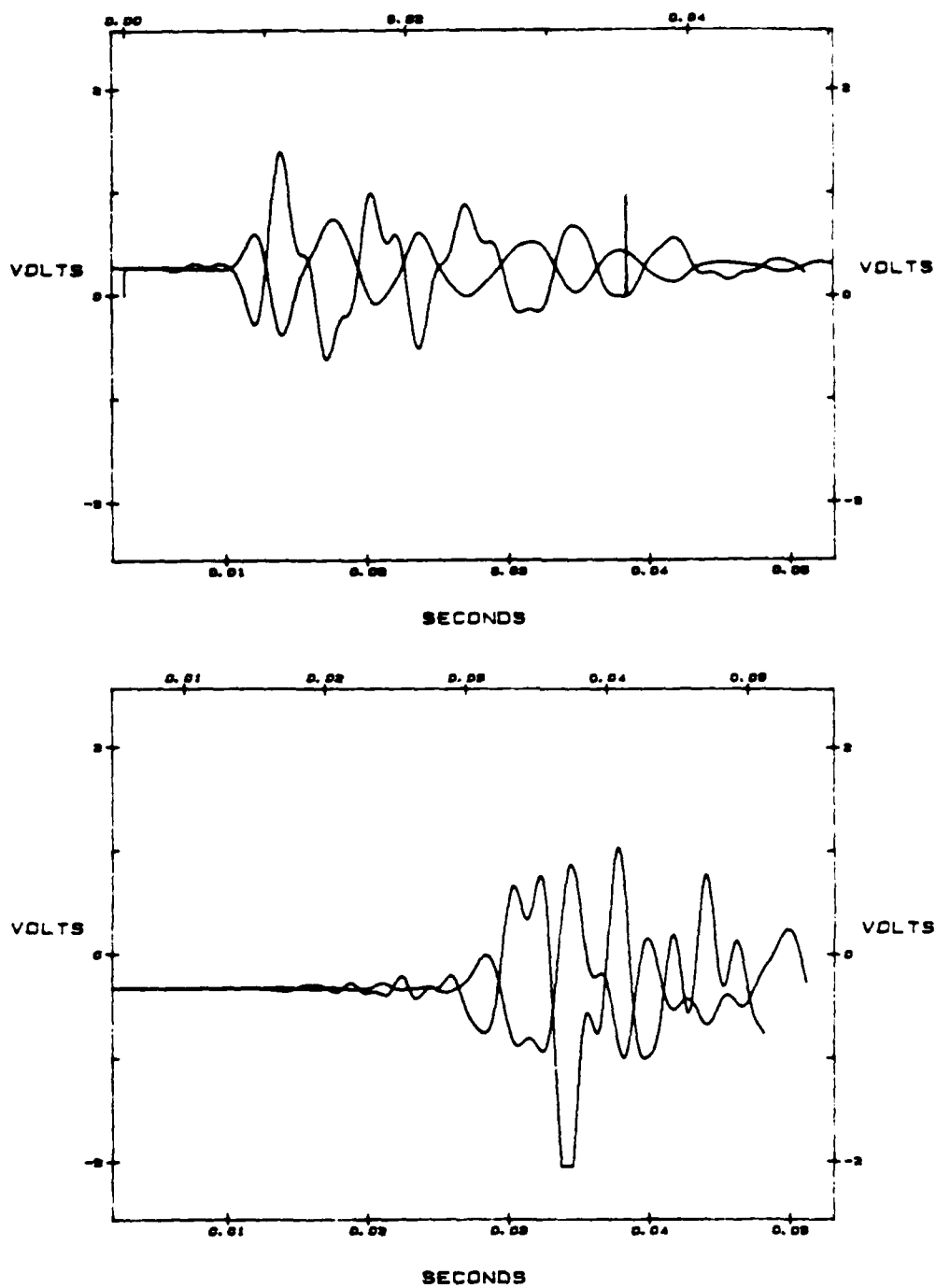


Fig. C.3 - Typical Shear Waveforms from Which V_{xz} Was Determined at $\bar{\sigma}_0 = 40$ psi Under Isotropic Confinement

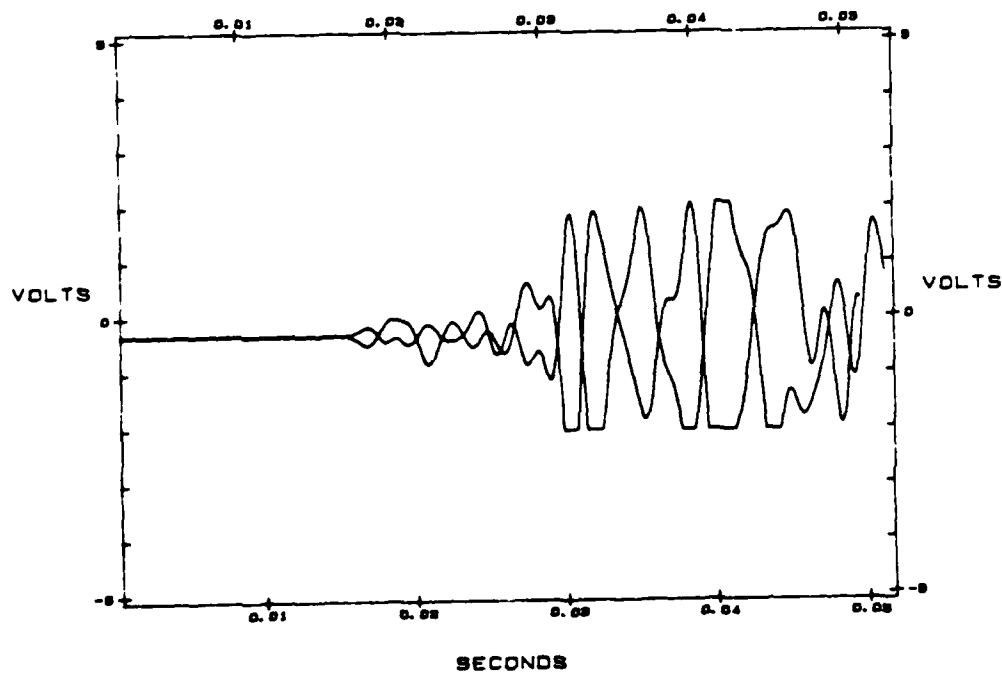
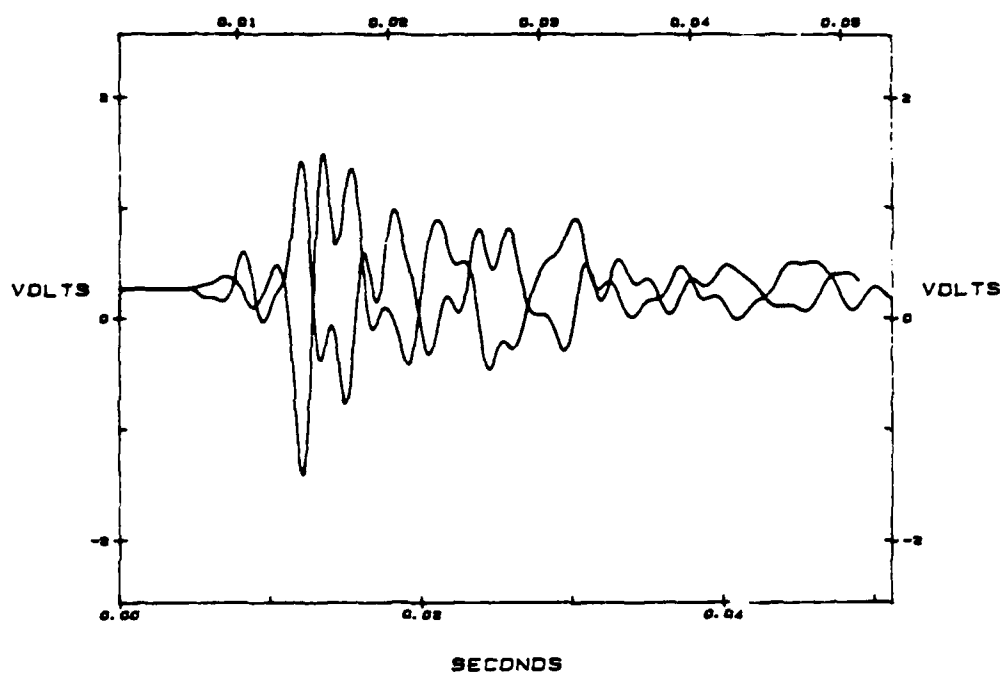


Fig. C.4 - Typical Shear Waveforms from Which V_{yz} Was Determined at $\bar{\sigma}_0 = 40$ psi Under Isotropic Confinement

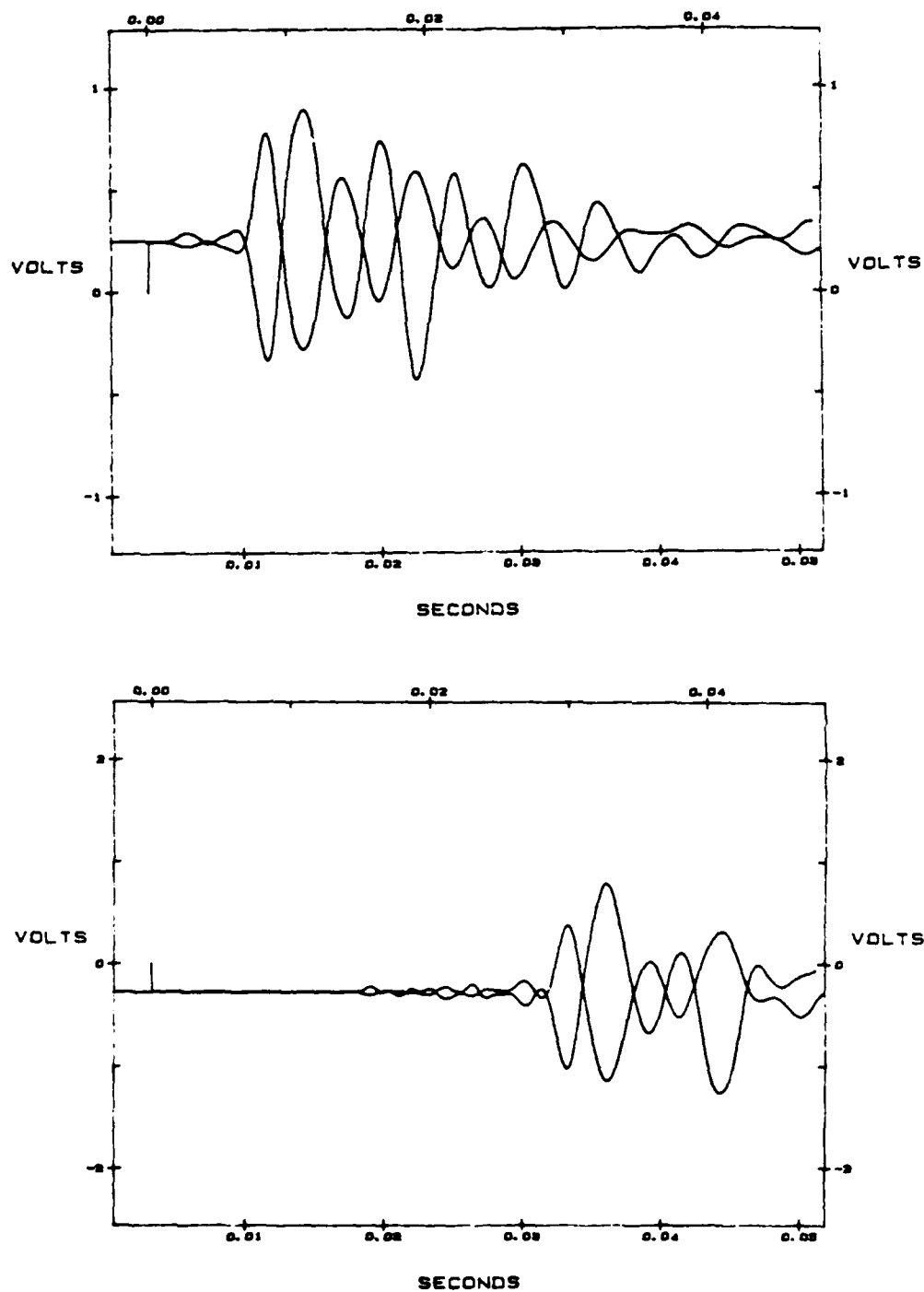


Fig. C.5 - Typical Shear Waveforms from Which V_{zx} Was Determined at $\bar{\sigma}_0 = 40$ psi Under Isotropic Confinement

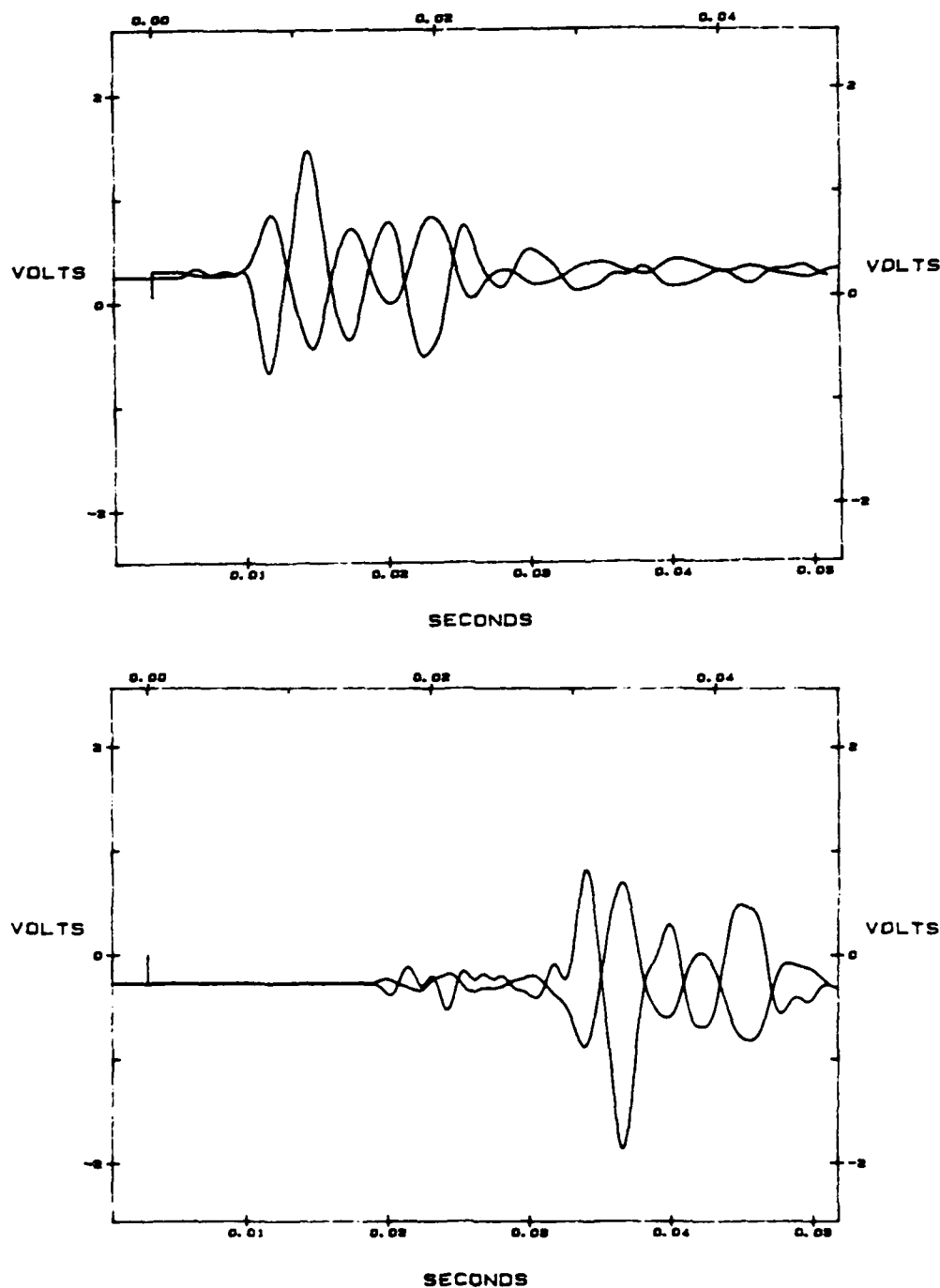


Fig. C.6 - Typical Shear Waveforms from Which V_{zy} Was Determined at $\bar{\sigma}_0 = 40$ psi Under Isotropic Confinement

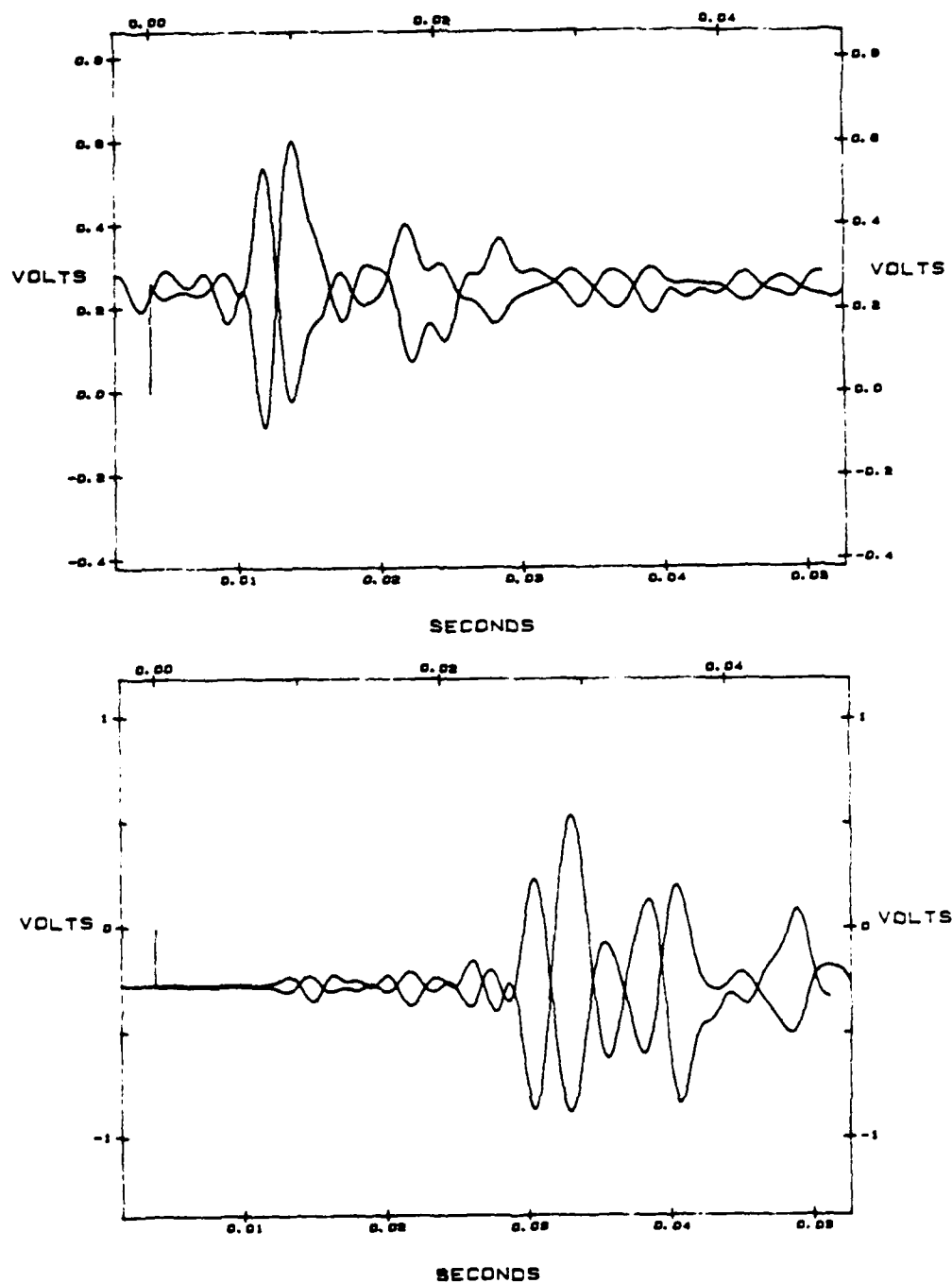


Fig. C.7 - Typical Shear Waveforms from Which V_{45} Was Determined at $\bar{\sigma}_0 = 40$ psi Under Isotropic Confinement

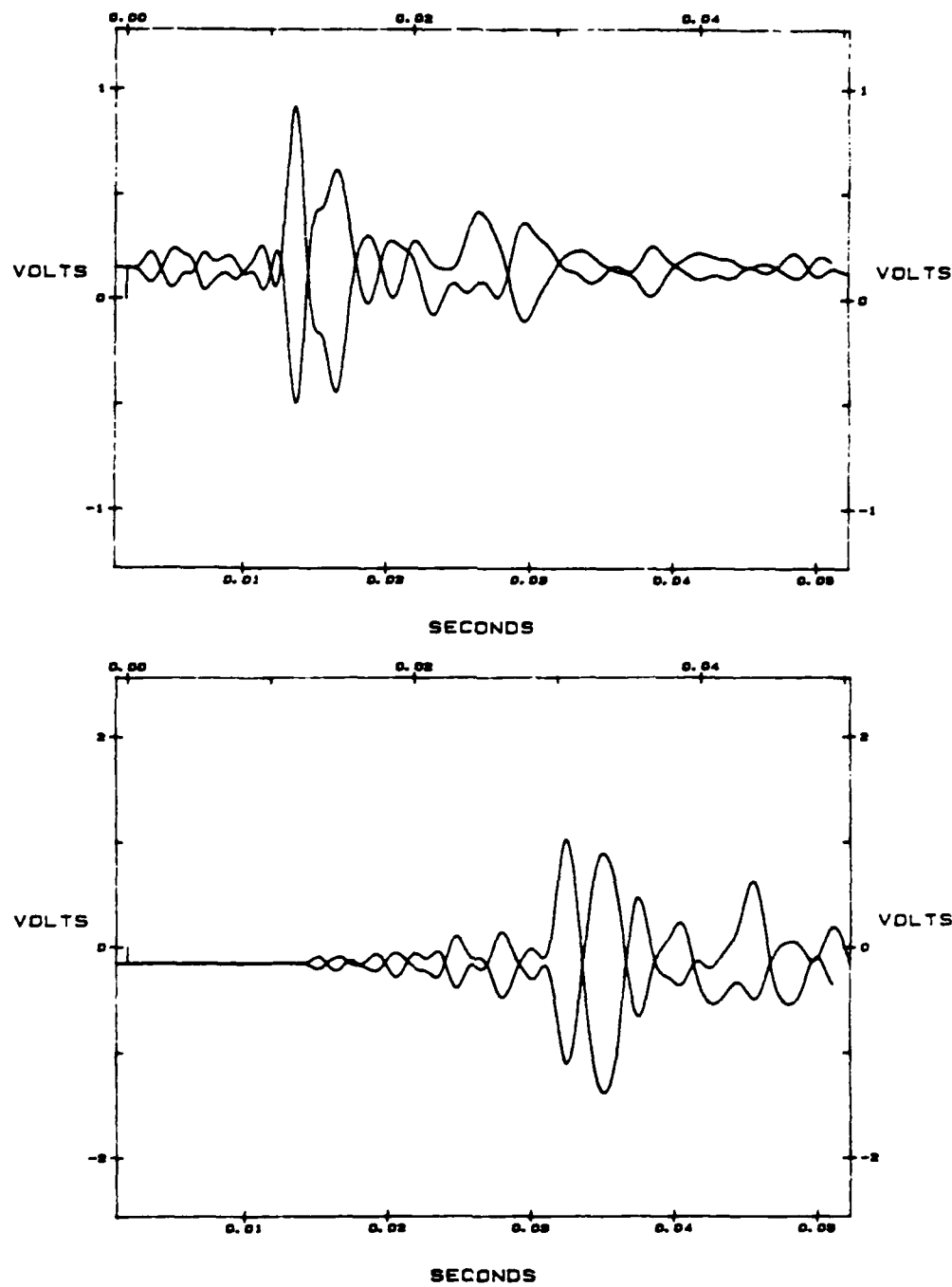


Fig. C.8 - Typical Shear Wave forms from which $V_{22.5}$ Was Determined at $\bar{\sigma}_0 = 40$ psi Under Isotropic Confinement

APPENDIX D

MAGNITUDE OF LINEAR SPECTRUM OF SHEAR WAVEFORMS IN APPENDIX C

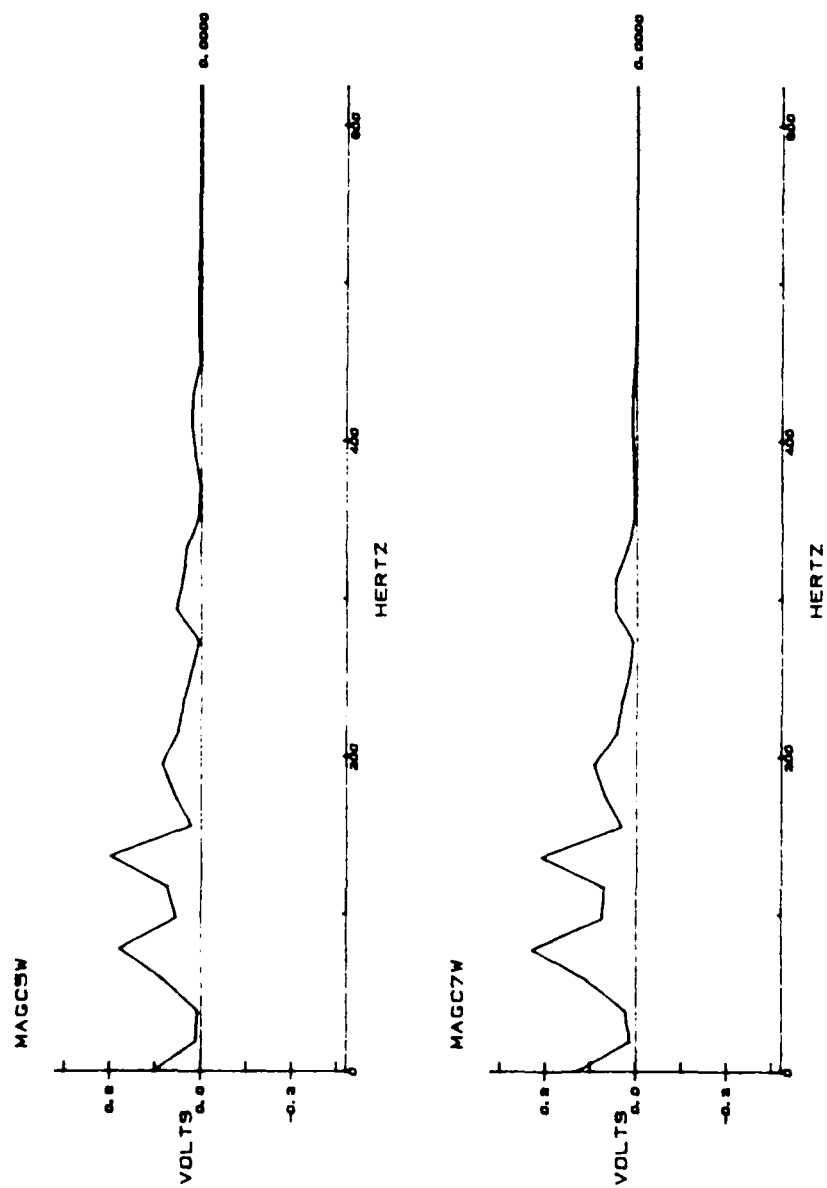


Fig. D.1 - Magnitude of Linear Spectrum of Waveform
of V_{xy} in Fig. C.1

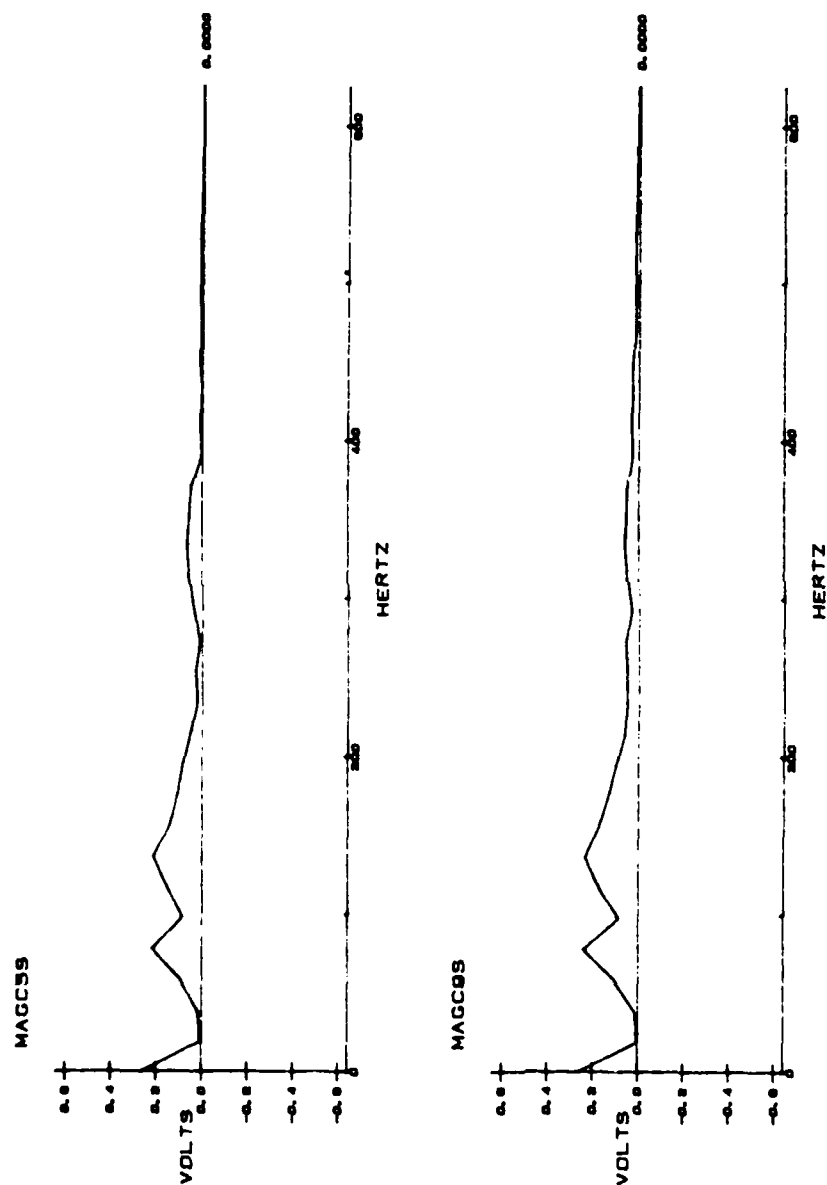


Fig. D.2 - Magnitude of Linear Spectrum of Waveform of V_{yx} in Fig. C.2

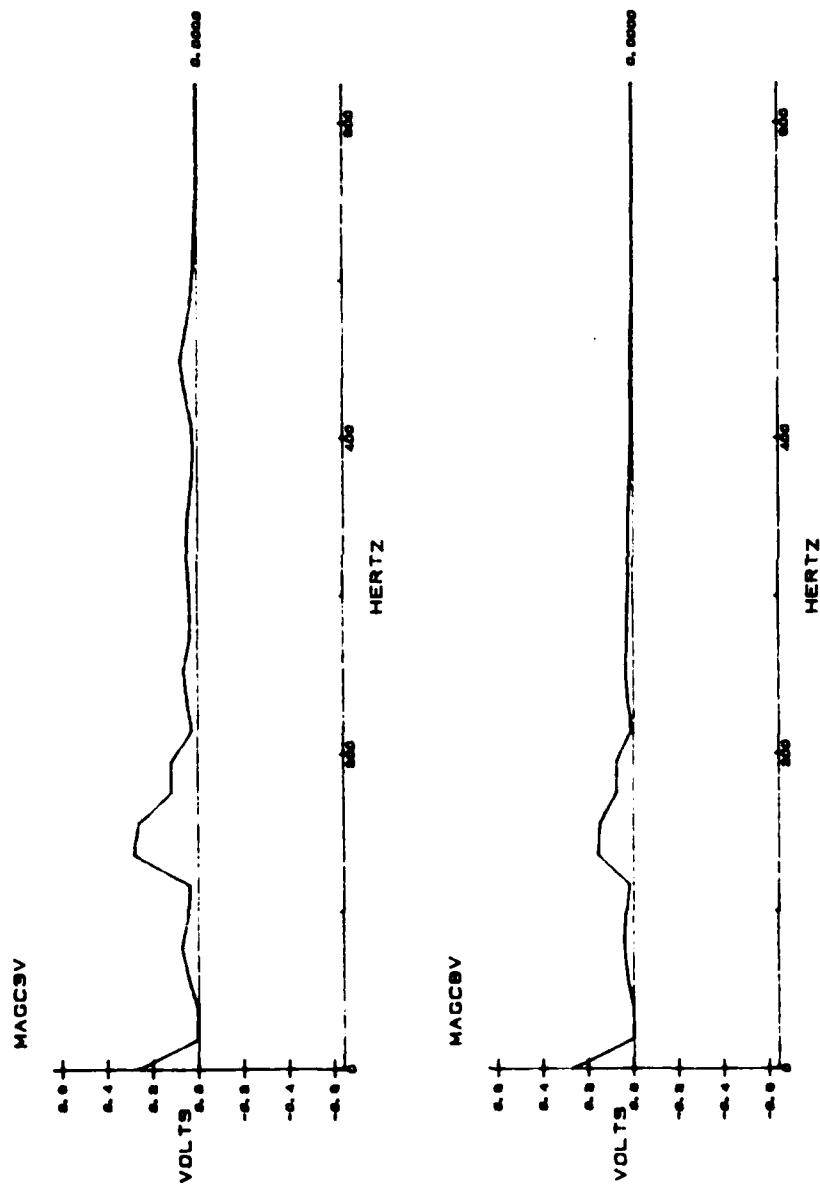


Fig. D.3 - Magnitude of Linear Spectrum of Waveform of V_{xz} in Fig. C.3

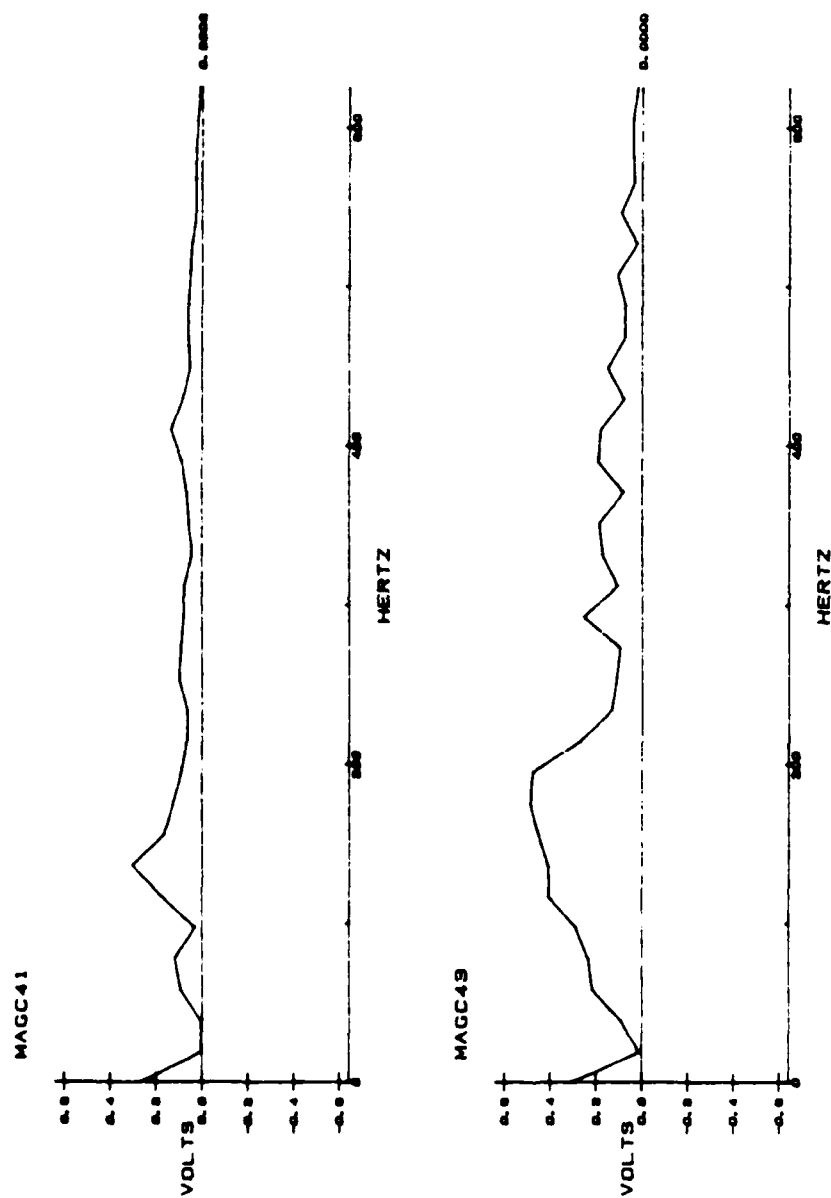


Fig. D.4 - Magnitude of Linear Spectrum of Waveform
of V_{yz} in Fig. C.4

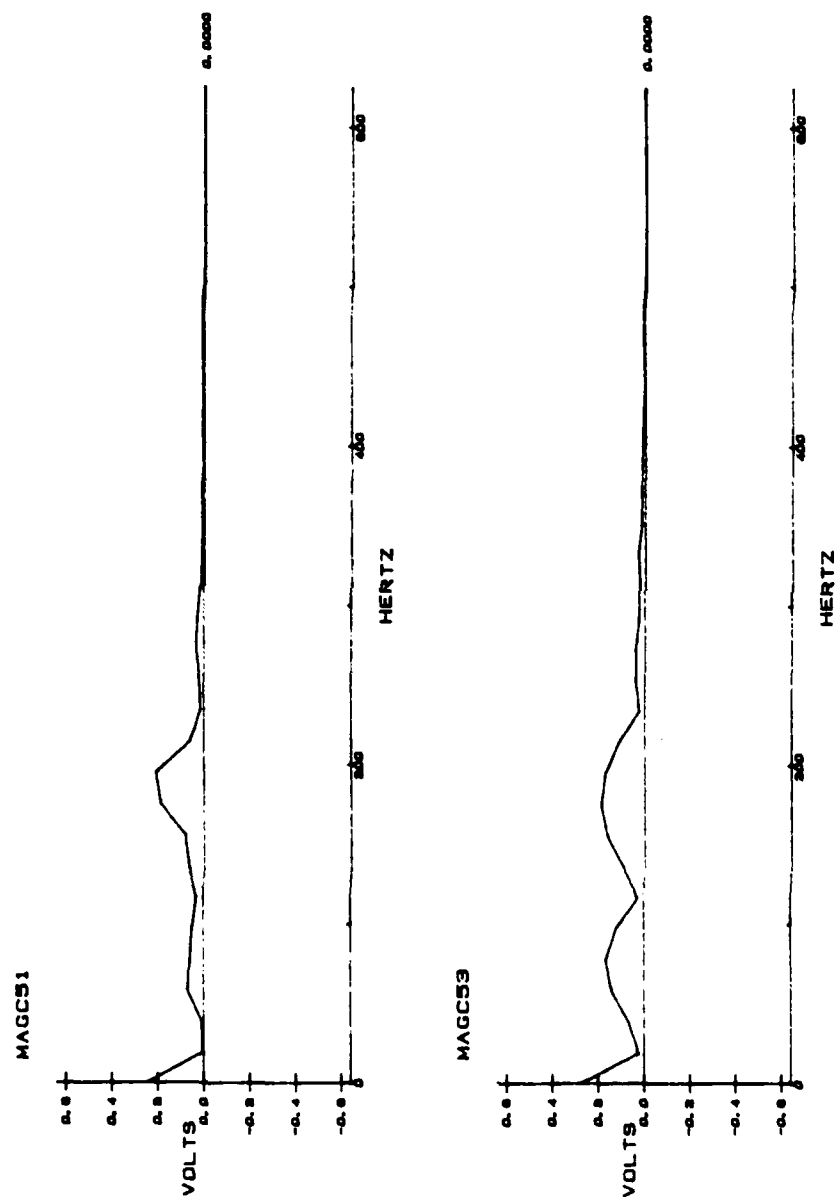


Fig. D.5 - Magnitude of Linear Spectrum of Waveform
of V_{zx} in Fig. C.5

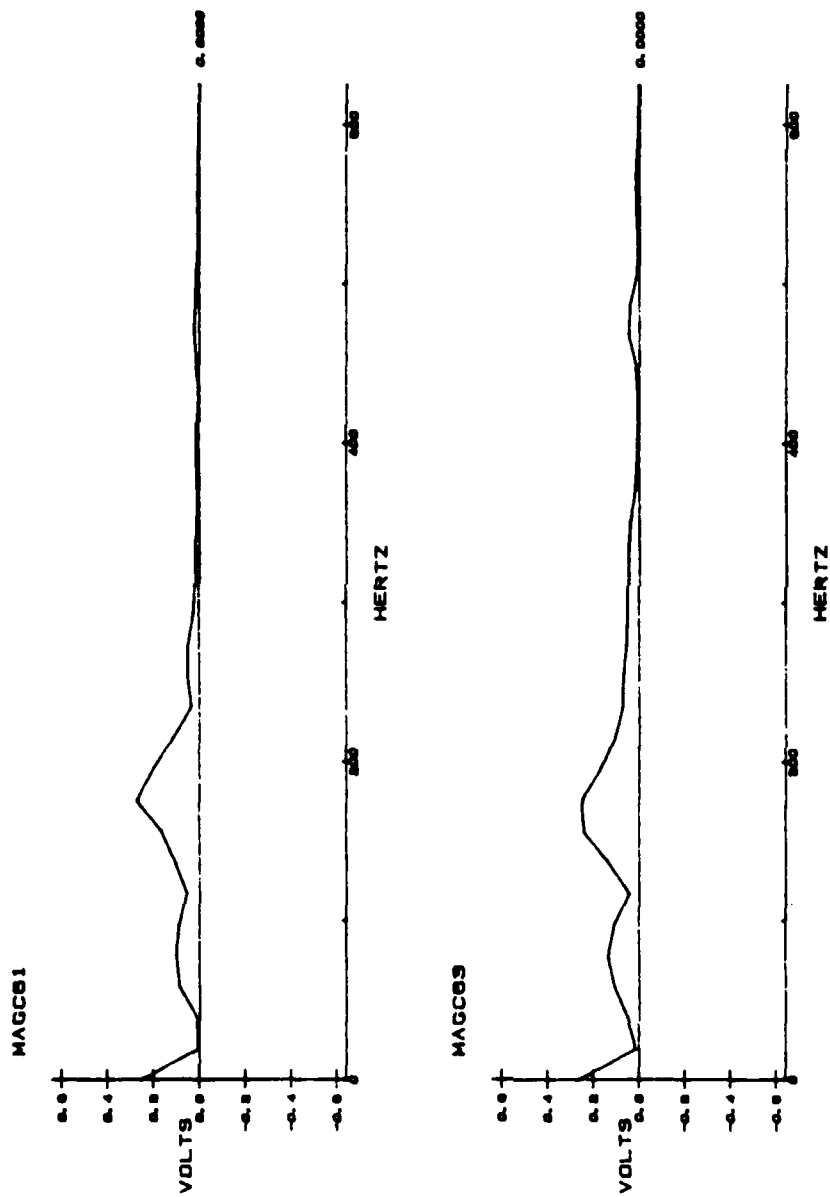


Fig. D.6 - Magnitude of Linear Spectrum of Waveform of V_{zy} in Fig. C.6

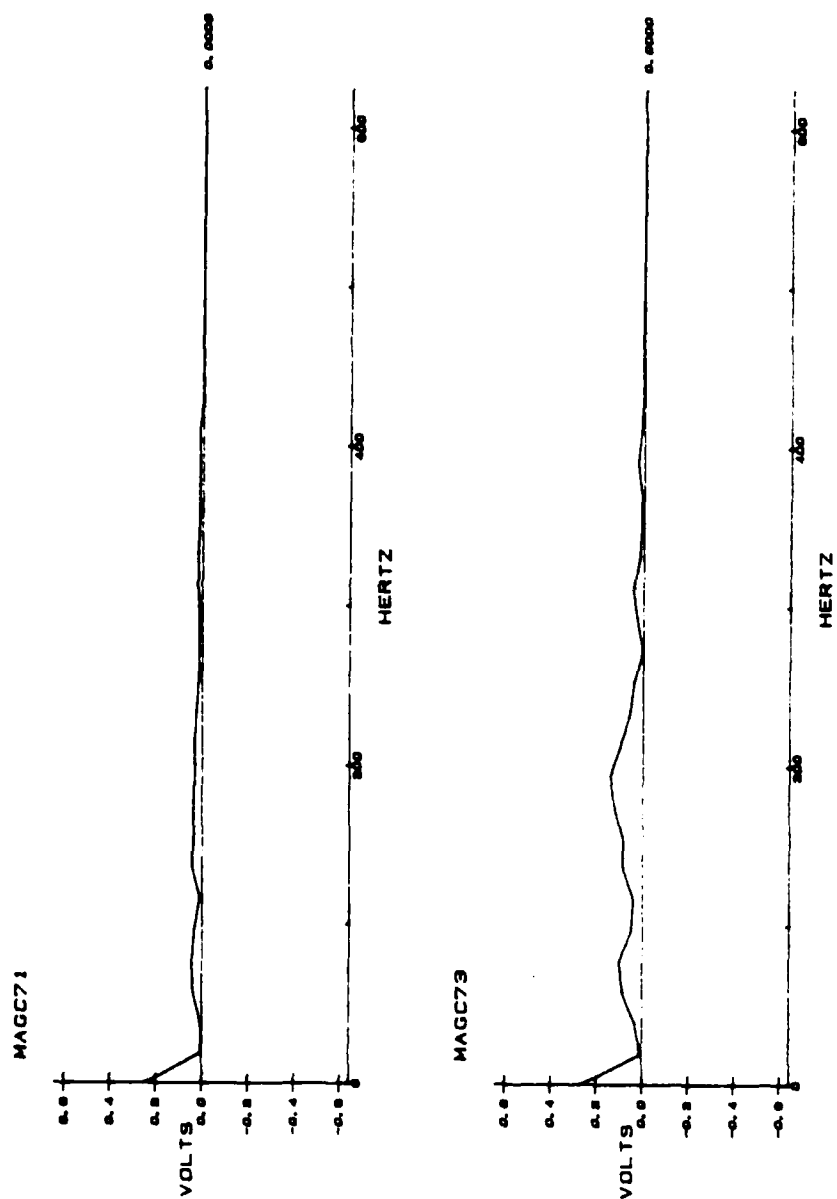


Fig. D.7 - Magnitude of Linear Spectrum of Waveform
of V_{45} in Fig. C.7

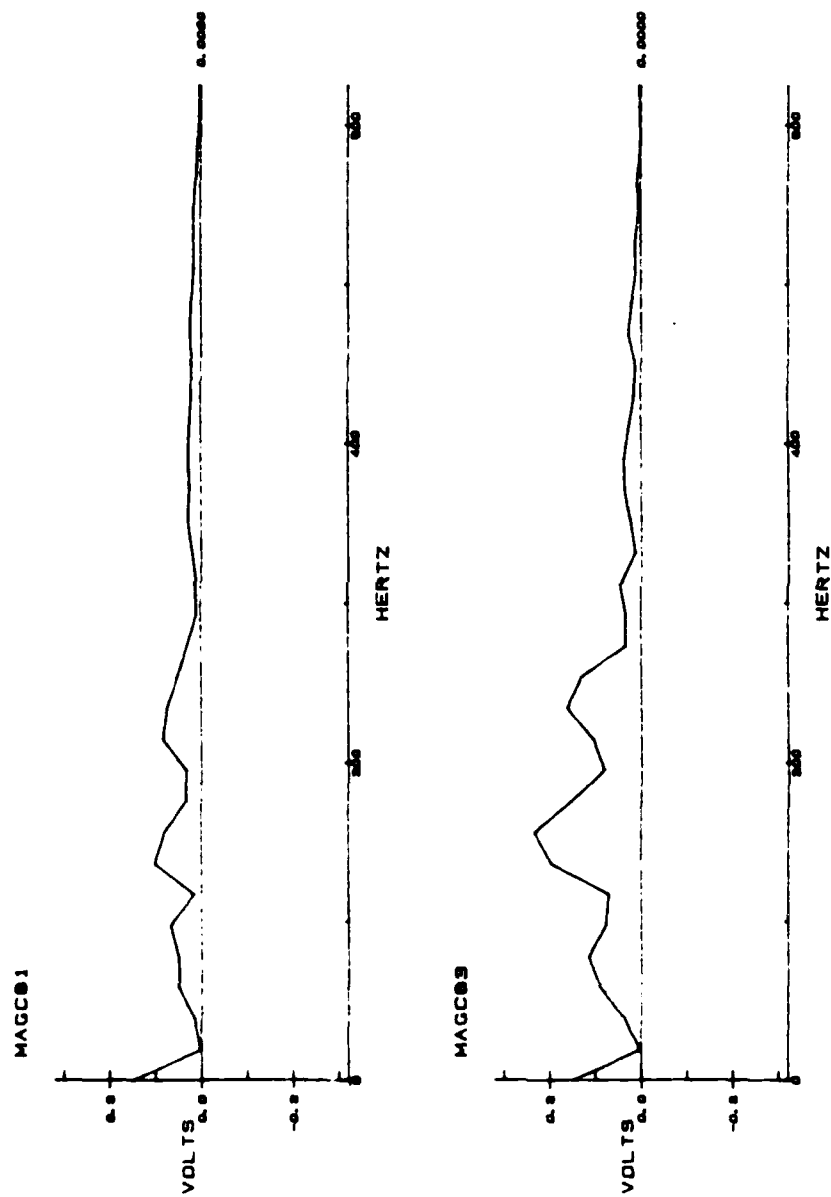


Fig. D.8 - Magnitude of Linear Spectrum of Waveform
of $V_{22.5}$ in Fig. C.8

REFERENCES

1. Abbiss, C. P. (1981), "Shear Wave Measurements of the Elasticity of the Ground," Geotechnique, Vol. 31, No. 1, pp. 91-104.
2. Acheson, C. H. (1963), "Time-Depth and Velocity-Depth Relations in Western Canada," Geophysics, Vol. 28, pp. 894-909.
3. Adams, L. H. and Williamson, E. D. (1923), "The Compressibility of Minerals and Rocks at High Pressure," Journal of Franklin Institute, 195, 475.
4. Afifi, S. E. A., and Richart, F. E., Jr. (1973), "Stress-History Effects on Shear Modulus of Soils," Soils and Foundations, International Society of Soil Mechanics and Foundation Engineering, Vol. 13, No. 1, pp. 77-95.
5. Air Force Weapons Laboratory (1977), "Cylindrical In Situ Test at Selected Nuclear and High-Explosive Test Sites," AFWL-TR-76-709, Kirtland Air Force Base, Albuquerque, NM.
6. Allen, J. C., and Stokoe, K. H., II (1982), "Development of Resonant Column Apparatus with Anisotropic Loading," Report GR82-28, Civil Engineering Department, University of Texas at Austin.
7. Anderson, D. G., and Stokoe, K. H., II (1978), "Shear Modulus: A Time Dependent Soil Property," Dynamic Geotechnical Testing, ASTM STP 654, American Society for Testing and Materials, pp. 66-90.
8. Ang, H. S. A, and Tang, W. H. (1975), Probability Concepts in Engineering Planning and Design, Vol. 1 - Basic Principles, John Wiley & Sons, Inc., New York, 409 pp.
9. Arango, I., Moriwaki, Y, and Brown, F. (1978), "In-Situ and Laboratory Shear Velocity and Modulus," Proceedings of the Earthquake Engineering and Soil Dynamics Conference, ASCE, Pasadena, CA, June 19-21, Vol. 1, p. 198-212.
10. Aremberg, D. L. (1948), "Ultrasonic Solid Delay Lines," Journal of Acoustical Society of America, Vol. 20, No. 1, pp. 1-26.
11. Auld, B. (1977), "Cross-Hole and Down-Hole Vs by Mechanical Impulse," Journal of the Geotechnical Engineering Division, ASCE, Vol. 103, GT12, pp. 1381-1398.
12. Bachman, R.T. (1983), "Elastic Anisotropy in Marine Sedimentary Rocks," Journal of Geophysical Research, Vol. 88, No. B1, pp. 539-545, January 10, 1983.
13. Backus, G. E. (1965), "Possible Forms of Seismic Anisotropy of the Uppermost Mantle under Oceans," Journal of Geophysical Research, Vol. 70, No. 14, July, pp. 3429-3439.

14. Ballard, R. F., Jr. (1976), "Method for Crosshole Seismic Testing," Journal of the Geotechnical Engineering Division, ASCE, Vol. 102, No. GT2, pp. 1261-1273.
15. Ballard, R. F., Jr., and McLean, F. G. (1975), "Seismic Field Methods for In Situ Moduli," Proceedings, Conference on In Situ Measurement of Soil Properties, ASCE, Vol. 1, pp. 121-150.
16. Ballard, R. F., Stokoe, K. H., II, and McLemore, R. (1983), "Proposed Standard Test Methods for Cross-Hole Seismic Testing," Geotechnical Testing Journal, GTJODJ, Vol 6, No. 4, December, pp. 210-219.
17. Banerjee, D. K., and Pao, Y. H. (1974), "Thermoelastic Waves in Anisotropic Solids," Journal of Acoustical Society of America, Vol. 56, No. 5, November, pp. 1444-1454.
18. Beiganousky, W. A., and Marcusson, W. F., III (1976), "Uniform Placement of Sand," Journal of the Geotechnical Engineering Division, ASCE, Vol. 102, No. GT3, March, pp. 229-233.
19. Bendat, J.S., and Piersol, A. G. (1980), Engineering Applications of Correlation and Spectral Analysis, John Wiley & Sons, New York, 302 pp.
20. Bendat, J.S., and Piersol, A. G., (1977), Random Data: Analysis and Measurement Procedures, John Wiley & Sons, 407 pp.
21. Berends, B. E. (1977), "Development of a Multiaxial Testing Cell for Cohesive Soils," M.S. Thesis, University of Colorado, Boulder, 1977.
22. Bianchini, G. F., and Saada, A. S. (1981), "Effect of Anisotropy on the Dynamic Response of Clay Soils," Proceedings, Tenth International Conference of Soil Mechanics and Foundation Engineering, Stockholm, Sweden, Vol. 3, pp. 189-192.
23. Biot, M. A. (1940), "The Influence of Initial Stress on Elastic Waves," Journal of Applied Physics, Vol. 2, August, pp. 522-530.
24. Biot, M. A. (1965), Mechanics of Incremental Deformations, John Wiley & Sons, Inc., New York.
25. Birch, F. (1960), "The Velocity of Compressional Waves in Rocks to 10 Kilobars," Journal of Geophysical Research, Vol. 65, 1083 pp.
26. Bjerrum, L., and Andersen, K. H. (1972), "In-Situ Measurement of Lateral Pressure in Clay," Proceedings, 5th European Conference on Soil Mechanics and Foundation Engineering, Vol. 1, Madrid, Spain, pp. 11-20.
27. Brace, W. F. (1965), "Some New Measurements of Linear Compressibility of Rocks," Journal of Geophysical Research, Vol 70, 391 pp.
28. Brandt, H. (1955), "A Study of the Speed of Sound in Porous Granular Media," J. Appl. Mech., Trans. ASME, Vol. 22, No. 4, pp. 479-486.

29. Bratton, J. L., and Higgins, C. J. (1978), "Measuring Dynamic In Situ Geotechnical Properties," Proceedings, Conference on Earthquake Engineering and Soil Dynamics, ASCE, Vol. I, Pasadena, CA, pp. 272-289.
30. Brodov, L. Y., Evstifeyev, V. I., Karus, E. V., and Kulichikhina, T. N. (1984), "Some Results of the Experimental Study of Seismic Anisotropy of Sedimentary Rocks Using Different Types of Waves," Geophysical Journal of the Royal Astronomical Society, Vol. 76, No. 1, January, pp. 191-200.
31. Byun, B. S. (1984), "Seismic Parameters for Transversely Isotropic Media," Geophysics, Vol. 49, No. 11, pp. 1908-1914.
32. Cattaneo, C., (1938), "Sul contatto di due corpi elastici," Accademia dei Lincei, Rendiconti, Vol. 27, pp. 342-348, 434-436, and 474-478 (from Hardin, 1961).
33. Chen, W. F. (1976), Limit Analysis and Soil Plasticity, McGraw-Hill Book Co., New York.
34. Chu, H.Y.F., Lee, S.H.H., and Stokoe, K.H., II (1984), "Effects of Structural and Stress Anisotropy on Velocity of Low-Amplitude Compression Waves Propagating along Principal Stress Directions in Dry Sand," Report GR84-6, Civil Engineering Dept., Univ. of Texas at Austin.
35. Dahlen, F. A. (1972), "Elastic Velocity Anisotropy in the Presence of an Anisotropic Initial Stress," Bulletin of the Seismological Society of America, Vol. 62, No. 5, October, pp. 11183-11193.
36. Dahlen, F. A. (1972), "The Effect of an Initial Hypocentral Stress Upon the Radiation Patterns of P and S Waves," Bulletin of the Seismological Society of America, Vol. 62, No. 5, October, pp. 1173-1182.
37. Dally, J. W., and Riley, W. F. (1978), Experimental Stress Analysis, 2nd edition, McGraw-Hill Book Co., New York.
38. Davis, A. M., and Schultheiss, P. J. (1980), "Seismic Signal Processing in Engineering Site Investigation - A Case History," Ground Engineering, Vol. 13, No. 4, pp. 44-48.
39. Dix, C. H. (1955), "Seismic Velocities from Surface Measurements," Geophysics, Vol. 20, pp. 68-86.
40. Dobrin, M. B. (1960), Introduction to Geophysical Prospecting, McGraw-Hill Book Co., New York, 435 pp.
41. Dranetz, A. I., and Orlacchio, A. W. (1976), "Piezoelectric and Piezoresistive Pickups," Shock and Vibration Handbook, 2nd edition, McGraw-Hill Book Co., New York, pp. 16-26.
42. Draper, N. R., and Smith, H. (1966), Applied Regression Analysis, 2nd Edition, Wiley, John & Sons, Inc., New York. 407 pp.

43. Drnevich, V. P. (1974), "Constrained and Shear Moduli for Finite Elements," University of Kentucky, Soil Mechanics Series, Report No. 18, pp. 24.
44. Drnevich, V. P. (1975), "Constrained and Shear Moduli for Finite Elements," Journal of the Geotechnical Engineering Division, ASCE, Vol. 101, No. GT5, May 1975, pp. 459-473.
45. Drnevich, V. P., Hall, J. R., Jr., and Richart, F. E., Jr. (1967), "Effects of Amplitude of Vibration on the Shear Modulus of Sand," Proceedings, International Symposium on Wave Propagation and Dynamic Properties of Earth Materials, Albuquerque, NM, August.
46. Drnevich, V. P., and Richart, F. E., Jr. (1970), "Dynamic Prestraining of Dry Sand," Journal of the Soil Mechanics and Foundations Division, ASCE, Vol. 96, No. SM2, pp. 453-469.
47. Duffy, J., and Mindlin, R. D. (1957), "Stress-Strain Relations of a Granular Medium," Journal of Applied Mechanics, Transactions ASME, Dec., pp. 585-593.
48. Eshelby, J. D. (1957), "The Determination of the Elastic Field of and Ellipsoidal Inclusion, and Related Problems," Proceedings, Royal Society of London, Series A, 241, 376.
49. Ewing, W. M., Jardetzky, W. S., and Press, F. (1957), Elastic Waves in Layered Media, McGraw-Hill Book Co., Inc.
50. Faust, L. Y. (1953), "A Velocity Function Including Lithologic Variations," Geophysics, Vol. 18, pp. 271-287.
51. Feng, C. C., Shiau, D. L., Liu C. C., and Tsai, Y. B. (1976), "Geophysical Survey of Taipei Basin," Proceedings, National Science Council, Taipei, Taiwan.
52. Ferrar, W. L. (1941), Algebra, A Test-Book of Determinants, Matrices, and Algebraic Forms, Oxford University Press, Clarendon, United Kingdom.
53. French, A. P. (1971), Vibrations and Waves, W. W. Norton & Company, New York, 316 pp.
54. Fry, Z. B. (1963), "A Procedure for Determining Elastic Moduli of Soils by Field Vibratory Techniques," Miscellaneous Paper No. 4-577, U. S. Army Engineer Waterways Experiment Station, Corps of Engineers, P. O. Box 631, Vicksburg, MS 39180.
55. Fry, Z. B. (1965), "Dynamic Soils Investigations Project Buggy, Buckboard Mesa Nevada Test Site, Mercury, Nevada," WES, Misc. Paper No. 4-666, January.
56. Fumal, T. (1978), "Correlations Between Seismic Wave Velocities and Physical Properties of Geologic Materials in the Southern San Francisco Bay Region, California," U.S.G.S. Open-File Report 78-1067, 114 pp.

57. Gardner, G. H. F., Wyllie, M. R. J., and Droschak, D. M. (1964), "Effects of Pressure and Fluid Saturation on the Attenuation of Elastic Waves in Sands," Petrol. Tec., Vol. 16, pp. 189-198.
58. Gassmann, F. (1951), "Elastic Waves Through a Packing of Spheres," Geophysics, Vol. 16, pp. 673-685.
59. Graff, K. F. (1975), Vibrations and Waves in Physics, Cambridge University Press, Cambridge, London, pp. 208-213.
60. Gregory, A. R. (1967), "Mode Conversion Technique Employed in Shear Velocity Studies of Rock Samples Under Axial and Uniform Compression," Soc. Pet. Engr. Jour., 7, p. 136.
61. Gregory, A. R., and Podio, A. L. (1970), "Dual-Mode Ultrasonic Apparatus for Measuring Compressional and Shear Wave Velocities of Rock Samples," IEEE Transactions on Sonics and Ultrasonics, Vol. SU-17, No. 2, April, pp. 77-85.
62. Hamilton, E. L. (1971a), "Elastic Properties of Marine Sediments," Journal of Geophysical Research, Vol. 76, pp. 579-604.
63. Hamilton, E. L. (1971b), "Predictions of In-Situ Acoustic and Elastic Properties of Marine Sediments," Geophysics, Vol. 36, pp. 266-284.
64. Hamilton, E. L. (1976a), "Attenuation of Shear Waves in Marine Sediments," Journal of the Acoustical Society of America, Vol. 60, No. 2, pp. 334-338.
65. Hamilton, E. L. (1976b), "Shear Wave Velocity Versus Depth in Marine Sediments: A Review," Geophysics, Vol. 41, No. 5, pp. 985-996.
66. Hamilton, E. L. (1979a), "Sound Velocity Gradients in Marine Sediments," Journal of Acoustical Society of America, Vol. 65, pp. 909-922.
67. Hamilton, E. L. (1979b), " V_p/V_s and Poisson's Ratios in Marine Sediments and Rocks," Journal of Acoustical Society of America, 66(4), October, pp. 1093-1101.
68. Hamilton, W. W. (1839), Proceeding of Royal Irish Academic, 1, 267, p. 341.
69. Hardin, B. O. (1961), "Study of Elastic Wave Propagation and Damping in Granular Materials," Ph.D. Dissertation, University of Florida, August, 207 pp.
70. Hardin, B. O. (1962), Discussion on "Foundation Vibrations," Transactions, ASCE, Vol. 127, Part 1, pp. 906-908.
71. Hardin, B. O. (1978), "The Nature of Stress-Strain Behavior of Soils," Proceedings of the Earthquake Engineering and Soil Dynamics Conference, ASCE, Pasadena, CA, June 19-21, 1978, Vol. I, pp. 3-90.

72. Hardin, B. O. (1983), "Plane Strain Constitutive Equations for Soils," Journal of Geotechnical Engineering Division, ASCE, Vol. 109, No. 3, March, pp. 388-407.
73. Hardin, B. O., and Black, W. L. (1966), "Sand Stiffness Under Various Triaxial Stresses," Journal of the Soil Mechanics and Foundations Division, ASCE, Vol. 92, No. SM2, March, pp. 27-43.
74. Hardin, B. O., and Drnevich, V. P. (1972a), "Shear Modulus and Damping in Soils: Measurement and Parameter Effects," Journal of the Soil Mechanics and Foundations Division, ASCE, Vol. 98, No. SM6, June, pp. 603-642.
75. Hardin, B. O., and Drnevich, V. P. (1972b), "Shear Modulus and Damping in Soils: Design Equations and Curves," Journal of the Soil Mechanics and Foundations Division, ASCE Vol. 98, No. SM7, July, pp. 667-692.
76. Hardin, B. O., and Music, J. (1965), "Apparatus for Vibration During the Triaxial Test," Symposium on Instrumentation and Apparatus for Soils and Rocks, ASTM STP, No. 392.
77. Hardin, B. O., and Richart, F. E., Jr. (1963), "Elastic Wave Velocities in Granular Soils," Journal of the Soil Mechanics and Foundations Division, ASCE, Vol. 89, No. SM1, February, pp. 33-65.
78. Haupt, W. A. (1973), "Discussion of In Situ Shear Wave Velocity by Cross-Hole Method," Journal of the Soil Mechanics and Foundation Division, ASCE, Vol. 99, No. SM2, February, pp. 224-228.
79. Heisey, S. (1981), "Determination of In Situ Shear Wave Velocity from Spectral Analysis of Surface Waves," M. S. Thesis, Civil Engineering Department., University of Texas at Austin, 300 pp.
80. Helbig, K. (1979), Discussion on "The Reflection, Refraction, and Diffraction of Waves in Media with an Elliptical Velocity Dependence," Geophysics, Vol. 44, No. 5, pp. 987-990.
81. Helbig, K. (1983), "Elliptical Anisotropy - Its Significance and Meaning," Geophysics, Vol 48, pp. 825-832.
82. Helbig, K. (1985), Workshop on Shear Waves, Shales and Anisotropy, Special Report 1984 SEG Workshops, Dec. 6-7, following SEG's 54th Annual Int. Meeting and Exposition in Atlanta, Geophysics, Vol. 50, No. 7, pp. 1188-1190.
83. Hoar, R. J. (1982), "Field Measurement of Seismic Wave Velocity and Attenuation for Dynamic Analyses," Ph.D. Dissertation, University of Texas at Austin, 478 pp.
84. Hoar, R. J., and Stokoe, K. H., II (1978), "Generation and Measurement of Shear Waves in Situ, Dynamic Geotechnical Testing, ASTM STP 654, pp. 3-29.

85. Hoar, R. J., and Stokoe, K. H., II (1980a), "In Situ Shear Wave Velocity Measurements, Lynn Ary Park, Anchorage, Alaska," report submitted to the United States Geological Survey, Branch of Engineering Geology, Denver, CO, 114 pp.
86. Hoar, R. J., and Stokoe, K. H., II (1980b), "Investigation of Variables Affecting In Situ Seismic Wave Velocity Measurements," report submitted to the U. S. Army Engineer Waterways Experiment Station, Corps of Engineers, P. O. Box 631, Vicksburg, MS, 39180, 63 pp.
87. Hoar, R. J., and Stokoe, K. H., II (1981), "Measurement and Analysis of Shear Waves in Crosshole Testing," Proceedings, Tenth International Conference on Soil Mechanics and Foundation Engineering, Stockholm, Sweden, June, Vol. 10, pp. 223-226.
88. Hughes, D. S., and Cross, J. H. (1951), "Elastic Wave Velocities in Rocks at High Pressures and Temperatures," Geophysics, Vol. 16, pp. 577-593.
89. Ingram, J. K. (1965), "The Development of a Free-Field Soil Stress Gage for Static and Dynamic Measurements," Instruments and Apparatus for Soil and Rock Mechanics, ASTM STP 392, American Society for Testing and Materials, pp. 20-36.
90. Ishimoto, J., and Iida, K. (1936), "Determination of Elastic Constants of Soil by Means of Vibration Methods, Part 1, Young's Modulus," Bulletin of Earthquake Research Institute, Tokyo Imperial University, Vol. 14.
91. Iwasaki, T., Tatsuoka, F., and Takagi, Y. (1978), "Shear Moduli of Sands Under Cyclic Torsional Shear Loading," Soils and Foundations, Japanese Society of Soil Mechanics and Foundation Engineering, Vol. 18, No. 1, pp. 39-56.
92. Januskevicius, C. K. and Vey, E. (1965), "Stresses and Strains in Triaxial Specimens," Instruments and Apparatus for Soil and Rock Mechanics, ASTM STP 392, American Society for Testing and Materials, pp. 37-54.
93. Jeffreys, H. (1926), "The Reflection and Refraction of Elastic Waves," Mon. Nat. Roy. At. Soc., Geophysics Supplement 1, pp. 321-334.
94. Jolly, R. N. (1956), "Investigation of Shear Waves," Geophysics, Vol. XXI, No. 4, pp. 905-938.
95. Jones, L. E. A. (1985), Workshop on Shear Waves, Shales and Anisotropy, special report 1984 SEG Workshop, Dec. 6-7, following SEG's 54th Annual Int. Meeting and Exposition in Atlanta, Geophysics, Vol. 50, No. 7, pp. 1188-1190.
96. Jose G. (1934), Theoretical Physics, English Translation, Glasgow: Blackie.

97. Kilbuszewski, J. J. (1948), "General Investigation of the Fundamental Factors Controlling Loose Packing of Sands," Proceedings, the Second International Conference on Soil Mechanics, Rotterdam, Vol. 7, pp. 47-49.
98. Kjellman, W. (1936), "Report on an Apparatus for Consummate Investigation of the Mechanical Properties of Soils," Proceedings of the 1st International Conference on Soil Mechanics and Foundation Engineering, Cambridge, Mass., Vol. 2, 1936, pp. 16-20.
99. Knox, D. P. (1982), "Effect of State of Stress on Velocity of Low-Amplitude Shear Waves Propagating Along Principal Stress Direction in Dry Sand," M.S. Thesis, University of Texas at Austin, 420 pp.
100. Knox, D. P., Stokoe, K. H., II, and Kopperman, S. E. (1982), "Effect of State of Stress on Velocity of Low-Amplitude Shear Waves Propagating Along Principal Stress Directions in Dry Sand," Report GR82-23, Civil Engineering Department, University of Texas at Austin, 420 pp.
101. Ko, H. Y. and Scott, R. F. (1967), "A New Soil Testing Apparatus," Geotechnique, Vol. 17, No. 1, pp. 40-57.
102. Kolsky, H. (1963), Stress Waves in Solids, Dover Publications, Inc., New York, 213 pp.
103. Kopperman, S. E., Stokoe, K. H., II, and Knox, D. P. (1982), "Effect of State of Stress on Velocity of Low-Amplitude Compression Waves Propagating Along Principal Stress Directions in Dry Sand," Report GR82-22, Civil Engineering Department, University of Texas at Austin, 267 pp.
104. Kovalev, O. I., and Molotova, L. V. (1960), "Borehole Percussion Device for the Excitation of Various Types of Elastic Waves," Bulletin of the Academy of Sciences of the USSR, Geophysics Series (Columbia Technical Translation), No. 7, pp. 639-646.
105. Kuribayashi, E., Iwasaki, T., and Tatsuoka, F. (1975), "Effects of Stress-Strain Conditions on Dynamic Properties of Sand," Proceedings of Japanese Society of Civil Engineers, No. 242, pp. 105-114.
106. Ladd, C. C. (1964), "Stress-Strain Modulus of Clay in Undrained Shear," Journal of the Soil Mechanics and Foundation Division, ASCE, SM5, September, pp. 103-131.
107. Lade, P. V., and Duncan, J. M. (1973), "Cubical Triaxial Tests on Cohesionless Soil," Journal of the Soil Mechanics and Foundations Division, ASCE, Vol. 99, SM10, pp. 793-812.
108. Lamb, H., (1945), Hydrodynamics, Dover Publications, New York, p. 380
109. Lash, C. C. (1985), "Shear Waves Produced by Explosive Sources," Geophysics, Vol. 50, No. 9, September, pp. 1399-1409.

110. Lawrence, F. V. (1963), "The Response of Soils to Dynamic Loadings," Report 14: Propagation Velocity of Ultrasonic Waves Through Sand, Massachusetts Institute of Technology, Department of Civil Engineering, Research Report R63-8, March, 54 pp.
111. Lawrence, F. V. (1965), "Ultrasonic Shear Wave Velocities in Sand and Clay," Massachusetts Institute of Technology, Department of Civil Engineering, Research Report R65-05, January, 24 pp.
112. Lee, S. H. H., and Stokoe, K. H., II (1986), "Effects of Structural and Stress Anisotropy on Velocity of Low-Amplitude Oblique Compression Wave in Dry Sand," GR86-16, Civil Engineering Department, University of Texas at Austin (In Preparation).
113. Levin, F. K. (1978), "The Reflection, Refraction, and Diffraction of Waves in Media with an Elliptical Velocity Dependence," Geophysics, Vol. 43, pp. 528-537.
114. Lew, M., and Campbell, K. W. (1985), "Relationships Between Shear Wave Velocity and Depth of Overburden", Proceedings, Measurement and Use of Shear Wave Velocity, Geotechnical Engineering Division, ASCE, Denver, Colorado, pp. 64-76.
115. Liaw, T. L., and Yeh, Y. H. (1983), "Crustal Structure of P-Wave Velocity in Northeastern Taiwan," Bulletin of the Institute of Earth Sciences, Academia Sinica, Vol. 3, pp. 55-70.
116. Love, A. E. H. (1927), A Treatise on the Mathematical Theory of Elasticity, Cambridge University Press, Cambridge, (reprinted by Dover Publication, Inc., 1944).
117. Ludeling, R. (1977), "Shear Wave Measurements Using the Seismic Up-Hole Method," Proceedings, Dynamical Methods in Soil and Rock Mechanics, Vol. 3, September, pp. 139-148.
118. Lysmer, J., (1966), private communication with F.E. Richart, Jr., dated Feb. 2. (From p. 91 of Richart, F.E., Jr., Hall, J.R., Jr., and Woods, R.D. (1970), Vibrations of Soils and Foundations, Prentice-Hall)
119. Ma, I. G. (1978), Vibrations and Waves in Physics, Cambridge University Press, Cambridge, 336 pp.
120. Mandel, J. (1984), The Statistical Analysis of Experimental Data, Dover Publications, Inc., New York, 410 pp.
121. Massarsch, K. R., and Broms, B. B. (1976), "Lateral Earth Pressure at Rest in Soft Clay," Journal of Geotechnical Engineering Division, ASCE, GT10, October, pp. 1041-1047
122. Massarsch, K. R., et al (1975), "Measurement of Horizontal In Situ Stresses," 1975 ASCE Specialty Conference on In Situ Measurements of Soil Properties, Raleigh, N.C., Vol. 1, pp. 266-286

123. Matsukawa, E., and Hunter, A. N. (1956), "The Variation of Sound Velocity with Stress in Sand," Proceedings of the Physical Society, Sect. B, Vol. 69, Part 8, No. 440.b, August, pp. 847-884.
124. Matsushima, S. (1960), "On the Deformation and Fracture of Granite Under High Confining Pressure," Bulletin of the Disaster Prevention Research Institute, Kyoto University, 36, 11.
125. Maxwell, A. A., and Fry, F. B. (1967), "A Procedure for Determining Elastic Moduli of In-Situ Soils by Dynamic Techniques," Proceedings, International Symposium on Wave Propagation and Dynamic Properties of Earth Materials, Albuquerque, NM, pp. 913-920.
126. McSkimin, H. J. (1961), "Notes and References for the Measurement of Elastic Moduli by Means of Ultrasonic Waves," Journal of Acoustical Society of America, Vol. 33, No. 5, pp. 606-627.
127. Meissner, R. (1961), "Wave-Front Diagrams from Up-Hole Shooting," Geophysical Prospecting, Vol. 9, No. 4, pp. 533-543.
128. Melia, P. J., and Carlson, R. L. (1984), "An Experimental Test of P-Wave Anisotropy in Stratified Media," Geophysics, Vol. 49, No. 4, pp. 374-378.
129. Menard, L. (1967), "Mesures in situ des proprietes physique des sols," Annales des Ponts et Chaussees (from Massarsh and Broms, 1976).
130. Miller, G. F., and Pursey, H. (1954), "The Field and Radiation Impedance of Mechanical Radiators on the Free Surface of a Semi-Infinite Isotropic Solid," Proceedings, Royal Society of London, Series A, Vol. 223, pp. 521-541.
131. Miller, G. F., and Pursey, H. (1955), "On the Partition of Energy Between Elastic Waves in a Semi-Infinite Solid," Proceedings, Royal Society of London, Series A, Mathematical and Physical Sciences, Vol. 233, pp. 55-69.
132. Mindlin, R. D. (1949), "Compliance of Elastic Bodies in Contact," Journal of Applied Mechanics, September, pp. 259-268.
133. Mindlin, R. D. (1954), "Mechanics of Granular Media," Proceedings, 2nd U. S. National Congress of Appl. Mech., ASME, September, pp. 327-344.
134. Mindlin, R. D., and Deresiewicz, H. (1953), "Elastic Spheres in Contact Under Varying Oblique Forces," Journal of Applied Mechanics, Trans ASME, September, pp. 327-344.
135. Mooney, H. M. (1954), "Seismic Shear Waves in Engineering," Journal of the Geotechnical Engineering Division, ASCE, Vol. 100, No. GT8, pp. 905-923.
136. Morse, R. W., "Acoustic Propagation in Granular Media," Journal of the Acoustical Society of America, Vol. 24, No. 6, pp. 696-700.

137. Murayama, S., and Shibata, T. (1960), "On the Dynamic Properties of Clay," Proceedings, the Second World Conference on Earthquake Engineering, Japan, Vol. 1, pp. 297-310.
138. Musgrave, M. J. P. (1970), Crystal Acoustics, Holden-Day, San Francisco, CA.
139. Nazarian, S., and Stokoe, K. H., II (1983), "Evaluation of Moduli and Thicknesses of Pavement Systems by Spectral Analysis of Surface Waves Method," Research Report 256-4, Center for Transportation Research, University of Texas at Austin, December, 122 pp.
140. Nur, A. (1971), "Effects of Stress on Velocity Anisotropy in Rocks with Cracks," Journal of Geophysical Research, Vol. 76, No. 8, pp. 2022-2034.
141. Nur A. and Simmons, G. (1969), "Stress-Induced Velocity Anisotropy in Rocks: An Experimental Study," Journal of Geophysical Research, Vol. 74, No. 27, pp. 6667-6674.
142. Nye, J. F. (1960), Physical Properties of Crystals, Oxford University Press, London.
143. Oda, M. (1972), "The Mechanism of Fabric Changes During Compressional Deformation of Sand," Soils and Foundations, International Society of Soil Mechanics and Foundation Engineering, Vol. 12, No. 2, pp.1-18.
144. Ogura, K. (1979), "Development of a Suspension Type S-Wave Log System," OYO Technical Note TN-34, OYO Corporation, Tokyo, Japan, 23 pp.
145. Ohta, Y., and Goto, N. (1978), "Empirical Shear Wave Velocity Equations in Terms of Characteristic Soil Indexes," Earthquake Engineering and Structural Dynamics, John Wiley & Sons, Vol. 6, No. 1, pp. 167-187.
146. Olson, H. F. (1967), Music, Physics and Engineering, Dover Publications, Inc., New York, 460 pp.
147. Parkin, A. K., Gerrard, C. M., and Willoughby, D. R. (1968), Discussion on "Deformation of Sand in Shear," Journal of Soil Mechanics and Foundations Division, ASCE, Vol. 94, SM1, pp. 336-340.
148. Paterson, N. R. (1956), "Seismic Wave Propagation in Porous Granular Media," Geophysics, Vol. 21, pp. 691-714.
149. Podio-Lucioni, A. (1968), "Experimental Determination of the Dynamic Elastic Properties of Anisotropic Rocks, Ultrasonic Pulse Method," Ph.D. Thesis, University of Texas at Austin.
150. Rayleigh, J. W. S. (1945), The Theory of Sound, Vol. 1, Dover Publications, New York, pp. 475-480.
151. Richart, F. E., Jr. (1962), "Foundation Vibrations," Transactions, ASCE, Vol. 127, Part 1, pp. 863-898.

152. Richart, F. E., Jr. (1975), "Some Effects of Dynamic Soil Properties on Soil-Structure Interaction," Journal Geotechnical Engineering Division, ASCE, Vol. 101, No. GT12, December, Proc. Paper 11764, pp. 1193-1240.
153. Richart, F. E., Jr., Hall, J. R., Jr., and Woods, R. D. (1970), Vibrations of Soils and Foundations, Prentice-Hall, 414 pp.
154. Rix, G. J. (1984), "Correlation of Elastic Moduli and Cone Penetration Resistance," M.S. Thesis, University of Texas at Austin, 110 pp.
155. Robertson, P. K., Campanella, R. G., Gillespie, D., and Rice, A. (1985), "Seismic CPT to Measure In-Situ Shear Wave Velocity," Proceedings, Measurement and Use of Shear Wave Velocity for Evaluating Dynamic Soil Properties, Geotechnical Engineering Division, ASCE, Denver, Colorado, May.
156. Roesler, S. K. (1979), "Anisotropic Shear Modulus Due to Stress Anisotropy," Journal of the Geotechnical Engineering Division, ASCE, Vol. 105, No. GT5, July, pp. 871-880.
157. Roscoe, K. H. (1953), "An Apparatus for the Application of Simple Shear to Soil Samples," Proceedings, Third International Conference on Soil Mechanics and Foundation Engineering, Zurich, Vol. 1, pp. 186-191.
158. Saada, A. S., Bianchini, G. F., and Shook, L. P. (1978), "The Dynamic Response of Anisotropic Clay", Proceedings of the Earthquake Engineering and Soil Dynamics Conference, ASCE, Pasadena, CA, June 19-21, Vol. 2, pp. 777-801.
159. Schmertmann, J. H. (1978), Effect of Shear Stress on Dynamic Bulk Modulus of Sand, U. S. Army Engineering Waterways Experiment Station, Technical Report S-78-16, October, 92 pp.
160. Seed, H. B., and Lee, K. L. (1966), "Liquefaction of Saturated Sands during Cyclic Loading," Journal of Soil Mechanics and Foundation Division, ASCE, Vol. 92, No. SM6, November, pp. 105-134.
161. Shannon, W. L., Yamane, G., and Dietrich, R. J. (1959), "Dynamic Triaxial Tests on Sand," Proceedings, First Panamerican Conference on Soil Mechanics and Foundation Engineering, Mexico City, Vol. 1, pp. 473-486.
162. Slotnick, M. M. (1950), "A Graphical Method for the Interpretation of Refraction Profile Data," Geophysics, Vol. 15, pp. 163-180.
163. Smoots, V. A., and Stickel, J. F. (1962), Discussion on "Foundation Vibrations," Transactions, ASCE, Vol. 127, Part 1, pp. 906-908.
164. Stewart, J. P., and Kulhawy, F. H. (1981), "Experimental Investigation of the Uplift Capacity of Drilled Shaft Foundations in Cohesionless Soil," Contract Report B-49(6), to Niagara Mohawk Power Corporation by Cornell University, May, 397 pp.

165. Stokes, G. G. (1883), Mathematical and Physical Papers, Vol. 2, p. 329, Cambridge University Press.
166. Stokoe, K. H., II (1977), "Field Measurement of Shear Wave Velocity by Crosshole and Downhole Seismic Methods," Proceedings, Dynamical Methods in Soil and Rock Mechanics, Vol. 3, pp. 115-137.
167. Stokoe, K. H., II (1980), "Field Measurement of Dynamic Soil Properties," Speciality Conference on Civil Engineering and Nuclear Power, ASCE, Sept. 15-17, Knoxville, TN, 31 pp.
168. Stokoe, K. H., II, and Arnold, E. J.; Hoar, R. J.; Shirley, D. J.; and Anderson, D. G. (1978), "Development of a Bottom-Hole Device for Offshore Shear Wave Velocity Measurement," Proceedings, Tenth Annual Offshore Technology Conference, Paper No. OTC 3210, pp. 1367-1380.
169. Stokoe, K. H., II, and Hoar, R. J. (1978a), "Field Measurement of Shear Wave Velocity by Crosshole and Downhole Seismic Methods," Proceedings, Conference on Dynamical Methods in Soil and Rock Mechanics, Karlsruhe, Germany, Vol. III, pp. 115-137.
170. Stokoe, K. H., II, and Hoar, R. J. (1978b), "Variables Affecting In Situ Seismic Measurements," Proceedings, Conference on Earthquake Engineering and Soil Dynamics, ASCE, Pasadena, CA, Vol. II, pp. 919-939.
171. Stokoe, K. H., II, and Lodde, P. F. (1978), "Dynamic Response of San Francisco Bay Mud," Proceedings, Conference on Earthquake Engineering and Soil Dynamics, ASCE, Pasadena, CA, Vol. II, pp. 940-959.
172. Stokoe, K. H., II, and Woods, R. D. (1972), "In Situ Shear Wave Velocity by Cross-Hole Method," Journal of the Soil Mechanics and Foundations Division, ASCE, Vol. 98, No. SM5, pp. 443-460.
173. Stokoe, K. H., II, Anderson, D. G., Hoar, R. J., and Isenhower, W. M. (1978), Discussion on "In-Situ and Laboratory Shear Velocity and Modulus," Proceedings of the Earthquake Engineering and Soil Dynamics Conference, ASCE, Pasadena, CA, June 19-21, Vol. 3, pp. 1498-1502.
174. Stokoe, K. H., II, Lee, S. H. H., and Chu, H. Y. F. (1985a), "Effect of Stress State on Velocities of Low-Amplitude Compression and Shear Waves in Dry Sand," Proceedings, the Second Symposium on the Interaction of Non-nuclear Munition with Structures, Panama City Beach, Florida, April, pp. 358-363.
175. Stokoe, K. H., II, Lee, S. H. H., and Knox, D. P. (1985b), "Shear Moduli Measurement Under True Triaxial Stresses," Proceedings Advances in the Art of Testing Soils Under Cyclic Conditions, Geotechnical Engineering Division, ASCE, Deroit, Michigan, pp. 166-185.
176. Stokoe, K. H., II, and Ni, S. H. (1985), "Effects of Stress State and Strain Amplitude on Shear Modulus of Dry Sand," Proceedings, Second Symposium on the Interaction of Non-Nuclear Munitions with Structures, Panama City Beach, Florida, April, pp. 407-412.

177. Stokoe, K. H., II, Roesset, J. M., Knox, D. P., Kopperman, S. E., and Suddhiprakarn C. (1980), "Development of a Large-Scale Triaxial Testing Device for Wave Propagation Studies," Report GR80-10, Civil Engineering Department, University of Texas at Austin, 182 pp.
178. Suddhiprakarn, C., and Roesset, J. M. (1984), "Wave Propagation in Heterogeneous Media," Report GR84-6, Civil Engineering Department, University of Texas at Austin, 182 pp.
179. Suddhiprakarn, C., Roesset, J. M., and Stokoe, K. H., II, (1983), "Effects of Rigid Inclusions on Wave Propagation," Report GR83-3, Civil Engineering Department, University of Texas at Austin, 175 pp.
180. Sykora, D. W., and Stokoe, K. H., II (1983), "Correlations of In Situ Measurements in Sands of Shear Wave Velocity, Soil Characteristics, and Site Conditions," Report GR83-33, Civil Engineering Department, University of Texas at Austin, 484 pp.
181. Tatsuoka, F., Iwasaki, T., Fukushima, S., and Sudo, H. (1979), "Stress Conditions and Stress Histories Affecting Shear Modulus and Damping of Sand Under Cyclic Loading," Soils and Foundations, Japanese Society of Soil Mechanics and Foundation Engineering, Vol. 19, No. 2, pp. 29-43.
182. Tatsuoka, F., Iwasaki, T., Yoshida, S., Fukushima, K., and Sudo, H. (1979), "Shear Modulus and Damping by Drained Tests on Clean Sand Specimens Reconstituted by Various Methods," Soils and Foundations, International Society of Soil Mechanics and Foundation Engineering, Vol. 19, No. 1, March, pp. 39-54.
183. Taylor, P. W., and Huges, J. M. O. (1965), "Dynamic Properties of Foundation Subsoils as Determined from Laboratory Tests," Proceedings, the Third World Conference on Earthquake Engineering, New Zealand, Vol. 1, pp. 196-209.
184. Thiers, G. R., and Seed, H. B. (1969), "Strength and Stress-Strain Characteristics of Clays Subjected to Seismic Loading Conditions," Vibration Effects of Earthquakes on Soils and Foundations, STP 450, American Society for Testing and Materials, pp. 3-56.
185. Thornhill, J., and Smith, C. C. (1980), Fourier and Spectral Analysis, Course Notes, University of Texas at Austin.
186. Timoshenko, S. P., and Goodier, J. N. (1951), Theory of Elasticity, McGraw-Hill Book Co., New York, 506 pp.
187. Tocher, D. (1957), "Anisotropy in Rocks Under Simple Compressions," Trans. Am. Geophys. Union, 38(1), 89.
188. Toki (1969), "Consideration of Homogeneous Layers from a Mechanical Point of View," Chidanken Technical Report No. 17, in Japanese.
189. Troncoso, J. H. (1975), "In Situ Impulse Test for Determination of Soil Shear Modulus as a Function of Strain," Ph.D. Thesis, University of Illinois, 322 pp.

190. Uchida, K., Sawada, and Hasegawa, T. (1980), "Dynamic Properties of Sand Subjected to Initial Shear Stress," Proceedings, International Symposium on Soils Under Cyclic Transient Loading, Swansea, pp. 121-133.
191. Van Steveninck, J. (1967), "Apparatus for Simultaneous Determination of Longitudinal and Shear Wave Velocities Under Pressure," Journal of Scientical Instrument, Vol. 44, pp. 379-81.
192. White, J. E. (1965), Seismic Waves: Radiation, Transmission, and Attenuation, McGraw-Hill Book Company, 302 pp.
193. Wilson, S. D. and Miller, R. P. (1962), Discussion of "Foundation Vibrations," Transactions, ASCE, Vol. 127, Part I, pp. 913-917.
194. White, J. E., Nicoletis, L. M., and Monash, C. (1983), "Measured Anisotropy in Pierre Shale," Geophysics, Geophysical Prospecting 31, pp. 709-725.
195. Wilson, S. D., Brown, F. R., Jr., and Schwarz, S. D. (1978), "In Situ Determination of Dynamic Soil Properties," Dynamic Geotechnical Testing, ASTM STP 654, American Society for Testing and Materials, pp. 295-317.
196. Woods, R. D. (1978), "Measurement of Dynamic Soil Properties," Proceedings of the Earthquake Engineering and Soil Dynamics Conference, ASCE, Pasadena, CA, June 19-21, 1978, Vol. I, pp. 91-178.
197. Wooster, W. A. (1938), A Textbook on Crystal Physics, Cambridge University Press, Cambridge.
198. Wroth, C. P., and Hughes, J. M. O. (1972), "An Instrument for the In Situ Measurement of the Properties of Soft Clays," CUED/C-SOILSTR 13, Department of Engineering, University of Cambridge, Cambridge, England.
199. Wyllie, M. R. J., Gregory, A. R., and Gardner, L. W. (1956), "Elastic Wave Velocities in Heterogeneous and Porous Media," Geophysics, Vol. 21, No. 1, pp. 41-69.
200. Yanagisawa, E. and Yan, R. S. (1977), "On Variation of Shear Modulus of Sand During Shearing," Proceedings, the 12th Annual Meeting, Japanese Society of SMFE, pp. 421-424, (in Japanese).
201. Yoshimi, Y., and Oh-oka, H. (1973), "A Ring Torsion Apparatus for Simple Shear Tests," Proceedings, Eighth International Conference on Soil Mechanics and Foundation Engineering, Vol. 1, Part 2, Moscow, pp. 501-506.
202. Yu, P., and Richart, F. E., Jr. (1984), "Stress Ratio Effects on Shear Modulus of Dry Sands," Journal of Geotechnical Engineering, ASCE, Vol. 110, No. 3, pp. 331-345.
203. Yu, S. B., and Tsai, Y. B. (1981), "Thickness and P-Wave Velocity of the Miocene to Oligo-Eocene Formations in Northeastern Taiwan," Bulletin of the Institute of Earth Sciences, Academia Sinica, Vol. 1, pp. 103-110.

END

5-87

DTIC